



Durham E-Theses

The Progressive Development and Post-failure Behaviour of Deep-seated Landslide Complexes

CAREY, JONATHAN,MARTIN

How to cite:

CAREY, JONATHAN,MARTIN (2011) *The Progressive Development and Post-failure Behaviour of Deep-seated Landslide Complexes*, Durham theses, Durham University. Available at Durham E-Theses Online: <http://etheses.dur.ac.uk/3186/>

Use policy

The full-text may be used and/or reproduced, and given to third parties in any format or medium, without prior permission or charge, for personal research or study, educational, or not-for-profit purposes provided that:

- a full bibliographic reference is made to the original source
- a [link](#) is made to the metadata record in Durham E-Theses
- the full-text is not changed in any way

The full-text must not be sold in any format or medium without the formal permission of the copyright holders.

Please consult the [full Durham E-Theses policy](#) for further details.

Academic Support Office, Durham University, University Office, Old Elvet, Durham DH1 3HP
e-mail: e-theses.admin@dur.ac.uk Tel: +44 0191 334 6107
<http://etheses.dur.ac.uk>

The Progressive Development and Post-failure Behaviour of Deep-seated Landslide Complexes

Jonathan Martin Carey

PhD thesis

This thesis is submitted in accordance with the regulations for the degree of Doctor of Philosophy in Durham University, Department of Geography, 2011

Declaration

I confirm that no part of the material offered has previously been submitted by me for a degree in this or in any other University. In all cases, where it is relevant, material from the work of others has been acknowledged.

The copyright of this thesis rests with the author. No quotation from the thesis should be published without the prior written consent of the author. All information derived from this thesis must be acknowledged appropriately.

A handwritten signature in blue ink, appearing to read 'Jm Chry', is positioned above the 'Signed:' label.

Signed:

Date: 09.09.2011

Abstract

The concept of progressive shear surface development remains to be fully understood. This study aims to investigate the mechanisms of progressive shear surface development to failure, and the subsequent post-failure behaviour, of deep-seated landslide complexes.

Field samples, collected from the Ventnor deep-seated landslide complex, Isle of Wight have been tested in a series of bespoke triaxial and back pressured shear box tests, in which field failure conditions are simulated by elevating pore water pressures under a constant deviator stress. These laboratory simulations have been calibrated with a detailed analysis of ground movement, groundwater and antecedent rainfall relationships from real-time site monitoring records from the site.

A model to explain the progressive failure of landslides in cohesive materials is proposed. The model demonstrates that pre-failure movement in landslides occurs during the progressive shear surface development through the development of micro-cracks within the slope. This process is active during periods when porewater pressures are sufficiently elevated in the slope. These micro-cracks eventually lengthen and coalesce as stresses concentrate at micro-crack tips, leading to the development of a singular shear surface which is observed as tertiary creep. The study confirms that the onset of 'Saito linearity' in $1/v - t$ space is associated with this tertiary creep phase. This mechanism can occur through time dependent creep at constant stresses from below the peak strength envelope. The results have been validated against real-world landslide monitoring data to provide a new understanding of the shear surface mechanisms operating within the Ventnor landslide.

The results contribute new knowledge regarding the mechanisms of shear surface development and provide an improved understanding of these mechanisms by developing one of the first high quality data sets that combines laboratory and field data. Finally, the study provides a new method to inform future landslide behaviour predictions for deep-seated slope failures.

Acknowledgements

This thesis has been made possible, in part, through the industrial sponsorship of the Halcrow Award Scheme. This award has provided financial support for my tuition fees and has allowed me to develop my keen interest in landslide research.

I am particularly grateful to my supervisor Professor David Petley for his guidance throughout my studies, including his intellectual stimulation and encouragement over such a long period. Dave has always been positive about my research and has provided prompt support from various remote locations around the world. I would also like to thank Professor Robert Allison who supported my studies in the early years and with whom I have had numerous invaluable discussions regarding the direction of my research.

I am very grateful to my line manager Professor Roger Moore, who has been influential in the development of this research opportunity and allowed me the flexibility to pursue my research whilst working full time at Halcrow. Special thanks also must go to Howard Siddle, Global Director of Ground Engineering at Halcrow, for supporting my award application and providing additional training time to maintain my studies.

I would like to acknowledge the support I have received from the Isle of Wight Council, Centre for the Coastal Environment. Dr Robin McInnes O.B.E and Peter Marsden have provided high level support and allowed me access to all of the Council's previous study data which has been invaluable. My appreciation is also given to James Houghton and Maddeline Clewett who have collected and provided monitoring data for the site during my studies.

I would like to thank all in the Geography Department Laboratory; particularly Alison Clarke, Chris Longley and Neil Tunstall, who have dedicated countless hours to my very demanding testing programmes. The quality of the data I have been able to present is a testament to the technical capability of these people and needs be acknowledged.

During my studies I have had the opportunity to work with a number of geotechnical specialists who have always expressed an interest in my research and provided invaluable advice, these include; Malcolm Turner, Mike Palmer, Colin Warren and Sarah Trinder. I also thank my colleagues Dr Andrew Mills, Dr Paul Fish and Dr Richard Johnson for valuable input and advice having all been through this process previously.

Finally I would like to especially thank my long suffering family for feeding me on numerous occasions, providing internet access at random hours of the night and putting up with my countless grumblings over the last few years. I would especially like to thank my sister Louise who has been cajoled into proof reading countless draft chapters.

Table of Contents

Title Page		i
Declaration		ii
Abstract		iii
Acknowledgements		iv
Table of Contents		vi
List of Tables		xii
List of Figures		xv
List of Plates		xxxi
List of Appendix Figures		xxxii
Chapter 1	Introduction	1
1.1	Global context of landslide geohazards	1
1.2	Landslide hazard management	7
1.3	Landsliding in the UK	8
1.4	Study aims, objectives and research questions	10
1.5	Study scope	11
1.6	Thesis structure	12
Chapter 2	Literature Review	15
2.1	Principles of landslide failure	15
	2.1.1 Mohr Coulomb failure criterion	16
2.2	Landslide definition and classification	18
2.3	Landslide triggers and failure mechanisms	23
	2.3.1 Landslide causes	23
	2.3.2 Slope weakening processes and creep mechanisms	24
	2.3.3 The role of porewater pressure	29
	2.3.4 Reactivation of pre-existing landslides	30
	2.3.5 Coastal landslide mechanisms in the UK	31
2.4	Material behaviour and their significance in landslide	33

	development	
2.5	Deformation properties of materials	39
2.6	Laboratory testing of rainfall induced landslides	42
2.7	Patterns of landslide movement	49
2.8	Conceptual models of progressive landslide development	55
	2.8.1 State and rate dependent friction model	60
	2.8.2 Progressive landslide model – micro-cracking and shear surface development	62
2.9	Calibrating the progressive failure models with landslide monitoring	65
2.10	Chapter summary	69
Chapter 3	Site Location	71
3.1	Introduction	71
3.2	Landslide investigation in the Undercliff	75
3.3	Climate (rainfall)	79
3.4	Structural geology	81
3.5	Quaternary geology and potential origin of the Undercliff landslides	84
3.6	Hydrogeology	86
3.7	Geological controls on landsliding	87
3.8	Geomorphology of the Ventnor landslide	88
3.9	Ventnor landslide stratigraphy	93
3.10	Site hydrogeology	96
3.11	Ventnor landslide ground model	101
3.12	Ventnor landslide evolution	108
	3.12.1 Previous evolutionary models	108
	3.12.1.1 Multiple rotational failures within Gault Clay	108
	3.12.1.2 Compound failure along clay layers	110
	3.12.1.3 Large singular catastrophic event	112
	3.12.2 Ventnor landslide Quaternary evolution	114
3.13	Chapter summary	116

Chapter 4	Methodology	119
4.1	Field site selection	119
4.2	Site investigation and sampling methodology	120
4.3	Analysis of landslide monitoring data	123
	4.3.1 Vertical and horizontal displacement - analysis of crackmeter and settlement cell data	126
	4.3.2 Shear surface depth - analysis of inclinometer data	128
	4.3.3 Analysis of groundwater data	130
	4.3.4 Analysis of rainfall data	130
4.4	Laboratory testing	131
	4.4.1 Physical properties testing	131
	4.4.2 Triaxial cell testing	133
	4.4.2.1 Triaxial cell apparatus	133
	4.4.2.2 Preparation of soil samples	135
	4.4.2.3 Stage 1 sample saturation	136
	4.4.2.4 Stage 2 sample consolidation	136
	4.4.2.5 Stage 3 (a) undrained compression (shear)	137
	4.4.2.6 Stage 3 (b) drained compression (shear)	137
	4.4.2.7 Stage 4 pore pressure reinflation	137
	4.4.3 Back pressure shear box testing	138
	4.4.3.1 Back pressure shear box apparatus	138
	4.4.3.2 Preparation of soil samples	140
	4.4.3.3 Stage 1 sample saturation	141
	4.4.3.4 Stage 2 sample consolidation	141
	4.4.3.5 Stage 3 sustained initial shear	142
	4.4.3.6 Stage 4 pore pressure reinflation	142
4.5.	Chapter summary	142
Chapter 5	Ventnor Landslide Monitoring Results	143
5.1	Introduction	143
5.2	Spatial and temporal patterns of ground movement	144
	5.2.1 Depth of ground movement	147

5.2.2	Differential GPS movement records	152
5.2.3	Movement patterns, Newport Road (Lowtherville Graben)	158
5.2.4	Movement patterns, Bath Road	164
5.2.5	Movement patterns, Winter Gardens	167
5.2.6	Implications of ground movement records on the landslide model	170
5.3	Groundwater and rainfall characteristics	173
5.4	Patterns of movement in relation to groundwater and rainfall characteristics	188
5.4.1	Ongoing slow creep mechanisms	189
5.4.2	Regular settlement and uplift cycles	192
5.4.3	Accelerated ground displacement at the Lowtherville Graben	195
5.5	Chapter summary	206
Chapter 6	Laboratory Results	209
6.1	Introduction	209
6.2	Physical properties	210
6.3	Geotechnical testing	215
6.3.1	Saturation stage	216
6.3.2	Consolidation stage	218
6.3.3	Material failure envelopes	221
6.4	Specialist Pore pressure reinflation (PPR) testing	229
6.4.1	Can PPR testing be used to construct a failure envelope and how does this compare to the standard undrained failure envelope in the triaxial cell?	230
6.4.1.1	Sustained initial shear stage	231
6.4.1.2	Pore pressure reinflation	231
6.4.2	How does the consolidation history of the shear surface materials affect the development of the shear surface to failure?	238
6.4.2.1	Sustained initial shear stage	239

6.4.2.2	Pore pressure reinflation	239
6.4.3	How does the rate of pore pressure reinflation affect the development of the shear surface to failure?	243
6.4.3.1	Sustained initial shear stage	244
6.4.3.2	Pore pressure reinflation	244
6.4.4	How does a material behaviour during different porewater pressure scenarios behave post-failure?	248
6.4.4.1	Sustained initial shear stage	249
6.4.4.2	Pore pressure reinflation	249
6.4.5	Variability of Gault Clay across sites	253
6.4.5.1	Sustained initial shear	253
6.4.5.2	Pore pressure reinflation	254
6.4.6	Is the nature of shear surface development different in the Gault Carstone interface material, and can this be compared to the Gault Clay?	258
6.4.6.1	Sustained initial shear	259
6.4.6.2	Pore pressure reinflation	261
6.5	PPR results in relation ICU and ICD PPR failure envelopes	267
6.6	Can failure be initiated from a constant p' long creep test?	271
6.7	Chapter summary	276

Chapter 7	Discussion	281
7.1	Introduction	281
7.2	Pre-failure displacement patterns in intact materials	282
7.3	Pre-failure behaviour in remoulded materials	293
7.4	Acceleration to failure in intact materials	295
7.5	Acceleration to failure in remoulded materials	301
7.6	Relationship between movement patterns and failure envelopes	304
7.7	Failure behaviour at constant stress – The long creep test	311
7.8	Patterns of deformation	320
7.9	The relationship to previous progressive models of shear surface development	323

7.9.1	Progressive failure (Bjerrum, 1967)	324
7.9.2	Three phase creep (Varnes, 1983)	324
7.9.3	Slider block model (Helmsetter <i>et al.</i> , 2004)	325
7.9.4	Crack Propagation (Petley <i>et al.</i> , 2005a)	326
7.10	Implications for the Ventnor Undercliff landslide	327
7.11	A model of progressive failure in a landslide	335
7.12	Implications for understanding rainfall and groundwater induced landslides	341
Chapter 8	Conclusion	345
8.1	Key findings	345
8.1.1	Patterns of deformation to failure	345
8.1.2	Time dependent failure at constant stress	347
8.1.3	The progressive failure of landslides	347
8.2	Limitations	349
8.3	Recommendations for further research	351
	References	355
	Appendix A: Laboratory Testing Results	377

List of Tables

Chapter 1 Introduction

Table 1.1	Selected Large Landslide events in terms of fatalities between 1920 and 2005 (after Petley and Bulmer, 2005)	4
Table 1.2	Economic and social impact of landsliding for selected countries across the world. From books and reports edited by Brabb and Harrod (1989), (adapted from Brabb, 1981; additional data from Salvati <i>et al.</i> , 2010)	6

Chapter 2 Literature Review

Table 2.1	Mass movement classification (after EPOCH, 1993; Dikau and Brunsden, 1996)	19
Table 2.2	Geotechnical landslide classification system (after Sassa, 1989)	20
Table 2.3	Summary of causes of landslide failures (after <i>Moore et al.</i> , 2006)	23
Table 2.4	Summary of landslide mechanisms and around the UK coastline (after Hutchinson, 1984)	32
Table 2.6	Critical limits of velocities (after Salt, 1988)	38

Chapter 3 Site Location

Table 3.1	Summary of development and population growth in Ventnor (after Halcrow, 2006)	74
Table 3.2	Table 3.2 Summary climate data for the Isle of Wight based on monthly average readings taken from the Newport Weather Station (Elevation 15m) between 2003 and 2010 (http://www.isleofwightweather.co.uk/)	79
Table 3.3	Weather station records used to develop a long term, composite rainfall dataset for the Undercliff (1839 - present)	80
Table 3.4	Summary geological stratigraphy of Ventnor (after Palmer <i>et al.</i> , 2007)	94
Table 3.5	Piezometer installation details in central Ventnor (after Halcrow, 2006)	97

Chapter 4	Methodology	
Table 4.1	Samples collected during the 2005 Ventnor ground investigation	122
Table 4.2	Landslide monitoring frequency and duration	125
Table 4.3	Summary laboratory testing schedule	132
Table 4.4	Summary of physical properties tests	132
Table 4.5	Summary back pressured shear box system capabilities and technical specification	139
Chapter 5	Ventnor Landslide Monitoring Results	
Table 5.1	Summary of landslide monitoring instruments, Ventnor Town	144
Table 5.2	Summary of inclinometer data 2002 to 2008	151
Table 5.3	Differential GPS measurements of horizontal and vertical displacement from baseline survey (December 2003)	154
Table 5.4	Summary installation details for automated standpipe piezometers, Winter Gardens, Ventnor Town	175
Chapter 6	Laboratory Results	
Table 6.1	Physical properties of the Gault Clay and Gault-Carstone transition samples	211
Table 6.2	Isotropic consolidated undrained (ICU) tests	215
Table 6.3	Isotropic consolidated drained (ICD) pore pressure re-inflation (PPR) tests	215
Table 6.4	Direct shear cut plane shear box (CPSB) tests	216
Table 6.5	Back pressured shear box (BPSB) pore pressure re-inflation (PPR) tests	216
Table 6.6	Change in ICU and ICD sample dimensions during the saturation of Gault Clay samples	217
Table 6.7	Change in CPSB and BPSB sample dimensions during the saturation of Gault- Carstone interface samples	217
Table 6.8	Axial strain (5) at failure during ICU testing	222
Table 6.9	Comparison of residual strength values proposed for Gault Clay	226

Chapter 7 Discussion

Table 7.1 Summary of ground movement records Ventnor (after Moore *et al.*, 2007a) 328

List of Figures

Chapter 1	Introduction	
Figure 1.1	Global distribution of Avalanche/Landslide Disasters by Country: 1974-2003 (Université Catholique de Louvain – Brussels – Belgium, http://www.emdat.be/maps-disaster-types)	2
Figure 1.2	Global distribution of near fatal landslide events between January 2006 and December 2009 (after Petley <i>et al.</i> , 2010)	3
Figure 1.3	Distribution of landslides in the BGS National Landslide Database (Foster <i>et al.</i> , 2008; after GSL, 1986/97)	9
Chapter 2	Literature Review	
Figure 2.1	The balance of forces in landslide development	15
Figure 2.2	Mohr Coulomb stress conditions at failure, (after Craig, 1992)	17
Figure 2.3	Conceptual model for geotechnical classification (after Sassa, 1989)	22
Figure 2.4	Model showing relative time frame of landslide development and significance of slope ripening and landslide triggering factors, adapted from Julian and Anthony (1996)	27
Figure 2.5	Conceptual model of coastal landslide development	29
Figure 2.6	Ground movement creep preceding a landslide (after Terzaghi, 1950)	34
Figure 2.7	Idealised pattern of material deformation through time proposed by varnes (1983)	35
Figure 2.8	Diagram illustrating the method for calculating the reciprocal of velocity from landslide surface displacement to predict the time of failure (after Fukuzono, 1989)	37
Figure 2.9	Idealised deformation patterns (a) Ductile deformation (b) Brittle deformation	41
Figure 2.10	The field stress path concept (FSP) in comparison to undrained (CU) and drained (CD) stress paths (after Brand, 1981; Ng, 2007)	43
Figure 2.11	The yield strength concept (after Orense <i>et al.</i> , 2004)	44
Figure 2.12	Patterns of deformation observed in PPR testing and their relationship to landslide movement patterns	45

Figure 2.13	(a) $1/v - t$ space plot of sample tested at 1000 kPa (b) Interpretation of three phase creep behaviour (after Petley and Allison, 2006)	47
Figure 2.14	Schematic diagrams illustrating 3 stages of landslide movement in residual soils (after Ng and Petley, 2009)	48
Figure 2.15	Plot of axial strain rates against time showing rapid acceleration under constant stress conditions prior to final failure (after Ng and Petley, 2009)	49
Figure 2.16	The Selbourne Cutting experiment (a) Patterns of displacement measured (b) $1/v - t$ patterns to final failure (after Petley, 2004)	51
Figure 2.17	Displacement patterns observed within the Tessina landslide (a) displacement against time for four representative monitoring points (b) asymptotic trend of movement in $1/v - t$ space (after Petley <i>et al.</i> , 2005c)	52
Figure 2.18	(a) A multiple stick-slip movement plot (b) a horizontal velocity plot of multiple stick-slip movement (after Allison and Brunsden, 1990)	53
Figure 2.19	(a) A graded movement plot (b) a horizontal velocity plot of graded movement (after Allison and Brunsden, 1990)	54
Figure 2.20	(a) A surge movement plot (b) a horizontal velocity plot of surge movement (after Allison and Brunsden, 1990)	54
Figure 2.21	Principle of development of a continual sliding surface by progressive failure (after Bjerrum, 1967)	58
Figure 2.22	Schematic illustrating Iverson's slider block model (after Iverson, 2005)	61
Figure 2.23	New model for the progressive development of a shear surface (after Petley <i>et al.</i> , 2005b)	64
Figure 2.24	Relationship between the three phase creep model (Varnes, 1978) and the displacement patterns to failure of the New Tredegar landslide in 1930	66
Figure 2.25	Landslide movement New Tredegar (after Carey <i>et al.</i> , 2007)	68
Figure 2.26	Transition from asymptotic to linear behaviour in $1/v - t$ space (a) Vaiont landslide (after Petley and Petley 2006) (b) New Tredegar	68

Chapter 3	Site Location	
Figure 3.1	Location of the Ventnor Undercliff, Isle of Wight	71
Figure 3.2	The Ventnor landslide, Lowtherville Graben and key highway infrastructure	73
Figure 3.3	Previous sites of investigation along the Undercliff	77
Figure 3.4	Plan of the Ventnor Ground investigations undertaken by IWC	78
Figure 3.5	Maximum 4 month annual effective rainfall and nine year running mean between 1839 and 1999	81
Figure 3.6	Mean monthly rainfall recorded in Ventnor between 1839 and 2009 (after Moore <i>et al.</i> , 2010)	81
Figure 3.7	Geology of the Isle of Wight and its implications on landsliding (after Bird, 1997)	82
Figure 3.8	Structural geology of the Isle of Wight and its implications on landsliding (after Chandler, 1984)	83
Figure 3.9	Isle of Wight stratigraphy (after Hutchinson and Bromhead, 2002)	84
Figure 3.10	Evolution of the Solent (after Bird, 1997)	85
Figure 3.11	Offshore Undercliff geology to St Catherines Deep (after Chandler, 1984)	86
Figure 3.12	Geomorphological map of the Ventnor landslide complex (from Halcrow, 2006, after GSL 1991)	91
Figure 3.13	Groundwater tables affecting the Ventnor landslide complex	99
Figure 3.14	Inclinometer plots from central Ventnor; BH5 2002-2008; BH4I 2005-2008 (provided by the Isle of Wight Council)	102
Figure 3.15	Ventnor landslide ground model (after Moore <i>et al.</i> , 2007b)	105
Figure 3.16	Proposed landslide development model, Folkestone Warren (after Hutchinson, 1969)	110
Figure 3.17	Proposed landslide model for the Bindon landslide, Dorset (after Pitts and Brunsden, 1982)	112
Figure 3.18	Proposed landslide model, Turnagain Heights landslide (after Seed and Wilson, 1967)	113
Figure 3.19	Proposed evolution of the Ventnor Undercliff landslide (after Moore <i>et al.</i> , 2007b)	115

Chapter 4	Methodology	
Figure 4.1	Sample locations along the Undercliff	121
Figure 4.2	Site monitoring sites and instrument location plan, Ventnor Town	124
Figure 4.3	Schematic of long range crackmeters installed at Bath Road and Newport Road (after Dias, 2002)	126
Figure 4.4	Schematic vibrating wire settlement cells installed at Bath Road, Newport Road and Winter Gardens (after Dias, 2002)	127
Figure 4.5	Schematic of inclinometer methodology used to monitor landslide deformation (after Mickelson, 2003)	129
Figure 4.6	Example of inclinometer grooved guide casing (after Transportation Research Board, 2008)	129
Figure 4.7	Orientation of probe with the inclinometer casing (after Transport Research Board, 2008)	130
Figure 4.8	Schematic diagram of the triaxial cell system (after GDS Instruments, 2005)	134
Figure 4.9	Schematic diagram of the GDS back pressured shear box (Figure obtained from D. Petley and used with permission)	140
Chapter 5	Analysis of Landslide Monitoring Results	
Figure 5.1	Ventnor ground monitoring instruments	145
Figure 5.2	Locations of inclinometers within the Ventnor landslide complex	147
Figure 5.3	Inclinometer movement recorded at BH2 between 2002 and 2004 (after de Freitas, 2009)	148
Figure 5.4	Cross section of landslide ground movement within the Ventnor landslide complex	149
Figure 5.5	Potential travel error within borehole measurements at BH2 (a) Ventnor inclinometer record (after de Freitas, 2009) (b) bias shift error (c) bias shift correction (adapted from Mikkelsen, 2003)	150
Figure 5.6	Differential GPS from Ventnor Town (after de Freitas, 2009). The arrows indicate the measured direction of movement of that point	152
Figure 5.7	Comparison of the differential GPS survey data (2005-2008) and site geomorphological mapping undertaken by GSL, (1991)	156

Figure 5.8	The spatial distribution of damage in relation to site geomorphological mapping undertaken by GSL (1991)	157
Figure 5.9	Monitoring instruments installed at Newport Road (Lowtherville Graben) in relation to the site geomorphology mapped by GSL (1991)	159
Figure 5.10	Settlement records at SC03 and SC04, Newport Road between 1995 and 2004	160
Figure 5.11	Running mean settlement records at SC03 and SC04, Newport Road between 1995 and 2004	160
Figure 5.12	Correlation of settlement measurements at the Newport Road between 1995 and 2004	161
Figure 5.13	Displacement against time recorded at C01 and C02, Newport Road between 1995 and 2002	162
Figure 5.14	Correlation of horizontal displacement measured at C02 and C01 between 1995 and 2002	162
Figure 5.15	Correlation of horizontal displacement with vertical displacement measured between 1995 and 2002 (a) SC03 (b) SC04	163
Figure 5.16	Monitoring instruments installed at Bath Road in relation to the site geomorphology mapped by GSL (1991)	165
Figure 5.17	Settlement records from settlement cell SC06, Bath Road (1995-2004)	166
Figure 5.18	Running mean settlement measured at SC06, Bath Road (1995-2004)	166
Figure 5.19	Displacement against time recorded at C03, Bath Road	167
Figure 5.20	Monitoring instruments installed at Winter Gardens in relation to the site geomorphology mapped by GSL (1991)	168
Figure 5.21	Settlement records at SC11, Winter Gardens (1995-2004)	169
Figure 5.22	Running mean settlement records at SC11, Winter Gardens (1995-2004)	170
Figure 5.23	Spatial movements of the Ventnor landslide units	172
Figure 5.24	Piezometer and weather station locations, Ventnor Town	174
Figure 5.25	Groundwater levels measured in P01 and P02, Winter Gardens between 1995 and 2004	175

Figure 5.26	Ventnor landslide hydrogeological characteristics (a) Elevation of piezometers and water tables within the landslide system and calculated including water table readings from automated piezometers at the Winter Gardens (P01 and 02) (b) Manual readings between January and October 2002 (c) Manual piezometer readings between June and November 2005	177
Figure 5.27	Daily rainfall records and 60 day running mean rainfall from the Ventnor Park weather Station between 1995 and 2004	179
Figure 5.28	Comparison of running 60 day running mean rainfall and porewater pressures at P02 between 1995 and 2004	180
Figure 5.29	Comparison of 60 day running mean rainfall and porewater pressures at P02 between 12/08/2001 and 16/09/2001	180
Figure 5.30	Relationship between daily porewater pressure and daily rainfall during the pore pressure rise (P02) between August and December 2000	181
Figure 5.31	Comparison of 60 day running mean rainfall and porewater pressures at P01 between 1995 and 2004	182
Figure 5.32	Comparison of 60 day running mean rainfall and porewater pressures at P01 between 12/08/2001 and 16/09/2001	182
Figure 5.33	Relationship between daily porewater pressure and daily rainfall during the pore pressure rise (P01) between August and December 2000	183
Figure 5.34	Comparison of 60 day running mean porewater pressures at P02 and running average total monthly rainfall between 1995 and 2004	184
Figure 5.35	Comparison of 60 day running mean porewater pressures at P01 and running average total monthly rainfall between 1995 and 2004	184
Figure 5.36	Comparison of 60 day running mean porewater pressures at P02 and running average total monthly rainfall between 1995 and 2004	185
Figure 5.37	Comparison of 60 day running mean porewater pressures at P01 and running average total monthly rainfall between 1995 and 2004	185
Figure 5.38	Comparison of 4 month running mean rainfall and porewater pressures at P02 between March 2000 and July 2002	186

Figure 5.39	Comparison of 4 month running mean rainfall and porewater pressures at P01	186
Figure 5.40	The relationship between average monthly porewater pressures in P02 and 4 month running average total monthly rainfall between March 2000 and July 2002	187
Figure 5.41	The relationship between average monthly porewater pressures in P01 and 4 month running average total monthly rainfall between March 2000 and July 2002	187
Figure 5.42	Relationship between cumulative rainfall and horizontal displacement at C01 and C02 between 1995 and 2000	190
Figure 5.43	Relationship between cumulative rainfall and vertical displacement at SC04 between 1995 and 2000	190
Figure 5.44	Comparison of displacement records at C01 and C02 and 60 day running mean porewater pressures in P01 between 1995 and 2000	191
Figure 5.45	Comparison of running mean daily velocities at C01 and C02 and porewater pressures in P01 between 1995 and 2000	191
Figure 5.46	Comparison of settlement velocities at SC03, SC06 and SC11 between 1995 and 2004	193
Figure 5.47	Comparison of daily rainfall characteristics and settlement velocities at SC03 between 1995 and 2003	194
Figure 5.48	Comparison of daily rainfall characteristics and settlement velocities at SC06 between 1995 and 2003	194
Figure 5.49	Comparison of porewater pressure at P02 and settlement velocities at SC06 between 1995 and 2003	195
Figure 5.50	Comparison of porewater pressure at P02 and settlement velocities at SC011 between 1995 and 2003	195
Figure 5.51	Running mean of horizontal displacement rates recorded at C01 and C02 between 1995 and 2002	196
Figure 5.52	Running mean of vertical displacement rates recorded at SC04 between 1995 and 2002	196
Figure 5.53	Comparison of running mean velocity patterns from C01 and C02 during accelerated ground displacement	197

Figure 5.54	Relationship between running mean velocities measured at C01 and C02 during accelerated ground displacement	197
Figure 5.55	Accelerated ground displacement at C01 plotted in $1/v - t$ space	198
Figure 5.56	Accelerated ground displacement at C02 plotted in $1/v - t$ space	199
Figure 5.57	Accelerated ground displacement at SC04 plotted in $1/v - t$ space	199
Figure 5.58	Comparison of running mean horizontal velocities at C01 and C02 and running mean porewater pressures in P02	200
Figure 5.59	Comparison of running mean vertical velocities at SC04 and running mean porewater pressures in P02	201
Figure 5.60	Relationship between velocity measured at the Newport Road (C01 and C02) and porewater pressure (P01) between 23/06/2000 and 28/07/2001	202
Figure 5.61	Comparison of porewater pressures in P02 and total monthly displacement at C01 between 15/03/2000 and 28/07/2001	203
Figure 5.62	Relationship between porewater pressure in P02 and total displacement at C01	203
Figure 5.63	Relationship between velocity measured at the Newport Road (C01 and C02) and total monthly rainfall between 23/06/2000 and 28/07/2001	204
Figure 5.64	Comparison of the 4 month running average total monthly rainfall and total displacement at C01 between 15/03/2000 and 28/07/2001	205
Figure 5.65	Relationship between 4 month running average total monthly rainfall and total displacement at C01	205
Chapter 6	Laboratory Results	
Figure 6.1	Particle size distribution chart for Gault Clay samples collected from BH4, BH5 and BS and Gault- Carstone transition zone in BH5	213
Figure 6.2	Comparison of particle size distribution with previous laboratory testing during the previous ground investigations by the Isle of Wight Council (after Halcrow, 2006)	213
Figure 6.3	Material classification of Gault Clay and Gault/ Carstone transition samples using the plasticity chart (after BSI, 1981)	214

Figure 6.4	Comparison of Atterberg limits in relation to previous testing on the Gault Clay at Ventnor	214
Figure 6.5	Volumetric strain plotted on a log scale against time for ICD and ICU Gault Clay samples at effective stress 250, 350, 450 and 550 kPa	218
Figure 6.6	Log volumetric strain against time for remoulded ICD Gault Clay samples at effective stress of 350 kPa	219
Figure 6.7	Consolidation curve for Gault-Carstone transition zone samples at effective stress of 150, 200, 300, 600 and 900 kPa	220
Figure 6.8	Vertical strain against time for Gault Clay samples at effective stress of 150 and 250 kPa	212
Figure 6.9	Peak and residual strength envelope, undrained triaxial cell testing	223
Figure 6.10	Peak and residual strength envelope, undrained triaxial cell testing (including results from Carey, 2002)	224
Figure 6.11	Construction of the peak strength failure envelope for ICU tests using the Mohr Coulomb approach	225
Figure 6.12	Construction of the residual strength failure envelope for ICU tests using the Mohr Coulomb approach	225
Figure 6.13	Peak and residual shear stress against normal stress using all CPSB tests on the Gault/ Carstone transition zone material	228
Figure 6.14	Construction of the peak and residual strength envelope failure envelope, Gault/ Carstone transition material	228
Figure 6.15	ICD stress path testing programme	230
Figure 6.16	ICD PPR stress paths at constant deviator stress 400, 500 and 550 kPa from effective stresses 350, 450 and 550 kPa	230
Figure 6.17	Displacement rate against p' , at constant q of 400, 500 and 550 kPa, samples ICD4, ICD8 and ICD9	232
Figure 6.18	$1/v$ against p' at constant q of 400, 500 and 550 kPa, samples ICD4, ICD8 and ICD9	232
Figure 6.19	Regression analysis of displacement to failure in $1/v - p'$ at constant q of 400, 500 and 550 kPa, samples ICD4, ICD8 and ICD9	233
Figure 6.20	Displacement rate against time at constant q of 400, 500 and 550 kPa, samples ICD4, ICD8 and ICD9	234

Figure 6.21	1/v - t at constant q of 400, 500 and 550 kPa, samples ICD4, ICD8 and ICD9	234
Figure 6.22	Change in sample volume through time at constant q of 400, 500 and 550 kPa, samples ICD4, ICD8 and ICD9	235
Figure 6.23	Comparison of p' at failure of PPR testing and the ICU failure envelope inclusive of Carey 2002 tests	236
Figure 6.24	Comparison of p' at failure of PPR testing and the ICU failure envelope based on thesis results	237
Figure 6.25	Comparison of the ICD PPR and ICU peak failure envelope constructed from samples ICD4, ICD8 and ICD9 and PPR rate = 10 kPa/hr	238
Figure 6.26	ICDPPR stress paths at constant deviator stress 400 kPa from effective stresses 350, 450 and 550 kPa	238
Figure 6.27	Displacement rate against p', at constant q of 400 kPa, samples ICD1, ICD2, ICD3 and ICD4	240
Figure 6.28	1/ velocity against p' at constant q of 400kPa, samples ICD1, ICD2, ICD3 and ICD4	241
Figure 6.29	Regression analysis of displacement to failure in 1/v -p' at constant q of 400 kPa, samples ICD1, ICD2, ICD3 and ICD4	241
Figure 6.30	Displacement rate against time at constant q of 400 kPa, samples ICD1, ICD2, ICD3 and ICD4	242
Figure 6.31	1 /v - t at constant q of 400 kPa, samples ICD1, ICD2, ICD3 and ICD4	242
Figure 6.32	Change in sample volume through time at constant q of 400 kPa, samples ICD1, ICD2, ICD3 and ICD4	243
Figure 6.33	ICDPPR stress paths at PPR rates of 5, 10, 18 kPa/hr at constant q of 400 kPa from initial p' of 350kPa	243
Figure 6.34	Displacement rate against p', at constant q of 400 kPa, samples ICD21, ICD4, ICD6 and ICD7	245
Figure 6.35	1/ velocity against p' at constant q of 400kPa, samples ICD2, ICD4, ICD6 and ICD7	245
Figure 6.36	Regression analysis of displacement to failure in 1/v -p' at constant q of 400 kPa, samples ICD2, ICD4, ICD6 and ICD7	233

Figure 6.37	Displacement rate against time at constant q of 400 kPa, samples ICD2, ICD4, ICD6 and ICD7	247
Figure 6.38	$1/v - t$ at constant q of 400 kPa, samples ICD2, ICD4, ICD6 and ICD7	247
Figure 6.39	Change in sample volume through time at constant q of 400 kPa, samples ICD1, ICD2, ICD3 and ICD4	248
Figure 6.40	ICDPPR stress paths for remoulded samples at PPR rates of 5, 10, 18 kPa/hr at constant q of 400 kPa from initial p' of 350kPa	248
Figure 6.41	Displacement rate against p' , at constant q of 400 kPa, samples ICDR1, ICDR2 and ICDR3	250
Figure 6.42	$1/v$ against p' at constant q of 400kPa, samples ICDR1, ICDR2 and ICDR3	250
Figure 6.43	Regression analysis of displacement to failure in $1/v - p'$ at constant q of 400 kPa, samples ICDR1, ICDR2 and ICDR3	251
Figure 6.44	Displacement rate against time at constant q of 400 kPa, samples ICDR1, ICDR2 and ICDR3	251
Figure 6.45	$1/v - t$ at constant q of 400 kPa, samples ICDR1, ICDR2 and ICDR3	252
Figure 6.46	Change in sample volume through time at constant q of 400 kPa, samples ICDR1, ICDR2 and ICDR3	252
Figure 6.47	ICDPPR stress paths for Gault Clay samples taken from BH4, BH5 and BS at PPR rates of 5, 10, 18 kPa/hr at constant q of 400 kPa from initial p' of 350kPa	253
Figure 6.48	Displacement rate against p' , at constant q of 400 kPa, samples ICD4, ICD10 and ICD11	255
Figure 6.49	$1/v$ against p' at constant q of 400kPa, samples ICD4, ICD10 and ICD11	255
Figure 6.50	Regression analysis of displacement to failure in $1/v - p'$ at constant q of 400 kPa, samples ICD4, ICD10 and ICD11	256
Figure 6.51	Displacement rate against time at constant q of 400 kPa, samples ICD4, ICD10 and ICD11	257
Figure 6.52	$1/v - t$ at constant q of 400 kPa, samples ICD4, ICD10 and ICD11	257
Figure 6.53	Change in sample volume through time at constant q of 400 kPa, samples ICDR4, ICD10 and ICD11	258

Figure 6.54	BPSB stress path testing programme, Gault-Carstone transition	259
Figure 6.55	BPSB stress path testing programme, Gault Clay	259
Figure 6.56	Shear strain against horizontal displacement during initial shear stage, Gault Clay samples BPSB3 and BPSB4	260
Figure 6.57	Vertical strain against horizontal displacement during initial shear stage, Gault Clay samples BPSB3 and BPSB4	261
Figure 6.58	Displacement rate against p' at constant $q = 250$ kPa from initial $p' = 600$ kPa, samples BPSB1 and BPSB1R	262
Figure 6.59	$1/v - p'$ at constant $q = 250$ kPa from initial $p' = 600$ kPa, samples BPSB1 and BPSB1R	262
Figure 6.60	BPSB1 Final phase of linearity to failure in intact sample BPSB1	263
Figure 6.61	Displacement rate against time at constant $q = 250$ kPa from initial $p' = 600$ kPa, samples BPSB1 and BPSB1R	264
Figure 6.62	$1/v - t$ at constant $q = 250$ kPa from initial $p' = 600$ kPa, samples BPSB1 ad BPSB1R	264
Figure 6.63	Displacement rate against p' at constant $q = 150$ kPa from initial $p' = 250$ kPa, sample BPSB2	265
Figure 6.64	$1/v - p'$ at constant $q = 150$ kPa from intial $p' = 250$ kPa, sample BPSB2	265
Figure 6.65	Displacement rate against time at constant $q = 150$ kPa from initial $p' = 250$ kPa, sample BPSB2	266
Figure 6.66	$1/v - t$ at constant $q = 150$ kPa from initial $p' = 250$ kPa sample BPSB2	266
Figure 6.67	Displacement and displacement rate against time at constant $q = 250$ kPa from initial $p' = 750$ kPa, sample BPSB4	267
Figure 6.68	Relationship between $1/v - p'$ and ICU and ICDPPR failure envelopes, intact Gault Clays samples	268
Figure 6.69	Relationship between $1/v - p'$ and the peak and residual strength envelopes, intact Gault-Carstone interface material	269
Figure 6.70	Relationship between displacement rate against p' and the peak and residual failure envelopes, intact Gault-Carstone interface material	269
Figure 6.71	Relationship between $1/v - p'$ and the peak (ICU, ICD PPR) and ICU residual strength envelopes, intact Gault sample from $p' = 500$ kPa	270

Figure 6.72	1/v – p' plots for remoulded (ICD PPR) Gault samples	271
Figure 6.73	1/ v – p' plot for remoulded (BPSB) Gault-Carstone transition samples	271
Figure 6.74	Displacement and pore water pressure through time	272
Figure 6.75	Displacement rate to failure at constant back pressure and porewater pressure	273
Figure 6.76	Comparison of sample volume and displacement rate at constant p' to failure	273
Figure 6.77	Displacement rate against time during last 11 days of the long creep test	274
Figure 6.78	1/v –t during final 11 days of long creep test	275
Figure 6.79	Regression analysis of the linear trend in 1/v – t space	275
Chapter 7	Discussion	
Figure 7.1	Concept of progressive landslide development and post failure creep (adapted from Varnes, 1978; Petley and Allison, 2006)	281
Figure 7.2	Potential Primary creep New Tredegar Landslide (a) Displacement and displacement rate (b) 1/v-t space (after Carey <i>et al.</i> , 2007).	283
Figure 7.3	Initiation of displacement in intact Gault ICDPPR tests (a) Change in sample volume plotted against p' (b) Change in back volume plotted against p'	284
Figure 7.4	Initiation of displacement in intact Gault ICDPPR tests (a) Displacement rate – p' (b) 1/V - p'	285
Figure 7.5	Initial deformation of intact Gault Carstone transition BPSB test (a) Sample volume and displacement rate – p' (b) Change in back volume and displacement rate – p'	287
Figure 7.6	initial deformation of intact Gault Carstone transition BPSB test in 1/v –p' space	288
Figure 7.7	Secondary creep, New Tredegar (a) average displacement and displacement rate (b) 1/velocity against time	290
Figure 7.8	Deformation of intact Gault Carstone transition BPSB test (a) displacement rate and back volume against p' (b) displacement rate and sample volume against p'	291

Figure 7.9	Deformation of Gault- Carstone transition BPSB test in $1/v - p'$ space	292
Figure 7.10	Initial displacements in remoulded Gault ICDPPR tests (a) change in sample volume against p' (b) change in back volume against p'	293
Figure 7.11	Initiation of displacement in remoulded Gault ICDPPR tests (a) Displacement rate against p' (b) $1/v - p'$ space	294
Figure 7.12	Acceleration to failure, New Tredegar (a) displacement and velocity against time (b) $1/v - t$ space	296
Figure 7.13	Acceleration to failure in intact Gault ICDPPR tests (a change in sample volume against p' (b) change in back volume against p'	297
Figure 7.14	Acceleration to failure in Intact Gault ICDPPR tests (a) displacement rate against p' (b) $1/v - p'$ space	298
Figure 7.15	Acceleration to failure in Gault Carstone transition BPSB test (a) displacement rate and back volume against p' (b) displacement rate and sample volume against p'	300
Figure 7.16	Acceleration to failure in Gault Carstone transition BPSB test in $1/v - p'$ space	301
Figure 7.17	Acceleration to failure in remoulded Gault ICDPPR tests (a) change in back volume against p' (b) change in sample volume against p'	302
Figure 7.18	Acceleration to failure in remoulded Gault ICDPPR tests (a) displacement rate against p' (b) $1/v - p'$ space	303
Figure 7.19	Axial strain to failure of intact Gault ICD PPR tests at 400kPa (a) undertaken at different initial confining pressures (b) undertaken at different PPR rates	306
Figure 7.20	Displacement to failure of intact Gault ICD PPR tests at 400kPa in relation to the undrained failure envelopes (a) undertaken at different initial confining pressures (b) undertaken at different PPR rates	307
Figure 7.21	$1/v-p'$ and displacement rate against p' in relation to undrained failure envelopes, sample ICD2, PPR 10 kPa/hr, 400kPa	308
Figure 7.22	$1/v-p'$ and displacement rate against p' in relation to undrained failure envelopes, sample ICD9, PPR 10 kPa/hr, 550kPa	309

Figure 7.23	Deformation to failure in remoulded Gault PPR tests in relation to the undrained failure envelope, (a) axial strain against p' (b) displacement rate against p'	310
Figure 7.24	$1/v-p'$ and displacement rate against p' in relation to undrained failure envelopes, sample ICDR2, PPR 10 kPa/hr, 400kPa	311
Figure 7.25	The long creep test (a) Comparison of back pressure and mean effective stress in relation to the failure envelope (b) Comparison of porewater pressure and sample displacement throughout the full test (c) Comparison of sample displacement and back pressure to failure	313
Figure 7.26	Deformation to failure during the final stage of the long creep test (a) Comparison of displacement rate with sample porewater pressure and back pressure, (b) Comparison of change in sample volume and sample mean effective stress	314
Figure 7.27	Comparison of log displacement rate and back volume during final stage of long creep test	315
Figure 7.28	Displacement rate plotted on a log scale against time	316
Figure 7.29	$1/v - t$ plot for the long term creep test at constant mean effective stress	317
Figure 7.30	Comparison of displacement rates to failure through linear PPR and during the long creep test	318
Figure 7.31	Comparison of linear PPR and long creep test (a) $1/v - t$ (b) $1/v - t$ during final stages of failure	319
Figure 7.32	Progressive shear surface development patterns observed in PPR test	323
Figure 7.33	Comparison of settlement and extension behaviour at the Lowtherville Graben between 1995 and 2002	329
Figure 7.34	Comparison of ground movement behaviour and porewater pressure characteristics	330
Figure 7.35	Ground movement velocity measured at the Lowtherville graben (23/06/2000 – 28/07/2001)	331
Figure 7.36	Ground movement pattern at the Lowtherville graben in $1/v - t$ space (23/06/2000 – 28/07/2001)	332

Figure 7.37	Comparison between ground movement velocity and porewater pressure (23/06/2000 – 28/07/2001)	333
Figure 7.38	Relationship between ground movement rate and porewater pressure, Ventnor	334
Figure 7.39	A conceptual model for the progressive development of a first time landslide	336
Figure 7.40	Total monthly rainfall and ground acceleration relationship, Ventnor	342
Figure 7.41	Landslide events in relation to Maximum 4 month WER within the Undercliff (after Moore <i>et al.</i> , 2007a)	343

List of Plates

Chapter 6

Plate 6.1	Classic Brittle failure through shear surface development sample ICU1	222
-----------	--	-----

List of Appendix Figures

Appendix A

Figure A1	Consolidation curves for ICD and ICU Gault Clay samples at effective stress 250, 350, 450 and 550 kPa	377
Figure A2	Initial void ratio against maximum effective stress (p') for ICD and ICU Gault Clay samples at effective stresses 250, 350, 450 and 550 kPa	377
Figure A3	Void ratio against mean effective stress for ICD and ICU Gault Clay samples at effective stresses 250, 350, 450 and 550 kPa	378
Figure A4	Change in void ratio against mean effective stress for ICD and ICU samples at effective stresses 250, 350, 450 and 550 kPa	378
Figure A5	Final void ratio against mean effective stress for ICD and ICU samples at effective stresses 250, 350, 450 and 550 kPa	379
Figure A6	Consolidation curves for remoulded ICD Gault Clay samples at effective stress of 350 kPa	379
Figure A7	Initial void ratio against mean effective stress for remoulded ICD Gault Clay samples at effective stress of 350 kPa	380
Figure A8	Volumetric strain against mean effective stress for remoulded ICD Gault Clay samples at effective stress of 350 kPa	380
Figure A9	Final void ratio against mean effective stress for remoulded ICD Gault Clay samples at effective stress of 350 kPa	381
Figure A10	Change in void ratio against mean effective stress for remoulded ICD Gault Clay samples at effective stress of 350 kPa	381
Figure A11	Change in axial load and axial displacement through time for Gault–Carstone transition zone sample at effective stress of 150, 250, 300, 600 and 900 kPa	382
Figure A12	Axial load against axial displacement for Gault – Carstone transition zone samples at effective stress of 150, 250, 300, 600 and 900 kPa	382
Figure A13	Vertical strain against effective normal stress for Gault – Carstone transition samples at effective stress of 150, 250, 300, 600 and 900 kPa	383

Figure A14	Change in axial load and axial displacement through time for Gault Clay samples at effective stress of 150 and 250 kPa	383
Figure A15	Axial load against axial displacement for Gault Clay samples at effective stress of 150 and 250kPa	384
Figure A16	Classic brittle failures through shear surface development in ICU samples	384
Figure A17	Standard stress path for the undrained triaxial tests on the Gault Clay	385
Figure A18	Shear stress against horizontal displacement during CPSB testing on the Gault -Carstone transition samples at effective stresses 300, 600 and 900 kPa	385
Figure A19	Vertical strain against horizontal displacement during CPSB testing on the Gault -Carstone transition samples at effective stresses 300, 600 and 900 kPa	386
Figure A20	Stress paths during initial drained shear to 400 500 and 550 kPa, samples ICD4, ICD8 and ICD9	386
Figure A21	Stress strain relationship during initial drained shear to 400, 500 and 550 kPa, samples ICD4, ICD8 and ICD9	387
Figure A22	Sample volume change during initial drained shear to 400, 500 and 550 kPa, samples ICD4, ICD8 and ICD9	387
Figure A23	Stress paths during initial drained shear to 400 kPa, samples ICD1, ICD2 ICD3 and ICD4	388
Figure A24	Stress strain relationship during initial drained shear to 400 kPa, samples ICD1, ICD2 ICD3 and ICD4	388
Figure A25	Sample volume change during initial drained shear to 400 kPa, samples ICD1, ICD2 ICD3 and ICD4	389
Figure A26	Stress paths during initial drained shear to 400 kPa, samples ICD2, ICD4, ICD6 and ICD7	389
Figure A27	Stress strain relationship during initial drained shear to 400 kPa, samples ICD2, ICD4, ICD6 and ICD7	390
Figure A28	Sample volume change during initial drained shear to 400 kPa, samples ICD2, ICD4 ICD6 and ICD7	390

Figure A29	Stress paths during initial drained shear to 400 kPa, samples ICDR12, ICDR2 and ICDR3	391
Figure A30	Stress strain relationship during initial drained shear to 400 kPa, samples ICDR1, ICDR2 and ICDR3	391
Figure A31	Sample volume change during initial drained shear to 400 kPa, samples ICDR1, ICDR2 and ICDR3	392
Figure A32	Stress paths during initial drained shear to 400 kPa, samples ICD4, ICD10 and ICD11	392
Figure A33	Stress strain relationship during initial drained shear to 400 kPa, samples ICD4, ICD10 and ICD11	393
Figure A34	Sample volume change during initial drained shear to 400 kPa, samples ICD4, ICD11 and ICD10	393
Figure A35	Shear strain against horizontal displacement during initial shear stage, Gault-Carstone transition sample BPSB1, BPSB1R and BPSB2	394
Figure A36	Vertical strain against horizontal displacement during initial shear stage, Gault Carstone transition samples BPSB1, BPSB1R and BPSB2	394
Figure A37	Model of shear surface development (after Main, 2000)	395
Figure A38	The consolidation curve for the long term creep test	395
Figure A39	The long term creep test stress path through initial drained shear and PPR	396

Chapter 1: Introduction

1.1 Global context of landslide geohazards

Landslides constitute a key natural mechanism that modifies the earth's surface. The variability and complexity of landslides has led to the development of numerous definitions of the phenomena. Varnes (1978) describes them, from an engineering perspective, as the movement of slope forming materials including, rock, soil, artificial fill, or a combination of these. Alternatively, Brunsden (1985) provides a more detailed geomorphological definition, suggesting they are the outcome of a set of natural processes of landform development in which materials forming a slope modify their geometry by moving to a lower position of inclination and ultimately from an unstable to a stable state. Whilst definitions may vary between disciplines, it is clear that landslides are a mass movement process prevalent in the upland and coastal areas of most continents, including North, Central and South America, Europe, Africa and Asia. Their occurrence relates to diverse and complex processes capable of affecting the landscape of any environment with topographic relief. Although landslides are viewed largely as natural phenomenon (e.g. Bromhead and Ibsen, 2007; Chigira *et al.*, 2010), the increasing demands placed upon upland and coastal environments through population growth and economic development have increased human exposure to landslide hazards and, in many instances, anthropogenic intervention has either instigated or exacerbated their occurrence (e.g. Lacey, 1972; Brunsden, 1993; Ulusay and Aksoy, 1994). In particular, the adoption of poor planning practices, or a lack of appreciation of natural processes operating within uplands during development, have often resulted in such events (e.g. Petley *et al.*, 2010).

According to the EM_DAT database (Gokceoglu and Sezer, 2009) an estimated 8,658 people died between 1990 and 1991 as a direct consequence of landslide activity throughout the world. Of these deaths, approximately 90% occurred within the Circum Pacific Rim region (Aleotti and Chowdhury, 1999). The impacts of landslides are particularly focused on

less developed countries (Fig 1.1). The database of fatality-inducing landslide occurrence developed by the International Landslide Centre, University of Durham illustrates a similar concentration of events in less developed countries (Fig 1.2). Table 1.1 catalogues the largest fatalities associated with landslide events within the database. It is acknowledged, however, that the annual fatalities from landslides may be much higher than almost all previous authors have estimated (Petley *et al.*, 2010). Whilst this database suggested that the number of fatalities from landslide events through the period 1980 to 2000 was approximately 72,000 worldwide or about 3,400 per annum (Petley and Bulmer, 2005), this figure has been argued be a significant underestimate. This has largely been attributed to the under-reporting of small events (i.e. those with few fatalities) and those that occur in very remote locations (Petley *et al.*, 2010) The reliability of this dataset has been discussed in a number of publications (Petley *et al.*, 2007; Petley, 2008) and has been shown to provide a good overview of the hazards, though with quite large error bars (Downton and Pielke, 2005).

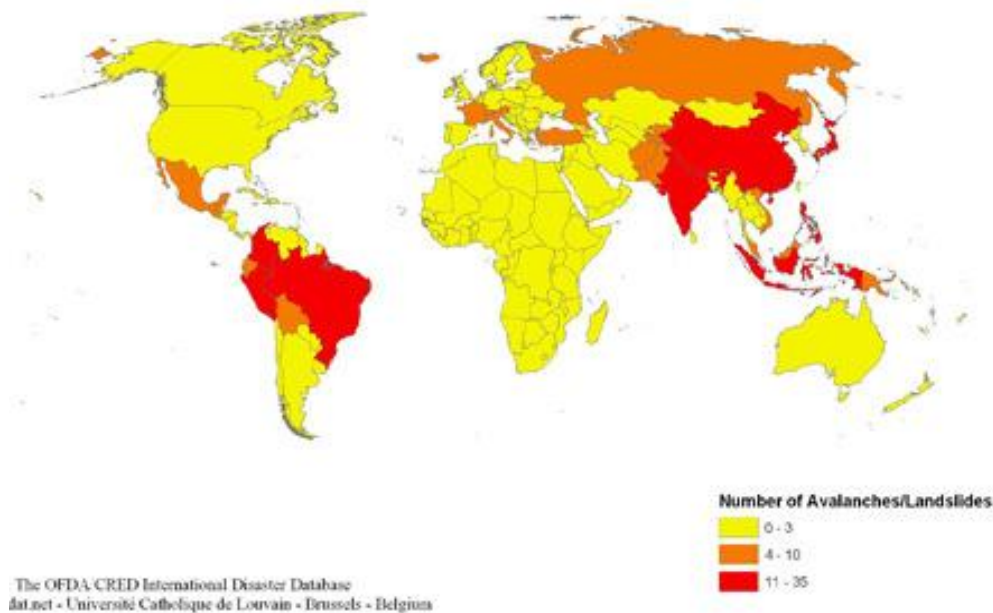


Figure 1.1 Global distribution of Avalanche/Landslide Disasters by Country: 1974-2003 (Université Catholique de Louvain – Brussels – Belgium, <http://www.emdat.be/maps-disaster-types>)

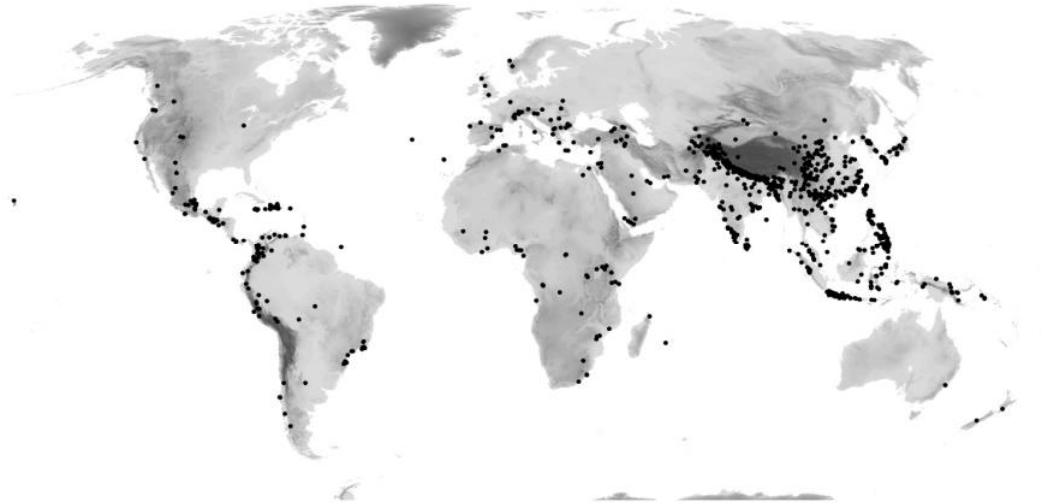


Figure 1.2 Global distribution of near fatal landslides events between January 2006 and December 2009 (after Petley et al., 2010)

In addition to loss of life landslides have an important impact on key infrastructures. These include transport links (roads, railways etc.) (e.g. Griffiths, *et al.*, 2004; Bromhead and Ibsen, 2007; Winter, *et al.*, 2007; Hearn and Massey, 2009); commercial and residential properties (e.g. Eisbacher and Clague, 1980; Mills *et al.*, 2007; Wong and Ko 2006); power generation and supplies such as oil and gas pipelines (e.g. Couperthwaite and Marshall, 1989; Lee *et al.*, 2009) and the disruption of key lifelines such as lakes, rivers and reservoirs (e.g. Dunning *et al.*, 2006).

Table 1.1 Selected Large Landslide events in terms of fatalities between 1920 and 2005 (after Petley and Bulmer, 2005)

Date	Country	Location	Estimated Fatalities	Trigger
26/12/1920	China P Republic	Kansu	200,000	Earthquake
15/12/1999	Venezuela	Vargas	30,000	Heavy rainfall
13/09/1985	Columbia	Nevado del Ruiz	23,000	Volcanic eruption
31/05/1970	Peru	Nevados Huascarán	18,000	Earthquake
30/10/1998	Nicaragua, Honduras, El Salvador, Guatemala		15,000	Hurricane Mitch
02/05/1905	Tajikistan	Khait	12,000	Earthquake
10/01/1962	Peru	Ranrahirca	4,500	Failure of hanging Glacier
20/09/1973	Honduras	Cholima	2,800	Heavy rainfall
30/10/1998	Nicaragua	Casita Volcano	1,680	Hurricane Mitch
24/05/2004	Haiti	Fonds-Verettes etc	1,800	Heavy rainfall
24/05/2004	Haiti	Gonaives	1,500	Hurricane Jeanne
09/10/1963	Italy	Vaiont Dam	1,189	Human
01/10/1968	India	Bihar, Bengal	1,000	Earthquake
05/03/1987	Ecuador	Revantador, Napa Province	1,000	2 earthquakes on rain saturated slopes
18/03/1971	Peru	Chungar, Lago Yanahuin, Pasco	600	Headward erosion
13/01/2001	El Salvador	Santa Tecla (Las Colinas)	518	Earthquake
08/07/1921	Kazakhstan	Zaili, Ala-Tau	500	Earthquake
23/03/1934	China P Republic	Canton	500	Heavy rainfall
18/09/1948	India	Assam	500	Heavy rainfall
25/04/1973	Peru	Andes	500	Heavy rainfall
18/09/1982	El Salvador	San Salvador Volcano	500	Heavy rainfall
08/08/2009	Taiwan	Shiaolin	500	Typhoon Morakot
07/08/2010	China P Republic	Zhouqu	1,117	Heavy rainfall

The impact of landslides can further lead to secondary hazards such as the damming of rivers and subsequent outburst floods (e.g. Costa and Schuster, 1987; Korup, 2005; Hancox *et al.*, 2005; Dunning *et al.*, 2005; Petley *et al.*, 2010) and the transfer of debris into river systems creating flood hazards and impacting water quality (McCahon *et al.*, 1987).

It is clear that the economic and social impact of landslide events is of global significance (Table 1.2). It has been estimated that in the United States alone, which may have as many as 20 million terrestrial landslide deposits, landslides are estimated to cause approximately \$3.5 billion dollars (2001 dollars) in damage, and kill between 25 and 50 people annually (Brabb, 1989, USGS, 2004). The casualties are primarily victims of rockfalls, rock slides and debris flows (Evans *et al.*, 2009).

Table 1.2 Economic and social impact of landsliding for selected Countries across the world. From books and reports edited by Brabb and Harrod (1989), (adapted from Brabb, 1991; additional data from Salvati et al., 2010).

Country	Description of social and economic impact
Canada	365 deaths caused by landslides in Canadian Cordillera since 1855. 100 rockslide fatalities in Quebec between 1836-1889. At least 1000 killed in sensitive clay slides
United States	Average annual cost of landsliding estimated to be \$1.5 billion with at least 25 fatalities
Costa Rica	\$12 million in damages and at least 3 landslide and fatalities in 1987
Panama	Estimated 700 sq km denuded by liquefaction and landsliding triggered by earthquakes in 1976
Andes	20,000 fatalities caused by Nevados Huascaran avalanche of 1970. At least \$1 billion losses and more than 25,000 fatalities Since 1940.
Ecuador	Fatalities have risen from 10 in 1955 to at least 1,290 in 1980's. Landslides in 1987 severed 33km of oil pipeline reducing government income by 35%.
Norway	Over 750 fatalities since 1345
Denmark	Cost of repairing and preventing landslides estimated to \$1-3 million annually
Poland	At least 1,000 landslides have damaged roads
Spain	Damages estimated at \$220 million per year. Total loss for next 30 years could exceed \$6 billion
Portugal	At least 31 landslide fatalities
Italy	Landslides between 843 and 2008 have resulted in 12,287 fatalities with some 4077 deaths and 177375 people evacuated between 1950 and 2008 (Salvati et al., 2010)
Former USSR	At least \$500 million worth of damage in Kasakhstan alone
Ghana	Estimated damage costs of between \$0.5 to \$1 million per annum
Nigeria	Millions of dollars annually in landslide damage to farmlands, villages and roads
Southern Africa	landslide damage costs to roads in 1987 was \$5-\$10 million; housing damage was \$2.5 million. Total cost of landsliding is estimated in the order of \$10 million
China	Annual losses exceed \$10.5 billion. Annual fatalities exceed 100. Over 100,000 killed when a landslide dam failed and impounded water rushed downstream and overran villages. Since 1310, at least 244,000 landslides fatalities
Australasia	Annual losses are in the tens of millions of dollars
Papua New Guinea	A landslide in 1988 killed at least 70 people
Indonesia	As many as 2000 fatalities each year. 5,110 fatalities in 1919 volcanic eruption and mudflows
Malaysia	246 fatalities after flow-slides from tin mine works between 1960 and 1980.
Hong Kong	250 fatalities resulting from landslides in 1972. 57 fatalities in 1976. Approximately 1,500 landslides occurred in 1982 causing 48 fatalities
Sri Lanka	149 fatalities in 1988
Thai Land	700 fatalities in 1988
Philippines	Several hundred people killed by landslides in gold mining areas
Japan	Estimated \$4 billion annual losses. At least 2,500 fatalities from 1967-1966

1.2 Landslide hazard management

Despite their devastating impact it could be argued that when compared to other natural hazards, such as volcanic activity, earthquakes and certain storm events, landslides are easier to manage and mitigate through engineering practices. This requires, however, that their location, spatial extent and potential impacts can be identified and quantified (e.g. Lee and Moore, 2007; Lee, 2009).

In recent years the need for greater scientific investment by decision makers to mitigate the losses caused by, and to manage the potential risk posed by, landslide hazards has stimulated a notable increase in the body of literature on the subject. In the majority of cases this research has concluded that these natural hazards cannot in general be prevented. As a consequence research has increasingly focused on the development of a greater appreciation of the mechanisms and processes of landsliding to allow predictions to be made of likely patterns of behaviour. In principle these are powerful tools in reducing human vulnerability and managing risk. Notable successes can be observed, for example in the field of spatial mapping of landslide hazard and risk. The development of hazard zoning techniques, based on specific attributes such as slope morphology and geology, have provided high level methods of quantifying landslide susceptibility (e.g. Pachauri and Pant, 1991; Hutchinson, 2001a).

Similarly, advances in the resolution of remotely sensed imagery, such as high resolution satellite technology (e.g. Quickbird and Ikonos) and satellite radar interferometry (INSAR), have demonstrated great potential in landslide identification, mapping and monitoring techniques (Petley and Bulmer, 2005; Yin *et al.*, 2010). These methodologies have been strengthened by the development of Geographical Information Systems (GIS). These data management systems provide a more sophisticated approach by manipulating numerous spatial data inputs (e.g. geological mapping, topographic surveys and aerial photographs) enabling landslide susceptibility mapping and statistical relationships of landslide frequency and distribution to be

determined (e.g Carrara *et al.*, 1999; Dai and Lee, 2002; Flentje *et al.*, 2005; Cheli *et al.*, 2006;Trigila *et al.*, 2010).

In spite of the apparent potential of these approaches results have, to date, been disappointing as the diffusion of such technologies is still hampered by factors such as practical challenges in acquiring appropriate data, the intrinsic complexity of natural systems, the lack of adequate graphical interfaces and the high cost of digitisation (Petley and Bulmer, 2005).

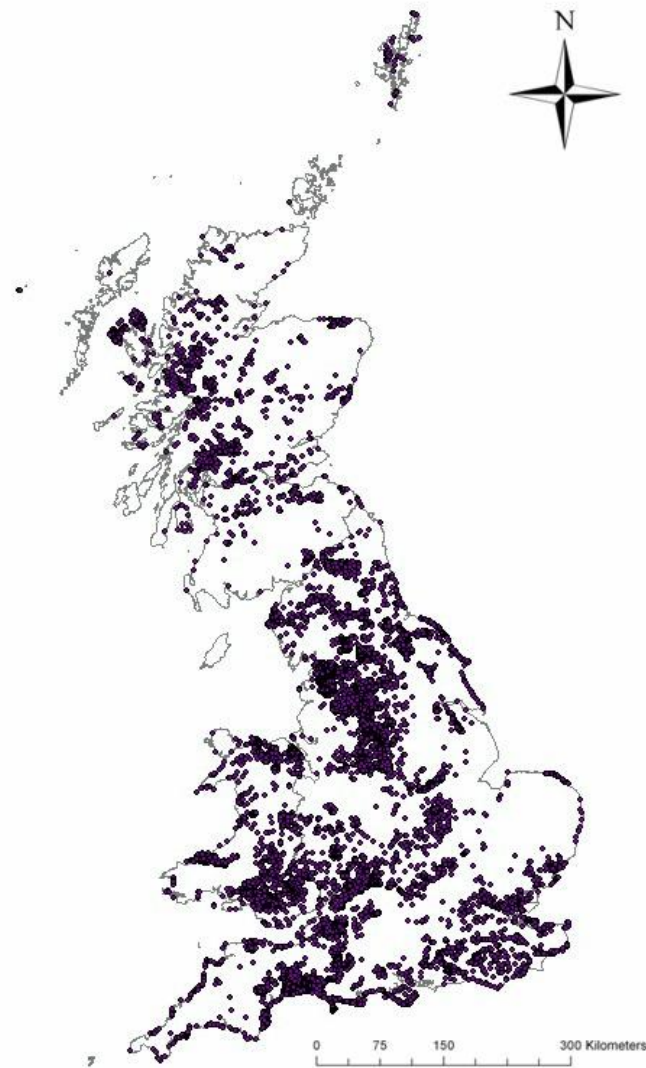
A key area in the development of remotely sensed datasets is the use of satellite technologies to monitor landslide displacements. In theory, techniques such as INSAR can produce high resolution displacement - time datasets (e.g. Casagli *et al.*, 2010). However, these are in reality somewhat limited in scope, and have yet to be developed into a useful tool in predicting the catastrophic ground movements that cause disaster. This largely results from the fact that most fatal landslides are of short duration, high velocity and comparatively spatially limited (Petley and Bulmer, 2005).

Ultimately, the fundamental cause of landslide-induced damage and loss of life is displacement of the landslide mass. The distance travelled and velocity of displacement largely controls the nature of the landslide risk and the associated damage incurred. Despite this knowledge, few studies have concentrated on analysing the mechanism of landslide displacement as a method to understand and potentially forecast future landslide behaviour. Where these studies have been successful (e.g. Saito, 1965, 1980; Fukuzono, 1990; Petley *et al.*, 2002), few countries have taken advantage of this knowledge to reduce landslide hazard.

1.3 Landsliding in the UK

Whilst the impact of landsliding within the United Kingdom (UK) may be considered to be relatively low from a global perspective, the risks posed by such events are still substantial and considerable resources are expended annually in mitigating and managing their effects. The British Geological Survey (BGS) have been managing a detailed database since 2002 based on

mapping undertaken by GSL (1986/87) that currently records over 14,000 landslides across the UK (Fig 1.3). Many UK landslides are slow moving (mm / year) (e.g. Ventnor; Folkestone Warren; Lyme Regis), which can often disguise their effects and the potential hazard. In some cases rapid movement events do occur in the UK, such as the 1966 Aberfan landslide and the 1993 Holbeck Hall event, both of which had catastrophic consequences. The impacts of landslides in the UK are particularly apparent along the coastline where, in many locations, a combination of weak and/or unfavourably dipping geology, coastal erosion and the potential high groundwater levels are commonly observed.



*Figure 1.3 Distribution of landslides in the BGS National Landslide Database
(from Foster et al., 2008; after GSL, 1986/87)*

Recent investment in UK coastal landslide monitoring has provided some detailed datasets that have yet to be fully interpreted in relation to landslide mechanisms. A more detailed analysis of these data in relation to understanding the mechanisms and patterns of landslide behaviour provides an opportunity to develop more appropriate methods for managing landslide risk in the UK.

It is clear that understanding the movement of both existing and first time landslides is fundamental in informing landslide hazard. These landslide movement patterns cannot be fully understood without a detailed knowledge of the processes and mechanisms of deformation occurring within the landslide mass. Central to this understanding is the process of shear surface development along which failure ultimately occurs. Whilst the progressive development of a landslide shear surface has been considered in many previous studies (e.g. Terzaghi, 1950; Skempton, 1969; Bjerrum, 1967) this process remains poorly understood in deep-seated landslides.

1.4 Study aims, objectives and research questions

This study aims to consider mechanisms of deep-seated landsliding by studying these processes within the Ventnor town deep-seated landslide complex on the Isle of Wight.

The objectives of this research are to:

1. examine the progressive development of shear surfaces under varying pore water pressure conditions using specialist laboratory tests to replicate field failure conditions,
2. evaluate the patterns of displacement observed in laboratory tests as a potential method to evaluate present and potential landslide behaviour through calibration with available monitoring data from Ventnor, a deep-seated urban landslide complex in the UK, and
3. develop a new model to describe the development to failure, and the subsequent post-failure behaviour of deep-seated landslide complexes.

To achieve these overarching research aims the following research questions will be answered:

1. Can the patterns of ground movement observed during the pre-failure strain of a first time landslide be related to the phases of creep associated with the development of the landslide shear surface?
2. How do these patterns of movement vary in relation to the mechanisms of shear surface development and the physical properties of the materials within the shear zone?
3. How do these mechanisms of shear surface development relate to the asymptotic and linear trends to failure in $1/v-t$ space?
4. How do the phases of creep relate to the Mohr Coulomb failure envelope?
5. Is final failure controlled by the shear stress being applied at the landslide shear zone or is there a time dependent factor in the development of the shear surface controlled by internal mechanisms such as the progressive development of strain?
6. What implications does this research have on understanding the potential future landslide behaviour of the Ventnor landslide complex?

1.5 Study scope

This study is focused on collating ground movement records for deep seated landslides with a suite of specialist laboratory tests in order to study the progressive development of landslide shear surfaces and their subsequent post-failure behaviour.

Field samples have been collected from the Ventnor Undercliff, on the south coast of the Isle of Wight, UK. The site is subject to complex deep-seated mass movement and represents the largest urban landslide complex in Northern Europe (Moore *et al.*, 2007). These samples have been tested using a suite of bespoke triaxial and back pressured shear box tests, in which field failure conditions are simulated by elevating pore water pressures under a constant deviator stress. These laboratory simulations have been calibrated with a detailed analysis of ground movement, groundwater and antecedent

rainfall relationships from real-time site monitoring records taken from field instrumentation managed and funded by Isle of Wight Council.

1.6 Thesis structure

The thesis has been subdivided into eight chapters, which are briefly outlined below.

- **Chapter 1** (this chapter) provides an introduction to the research, its context and relevance to the wider landslide study literature. It identifies the key aims and objectives, and describes the structure and research questions the thesis will address.
- **Chapter 2** provides a detailed review of the current state of knowledge on the mechanisms of landsliding; the methods of landslide monitoring; the proposed models for understanding shear surface development, and the significance and role of material properties in developing these understandings and interpretations.
- **Chapter 3** describes the site of this study including its climate, geomorphology, geology, hydro-geology, Quaternary history and the historical context of landsliding that has impacted the site.
- **Chapter 4** outlines the methodologies developed; the collection of historical records of ground movement, groundwater and rainfall; the collection of suitable field samples of the landslide material; and the methods used to undertake laboratory tests to classify both material properties and simulate field failure conditions.
- **Chapter 5** provides an analysis of the monitoring data available for the Ventnor landslide, including automated groundwater, rainfall and ground movement records collected from 1997 onwards. The analyses seeks to establish empirical relationships between periods of accelerated ground movement, elevated pore water pressures and the antecedent rainfall conditions at site.

- **Chapter 6** provides an analysis of the data collected from the standard laboratory tests and the specialist triaxial and back pressure shear box tests designed to replicate field failure conditions. The laboratory testing is focused on field samples collected in the key basal materials from the Ventnor landslide shear zone, examining specific locations within the landslide mass and stratigraphic equivalent samples collected locally.

- **Chapter 7** discusses the implications of the findings of Chapters 5 and 6 to develop an understanding of the progressive development of shear surface in deep seated landslides, assess the validity of existing landslide prediction methods and calibrate the shear surface behaviour observed in the laboratory testing with real landslide monitoring records available for the Ventnor landslide.

- **Chapter 8** concludes the thesis by outlining the key findings of the research, the contribution that these findings have made to the knowledge of the understanding of landslide mechanisms and outlines recommendations for further study to improve our understanding of deep seated landslide mechanisms.

Chapter 2: Literature Review

2.1 Principles of landslide failure

All landslide events result from gravitational forces that cause the materials to fail and move downslope from an unstable to a more stable position. In the majority of cases failure occurs along a failure surface, or within a failure zone, where a balance of forces exists between the weight component of the potential landslide body (shear force) and the inherent strength of the soil or rock within the hillside (shear strength) (Fig. 2.1). This balance of forces can be considered as a Factor of Safety (FoS) (Selby, 1993).

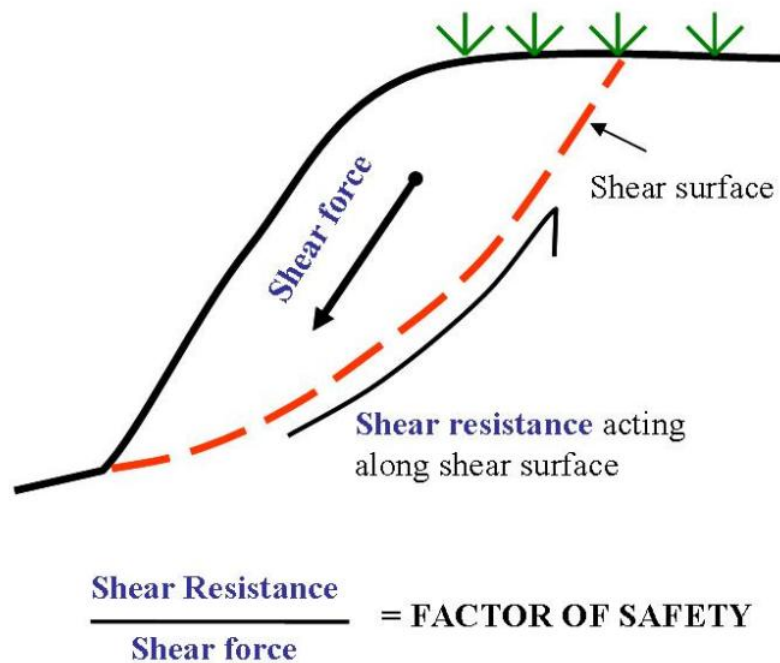


Figure 2.1 The balance of forces in landslide development

FoS = 1 represents a state in which the forces are acting in equilibrium. In this case the slope is considered to be at the failure point. When the shear forces acting in the slope exceed the forces acting to promote failure, the slope can be considered to be stable (FoS > 1). Conversely, when shear forces are sufficiently reduced, or the forces acting to promote failure are increased such that the shear strength is exceeded (i.e. FoS < 1), the slope

will fail. In this respect landslides may be viewed as a dynamic geomorphological process acting to rebalance the forces within a slope from an unstable to more stable state. To fully understand landslide failure conditions an appreciation of the key strength operating within, and the stress components acting upon, a slope is needed.

2.1.1 Mohr Coulomb failure criterion

The resistance of a soil or materials to shear is defined by its shear strength (τ_f). The shear strength of a soil was originally expressed is expressed by the Mohr Coulomb law (Lambe and Whitman, 1969) as a linear function of the normal stress (σ_f) on the plane at the same point;

$$\tau_f = c + \sigma_f \tan \phi$$

(Eq. 2.1)

where c refers to the cohesion or apparent cohesion and ϕ refers to the angle of shearing resistance or angle of internal friction. Terzaghi's fundamental concept of effective stress states that soil shear stress can be resisted only by the skeleton of the solid particles, and therefore shear strength should be expressed as a function of its effective normal stress;

$$\tau_f = c' + \sigma'_f \tan \phi'$$

(Eq. 2.2)

where c' and ϕ' are the shear strength parameters in terms of effective stress. As a consequence, failures occur when a critical combination of shear stress and effective normal stress develops (Craig, 1992). In terms of the Factor of Safety (F) this can be calculated using;

$$F = \frac{c' + (\gamma \cos^2 \beta - u) \tan \phi'}{\gamma z \sin \beta \cos \beta}$$

(Eq. 2.3)

where c' is the effective cohesion, γ is the bulk unit weight of saturated soil, β - u is the porewater pressure, z is the soil depth the direction of the normal stress, β is the angle of the slope to the horizontal and ϕ' is the effective angle of internal friction.

The shear strength of a slope is also frequently assessed in terms of its effective major and minor principal stress, σ'_1 and σ'_3 , of the soil at the failure point in question. At the point of slope failure a straight line, as represented by Equation 2.2, will be tangential to the Mohr circle, representing the state of stress (Fig 2.2).

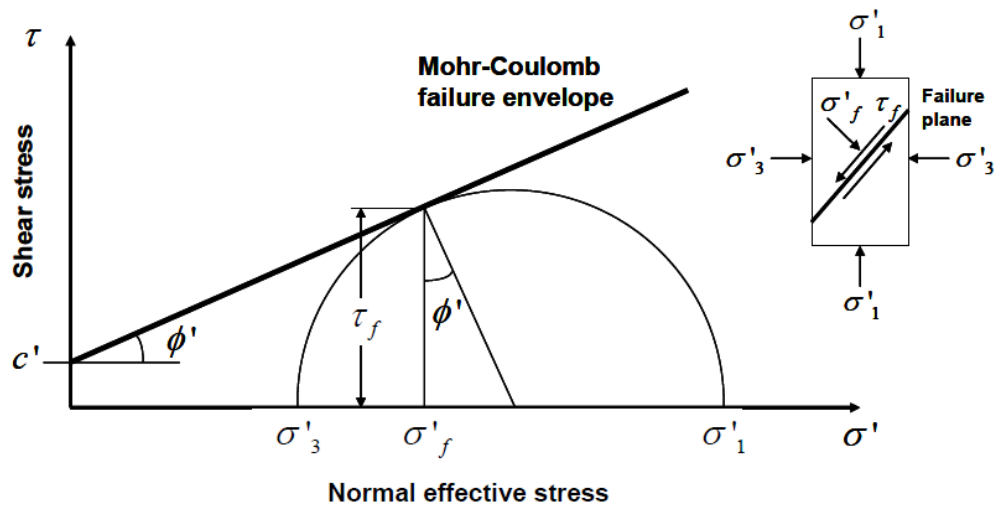


Figure 2.2 Mohr Coulomb stress conditions at failure (after Craig, 1992)

The Mohr Coulomb failure criterion, largely as a result of its simplicity, is the most commonly used method to represent states of stress of material at failure. Any stress state plotted above the failure envelope (Fig 2.2) is deemed to be in an impossible state. It is important to recognise however that whilst this is most popular criterion for establishing material strength, the failure state of stress plotted by this method can be criticised for not considering the strains either at, or prior to, the failure. The condition expressed, further assumes that the effective intermediate principal stress σ'_2 has no influence on the shear strength of the soil. Whilst the Mohr Coulomb failure criterion is widely used and practiced it should not be considered as the only possible failure criterion for soils (Craig, 1992).

2.2 Landslide definition and classification

The very nature and complexity of the natural environment, in terms of the potential combinations of controls, causes, mechanisms and forms of landslides, is so varied that correct identification and classification is a notorious academic 'battlefield' (Brunsden, 1985). As a consequence, a plethora of definitions have been proposed to describe landslides. Cruden (1991) defined a landslide as a movement of a mass of rock, earth or debris down a slope. Alternatively, Varnes (1978) describes a landslide as a downward and outward movement of slope forming materials under the influence of gravity, suggesting that slope movement would be a more suitable term as it does not infer a process. Brunsden (1984, cited in Dikau and Brunsden, 1996), described landslides as a mass movement process distinguishable from mass transport as being a process which did not require a specific transporting medium such as water, air or ice.

This range of definitions has resulted in the development of various landslide classification systems that attempt to differentiate landslide types and failure mechanisms (e.g. Skempton and Hutchinson, 1968; Brunsden, 1973; Varnes, 1978; Crozier, 1984; EPOCH, 1993). The majority of these definitions have evolved from Varnes, (1958) and are based on the type of material involved in the process (e.g. Varnes, 1978), and/or the movement type and/or the movement rate (e.g. Brunsden, 1993). One of the most successful schemes, proved in practice in the UK, was proposed by Hutchinson (1968). This scheme, which adopted the mode of failure as the main criteria, allowed for the simple division of landslide types and avoided the complications of schemes based on material, coherence, size, geology, rates, water, trigger mechanism or morphological components (Brunsden, 1985). Later, Hutchinson (1988) developed a more comprehensive scheme that classified slope movements into eight categories based on the morphology, mechanism, material and movement rate. More recently a European classification scheme (EPOCH, 1993) has been established that provides a simple division into seven distinct types that are suitable for European conditions (Table 2.1).

Table 2.1. Mass movement classification (after EPOCH, 1993; Dikau and Brunsden, 1996)

Type	Rock	Debris	Soil
Fall	Rock fall	Debris fall	Soil fall
Topple	Rock topple	Debris topple	Soil topple
Slide (rotational)	Single (slump)	Single multiple	Single multiple
	multiple successive	successive	successive
Slide (translational)	Block slide	Block slide	Slab slide
Planar	Rock slide	Debris slide	Mudslide
Lateral spreading	Rock spreading	Debris spread	Soil (debris) spreading
Flow	Rock flow (Sackung)	Debris flow	Soil flow
Complex (with run-out or change of behaviour downslope)	Rock avalanche	Flow slide	Slump
			earthflow

Within this scheme a 'fall' can be identified as a free-fall movement of material from a steep slope or cliff, whilst 'topples', although similar, tend to involve a pivoting action rather than complete separation at the failure base. Sliding movements involve material displacement along one or more discrete shear surfaces or shear zones, and can be further subdivided into either 'rotational' or 'translational slides' according to the form of failure surface (Dikau and Brunsden, 1996). 'Rotational' landslides occur along a circular slip surface whereas 'translational' failures occur on a planar slip surface, which is often bedding controlled. 'Lateral spreading' is a characteristic of low angled slopes and generally very slow rates of movement, whereas a 'flow' failure can occur over a range of slope angles and generally behaves similarly to fluids due to the significant volumes of water or air involved. 'Complex' landslide failures in this classification consist of failures that comprise a combination of two or more of the failure mechanisms (Table 2.1). In natural environments nearly all landslides involve several types of movement. This can involve mechanisms acting concurrently in different parts of the failure resulting in a compound failure, or mechanisms evolving over time as the failing mass moves and deforms downslope resulting in a 'complex' landslide (Dikau and Brunsden, 1996).

Whilst it is noted that the development of these schemes has enabled much progress in understanding the variability of landslides in terms of their form, under such schemes the majority of large landslide systems are categorised as 'complex' due to the fact that failures often initiate in a certain form and evolve a multitude of failure characteristics as materials deform and move downslope. Although these schemes consider general material characteristics, and potential movement rates, none of the classification systems presented consider the geotechnical characteristics and process mechanisms involved in landslide development (Brunsden, 1985).

Sassa (1989) developed a geotechnical landslide classification based on the type of shear and the material grain size (Table 2.2). The shear types were described as 'slide', 'liquefaction' and 'creep' and were outlined by use of a simplified stress path (Fig 2.3).

Table 2.2 Geotechnical landslide classification system (after Sassa, 1989)

Type of shear	Grain size of material		
	Rock (20mm)	Sandy soil (20-0.074mm)	Clayey soil (0.074mm)
1. Slides-			
a)Peak strength	Rock avalanche	Sandy peak strength slide	Clay peak strength slide
b)Residual strength	Residual strength rock failure	Sandy residual strength slide	Clay residual strength slide
2. Liquefaction	None	Soil creep	Quick clay landslide
3. Creep	Rock creep	Soil creep	Clay creep

A 'peak strength slide' results when a slope reaches its undisturbed failure envelope, allowing motion to occur along a single slip surface. When pore pressure increases in the slope the normal effective stress reduces toward the peak failure envelope (Fig 2.3, Type 1a). As the peak strength envelope is reached failure is initiated at point Pp, and movement occurs (Sassa, 1989). The state of the shear surface rapidly moves to the residual state line. As this

occurs the imbalance of forces between the shear stress and shear resistance causes acceleration of the sliding mass. In these circumstances a rapid landslide can occur if the difference between shear resistance and shear stress is large.

Alternatively, a 'residual strength slide' occurs when a slip surface or shear zone is already in a residual state. In these circumstances movement is initiated when the stress reaches the residual strength envelope (point Pr, Fig 2.3 Type 1b). Shear resistance is more likely to remain constant, such that movement is often less rapid. In this case a small recovery in the stress condition would therefore stabilise the disturbed mass.

'Liquefaction' occurs when a loose, saturated soil mass is subjected to undrained loading. As a consequence the soil structure may suddenly fail without exerting its frictional shear resistance (before reaching the failure envelope) and the effective stress decreases significantly to a very low stress point (Fig 2.3. Type 2). This is the initiation of flow as frictional resistance is so low that it is comparable to viscous resistance.

'Creep' is referred to as a phenomenon that occurs inside natural slopes, when stresses vary due to groundwater fluctuation but sufficient to cause very slow motion during the resultant fluctuations in stress (Fig 2.2 Type 3). In this description slow movement occurs inside a slope when some very unstable grains/ fractured rock can partly move, accompanied by saturation and drainage (Sassa, 1989). Whilst slow movements have been observed in slopes, true creep, by definition, refers to continuous deformation at constant stress (Varnes, 1978). In Sassa's description therefore, creep is incorrectly identified as very slow movement in pre-existing landslides.

Type	Stress path	Description
1a		<p>Peak strength slide</p> <p>As shear resistance decreases after failure to residual value, the failed mass will be accelerated by force</p>
1b		<p>Residual strength slide</p> <p>Shear resistance remains almost constant after failure. The sliding mass is not much accelerated</p>
2		<p>Liquefaction</p> <p>After sudden failure, shear resistance reaches so low that it may be compared to liquid</p>
3		<p>Creep</p> <p>Stress remains under the failure envelope, however a slight deformation takes place within grains/joints due to fluctuation of groundwater level and infiltration</p>

Figure 2.3 Conceptual model for geotechnical classification (after Sassa, 1989)

Although the landslide classification schemes presented have proved useful for establishing landslide types based on their component materials, morphology, mode of failure and movement behaviour, their limitations in accounting for the geotechnical properties of materials and the variable mechanisms of failure operating in landslides are clearly evident. It is for this reason that in the vast majority of cases landslides are referred to as 'complex'. To improve the relevance of these methods of classification a greater understanding of the mechanisms of failure operating within a slope, their relationship to potential external and internal causal factors and their implications for landslide displacement rates is required.

2.3. Landslide triggers and failure mechanisms

2.3.1 Landslide causes

Whilst landslide failure can be easily understood in terms of forces when considering individual failure events, the actual causes of landslides can be considered complex due to the great diversity of causal factors that may act upon and within a slope. In broad terms these causes may be subdivided into two groups (Table 2.3):

- **internal causes** that lead to a reduction in shear strength, and
- **external causes** that lead to an increase in the shear stress.

In the context of deep-seated UK landslides the key driving mechanisms tend to be weathering and erosion, and the variations in porewater pressures driven by rainfall events. However, the actual cause and mechanism of a UK landslide can be complicated to understand as often these causes vary both spatially and temporally within a landslide system.

Table 2.3 Summary of causes of landslide failures (after Moore et al., 2006)

Internal Causes	External Causes
<p style="text-align: center;">Materials:</p> <ul style="list-style-type: none"> • Soils subject to strength loss on contact with water or as a result of stress relief (strain softening) • Fine grained soils which are subject to strength loss or gain due to weathering • Soils with discontinuities characterised by low shear strength such as bedding planes, faults, joints etc. 	<p style="text-align: center;">Removal of slope support:</p> <ul style="list-style-type: none"> • Undercutting by water (waves and stream incision) • Washing out of soil (groundwater flows) • Human intervention (e.g. Cutting, excavations, tunnelling and mining)
<p style="text-align: center;">Weathering:</p> <ul style="list-style-type: none"> • Physical and chemical weathering of soils causing loss of strength (apparent cohesion and friction) • Slope ripening and soil weakening processes (e.g. loss of vegetation, shrink and swell, desiccation and surface cracking) 	<p style="text-align: center;">Increased loading:</p> <ul style="list-style-type: none"> • Natural accumulations of water, snow, talus • Human intervention (e.g. fill, tips, buildings)
<p style="text-align: center;">Pore-water pressure:</p> <ul style="list-style-type: none"> • Elevated pore-water pressures causing a reduction in effective shear stress. Such effects are most severe during wet periods or intense rainstorms. 	<p style="text-align: center;">Transient Effects:</p> <ul style="list-style-type: none"> • Earthquakes and tremors • Shocks and vibrations

2.3.2 Slope weakening processes and creep mechanisms

Long-term weathering process acting within a slope can act to weaken soils and rocks, which in turn make the slope more susceptible to failure. These processes are referred to as slope ripening or preconditioning factors. These processes, when active in the slope, can occur over varying time scales. Long-term changes in soil strength can relate to: weathering, for example in tropical environments (Ng, 2007); physio-chemical effects, for example in coastal mudslides where sea spray can add salt to the pore fluid (e.g. Moore and Brunsten, 1996); and rock shattering due to changes in stress state (e.g. Monma *et al.*, 2000). Conversely, short-term oscillations in soil strength, resulting from pore pressure fluctuations, may be active on annual timescales as a result of rainfall and seasonal groundwater fluctuations. Progressive changes in soil strength may result from gradual increases in shear stress through slope steepening by basal erosion (e.g. fluvial incision, coastal erosion).

The term 'creep' has been used in a range of hillslope studies, and the distinctions between them often go unrecognised (Selby, 1993). True engineering creep, however, refers to acceleration in ground movement at constant stress (e.g. Varnes, 1978), in geological studies 'creep' often refers to the very slow-motion movement of materials due to fluctuations in stress (e.g. Basset, 1979; Sassa, 1989). These creep processes can be active in a slope where slope weakening or weathering processes are in operation and can be either seasonal or continuous.

'Seasonal creep' results from seasonal changes in moisture and temperature by thermal expansion and contraction, swelling and shrinking, freezing and thawing and other seasonal processes, which generally result in the movement in the upper surface of the slope (Terzaghi, 1950). Alternatively, 'continuous creep' processes often result in a downhill movement of a sheet of earth produced only by the force of gravity, unaided by other agents. As the force of gravity remains constant the resultant rate of ground creep is relatively constant over time (Basset, 1979).

Creep processes that produce slow mass movements have, in the main, been related to four principal mechanisms comprising; 'pure shear', 'viscous flow', 'expansion and contraction', and 'particle diffusion' (Donoghue, 1986). The 'pure shear' mechanism describes deformation of a soil mass along a plane narrow zone (Gueguen and Besuelle, 2007; Logan, 2007), without the significant rotation of individual particles, by the action of deviator stress (Donoghue, 1986). Whilst all slopes are subjected to shear stresses inter-granular readjustments only occur when grain to grain bonds are ruptured and friction resistance is overcome (e.g. Ng and Petley, 2007). Viscous flow occurs in instances where deforming soils behave as a viscous fluid, allowing them to deform continually when subjected to shear stress. Volume change in soil particles and soil pore liquids and gases will tend to cause downslope movement on hillslopes. This occurs because 'expansion and contraction' is retarded by gravity in an upslope direction and assisted by gravity in a downslope direction. Volume changes in soils caused by freezing of pore

fluids may be considerable in soils susceptible to frost action where ice needles and ice lenses can form. The novel approach of particle diffusion established by Culling (1963; 1983) suggests a diffusion model for granular soils, characterised by a random and a downslope component in the particles subjected to all natural disruptive forces. Such forces, whether internally or externally produced, cause particles to be displaced into adjacent free voids in the soil structure. This process requires particles to behave independently of neighbours, such that movement is controlled by local stresses and inter-particle bond distributions, providing suitable recipient voids are available to accept particle translation.

A number of authors studying slope and landslide movement characteristics have identified pre-failure creep phases in earth materials prior to final failures (eg. Moriwaki, *et al.*, 2004; Zhou *et al.*, 2008; Lui, 2009). Results from laboratory investigations of the slow mass movement mechanisms, combined with catchment monitoring observations, suggested that this shear mechanism alone is not capable of producing the movements observed (Donoghue, 1986). These results indicate that other processes may be operating within slopes related to long term change in the overall fabric of the deforming material. This correctly challenges the, often misunderstood, nature of earth materials as being static in space and time. Earth materials are in reality dynamic entities that change continually in time and space. It also emphasises the potential for progressive transition of mass movement processes from a stable to unstable state, commonly referred to in landslide studies as slope ripening (Picarrelli *and Russo*, 2004), to a high strain (catastrophic) phase.

This concept of long-term slope soil strength reduction (Fig 2.4), with corresponding fluctuations in shear stress, has been discussed by numerous authors (e.g. Allison, 1996; Julian and Anthony, 1996).

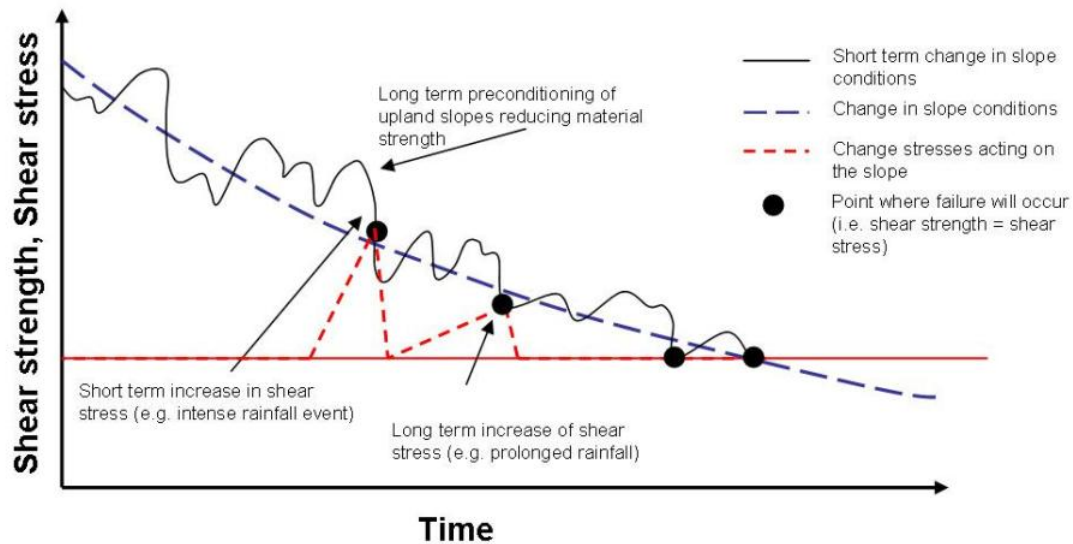


Figure 2.4 Model showing relative time frame of landslide development and significance of slope ripening and landslide triggering factors, adapted from Julian and Anthony (1996).

Whilst Figure 2.4 illustrates the dynamic nature of slope conditions, and the variability of stress conditions that may impact it though time, it does not fully account for field failure conditions in the majority of natural landslide systems. The graph suggests that a slope may progress to failure, regardless of the stress characteristics imposed upon it, as a result of decreasing material shear strength over time. In the majority of landslides systems any fluctuations in the shear surface strength are the result of a reduction in the mean effective stress, through elevated porewater pressures. The relevance of these strength reduction processes is likely to vary considerably due to the nature of the environment and properties of the materials in the slope. Deep seated landslide systems, for example, are likely to sustain almost constant shear stress, whilst weathering processes in shallow topical soils are likely to be a major factor in reducing normal stress within the slope. This interpretation further implies that only short-term stress fluctuations sufficient to create failure are significant in slope failure development, with any minor fluctuations having a negligible impact on the overall strength of the slope. The many instances in which landslides have occurred with little or no evidence of a definable trigger (e.g. Wataru and Tsukasa, 2004) suggests that minor

fluctuations in stress may initiate creep processes, which could lead to failure over time.

It is possibly more appropriate to consider failure in terms of two potential variable stresses acting to destabilise the slope which comprise reductions in mean effective stress (p') and increases in the deviator stress (q) or principal stress difference ($\sigma_1 - \sigma_3$). A conceptual model of such conditions for a dynamic coastal landslide system is presented (Fig 2.5). In this model the failure initiation line is a line which is governed by the relationship between p' and q and is therefore considered a constant line in time. The model demonstrates that failure in a coastal landslide can occur through a number of processes as a result of short and long term fluctuation in the mean effective stress (in this instance caused by fluctuations in porewater pressure) and deviator stress (e.g. toe unloading through coastal erosion).

The role and processes of creep in a slope and its implications for the development of slope failure remains a key area of uncertainty in landslide research (Furuya *et al.*, 1999). Whilst creep mechanisms have been studied using laboratory testing and field measurements, its detection remains difficult (Donoghue, 1986; Selby 1993; Ng, 2007). A major constraint has been that both field and laboratory based studies have been generally undertaken over short-time periods, using methods of varying precision. In particular the identification of true engineering creep, for example acceleration in slope deformation and constant stress, has yet to be confirmed as a time dependent landslide mechanism (e.g. Terzaghi, 1950; Bjerrum, 1967; Ng and Petley, 2009).

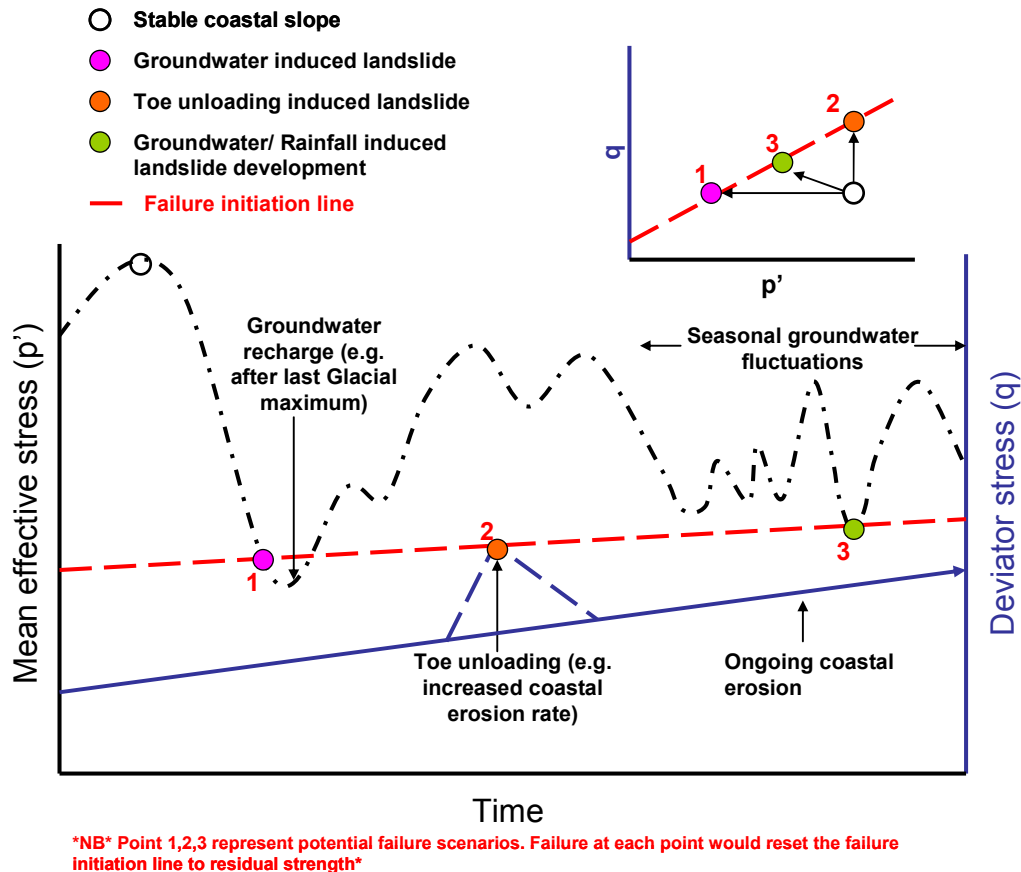


Figure 2.5 Conceptual model of coastal landslide development

2.3.3 The role of pore water pressure

The saturation of slopes by water is one of the Primary causes of landsliding and can be caused by intense rainfall; snow-melt; elevated groundwater levels and water level changes along the coast, earth dams and the banks of reservoirs, canals and rivers (USGS, 2004). Water seeping into slopes affects the stability in several ways. Firstly, if voids in the materials are only partially filled with air the water eliminates surface tension, which imparts to fine-grained, cohesionless soils apparent cohesion (Terzaghi, 1950). Secondly, some soils, such as loess, owe their cohesion to soluble binders. Slopes consisting of such materials, when submerged or saturated for the first time, can have their binder removed by solution leading to a loss of cohesion (Terzaghi, 1950). Finally, elevated groundwater levels cause a subsequent rise in the piezometric surface, which in turn leads to increased porewater pressures and decreases in mean effective stress (shear resistance) in the soil.

Rainfall-induced landslides occur frequently and are very dependent on the characteristics of the rainfall in terms of duration and intensity, and on the nature of the soils being affected. Storm intensity is of particular importance in determining the nature, size and type of failure (Tsai, 2008; Allison, 1996). Intensive storms often lead to the development of relatively shallow, fluidised landslides and debris flows that can often occur unexpectedly, with rapid movement and long runout features making them particularly hazardous (Wang *et al.*, 2003). In some instances soils may experience a sudden loss of a large proportion of their shear resistance due to the generation of high porewater pressures.

2.3.4 Reactivation of pre-existing landslides

The study of landslide movement mechanisms has commonly concentrated on the initiation of first time landslides (e.g. Varnes, 1958; 1978). Movement of pre-existing landslides, where displacement generally occurs along pre-existing shears, are often subject to slow displacement rates. These are controlled by non-brittle deformation, or by movement along an associated slip surface (Skempton and Hutchinson, 1969). Under some circumstances, however, large rapid displacements can occur and due to the commonly unanticipated nature of these failures, these events can be particularly hazardous (Hutchinson, 1987a).

Hutchinson (1987a) suggests that the causes of these failures can be subdivided into six types:

1. Water induced mechanisms
2. Changes to the surface profile of the landslide
3. Mechanisms involving brittleness within a sliding mass
4. Mechanisms involving the modification of pre-existing shears
5. Seismic effects
6. Coalescence of landslides

The causes reviewed by Hutchinson (1987a) provide an insight into the potential mechanisms of movement and the likely terrain characteristics in

which they may occur. The review further illustrates the importance of material characteristics as a key control of the reactivation type. However, the review does not provide information on the anticipated magnitudes and patterns of ground movement that may be anticipated as a result of these shear reactivations.

2.3.5. Coastal landslide mechanisms in the UK

The causes and mechanisms of coastal landsliding in the UK are highly variable, reflecting the diverse geology, morphology, scale, age and exposure to marine attack that are experienced along the UK coastline. Estimates of average annual recession rates can vary from as low a centimetre on hard coastal cliffs (e.g. Rosser *et al.*, 2005; Allison, 1989), to metres in lower cliffs comprised of weak glacial materials (e.g. Hutchinson, 1984). The ages of landslides along the coastline range from the ancient deep-seated failures that are believed to have initiated thousands of years ago (e.g. Stephens *et al.*, 1975; Fish *et al.*, 2006), to active landslide deposits which can be eroded and steepened rapidly by marine erosion (e.g. Hutchinson, 1976; Dixon and Bromhead, 1991; 2002). Hutchinson (1984) divided UK coastal landslides into five categories based on their material properties and relative susceptibility to marine erosion. These are summarised in Table 2.4.

*Table 2.4 Summary of landslide mechanisms and around the UK coastline
(after Hutchinson, 1984)*

Landslide category	Description	Example
i. Coastal landslide in stiff fissured clay undergoing strong toe erosion	Particularly evident along cliffs up to approximately 40m height such as the cliffs to the north and south of the Thames Estuary (1). On the north and north-east facing cliffs where materials are exposed to high marine activity large deep seated single rotational landslides occur. Further east sandstones underlying London Clay rise until only a few meters below ground level. In these locations rotational failures are inhibited and compound landslides with distinct graben features occur (2).	(1) Warden Point, Isle of Sheppey (2) Herne Bay
ii. Coastal landslides in stiff fissured clay undergoing moderate toe erosion	Occur along similar London Clay cliffs with lower energy coastal environments leading to different patterns of landsliding as a result of more moderate coastal erosion. These failures are often characterised by mudslides occurring in regular embayments. The mudslides are generally stationary during summer months with ground movements occurring in the winter as a result of undrained loading at the head of the failures. Other mudslide failures are located at the flanks of deep-seated landslides as they degrade. The largest coastal mudslides occur in Jurassic Clays and shales on the south coast (3).	(3)Black Ven, Dorset
iii. Stiff fissured clay with a rigid, jointed cap-rock	The largest landslides in UK occur where thick glacial over-consolidated Clay is found between stronger rock formations. Characteristically failure tend to be multiple rotational slides	Undercliff, Isle of Wight Folkestone Warren, Kent Dowlands, Dorset Garron Point, Northern Ireland
iv. Coastal landslides in Quaternary deposits (tills) commonly with interbedded sands and laminated clays	Materials form much of the north Yorkshire and East Anglian coastline comprise generally weak glacial till deposits which are highly susceptible to erosion from the intense marine activity of the North Sea. Generally landslides and slipped masses are rapidly eroded along the coastline leading to further costal instability.	Holderness, East Yorkshire
v. Coastal landslides in hard rock cliffs	Rockfalls occur along the UK coastline, chiefly in Chalk Cliffs but also in Upper and Lower Greensands. Often failures form a steep talus at the toe of the cliff although as cliff height and slides volumes increase a runout flow may occur. These flows are generally believed to occur due to elevated porewater pressures. Toppling failures occur in steeply dipping rocks and in horizontally bedded strata with steep joints.	Sidmouth, Devon Beach Head, Sussex

2.4 Material behaviour and their significance in landslide development

It has long been understood that to determine the safety and future potential of landslide initiation and reactivation, a detailed understanding of the material's physical, hydrological and geotechnical properties is essential (e.g. Varnes, 1978 Hutchinson, 1967; 1984; 2001b). These processes have been recognised as key in controlling material deformation and the resultant movement characteristics of a slope (Petley, 2004; Petley *et al.*, 2005a). Despite this notion, progress in this field has been surprisingly limited and only improved over the last five years (e.g. Petley *et al.*, 2005a; 2005b; Lui, 2009).

The concept of understanding pre-failure behaviour within a landslide mass was first recognised by Terzaghi (1950), who identified the connection between material creep and landslides (Fig 2.6). It was noted that even landslides that appear to occur with no prior warning could not take place unless the ratio between the average shearing stress on the potential surface of sliding has previously decreased from an initial value greater than one to unity at the instant of the landslide event. This highlights the requirement for a preceding gradual decrease of the ratio from a FoS of above 1, which in turn involves a progressive deformation of the slice of the material located at the landslide shear surface (Federico *et al.*, 2002). Field observation of the opening of tension cracks, toe bulging and other site features are a sign of a slope in distress. In general, landslides that occur as a surprise to an eyewitness would actually show pre-failure strain indicators that had not been detected by the observer (Terzaghi, 1950).

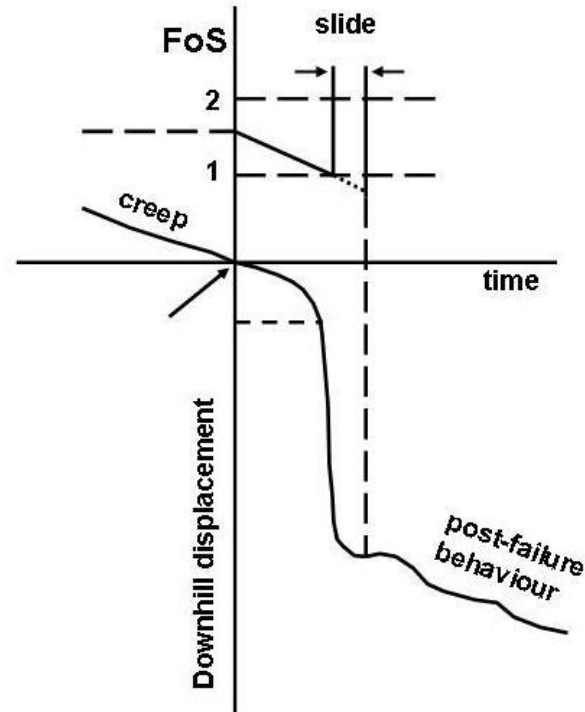


Figure 2.6 Ground movement creep preceding a landslide (after Terzaghi, 1950)

Varnes (1983) noted that a deforming material would progress through phases of strain development related to the characteristics of the deformation occurring (Fig 2.7). This is characterised by an early 'Primary creep' phase of acceleration, related to recoverable elastic deformation, followed by a 'Secondary creep' phase of slower plastic deformation as the material continues to deform. The displacement curve then becomes concave upwards as a Tertiary creep phase of brittle deformation develops, in which the strength of the material reduces from peak to residual values and as a consequence accelerates to final failure. However, damage mechanics literature (Main, 2000) suggests that the three phase creep model can be explained by contrasting strain hardening and strain weakening forces acting within the material. In Main's hybrid model, during 'Primary creep' the initial increase in deformation relates to an early form of damage dominated by strain hardening forces acting locally at crack tips. At this stage cracking is stable and decelerating as a result of stress relaxation and micro-scale

dilatancy hardening. During 'Secondary creep', strain hardening and weakening forces are both occurring almost in balance and therefore the rate of deformation is slower and almost constant. The relationship between these forces slowly transfers during this stage toward the dominance of strain weakening forces. As a consequence, deformation begins to increase, which may explain the inflection point often observed in many creep deformation patterns. During the Tertiary phase the weakening forces clearly dominate deformation and eventually local softening feedback mechanisms cause the run-away to final failure along a singular shear surface.

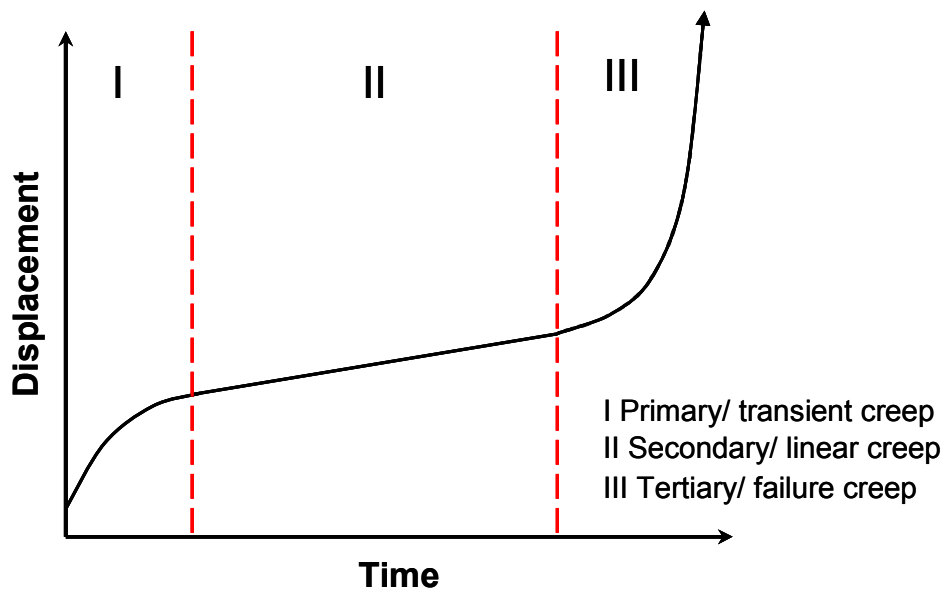


Figure 2.7 Idealised pattern of material deformation through time proposed by Varnes (1983)

Based on these observations, approaches for monitoring the pre-failure surface movements to forecast the times of failure have been established. This was first characterised mathematically by Saito (1969) who established that the relationship between the reciprocal strain rate and the time of rupture were inversely proportional.

Forecasting approaches have been successfully adopted by a number of authors (e.g. Voight 1988; Fukuzono, 1985, 1989; Main *et al.*, 1999; Main, 2000) following the creep curve methods proposed by Saito (1965). These methods have been based on the concept that the time of failure of a slope

can be predicted from creep rupture. This is based on the observation that the increment of the logarithm of acceleration was proportional to the logarithm of velocity of the surface displacement immediately before catastrophic failure (Fukuzono, 1990). The relationship is represented by;

$$\frac{d^2x}{dt^2} = A \left(\frac{dx}{dt} \right)^m$$

(Eq. 2.4)

where x is surface displacement, t is time and A and m are constants. The concept above has been applied to other catastrophic phenomena by Voight (1988,1989). The integrated velocity is a power function of t for $0 < m < 1$, an exponential function of t at $m = 1$ and a negative power function of t at $m > 1$. Experimental studies (e.g. Varnes, 1983; Fukuzono, 1985, 1989a) demonstrate that $m > 1$ for approximately 80% of all measured landslide surface displacements, and $m = 2$ for about 50% of those measured (Fukuzono, 1990). Assuming that $m > 1$ it was proposed that the time of failure could be predicted using the reciprocal of mean velocity.

Using this method final failure can be calculated at the time when $1/v = 0$, and therefore the acceleration of the slope is theoretically infinite (Fig 2.8). Successful estimates (e.g. Voight, 1989) have been made of landslide failure time based on the reciprocal of movement velocity against time as proposed by Fukuzono (1989, 1990).

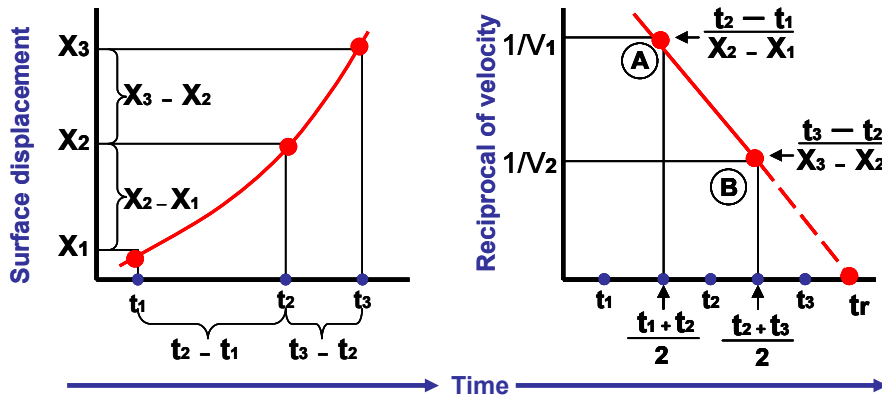


Figure 2.8 Diagram illustrating the method for calculating the reciprocal of velocity from landslide surface displacement to predict the time of failure (after Fukuzono, 1990).

Hayashi *et al.* (1988) have undertaken analyses of surface displacement measurements from landslides and used these to propose a concept of landslide prediction in which Tertiary creep includes two stages. In this method it was noted that the relationship between velocity and surface displacement were linear during the first stage of movement, and that the increment of logarithmic velocity was proportional to surface displacement during the second stage of movement. These can be expressed as:

Stage 1

$$v = al + v_0 \tag{Eq. 2.5}$$

Stage 2

$$v = v_0 \cdot e^{b(l-l_0)} \tag{Eq. 2.6}$$

Where v is velocity v_0 is the initial value of velocity, l is the surface displacement, l_0 is the initial value of surface displacement and a and b are constants. In this methodology the first phase of Tertiary creep, occurring immediately after Secondary creep, takes up the largest proportion of time followed by the relatively short second phase of Tertiary creep. Hayashi *et al.* (1988) identified that whilst the relationship during the second phase of

Tertiary creep was equivalent to the observation of Saito linearity, the earlier relationship during the first phase may allow time prediction to failure to be achieved in an earlier period of displacement. The higher the velocities achieved in the first period the shorter the time to failure. Hayashi proposed a power function to express this relationship as;

$$t_r - t_0 = \alpha(\Delta t)^n$$

(Eq. 2.7)

where a and n are constants. Based on this relationship it may be possible to approximately predict the time of failure at an earlier stage.

Salt (1988) proposed an empirical alarm criterion using critical velocity and acceleration following a detailed review of landslide field data which included both landslides that had failed catastrophically and those that had not. The critical velocities for different landslide types are summarised in Table 2.5 below.

Table 2.5 Critical limits of velocities (after Salt, 1988)

Failure type	Critical limits of velocities and accelerations
Residual strength conditions	50 mm / day and 5 mm day/ day
Peak strength conditions (First time failures)	10-5 mm / day and 1-0.5 mm / day / day

Although the data for the alarm criterion have been primarily derived from field data the above thresholds do have some credit from a geotechnical perspective in terms of both residual strength testing and frictional heat concepts (Fukuzono 1989b). Whilst this may be considered a potential approach to warn of hazardous movement in pre-existing landslide deposits, in the case of most first time failures this approach is clearly not suitable to mitigate large scale landslide risk. It is frequently the rapid development of first

time failures which occur from a position of almost no discernable ground movement to failure that cause the most serious damage and loss of life.

Whilst the methods discussed have provided some success in approximating the time to failure of previous landslides, these methods are limited by the level of uncertainty in their estimated failure times. This is because the fundamental physics controlling the nature and shape of the deformation to failure have yet to be elucidated (Hutchinson, 2001b). To develop the credibility of these methods in interpreting landslide behaviour a more detailed understanding of progressive landslide development and the mechanics of shear surfaces development are essential. This must be critically dependent on the deformation properties of the failing materials, the groundwater and hydro-climatic regime of the landslide, and the dynamic interaction of these fundamental properties.

2.5 Deformation properties of materials

A number of laboratory studies conducted on remoulded clays (e.g. Parry, 1960; Schofield and Wroth, 1968; Bishop and Lovenbury, 1969) have revealed that at any given mean effective stress, shear failure of the material occurs at constant deviator stress irrespective of strain. In such conditions the material is theoretically able to deform at a constant pore volume to infinite strain. In real systems, however, this is likely to occur only until geometric changes force a change in the stress system or magnitude. The sediment in such conditions is behaving as a perfectly plastic material in the sense that it is undergoing a permanent change in shape without fracturing or without hardening or softening. This form of material behaviour is commonly referred to as ductile deformation (e.g. Petley and Allison, 1997) and can be illustrated by a standard stress strain curve (Fig 2.9a).

Ductile deformation has been identified to occur in most geological materials at high effective stresses, and may also be characteristic of materials with little or no interparticle bonding. Critically, under these conditions strains are not able to localise to form a shear surface and as a consequence the material is not able to either sustain an increase in load or to strain-weaken, resulting in a

phase of purely plastic, or cataclastic, deformation at constant stress (Petley and Allison, 1997). The mechanism of internal deformation is thus an internal restructuring of the material, at constant porosity. Such deformation is considered to occur at a 'critical state'.

Strictly, this critical state concept applies only to homogenous materials that behave in a perfectly plastic manner. In reality, most natural sediments exhibit an initial shear strength that is greater than that of the critical state due to the presence of interparticulate (cohesive) forces. This higher shear strength is generally referred to as the peak strength. Once the peak strength is exceeded, the deviator stress sustained by the sediment decays until the critical state (residual strength) is attained. As the shear force is constant but the shear resistance is reducing, the material must respond by deforming and thus developing strain. Under these conditions sediments will continue to deform until either the shear forces reduce, or until changes in geometry or deformation mechanism promote a change in either the stress state or the sediment's strength. Thus in conventional soil mechanics theory, stress and strain can be seen to be a coupled phenomenon, with the state of stress, and its inter-relationship with the properties of the material, defining the strain, and vice-versa.

During brittle deformation resulting from increased stress, the material initially undergoes a short phase of elastic (recoverable) strain caused by the bonds, which result from grain-grain adhesion between particles, being loaded but not breaking (Fig 2.9(b) - 3). Eventually the load will become sufficiently large that the weakest or most intensely stressed bonds will begin to break (Petley and Allison, 1997). At this point the material is undergoing a combination of elastic and plastic deformation, characterised by a decrease in the gradient of the stress-strain curve. Eventually the material will reach a point at which so many bonds have been broken that it is unable to bear the applied load or stress. At this point a shear surface will develop as a consequence of strain weakening, and strength will decrease. Thereafter, deformation in the material will occur primarily as displacement across the shear surface, with the friction across it

determining the material strength. Typically, the strength of the material decreases towards the critical state.

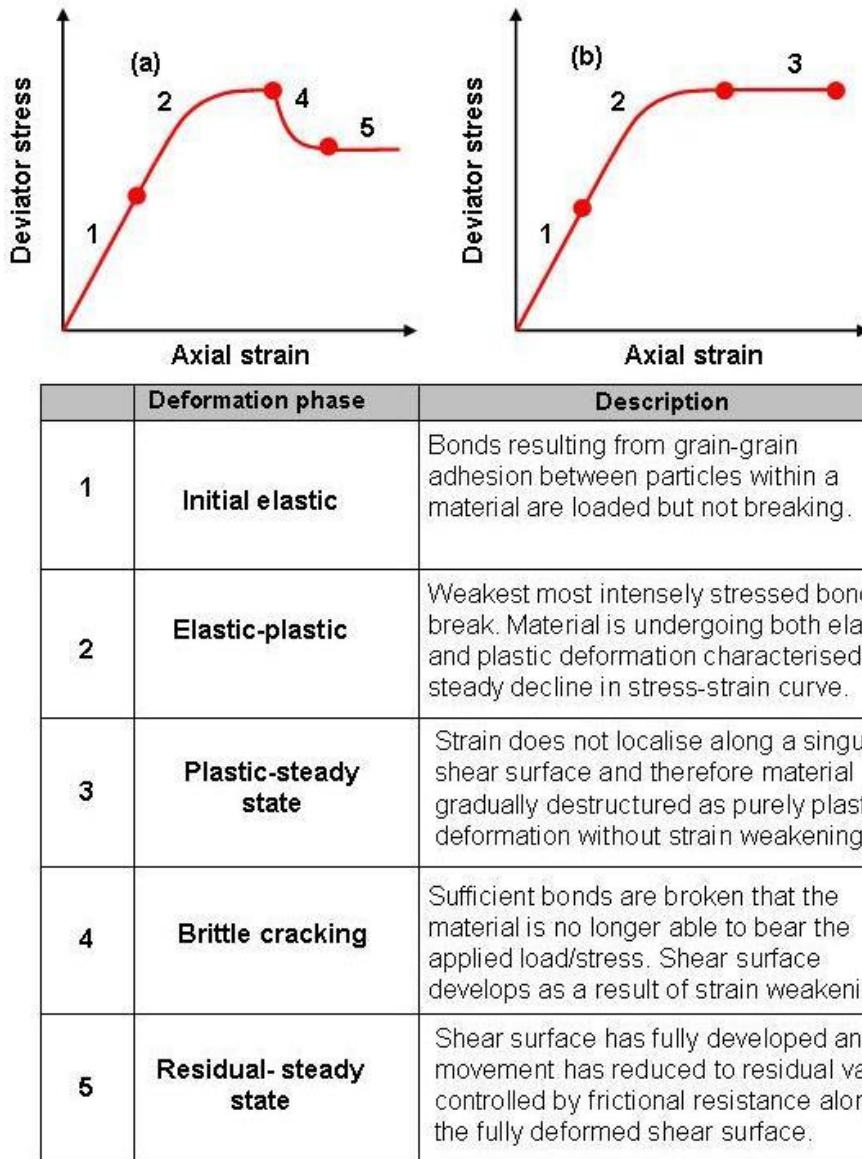


Figure 2.9 Idealised deformation patterns (a) Ductile deformation (b) Brittle deformation

Brittle failure commonly occurs in bonded, cemented or cohesive materials at relatively low confining pressures. At a confining pressure in the range of 1-250 kPa, most engineering soils will display brittle behaviour (Petley and Allison, 1997). As a consequence, it is logical that these distinctive forms of material behaviour will have key control of the movement patterns recorded at the earth's surface during landslide initiation.

2.6 Laboratory testing of rainfall induced landslides

Conventional investigations of landslide mechanisms and behaviour have relied heavily on conventional soil mechanics tests to establish the strength characteristics of the deforming shear surface. These conventional tests largely comprise drained and undrained triaxial and shear box tests to establish c' and ϕ' parameters for use in slope stability analysis. Whilst these methods may be suitable for establishing existing stability of the slope and for the design of slope remediation measures, their ability to allow interpretation of failure mechanisms is limited, and relying heavily on back analysis of slope strength parameters. This can often lead to inaccurate landslide ground models that may not be suitable to accurately assess landslide hazard potential.

A major weakness of these methods is that conventional geotechnical tests initiate shear surface development by increasing deviator stress to failure at a constant displacement rate, whilst most landslide failures occur as a result of increasing pore pressures acting within the slope, which lead to a reduction in mean effective stress at approximately constant deviator stress. It is also well established that the conventional geotechnical methods described above are weak at defining the true failure envelope in a slope (Zhu and Anderson, 1998, Orense *et al.*, 2004).

Laboratory based testing procedures that simulate failure processes caused by increasing pore pressures were initially identified by Bishop and Henkel (1962) and later progressed by Brand (1981) with the development of the field stress path concept (Fig 2.10). The key feature comprises the concept of increasing pore pressures within a soil sample at constant total normal stress and constant shear stress. This testing procedure replicates the most realistic field conditions for the majority of rainfall and groundwater induced landslides. Numerous testing procedures have been adopted using this general testing concept (e.g. Anderson and Sitar, 1995; Zhu and Anderson, 1998; Dai *et al.*, 1999).

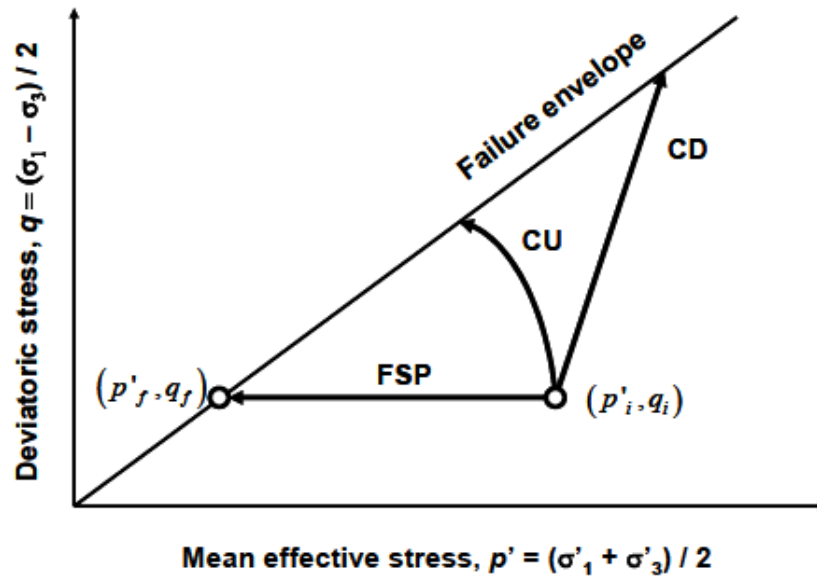


Figure 2.10 The field stress path concept (FSP) in comparison to undrained (CU) and drained (CD) stress paths (after Brand, 1981; Ng, 2007)

A range of tests were undertaken by Orense *et al.* (2004) in samples of cohesionless sandy soils where field shear conditions were replicated. The study demonstrated that for the cohesionless soils tested a failure initiation line could be defined, which for any reinflation stress path represents the point at which the sample reaches its yield strength and large scale strain accumulation is initiated (Fig 2.11).

Whilst these testing procedures have yielded some useful results, their applicability to understanding landslide behaviour has been limited. Often the rationale behind rates for pore pressure reinflation has not been considered in detail and the system capabilities for controlling pore pressures and deviator stress acting on the sample have been insufficient. Testing has also been focused largely on tropical and subtropical soils, which mainly comprise weathered soils subject to shallow failure (<5 m) in intense rainfall conditions. As a consequence testing has been skewed toward understanding residual strength materials at low mean effective stresses and very high rates of pore pressure reinflation.

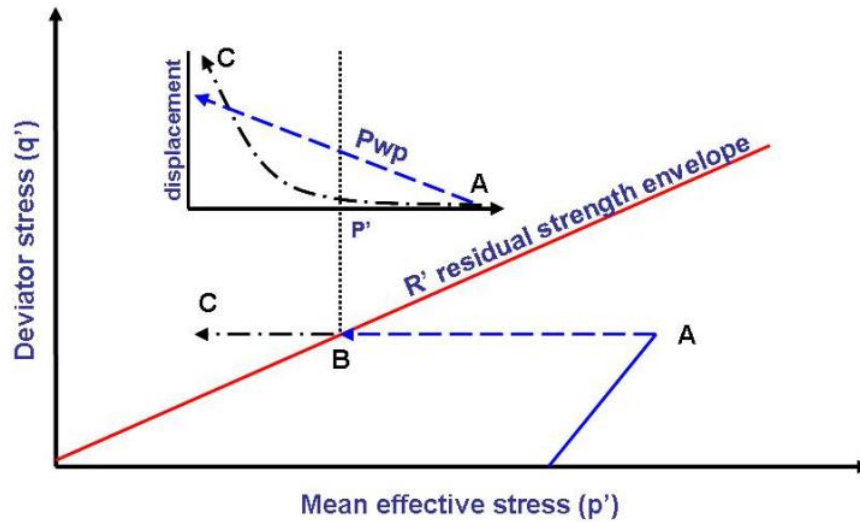


Figure 2.11 The yield strength concept (after Orense *et al.*, 2004)

Other developments have considered a range of porewater pressure inflation rates on a variety of materials in order to determine failure behaviour (Petley *et al.*, 2005a; Petley and Allison 2006; Ng and Petley, 2009). These pore pressure reinflation (PPR) tests have been conducted using a standard triaxial cell in which samples are initially isotropically consolidated to pre-determined mean effective stress. Samples are then subjected to a period of standard drained or undrained shear to a predetermined mean effective stress. The deviator stresses are then held constant and failure is initiated by increasing porewater pressures in the sample (Fig 2.12). The results of these tests, conducted over a range of materials, have illustrated two distinct patterns of deformation to failure when plotted in $1/v - t$ space. First, a negative linear trend in $1/v - t$ space that, in all circumstances, relates to brittle failure and the development of a singular shear surface. Second, an asymptotic trend in $1/v - t$ space associated with ductile or plastic deformation in samples where brittle failure is not able to occur (Petley *et al.*, 2005a).

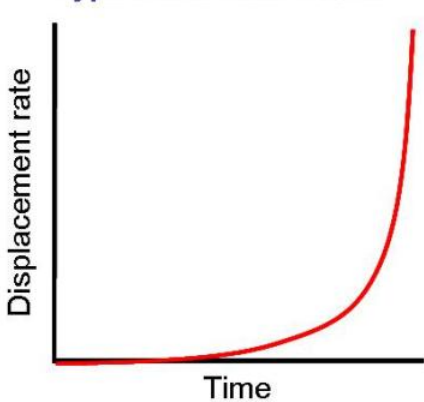
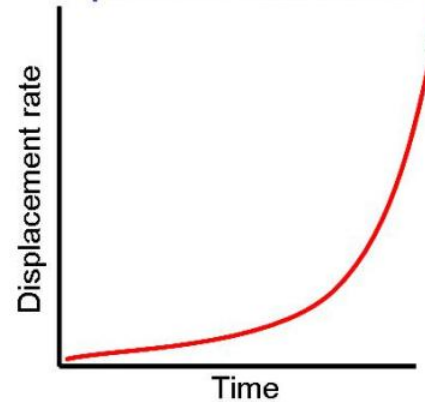
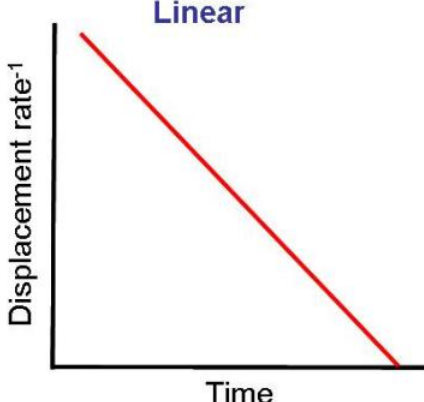
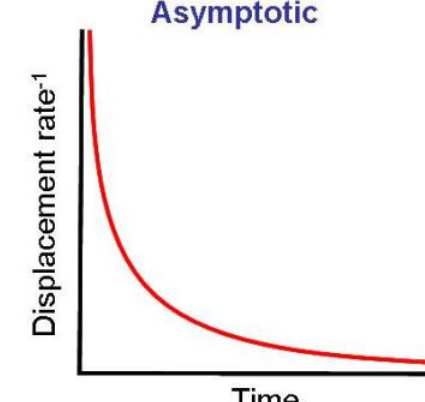

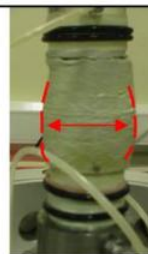
	Type I	Type II
Displacement characteristics	<p>Hyperbolic acceleration</p> 	<p>Exponential acceleration</p> 
Saito characteristics	<p>Linear</p> 	<p>Asymptotic</p> 
Shear surface characteristics	<p>Brittle</p> 	<p>Ductile</p> 
Landslides exerting movement pattern	<p>Vaiont landslide 1963, Italy (Petley and Petley, 2006)</p> <p>Intact Foxmould, Black Ven (Petley et al., 2005)</p> <p>Gault Clay, Gore Cliff. Ventnor (Petley et al., 2005)</p> <p>Gault Clay, Selbourne cutting experiment (Petley et al., 2002)</p>	<p>Vaiont landslide 1960, Italy (Petley and Petley, 2006)</p> <p>Tessina, Italy (Petley et al., 2005)</p> <p>Remoulded Foxmould, Black Ven (Petley et al., 2005)</p> <p>Lantau Island, Hong Kong, (Ng and Petley 2009)</p>

Figure 2.12 Patterns of deformation observed in PPR testing and their relationship to landslide movement patterns

Petley and Allison (2006) considered the relationship between the patterns brittle material deformation and the peak strength and residual strength failure envelopes. The results illustrated that the $1/v - t$ plots were informative in showing a more complex trend in $1/v - t$ space (Fig 2.13a). In this instance the early stages of deformation show a rapid increase in strain rate followed by a period of strain decline. The strain increases again at 110 000 seconds displaying a curved trend through time. The trend then becomes linear at approximately 166 000 seconds but with small fluctuations from the linear trend.

When the same dataset was plotted against mean effective stress (Fig 2.13b) measurable deformation began shortly after the residual strength failure envelope. After the residual strength had been surpassed a continual increase in strain rate was recorded but the pattern was not linear until the peak strength envelope had been reached (Petley and Allison, 2006). This linearity was then maintained to final failure but with cyclical fluctuations in strain rate.

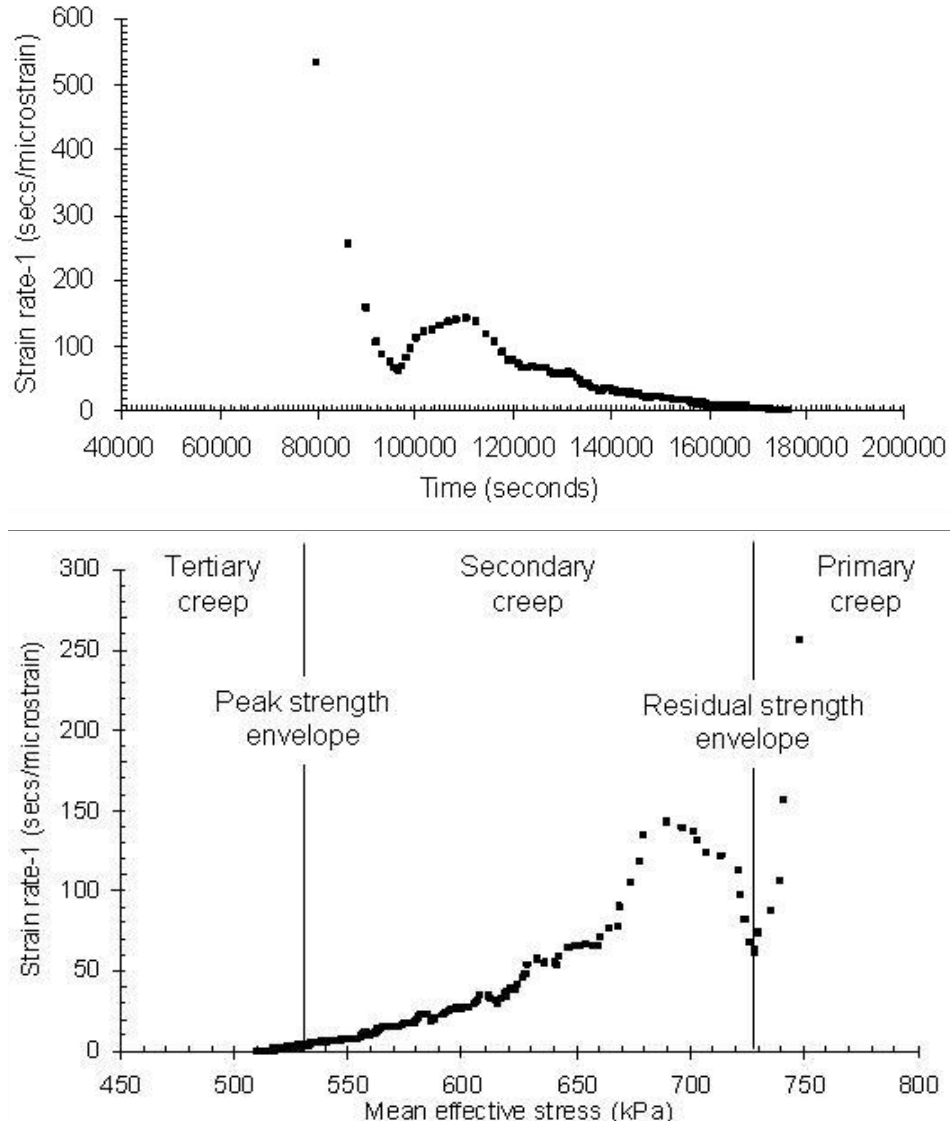


Figure 2.13(a) $1/v - t$ space plot of sample tested at 1000 kPa (b)

Interpretation of three phase creep behaviour (after Petley and Allison, 2006)

Further specialist PPR triaxial testing has been undertaken on landslide headscarps comprised of Mesozoic rhyolite lava and tuff at Tung Chung on Lantau Island, Hong Kong (Ng and Petley, 2009). In this study a series of different pore pressure rates, calculated from representative rainstorm periods, were chosen and a separate series of tests where porewater pressure was increased in steps rather than linearly. The results of these tests have been used to develop an understanding of the patterns of movement that are observed in shallow plastic landslides (e.g. Allison and Brunsden,

1990). The progressive patterns of movement have been defined as three stages (Fig 2.14):

1. Stage 1 is characterised by very low strain rates when the mean effective stresses are still high.
2. Stage 2 occurs as the mean effective stress decreases and associated strain increases. During this phase non-linear pulses in pore pressure increase lead to the development of measureable but significantly variable strain rates are observed.
3. Stage 3 occurs where porewater pressures are increased to a sufficient level that the landslide accelerates to final failure. This phase is believed to be associated with the restructuring of material within the landslide shear zone towards the critical state.

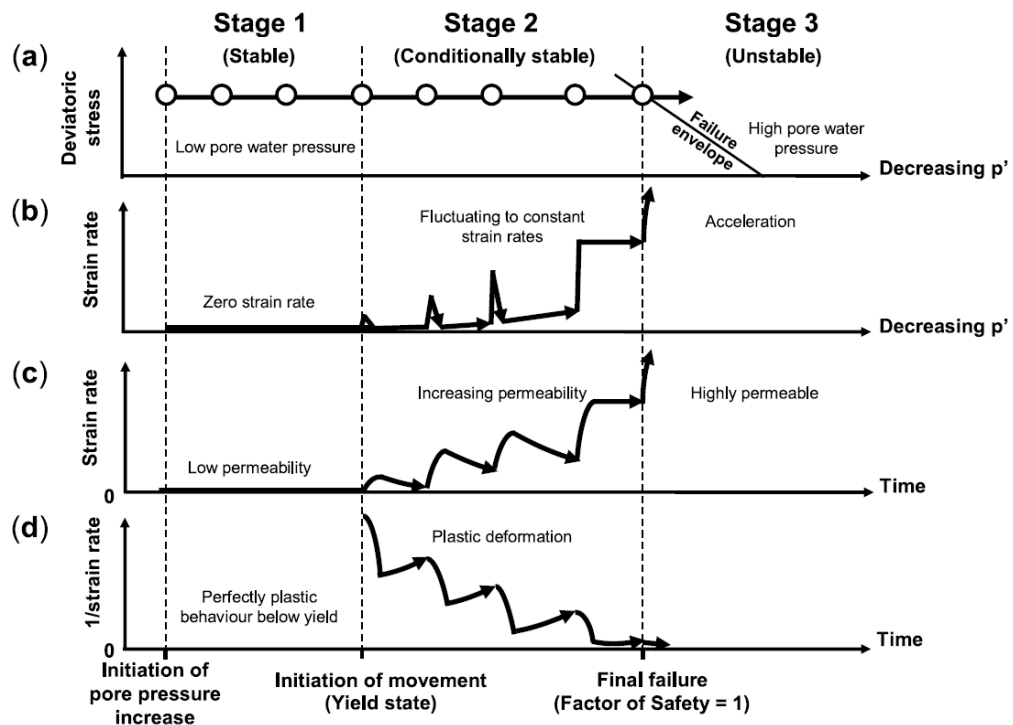


Figure 2.14 Schematic diagrams illustrating 3 stages of landslide movement in residual soils (after Ng and Petley, 2009)

Importantly, Ng and Petley (2009) demonstrated that final failure can occur even with pore pressures being held constant, which indicates that the rapid development of strain to failure is associated with the internal restructuring of the material at the shear surface (Fig 2.15).

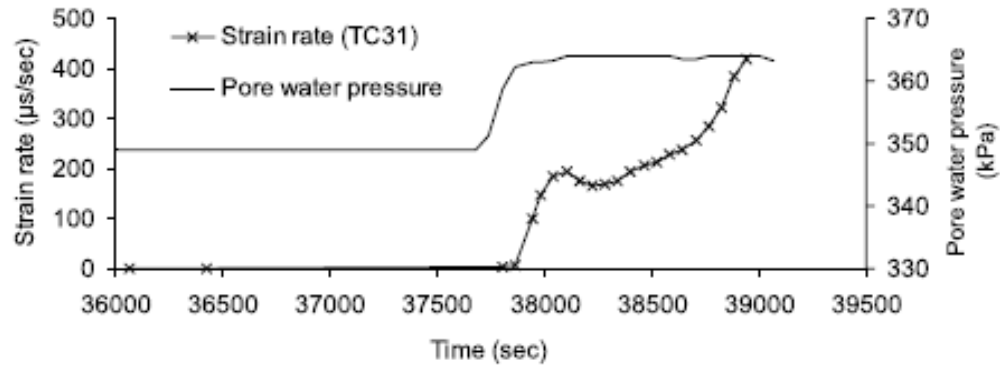


Figure 2.15 Plot of axial strain rates against time showing rapid acceleration under constant stress conditions prior to final failure (after Ng and Petley, 2009)

2.7 Patterns of landslide movement

Landslide data collected through real-time monitoring has been compiled from a wide range of landslide sites globally. These show distinctive patterns of movement during phases of landslide acceleration and deceleration. Petley *et al.* (2002) recognised the existence of landslide behaviour styles ranging from long term creep, catastrophic accelerations with no creep, and catastrophic movements with creep.

Petley *et al.* (2002) analysed these patterns of movement in a variety of landslides and successfully recognised two distinct trends related to different basal deformation regimes. These are: (1) a negative linear trend characteristic of a large surge or catastrophic event; and (2) an asymptotic trend characteristic of a landslide undergoing creep movements, though the rate of strain can be very high.

In general, first time failures tend to exhibit considerable, and sometimes rapid, displacements during failure, while renewals of movement in landslides

on pre-existing shears are usually associated with slow and relatively limited displacements (Hutchinson, 1967). This pattern of behaviour is consistent with the nature of the corresponding stress-displacement curves for the respective slip surfaces. In first time slides these commonly have a significant degree of brittleness, arising from the existence of a peak strength followed by strain softening, whereas in slides on a pre-existing shear, the slip surface is at or near its residual strength and thus approximates to rigid plastic or elasto-plastic behaviour with negligible brittleness (Hutchinson, 2001). Thus, in many cases the catastrophic movement is associated with the reduction from peak to residual strength associated with brittle failure.

Petley *et al.* (2002) and Kilburn and Petley (2003) successfully linked the linear trend to crack nucleation and shear surface development. This work showed that in brittle materials the development of strain rate with time follows a hyperbolic function, giving the linear trend in $1/v - t$ space, as the inverse rate of displacement changes linearly with time, and thus at the point of failure the strain rate will become infinitely large. Failure, therefore, occurs where $1/v = 0$ (Petley *et al.*, 2002). Voight (1988) noted an inverse linear trend in $1/v - t$ space and has attempted to describe these trends on empirical grounds. Kilburn and Petley (2003) used this relationship to propose a slow cracking model, which may provide a quantitative forecasting of slope movement to failure. The slow cracking model also accounts for the minimum volumes required for catastrophic collapse, and is readily catalysed by circulating water. It thus offers a natural mechanism for explaining the catastrophic acceleration to failure in deep-seated landslides.

The linear trend has been demonstrated for a number of monitored landslide failures. For example, it is clearly demonstrated for the Selbourne Cutting experiment, which consisted of a 9 m deep cut slope in Gault Clay that was brought to failure through pore pressure recharge (Cooper *et al.*, 1998). The site was extensively instrumented using piezometers, inclinometers and surface extensionometers, and detailed information obtained. Inclinometer records from within the landslide provided an insight into the initiation and progressive failure of the slope (Fig 2.16). The general effects indicate that the

early phases of movement were dominated by internal deformations, whilst the later stages are dominated by rapid acceleration suggesting propagation of a fracture up-slope (Petley *et al.*, 2002; Petley, 2004).

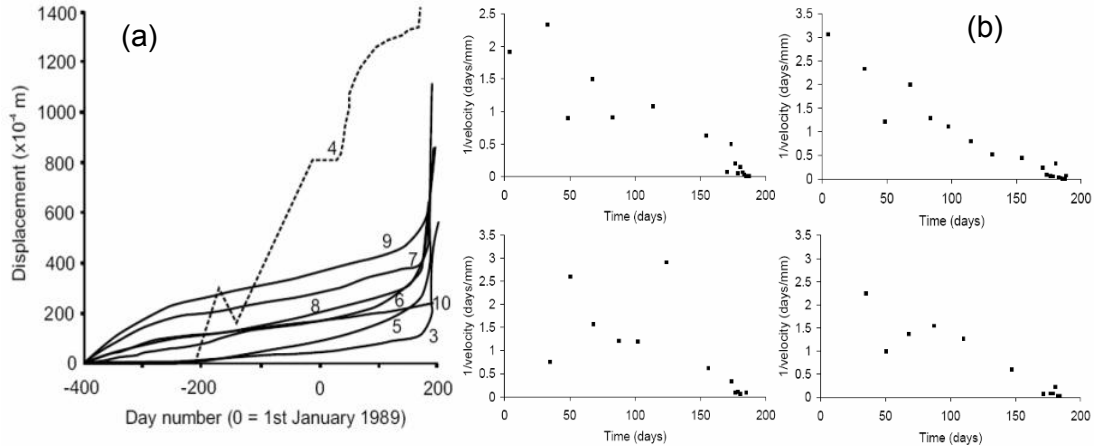


Figure 2.16 The Selbourne Cutting experiment (a) Patterns of displacement measured; (b) 1/velocity patterns to final failure, (after Petley, 2004)

Saito linearity only correlates with brittle deformation characteristics and therefore has only been linked to landslides in cohesive materials undergoing first time failure. In the case of seasonally active slopes, analysis in $1/v - t$ space generates an asymptotic trend suggesting acceleration to a constant velocity or creep rate. Evidence of these asymptotic movement patterns have been displayed within the Tessina landslide (Fig 2.17), where examination of the movement patterns using EDM data sets (Petley *et al.*, 2005c) revealed four distinct patterns of movement within the landslide complex: (1) very slow movements (less than 1mm per day); (2) low movement rates (2-3 mm per day); (3) moderate movement rates (approximately 10mm per day); and (4) episodic, very rapid movements (1-2 m per day).

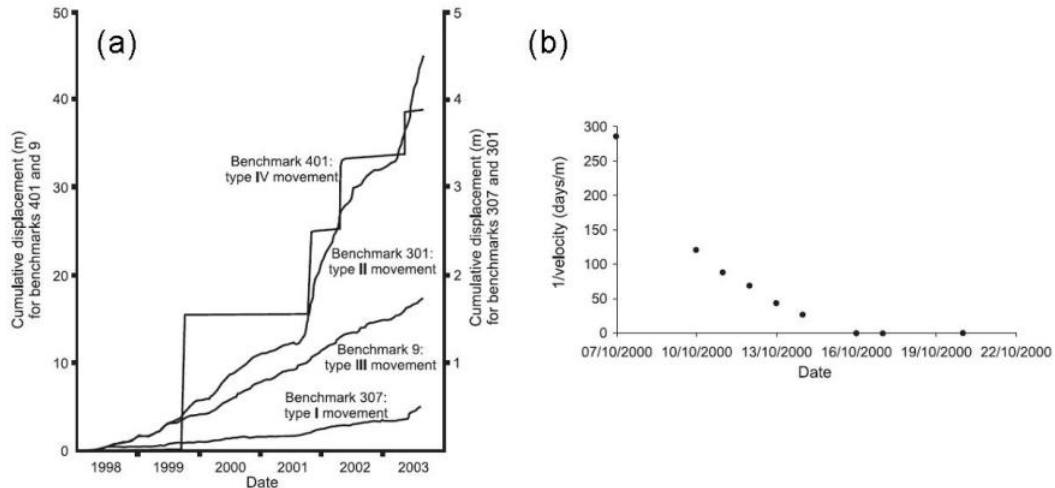


Figure 2.17 Displacement patterns observed within the Tessina landslide (a) displacement against time for four representative monitoring points (b) asymptotic trend of movement in $1/v - t$ space (after Petley et al., 2005c)

These results, although supporting the notion of the asymptotic trend materials displacing along non-brittle failure surfaces, further illustrate the complexity and variability of different movement patterns. This suggests that further geotechnical testing is required to understand the subtleties of movement in these materials and how they may inform on the behaviour of pre-existing landslides and non-cohesive materials.

Further investigations into reactivated landslides, however, often show complex movement behaviour to be related to groundwater fluctuations (e.g. Fort *et al.*, 2000). This is probably most evident in the patterns of movement in mudslides (e.g. Hutchinson 1970; 1983; Hutchinson and Bhandari 1971; Prior and Stephens, 1972). However, detailed analysis of mudslide movement patterns on the Isle of Purbeck (Allison, and Brunsden, 1990) suggested that mudslide movement could be divided into four multiple components: (1) 'stick slip'; (2) gradual or graded slips; (3) 'rapid surge' events over short time periods; and (4) unexplained 'random movements.' Each pattern of movement was shown to display a characteristic pattern of porewater pressure change.

In the case of multiple 'stick slip', movements were related to relatively slow or gradual rises and falls in porewater pressure and typically resulted in a downslope movement of approximately 8 cm (Fig 2.18).

In contrast, graded slip movements however showed a maximum displacement downslope of 35 cm and were generally characterised by greater displacements over a proportionally shorter time than multiple stick slip movements. Porewater pressure readings illustrated a gradual rise in porewater pressure at the start of movement, followed by a more rapid rise in groundwater and subsequently larger movement of the monitoring pins, which continued as the porewater pressures began to slowly decline (Fig 2.19).

Surge movements involved large spatial displacements of 3 m occurring over short time periods of approximately 20 minutes. Each surge was further preceded by increasing porewater pressure at the top and toe of the mudslide, and immediately before the event groundwater rise was significantly faster than in either the multiple or graded movement events (Fig 2.20).

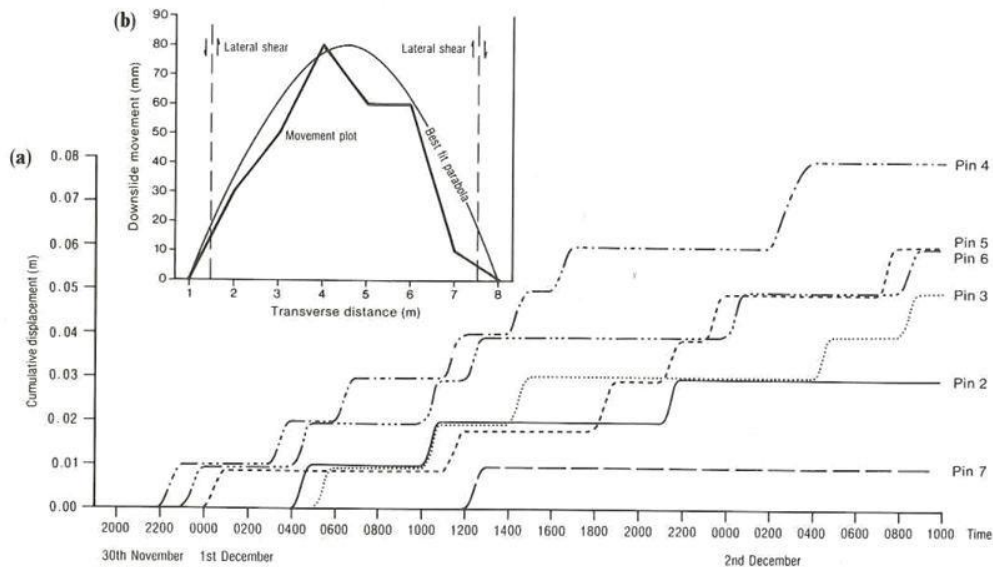


Figure 2.18 (a) A multiple stick slip movement plot (b) a horizontal velocity plot of a multiple stick-slip movement (after Allison and Brunsden, 1990)

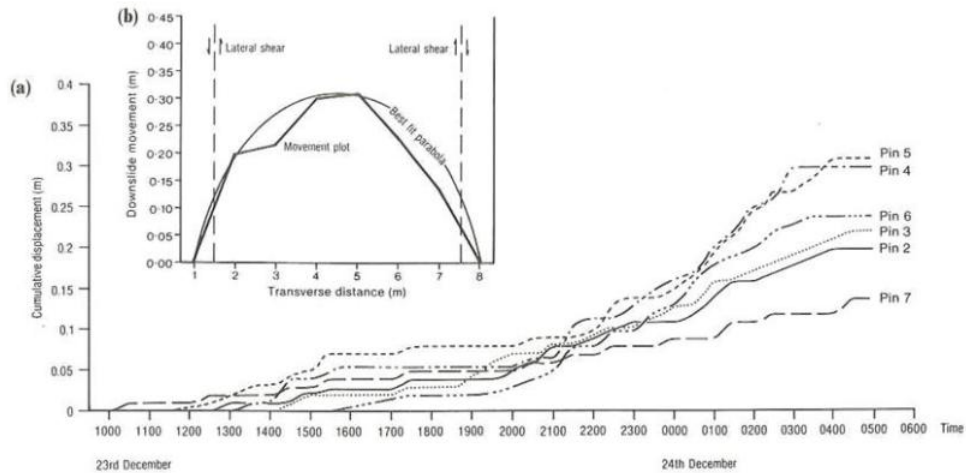


Figure 2.19 (a) A graded movement plot (b) a horizontal velocity plot of graded movement (after Allison and Brunsden, 1990)

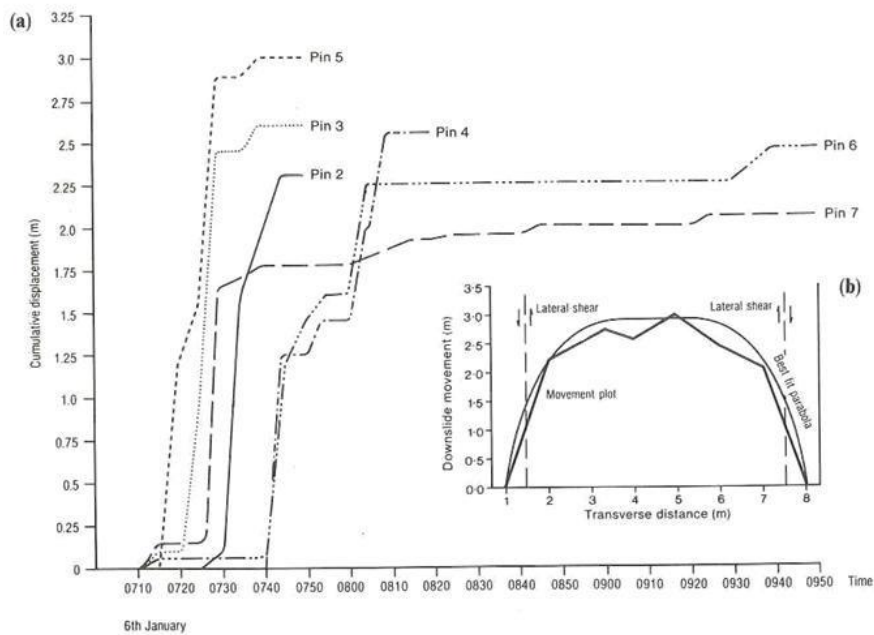


Figure 2.20 (a) A surge movement plot; (b) a horizontal velocity plot of surge movement (after Allison and Brunsden, 1990)

These results illustrate that the complex relationships between material properties, landscape inheritance and groundwater conditions have a fundamental influence on the movement patterns and behaviour experienced in a landslide system. Understanding the relationships between these factors

and the deformation characteristics is essential if effective remediation and management of landslide hazards is to be achieved.

2.8 Conceptual models of progressive landslide development

Whilst the initial concept of progressive landslide development can be traced as far back as Terzaghi (1950), the first attempt to explain the *mechanisms* associated with the development of the concept were made by Bjerrum (1967) who identified this as one of the difficult problems in soil mechanics. Bjerrum's progressive shear surface concept was based on the advances made by Skempton (1964) in relation to the residual strength properties of overconsolidated clay. Skempton concluded:

1. The residual shear strength of overconsolidated clay (σ'_r) is independent of the original strength of the clay and associated material properties such as moisture content and liquidity index. The residual strength seems only dependent on the size, shape and mineralogical composition of the constituent particles.
2. Calculated average shear stresses along failure surfaces of a number of overconsolidated clays show a greater resemblance to the residual strength than the peak strength, and in some analyses slides in natural slopes have demonstrated shear stresses at failure can be nearly equal to the residual shear strength.
3. As a consequence of (1) and (2) it was concluded that slides in overconsolidated clays were preceded by the progressive development of a failure surface. In natural slopes, where sufficient time has been available for the development of sliding surfaces by progressive failure, the ultimate stability depends on the residual shear strength only.

This theory suggests that, in slopes where sufficient time is available for the progressive development of a sliding surface, ultimate stability is governed by the residual strength value. This theory represented a great advance in understanding slope failure development and as a consequence slope engineering has become much more focused on predicting the minimum resistance of clay. Whilst such an advance has had undoubted benefits in the

appropriate development and design of specification slope remediation structures, this approach can clearly lead to the development of over conservative and often commercially unviable stabilisation solutions. The approach also offers a suitable understanding of progressive development mechanisms in order to accurately advise landslide hazard and risk management strategies. Despite this advance there is still a need to understand the mechanisms of progressive strength reduction along a given shear surface.

Bjerrum (1967) postulated a generalised model for the progressive failure of slopes in over-consolidated clays leading to the development of a continuous sliding surface. Bjerrum's model considers a simplified small-scale uniform slope of inclination (α) as illustrated in Figure 2.21a. The model focuses on the stresses acting along a surface parallel to the ground surface, at a depth (z) of an equilibrium block (OAA'O'). Originally, the only shear stresses existing along OA are those produced by the gravitational force of the block, the lateral earth pressures (E) acting at either end of the block being equal and opposite. The shear stress due to gravity can therefore be expressed as:

$$\tau = \gamma Z \sin \alpha \cos \alpha \quad (\text{Eq. 2.8})$$

As the slope is currently stable shear stress due to gravity is less than the peak strength of the clay.

For progressive failure to initiate Bjerrum (1967) argues that a discontinuity must exist somewhere in the slope and therefore suggests a cutting with vertical walls is made down to depth z adjacent to the considered section. The removal of lateral support on O'O by excavation produces a redistribution of the internal stresses in the block OAA'O'. Provided that AA' is a sufficient distance from OO', and that the lateral stress AA' has remained unaltered, the equilibrium of the block OAA'O' can only be maintained if the shear force

along OA increases by the amount E , the total internal lateral earth pressure on AA'.

This additional shear stress will not be uniformly distributed. The maximum additional stress will occur at O and the will be approximately as illustrated in Figure 2.21b.

The occurrence of a shear failure at the base of block OO'P₁P₁ will, in the first instance, mean a reduction of the shear stresses on OP₁ from the theoretical value expressed above to the peak strength. Correspondingly, the internal lateral stresses in the clay block OO'P₁P₁ will diminish. Due to the elastic behaviour of the clay this lateral unloading will cause the clay to expand towards the excavation by sliding on the newly formed failure plane OP₁ (Fig 2.21c). The resulting differential strain (Fig 2.21d) across the failure zone is governed by the recoverable strain energy of the clay. If this is large enough the strain will be sufficient to reduce the shear strength from the peak to residual value. Providing the residual shear strength is low compared with the peak shear strength, the shear failure and consequent strain will cause a large reduction of the shear stresses along OP₁ and a corresponding increase in shear stresses on the surface to the right of P₁.

The conditions above illustrate how a shear surface can progress along a shear plane up to point P₁. For the shear surface to advance further Bjerrum considered the equilibrium of the next block, P₁BB'P₁', where section BB is a sufficient distance from P₁P₁' that the lateral stresses on BB' are unaffected by what has happened to up to point P₁. As before the shear stresses along the base P₁B of the block are considered, but in this instance the additional shear stresses due to the internal lateral stresses in the clay, are dependent upon the difference between the lateral forces E and E_p acting on the upslope and downslope sections of the block.

If the maximum shear stress is greater than the peak shear strength of the clay the local failure will develop into a progressive failure. This in turn means that the smaller the value of E_p the greater the likelihood of the failure

progressing. Prior to the excavation E_p would have been equal to E . The local unloading caused by the excavation and the reduction in shear stresses along OP1 when the initial failure occurred resulted in a reduction of E_p .

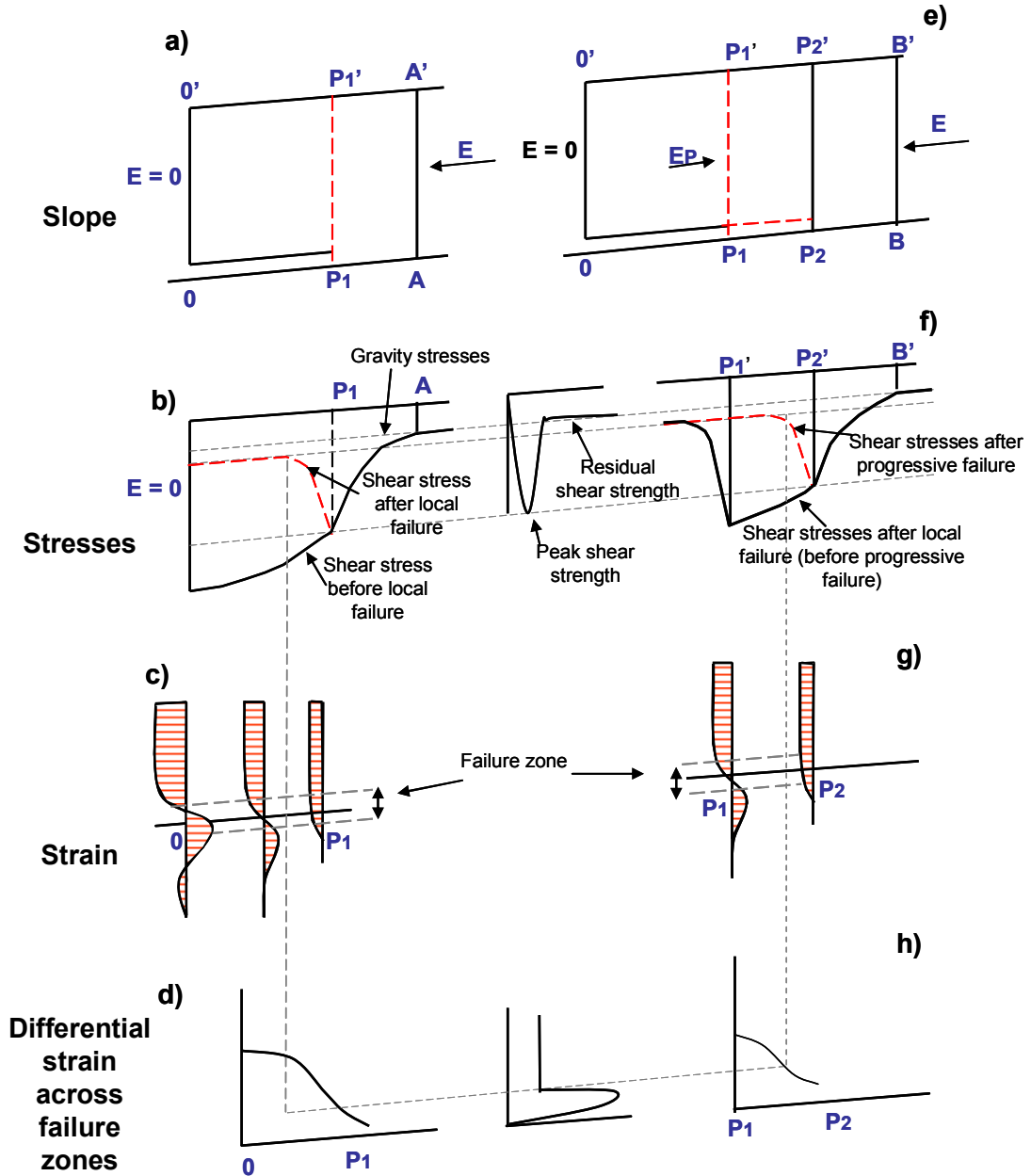


Figure 2.21 Principle of development of a continual sliding surface by progressive failure (after Bjerrum, 1967)

Bjerrum concludes that, under this model of shear surface development, progressive failure can only occur when the following three conditions are satisfied:

1. The development of a continuous shear surface by progressive failure only occurs if local shear stresses exceed the peak strength of clay.
2. The progression of the shear surface must be accompanied by a local differential strain in the zone of shear failure, sufficient to strain the clay beyond failure.
3. The clay must show a large and rapid decrease in shear strength with strain after the failure strength has been mobilised. In these circumstances the shear resistance in the failure zone will not obstruct the movement required to obtain the differential strain and as a consequence, the zone of stress concentration is moved into the neighbouring zone of unfailed clay.

Whilst Bjerrum's model provides a simplified concept for understanding the progressive development of a shear surface in over-consolidated clays it has been developed only for simple slopes of homogenous materials along a linear shear surface. As discussed previously (see Section 2.2.) in the majority of cases landslides can be classified as 'complex' occurring along a non linear shear surface and often through several heterogeneous material types. Similarly, the model focuses on a landslide initiation event caused by toe unloading. This in turn leads to a widely held view that crack development occurs from the slope toe and later retrogresses upslope. Whilst there is much evidence of landslide events which have been caused by toe unloading (e.g. Varley *et al.*, 1996) there is also a significant occurrence of landslides caused by other mechanisms, such as through raised pore pressures, which are unlikely to result in the same differential stresses acting across the shear surface.

Finally, the Bjerrum model requires a localised increase in shear stresses that exceeds the peak strength of the material. As a consequence the model is not consistent with the pre-failure strain behaviour of materials as identified in PPI testing by Petley and Allison (2006). The results of these tests demonstrated

progressive development to failure of shear surfaces before the material peak strength is reached, which indicated deformation of the shear surface is occurring prior to failure. This assertion is further supported by other studies on the initiation of slip surfaces (e.g. Burland, 1990; Georgiannou and Burland, 2006).

2.8.1 State and rate dependent friction model

A power law model to explain the acceleration to failure within landslides has been proposed by Helmstetter *et al.* (2004). The model provides a physical basis for this law based on a slider block model that uses the state and velocity dependent friction law established through laboratory testing and used to model earthquake friction (Fig 2.22). This slider block model attempts to explain the acceleration of the landslide by assuming the landslide is a rigid sliding slab of material, the motion of which is governed by the friction acting at the base of the block under gravity (Helmstetter *et al.*, 2004). Within such a conceptual model, the complexity of the landslide behaviour results from:

1. the dynamics of the block behaviour;
2. the dynamics of interactions between the block and the stratum, and
3. the history of external loading.

Previous attempts at modelling landslides using a rigid slider-block have taken either a constant friction coefficient or a slip- or velocity-dependent friction coefficient between the rigid block and the surface.

In this model four possible regimes are required to explain the displacement of a landslide mass:

1. Velocity weakening / unstable acceleration
2. Velocity strengthening/ stable or constant acceleration
3. Deceleration regime III
4. Deceleration regime IV

The model correlated well with displacement records from both the Vaiont and the La Clapiere landslides. The model suggested that the Vaiont landslide was in the 'unstable velocity weakening' regime, whilst the La Clapiere landslide was in the 'stable velocity strengthening' regime. The model was

further validated by Sornette *et al.* (2004), who assessed the predictability of movements within the two landsides, concluding that failure of the Vaiont landslide was predictable some 20 days prior to final failure.

The simplicity of this method, however, limits the shear surface conditions that could be modelled. Critically, the slider block model cannot account either for a landslide, deforming along a ductile shear zone, or for the significance of variable porewater pressures acting at the shear surface.

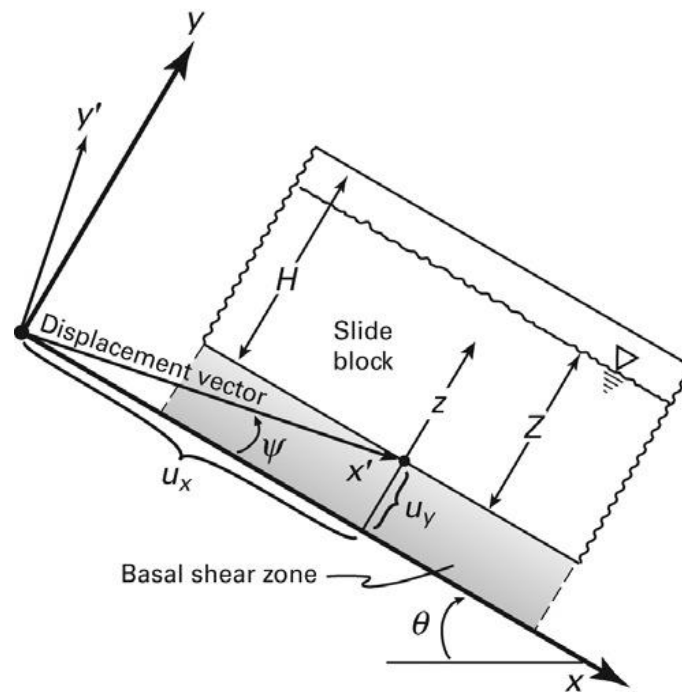


Figure 2.22 Schematic illustrating Iverson's slider block model (after Iverson, 2005).

Pore pressure variability has been analysed in more recent slider block models (e.g. Iverson, 2005). In Iverson's model the stress state is treated as one dimensional and statically determinate, making the use of stress-strain formulae unnecessary. Instead the motion of the landslide obeys Newton's second law and is resisted only by basal Coulomb friction. The model devised was based on Hutchinson's sliding-consolidation model (1986a) in which the translation of the block is regulated by a basal pore fluid pressure that obeys a

one-dimensional diffusion (Iverson, 2005). The results conclude that the rates and styles of landslide motion were dependent on the effects of porewater pressure, which are governed by dilatancy and contraction at the basal shear zone. Iverson (2005), concludes that landslide motion resulting from pore pressures, acting to overcome Coulomb friction within the shear zone, can lead either to rapid acceleration or to longer term stabilisation, depending on the effects of dilation and negative pore pressure feedback mechanisms acting in the shear zone. The transition between these two states is argued largely to result from the physical properties of the landslide materials and the history of forcing by rain infiltration. In the case of clay-rich landslides, slow motions may be stabilised permanently by dilatancy feedback. In typically sand-rich soils, however, transition from slow, to nearly steady motion to rapid acceleration, can occur quickly (Iverson, 2005).

Whilst these models have successfully represented a series of different landslide movement patterns, neither slider block model, described above, provides an adequate explanation of episodic 'stick-slip' ground movements, as previously observed at a series of landslide sites (e.g. Allison and Brunsden; Petley *et al.*, 2005c). Similarly, whilst Iverson (2005) and Helmstetter *et al.* (2004) both recognise the significance of material properties in controlling ground movement patterns, laboratory testing data to support these models have been limited and are largely based on high permeability soils, as traditional laboratory testing for clay rich soils has often suffered from difficulties in generating reproducible results (e.g. Watry and Ehlig, 1995).

2.8.2 Progressive landslide model- micro-cracking and shear surface development

Recent studies have analysed deformation mechanisms and movement type, together with novel pore pressure reinflation testing, using a triaxial cell (Petley *et al.*, 2005a). This research has been used to propose a new conceptual model for the progressive development of landslide failures (Fig 2.23) (Petley *et al.*, 2005a; 2005b).

This reveals that a slope, initially with no signs of instability (zero displacement), will undergo micro-cracking once pore pressures are elevated to a point where the effective strength of the material is reduced sufficiently to allow micro-crack development. Because this process will cause permanent damage to the shear surface, some displacement will be observed. When the pore pressure rises once again beyond a key threshold, the effective strength is again lowered to a point where more micro-cracking will take place and further strain will develop. This continual damage through raised pore pressure may occur multiple times over long timescales. For example, in some slopes the 1 in 100 year return interval rainfall event may be required to promote micro-cracking. The progressive weakening of a material to the point of failure, therefore, may occur over timescales that range from seconds to millennia. The continued process will therefore reduce the overall strength of the shear zone. Final failure begins when the failure initiation line is reached (Petley *et al.*, 2005b). At this point the micro-crack density within the sample becomes sufficiently high that interaction between them can occur, leading to an increase in the stress intensity at the tip of the adjacent micro-cracks, causing them to lengthen without a need for an associated change in the bulk stress state (Petley *et al.*, 2005b). The lengthening of micro-cracks in turn increases the stress intensity at the crack tips of adjacent micro-cracks with each step, and thus the processes 'runs away' catastrophically leading to a hyperbolic increase in strain rate. Eventually the micro-cracks coalesce and a shear surface is developed. At this point displacement is controlled by other factors such as the deviator stress acting upon the mass, the frictional resistance of the shear surface and the drop from peak to residual strength in the material. In all cases the landslide will fail but the rate of strain during runout is likely to be controlled by these other influences.

This model, initially proposed by Petley *et al.* (2005a), and further developed by Petley *et al.* (2005b), explains the linearity in $1/v - t$ space as proposed by Saito (1965) and Voight (1988), the movement patterns observed in cohesive materials in natural landslides and correlates well with pore pressure inflation testing results (e.g. Zhu and Anderson, 1998; Tsukamoto, 2002; Petley *et al.*,

2005a). This model requires further validation using real complex landslide systems, especially those associated with continual creep reactivation and landslides occurring in materials with little or no cohesion. Therefore, further testing of landslides moving on pre-existing shear surfaces is required to develop these methods into real-time methods for assessing landslide behaviour and forecasting the potential and likelihood of future failure.

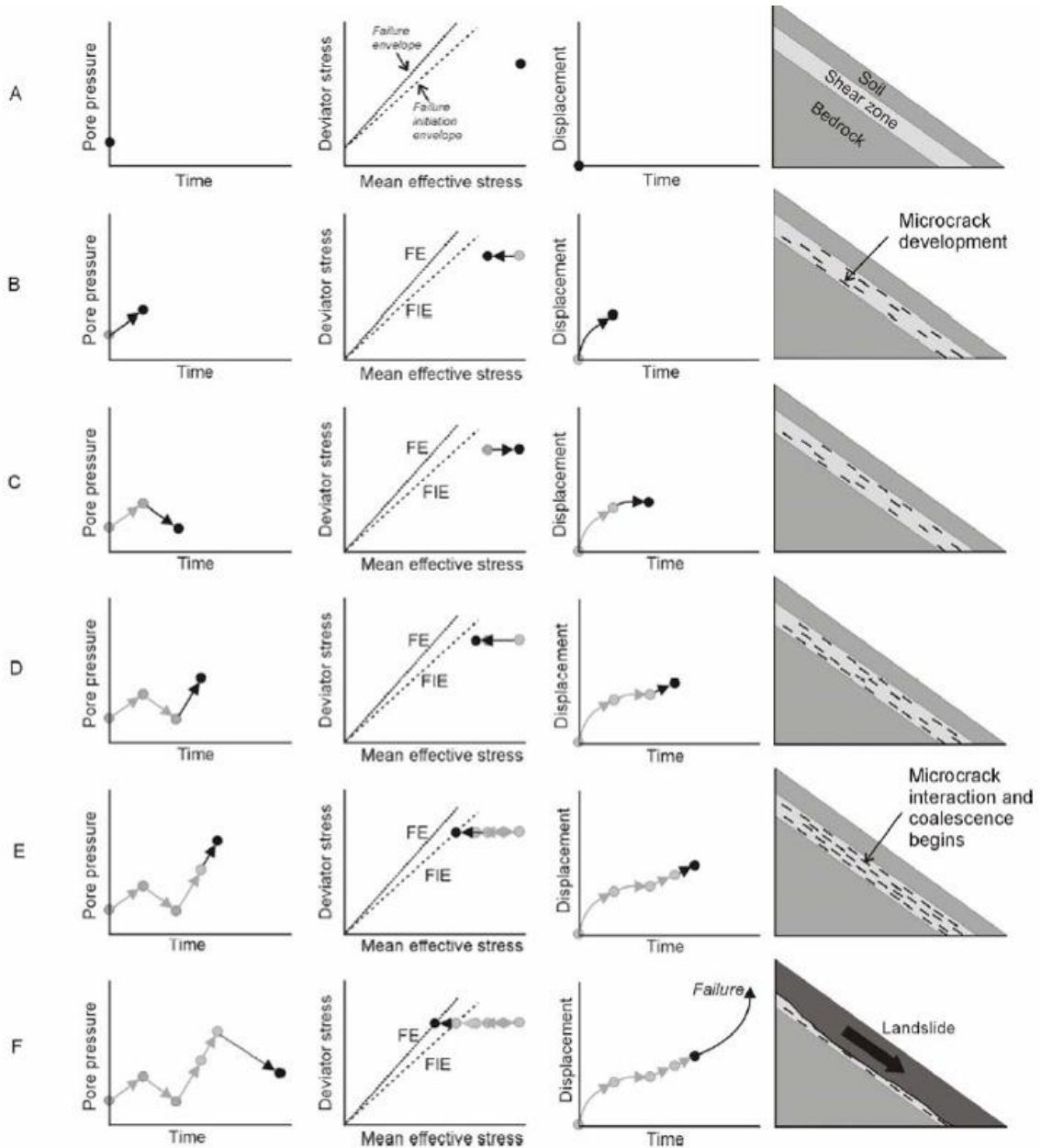


Figure 2.23 New model for the progressive development of a shear surface after Petley et al. (2005b)

2.9 Calibrating the progressive failure models with landslide monitoring

The New Tredegar Landslide, which occurred in 1930, offers an opportunity to assess the validity of the progressive landslide model against the pre-failure behaviour of a first time landslide. At this site daily surface movement monitoring occurred for approximately 60 days before the landslide catastrophically failed (Bentley and Siddle, 2000). The earliest evidence of ground movements in the area consist of unsubstantiated reports of displacement in nearby slopes during and after construction of a railway in 1856 (Knox, 1927). In 1905 an adjacent landslide caused damage to the colliery shafts and road and localised movement continued thereafter. In the early part of 1930, new movements began causing concern when fissures appeared in the upper part of the slope and daily monitoring was initiated. On the 12th April 1930, a catastrophic failure occurred, completely overwhelming the road and destroying the colliery building and shafts (Bentley and Siddle 2000).

Daily monitored displacement records (Fig 2.24) illustrate a pattern similar to the three phases of deformation to failure as described by Varnes (1983). Monitored displacement records have been analysed in $v - t$ space, showing a series of periods of accelerated creep prior to final failure. These patterns of acceleration have been analysed in $1/v - t$ space, which illustrates different patterns of displacement associated with the three phases of creep. Firstly, there are a series of pre-failure asymptotic trends, suggesting a period of initially recoverable plastic deformation. This is followed by a transition from the ductile deformation phase to the brittle phase. In the final days prior to failure the landslide displays the linear trend, with movement no longer being related to the groundwater conditions.

This pattern of behaviour to final failure is similar to previous published patterns of movement at Vaiont (Petley and Petley, 2006), where the same three patterns of $1/\text{velocity}$ was experienced, although over a much longer time period. This behaviour has also been illustrated in triaxial reinflation testing (Petley *et al.*, 2005a; 2005b).

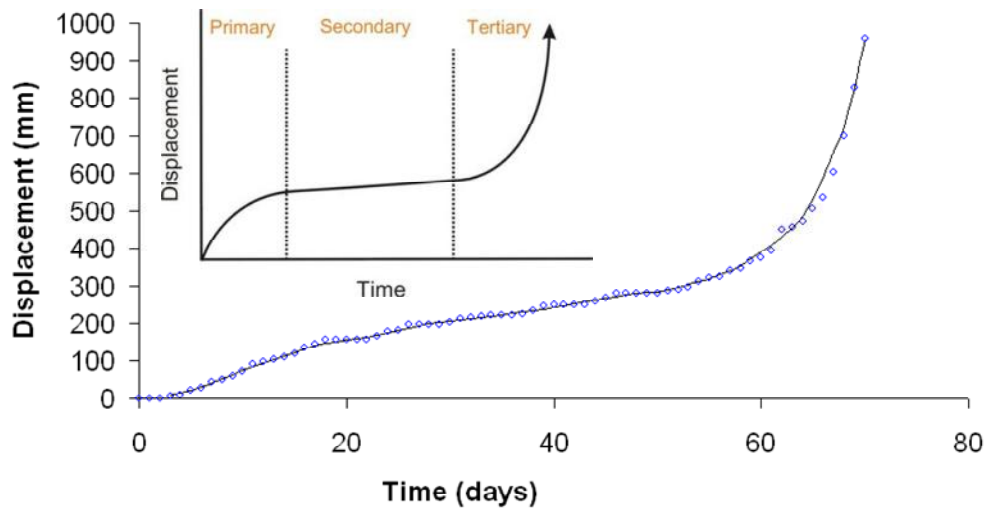


Figure 2.24 Relationship between the three phase creep model (Varnes, 1978) and the displacement pattern to failure of the New Tredegar landslide in 1930

This model has been applied to the New Tredegar landslide (Fig 2.25). The initial movement occurs as pore pressures are elevated to a point where deformation begins. At this stage strain hardening processes are elevated above the strain weakening processes (Fig 2.25(1)), expressed in $1/v - t$ space as an asymptotic trend that represents initial creep (Fig 2.25a). This period is followed by Secondary creep, characterised by a period of slower deformation related to the increase in weakening processes which act to balance the strain hardening processes (Fig 2.25(2)). This movement is characterised by continued accelerated creep phases during periods in which pore pressures are inflated sufficiently to reduce mean effective stresses and develop further micro-cracking. At this stage micro-cracking is still distributed throughout a large area of the material and therefore movements are asymptotic to reflect the apparent overall ductile behaviour of the landslide (Fig 2.25b). During these periods the overall material shear strength of the shear zone is reducing, and so it is likely that the mean effective stress state at which movement can occur is continually increasing. Eventually, the landslide transitions into Tertiary creep (Fig 2.25 (3)), which in this case occurs at an elevated but not exceptional groundwater level. This causes a

transition in the behaviour of the shear surface, similar to phase E in the Petley *et al.* (2005b) model (Fig 2.23), in which the material strength properties reduce, and the micro-crack density within the shear zone is sufficiently high that interaction between them occurs. At this stage strain hardening processes have been dramatically reduced and strain weakening processes are dominant as a singular shear surface develops. The shear stresses are now concentrated at the micro-crack tips. The stress concentration in the non-sheared material, under a constant shear load, allows the rate of deformation to accelerate hyperbolically. This period of final shear surface development is depicted by the linear trend in $1/v - t$ space (Fig 2.25c). It is clear at this stage that the shear surface development is now strain controlled until a singular shear surface is formed. At this point the landslide fails as the theoretical displacement rate becomes infinite and other processes start to reduce the strain rate.

During the final stages of deformation a transition occurs between ductile/plastic to purely brittle behaviour, which is reflected in the $1/v - t$ plot (Fig 2.26b). This pattern of deformation is similar to that demonstrated at Vaiont (Fig 2.26a) prior to the catastrophic 1963 disaster (Petley and Petley, 2006).

The 1930 New Tredegar landslide event supports the proposed models of progressive development of landslide failure proposed by Petley *et al.* (2005a; 2005b). The data supports the recent analysis of the Vaiont dam landslide (Petley and Petley, 2006), illustrating the early ductile movement patterns followed by a transitional trend from pure ductile deformation to brittle deformation. It further supports the existence of 'Saito' linearity during the final phase of failure (Fukuzono, 1990). The development of the linear trend in $1/v - t$ is recognisable at approximately day 56, which further highlights the potential use of this method as an effective forecasting and landslide hazard warning system

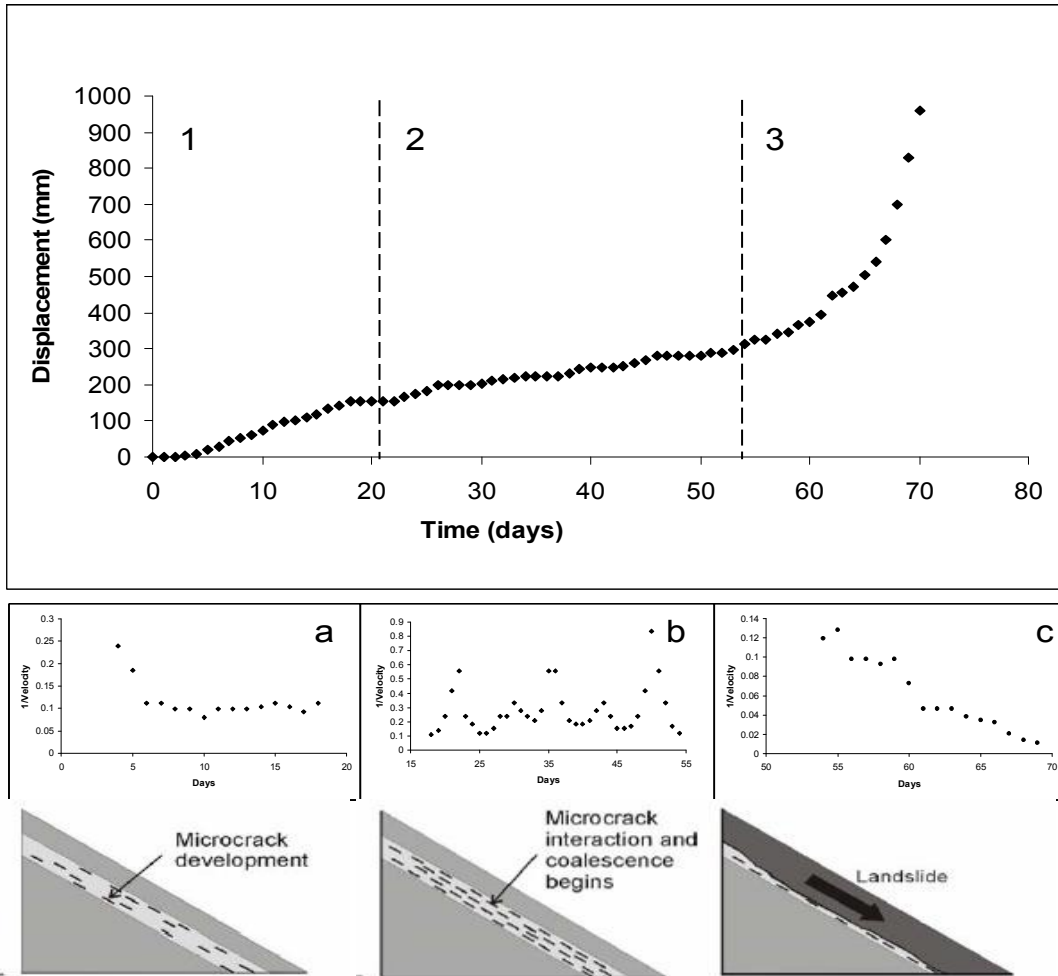


Figure 2.25 Landslide movement, New Tredegar (after Carey et al., 2007).

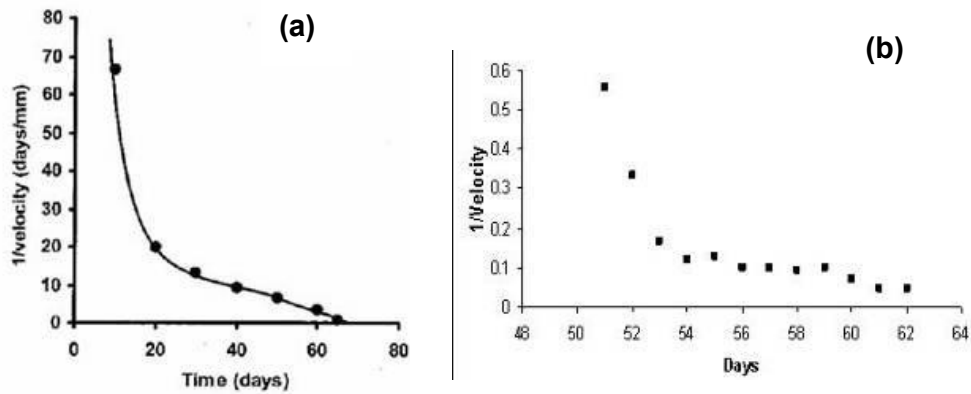


Figure 2.26 Transition from asymptotic to linear behaviour in $1/v - t$ space (a) Vaiont landslide (after Petley and Petley, 2006) (b) New Tredegar

2.10 Chapter Summary

This chapter has demonstrated how landslides represent a key natural agent or process in landform development in most upland and mountainous regions of the world. Where communities and infrastructure assets are located in these regions landslides represent a major geological hazard where significant resources and expenditure are used in mitigating landslide risk.

Whilst numerous publications have analysed and categorised landslide types based on their form, material components and movement characteristics, these classifications systems have provided only an elementary understanding of the geotechnical properties of the shear surface materials and their significance on mechanisms of failure. In particular, limited progress has been made in understanding how a hillslope progresses from a stable to unstable state at which point failure can occur. As a consequence a similar lack of knowledge of the mechanisms of landslide reactivation along pre-existing shear surfaces exists.

Although the concept of progressive failure in landslide systems has been used for over 40 years, since its formulation by Bjerrum (1967), surprisingly the detailed mechanisms through which this process occurs remain poorly understood. As a consequence, common landslide stability and management practices rely heavily on factor of safety analysis based largely on an understanding of failure envelopes using a Mohr Coulomb approach, which may not be the only possible failure criterion (Craig, 1992). Most significantly these practices do not consider the strain at or prior to failure, which may have significant implications on the stress conditions failure.

Whilst such methods may be considered adequate in developing suitable slope remediation measures for simple slope and landslide failure, their suitability for interpreting complex landside systems and assessing future landslide risk is limited. One particular weakness is the lack of correlation between observations of movement in real landslide systems and the understanding of the deformation processes occurring in the basal shear zone (Martel, 2003).

Numerous authors have developed methods of landslide prediction based on the pre-failure movement of unstable slopes (e.g Salt, 1988; Fukuzono 1988, 1990; Hayashi *et al.*, 1989) based on the Saito (1965) method of assessing patterns of linearity in $1/v - t$ space. Such methodologies have shown some success as predictors of slope failure (e.g. Voight, 1988, Petley *et al.*, 2002). The relative merits of these methodologies have been questioned (e.g. Hutchinson, 2001b) as they fail to take into account the geotechnical parameters or potential variations in porewater pressures that may impact on the time and behaviour of a landslide at failure. Furthermore, assessment of landslide failure movement patterns (e.g. Petley *et al.*, 2002; Petley and Petley, 2006) has demonstrated that two distinct movement patterns in $1/v - t$ space can occur. These patterns have subsequently been linked to the deformation properties of the materials at the shear zone, through a series of specialist pore pressure reinflation tests that replicate rainfall or groundwater induced landslide failure.

The results of these studies have led to the development of two potential models of landslide development. The first, a progressive failure slider block model (e.g. Helmsetter, 2004) and the second, a progressive failure model associated with crack nucleation and coalescence to form a brittle shear surface (e.g. Petley *et al.*, 2005).

Further research is required to link movement patterns in both first time landslides and reactivation failures to the patterns and mechanics of shear surface development in different materials, if accurate landslide failure prediction and behaviour forecasting methodologies can be established.

Chapter 3: Site Location

3.1 Introduction

The Ventnor Undercliff represents one of the deepest and largest landslide complexes in the UK, with potential impacts on a population of over 6000 residents (Fig 3.1). A review of landsliding in the UK (GSL, 1987) identified the Ventnor Undercliff as the largest urban area affected by landsliding, and as such has been subject to a number of previous studies (e.g. Chandler, 1984; Hutchinson *et al.*, 1991a, 1991b; Lee and Moore, 1991; Moore *et al.*, 1995; Hutchinson and Bromhead, 2002; Moore *et al.*, 2007a, 2007b).

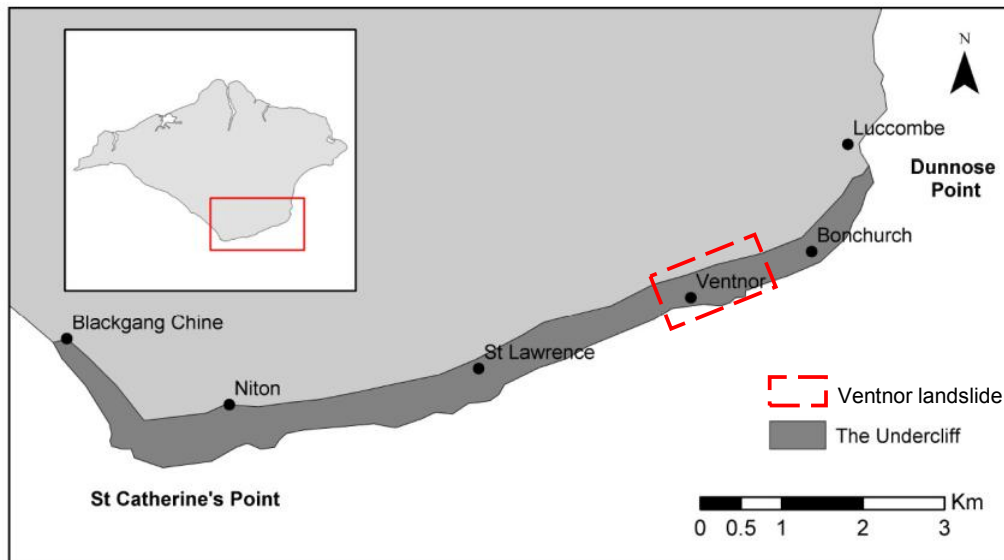


Figure 3.1 Location of the Ventnor Undercliff, Isle of Wight

Ventnor is located on the south coast of the Isle of Wight (Fig. 3.1), centred at national grid reference SZ 4557 0774. The Ventnor landslide system comprises a total area of 0.7 km² of unstable ground (Fig 3.2), with a large depression feature known as the 'Lowtherville Graben' delimiting the current landward extent of instability.

The area underlain by the landslide includes a number of notable economic assets, such as residential properties, hotels, guest houses, public houses and important roads. Halcrow (2006) identified the following key assets:

- The Newport Road (B3327)
- Steephill Down Road
- St Alban's Road and St Alban's Gardens
- Castle Road
- Park Avenue
- La Falaise car park (Bath Road)
- Spyglass Inn (Western Esplanade)
- The Royal Hotel (Belgrave Road)
- Ventnor Park (Park Avenue), and
- The Western Cliffs

The town has been subject to a number of periods of development (Table 3.1). Prior to 1828 Ventnor was a small fishing village. Considerable expansion occurred from 1828 onwards, with the development of new infrastructure and properties taking advantage of the existing terraces within the Undercliff. Significant cutting and filling operations took place and building stone was quarried along the present site of Lower Gill's Cliff Road and Belgrave Road.

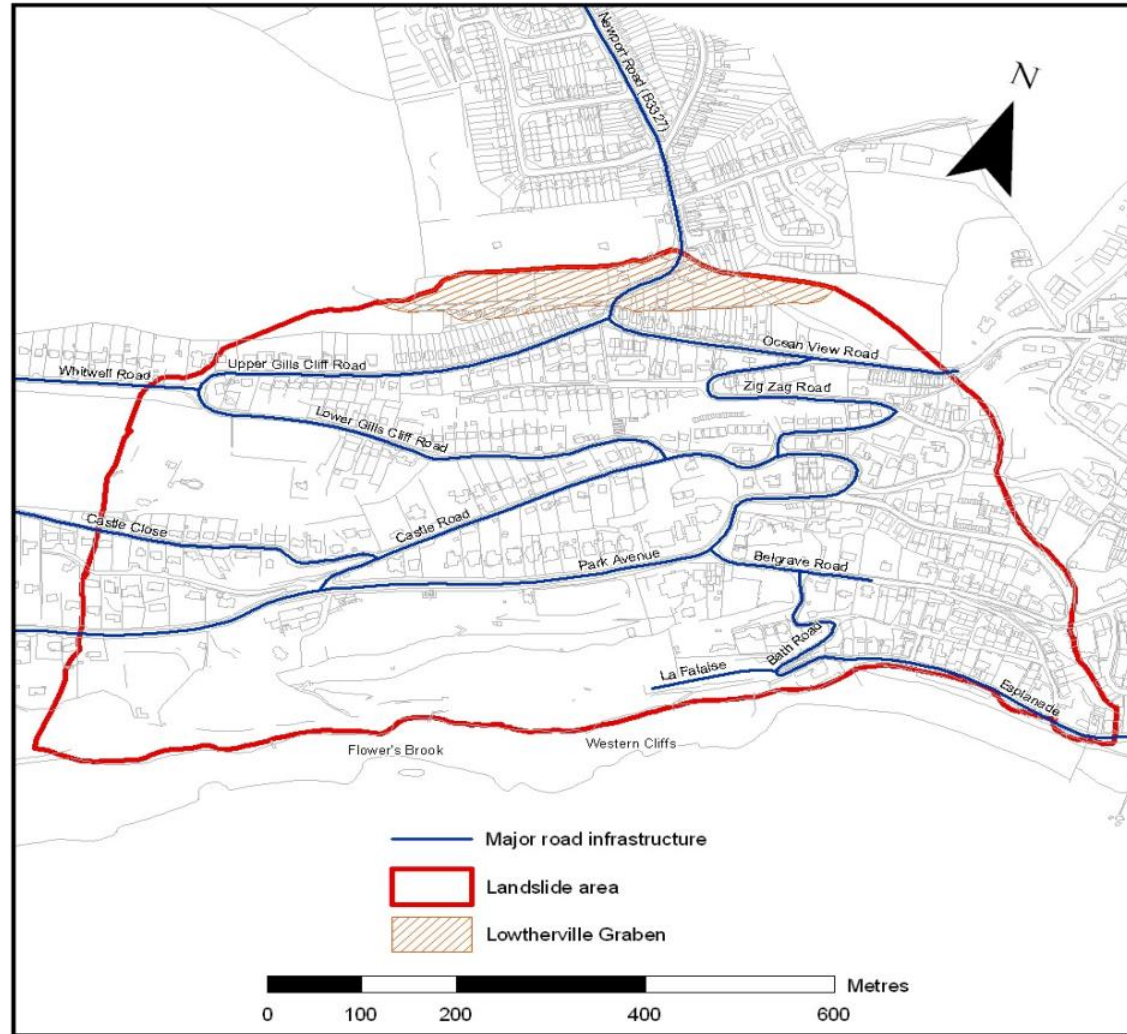


Figure 3.2 The Ventnor landslide, Lowtherville Graben and key highway infrastructure

Table 3.1 Summary of development and population growth in Ventnor (after Halcrow, 2006)

Period	Description	Estimated Population
1760's	One of the earliest properties 'St Boniface Cottage' was built at this time.	10
1795	Albin referred to small village of Ventnor.	77
1828	Expansion of Ventnor began on the sale of Earl Dysart's property at Steephill to John Hambrough who proposed plans and funded development of the area. Cove Cottage in Belgrave Road was first property in New Ventnor.	100
1829	Publication of the 'influence of climate in the prevention and cure of chronic disease' by Sir James Clark, promoting the virtues of the Undercliff climate nationally saw a rapid increase in visitors and resident population.	150
1836	The diarist Mark William Norman described the development fever in Ventnor as an 'El Dorado' with the town emerging from obscurity to notoriety.	350
1844	Ventnor Improvement Committee formed. Roads widened and new roads constructed including Zig Zag Road.	1800
1847	Ventnor esplanade constructed	2070
1851	76,000 people conveyed by horse drawn carriage between Ryde and Ventnor.	3000
1863	Attempts to construct a harbour fail.	5100
1866	Ventnor railway station completed.	5300
1880	Pier constructed but damaged soon after when a large section was swept away in December.	6000
1890's	Ventnor broadly similar in appearance to the town today.	6500
1939-45	Ventnor suffers extensive bomb damage during the war.	
1963	Closure of the Shanklin to Ventnor railway line.	7200
1990's	Coast protection works to Western Cliffs and the Esplanade.	
2003	Construction of Ventnor Haven	6050

Note: the rapid development of Ventnor between 1830 and 1844, saw many houses and walls of poor standard being built, a legacy that has contributed to the vulnerability of many structures to ground movement. Building stone was probably quarried along Lower Gill's Cliff Road and Belgrave Road.

3.2 Landslide investigation in the Undercliff

In the late 1980's a major pilot study of landsliding potential at Ventnor was commissioned by the Department of Environment as part of government research. This led to the development of Planning Policy Guidance Note 14, 'Development on Unstable Land.' The study aimed to identify the nature of ground movement in central Ventnor. It concluded that over the last 200 years Ventnor had been relatively slow moving and large-scale failures were not typical of movement experienced in many areas of the Undercliff. The pilot study led to the development of a geomorphological approach, relying on the review and analysis of available historical records of ground movement, and the understanding of landform features and processes in order to derive models of landslide behaviour. These in turn have assisted the local planning authority in managing the ground condition constraints in the Undercliff.

The requirement for detailed subsurface investigation of the Undercliff landslides was emphasised by Hutchinson and Bromhead (2002). Their paper states, "a major decision concerns whether the landslides are benign enough to live with or could generate a future unacceptable hazard and risk, to guard against which appropriate intervention would be needed." Hutchinson and Bromhead (2002) raise particular concerns over the potential failure of the depression in upper Ventnor known as the Lowtherville Graben. In their view this feature provided some of the clearest evidence in the Undercliff of a potential landslide event of considerable size.

Subsequently, the Isle of Wight Council have commissioned several subsurface investigations in Ventnor and on the Undercliff landslides including The Landslip in Upper Bonchurch and along the Undercliff Drive, near Mirables and the Orchard (Fig 3.3) (Halcrow, 2006).

Detailed ground investigations were conducted in central Ventnor in both 2002 and 2005 (Fig 3.4). Investigations comprised the drilling of five deep boreholes to confirm the landslide stratigraphy, installation of landslide movement and groundwater monitoring instruments and the collection of

samples for geotechnical testing. The investigation was conducted in order to improve understanding of the Ventnor landslide system and to assess the potential cost benefit of undertaken landslide stabilisation measures.

Despite these investigations further analysis is required to develop a better understanding of landslide failure mechanisms and future potential landslide risk; specifically those associated with the Lowtherville Graben. The site is situated in typical geological, hydro-geological and climatic conditions for deep-seated coastal landsliding in the UK and a wealth of historical and contemporary landslide monitoring and landslide mapping is available that would be difficult to replicate for any other coastal landslide sites in the UK.

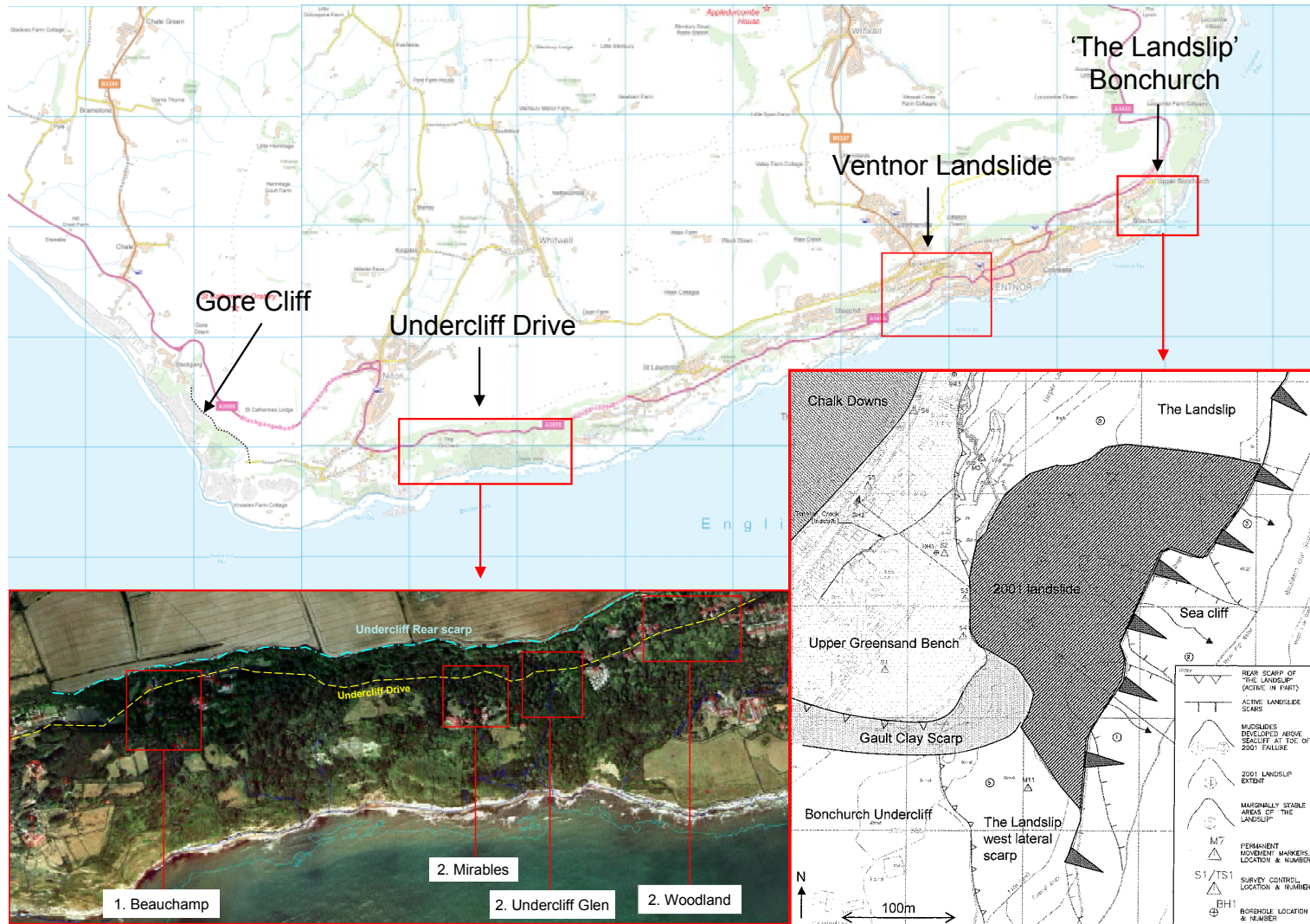


Figure 3.3 Previous investigations sites along the Undercliff

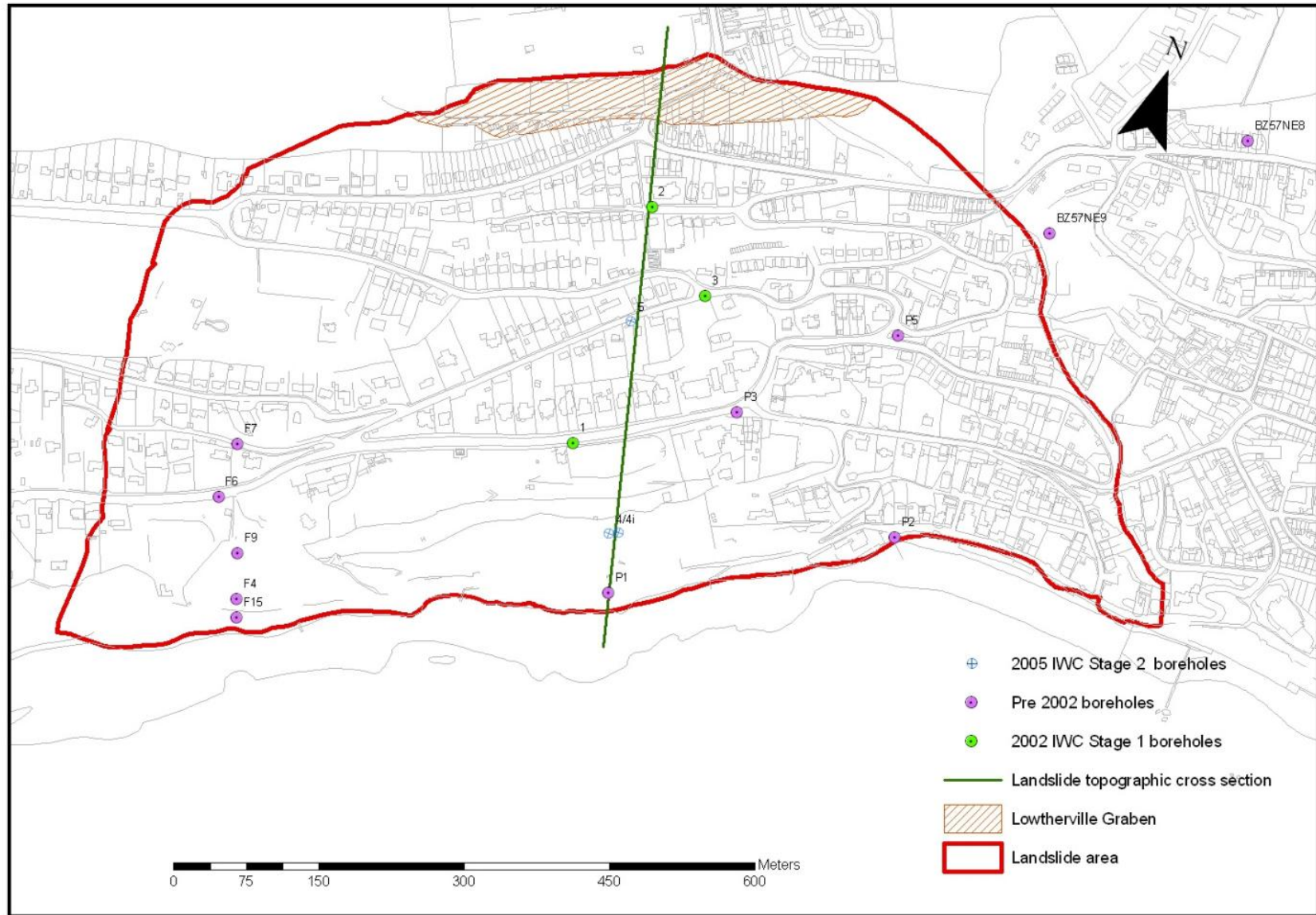


Figure 3.4 Plan of the Ventnor Ground investigations undertaken by IWC

3.3 Climate (Rainfall)

The Isle of Wight experiences one of the mildest climates in the UK due to its southerly location. Table 3.2 illustrates the average high, average, minimum and mean monthly temperatures and average monthly precipitation anticipated for the island.

Table 3.2 Summary climate data for the Isle of Wight based on monthly average readings taken from the Newport Weather Station (Elevation 15m) between 2003 and 2010 (<http://www.isleofwightweather.co.uk/>)

	Jan	Feb	Mar	Apr	May	June	July	Aug	Sept	Oct	Nov	Dec
Av High (°C)	8	8	10	12	16	18	21	21	18	15	11	9
Av Min (°C)	3	3	4	5	8	10	12	13	11	8	5	4
Mean (°C)	6	6	7	10	13	15	17	17	15	12	9	7
Av Precip (mm)	89	61	66	48	56	53	41	56	66	79	84	89

Previous references to climate and rainfall events are very limited prior to the late 19th Century. Chandler (1984) analysed weather data for three weather stations at St Catherine's Point, Royal National Hospital and Ventnor Park between 1920 and 1983. Analysis of these data sets (DOE, 1991) demonstrated a number of key observations:

- an increase in mean annual rainfall along the Undercliff from St Catherine's Point (762.3 mm) in the west to Ventnor (840 mm), and Shanklin (888.4 mm) to the east;
- an apparent trend of increasing annual rainfall totals since approximately 1920, with rainfall averaging 700-750 mm per year between 1839-1920 and over 800 mm per year since 1920, and
- three main periods of significantly higher rainfall (averaging 800 mm per year); 1874-1884, 1922-1941 and 1950 to present.

Halcrow (2006) analysed rainfall records available for the Undercliff between 1839 and 2001. A composite data set was derived from rain gauges using rainfall datasets from several sites a summarised in Table 3.3.

Table 3.3. Weather station records used to develop a long term, composite rainfall dataset for the Undercliff (1839 – present)

Station	Reading period	Easting	Northing	Elevation (m)
St Catherine's Point	1920-1988	449880	75338	20
Royal National Hospital	1839-1950	454800	76900	18
Ventnor Cemetery	1932-1988	455600	77700	135
Ventnor Park	1926-1983; 1992-present	45787	77298	60

These long-term records have been used to estimate effective rainfall (rainfall minus evapo-transpiration), which has been calculated using the methods of Thornthwaite(1948) for historical records and Penman-Montieth (1948) where direct measurement of potential evapo-transpiration is available from the automatic weather station installed at Ventnor Park.

Analysis of these records using a nine year running mean illustrates an apparent trend of increasing annual rainfall, particularly since 1920 (Fig 3.5). Mean annual rainfall of 700-750 mm occurred over the period 1839-1920 increasing to about 800 mm since 1920. The trend includes three notable periods of significantly higher rainfall (averaging over 800 mm per year) between 1874-1884, 1922-1941 and 1950 to 1975. There is also a notable seasonal variation in monthly rainfall at Ventnor comprising a typical dry period between February and August and a wetter period between September and January, with maximum monthly rainfall typically occurring in November (Fig 3.6).

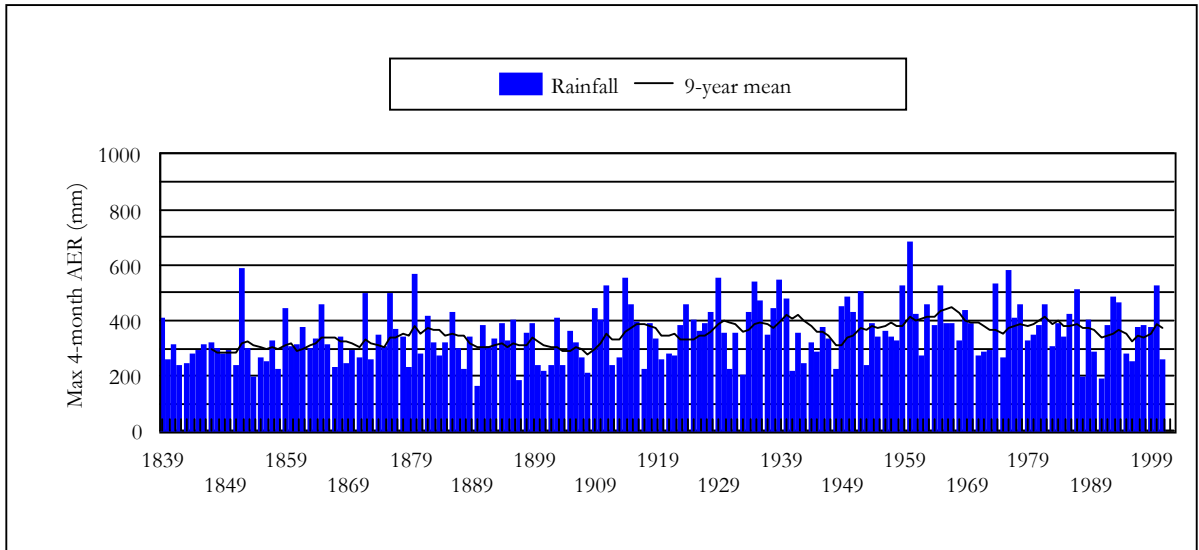


Figure 3.5 Maximum 4 month annual effective rainfall and nine year running mean between 1839 and 1999

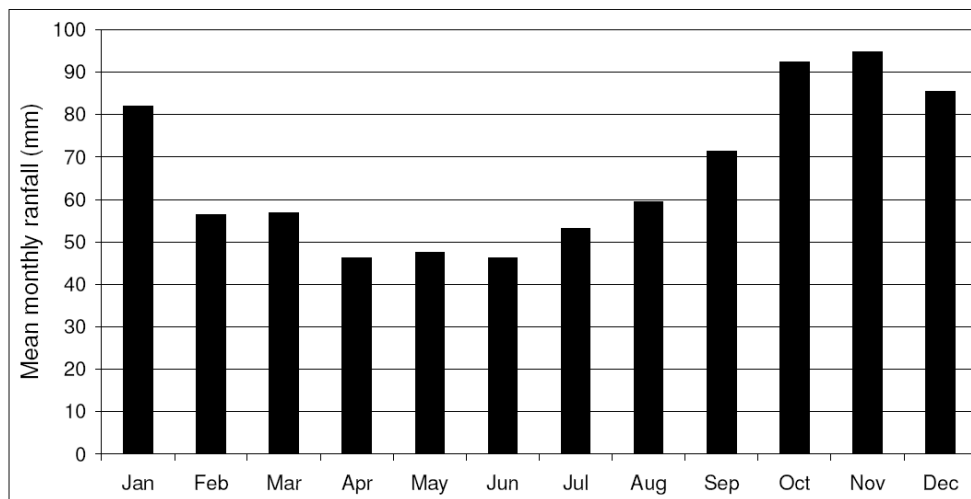


Figure 3.6 Mean monthly rainfall, Ventnor between 1839 and 2009 (after Moore et al., 2010)

3.4 Structural geology

The Isle of Wight lies within the Wessex Basin. This originated as a structural series of fault controlled basins, with much of the present day structure reflecting tectonic movements during the Variscan and Alpine Orogenies (White, 1921). The main structures of the island are two north-facing monoclinial flexures which trend E-W, parallel to the long axis of the island (Fig 3.7).

The geology of the Undercliff forms an important structural control on the development of the coastal landslide complexes (Fig 3.8). The site itself is situated on the southern limb of the asymmetric Sandown Anticline, and is composed of a complex sequence of interbedded sedimentary rocks with a seaward dip of approximately 1.5 to 2° (Moore *et al.*, 2007b). These sedimentary rocks were formed by sediments laid down during the Cretaceous period, approximately 80-120 million years BP. This generally southerly dip is superimposed with the dip of the St Lawrence syncline (Chandler, 1984) although the relative position of this feature is difficult to confirm due to the degree of disturbance to the strata as a result of landsliding.

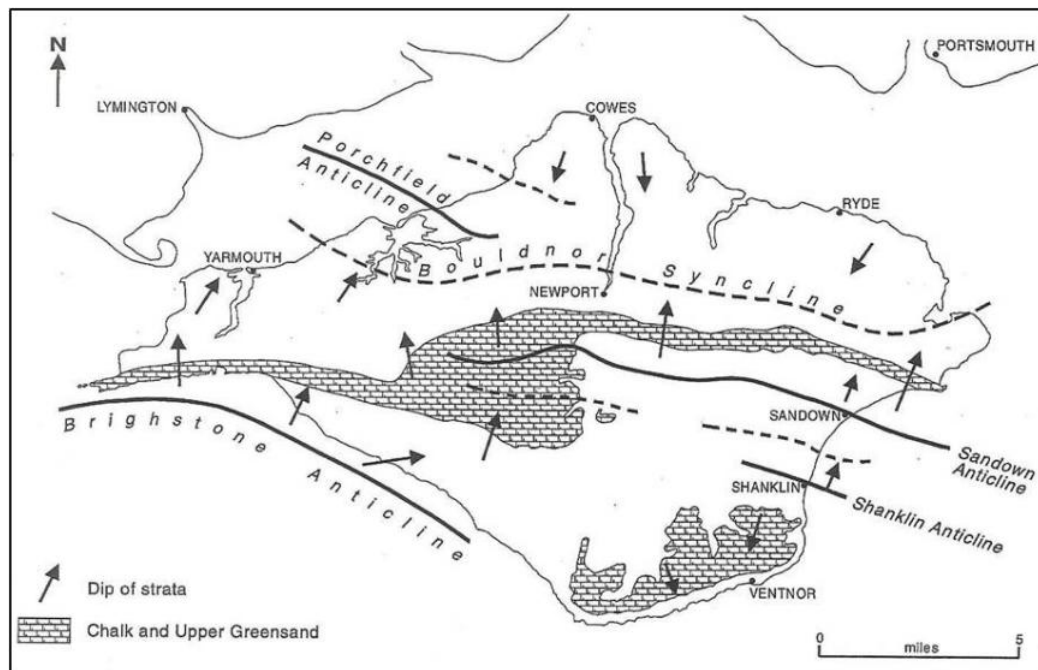


Figure 3.7 Geology of the Isle of Wight and its implications on landsliding, (after Bird, 1997)

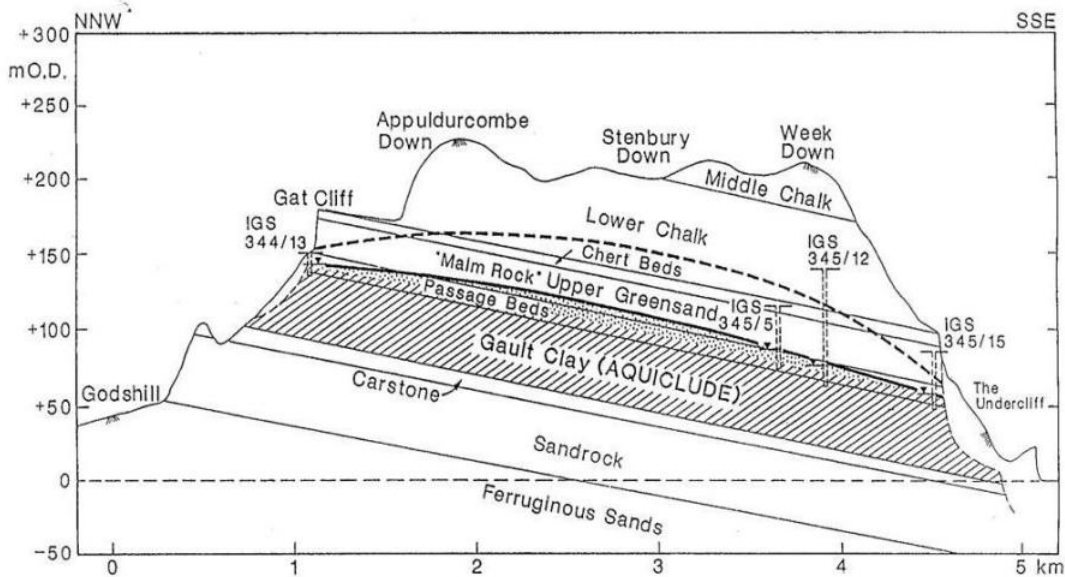


Figure 3.8 Structural geology of the Isle of Wight and its implications on landsliding, (after Chandler, 1984)

The Lower Cretaceous formations on the Isle of Wight begin with the Wealden Beds (Fig 3.9), which comprise the Wessex Marls deposited within a broad floodplain environment. These Marls were overlain by Vectis Shales, deposited within a coastal lake or lagoon environment until a period of uplift and subsequent sea level rise in the Aptian marine transgression, which subsequently led to the deposition of the Lower Greensand. The deepening sea led to the development of the Atherfield Clay Formation of the Lower Greensand Group. This group contained five distinct units; namely the Perna Beds, Chale Clay, Lower Lobster Bed, Cracker Bed, and the Upper Lobster Bed. These units comprise a series of brown-grey silty muds, silts and fine sands, with some sandier calcareous layers present in the Cracker Bed. Following this a long period of sand sedimentation, with some clay and silt inclusions, produced the Ferruginous Sand Formation.

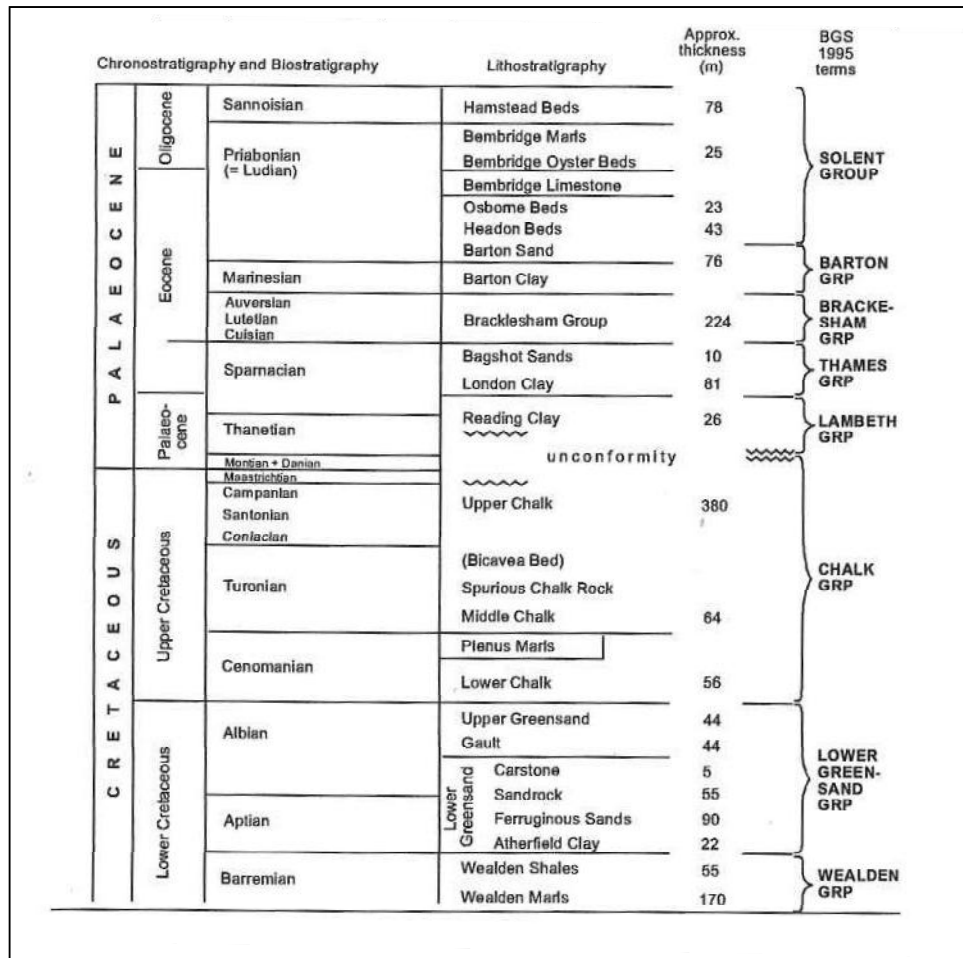


Figure 3.9 Isle of Wight stratigraphy (after Hutchinson and Bromhead, 2002)

3.5 Quaternary geology and potential origin of the Undercliff landslides

The Isle of Wight has never been glaciated, but has experienced several periods of severe periglacial conditions, and widespread periglacially-triggered landslides and periglacial solifluction deposits can thus be expected (Hutchinson and Bromhead, 2002). During the Pleistocene, prior to the breaching of the former Chalk ridge between The Needles and Ballard Point, near Swanage, it is inferred that the Solent River, a major eastward-flowing stream flowed out from Poole Harbour (Velegrakis *et al.*, 1999; Tomalin, 2000) (Fig 3.10).

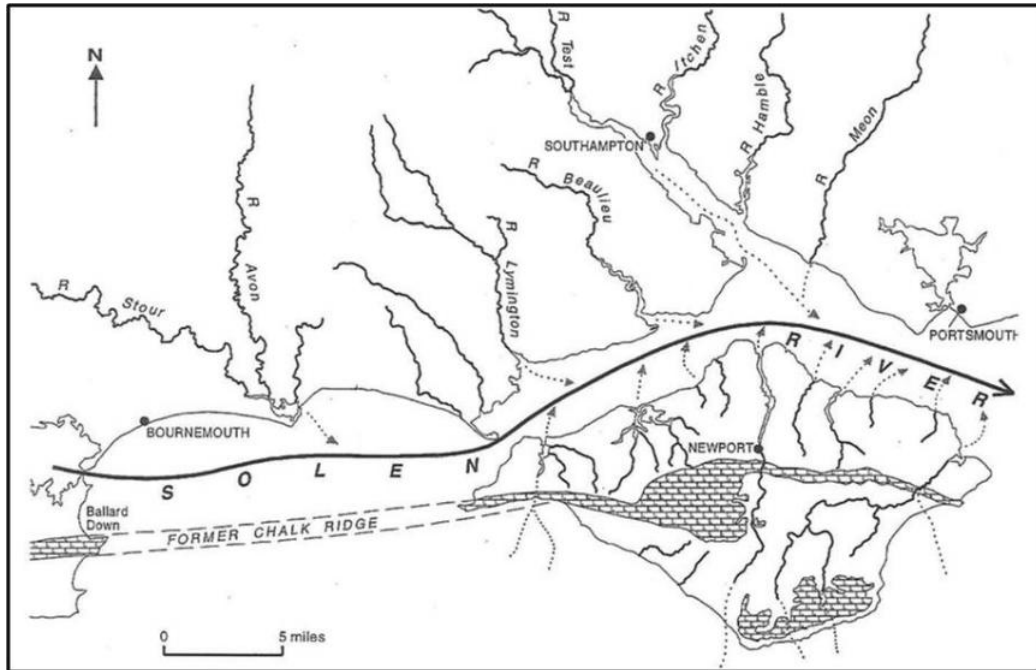


Figure 3.10 Evolution of the Solent River and former Chalk ridge that once linked the Isle of Wight to Ballard Down in Dorset (after Bird, 1997)

Defining the age and the timing of the initiation of the Undercliff landslides has been difficult. Hutchinson and Bromhead (2002) suggest that they probably initiated some distance south of the current shoreline. This would most likely have occurred on the dip slope of the Upper and Lower Cretaceous, which declines to St Catherine's Deep approximately 2.8 km offshore and with a bottom level of approximately -60 mOD (Fig 3.11). Offshore investigation has confirmed that the submarine slope is mantled by the remnants of old, deep-seated landslides to a depth of 20 m to 40 m (Clark *et al.*, 1994). Hutchinson and Bromhead (2002) suggest this provides evidence that the northern slope of St Catherine's Deep is likely to be formed of failed landslide debris.

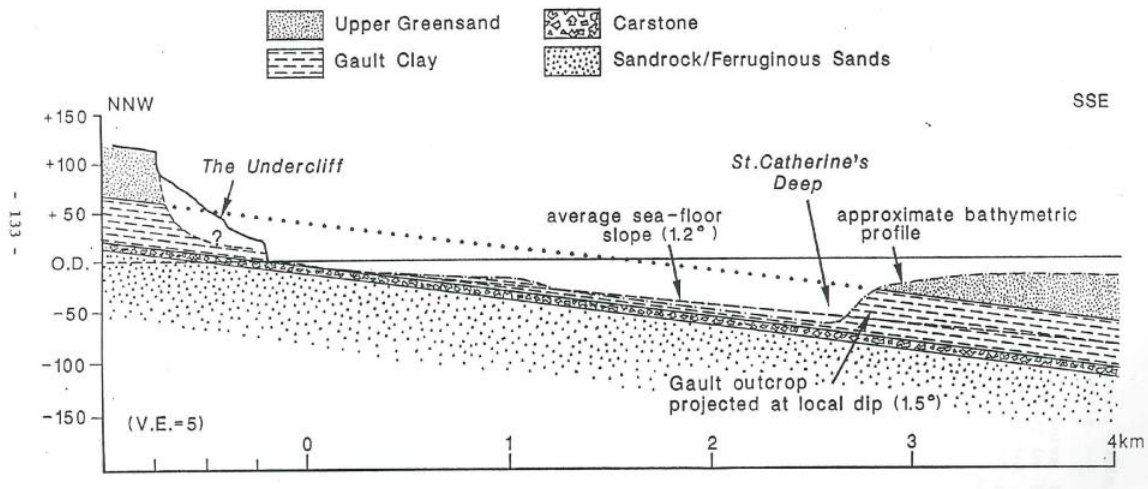


Figure 3.11 Offshore Undercliff geology to St Catherines Deep (after Chandler, 1984)

3.6 Hydrogeology

The Southern Downs of the Isle of the Wight contain two major aquifers:

1. The Chalk and Upper Greensand aquifer (referred to as 'Southern Downs Aquifer' (Chandler, 1984)), and
2. The Lower Greensand aquifer

These aquifers are separated by approximately 44 m of impermeable Gault Clay, which forms an aquiclude. The impermeable nature of the Gault Clay has led to the development of the spring line towards the base of the Upper Greensand. Whitaker (1910) observed that dips in the Southern Downs strata are sufficiently gentle to account for springs emerging along nearly the whole Gault Clay outcrop, although he noted that the most copious springs are to be expected along hillsides where the Gault Clay is at its lowest level. Alternatively, Chandler (1984) suggested that this spring line corresponds with the Passage Beds, rather than the Gault Clay, with springs issuing at a level approximately 3.5 m below the base of the Malm Rock.

The initiation of the landslides has not been fully explained, although previous research has suggested that a combination of the erosion of St Catherine's

Deep, by fluvial action possibly associated with the River Solent and Channel River, combined with marine erosion associated with past glacio-eustatically controlled sea levels, are the most likely triggers. Once formed, this landslide complex would tend to be reactivated during interglacials, when the rising sea levels would have increased coastal erosion rates.

3.7 Geological controls on landsliding

The lithological characteristics of the Cretaceous rocks, as found in the study area, have been identified elsewhere as being particularly prone to landsliding, especially in the coastal environment. The combination of hard, competent sandstones and chert beds, overlying thick overconsolidated clays has resulted in many large coastal landslides along the south coast of England. Examples of landslides in this type of geological setting include Folkestone Warren, Kent (Hutchinson *et al.*, 1980); the abandoned sea cliff behind Romney Marsh, Kent (Hutchinson *et al.*, 1985b); Fairlight Glen, East Sussex (Moore, 1986); and the Bindon landslide, East Devon (Pitts and Brunsden, 1987).

The overconsolidated Gault is underlain by alternating sandstones and clays of the Lower Greensand formations. These strata are particularly susceptible to both marine erosion and erosion by seepage at the interface of the clay layers with the overlying sandstone. An example of the erosion of Lower Greensand strata may be found at Chale Bay, Isle of Wight (Hutchinson *et al.*, 1981).

Previous reconnaissance of joint systems across the south east coast identified a number of factors that may contribute to landslide development in the area (DOE, 1991). This structural analysis revealed that exposed Cretaceous rocks are dissected by steeply dipping (between 70° and vertical), orthogonal joint sets, which exert a primary control on the morphology of rock masses involved in landslides along the coastline. The Upper Greensand Units exposed a Gore Cliff and along the rear scarp of the Undercliff show a regular spacing with the result that the cliff is dissected by a grid-like fracture pattern DOE (1991). The configuration of joints in the Cretaceous rocks is

considered to be a major control on landslide development. These previous observations of high angle structures in the Upper Greensand units exposed in at Gore Cliff pass down into the passage beds and Gault Clay suggests a possible method by which shear surfaces, developed in the Gault Clay can propagate upwards through the more competent Greensand. These joint set may, therefore, act as a major control on landslide development. Large blocks of Upper Greensand along the Undercliff and beneath Gore Cliff (Fig 3.3), whose morphology is clearly controlled by major orthogonal joint sets, have suffered detachment and horizontal movement along shear zones, likely to be located in the Gault Clay (e.g. Chandler, 1984) or the clay layers in the Sandrock (Hutchinson *et al.*, 1985).

3.8 Geomorphology of the Ventnor landslide

The geomorphology of the Ventnor Undercliff was most recently mapped in the 1990's as part of the Department of Environment pilot study of central Ventnor (GSL, 1991). These maps define the surface morphology and nature of the landslides.

The key geomorphological features identified at Ventnor (Fig 3.12) were:

- the Chalk Downs located landward of the Undercliff, which are largely unaffected by landsliding;
- an upper tier of apparent multiple rotational blocks of Upper Greensand and Chalk which account for the presence of shore parallel beaches separated by steep scarp slopes;
- the Lowtherville graben, a 450 m by 20 m subsiding block of Upper Greensand and Chalk located at the upslope margin of the upper tier landslide units. This feature has been sharply defined by two active parallel tension scarps subject to differential horizontal and vertical movement;
- a lower tier of apparently compound slides, comprising a shore parallel linear ridge of displaced Chalk debris about 500 m wide and 20 m high;
- a low-lying depression landward of the compound slide, formed from infilled Chalk debris.

The shoreline of the Undercliff runs parallel with St Catherine's Deep, a submerged valley depression described earlier (see Section 3.5). Offshore seismic survey data, collected in the intertidal zone, have indicated the presence of planed-off remnants of landslide blocks on the seabed seaward of the Western Cliffs

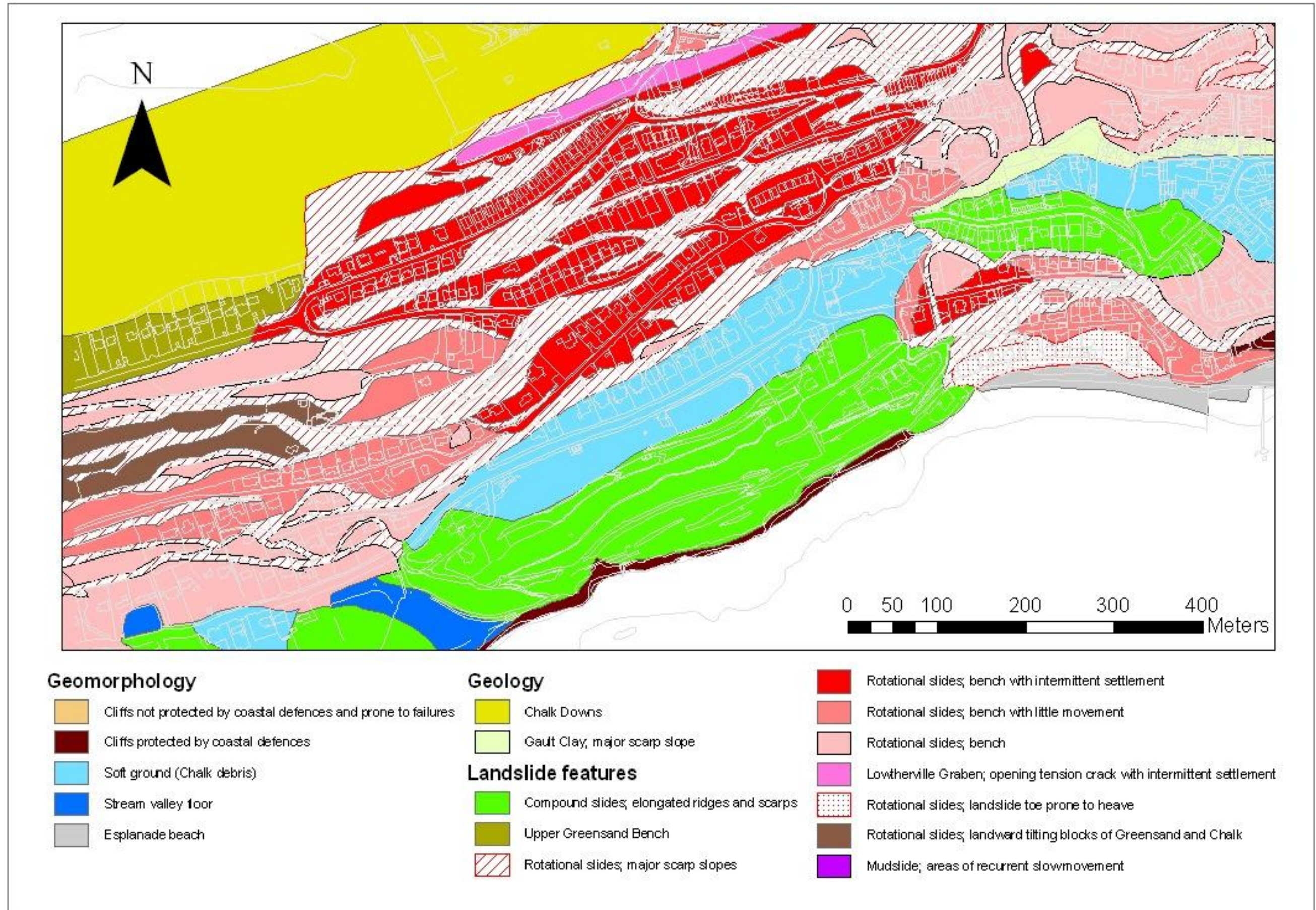


Figure 3.12 Geomorphological map of the Ventnor landslide complex (from Halcrow, 2006 after GSL, 1991)

3.9 Ventnor landslide stratigraphy

Two ground investigations at Ventnor have obtained detailed geological information to a depth of up to 150 m below ground level in Upper Ventnor, allowing correlation with previous boreholes in the region. Earlier boreholes are generally shallow, having been optimised for localised investigations. Ground investigations carried out in 2002 (Soil Mechanics Ltd) and 2005 (Fugro Engineering Services Ltd) comprised; the drilling of five deep rotary and open-cored boreholes; engineering and geophysical logging of materials; laboratory based testing of samples; and the installation of subsurface inclinometers and standpipe piezometers. In a number of deep boreholes, down-hole geophysical gamma logs have been run to enable a composite geophysical profile to be generated and cross-referenced. The logs provide graphic representations of lithological variation throughout the sequence and, with sufficient confidence in the interpretation of the profiles, allows for boreholes to be drilled without coring. Interpretations can be made solely from the down-hole gamma logs. A combination of both engineering logs and geophysical logs were used to develop detailed stratigraphic description of the site materials.

A previous stratigraphic description has been provided as part of a coastal assessment of landslide potential (Lee and Moore, 1991). Following detailed examination of cores across the Undercliff this classification has been confirmed and expanded within this thesis to include greater detail within some units (Table 3.4).

The general sequence of strata was disrupted as a result of the formation of the Undercliff landslides, although strata thicknesses appear to be reasonably consistent when the block geometry of the landslide and strata loss due to shear and displacement are taken into account. The typical thicknesses have been compared with deep borehole records from Bonchurch in the eastern part of the Undercliff.

STAGE	FORMATION	UNIT	THICKNESS (m)			LITHOLOGICAL DESCRIPTION
			Lee & Moore (1991)	Ventnor	Bonchurch	
CENOMANIAN	Chalk			15-31.4		<div style="border: 1px solid black; padding: 5px;"> 2b(iv) 3.3-3.8 Dark green grey clayey sand 2b(iii) 0.9-2.6 Mainly clay with some bioturbation 2b(ii) 1.5-3.0 Sandy clay overlying dark coloured sand (sand absent in BH1) 2b(i) 0-1.1 Brown grey clay (translational to 2a) unit only present in Bh1 </div>
		6b	>5.5	33.1-3.4	4.4-5.0	Chalk Marl Member Grey marly chalk generally with no flints
		6a	2.1	6.6	7.8-8.7	Chalk Marl Member Calcareous glauconitic sand distinctive basal unit heavily bioturbated
		5c	6.2-8.8	20.5-22	16.5	Chert Beds prominent Chert and limestone bands in glauconitic sandstones
UPPER ALBIAN	Upper Greensand	5b	23.3	2.1-5.3	6.7-8	Malm Rock buff and grey coloured fine sandstone
		5a	12.0	45.1	44.2	Passage Beds grey and buff coloured silts and clays
		4b	44.0	36-42	36.4	Gault very stiff dark grey (silty) clay
4a	3.1-6.6	7.6		Gault very stiff brown (silty) clay		
LOWER ALBIAN	Gault Clay	3	10.5	4.1-9.2	>0.1	Carstone grey blue angular sand with pebbles and clayey sand interbeds
		2e	6.4	8.5-10.1		Sandrock light grey and buff sand
	2d	3.0	2.3-2.6		Sandrock dark grey or mottled sandy clay or sand	
	2c	17.7	20.0-21.3		Sandrock dark grey or mottled sandy clay or sand	
	(iii)		(iii) 5.3-6.3 (i) 14.5-615.4			
UPPER APTIAN	Lower Greensand	2b (iv-i)	5.1	6.3-9.3		Sandrock homogeneous glauconitic pebbly mud sand and sandy mud
		2a	10.6	3.6-4.6		Sandrock light grey weakly cemented sand
LOWER APTIAN		1c	>3	>11.4		Ferruginous Sands dark grey green glauconitic sands

Table 3.4 Summary geological stratigraphy of Ventnor (after Palmer et al., 2007)

The Ferruginous Sands form the basal material in the deep boreholes, approximately 150 m below ground level. The unit was typically recovered as dark grey-green, fine to medium glauconitic sands. Observations suggest landslide movements have not affected the unit. The Ferruginous Sands are overlain by a thick Sandrock Formation, which is comprised of a number of interbedded units of Sands and Clays. This has been subdivided by Palmer et al. (2007) for simplicity. Sandrock 2a is typically light grey, weakly cemented sand with pockets and partings of lignite. Sandrock 2b (ii) is generally recorded as sandy clay overlying dark coloured sand, which rests directly on Sandrock 2a. Sandrock 2b was identified as brown grey clay, although both units 2b (i) and 2b (ii) were found to be absent in a number of locations. The most significant horizons identified with regards to instability are the Sandrock units 2d and 2b (iii). These units comprise clay beds with evidence of slickensides and polished surfaces, representing flexural landslide shear surfaces. Above the Sandrock was a band of Carstone of variable thickness across the site, with a condensed sequence recorded in the geophysical logs depicting the same signature over a shorter length. The Carstone is typically grey brown, angular sand with occasional fine gravel and interbeds of sandy clay and clayey sand. A thin pebbly band also often marks the base of the clay. The Carstone was overlain by a variable thickness of the Gault Formation, which despite its importance in the landslide development, remains poorly described in Ventnor. The thickness of 45.1 m of Gault that was encountered in BH2 is typical of the maximum thickness of the formation in the Undercliff. In BH3 and BH5 this formation progressively thins down slope with the loss of the top most sequence of the Gault. This could be the result of solifluction processes during the Quaternary, or non-recovery related to complexities of the subsurface landslide geometry and general disruption of landslide blocks in these locations. Palaeosols were identified within the chalk debris at 2.9 m and 20.6 m below ground surface, providing a potential opportunity to date the soils. At the shallower depth, poorly preserved pollen was linked to the Late Bronze Age or a later period. At 20.6 m, a well-preserved pollen assemblage was dated between 9500 to 9000 years BP (i.e. Boreal period, Flandrian chronozone Ib). However, small numbers of spruce pollen were found, which were not native during the Boreal. The pollen may

be derived from earlier sediments, which would indicate a much earlier age of Middle Pleistocene. These dates lend support to the view that the lower parts of the Ventnor Undercliff landslides are considerably older than its upper parts (Hutchinson and Bromhead, 2002).

3.10 Site hydrogeology

The site stratigraphy demonstrates a series of materials of contrasting permeability, which led to the formation of several aquifers in Ventnor (Halcrow, 2006). During ground investigations a series of piezometers were installed in various strata horizons to monitor the conditions of the different water tables. Summaries of the piezometers installation details for each borehole are presented in Table 3.5.

Groundwater monitoring results demonstrate that the hydro-geological regime within the slope is complex (Fig 3.13).

- Water table 1 (WT1) comprises a perched aquifer within the Upper Greensand, believed to be in hydraulic continuity with groundwater within the Chalk debris.
- Water table 2 (WT2) represents a water table, which is confined between the base of the Gault and Sandrock 2d that applies hydrostatic pressures to Sandrock 2c.
- Water tables 3 and 4 (WT3 and WT4) represent different water tables within the Sandrock.

Table 3.5 Piezometer installation details, Ventnor Undercliff

Borehole	Piezometer (installation depth, m)	Date installed	Installation position
BH1	P1		Installed below clay layer (presumed aquiclude) of Sandrock 2b to measure water pressures acting on the potential shear surface in that layer (WT4).
	P2		Installed above clay layer (presumed aquiclude) of Sandrock 2d to measure water pressures in the permeable Chalk debris related to the uppermost table WT1 and WT2.
BH2S	P1		Installed in Sandrock 2c just below Sandrock 2d and measuring groundwater levels in WT3 which applies to Sandrock 2c.
	P2		Installed in the Gault and at the level of maximum disturbance in that stratum to measure groundwater in WT1 (applies to the cap rocks and upper part of Gault).
BH3	P1		Installed in Sandrock 2c to measure groundwater levels affecting that layer, related to WT3.
	P2		Installed in Passage Beds to measure groundwater levels of WT1.
BH4	P1		Installed at the base of Sandrock 2c to measure water levels in WT4.
	P2		Installed at the base of the Chalk to measure WT1 and WT2.
BH5	P1		Installed in Sandrock 2a to measure WT4, confined by the aquiclude of Sandrock 2b clay layer.
	P2		Installed just above presumed shear surface at the base of Gault. This piezometer measures the water levels in WT2 which is applied to the base of the Gault, Sandrock 2e and Sandrock 2d.

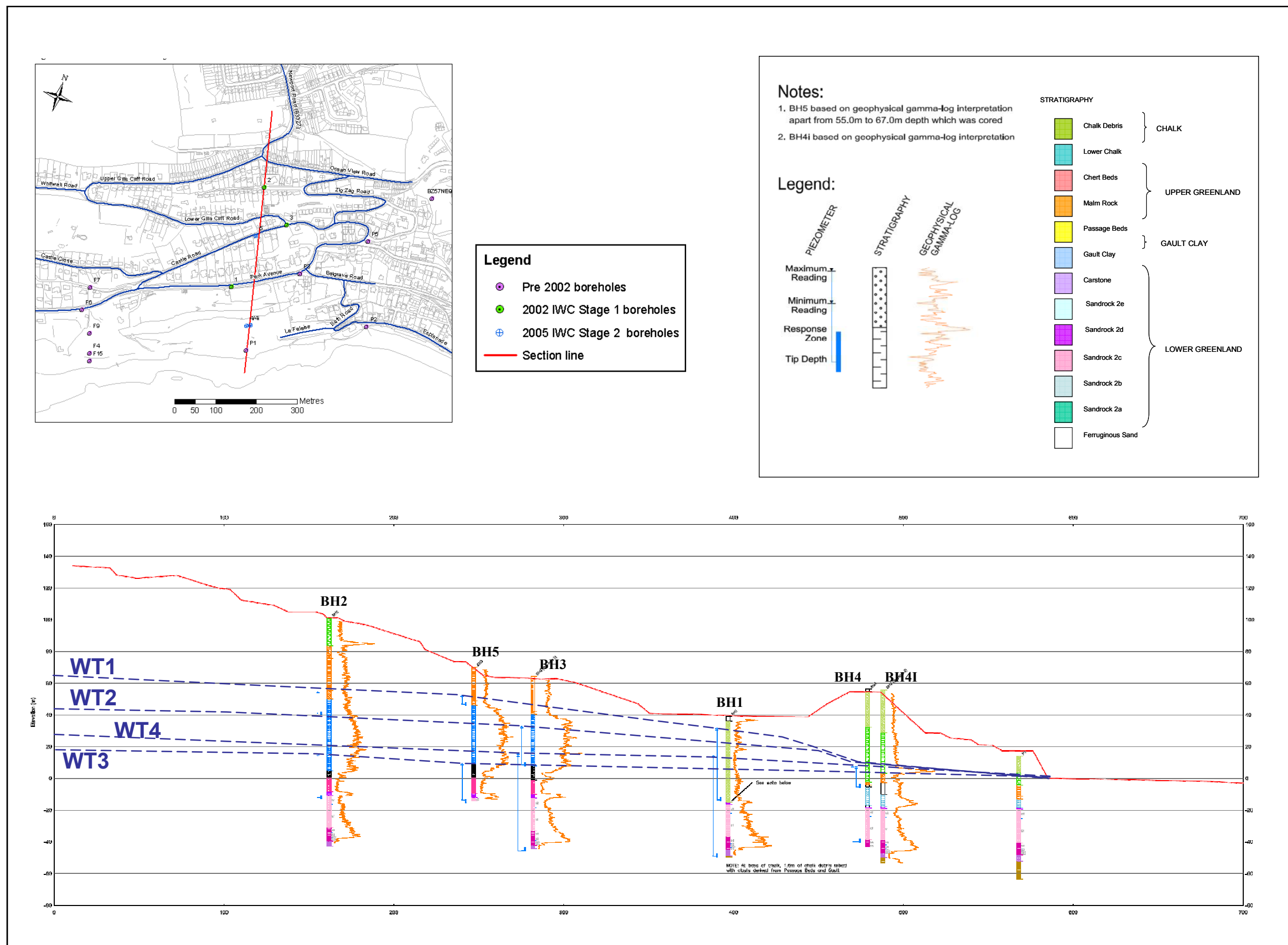


Figure 3.13 Groundwater tables affecting the Ventnor landslide complex

3.11 Ventnor landslide ground model

Interpretation of the causes, mechanisms and ground behaviour in the Undercliff depends on developing a consistent explanation that accounts for all of the features (geological, geomorphological, geotechnical, ground behaviour) in a logical and scientific way. Models of the Ventnor Undercliff landslides have been developed by a number of authors in the past and are conveniently summarised by Hutchinson and Bromhead (2002). The most favoured models include multiple rotational failures in the Gault, and compound (non-rotational) failure in the Sandrock at different shear surface depths.

Figure 3.2b illustrates the stability section line that was used to locate boreholes for the purpose of calibrating a ground model, identifying the principal failure mechanisms (landslide model) and for undertaking stability analysis. The section is generally representative of the Ventnor Undercliff landslide system and is aligned to the maximum dip of strata. The section line is not necessarily orthogonal to the coastline or the surface geomorphology, however, slight changes in the orientation of the section were found to have little effect on the stability of deep shear surfaces.

The strata boundaries were plotted on the section from the borehole records and geophysical logs and cross-referenced to the litho-stratigraphic framework (Palmer *et al.*, 2007). All boreholes along the section line penetrated the base of the landslide complex into the Sandrock beneath. Correlation of the Sandrock units were tied back to landward of the Undercliff to reconstruct the in situ Upper Greensand and Lower Chalk strata above, using the stratigraphic framework.

Inclinometer readings are available from the Isle of Wight Council from installation in 2002 to 2008 at BH2 and from installation in 2005 to 2008 at BH4I. Reading though this period provide evidence of a potential zone of movement recorded at approximately 93 m bgl at BH2 in Upper Ventnor and 76mbgl at BH4 in Lower Ventnor (Fig 3.14). BH2 readings indicate 30 mm of

movement has occurred between September 2002, and 2008. Readings at BH4I indicate 32 mm of movement has occurred between 2005 and 2008/

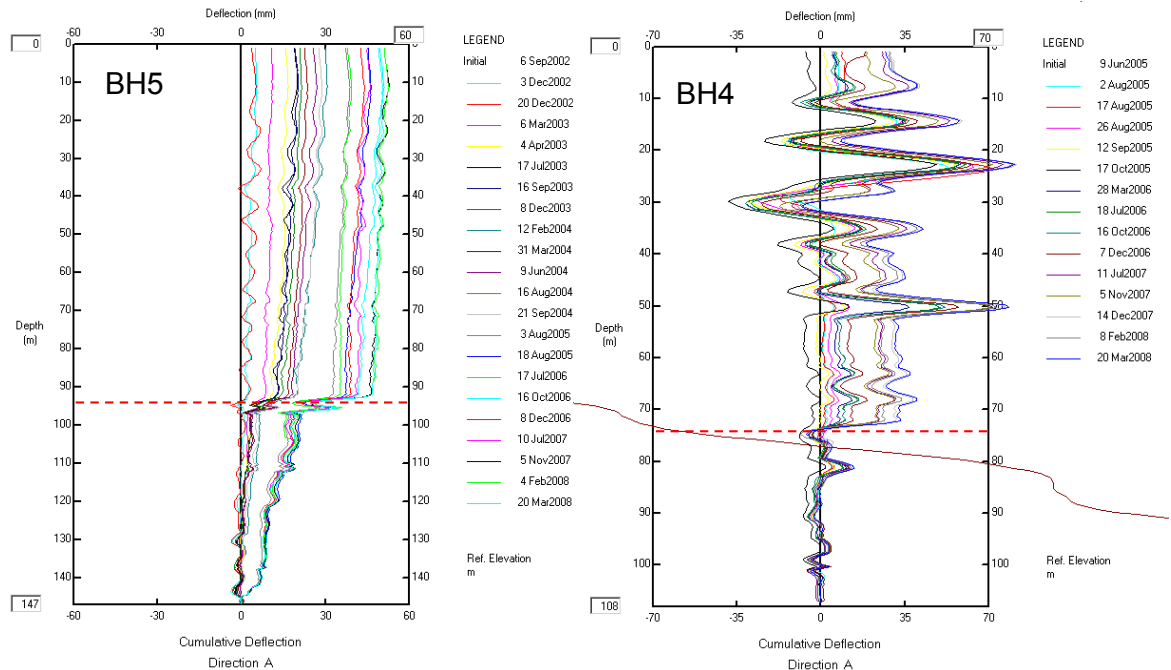


Figure 3.14 Inclinometer plots from central Ventnor; BH5 2002-2008; BH4I 2005-2008 (provided by the Isle of Wight Council)

Inclinometer records have been collated the findings of the 2005 ground investigations to develop a landslide model for the Ventnor Undercliff (Moore *et al.*, 2007b). This model hypothesises the presence of a retrogressive two-tier landslide model comprising a distinct upper and lower landslide section, as follows:

1. The upper landslide section is the area between the Lowtherville graben and Park Avenue. The sequence is characterised by distinct rotational failure blocks seated at the base of the Gault that have undergone displacement to varying degree. The landslide blocks are capped by Chalk debris, Lower Chalk, Malm Rock and Passage beds over a substantial thickness of Gault clay, under which lies Carstone and Sandrock.

2. The lower landslide section comprises the area from Park Avenue to the sea. It is distinguished by a prominent ridge at Ventnor Park and fronted by the Western Cliffs. The ground along Park Avenue is formed of a thick sequence of chalk debris, whilst the seaward block is thought to comprise a remnant multiple rotational landslide block sequence draped by chalk debris. Notably, the lower landslide section is seated upon disturbed Gault and Sandrock 2d.

The landslide blocks may act singly or interactively. It is not yet possible to clarify this, although it has been recognised that future monitoring could provide the basis for confirming the model (Moore *et al.*, 2007b). The strata of the lower landslide section are highly disrupted and are fundamentally different to the upper landslide section. This interpretation adds support to the view that the lower landslide section forms the head of an ancient landslide system that once extended offshore prior to submergence by rising sea level during the Holocene.

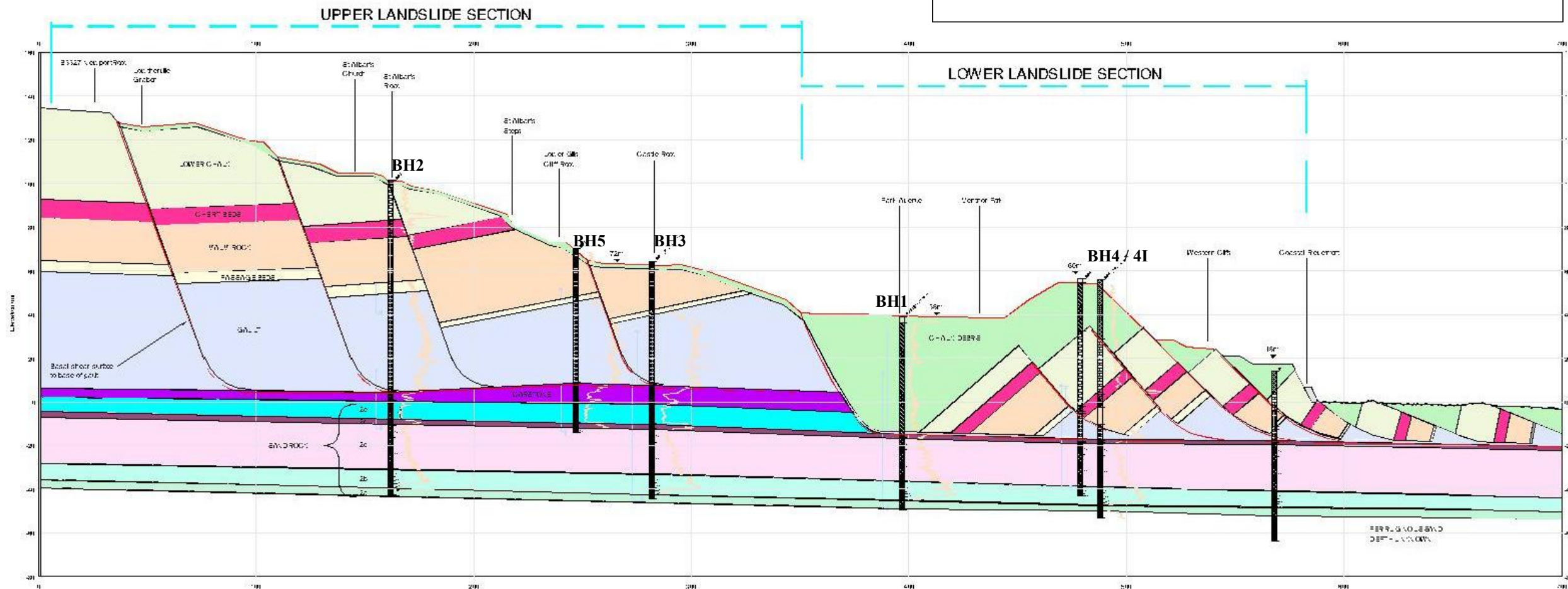
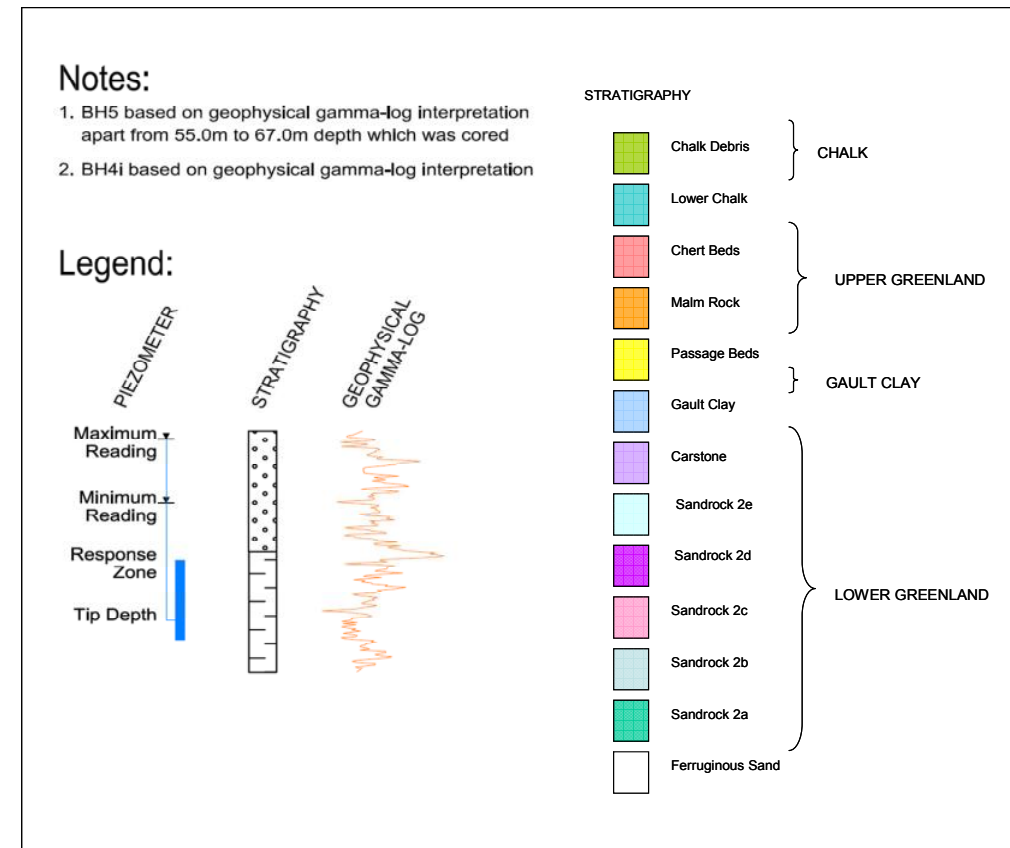
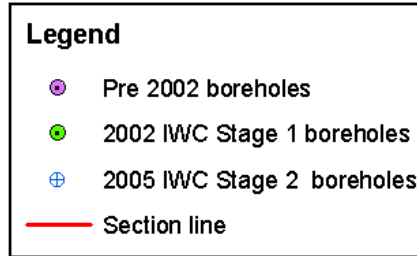
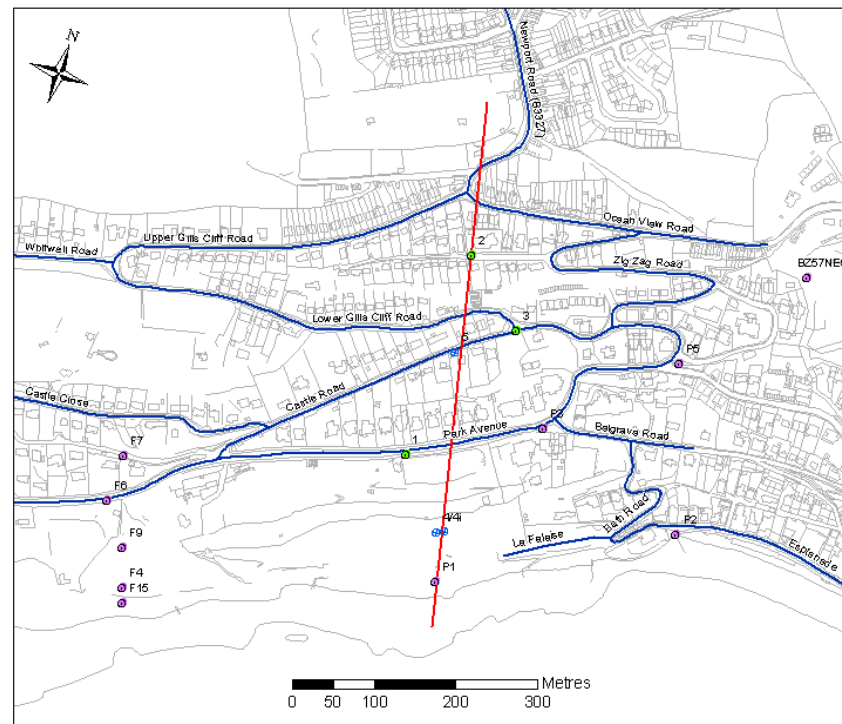


Figure 3.15 Ventnor landslide ground model (after Moore et al., 2007b)

The interpretation of the landslide stratigraphy is reasonably well defined in the upper section of the Ventnor Undercliff, providing a multiple rotational model is invoked. The interpretation correlates key strata (or marker horizons) with the key surface morphology to identify probable boundaries between the deep-seated rotated blocks. The model shows greater displacement and backtilt of the landslide blocks downslope, a characteristic of retrogressive multiple-rotational landslides.

The model correlates evidence of deep failure within the upper section that is manifest at the ground surface by distinct morphological features, such as scarp slopes, indicating that the Lowtherville Graben is the uppermost and most recent failure of a series of deep shear surfaces in that area. The model assumes that the development of the upper landslide section has occurred subsequent to the formation of the lower landslide section.

The origin, nature and composition of the chalk debris and landslide blocks forming the lower section remain partly conjectural. The large thickness of chalk debris in BH1 was unexpected and the structure of the landslide block at BH4 shows chalk debris over largely intact chalk, with significant differences between BH4 and BH4I, even though these are only about 10 m apart. The nature of the contact between the chalk debris and slope above is also a matter of conjecture. This may be a shear surface but may also be chalk washed against extruded and rotated Gault.

Only a restricted amount of information is known about the landslide stratigraphy out to sea. The work of Clark *et al.* (1994) shows this submarine slope is mantled by planed off remnants of old, deep-seated landslides to a depth of at least 25 m, and possibly 40 m. This would suggest that at least the seabed between the current shoreline and St Catherine's Deep, about 2 km offshore, is formed of pre-glacial slide remnants and debris. While St Catherine's Deep is sufficiently far from the shore to have little effect on the Undercliff landslides, it would be desirable to confirm that there are no major features of seabed instability within influencing distance.

The main uncertainty with the landslide model is the configuration of the multiple rotational landslide blocks between the boreholes. The basal shear surface is reasonably well defined, although it was anticipated that monitoring of the inclinometer and slip indicators would have revealed the depths of ground movement, this has only been achieved at BH2. Consequently, stability modelling of several potential failure surfaces has been carried out based on geomorphology and suspected shear zones encountered within the boreholes. These cannot be considered definitive until proved by further monitoring of borehole deformations and surveys of surface displacements.

3.12 Ventnor landslide evolution

3.12.1 Previous evolutionary models

A number of previous landslide models have been hypothesised to explain the long-term development of the Ventnor Undercliff. They have suggested different mechanisms of failure and differing depths of the landslide shear surface. These models include:

- Multiple rotational failure within the Gault Clay (e.g. Bass, 1954; Hutchinson, 1965; Hutchinson *et al.*, 1981, Chandler, 1984);
- Compound failure along clay layers within the Sandrock (e.g. Hutchinson *et al.*, 1985; Bromhead *et al.*, 1988);
- A singular catastrophic failure event causing multiple landslide failure mechanisms (e.g. Seed and Wilson, 1967).

3.12.1.1 Multiple Rotational failures within the Gault Clay

The multiple rotational failure model is largely based on previous studies undertaken at Folkestone Warren (Fig 3.16) (Hutchinson, 1969). Here progressive failure of the Gault was identified as the key control on landslide development, with lateral expansion in response to long-term unloading initiating the generation of shear surfaces at residual strength near the base of the Gault Clay (DOE, 1991). It is believed that lateral expansion and tensile stress probably causes joint widening in the Upper Greensand along the Undercliff, forming the deep fissures or vents that are evident across the site. As these fissures enlarge and extend deeper towards the Gault Clay they

create potential shear surface that extend from the base of the Gault through the Upper Greensand. At Folkestone, Hutchinson (1969) identified that it was these lateral expansion shears in the Gault Clay that have allowed for the relatively rapid cycles of landslide activity. Under this model of landslide development, improvements in stability may occur following failure as the slipped or detached provide toe support to the rear scarp. Removal of this support, however, can lead to a dramatic landslide reactivation (DOE, 1991).

The evidence for multiple rotational failures in the Gault is widespread throughout Ventnor. These include:

- The presence of vents in locations such as Whitwell Road
- The presence of fissures such as those observed in the railway station quarry
- Evidence of large back rotated blocks in the Upper Greensand
- Evidence of support from lower landslide blocks such (e.g. St Albans Steps).

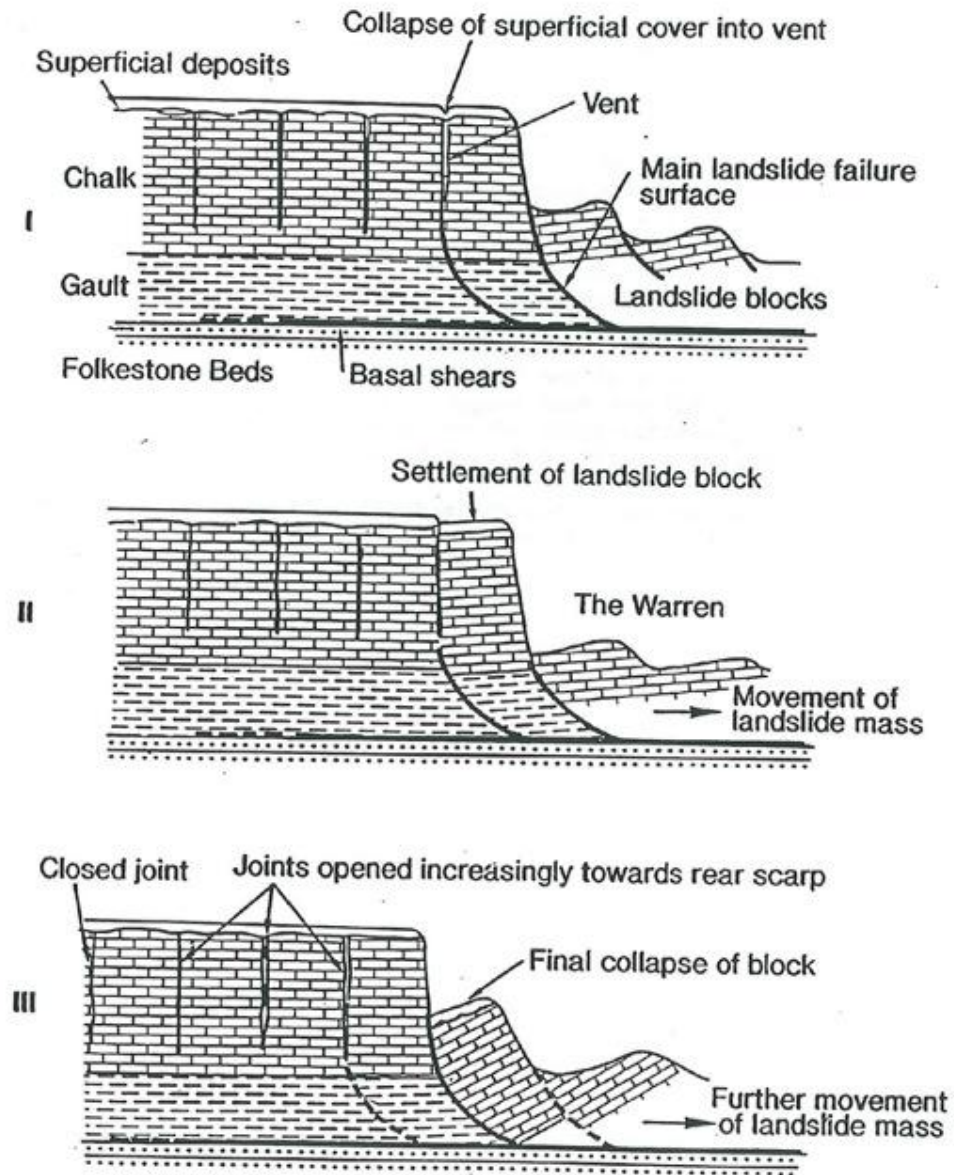


Figure 3.16 Proposed landslide development model, Folkestone Warren, (after Hutchinson, 1969)

3.12.1.2 Compound failure along the clay layers

The proposed compound landslide failure along the weak clay bands within the lower Sandrock has been proposed in a number of previous publications (e.g. Hutchinson *et al.*, 1985; 1987b; Bromhead *et al.*, 1988) and has been used specifically to explain the development of the deep landslide at St

Catherine's Point. The landslide complex comprises two linear ridges upslope of a broad debris apron. Surface evidence suggests that both ridges appear to have resulted from rotational failure. The site investigation indicated that the front block slid seawards along a bedding plane and the ridges were the surface expression of a graben. The basal shear surface of this block was identified to be occurring in the clay layers within the Sandrock, approximately 50 m beneath the base of the Gault.

Hutchinson *et al.* (1985) has drawn parallels between this system and the Bindon landslide, which occurred on the Dorset coastline on 25th December 1839 (Pitts and Brunnsden, 1987). The Bindon landslide (Fig 3.17) is one of the largest recorded landslide events in Great Britain and comprised a complex seaward movement forming Goat Island, with a rear graben developing behind the displaced block, and the temporary formation of an offshore reef. Stability analysis carried out in a re-evaluation of the landslide mechanisms suggests that failure was triggered by a sudden loss of support to the cliff following a large non-circular slide downslope (Pitts and Brunnsden, 1987).

Woodruff (1986) put forward a variation of this block slide model based on site investigations conducted at The Cascades. Woodruff's model suggests that the landslide comprises a zone of rotational failure at the rear of the Undercliff, with debris being moved subsequently seaward across a platform in the Sandrock, in response to continued marine erosion. The presence of elongated linear ridges and landward grabens in parts of the Undercliff, such as at Ventnor Park and Bonchurch (DOE, 1991), suggest that sections of the Undercliff have resulted from compound failures. It has been argued that the basal slip surfaces are situated within the Sandrock but with no clear indication along which clay layer this could have occurred.

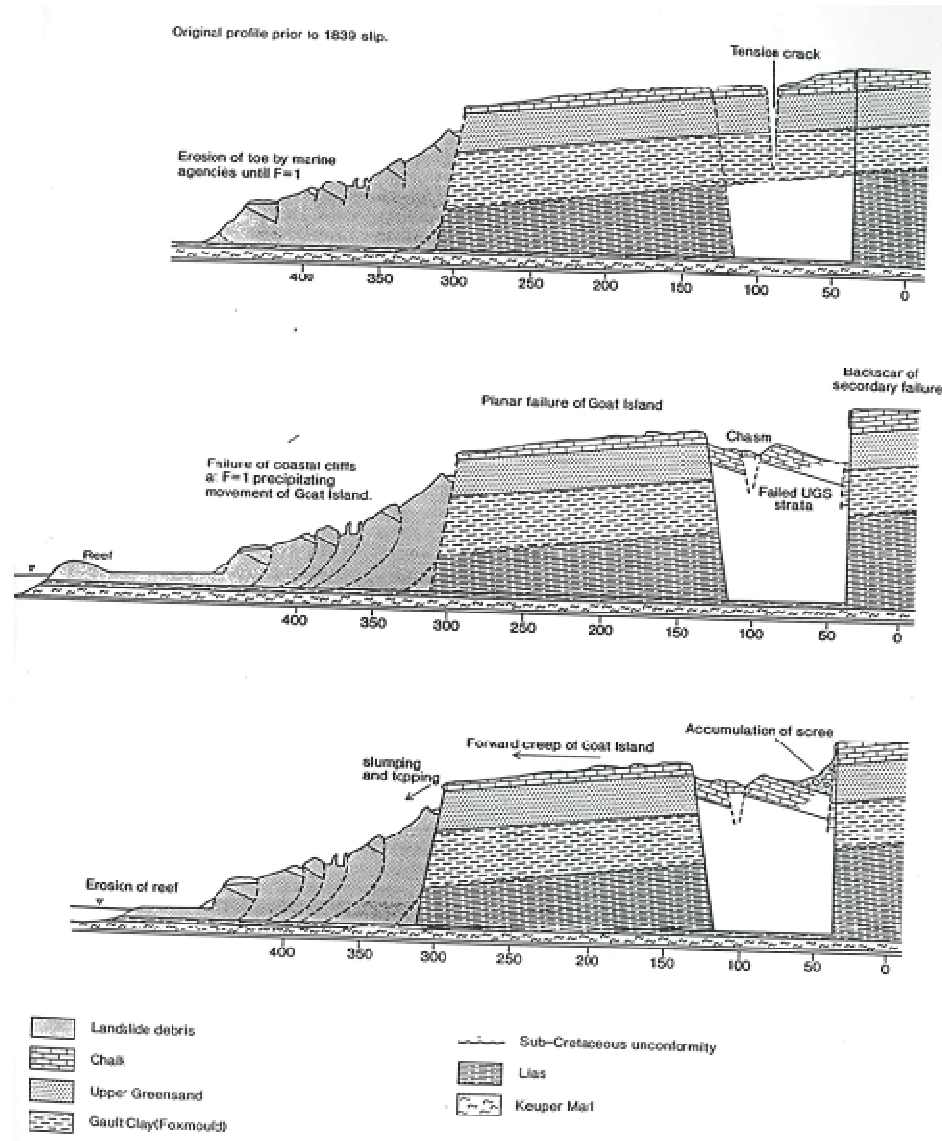


Figure 3.17 Proposed landslide model for the Bindon, Dorset (after Pitts and Brunsden, 1982)

3.12.1.3 Large singular catastrophic event

Extensive reviews of both UK and overseas literature carried out by the DOE (1991) highlighted a third possible model which could account for the close association between compound spreading failures and rotational slides in chalky debris which have been identified locally at sites such as Bonchurch. Broad similarities in form have been identified with the Turnagain Heights landslide in Anchorage, which occurred during the 1964 Alaskan earthquake

(Fig 3.18). In Anchorage, 21 m high coastal bluffs in sand and gravel, underlain by clay, failed causing a spreading failure to occur over an area of 52 hectares (Seed and Wilson, 1967). The slide resulted in the liquefaction of sand layers during the earthquake. Within the area of the slide the original ground surface was broken up into a series of elongate ridges and depressions, similar to those seen within the Undercliff. Seed and Wilson (1967) simulated the failure in a series of model tests where a very weak clay layer was overlain by layers of stronger clay. Toe support was removed from the model and slope failed through a complex sequence of slides, involving a series of rotational slides followed by block sliding and spreading failure.

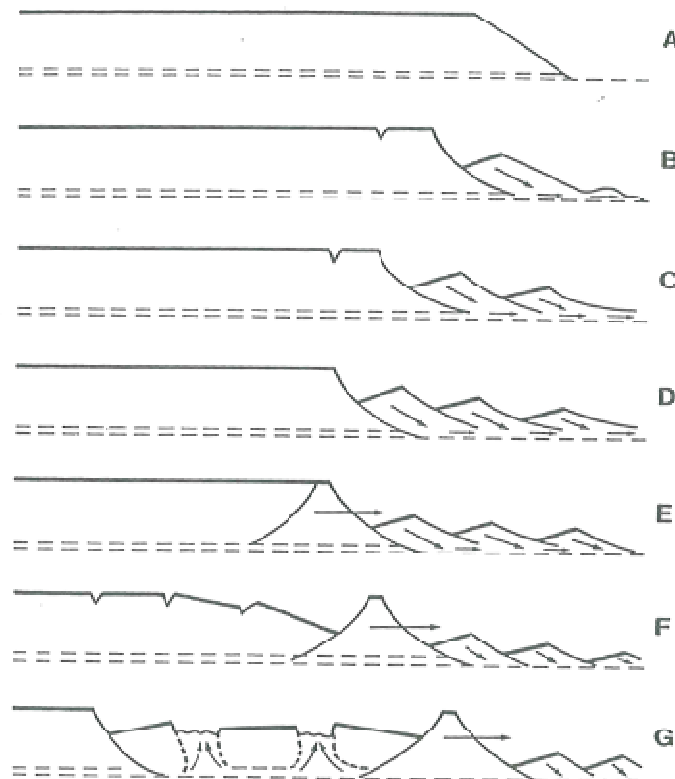


Figure 3.18 Proposed landslide model, Turnagain Heights landslide (after Seed and Wilson, 1967)

Although it must be remembered that the Turnagain Heights landslide was the direct consequence of a major earthquake ($M = 8.5$), the model test results demonstrate how complex patterns of landsliding can develop over short distances as a result of a singular event (DOE, 1991). Although it is not suggested that the features identified in the Undercliff are seismically induced it is possible that the different forms present today could have been formed by a singular event.

3.12.2 Ventnor landslide Quaternary evolution

An evolutionary model proposed by Moore *et al.* (2007b) suggests that a large pre-existing deep landslide complex probably existed offshore of its current position at the Western Cliffs to the St Catherine's Deep (Fig 3.19).

A series of previous investigations have suggested that the Undercliff was formed as a result of two phases of landsliding, which took place after the last glacial high stand at approximately 8,000 to 4,500 and 2,500 to 1,800 years before present (Long and Tooley, 1995). Both periods were characterised by major changes in climate and sea level and the consequent effects of marine erosion, island-wide. More recent investigations (Halcrow, 2006) have suggested that the ancient landslides forming the lower slopes extending offshore are likely to be much older and existed in pre-glacial times.

During the Flandrian transgression the decay of the UK ice sheets is believed to have raised sea level from -100 mOD approximately 14,000 years before present to -20 mOD at approximately 8,000 year before present (Long and Tooley, 1995). This rapid change in sea level would have occurred with elevated groundwater levels and major erosion transport and deposition of vast volumes of calcareous debris (mostly chalk) through solifluction processes at the cessation of the last glacial maximum (Hutchinson, 1987b). The latter will have resulted in the formation of the large debris aprons that exist along the Undercliff (Hutchinson and Bromhead, 2002).

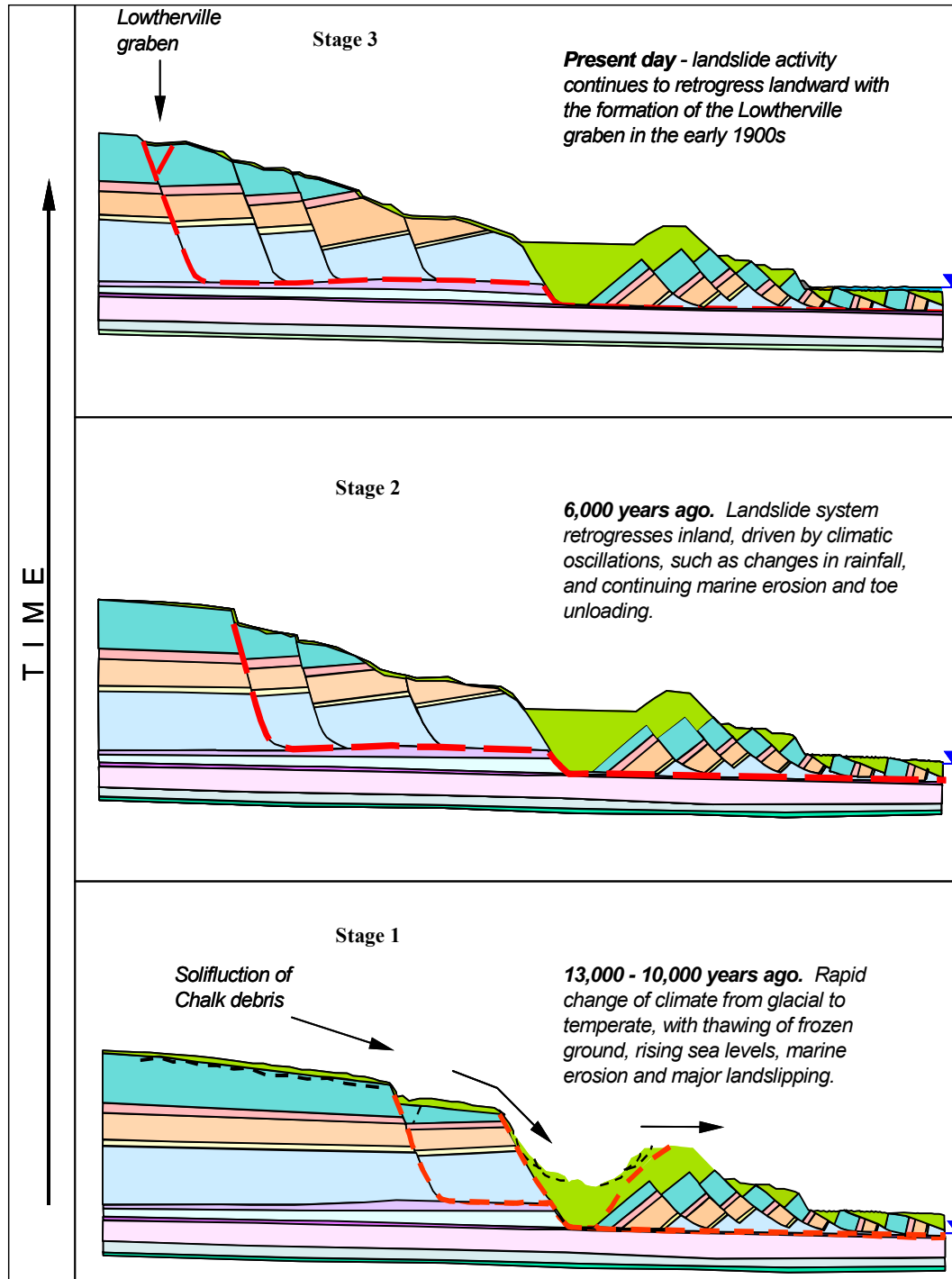


Figure 3.19 Proposed evolution of the Ventnor Undercliff Landslide (after Moore et al., 2007b)

The rise in groundwater levels, combined with sea level rise and episodic loading of the pre-Holocene landslide head, is believed to have caused a compound failure of Sandrock 2d. The rapid displacement of this block would have resulted in the formation of a depression in the current area of Ventnor Park, which would have rapidly infilled with chalky debris from subsequent solifluction events (Halcrow, 2006). This compound landslide failure would have removed substantial toe support to the upper slopes in the area of Upper Ventnor. The stress release is believed to have allowed the development of a retrogressive landslide system with a shear surface at the base of the slope. During the Mid-Holocene this landslide is believed to have retrogressed as groundwater levels were elevated. These raised porewater pressures would have acted to allow the landslide to retrogress further upslope. Rising sea levels and increased marine erosion is likely to have caused localised failures from the Western Cliffs, further contributing to the instability in Upper Ventnor. This retrogression in Upper Ventnor would have continued through the Holocene until reaching its current position at the Lowtherville graben. It is not clear when this feature developed, although no evidence of ground movement was recorded in the area until the early 1900's. Since then ground movement has occurred regularly usually as a result of fluctuations in winter rainfall and subsequent groundwater levels.

3.13 Chapter Summary

The Ventnor Undercliff landslide has been chosen as the study site for this research as recent ground investigations provide a unique opportunity to study landslide behaviour within a deep-seated landslide complex in typical environmental setting for UK coastal instability. The recent 2005 ground investigation, commissioned by the Isle of Wight Council, has provided the author a unique opportunity to collect intact samples of a number of materials for further laboratory based geotechnical investigation in order to assess the mechanisms of shear surface development through a series of specialist laboratory tests.

The nature of historical ground movement at Ventnor provides an excellent contemporary site to study the nature of continuous creep in landslides deep-

seated landslides. The council's long-term commitment to monitor the site has provided records of ground movement, groundwater and rainfall from 1992 onwards which can be analysed in conjunction with specialist materials testing to assess the mechanisms and causes of ground acceleration.

This chapter has provided an overview of the current knowledge of coastal landsliding characteristics along the Undercliff and has discussed the key factors in controlling landslide development at Ventnor. In summary these include; the nature and structure of the underlying geology, the hydrogeological characteristics, climatic (specifically rainfall) characteristics and the past environmental conditions which have impacted the landscape through the Quaternary. A number of previous explanatory landslide models have been proposed for the site, which have been discussed and developed by the sub-surface investigations in 2002 and 2005. Whilst these investigations have vastly improved the understanding of the Ventnor landslide and its evolutionary development over geological time the mechanism of landslide initiation and potential future risk of landslide reactivations remain poorly understood.

Ventnor offers a rare opportunity to improve our understanding of the mechanisms of deep-seated landslide movement and provide new insights into the potential reactivation of coastal landslide complexes in the UK.

Chapter 4: Methodology

The methods utilised in order to undertake this research, directly correspond to the research questions raised at the outset of this investigation, and can be summarised as:

1. Selecting suitable field sites for the study (section 4.1);
2. Site investigation and sampling methodology (section 4.2);
3. Assessment of landslide monitoring data (section 4.3);
4. Detailed laboratory investigations; (section 4.4).

4.1 Field site selection

The Ventnor landslide has been the subject of numerous previous investigations due to its scale and the perceived risk to the local population. The author supervised a landslide ground investigation on behalf of the Isle of Wight Council in 2005 and was involved in final report (Halcrow 2006), in which an interpretation of the current landslide mechanisms and a quantification of future potential landslide risk were presented. The ground investigation and monitoring being conducted by the Isle of Wight Council provided a rare opportunity to undertake complementary research into landslide behaviour.

The Ventnor Undercliff was considered a suitable field site for this study as it meets the following criteria:

- It is a known pre-existing deep-seated landslide complex in the UK
- There are existing ground movement, ground water and rainfall monitoring records available.
- It is a natural landslide complex caused by changes in groundwater conditions occurring in the basal shear zone.
- Outcrops of the suspected failing materials were available.

4.2 Site investigation and sampling methodology

The Ventnor landslide has been the subject of two detailed previous subsurface investigations. Soil Mechanics Limited carried out an initial ground investigation between 15th May and 16th August 2002. This comprised three deep boreholes and associated instrumentation; ground monitoring; and laboratory testing. Rotary drilled borehole cores were inspected and logged to develop a detailed understanding of the soil stratigraphy and soil fabrics.

A second stage ground investigation was undertaken in 2005 by Fugro Engineering Services and supervised by Halcrow Group Ltd. This investigation was designed to improve the existing understanding of the current Ventnor landslide and comprised the rotary drilling of three further boreholes. Two of the boreholes were drilled in a prominent ridge close to the landslide toe at Ventnor Park (BH4, BH4I) with associated instrumentation and testing (Fig 4.1). Both boreholes were logged using geophysical and standard core logging methodologies. A further borehole was drilled in Castle Road (BH5). Its purpose was to improve the understanding of the groundwater regime at the proposed shear surface (see Chapter 3).

The results of both investigations have been made available for this study and selected samples collected during the 2005 ground investigation were used for detailed laboratory testing as discussed in Chapter 3. Further samples were taken from geological exposures of stratigraphical equivalent materials. Samples of the Gault Clay were taken from Blackgang Chine, to the west of Ventnor, and samples of Carstone were collected from Monks Bay to the east of Ventnor (Fig 4.1). These samples were extracted from the cliffs as undisturbed, unweathered blocks dug out from the cliff.

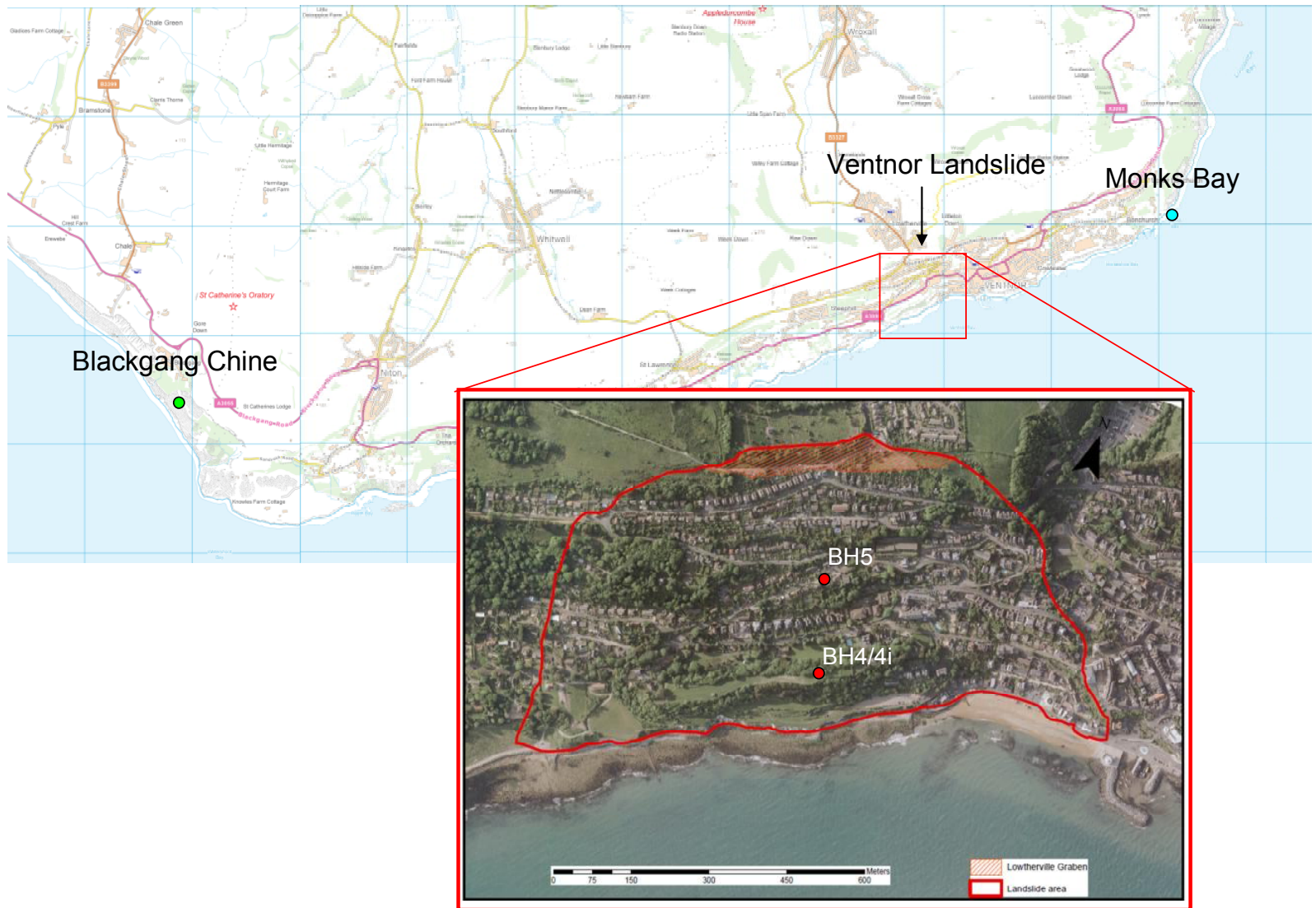


Figure 4.1 Sampling locations along the Undercliff

The selected samples from both the ground investigation and exposure sites were logged and recorded before being sealed using cling film and wax. The samples were then placed within plastic containers that were transported from the site to the laboratories using padded wooden core boxes. Disturbed samples were collected in plastic sealed bulk bags to prevent moisture loss. The samples were carefully transported by vehicle from the Isle of Wight to the University of Durham. The samples were then transferred to the departmental fridges and stored until required for testing.

Table 4.1 Samples collected during 2005 Ventnor ground investigation

BH	Ref	Material	Depth (m)	Size (mm)	State	Comments
4	C1	Chalk debris	25.80m - 26m	200 x 105	Undisturbed	Intact upper chalk with evidence of shear surfaces and disturbance above
4	C2	Chalk Debris	36.30- 36.50	200 x 105	Undisturbed	Intact weak upper chalk
4	C3	Chalk	41.60 - 42	400 x 105	Undisturbed	Intact strong upper chalk
4	C4	Chalk/ Upper Greensand	59.10 - 59.50	400 x 105	Undisturbed	Very hard siltstone possibly intact sample of the Upper Greensand
4	C5	Gault	62.65 - 63m	350 x 105	Undisturbed	Upper part of Gault sequence Section intact but likely to have disturbed by movement
4	C6	Gault	63.90 - 64.25	350 x 105	Undisturbed	Upper Intact section of Gault likely to have been disturbed by movement
4	C7	Gault	71.10 - 71.50	400 x 105	Undisturbed	Lower section of intact Gault with evidence of polished surface immediately above. Potentially just below a shear surface.
*4	C8	Gault	73.20 - 73.50	300 x 105	Undisturbed	Lowest section of intact Gault evidence of disturbance above and potential shear surfaces
4	C9	Sandrock clay (2b)	98.00 - 98.90	900 x 105	Undisturbed	Lowest section of intact Sandrock 2b. Sample taken from area where deepest potential shear surfaces have been hypothesised.
*5	C10	Lower Gault	55.0 - 55.30	300 x 105	Undisturbed	Section of intact Gault with less disturbance and fissuring than the Gault sampled from BH4
*5	C6	Lower Gault	55.75 - 56.0	250 x 105	Undisturbed	Section of intact Gault above the possible shear surface.
*5	C1	Gault/ Carstone transition	56.0 - 56.50	500 - 105	Undisturbed	Potential shear surface in a sandy transition zone between the Gault and Carstone.
*5	C2	Gault/ Carstone interface	56.50- 57.0	500 - 105	Undisturbed	Gault/ Carstone transition immediately beneath the potential shear surface.
5	C3	Carstone	57.05 - 57.35	300 x 105	Undisturbed	Intact Upper Carstone beneath potential shear zone

5	C4	Carstone	58.70 - 59.0	300 x 105	Undisturbed	Intact Carstone (V hard stone)
5	C5	Carstone	59.20 - 59.50	300 x 105	Undisturbed	Intact Carstone
5	C7	Carstone	62.50 - 63	500 x 105	Undisturbed	Intact Carstone (Sandy)
5	C9	Carstone/ Sandrock transition	63.50- 63.90	400 x 105	Undisturbed	Lower Carstone Sandrock transition becoming increasingly sandy
<i>*samples retained by the University of Durham and used for specialist testing</i>						

4.3 Analysis of landslide monitoring data

Ventnor has been subject to a detailed landslide management strategy which has involved the continual collection of ground movement, groundwater and climatic data from various locations within the town as summarised in Table 4.2. Systematic review of this data has previously been used to consider the condition of the landslide and provide advice to local residents on the potential for future ground movement. These data have been collected and managed by the Isle of Wight Council using techniques that include automated standpipe piezometers and crackmeters; differential GPS surveys; and manually measured standpipe piezometers and inclinometers (Fig 4.2).

These records have been used to assess the nature, mechanisms and causes of landslide behaviour as summarised below:

- The nature of landslide creep with particular focus on landslide acceleration and deceleration;
- The potential depth of landsliding and the nature and of the shear surface;
- The significance of groundwater and porewater pressures acting at the landslide shear surface as a control on ground movement behaviour;
- The climatic controls and relationships between rainfall patterns, groundwater and ground movement.

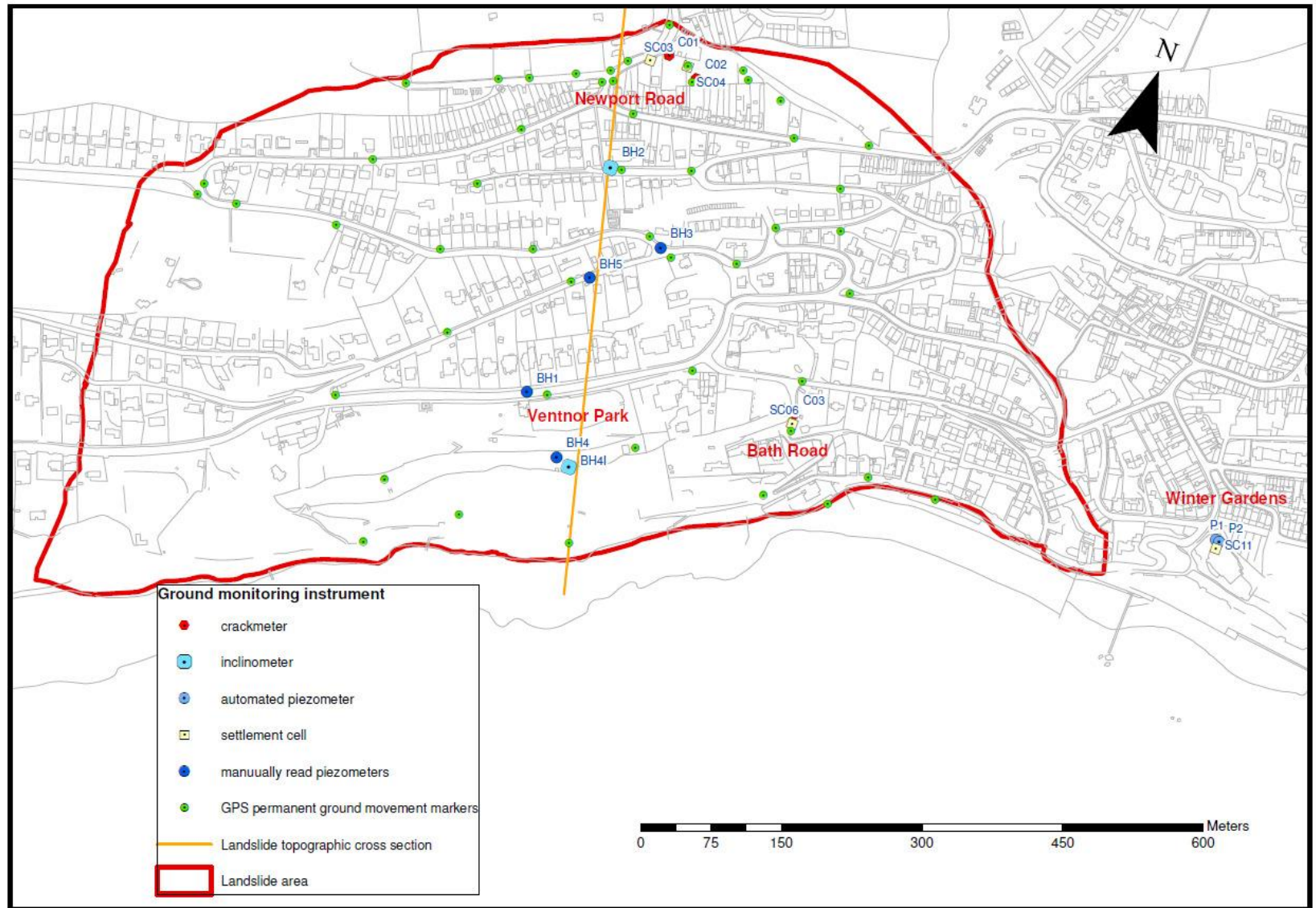


Figure 4.2 Site monitoring sites and instrument location plan, Ventnor Town

Table 4.2 Landside monitoring frequency and duration

Installation type	Location	Monitoring Duration (Year)																			
		92	93	94	95	96	97	98	99	00	01	02	03	04	05	06	07	08	09	10	
Vibrating wire piezometer	Winter Gardens (P01, P02)	Continuous monitoring (3 min intervals)																			
Vibrating Wire Crackmeters	Bath Road (C03) Newport Road (C01, C02)	Continuous monitoring (3 min intervals)												Annual site visits							
Vibrating wire settlement cells	Bath Road (SC06) Newport Road(SC03, SC04) Winter Gardens (SC11)	Continuous monitoring (3 min intervals)																			
Annual Movement Marker Survey	Ventnor Town (Fig 5.1)												Annual site visits								
Manually Read Piezometers	BH1, BH2, BH3 BH1, BH2, BH3, BH4, BH5											Regular monitoring visit (Bi-annual to monthly)			Regular monitoring visit (Bi-annual to monthly)						
Manually read inclinometers	BH2, BH4											Regular monitoring visit (Bi-annual to monthly)			Regular monitoring visit (Bi-annual to monthly)						
Weather Station	Ventnor Park	Continuous monitoring (3 min intervals)																			

Monitoring Frequency: Continuous monitoring (3 min intervals), Annual site visits, Regular monitoring visit (Bi-annual to monthly).

4.3.1 Vertical and horizontal displacement- analysis of crackmeter and settlement cell data

A series of crackmeters and settlement cells and differential GPS monitoring stations have been installed throughout Ventnor to assess both the spatial and temporal variability of ground movement.

Vibrating wire crackmeters records have been made available by the Isle of Wight Council from 1992 to 2005. The crackmeters consist of a sensor body with a vibrating wire transducer attached at one end. This is connected to a spring inside a tube with a protruding connecting rod (Fig 4.3). The instrument is buried within a shallow excavation and anchored to the ground either side of the crack at both the transducer and connecting rod ends of the crackmeter. Any change in distance is recorded through by the change in tension on the spring which alters the resonant frequency of the wire. The sensors are connected to an automated data logger which downloads readings, of crack extension in mm, at three hourly intervals. These instruments provide a continuous record of horizontal ground movement, including periods of ground acceleration and deceleration.

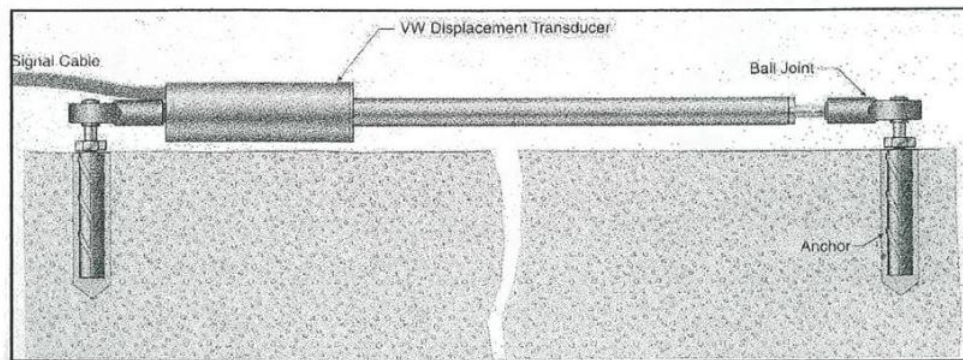


Figure 4.3 Schematic of long range crackmeters installed at Bath Road and Newport Road (after Dias, 2002)

Vibrating wire settlement cells have been installed at the site since 1992 to measure relative vertical deformation. The settlement cells comprise a pressure transducer, a liquid filled tube and liquid reservoir (Dias, 2000). The pressure transducers are buried within a shallow excavation together with the

liquid reservoir (Fig 4.4). As the ground settles the pressure exerted in the liquid column is converted to a measurement of settlement (cmHg) and automatically recorded by a data logger.

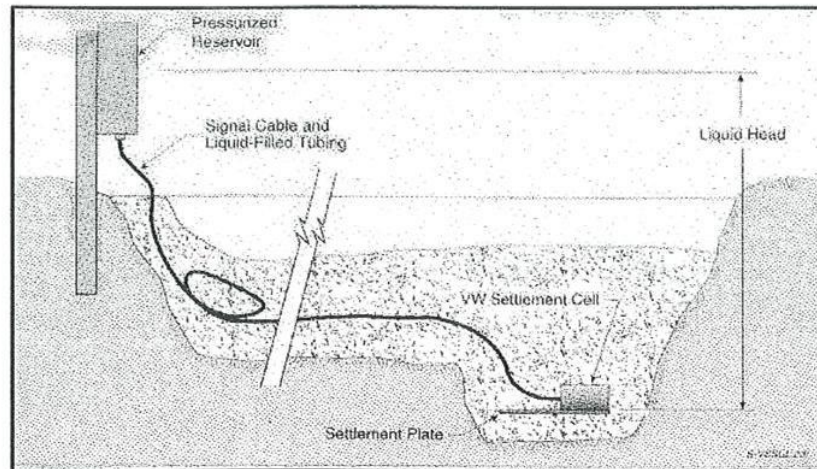


Figure 4.4 Schematic of vibrating wire settlement cells installed at Bath Road, Newport Road and Winter Gardens (after Dias, 2002)

Data from both the crackmeters and settlement cells have been regularly downloaded to a laptop during site visits over this period and has thus been available for analysis. The downloaded raw data provides time-stamped crackmeter extension measurements. Using this data it is therefore possible to assess the timing and patterns of ground displacement events and the rates of ground acceleration and post event deceleration by calculating the average velocity of movement over a given period.

Permanent ground movement markers were installed at numerous locations across the Ventnor landslide in December 2003 (Fig 4.2). On installation the position of each marker was accurately surveyed during a different GPS baseline survey. Subsequent surveys have been undertaken in 2005, 2007, 2007 and 2008 by the Isle of Wight Council. The repeat surveys, therefore, provide records of both the spatial distributions and direction of ground movement behaviour across the site.

4.3.2 Shear surface depth – analysis of inclinometer data

The depth of ground movement has been studied using records from inclinometers installed in BH5 and BH4I (Fig 4.3). A slope inclinometer is a device that monitors the onset and continuation of deformation normal to the axis of a borehole casing by passing a probe along the casing (Fig 4.5). An inclinometer therefore monitors deformation normal to the axis of the casing providing a profile of subsurface horizontal deformation (Stark, 2008).

Measurements have been taken using a traversing inclinometer probe. This is inserted to the base of the guide casing and lowered to the base of the hole (Fig 4.5). The probe is allowed to rest at the end of the casing for 15 to 20 minutes to allow the sensor to stabilise with ground temperatures (Dunnicliff, 1997). The measurement process is repeated by rotating the probe 180 degrees and reinserting it into the same groove set of the guide casing (Fig 4.7). Measurements of the shape of the guide casing are made by taking successive measurements at 50cm increments from the base to the top of the guide casing (Conforth, 2005).

The depths at which measurements are made are selected, for example no measurement is taken where the wheels of the probe coincide with a casing joint. Repeat measurements have been undertaken in order to develop accumulative plots of the shape of the casing.

In the case of landslide investigations the depth at which movement is detected by the inclinometer provides evidence of the depth of the landslide shear surface. An inclinometer has been installed and monitored intermittently since 2002 in Upper Ventnor (BH2). This installation extends from ground level to a depth of 150 m into the Ferruginous Sands below the deep Sandrock. A further inclinometer was installed in Ventnor Park (Fig 4.2) in Lower Ventnor (BH4I). Similarly an inclinometer was installed to a depth of 110 m into the Ferruginous Sands. Inclinometer readings provide a profile of the installed tube, which can be used to determine the depth of the landslide shear surface, and potentially the nature of shearing based on the area of

deformation within the landslide shear zone (e.g. Zhou *et al.*, 2010; de Freitas, 2009; Stark, 2008).

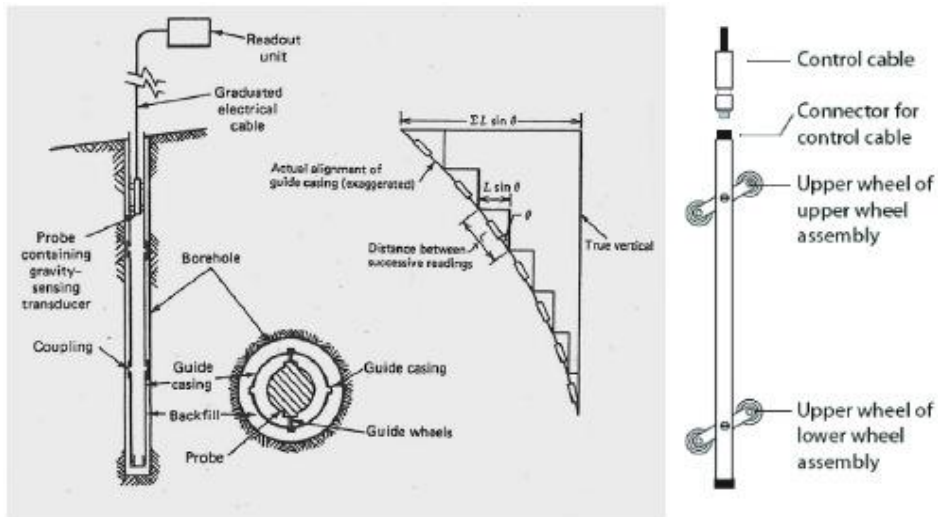


Figure 4.5 Schematic of inclinometer methodology used to monitor landslide deformation (after Mikkelsen, 2003)

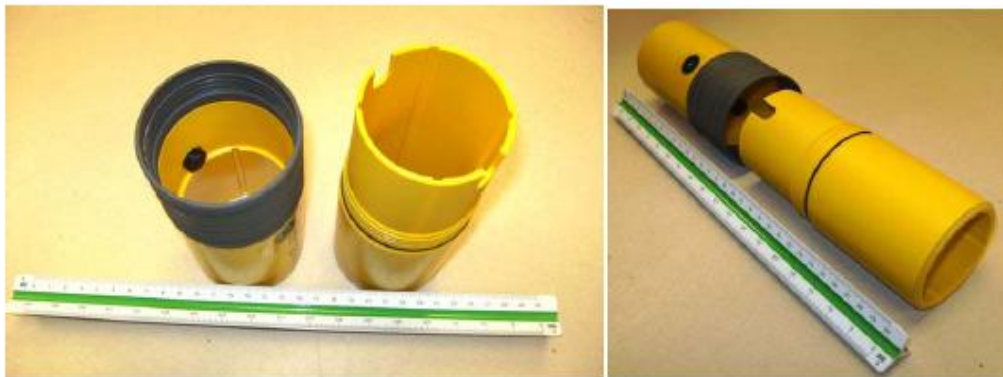


Figure 4.6 Example of inclinometer grooved guide casing (after Transportation Research Board, 2008)

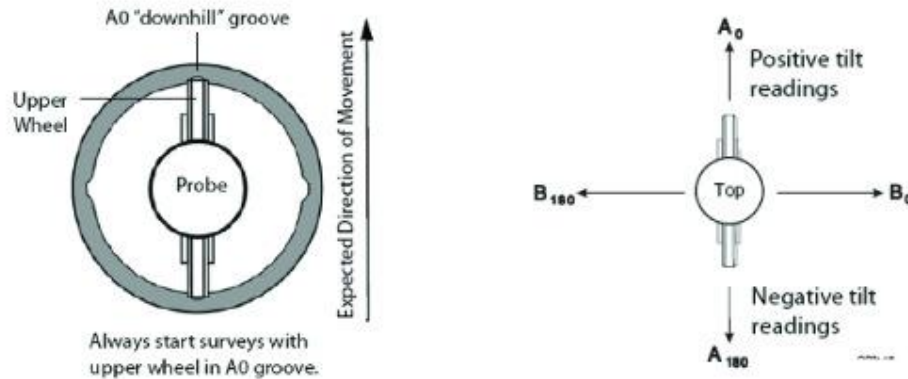


Figure 4.7 Orientation of probe within the inclinometer casing (after Transportation Research Board, 2008)

4.3.3 Analysis of groundwater data

During a ground investigation in 1995 two vibrating wire piezometers were installed at the Winter Gardens in Lower Ventnor (Fig 4.2). These were installed at different depths in order to monitor key groundwater levels within water-bearing strata (Fig 3.13). The piezometers recorded groundwater level continually between 1995 and 2002 at three hourly intervals. After 2002 no further readings were available through the Council. The data was converted to porewater pressures (kPa) and correlated with ground movement data to assess the relationships between porewater pressures within the different water tables and ground movement through the entire monitoring period.

4.3.4 Analysis of rainfall data

Rainfall records have been collected along the Undercliff since 1920 and specifically from Ventnor since 1926 at various rain gauges and weather stations within the Town (see Section 3.10). The most recent weather station data has been collected at Ventnor Park between 1992 and the present and records daily rainfall, temperature, evapo-transpiration and wind conditions. Both total daily and total monthly rainfall were calculated and similarly effective rainfall was calculated for both time periods. The rainfall calculations were used for collation with groundwater and ground movement records.

4.4 Laboratory testing

A suite of detailed laboratory tests were undertaken to determine the standard and specialist physical and geotechnical characteristics of the materials within the Ventnor landslide complex and to simulate the porewater pressure conditions that may occur in the landslide during failure. The testing suite is summarised in Table 4.3 and in summary involved:

1. Physical properties testing of the landslide materials
2. Isotropically undrained triaxial testing (ICU) to determine the failure envelopes of the failing materials
3. Isotropically consolidated drained triaxial testing, with a pore pressure reinflation stage (ICD PPR), to simulate landslide failure scenarios under elevated pore pressures at constant deviator stresses
4. Standard undrained direct shear box tests (SB) and specialist direct shear tests with a pore pressure reinflation stage at constant stress using the newly developed back pressure shear box (BPSB) to simulate landslide failure under elevated pore pressures at constant deviator stress in direct shear.

4.4.1 Physical properties testing

A detailed suite of standard soil classification tests were undertaken to establish the physical properties of the landslide materials at the basal shear zone. A representative number of samples were tested for each material sample collected from the Undercliff to establish and physical variability in the samples collected at the site, and to establish sample groups for further testing. These tests comprised particle size analysis, specific gravity, loss on ignition and Atterberg limits for each core and box sample. Further physical properties were established during triaxial and shear box testing, these included; moisture contents, bulk density, dry density, and void ratio. A summary of the physical properties tested and their associated methodologies is provided in Table 4.4.

Table 4.3 Summary laboratory testing schedule

Location	Sample no.	Laboratory testing schedule								
		ICU	ICD PPR	ICDR PPR	SB	BPSB	Moisture content	Atterberg Limits	Particle Size	Dry Density
Ventnor BH4	C8	-	1	1	-	-	3	3	3	3
Ventnor BH5	C1	-	2	-	-	-	4	3	3	2
	C2	-	-	-	3	5	8	3	3	8
	C6	-	-	-	2		3	3	3	2
Gore Cliff Block Sample	B1	7	9	3	-		19	3	3	19

Table 4.4 Summary of physical properties tests

Physical property	Method description
Moisture content	Calculated a proportion by mass of the dry solid particles. The moisture content has been obtained by a standard oven drying method where the soil is deemed as dry when no further water can be removed at a temperature of 105-110°C in accordance with BS 1377:1990a (section 3).
Atterberg Limits	Liquid limit Moisture content at which soil passes from a liquid state to plastic state and provides a means of soil classification. Testing was conducted using the one point cone penetrometer method in accordance with BS 1377:1990a (section 4)
	Plastic limit Moisture content at which a soil becomes too dry to behave in a plastic manner. Samples were proposed in accordance with BS 1377:1990 and the plastic limit was calculated as the lowest moisture content that a 20g sample could be rolled to a 3mm diameter. Further details of the testing methodology are provided in BS 1377:1990a (section 5).
	Plasticity index Calculated as the difference between the liquid and plastic limit by subtracting the liquid limit from the plastic limit in accordance with BS 1377:1990a (section 5).
Loss on ignition	Samples weighed and dried before being furnace dried for 6 hrs at 450 degrees. The organic content of the sample is then calculated
Particle size distribution	Particle size of site materials conducted using a Coulter granulometer to determine the relative percentage passing of sand, silt and clay size particles
Bulk density	Calculated as the mass per unit volume of the soil including any water contained. Measured using linear measurement method where samples are cut into a standard dimensions as described in BS 1377:1990a
Dry density	Calculated as the mass of dry soil contained in a unit volume. Measured using linear measurement method where samples are cut into a standard dimensions as described in BS 1377:1990a

4.4.2 Triaxial cell testing

Conventional soil mechanics requires the calculation of a number of key soil strength parameters that are fundamental in determining the stability, strength and deformation behaviour of any material. These comprise the effective angle of internal friction (ϕ') and the effective cohesion (c') derived from the construction of the failure envelope or Mohr Coulomb envelope. A minimum of three undrained triaxial tests is required, respectively carried out at three different initial confining pressures.

In the case of cohesive materials, a residual strength envelope can also be constructed which consists of the relationship between post failure strength of the material and the frictional resistance between randomly aligned particles along the shear surface. The residual strength envelope, by definition, should have a lower effective friction angle (ϕ') value and an effective cohesion (c') value tending toward zero. The peak and residual strength envelope delimit the behavioural boundaries of a given material under various stress and strain conditions and provide the initial stress conditions (pre-failure stress conditions) required for the design of the pore pressure reinflation tests. The development of pre-failure strain during the pore pressure reinflation tests can also be assessed against the stress-strain characteristics derived during conventional testing.

4.4.2.1 Triaxial cell apparatus

Triaxial testing was undertaken using a PC-controlled stress path triaxial testing system, designed and manufactured by GDS Instruments. The system uses the classic Bishop and Wesley (1975) hydraulic stress path triaxial cell. It uses a 38 mm diameter pedestal and top caps, one 4KN submersible load cell and 50 mm range displacement transducers (Fig 4.8). The parameters that can be controlled and measured are:

- Cell pressure
- Back pressure
- Specimen volume change
- Pore pressure

- Axial force
- Axial displacement

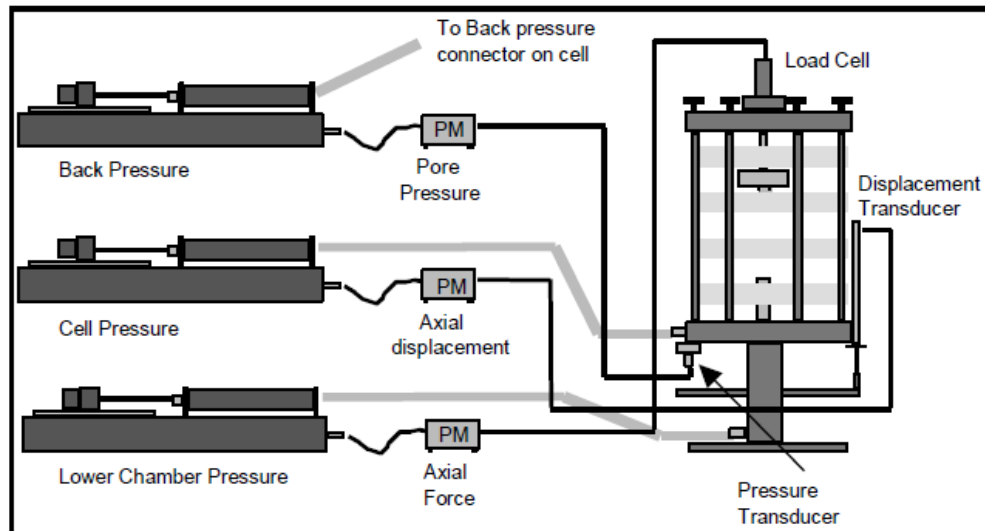


Figure 4.8 Schematic diagram of GDS triaxial cell system (after GDS Instruments, 2005)

An axial load/ displacement controller was used as the pressure controller; with axial force generated by the pressure in the cell's lower chamber. The controller uses a Remote Feedback Module (RFM) to control the axial load via an internal submersible load cell. The pressure controller precisely regulates the system using a closed loop servo control from the onboard pressure transducer. The system allows single, continuous, linear stress paths to be programmed in stress space. It can also perform constant rate of strain rate controlled tests at positive effective stresses.

There are four identical pressure transducers in the triaxial cell and one in each of the three pressure controllers as follows:

- Lower chamber pressure controller
- Cell pressure controller
- Back pressure controller

An additional fourth transducer measured pore pressure, routed through a data acquisition pad.

De-aired water was supplied by the Nold de-aerator which utilises cavitation by a high speed rotated vane to release air from tap water. The air was then removed through to a vacuum pump. The water stored in the tank was de-aired and maintained through a continuous vacuum generated by the internal pump above the water level.

The triaxial cell and data acquisition is controlled by GDSLAB v2 specialist software (GDS Instruments, 2005). The program runs using Microsoft Windows and provides a display on screen for the transducer readings, data logging and storage at regular time intervals (a minimum of every 10 seconds). It also provides automatic and manual control of the BP, CP, RP and CRS pump devices through user-defined equations and tolerance bands. Tolerance values were set at ± 0.5 kPa for the pressure controllers (i.e. CP, BP, RP), and ± 0.01 mm for the CRS pump, which were found to be suitable for the GDS stress path system without surpassing the target value.

4.4.2.2 Preparation of soil samples

Sample preparation involved two separate methodologies, dependent on whether the sample was undisturbed or remoulded. Undisturbed samples were taken and cut into a cylindrical shape, 38 mm in diameter and 76 mm in height. The sample was mounted on a cutting lathe and trimmed to the required dimensions using scalpels and sharp, straight edge, knives. The final height and diameter of each sample was measured, using a digital calliper, in millimetres to two decimal places. Samples that were observed to have cracked or had damaged surfaces during the trimming process were discarded and the material was used for other physical properties testing.

Disturbed samples were prepared by initially grinding dried soil samples using a pestle and mortar, before being passed through a 2 mm sieve in accordance with BS1377 (1990b). The soil particles which passed through the sieve were then mixed with distilled water to replicate original undisturbed

sample moisture contents and placed into the shear box mould. The sample was added as a series of layers and compacted to achieve the correct sample height. This enabled replication of the original samples undisturbed bulk density.

4.4.2.3 Stage 1: sample saturation

The soil samples were initially saturated in the triaxial cell, to simulate the recorded groundwater conditions at the Ventnor landslide shear surface. The saturation process is also required in order to remove the potential complication of pore air pressures, which differ from the porewater pressures and may produce misleading results (Head, 1998).

Initially each sample was flushed with carbon dioxide at a slow rate before de-aired water was flushed into the sample to fill the pore air voids (BSI, 1990b). Following this process a simultaneous increase in the back pressure and cell pressure was undertaken to dissolve the carbon dioxide into solution in the sample. During this period the cell pressure was always kept 10 kPa higher than the back pressure to maintain a positive effective stress and to prevent sample swelling during the saturation process.

4.4.2.4 Stage 2: sample consolidation

Following the saturation stage each sample was isotropically consolidated by the application of a confining pressure. Confining pressures were chosen as representative of the field stress conditions. The selected field stress conditions were further selected to be comparable with previous research on deep-seated landslide complexes on the South Coast of the UK (Petley *et al.*, 2005). The samples were consolidated at effective stresses ranging from 250 to 550 kPa.

Isotropic consolidation was undertaken by raising cell pressure within the triaxial cell from an initial value of 210 kPa to the desired confining pressure at a rate of 1 kPa/ hr. During the consolidation phase the back pressure was held at a constant of 200 kPa. The consolidation phase was completed when

there was no further significant volume change, and the excess pore pressure due to applied stress was dissipated (BSI, 1990).

4.4.2.5 Stage 3(a): undrained compression (shear)

Following the consolidation phase a series of samples were subject to an undrained shear at constant axial strain. During the undrained tests no drainage was allowed to occur during the shear stage and shear rates were kept low at 0.01 mm/min to prevent the development of uneven porewater pressures within the sample. The slow rates of shear allow for excess porewater pressure to equalise in the sample (BSI, 1990). Undrained tests were performed to define the failure envelope for the cohesive materials tested and to provide a suitable design parameter for the specialist pore pressure reinflation testing.

4.4.2.6 Stage 3(b): drained compression (shear)

Following the consolidation phase a series of samples were subject to a drained shear at constant axial strain to a predefined deviator stress. During this test further drainage was allowed to occur following consolidation, as the samples were sheared at 0.01 mm/min. Drained shears were performed on the samples used in specialist pore pressure reinflation testing.

4.4.2.7 Stage 4: pore pressure reinflation

A series of specialist pore pressure reinflation tests were undertaken to simulate groundwater-induced landslide development. In these tests failure occurs at a constant deviator stress, with strain development being caused by a reduction in the mean effective stress by increasing the porewater pressure in the sample. The rates of pore pressure reinflation were selected to replicate plausible groundwater recharge rates from the Ventnor piezometric data. During the tests the displacement of the sample through time was monitored to assess the progressive development of the shear surface under different conditions. Sample deformation is measured using a displacement transducer located at the top of the sample. Similarly, porewater pressure measurements were recorded at the top of bottom of the sample. Whilst these are unable to measure the exact conditions experienced at the shear surface, any error is

considered to be very minor and provides the best form of measurement without interfering with the conditions developing at the shear surface. The location of transducers at the shear surface, however, would have likely impacted on the progressive development of the shear surface. The method used is therefore believed to be the most accurate representation of the field landslide failure conditions.

4.4.3 Back pressured shear box

4.4.3.1 Back pressured shear box apparatus

Experimental testing was carried out in direct shear at constant deviator stress using the unique back-pressured shear box apparatus developed by the University of Durham and constructed by GDS (Fig 4.9). The GDS back pressured shear box (BPS) provides the opportunity to carry out direct shear testing on soil samples with varying degrees of saturation by controlling the porewater and pore air pressures of the specimen. The BPS is based on a standard direct shear device, modified to allow the measurement and control of matric suction. The apparatus can function as both a conventional direct shear and back pressured shear machine, using 100 mm x 100 mm samples. Control parameters comprise:

- Shear force and displacement
- Effective stress control
- Total stress control
- Pore air and water pressure
- Axial (normal) force and displacement (with optional axial actuator)

The back pressured shear box comprises both an upper and lower section of the sample vessel which are assembled using connecting screws. The lower section of the sample vessel contains a porous disk that is placed into a lower circular recess. Soil samples are placed into the sample vessel with filter papers of the same dimensions placed on the upper and lower sides of the sample. The sample vessel is then securely mounted in a sealed pressure vessel, an upper porous plate is placed on top of the specimen and vertical spacer is placed on the sample vessel from which the connecting screws have

been removed. The vessel is sealed by the upper section of the back-pressured shear box apparatus using twelve fastening screws. The load cell fits directly onto the upper porous disc. A vertical beam is connected to the apparatus and can apply a normal load to the sample, which is controlled by a hydraulic pressure controller.

The pressure vessel is flooded with de-aired water, and fluid pressure within the chamber is measured using two transducers, one mounted adjacent to the sample and the other on the fluid pressure control line.

The system was controlled and data logged using a lab software system (GDSLAB control software) designed and developed by GDS. The software was run using a high specification PC.

Table 4.4 Summary back pressured shear box system capabilities and technical specification

Feature	Specification
Overall dimensions (length)	875mm
Overall dimensions (width)	350mm
Displacement range (axial)	+/- 15mm
Displacement range (shear)	+/- 25mm
Maximum sample pore pressure	2 MPa
Maximum consolidation force	25 kN
Force accuracy	<0.1 %
Maximum consolidation stress	2.5 MPa
Maximum shear force	5 kN
Maximum shear stress	1000 kPa
Electrical Specification	240V or 110V 50/60 Hz single phase

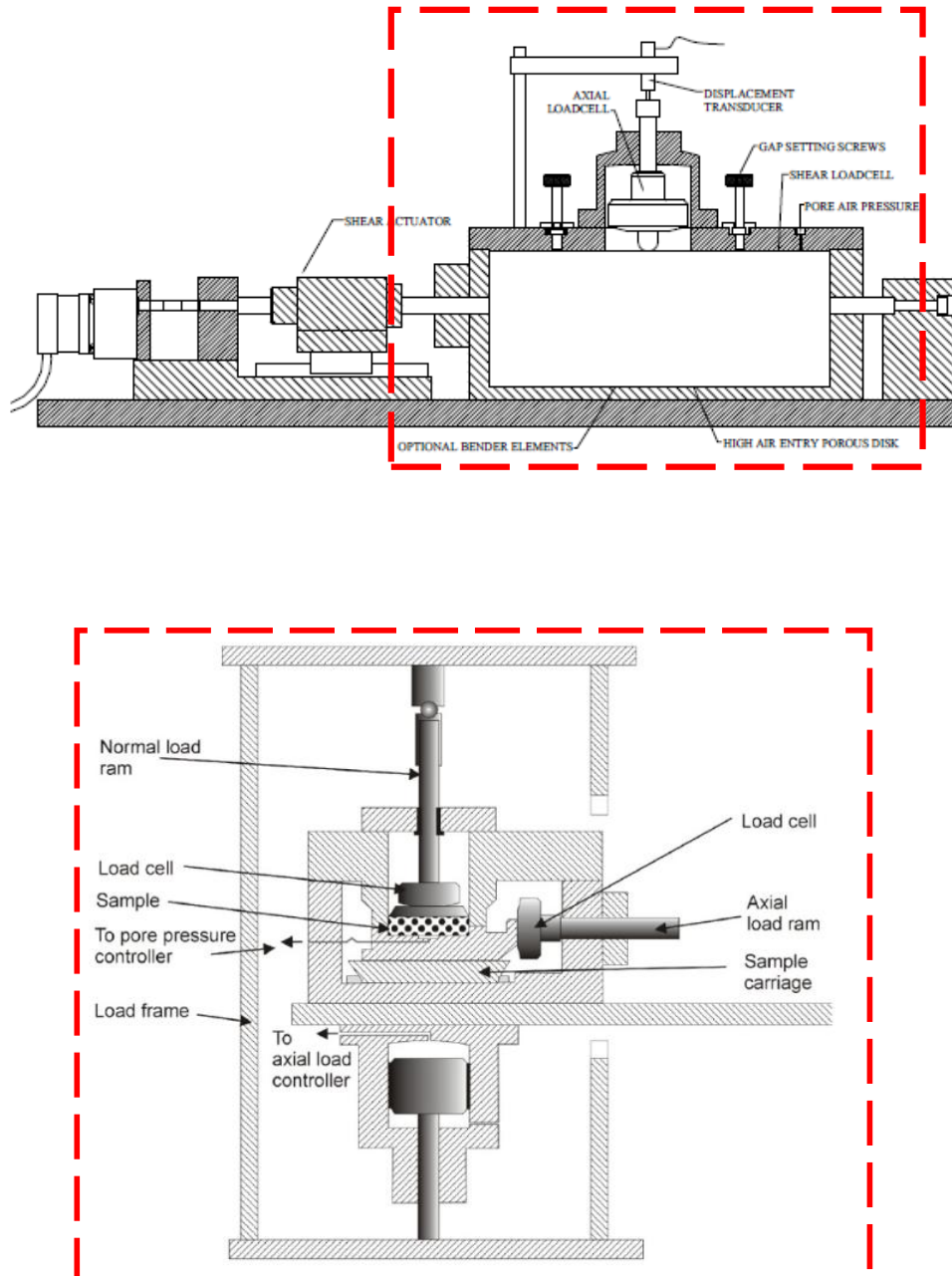


Figure 4.9 Schematic diagram of the GDS Back Pressured Shear box (Figure obtained from D. Petley and used with permission)

4.4.3.2 Preparation of soil samples

Samples were taken from the undisturbed core samples and stratigraphic equivalent block samples collected on the Isle of Wight. Small blocks were removed from the larger block samples, and excess material was trimmed away using a straight edged knife and the block template cutter, so that the

sample could be carefully placed within the carriage. Samples taken from drilling core and were carefully emplaced within the carriage. The corners of the carriage were then carefully filled with compacted sample trimmings without disturbing the main sample. Disturbance to the material was monitored during this process to ensure that negligible damage occurred to the sample during preparation. Each sample was weighed using a scientific balance and dimensions were measured using digital callipers. Any excess material from the trimming process was used to determine sample moisture content.

4.4.3.3 Stage 1: sample saturation

The soil samples were initially saturated in the back pressured shear box to simulate the recorded groundwater conditions at the Ventnor landslide shear surface. Pore air pressures were further removed by flushing the sample with carbon dioxide at a slow rate, before de-aired water was flushed into the sample to fill the pore air voids and ensure each sample was saturated. Following this process a simultaneous increase in the back pressure and cell pressure was undertaken to dissolve the carbon dioxide into solution in the sample. During this period the cell pressure was always kept 10 kPa higher than the back pressure to maintain a positive effective stress and to prevent sample swelling during the saturation process.

4.4.3.4 Stage 2: sample consolidation

Consolidation of the samples was undertaken by applying a normal load to the sample. The normal loads applied were calculated to replicate comparable conditions for the triaxial cell tests and previous tests undertaken on deep-seated landslides on the South Coast of the UK (Petley *et al.*, 2005a). The samples were consolidated at effective stresses ranging from 250 kPa to 750 kPa. The normal load is applied through a feedback controlled actuator which again permits the control of stress and sample displacement.

4.4.3.5 Stage 3: sustained initial shear

On successful completion of the consolidation stage of the test an initial stage of direct shear was undertaken. A shear force was applied to the sample at a predefined strain rate of 0.01 mm/min. The sample was subjected to this shear stage until a predetermined mean effective stress was reached, at which point the shear force was held constant.

4.4.3.6 Stage 4: pore pressure inflation

To simulate field conditions of groundwater induced failure, each sample was then subject to a pore pressure reinflation stage. During this stage the back pressure was raised at a predefined rate of between 5 and 10 kPa/hr, whilst both the normal load and shear force applied to the sample remained constant. The elevation of back pressure created an increase in porewater pressures within the sample, which reduced the mean effective stress in the sample until failure initiated. During this phase sample strain, porewater pressure, and displacement through time were measured and recorded at between 10 to 30 second intervals.

4.5 Chapter summary

This chapter has provided an outline of the methodological approach adopted in this study in order to meet the objectives in section 1.4. It has introduced the rationale for using Ventnor as the preferred field site and the field monitoring and laboratory techniques that will be used to understand the progressive development and past failure behaviour of a deep-seated landslide complex. The methodology draws on techniques from a number of disciplines including Geomorphology and Soil Mechanics, which reflects the multifaceted nature of this study and the significance of this field of study in understanding the nature and development of the landscape, slope stability and Engineering Geology.

Chapter 5: Ventnor Landslide Monitoring Results

5.1 Introduction

A key objective of this research is to compare the mechanisms of shear surface development observed under specialist PPR testing with the patterns of movement recorded in deep-seated landslide complexes in order to understand landslide behaviour. Whilst a number of studies based on the 'Saito approach' have confirmed a negative linear trend in $1/v - t$ space during the development of failure (e.g. Voight 1989; Fukuzono, 1989, 1990; Kilburn and Petley, 2003), others suggest that a more complex relationship may exist between basal deformation mechanisms and surface displacements (e.g. Petley *et al.*, 2002, 2005c; Piccarelli, *et al.*, 2004; Gonzalez *et al.*, 2008).

Section 5.2 reviews the landslide ground movement records, comprising automated inclinometer, settlement cells, inclinometers and differential GPS surveys. The analysis of these records is considered in the context of the earlier geomorphological mapping, historical damage surveys and the landslide stratigraphy presented in Chapter 3 to develop a holistic model for landslide movement behaviour for the Ventnor landslide complex.

Section 5.3 analyses the groundwater monitoring data collected in Ventnor to consider the establishment of key groundwater tables within the landslide, their location in relation to the landslide shear surfaces confirmed in section 5.1 and the relationship between groundwater and rainfall conditions.

Section 5.4 provides an assessment of the potential mechanism of ground movement behaviour observed in section 5.2, their relationship with groundwater and rainfall characteristics. The assessment analyses the existing landslide behaviour to consider the current stability of the site, its sensitivity in relation to future changes in groundwater and rainfall conditions, and the potential to forecast future ground behaviour under future rainfall scenarios.

5.2 Spatial and temporal patterns of ground movement

Detailed monitoring records of ground movement have been collected by the Isle of Wight Council in central Ventnor since 1995 as part of the ongoing landslide management strategy. This strategy has involved the installation of automated monitoring instruments such as crackmeters and vibrating wire settlement cells, which have been complimented by manual readings of deep inclinometers installed into the landslide to establish the nature and depths of landslide shear surfaces. In addition a series of differential GPS movement markers have been installed throughout the town and have been subject to repeat surveys. A detailed overview of the site instruments is provided in Table 5.1 and the location of instruments and is shown in Figure 5.1.

Table 5.1 Summary of landslide monitoring instruments, Ventnor Town

Installation	No. of instruments	Locations	Monitoring period
Vibrating wire crackmeter	3	Bath Road	1995 – 2004
		Newport Road	1995-2002
		Bath Road	1995-2004
Vibrating wire settlement cell	4	Newport Road	1995 – 2004
		Winter Gardens	
Vibrating wire piezometer	2	Winter Gardens	1992 – 2004
Manual inclinometers	2	BH2	2002 -2008
		BH4I	2005 – 2008
Annual movement marker Survey	57	Ventnor Town	2003 - 2008

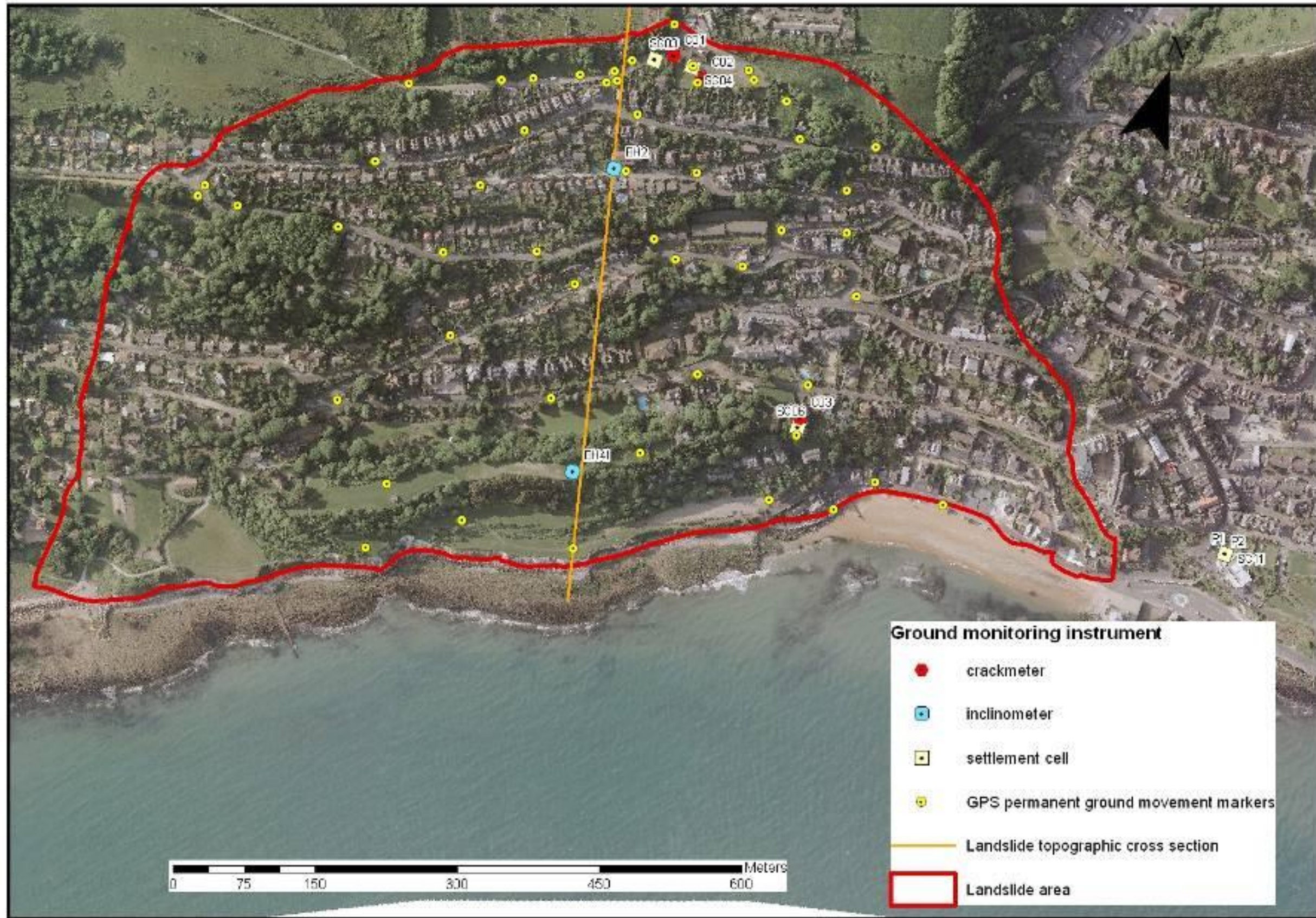


Figure 5.1 Location of the Ventnor ground monitoring instruments

5.2.1 Depth of ground movement

Two deep inclinometers have been installed on a transect through the centre of the landslide complex to establish the depth of movement; the depth and shape of the shear surface; and the behaviour of the shear surface in Upper and Lower Ventnor (Fig 5.2).



Figure 5.2 Location of Inclinometers within the Ventnor landslide complex

A previous interpretation of the inclinometer records at BH2 was undertaken by de Freitas (2009). The analysis was based on inclinometer readings taken between 2002 and 2004 and as been used to suggest that the landslide can be divided into four parts (Fig 5.3). At the base of the landslide a viscous layer was postulated, extending to c. 95 m bgl (A), which is separated from an upper layer of similar viscosity (C) by a layer of much lower viscosity (B) at the base of the Gault, where much of the shear displacement is concentrated. An upper zone of inactive ground (D) has then been hypothesised from ground level to approximately 20 m bgl, which is translating on the surface of zone (C).

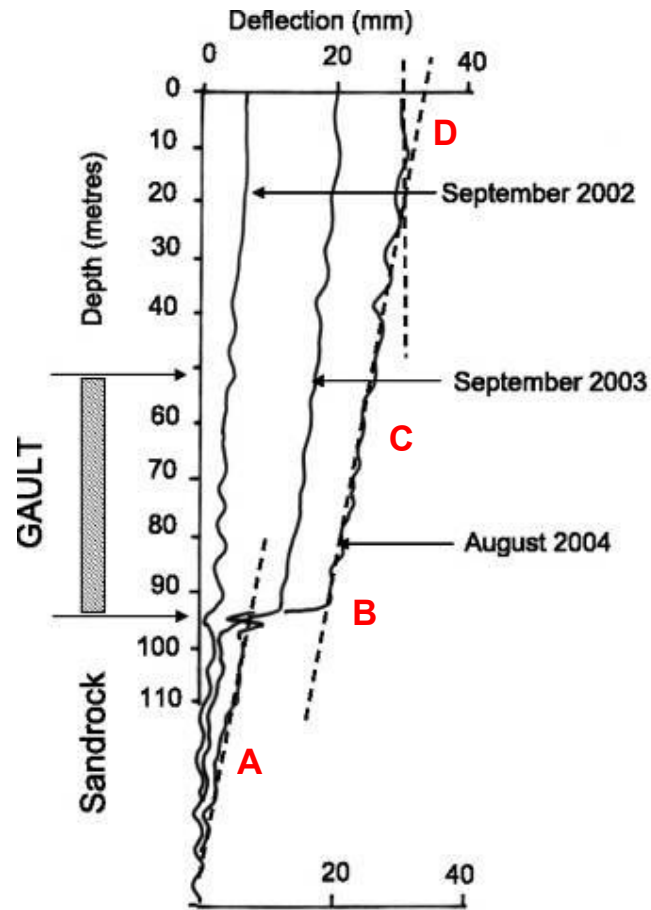


Figure 5.3 Inclinometer movement recorded at BH2 between 2002 and 2004
(after de Freitas, 2009)

These readings have been collated with additional inclinometer records collected by the Isle of Wight Council between 2002 and 2008 at BH2 and analysed in conjunction with reading taken between 2005 and 2008 of a separate at BH4I. The results from these inclinometers have been plotted along the topographic cross section surveyed through the centre of the landslide and analysed in relation to the landslide stratigraphy inferred from the geological logs at each borehole (Fig 5.4). In addition to the inclinometer records a distinct shear zone was observed within the recovered borehole core at BH5 located a base of the Gault Clay within the Gault/Carstone transition zone. The results indicate the presence of a two tiered landslide system which comprises of a single shear surface at the base of the Gault Clay measured in BH2 and a lower tier shear surface seated at the base of the Gault clay in BH4. Core logs from the BH4 record disturbed Gault Clay

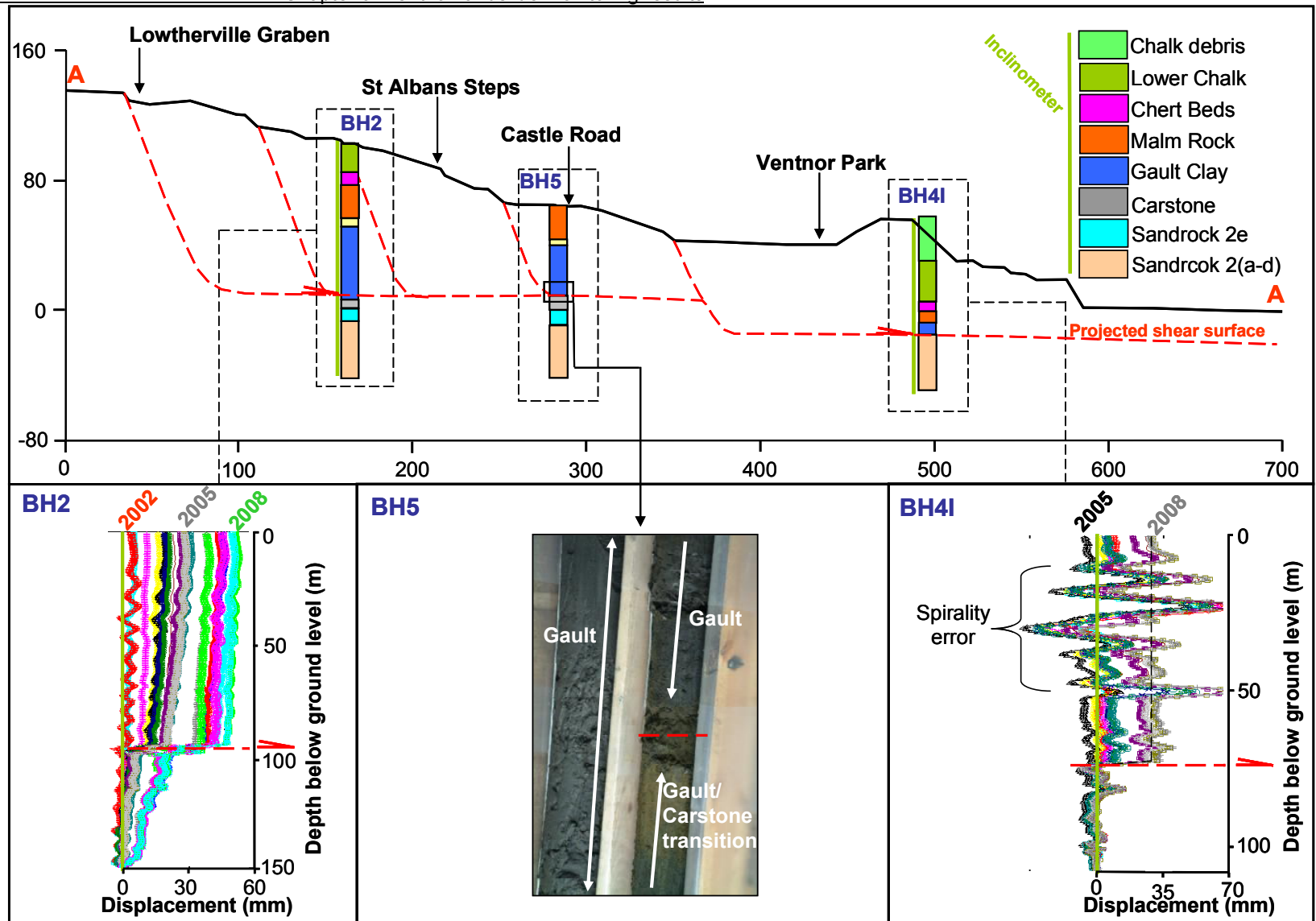
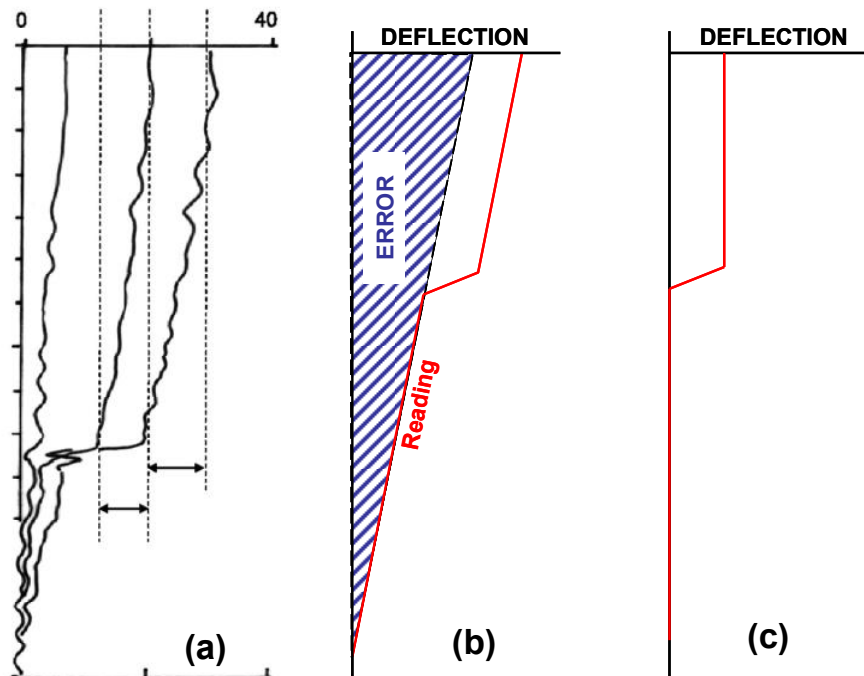


Figure 5.4 Cross section of landslide ground movement within the Ventnor landslide complex

overlying intact Sandrock unit 2d which indicates Sandrock unit 2e is absent at this location (Halcrow, 2006). The results confirm the shear surface is structurally controlled by the 2° south (seaward) dipping strata present in the Undercliff. This suggests movement is occurring within a discrete shear zone; there is little evidence to support the hypothesis of viscous flows at varying depths proposed by de Freitas (2009). The flow movements considered by de Freitas are more likely to be as a biased shift error caused by inconsistency in the inclinometer readings (Fig 5.5). Such errors in readings have been known to create misleading interpretations of ground movement (e.g. Mikkelsen 2003; Transportation Research Board, 2008). These errors are particularly common at the base of boreholes where instrument warm up drift is most acute, the borehole inclination is steepest and the reading is the greatest distance from the top reference point (Mikkelsen, 2003)



*Figure 5.5 Potential travel error within the borehole measurements at BH2
 (a) Ventnor inclinometer record (after de Freitas, 2009) (b) bias shift error (c)
 bias shift correction (adapted from Mikkelsen, 2003)*

The available inclinometer records have been used to analyse the annual rate and depth of movement within the Ventnor landslide system (Table 5.2). The results show a relatively consistent rate of movement of typically between 7 and 9 mm / yr in at a depth of 93 m bgl in BH2 and 76 m bgl in BH4I. The overall movement rates however illustrate that horizontal displacement is consistently higher at BH4I. Annual rates suggest that during this time displacement rates in lower Ventnor (BH4I) are over twice the rates measured at BH2.

Table 5.2 Summary of inclinometer data 2002 to 2008

DATE	Measured displacement (mm)	
	BH2 (Upper Ventnor)	BH4I (Lower Ventnor)
	Depth	Depth
	93 m bgl	76mm bgl
2002 - 2003	15	-
2003 - 2004	9	-
2004 - 2005	9	-
2005 - 2006	7	9
2006 - 2007	0	14
2007 - 2008	8	9
Total	48	32
Annual Rate (2002-2008)	8.0	-
Annual Rate (2005-2008)	5.0	10.7

Whilst the difference in displacement rate appears to relate largely to movements recorded between 2006 and 2007, these measurements provide the first evidence that displacement rates are higher toward the landslide toe in comparison to the Upper landslide blocks. This analysis suggest that the entire landslide complex is currently moving and that the ongoing development of graben may be related to toe unloading as a result of differential displacement in the lower tier landslide blocks.

5.2.2 Differential GPS movement records

The spatial patterns of ground movement have been monitored through a series of repeat differential GPS surveys of permanent ground movement markers across the town. The markers were installed in 2003 and subsequently repeat surveys have been undertaken in 2005, 2006, 2007 and 2008. Following the 2008 survey no further data has been provided from the Council.

Previous analysis of the GPS data from the Town has been considered by de Freitas (2009) and has been used to suggest that movement is occurring in a number of directions across the site, which does not correspond to any specific behaviour. This has been related to a hypothesis that the slope is cut through a number of polished surfaces and therefore movement in any direction is possible (Fig 5.6).

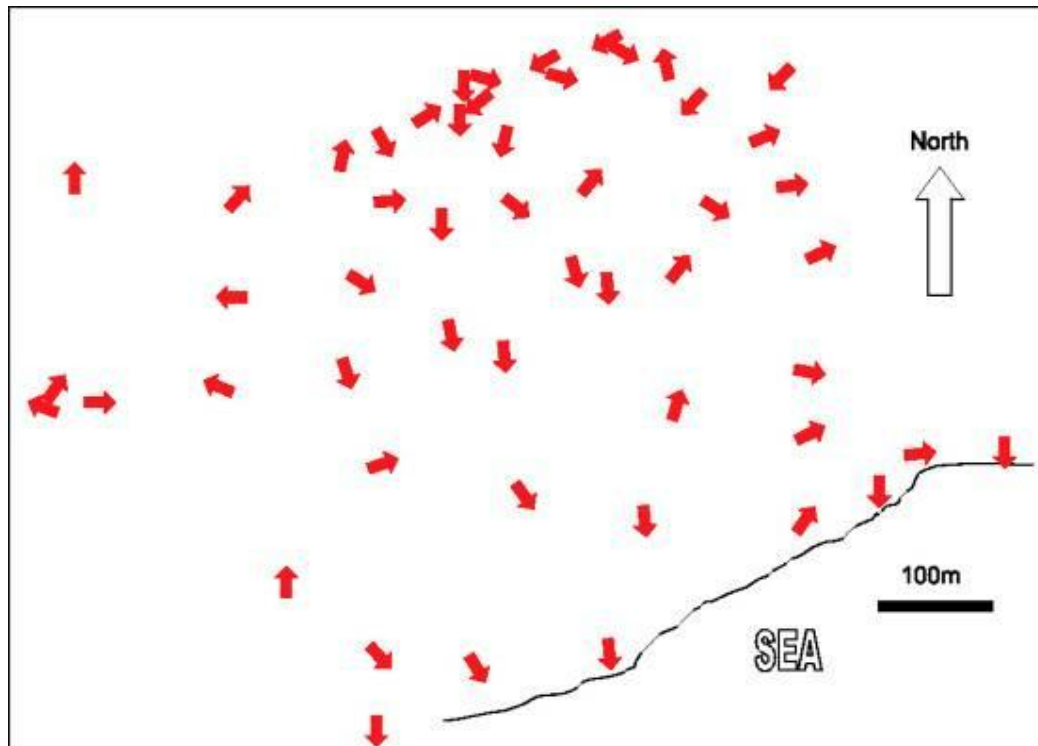


Figure 5.6 Differential GPS from Ventnor Town (after de Freitas, 2009). The arrows indicate the measured direction of movement of that point.

The differential survey data has been used to calculate both the horizontal and vertical displacement of each movement marker position from its baseline position recorded in the 2003 survey (Table 5.3). The results indicate that, in most locations, no specific direction of movement can be ascertained through the surveys, with both uplift and settlement occurring in many locations, in addition to landward and seaward movement depending on the chosen surveys used to establish movement vectors. This variability in displacement rates and direction is inconsistent with the ground movement evidence presented in the inclinometers at the site (Fig 5.4). It is more plausible that given the relative low displacement distances indicate only millimetres of change at most marker locations this variability is a function of measurement error rather than true measure of landslide displacement. Such marker surveys therefore may only provide real displacement measurements over longer time periods greater levels of displacement have occurred at the site.

Despite the inaccuracies in the potential ground displacement and settlement rates the overall direction and degree of movement between 2003 and 2008 have been overlain with the geomorphological mapping of the Town (Fig 5.7). The map indicates that whilst some vectors of movement are not credible (such as those suggesting movement upslope) in some locations movement is consistent with the orientation of mapped landslide blocks. In particular the arcuate headscarp of a lower landslide system associated with the Esplanade and Winter Gardens (area A) and the spreading movement of the large translational landslide blocks in Upper Ventnor (area B)

Table 5.3 Differential GPS measurements of horizontal and vertical displacement from baseline survey (December 2003)

Marker Number	Horizontal displacement (mm)				Vertical displacement (mm)			
	2005	2006	2007	2008	2005	2006	2007	2008
V1	31	47	71	12	-7	124	47	-2
V2	39	26	30	39	-30	-42	-27	-23
V3	8	10	17	error	-1	-12	2	22
V4	18	16	29	error	-8	-12	8	-34
V5	45	error	error	45	-40	error	error	-136
V6	56	24	31	24	-46	-26	-25	-33
V7	error	error	error	6	error	error	error	-47
V8	300	78	43	134	error	error	error	error
V9	15	9	8	8	0	-17	-11	-17
V10	45	40	76	28	-43	26	-6	6
V11	25	7	17	76	22	-21	42	159
V12	15	33	13	-	-4	24	-20	error
V13	13	16	45	30	-10	-1	-18	11
V14	85	33	13	-	71	-51	-44	-48
V15	12	3	8	-	-9	1	8	error
V16	29	22	17	29	-24	-31	-29	-29
V17	116	30	12	6	-113	33	-28	-13
V18	69	22	26	7	66	-21	-17	-14
V19	49	18	9	20	46	-45	12	-30
V20	45	13	16	19	-43	-44	-48	-68
V21	11	11	14	22	-8	-26	-7	-14
V22	24	9	26	26	-22	-12	-20	-28
V23	466	86	86	86	-6	-70	-90	-113
V24	33	25	35	49	-27	5	8	-49
V25	88	23	103	57	-88	-49	-140	-229
V26	52	27	31	22	-26	-70	-85	-95
V27	17	15	10	11	-11	-8	-3	-23
V28	89	103	69	101	35	103	63	51
V29	42	22	20	16	-37	-42	-37	-55
V30	26	13	11	9	-21	-29	-35	-74
V31	26	0	26	0	-17	0	-47	0
V33	58	19	23	33	-56	-48	-53	-65
V34	84	20	12	20	75	-45	-14	-48
V35	24	19	23	19	-22	-21	-19	-39
V36	185	116	115	114	-17	0	-47	0
V37A	7	5	8	10	-7	-23	-17	-11
V38	16	18	14	19	-14	-38	-32	-38
V39	101	175	28	24	70	21	-124	-73
V40	36	31	47	33	-31	13	-42	-71
V41	16	5	41	62	-7	-6	5	48
V42	19	14	11	22	-14	-11	-15	-14
V43	42	21	4	12	32	-6	2	-26
V44	23	27	21	31	17	-39	-16	-26
V45	66	14	181	19	65	8	-76	-11
V46	30	21	20	26	-27	-25	-17	-36
V47	29	19	3	38	-29	-1	-25	-24
V48	28	27	23	33	-20	-22	-5	-22
V49	4	5	12	32	-3	-8	8	5
V50	15	16	11	34	-4	-14	-22	-29

This potential indicative pattern of movement observed depicted by the GPS survey can be supported further by overlaying the historical damage survey records on the geomorphological mapping (Fig 5.8). These surveys have included settlement measurements of bench marks, analytical photogrammetry, short term measurements of crack separation and direct measurement of crackmeter and settlement gauges (Chandler, 1984; Woodruff, 1989).

The results conclude that the most severe damage has occurred within the area of the Lowtherville Graben, which forms the current headscarp of the Ventnor landslide system and the current landward extent of movement. The damage mapping further demarcates evidence of lateral shear between two distinct landslide units, which extends seaward from the graben in upper Ventnor to the west of Bath Road. In addition damage is observable at Bath road and along the Esplanade, which is consistent with the GPS movement vectors in this area and explains the presence of separate arcuate landslide headscarp which is likely to extend offshore. Less severe damage is concentrated along the separate landslide blocks in upper Ventnor and along the Ventnor park road in Lower Ventnor. This damage records support the hypothesis of an upper and lower tiered landslide system with differential movement occurring in each landslide unit.

The historical damage measurements taken across Ventnor have been used to conclude that the majority of sites have either been moving at less than 6 mm/yr, or show no signs of movement (Moore *et al.*, 2007). In the instances where short term measurement overlapped with long term studies the rates of movement were considered to be consistent. The only exception to this was the movements measured at the Lowtherville Graben, which have been measured at between 53 mm / yr and 125 mm / yr (Chandler 1984), with long term trends (from 1988 onwards), based on council data, of about 28 to 30 mm / yr. This is reflected in the distribution of damage across the town, which is clearly concentrated in Upper Ventnor (Fig 5.8). The annual movement rates indicate in historical studies are consistent with the movement rates recorded in the inclinometers of between 5 and 10.7 mm / yr.

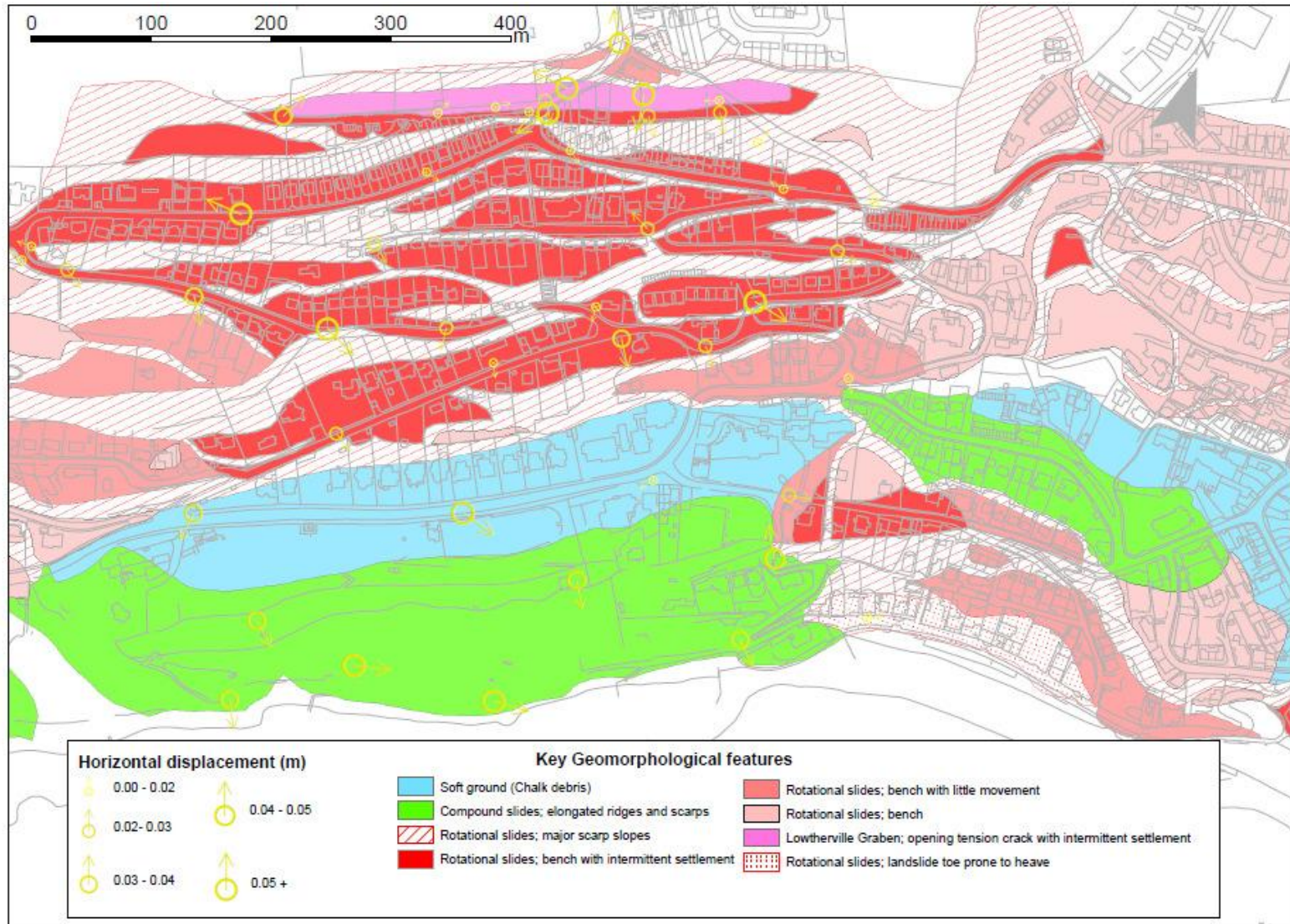


Figure 5.7 Comparison of the differential GPS survey data collect by IWC (2005-2008) and site geomorphological mapping undertaken by GSL, (1991)

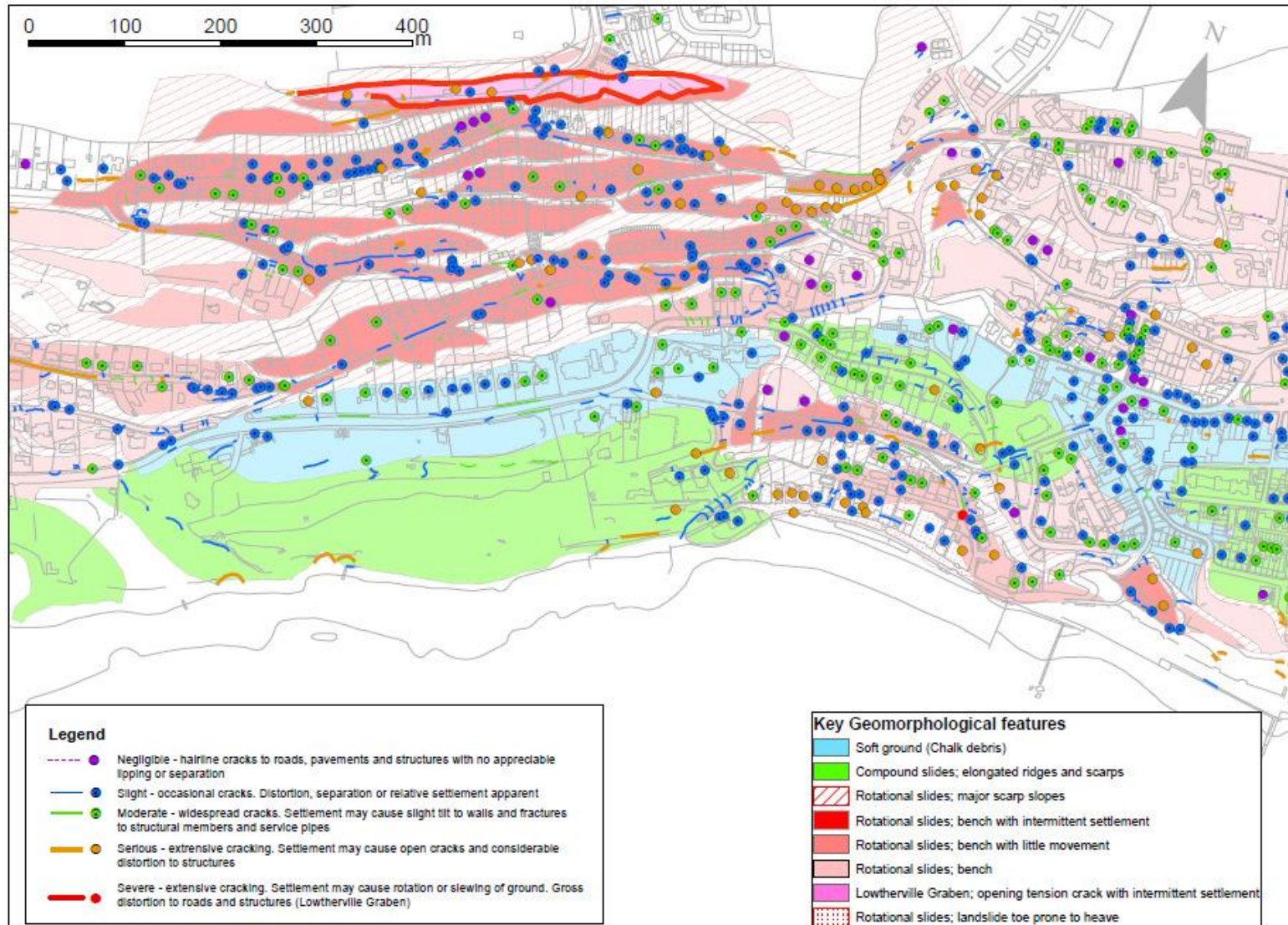


Figure 5.8 The spatial distribution of damage in relation to site geomorphological mapping undertaken by GSL (1991)

5.2.3 Movement patterns, Newport Road (Lowtherville Graben)

Settlement cells and crackmeters have been installed at Newport Road in the area of the Lowtherville Graben (Fig 5.9). The graben feature delimits the present extent of the Ventnor landslide complex as the landward extent of a series of large translational landslide blocks as identified in the geomorphological mapping. Crackmeters C01 and C02 have been installed to measure the horizontal displacement of the rear scarp and reverse scarp respectively. In addition settlement cells SC03 and SC04 are located within the graben feature to measure vertical displacement.

Detailed analysis of monitoring records at SC03 and SC04 demonstrates that ground settlement has occurred at a relatively uniform creep rate of between 38.7 to 46.7 mm / yr throughout the monitoring period (Fig 5.10). A series of regular fluctuations are also observable in both settlement records, suggesting a series of settlement and uplift cycles are occurring within the long term trend (Fig 5.11). The analysis of SC03 shows much greater annual variability in comparison to SC04, which shows only minor fluctuations in settlement. These seasonal episodes of heave and settlement are superimposed on a general trend of continual settlement that is consistent in both SC03 and SC04. The records further illustrate a distinct period of increased settlement rate at SC04 that occurred between October 2000 and April 2001. This period of acceleration has not been observed in SC03 records. Whilst some variability is observed between the two cells results indicate a strong linear correlation in settlement over the study period with an R^2 value of 0.90 (Fig 5.12).

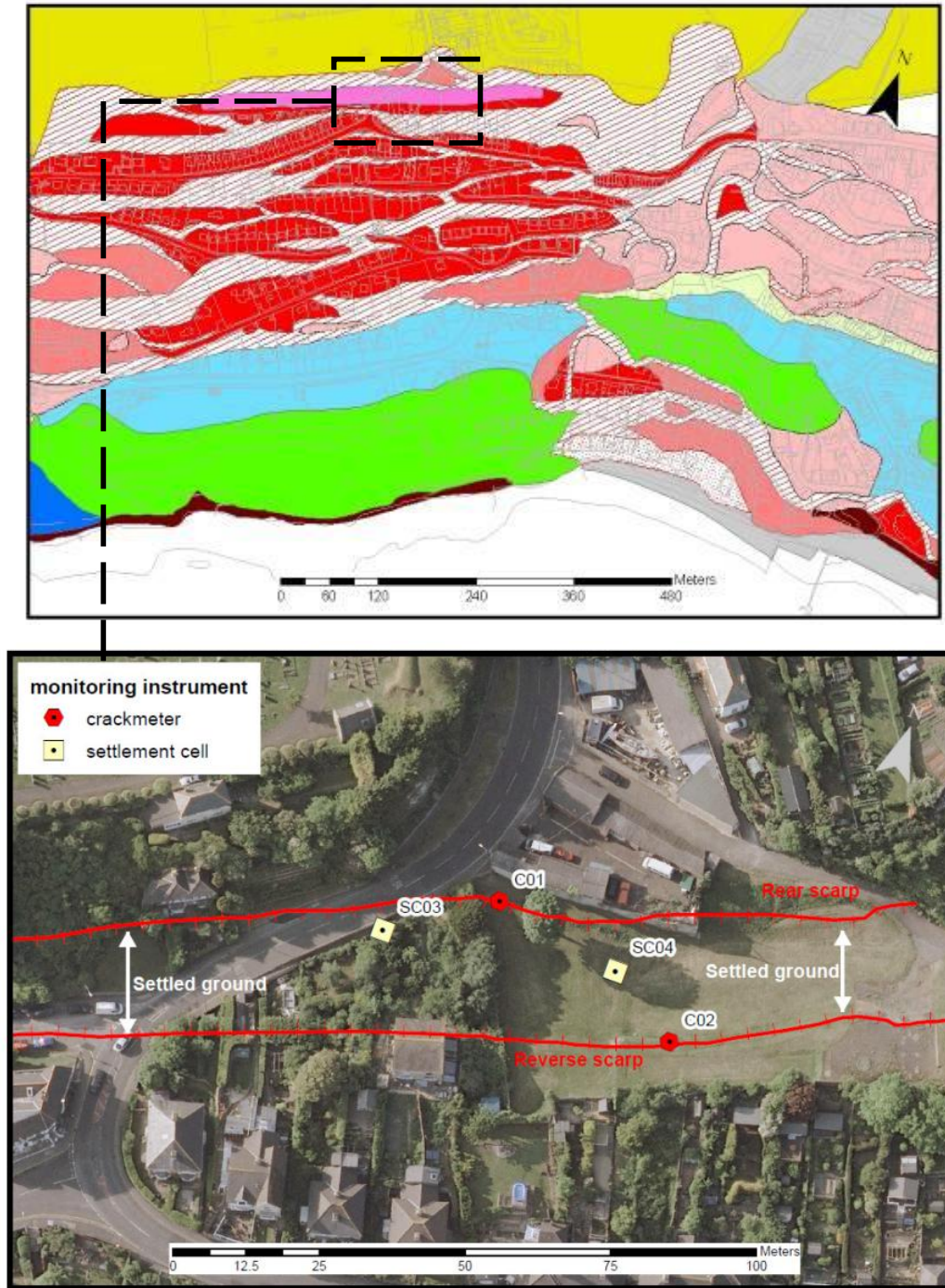


Figure 5.9 Monitoring instruments installed at Newport Road (Lowtherville Graben) in relation to the site geomorphology mapped by GSL (1991)

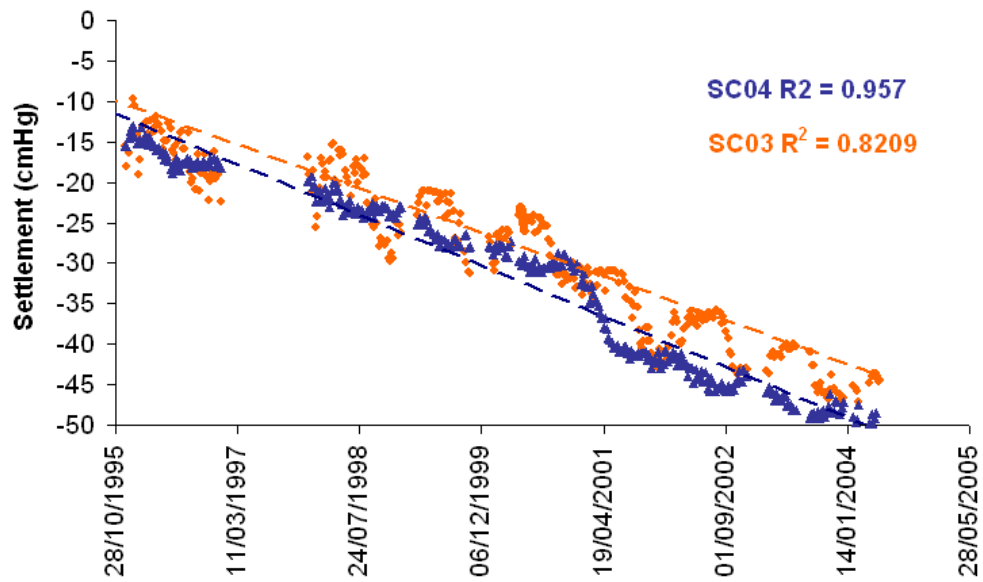


Figure 5.10 Settlement records at SC03 and SC04, Newport Road between 1995 and 2004

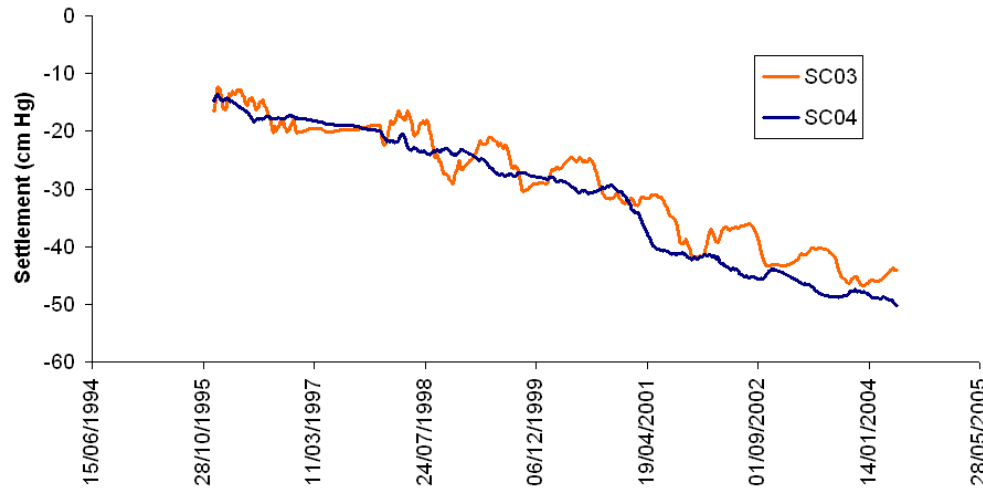


Figure 5.11 Running mean settlement records at SC03 and SC04, Newport Road between 1995 and 2004

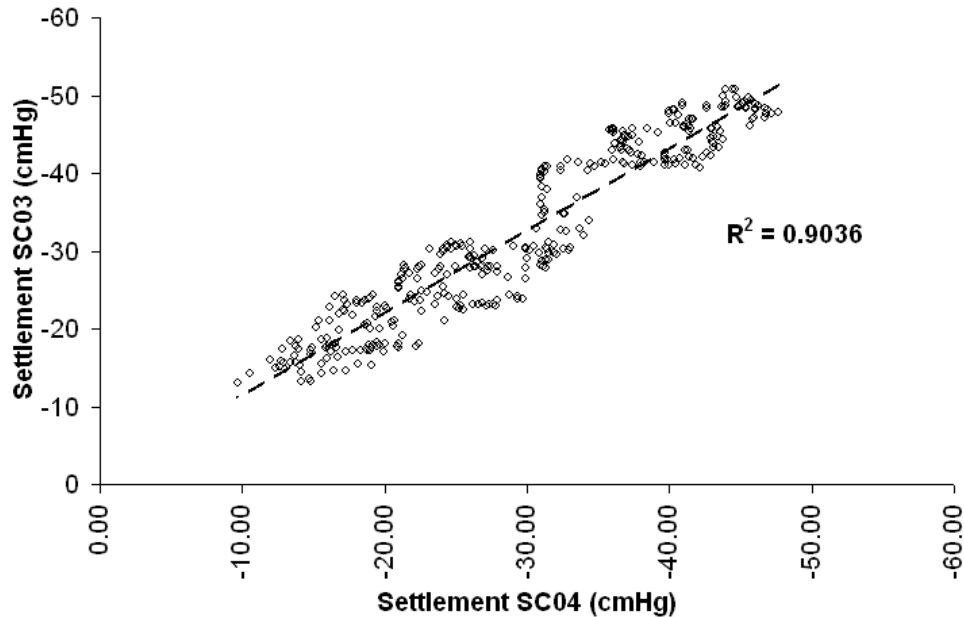


Figure 5.12 Correlation of settlement measurements at the Newport Road between 1995 and 2004

Analyses of crackmeter records at C01 and C02 over the same period suggest similarly consistent horizontal displacement (Fig 5.13). In the case of C01 the results illustrate that displacements occurred at a relatively uniform displacement rate of approximately 6.6 mm/yr between 1994 and 2000. This was followed by a period of acceleration from November 2000 to February 2001 when movement increased to a rate of 19.2 mm/yr for a four month period. Displacement rates then reduced to a continuous rate of 2.0 mm/yr between 2001 and 2002. Analysis of the displacement records illustrates that movements at the headscarp (C01) are greater than that measured at the reverse scarp (C02). The relationship between these two datasets also shows a statistically significant linear correlation (Fig 5.14), which indicates that whilst movement was greater at the rear scarp consistent horizontal displacement was recorded at both locations. Whilst greater displacements have been measured at the headscarp, the extension of C02 demonstrates overall extension of the landslide and, interestingly, higher rates of extension at C02 can occur without an increased displacement response at C01. This displacement behaviour provides clear evidence that the graben moves as a single block.

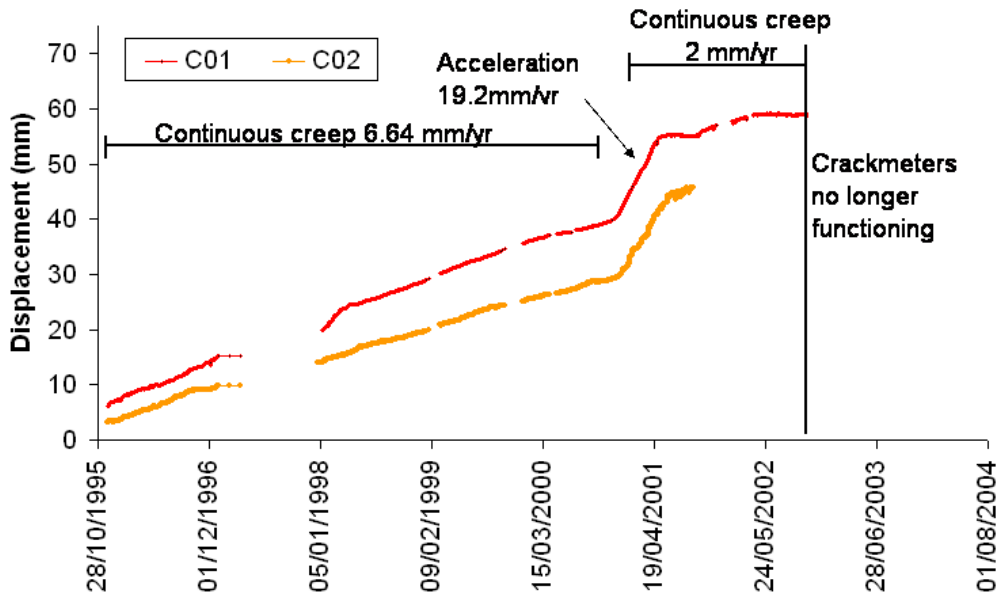


Figure 5.13 Displacement against time recorded at C01 and C02, Newport Road between 1995 and 2002

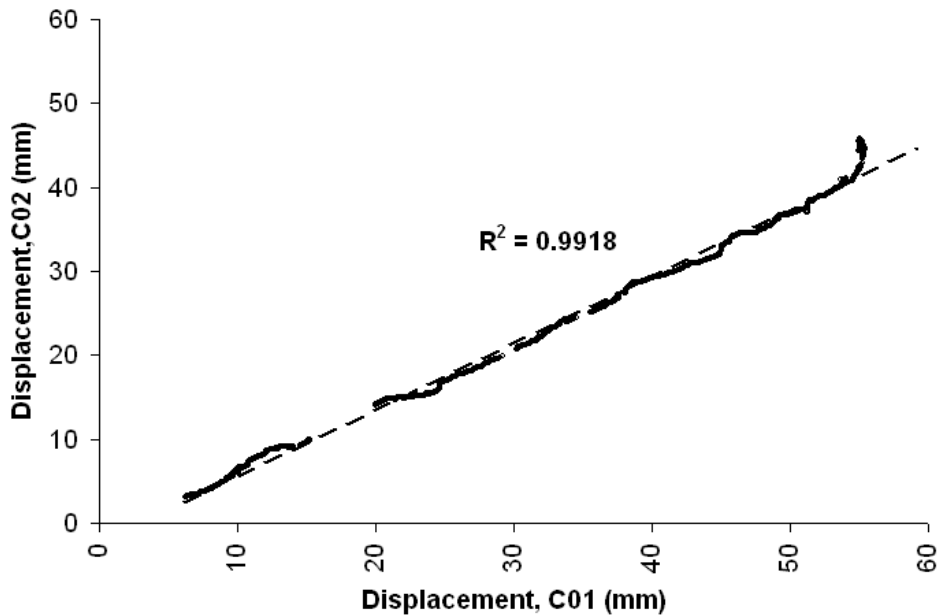


Figure 5.14 Correlation of horizontal displacement measured at C02 and C01 between 1995 and 2002

Correlation of the horizontal displacements measured at C01 and C02 and vertical displacement measured at SC04 (Figure 5.15a) and SC03 (Figure

5.15b) demonstrate statistically significant linear relationships. Whilst data has only been collected from two locations to date, this indicates that the patterns of long term displacement across the graben are consistent both horizontally and vertically. The analysis indicates that vertical displacement rates were significantly higher throughout study period. This regression analysis demonstrates a much closer relationship between horizontal displacement and settlement at SC03 when compared to SC04, which is related to the greater variation in the settlement and uplift cycles measured within the longer term settlement trend at SC04.

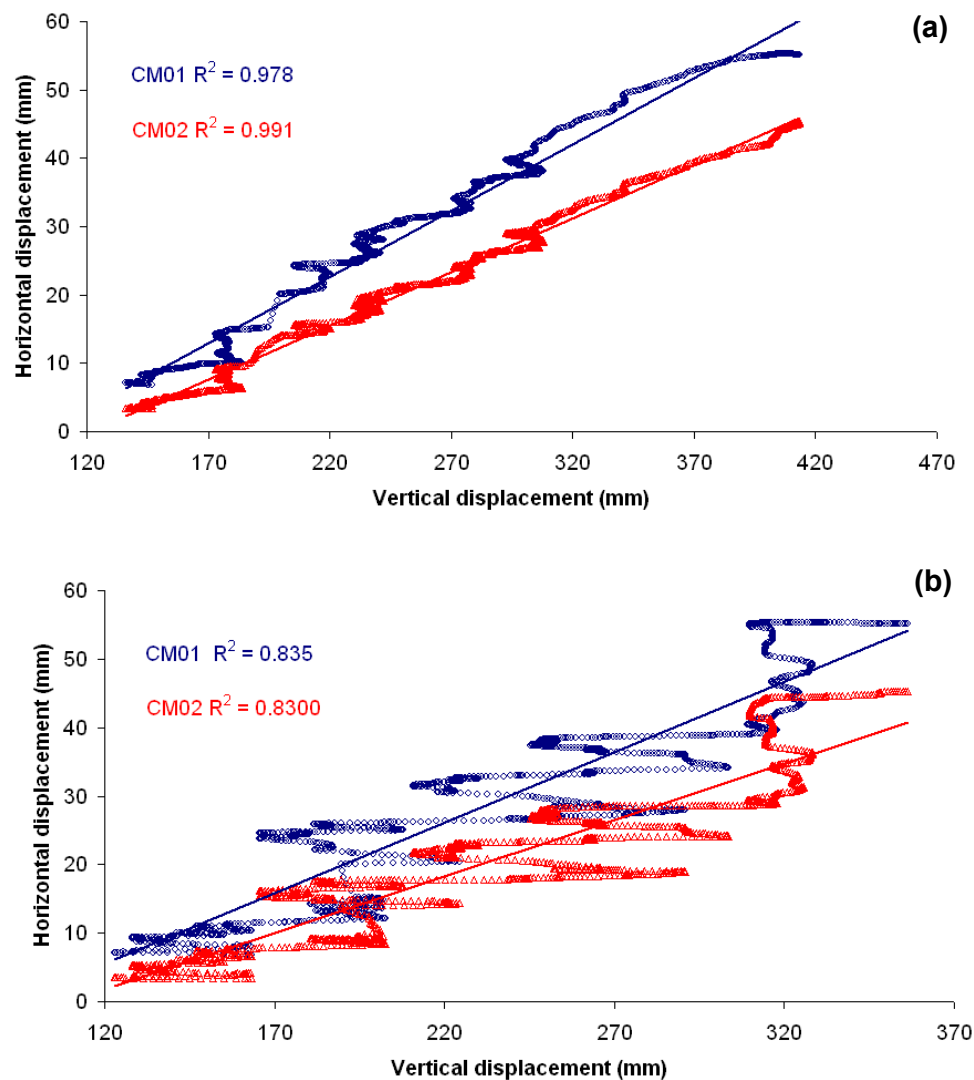


Figure 5.15 Correlation of horizontal displacement with vertical displacement measured between 1995 and 2002 (a) SC03 (b) SC04

5.2.4 Movement patterns, Bath Road

A single crackmeter (C03) and settlement cell (SC06) are installed at Bath Road in Lower Ventnor, providing records of vertical and horizontal displacement between 1995 and 2004 of an area of steep road which has been subject to previous episodes cracking and damage. The geomorphological mapping illustrates that this location is an active area of instability depicted by a series of landslide blocks (Fig 5.16).

Analysis of settlement records at SC06 demonstrates a statistically significant linear trend in settlement rate throughout the study period, with an overall vertical displacement of 15 cm with an annual rate of 1.67 cm / yr (Fig. 5.17). Despite settlement rates being significantly lower than those recorded at the Lowtherville Graben the elevations and location of the settlement cells toward the toe of the landward section of the landslide indicate that significant ground displacement is occurring in this area, consistent with previous damage records.

As observed in the Lowtherville Graben settlement, records at SC06 illustrate a regular cyclical settlement and uplift cycle consistent with the records at SC03 and SC04 (Figure 5.18).

The crackmeter records from C03 illustrate little evidence of crack displacement (Fig 5.19). There is a period of crack extension and contraction identifiable between 1995 and 1996. Following this the readings suggest that the crackmeter was reset in 1998 without further calibration resulting in a 40mm change in displacement readings. From 1998 to 2004 no crack extension was measured. Whilst the variation in the readings indicate that this record should be treated with caution the results indicate that any horizontal displacement measured at Bath Road occurred through movement of the entire landslide mass as opposed to the individual landslide unit.

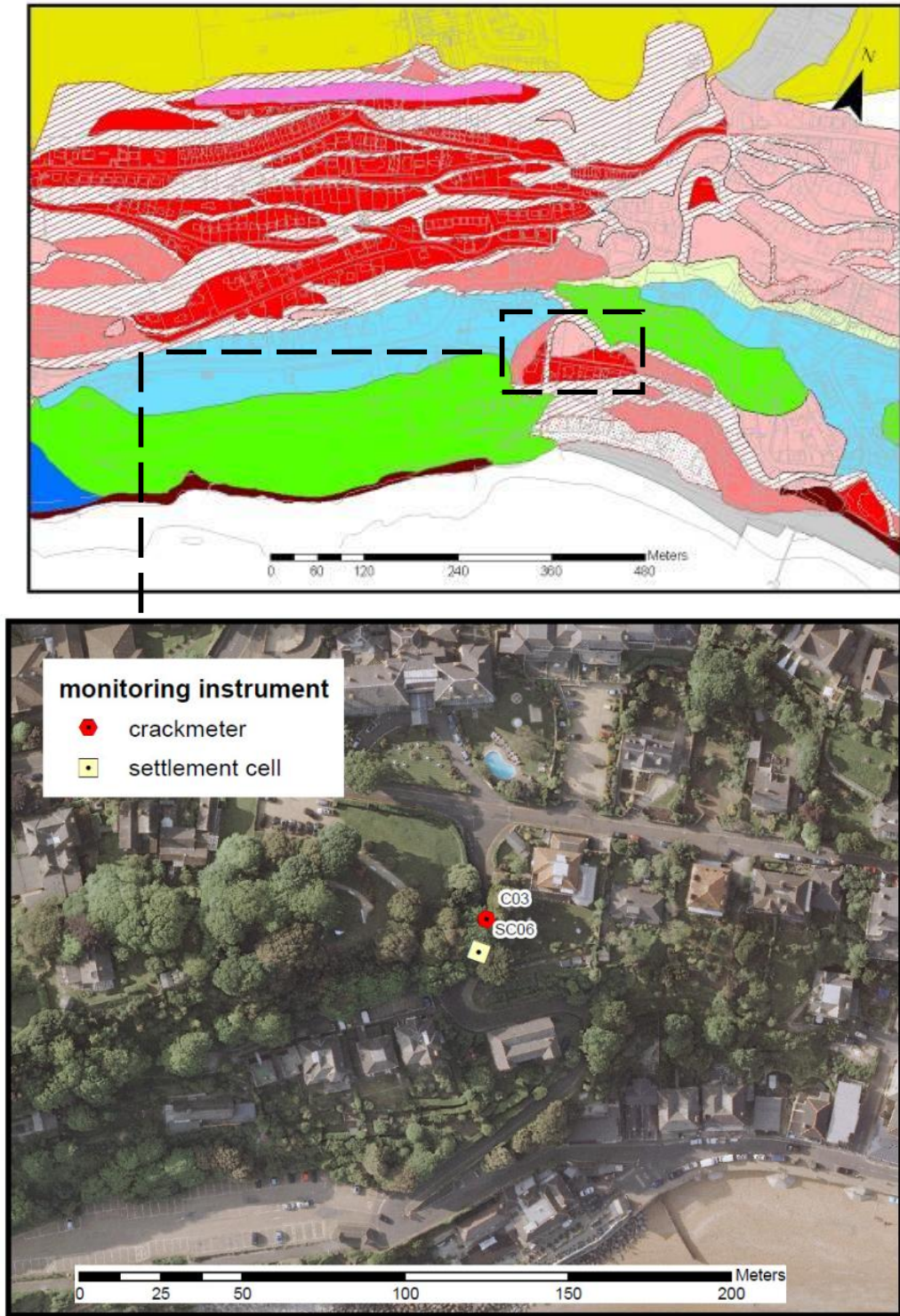


Figure 5.16 Monitoring instruments installed at Bath Road in relation to the site geomorphology mapped by GSL (1991)

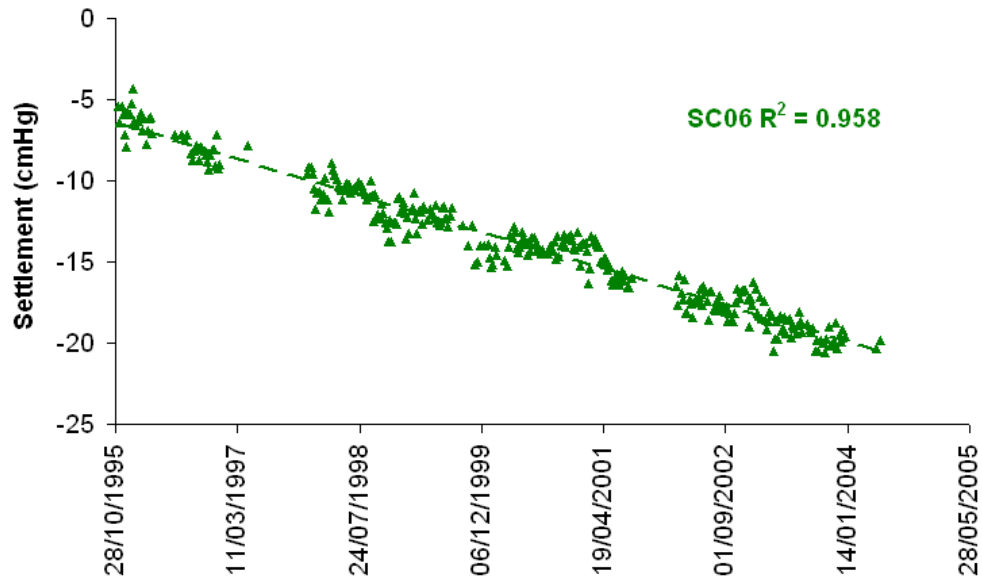


Figure 5.17 Settlement records from settlement cells SC06, Bath Road (1995-2004)



Figure 5.18 Running mean settlement measured at SC06, Bath Road (1995-2004)

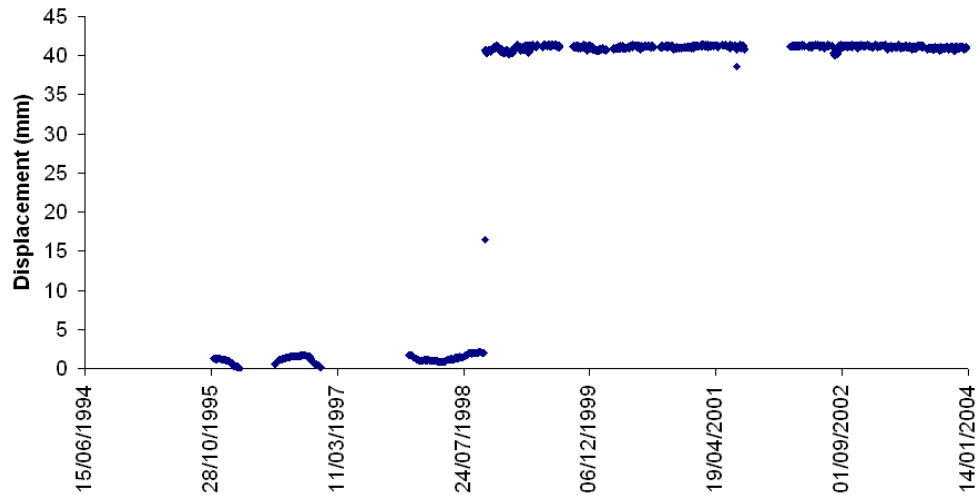


Figure 5.19 Displacement against time recorded at C03, Bath Road

The settlement rates measured at Bath Road, together with limited horizontal displacement measurements for C03, indicate that the area may form the headscarp of a lower tier landslide. This hypothesis is supported by the geomorphological mapping (GSL, 1991), which suggests the presence of a separate landslide unit. The lower rates of settlement are consistent with the direction of movement anticipated lower down the landslide system, where the majority of displacement would occur along a near horizontal axis. The consistent settlement behaviour and lack of extension evidence in C03 demonstrate that the landslide units generally behave as a single mass during periods of ongoing creep.

5.2.5 Movement patterns, Winter Gardens

An additional settlement cell settlement has been installed at the Winter Gardens in Lower Ventnor, which provides a further record of ground displacement between 1995 and 2004. The damage survey data and geomorphological mapping indicate this to be located in the same area of active instability as the Bath Road monitoring instruments (Fig 5.20).

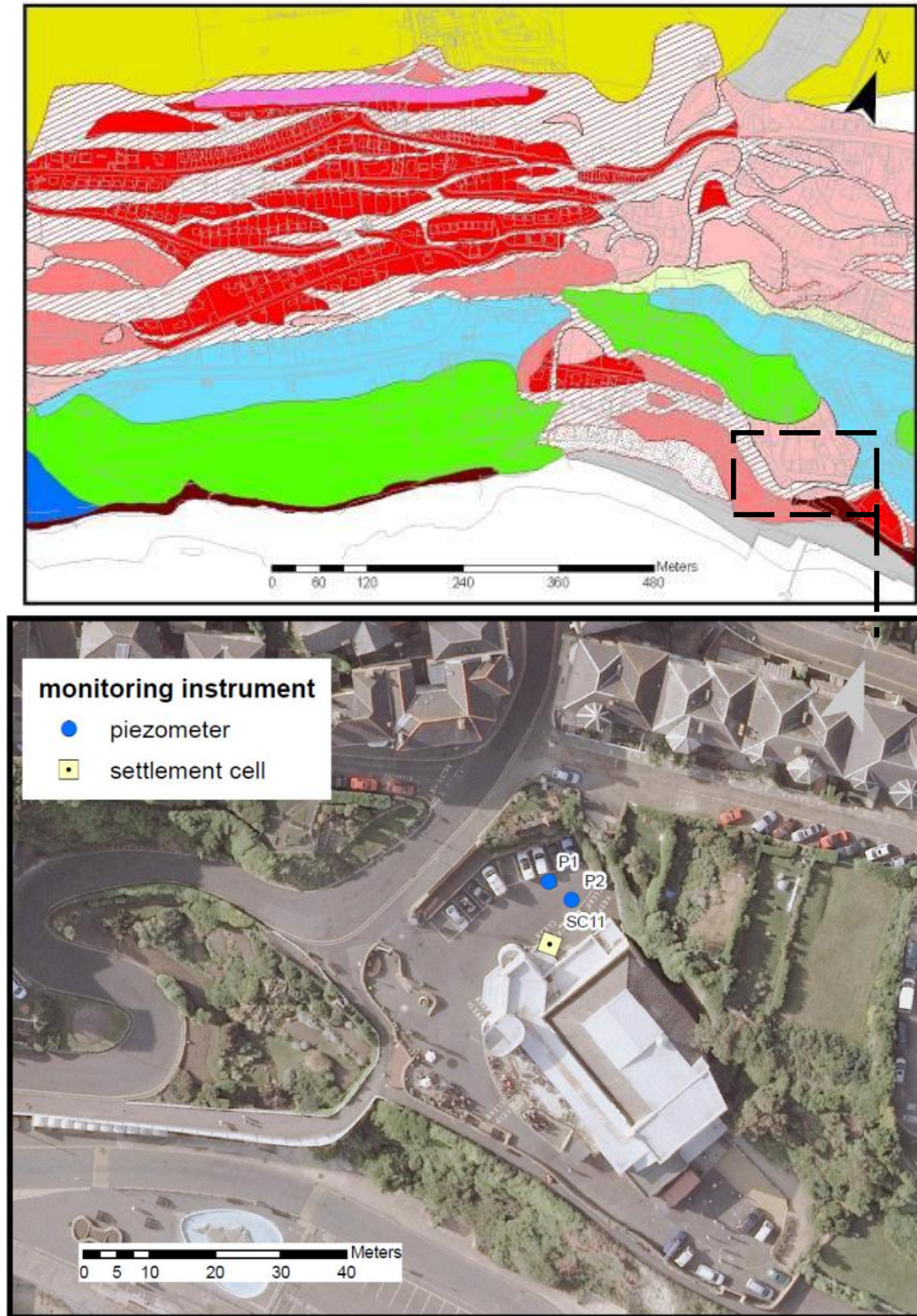


Figure 5.20 *Monitoring instruments installed at Winter Gardens in relation to the site geomorphology mapped by GSL (1991)*

The readings reveal the statistically significant linear trend in settlement as observed in both Newport Road and Bath Road monitoring records (Fig 5.21). SC11 records an overall settlement of approximately 8 cm between 1995 and 2004, which is comparable to the overall settlement records from within the same landslide unit at Bath Road. SC11 illustrates similar short-term variability in settlement rates with cyclic episodes of uplift and settlement as has been observed within all of the settlement cell records (Fig 5.22). The variation settlement within these cycles however is greater with a range of up to 4 cm recorded.

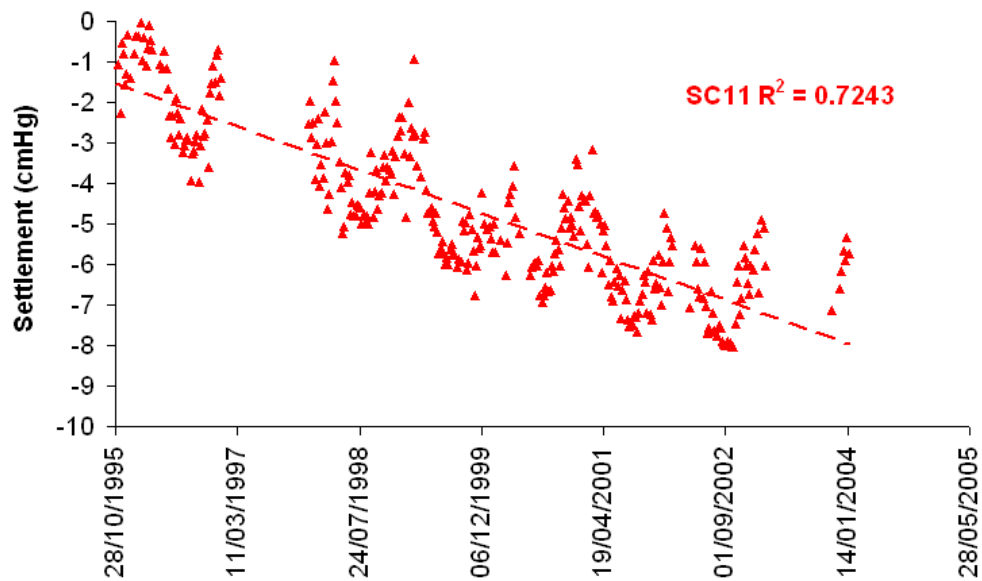


Figure 5.21 Settlement records at SC11, Winter Gardens (1995-2004)

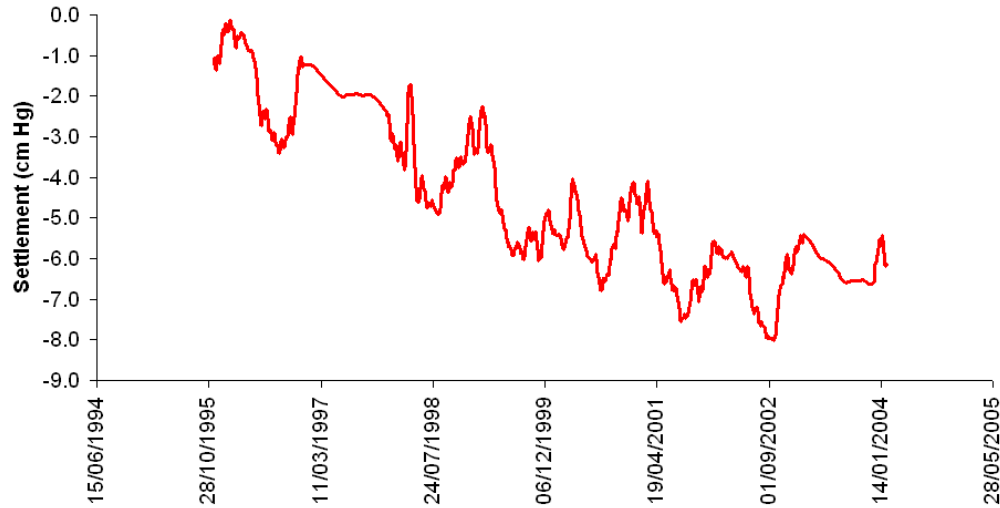


Figure 5.22 Running mean settlement records at SC11, Winter Gardens (1995-2004)

5.2.6 Implication of ground movement records on the landslide model

An assessment of the spatial distribution of ground movement has been conducted by collating all the available landslide movement data currently available for the Ventnor landslide complex. The results have illustrated that differential rates of ground movement can be observed across the landslide complex which provide a new knowledge of the landslide ground model.

The variation in ground behaviour within the complex can be related to discrete landslide blocks, which is supported by the geomorphological mapping. This differential movement is observed in all datasets, including the inclinometers, automated crackmeters and settlement cells and the damage surveys and differential GPS. The results indicate three distinct landslide units in which movement is taking place (Fig 5.23). These comprise:

1. A lower tier landslide incorporating the area of Park Avenue which is likely to extend offshore along an active shear surface confirmed at 73 m bgl (-20 m OD) at BH4I. The landslide stratigraphy recoded within this landslide unit is composed of a

series of large relict landslide blocks which include the prominent ridge in Ventnor Park (Fig 5.4) seated on a bedding controlled shear surface which is seated at base of the Gault Clay and in Sandrock 2d. A combination of movement data sources indicates that the unit is subject to ongoing horizontal displacement, leading to the development of significant damage at the headscarp. Inclinator data confirms that this area is displacing horizontally toward the sea which is actively unloading the upper landslide block.

2. A series of large translational landslide blocks forming an upper tier landslide unit which extends from the Lowtherville Graben to Park Avenue. Evidence confirms this unit is displacing along a bedding controlled shear surface 95 m bgl at the base of Gault Clay at BH2. Geological evidence (Palmer *et al.*, 2007) indicates that the landslide benches are back rotated, which is likely to have occurred as the blocks move downslope. Consistent with the model are monitoring results that have confirmed that settlement rates are currently higher than horizontal displacement rates.
3. A second lower tier landslide unit with an unconfirmed shear surface. Evidence has revealed that this landslide unit is subject to ongoing settlement of the entire block which is likely to be actively unloading the Upper tier landslide (2) above Park Avenue.

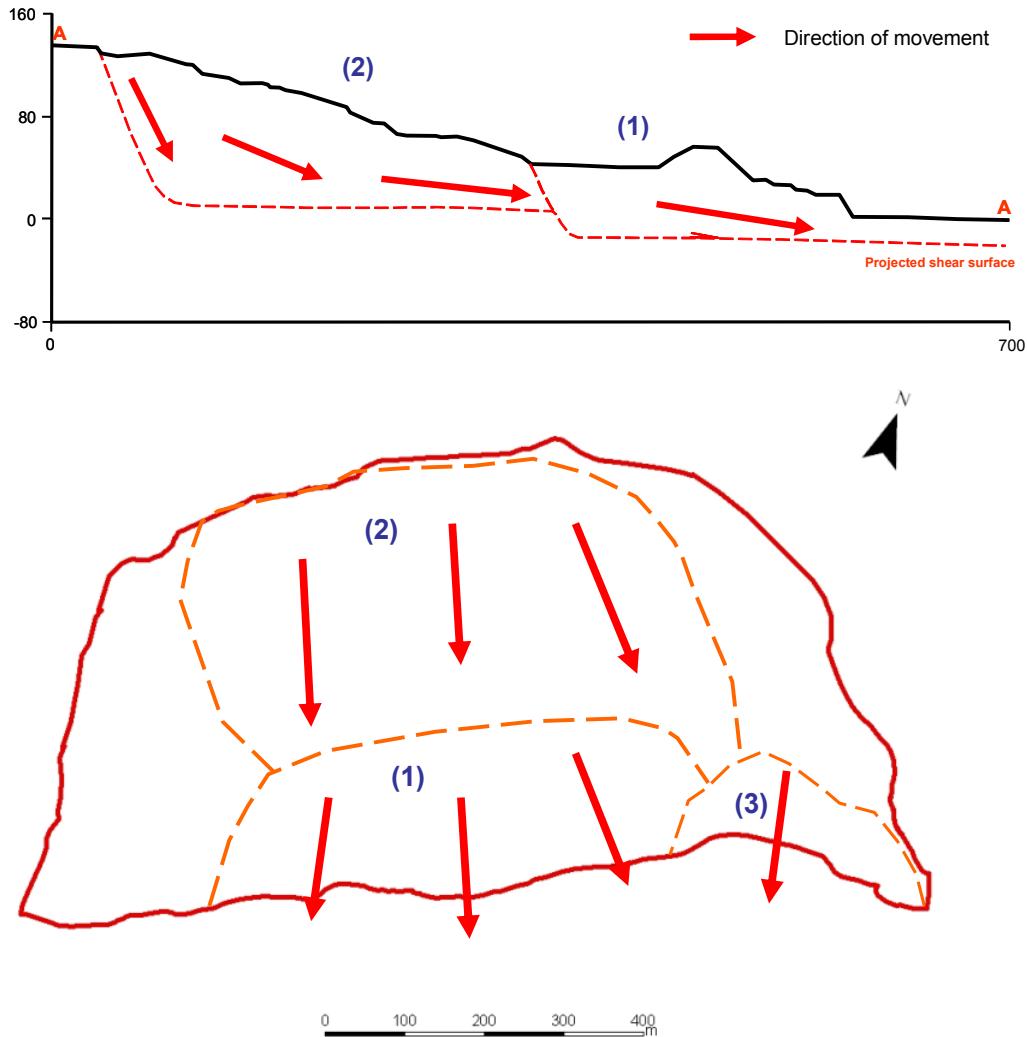


Figure 5.23 Spatial movements of the Ventnor landslide units

The monitoring analysis has revealed that three ground movement patterns are occurring within the landslide body, which are acting at different temporal and spatial scales. These include:

1. A long term ongoing slow creep displacement of the entire landslide mass has been observed across all three landslide units in both the settlement cell and ground movement records, consistent with the movement behaviour described in the two tier landslide model;

2. A period of accelerated ground creep that has been observed at the Lowtherville Graben only in crackmeters C01 and C02 and settlement cell SC04. This period of accelerated ground creep was sustained through the winter period of 2000 and 2001 and is consistent with the graded acceleration patterns previously observed at other sites (Allison and Brunsden, 1990); and
3. A short duration cyclical pattern of settlement and uplift which has been observed only within settlement cells but across all landslide units. This was most notable at SC03, SC06 and SC11.

The results provide a new insight into the Ventnor landslide ground model and indicate a series of complex movement behaviours and potential landslide mechanisms that require further analysis in relation to hydro-geological and rainfall characteristics which have impacted the site through this period.

5.3 Groundwater and rainfall characteristics

Groundwater data has been collected using both automated and manually-read standpipe piezometers installed at various locations across the site. Hand-read standpipe piezometers were installed through the centre of the Ventnor landslide complex during the 2002 and 2005 ground investigations whilst automated vibrating wire piezometers were installed in boreholes at the Winter Gardens during 2002 and provide continuous groundwater readings between 1992 and 2004. In addition automated rainfall records have been collected since 1992 at the weather station in Ventnor Park (Fig 5.24).



Figure 5.24 Piezometer and weather station locations, Ventnor Town

The installation details for the automated piezometers installed at the Winter Gardens are provided in Table 5.4. The automated piezometers readings at P01 and P02 have been converted into groundwater elevations in relation meters above or below to Ordnance Datum (Fig 5.25). The groundwater data illustrates a near constant water table at 0 m OD in P01, which shows only a minor fluctuation of less than 3 m in groundwater level through 2000 and 2001. A deeper water table is observed at P02 at -10 m OD, which demonstrates seasonal fluctuations in groundwater level. The groundwater elevation in P02 is recorded below Ordnance Datum suggesting that, the water table is not connected to the sea.

Table 5.4 Summary installation details for automated standpipe piezometers, Winter Gardens, Ventnor Town

Piezometer	Installation	Borehole	BH number
ref	depth (m bgl)	elevation (mOD)	
P01	41.6	22.44	BH9 (Winter Gardens)
P02	33.7	22.43	BH9 (Winter Gardens)

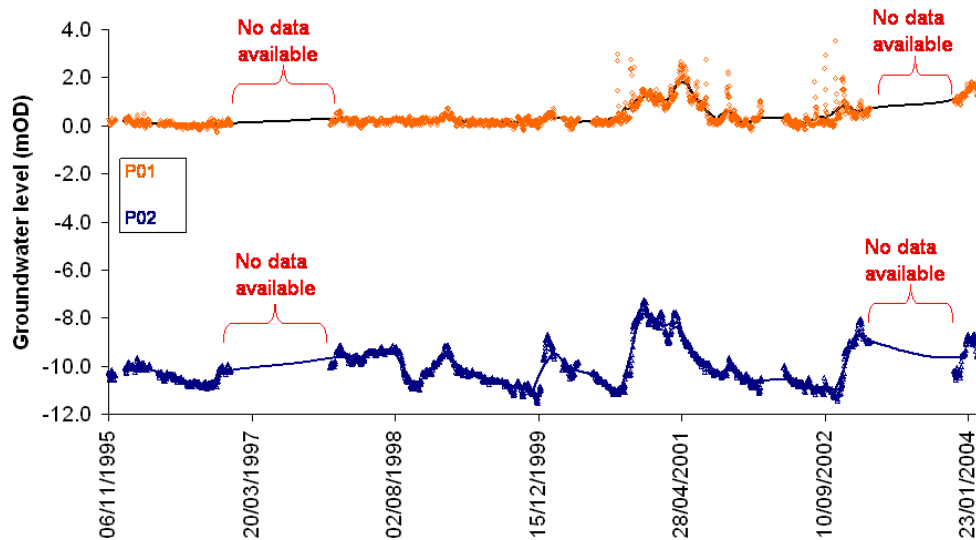


Figure 5.25 Groundwater levels measured in P01 and P02, Winter Gardens between 1995 and 2004

The water tables have been plotted on the landslide cross section in relation to readings taken from the manual standpipe piezometers during the 2002 and 2005 ground investigations (Fig 5.26). The cross section demonstrates a series of water tables as previously described in section 3.9. The groundwater levels measured at the Winter Gardens appear to be deeper than those recorded within Ventnor Park, although both water tables are higher than the landslide shear surface in the lower tier landslide, which suggests that the porewater pressures in the lower landslide could be acting upon it.

The deeper water tables highlight the complexity of the groundwater regime within the landslide complex and demonstrate how a series of water tables

may be affecting its behaviour. Whilst the groundwater regime remains to be fully understood at the site, the Winter Gardens provides the only continuous record of groundwater levels. Given the analysis of ground movement has indicated that displacement may initiate at the landside toe, it can be argued that these water tables may have impact on the shear surface in lower Ventnor and should be analysed further to determine their relation with the site rainfall and ground movement characteristics.

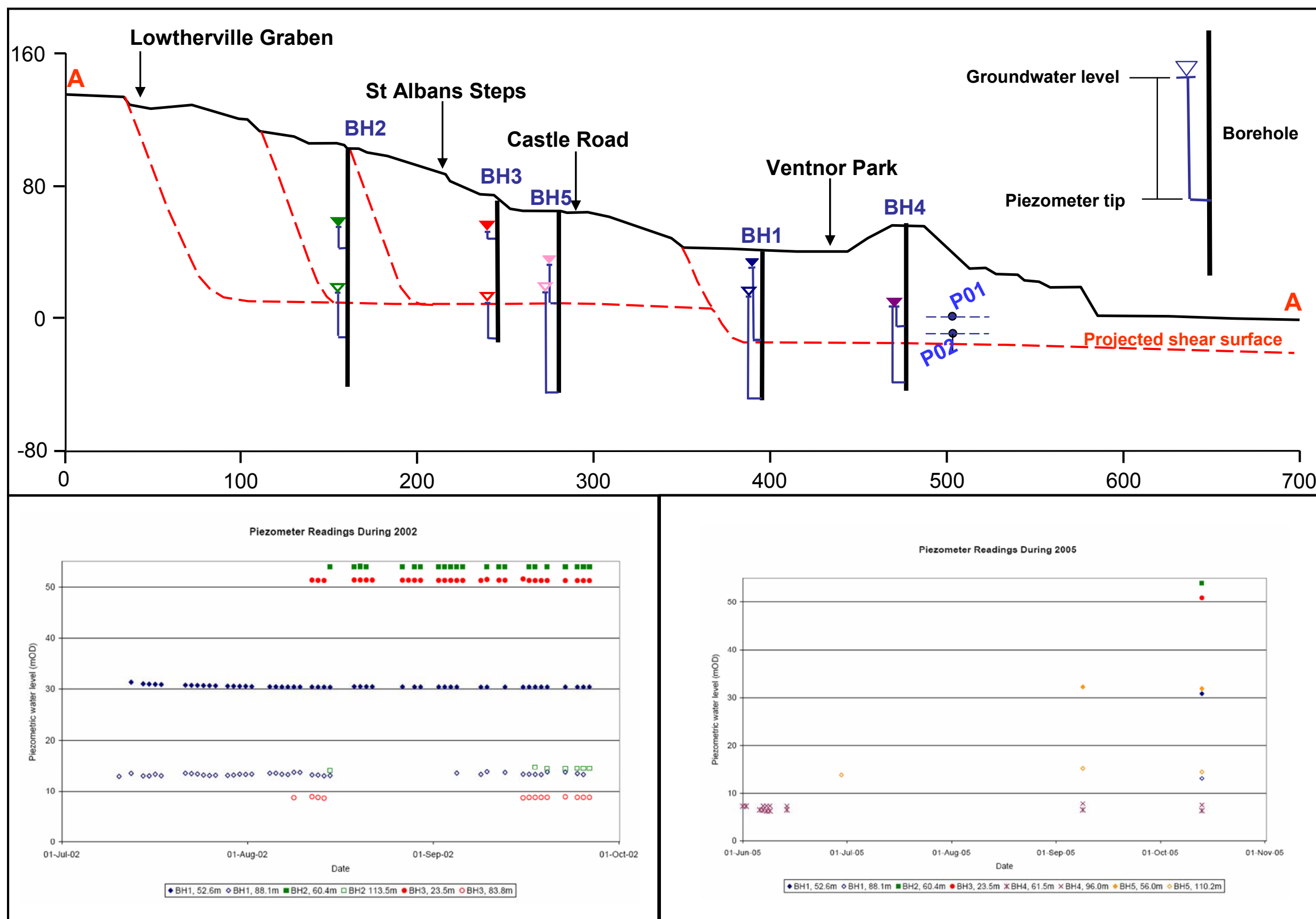


Figure 5.26 Ventnor landslide hydrogeological characteristics (a) Elevation of piezometers and water tables within the landslide system and calculated including water table reading from automated piezometers at the Winter gardens (P01 and _02) (b) Manual piezometer readings between January and October 2002 (c) Manual piezometer readings between June and November 2005

Daily rainfall records are available from the Ventnor Park Weather Station between 1995 and 2003 (Fig 5.27), providing a suitable record of rainfall for comparison with the groundwater records from the Winter Gardens. The rainfall records show typical seasonal variability in rainfall with a particularly wet winter period recorded through 2000 into early 2001.

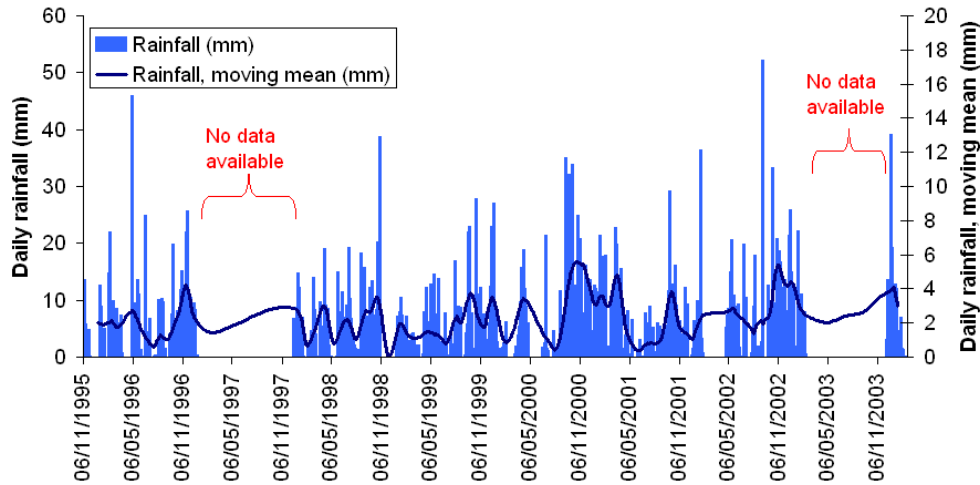


Figure 5.27 Daily rainfall records and 60 day running mean rainfall from the Ventnor Park Weather Station between 1995 and 2004

The rainfall conditions have been compared with the porewater pressure records at P02 (Fig 5.28). The results reveal a relationship between peak rainfall conditions and between 2000 and 2004. Interestingly prior to 2000 peaks in porewater pressure are generally lower and do not appear to show comparable patterns with the daily rainfall record.

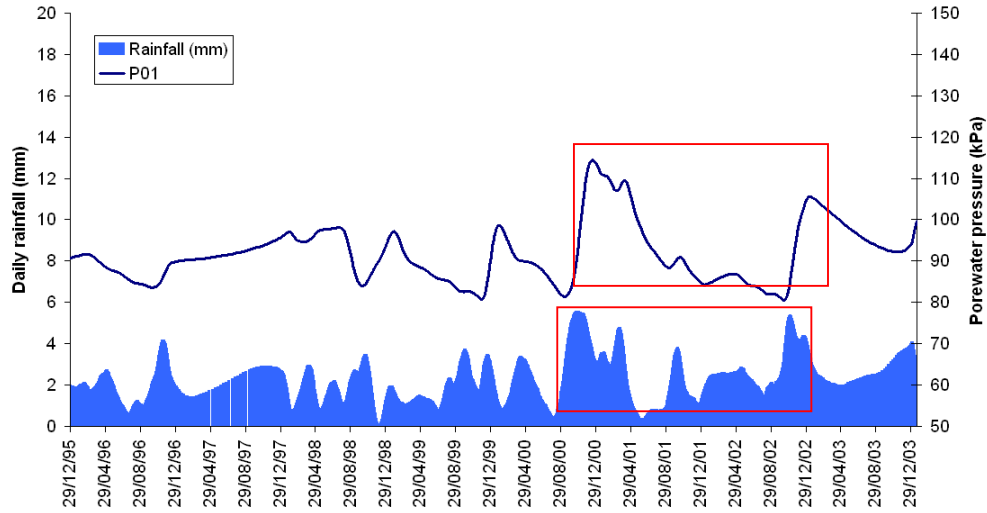


Figure 5.28 Comparison of 60 day running mean daily rainfall and porewater pressures at P02 between 1995 and 2004

The relationship has been analysed further by plotting porewater pressures recorded in P02 through the particularly wet winter between 2000 and 2001 (Fig 5.29). This illustrates a lag of 2 months between peak daily rainfall and peak daily porewater water pressure, which when correlated for the period of groundwater rise provides a statistically significant linear trend with the peak rainfall (Fig 5.30). This demonstrates a direct response in groundwater level in P02 to rainfall during this event.

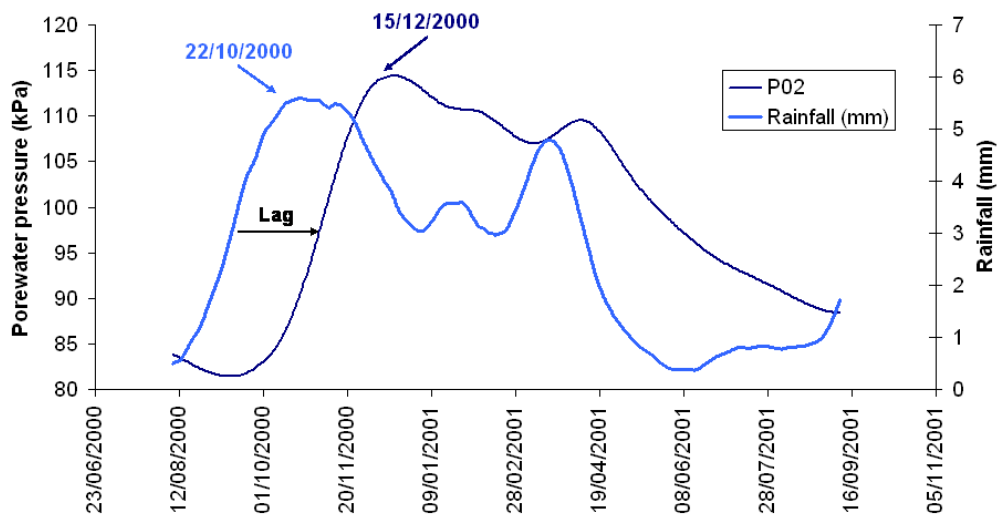


Figure 5.29 Comparison of 60 day running mean rainfall and porewater pressures at P02 between 12/08/2001 and 16/09/2001

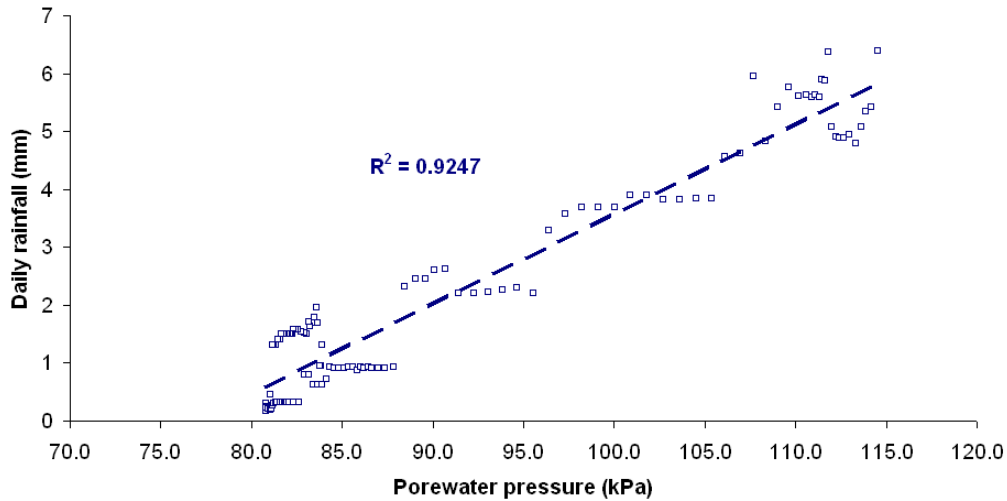


Figure 5.30 Relationship between daily porewater pressure and daily rainfall during the pore pressure rise (P02) between August and December 2000

A similar comparison of daily rainfall records and porewater pressures in P01 has been undertaken (Fig 5.31). The results indicate minimal relationship between the daily rainfall and porewater pressure readings between 1995 and 2000. From 2000 and 2003 the porewater pressure records appear to correlate with the daily rainfall patterns. The comparative analysis is consistent with the records from P02, although the variations in porewater pressures are lower in P01 with a maximum range of 17kPa in comparison to a range of 35 kPa in P02.

The relationship between rainfall and porewater pressure response recorded in P01 has been analysed further for the wet winter between 2000 and 2001 (Fig 5.32). Comparative analysis illustrates a lag of two months between peak rainfall and porewater pressure, which is consistent with the lag observed in P02. When the peak daily porewater pressure recorded on 03/05/2001 is plotted with the second peak in daily rainfall, a weak linear trend can be observed during the rising limb of both data sets, which regression analysis has proven to be statistically significant (Fig 5.33). As observed in P02, the analysis confirms a potential relationship between porewater pressures in P01 and rainfall during this period.

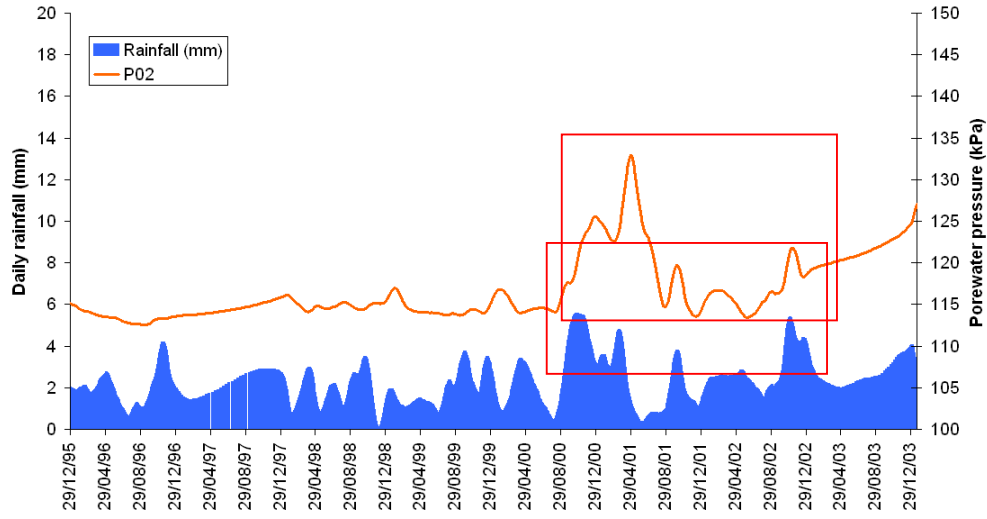


Figure 5.31 Comparison of 60 day running mean rainfall and porewater pressures at P01 between 1995 and 2004

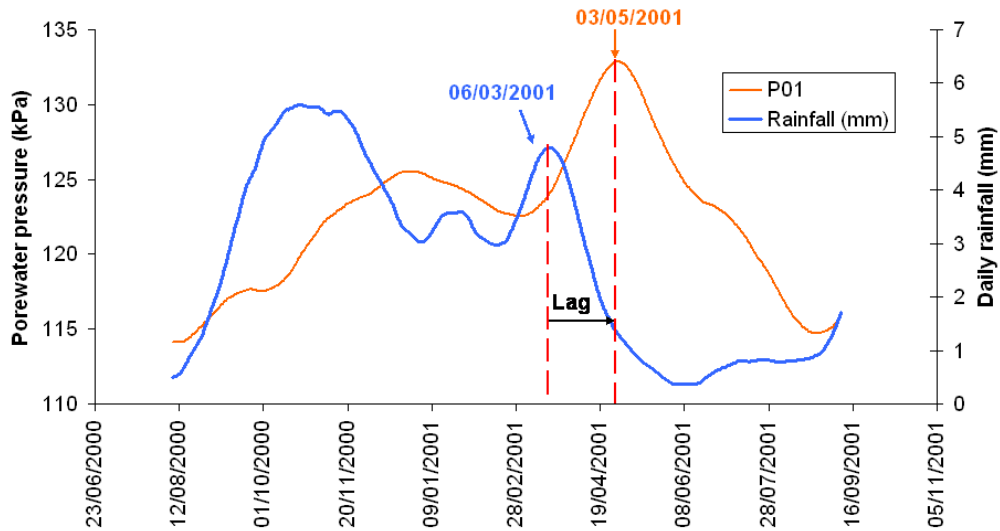


Figure 5.32 Comparison of 60 day running mean rainfall and porewater pressures at P01 between 12/08/2001 and 16/09/2001

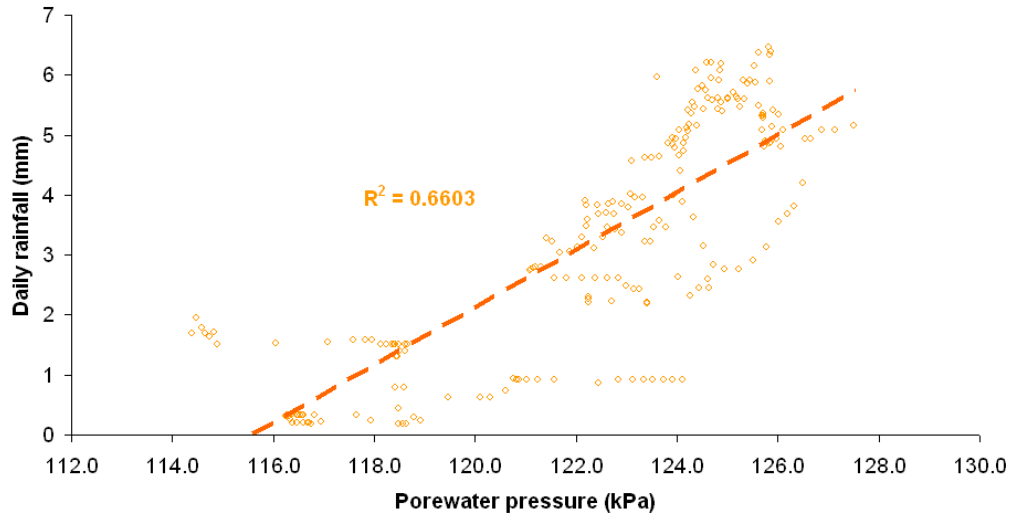


Figure 5.33 The relationship between daily porewater pressure and daily rainfall during the pore pressure rise (P01) between August and December 2000

A similar relationship is observed when the porewater pressures P02 are compared with total monthly rainfall (Figure 5.34). This demonstrates that porewater pressure peaks lag particularly wet winter months. This suggests that significant periods of elevated porewater pressure only occur after prolonged periods of heavy or sustained rainfall. This relationship, however, is not observed when total monthly rainfall is compared with the porewater pressures recorded at P01 (Fig 5.35).

The four month running average total monthly rainfall has been plotted against the average monthly porewater pressures at P01 (Fig 5.36) and at P02 (Fig 5.37). Similarly the graph illustrates the close relationship between antecedent rainfall conditions and groundwater response at P02, with no relationship observable with P01.

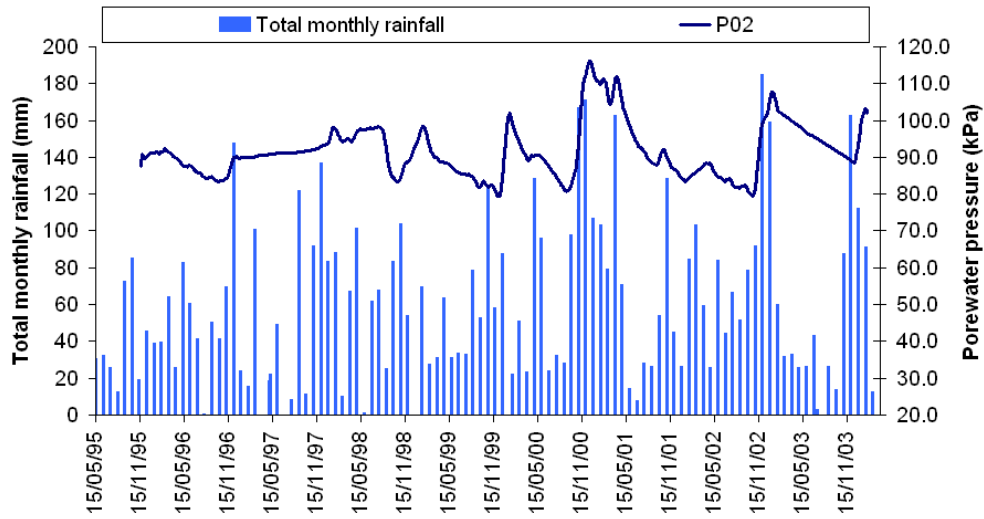


Figure 5.34 Comparison of 60 day running mean porewater pressures at P02 and running average total monthly rainfall between 1995 and 2004

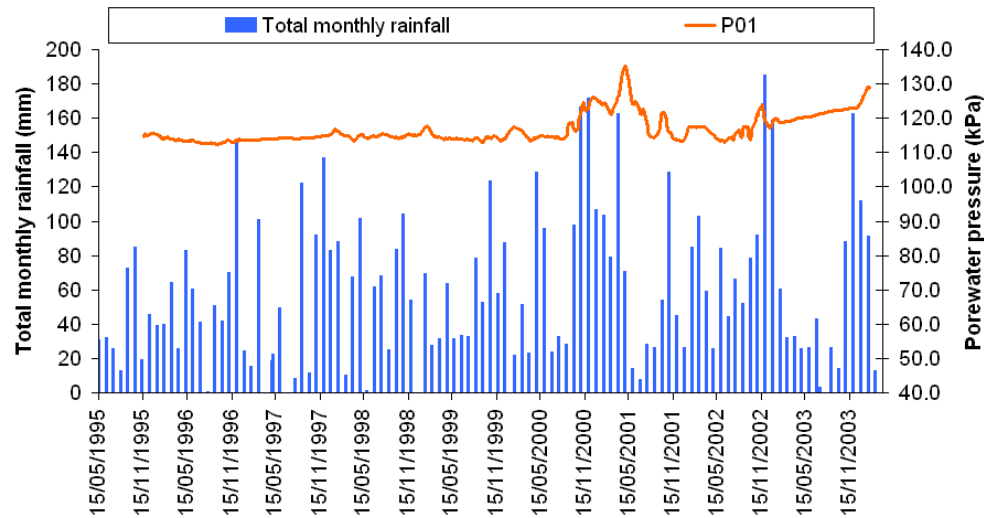


Figure 5.35 Comparison of 60 day running mean porewater pressures at P01 and running average total monthly rainfall between 1995 and 2004

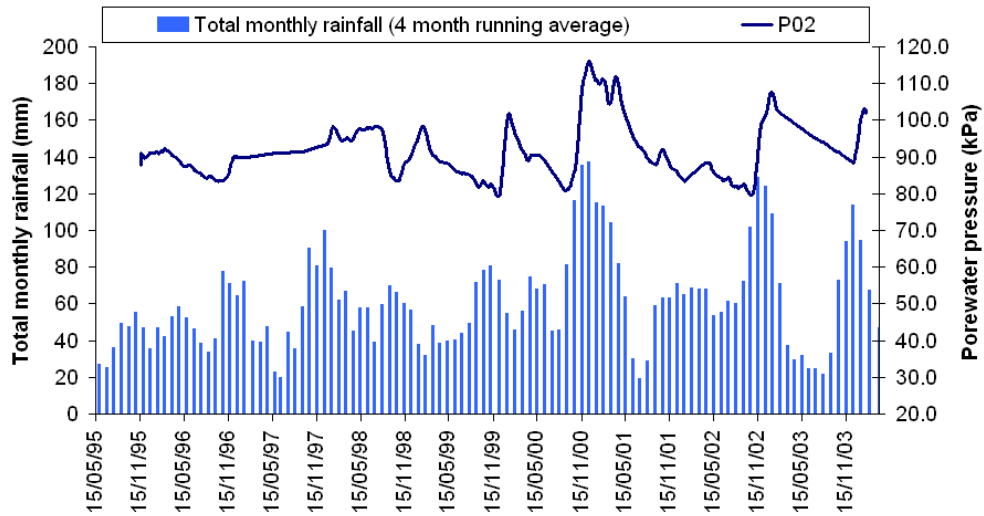


Figure 5.36 Comparison of 60 day running mean porewater pressures at P02 and running average total monthly rainfall between 1995 and 2004

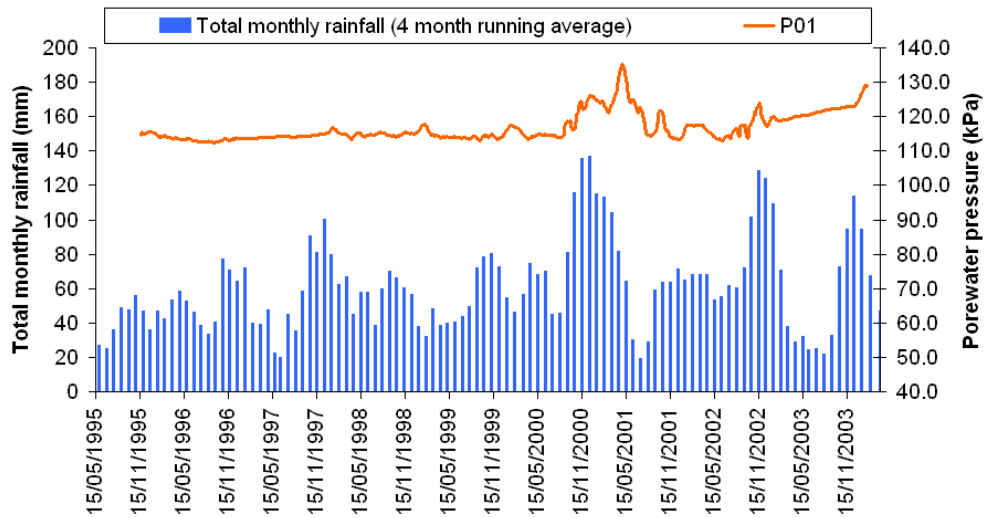


Figure 5.37 Comparison of 60 day running mean porewater pressures at P01 and running average total monthly rainfall between 1995 and 2004

A detailed analysis of the period of elevated porewater pressures between 2000 and 2001 has been undertaken by plotting the four month running mean total monthly rainfall with porewater pressures at P02 (Fig 5.38) and P01 (Fig 5.39). This analysis demonstrates that a clear relationship can be observed between antecedent rainfall and porewater pressure, which when plotted together confirms a statistically significant linear relationship (Fig 5.40). In the

case of P01, however, a relationship between these two variables cannot be demonstrated (Fig 5.41).

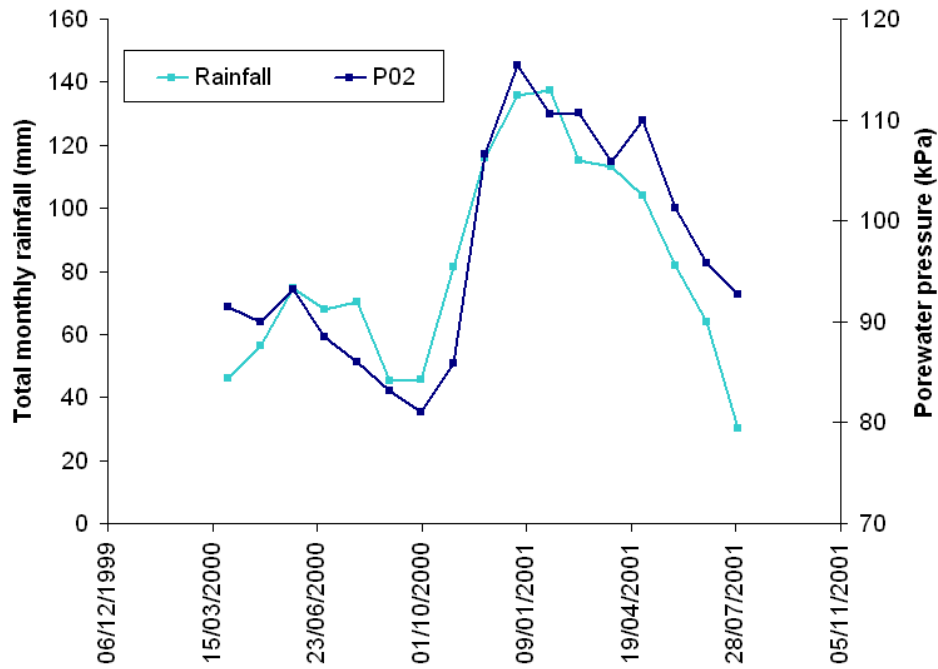


Figure 5.38 Comparison of 4 month running mean rainfall and porewater pressures at P02 between March 2000 and July 2002

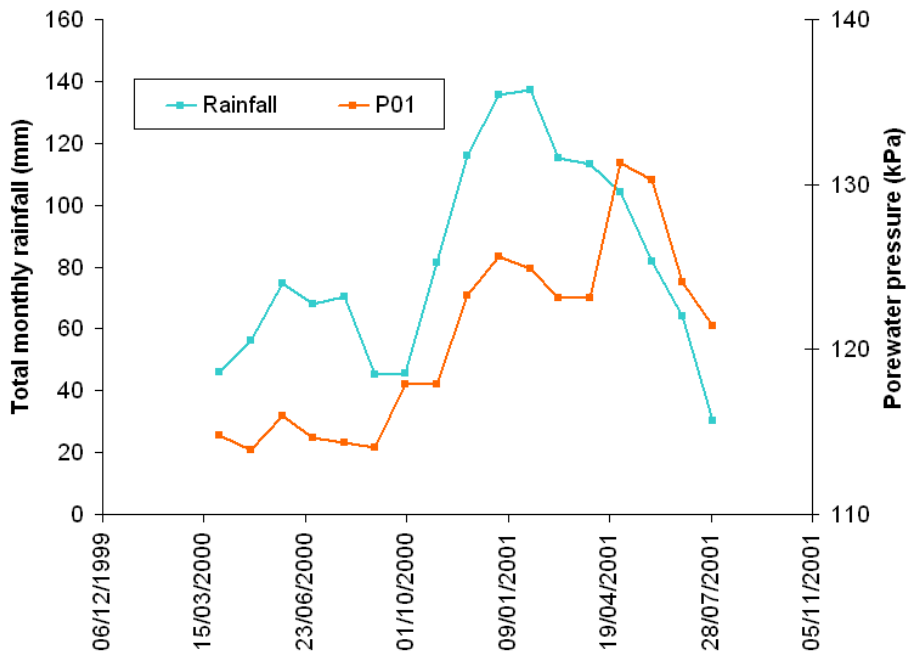


Figure 5.39 Comparison of 4 month running mean rainfall and porewater pressures at P01

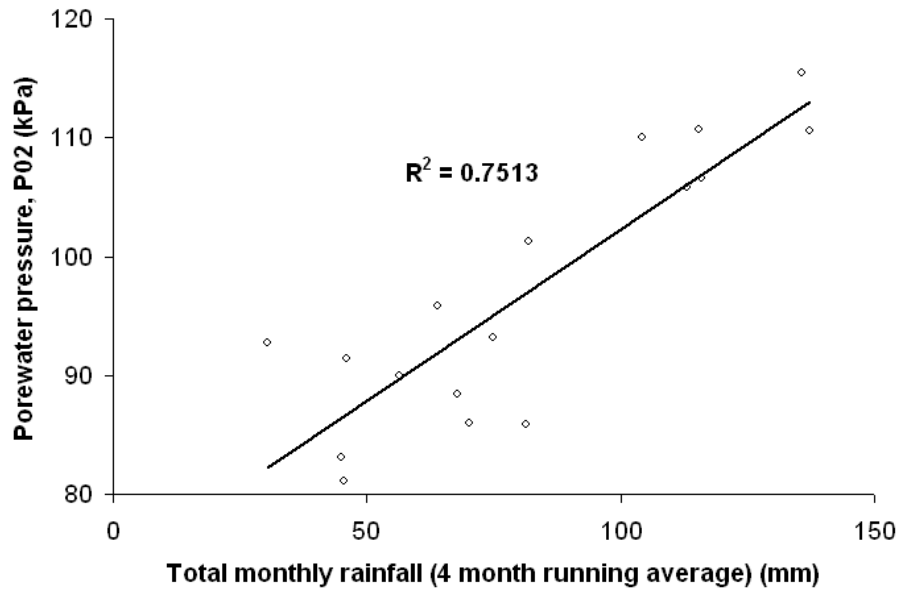


Figure 5.40 The relationship between average monthly porewater pressures in P02 and 4 month running average total monthly rainfall between March 2000 and July 2002

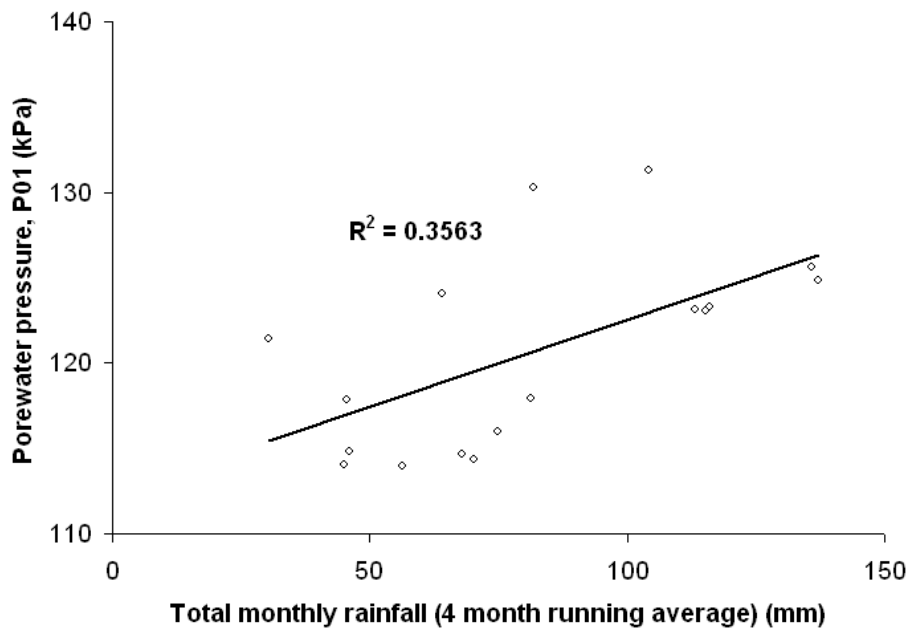


Figure 5.41 The relationship between average monthly porewater pressures in P02 and 4 month running average total monthly rainfall between March 2000 and July 2002

The analysis has illustrated a clear relationship between the groundwater characteristics measured in P02 and the rainfall records measured at Ventnor Park. Analysis has shown that porewater pressures increase linearly with rainfall following a lag of three months. This lag in groundwater response relates to the time required for the rainfall to percolate to the deep water table which is being measured at -10 m OD. The assessment, however, has concluded that the depth of this groundwater table is higher than the confirmed landslide shear surface beneath Ventnor Park, and is therefore likely to impact on mechanisms of ground movement that have been observed at the site (see section 5.1).

The relationship between rainfall characteristics and groundwater levels measured at P01 do not provide the same relationships. Whilst elevated porewater pressures have been observed, the relative change and pattern of porewater pressure elevation do not correlate well with rainfall characteristics assessed.

The results indicate that the groundwater characteristics measured at P02 provide a more realistic measure of the porewater pressures acting on the landslide shear surface. As a consequence the porewater pressure records at P02 have been taken forward to analyse the relationships between ground movement patterns, groundwater and rainfall.

5.4 Patterns of movement in relation to groundwater and rainfall characteristics

Analysis of landslide monitoring data in section 5.2 has confirmed a series of patterns of ground movement which vary both spatially and temporally. Similarly the analysis of the landslide hydrogeology (section 5.3) has confirmed groundwater tables at elevations within the landslide complex that are sufficient to impact the confirmed shear surface in the lower tier landslide unit. Analysis of the groundwater records has identified a close correlation to peak groundwater levels in P02 and antecedent rainfall conditions.

Further analysis is required to determine the relationship between the movement patterns observed and the rainfall and groundwater characteristics at the site. The relationships between these variables are analysed in terms of the patterns of movement observed. These can be summarised as:

- Section 5.4.1 considers the ongoing slow creep displacements which appear to be occurring across the site;
- Section 5.4.2 analyses the regular settlement and uplift cycles observed in settlement cells SC03, SC06 and SC11;
- Section 5.4.3 assesses the period of acceleration ground displacement through the winter period of 2000 and 2001 observed in crackmeters C01 and C02 and in settlement cell SC04 at the Lowtherville Graben.

5.4.1. Ongoing slow creep mechanisms

Long term displacement in terms of both ground settlement and displacement has been observed at all monitoring sites, suggesting ongoing slow creep of the entire landslide system. Analysis of the long term displacement records at C01 and C02 in the Lowtherville Graben provide the clearest indication of this type of movement between 1995 and 2000, prior to the onset of accelerated ground creep (Fig 5.38). Whilst this continuous movement occurs at a near constant displacement rate of 6.64 mm / yr, minor fluctuations can be observed in the displacement when the crackmeter records from C01 and C02 are plotted against cumulative rainfall (Fig 5.42). When the same period vertical displacement recorded at SC04 is plotted with cumulative rainfall a similar pattern of behaviour is revealed within the general linear trend (Fig 5.43).

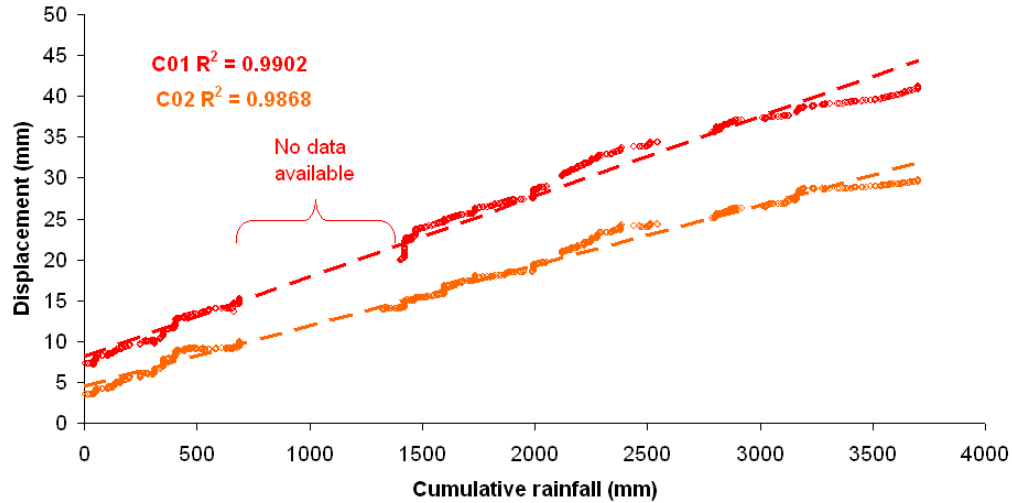


Figure 5.42 Relationship between cumulative rainfall and horizontal displacement at C01 and C02 between 1995 and 2000

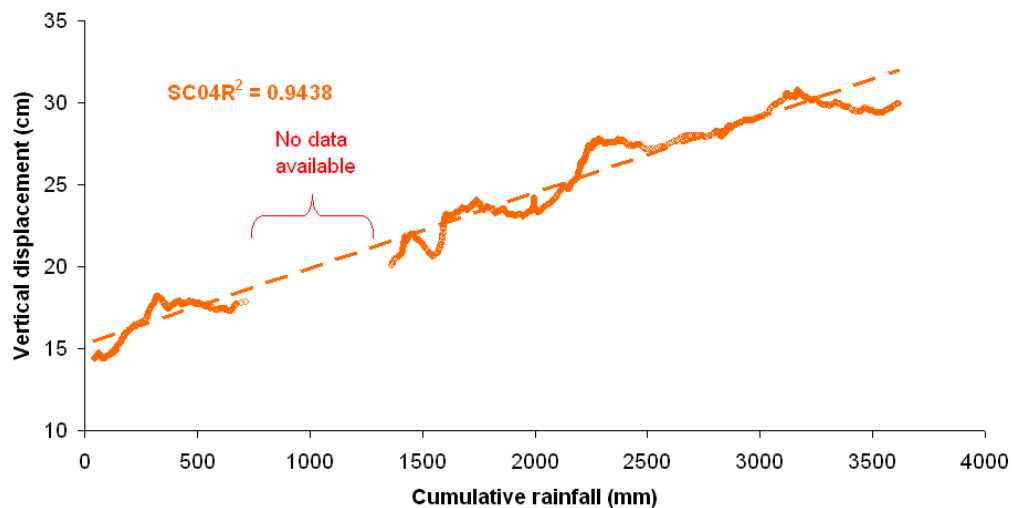


Figure 5.43 Relationship between cumulative rainfall and vertical displacement at SC04 between 1995 and 2000

This ongoing slow creep behaviour is consistent 'multiple stick-slip' movements as observed by Allison and Brunsten (1990), in which small movement events were preceded and followed by low or near zero displacement. These stick-slip patterns had little or no direct correlation with groundwater readings at the site and instead appeared to behave independently of the measured groundwater table. Similarly comparisons of the slow creep phase at Ventnor with porewater pressures recorded at P02

demonstrate little relationship between groundwater levels and movement, as can be observed at the Lowtherville graben (Fig 5.44). The stick slip behaviour may be better interpreted by plotting displacement as velocities (Fig 5.45). This demonstrates that whilst velocities generally show a constant trend of approximately 0.01 mm / day, regular fluctuations in velocity can be observed which are independent of fluctuations in the porewater pressures.

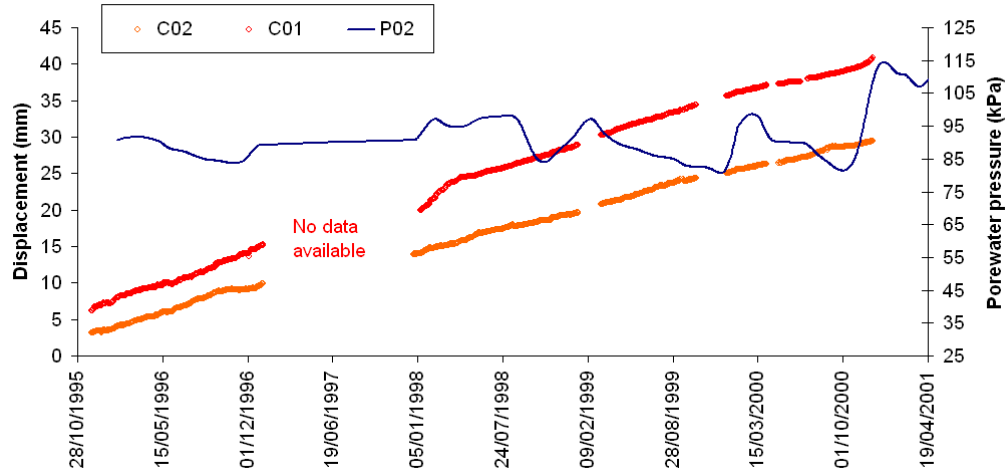


Figure 5.44 Comparison of displacement records at C01 and C02 and 60 day running mean porewater pressures in P01 between 1995 and 2000

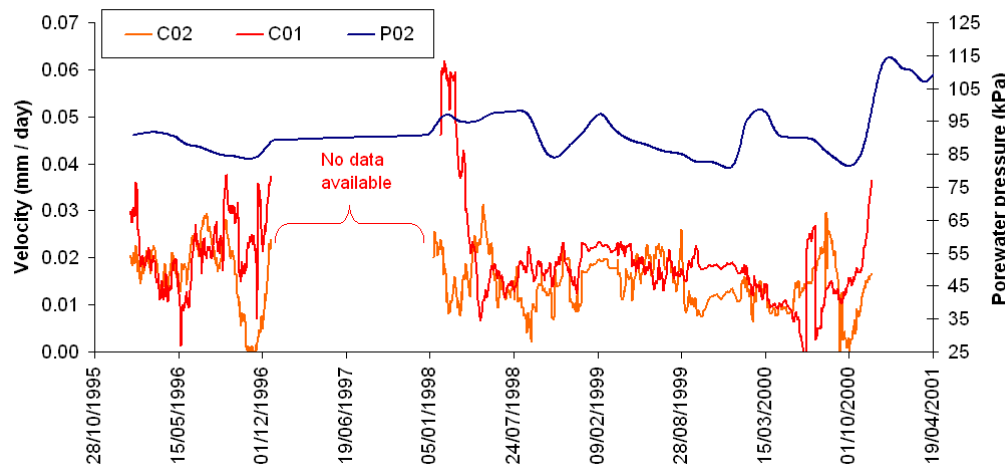


Figure 5.45 Comparison of running mean daily velocities at C01 and C02 and porewater pressures in P01 between 1995 and 2000

The analysis of the slow creep phase indicates a statistically significant linear trend in both vertical and horizontal displacement, with a distinct stepped pattern. The ongoing slow creep behaviour indicates that the landslide is currently only marginally stable and requires only minor alterations in the conditions at the shear surface to promote movement. As the landslide is subject to ongoing movement it is possible to conclude that the groundwater table remains of sufficient height to allow ongoing creep to occur. This creep occurs as a very slow 'stick-slip' mechanism. The groundwater table fluctuations measured during this phase are therefore not sufficient to promote any accelerated ground movement.

5.4.2 Regular settlement and uplift cycles

A series of regular cycles of settlement and uplift were observed within the long term records of ongoing settlement. These fluctuations were observed at all three settlement monitoring locations, although the variation in the rates and patterns varied. The settlement records at SC03 (Newport Road), SC06 (Bath Road) and SC11 (Winter Gardens) have been used to calculate a running average velocity record for each settlement cell (Fig 5.42). Comparison of velocity patterns at the three settlement cells shows significant variability in both the rates and patterns of settlement across the sites. There is some consistency in the velocity patterns at SC06 and SC11, suggesting that the lower tier landslide unit 3 is acting as a single landslide block. Velocities measured at SC03 at the Lowtherville Graben show regular peaks in velocity (settlement) between September and August, with lows (uplift or heave) occurring in February. A similar general pattern is observed at SC06 and SC11, although much less pronounced.

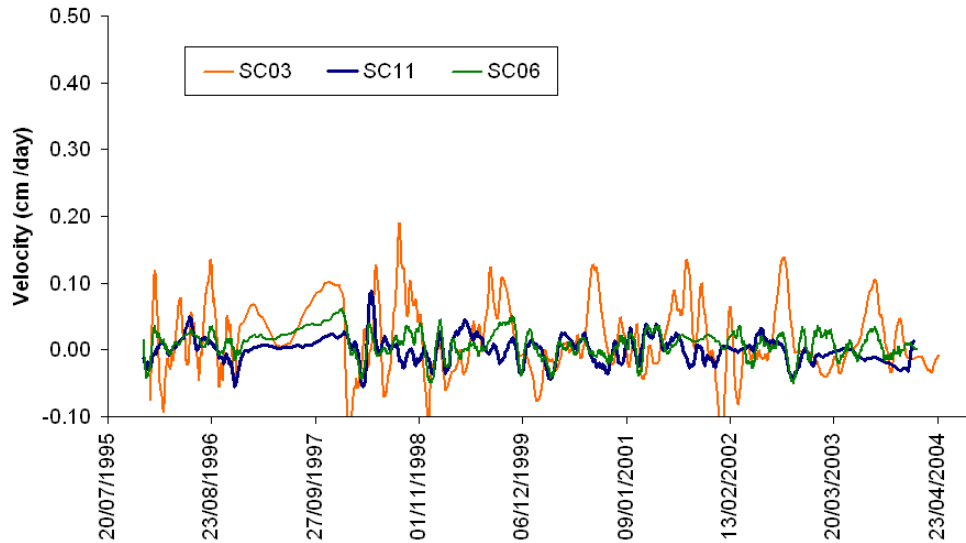


Figure 5.46 Comparison of settlement velocities at SC03, SC06 and SC11 between 1995 and 2004

The velocity measured at settlement cells SC03, SC06, and SC11 have been compared with daily rainfall readings. The readings at SC03 (Fig 5.47), SC06 (Fig 5.48) and SC11 (Fig 5.49) demonstrate little correlation between daily rainfall characteristics and the settlement – uplift cycle.

Similar analysis has been conducted using the porewater pressures at P02 and the settlement velocities measured at SC03 (Fig 5.50), SC06 (Fig 5.51) and SC11 (Fig 5.52). Similarly little correlation can be observed at all three sites.

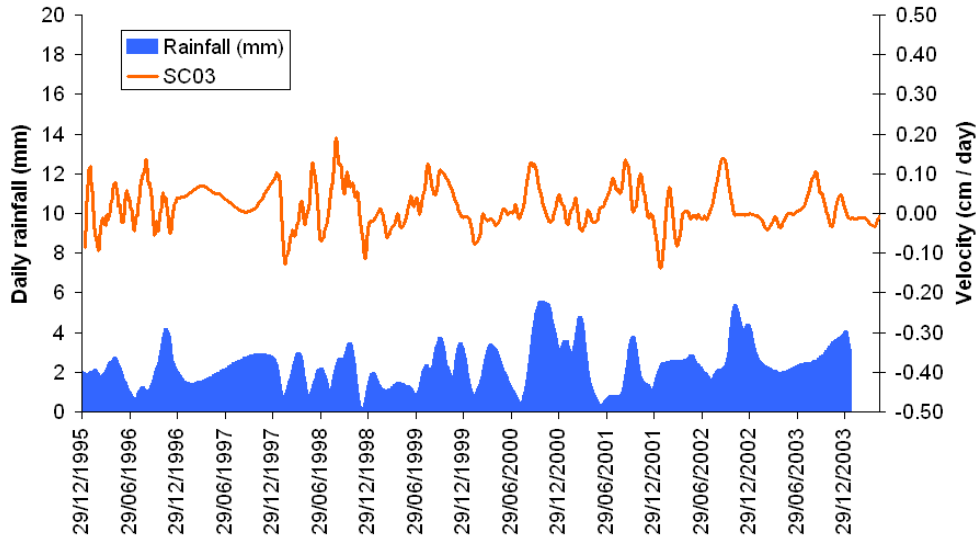


Figure 5.47 Comparison of daily rainfall characteristics and settlement velocities at SC03 between 1995 and 2003

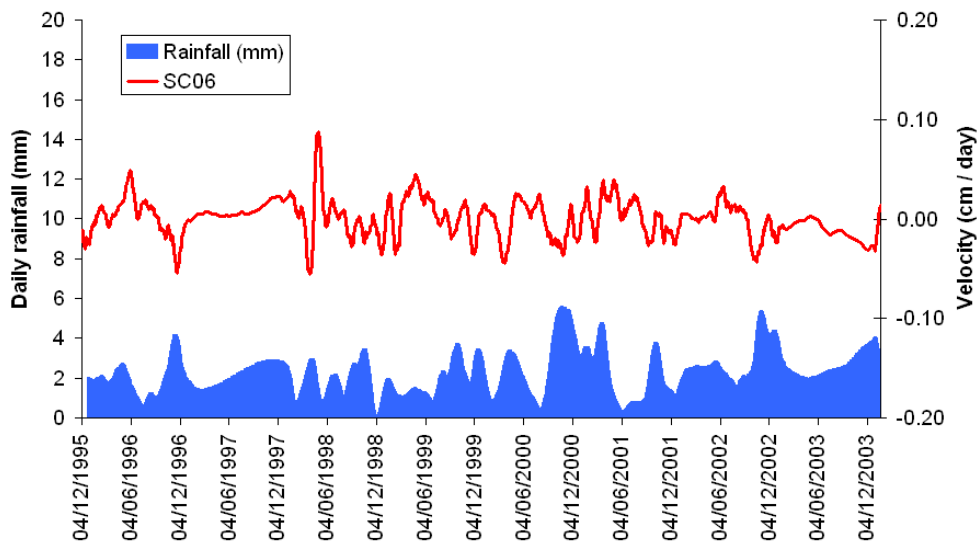


Figure 5.48 Comparison of daily rainfall characteristics and settlement velocities at SC06 between 1995 and 2003

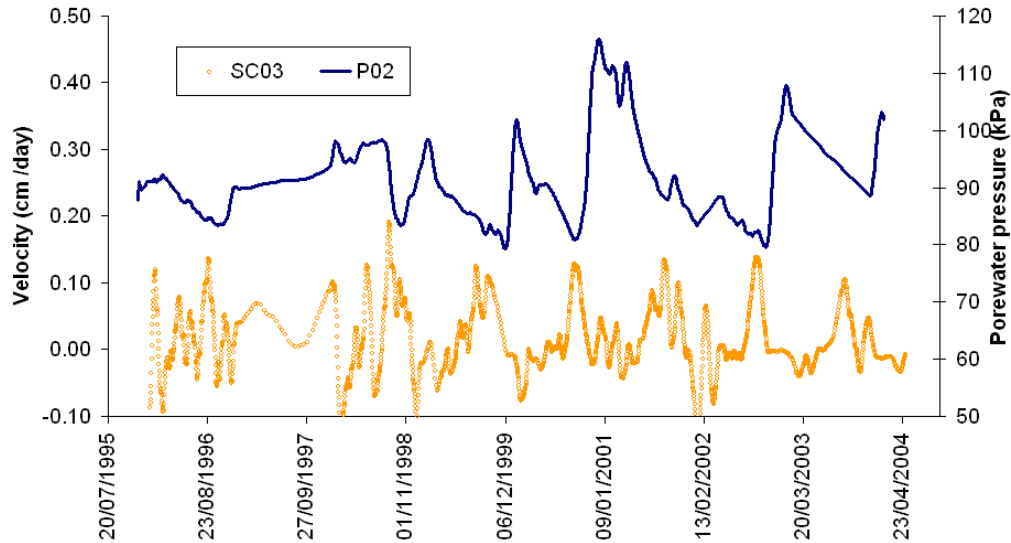


Figure 5.49 Comparison of porewater pressure at P02 and settlement velocities at SC06 between 1995 and 2003

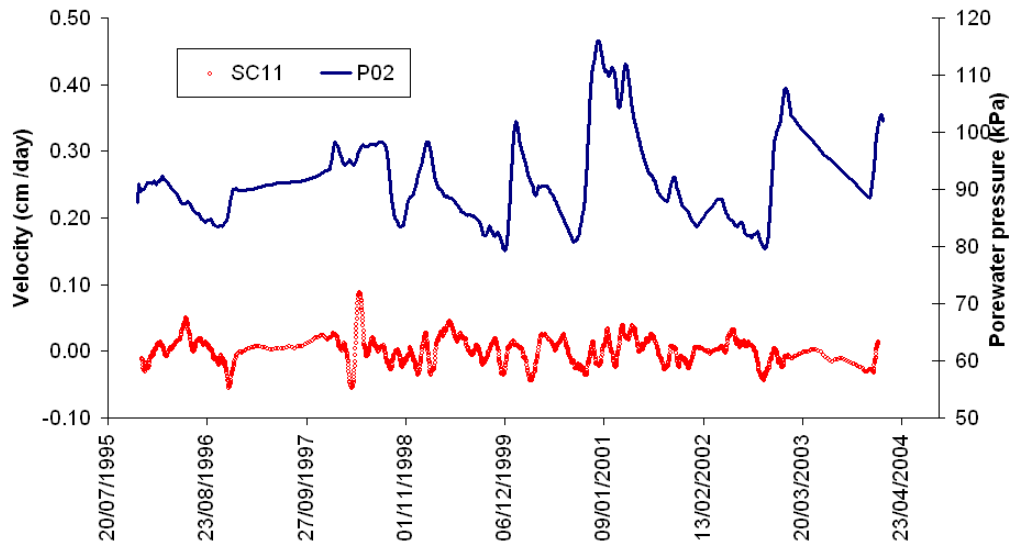


Figure 5.50 Comparison of porewater pressure at P02 and settlement velocities at SC011 between 1995 and 2003

5.4.3 Accelerated ground displacement at the Lowtherville Graben

A distinct period of ground acceleration has been observed at the Lowtherville Graben. The velocity data from C01 and C02 demonstrates that a distinct period of accelerated ground displacement occurred following a period of through 2000-2001 following a period of slow creep that has been discussed in section 5.4.2 (Fig 5.51).

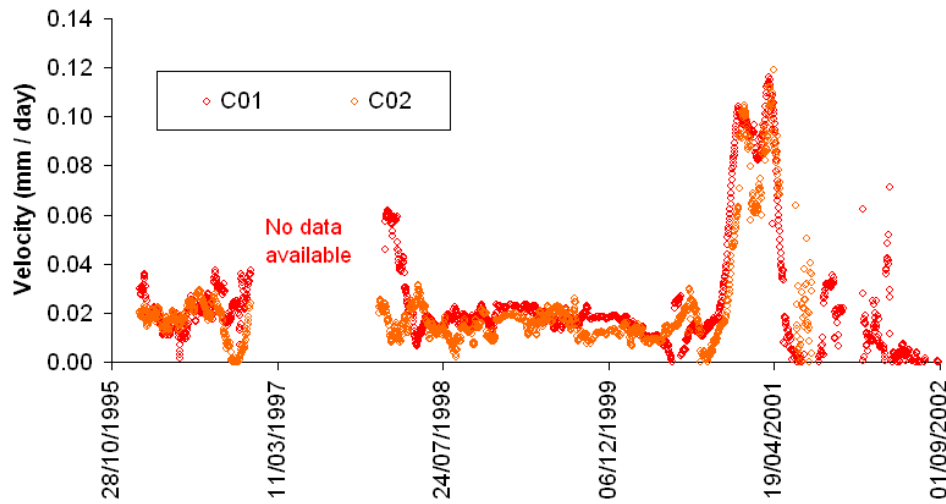


Figure 5.51 Running mean of horizontal displacement rates recorded at C01 and C02 between 1995 and 2002

A similar distinct period of ground acceleration can be observed through this period in the settlement records at SC04, although this pattern is not as easy to observe given the localised fluctuations in settlement and uplift discussed in section 5.3.2 (Fig 5.52).

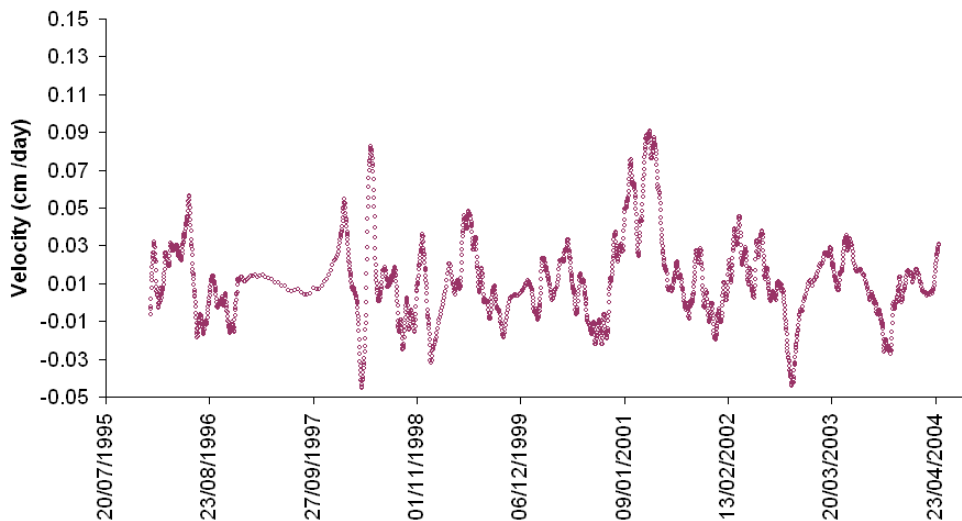


Figure 5.52 Running mean of vertical displacement rates recorded at SC04 between 1995 and 2002

The velocities measured at C01 and C02 have been plotted together to demonstrate that both the patterns and rates of displacement are similar during this period (Fig 5.53). When the velocities from these crackmeters are plotted together a statistically significant linear relationship can be observed. This demonstrates that the behaviour of accelerated ground creep occurring through this period is consistent across the graben.

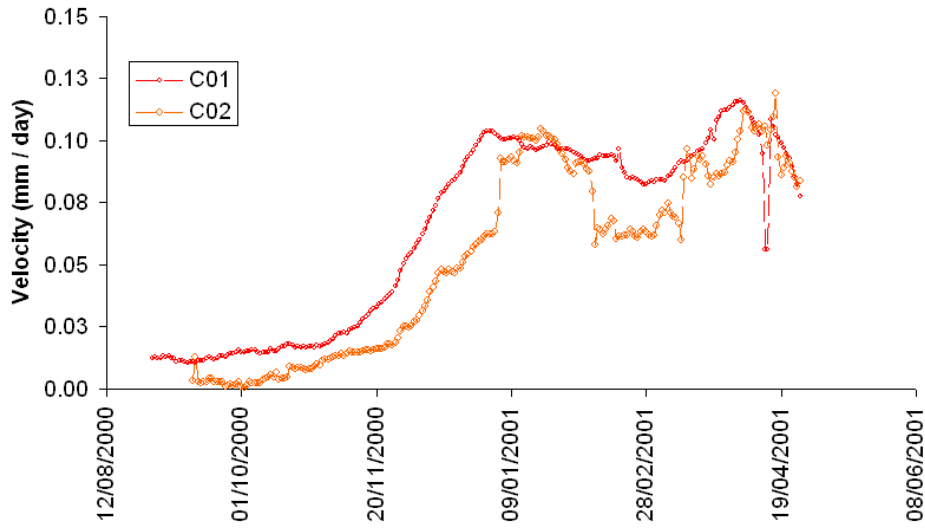


Figure 5.53 Comparison of running mean velocity patterns from C01 and C02 during accelerated ground displacement

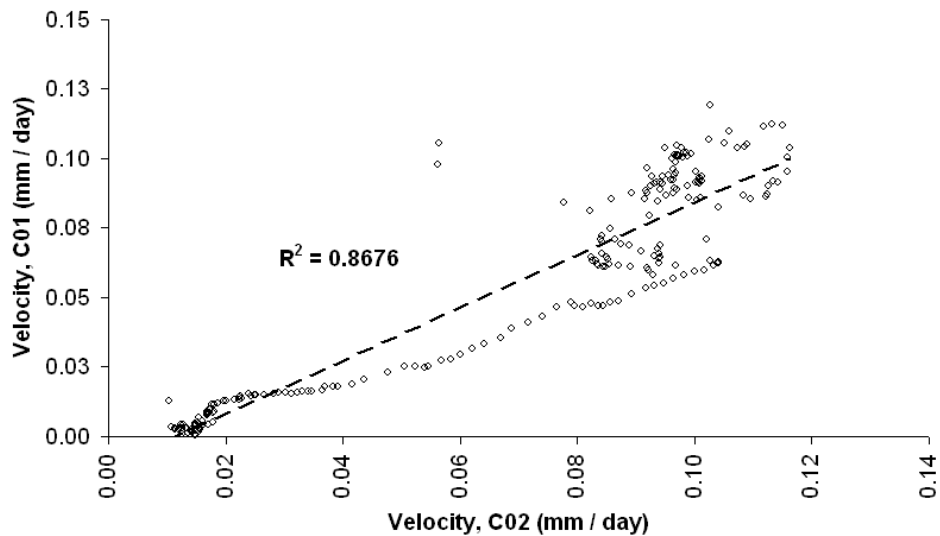


Figure 5.54 Relationship between running mean velocities measured at C01 and C02 during accelerated ground displacement

The specific period of accelerated ground creep between 12/08/2000 and 19/04/2001 has been analysed in $1/v - t$ space, demonstrating an asymptotic trend in both C01 (Fig 5.55) and C02 (Fig 5.56). The asymptotic curves have been shown to be statistically significant with R^2 values of 0.92 and 0.95. A similar asymptotic curve can be observed in vertical displacement rates at SC04 (Fig 5.57). The R^2 value however is notably lower which is likely to relate to variability in velocity readings observed in the settlement cells as previously discussed in section 5.3.2. The consistent asymptotic patterns of movement indicate that movement is occurring along a pre-existing shear surface or within a ductile shear zone (Petley *et al.*, 2005c).

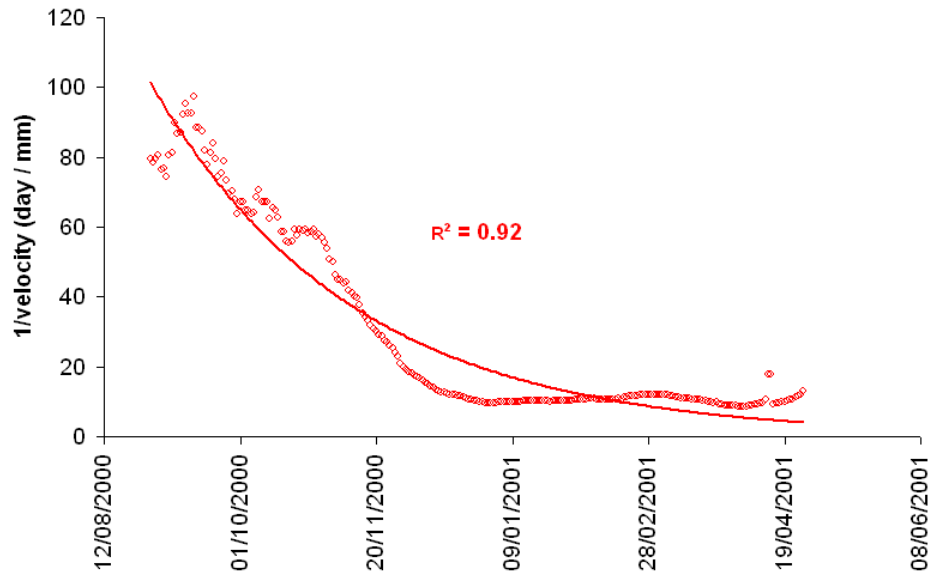


Figure 5.55 Accelerated ground displacement at C01 plotted in $1/v - t$ space

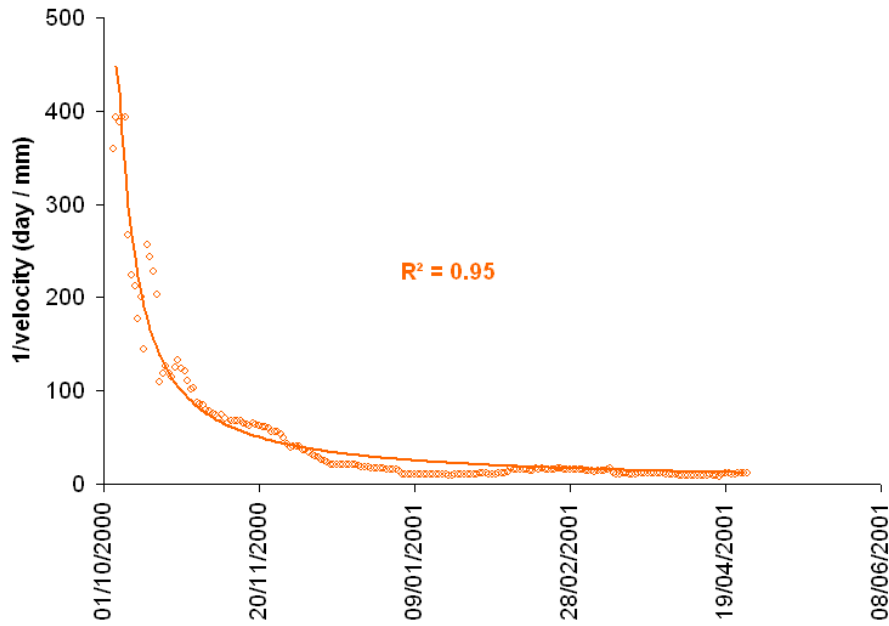


Figure 5.56 Accelerated ground displacement at C02 plotted in $1 / v - t$ space

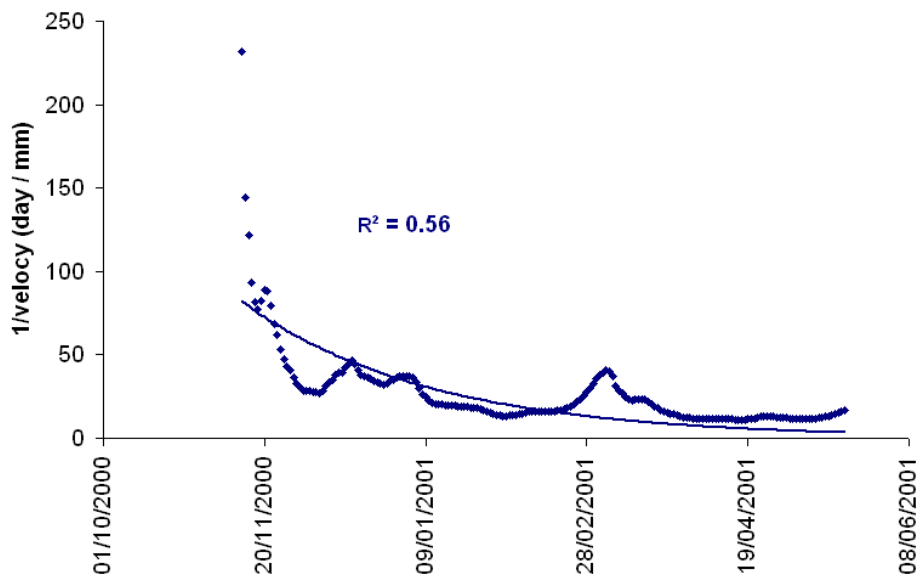


Figure 5.57 Accelerated ground displacement at SC04 plotted in $1 / v - t$ space

The daily displacement velocities from C01 and C02 have been plotted with porewater pressure readings at P02 for the period between 1995 and 2005. The graph indicates that whilst variations in the porewater pressures between 1995 and 2000 have had minimal impact on the slow creep rates, the higher

pore pressures recorded between 2000 and 2001 are mirrored by velocity patterns in the graben crackmeters (Fig 5.58) and similarly in the vertical velocity records at SC04 (Fig 5.59). The results illustrate that whilst the slow creep movement observed between 1995 and 2000 do not respond to changes in the porewater pressure, a significant change in displacement rate is observed following the higher porewater pressures measured in November and December 2000. This sudden change in behaviour must be associated with a specific porewater pressure threshold. Such threshold movements have been observed in other deep seated landslides such as Lyme Regis (Brunsdon, 2002).

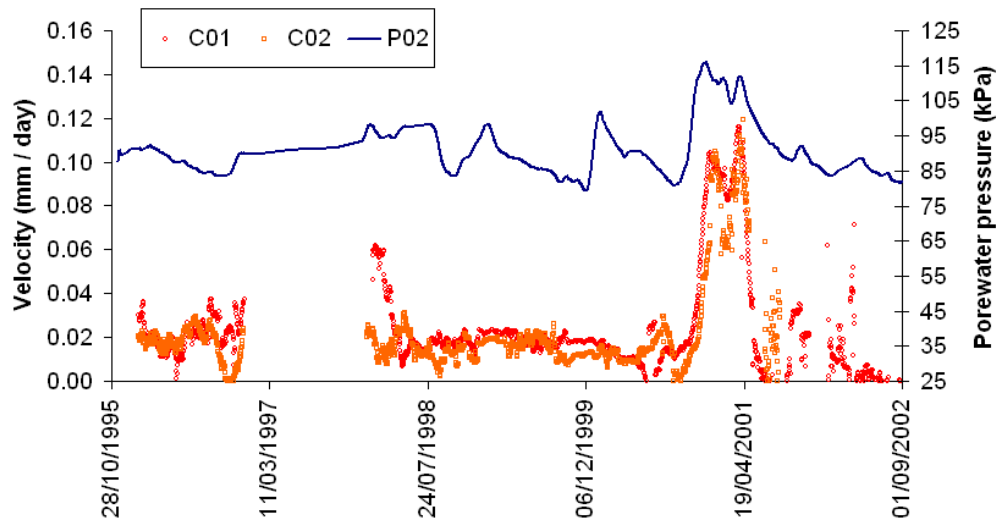


Figure 5.58 Comparison of running mean horizontal velocities at C01 and C02 and running mean porewater pressures in P02

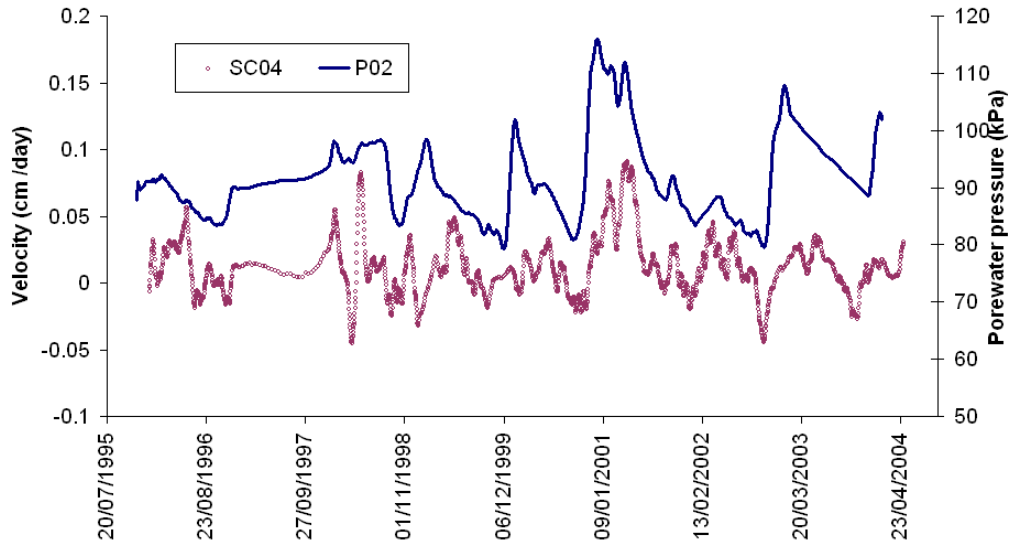


Figure 5.59 Comparison of running mean vertical velocities at SC04 and running mean porewater pressures in P02

The period of accelerated ground movement between 2000 and 2001, recorded in both C01 and C02, has been plotted with the porewater pressure readings in P02 (Fig 5.60). The results confirm that ground acceleration in both crackmeters occurs after a similar increase in porewater pressure. Once peak ground acceleration is achieved, ground movement continues at a near constant velocity before decreasing back to a background creep rate. This analysis suggests that the graben experienced accelerated ground creep in response to elevated porewater pressures acting at the landslide shear zone. The consistency in the patterns of porewater pressure in P02 and ground movement provide evidence that ground movement rates are controlled by porewater pressures which when elevated at the shear zone lead to a reduction of effective stress allowing displacement to occur. As porewater pressures dissipate the ground movement rates return to the background displacement rate. This behaviour is consistent with previously observed patterns of movement (e.g. Allison and Brunsden, 1990; Petley *et al.*, 2005c) and in laboratory testing (Ng and Petley, 2009), where deformation is occurring along a ductile shear zone or pre-defined shear surface.

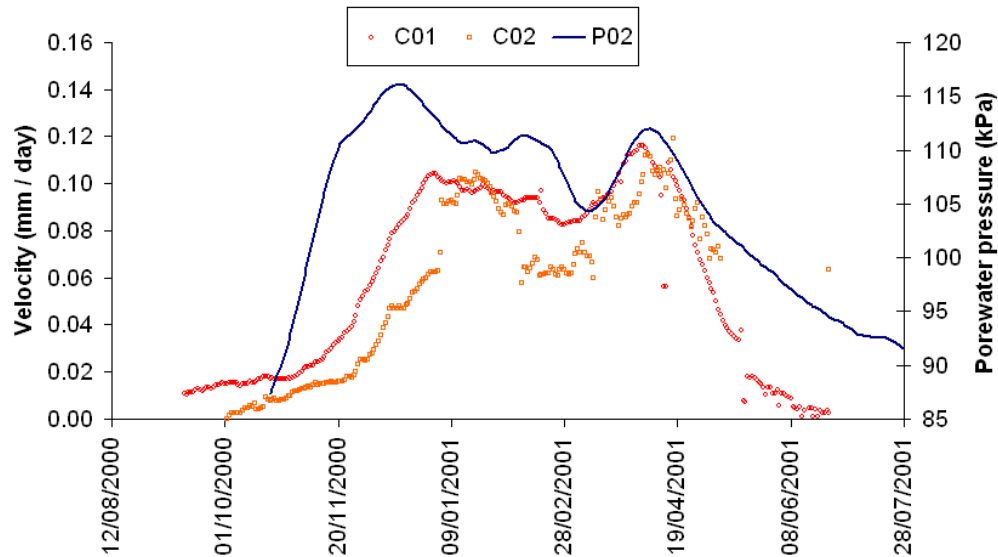


Figure 5.60 Relationship between velocity measured at the Newport Road (C01 and C02) and porewater pressure (P01) between 23/06/2000 and 28/07/2001

The relationship between porewater pressures at P02 and the ground movement have been analysed further by plotting average monthly porewater pressure with total monthly displacement (Fig 5.61). The graph illustrates the consistency between elevated porewater pressure and high total monthly displacement. Analysis of these two datasets provides a statistically significant linear trend with a R^2 value of 0.71 (Fig 5.62). Such analysis may provide a potential tool for forecast displacement events for a given porewater pressure scenario.

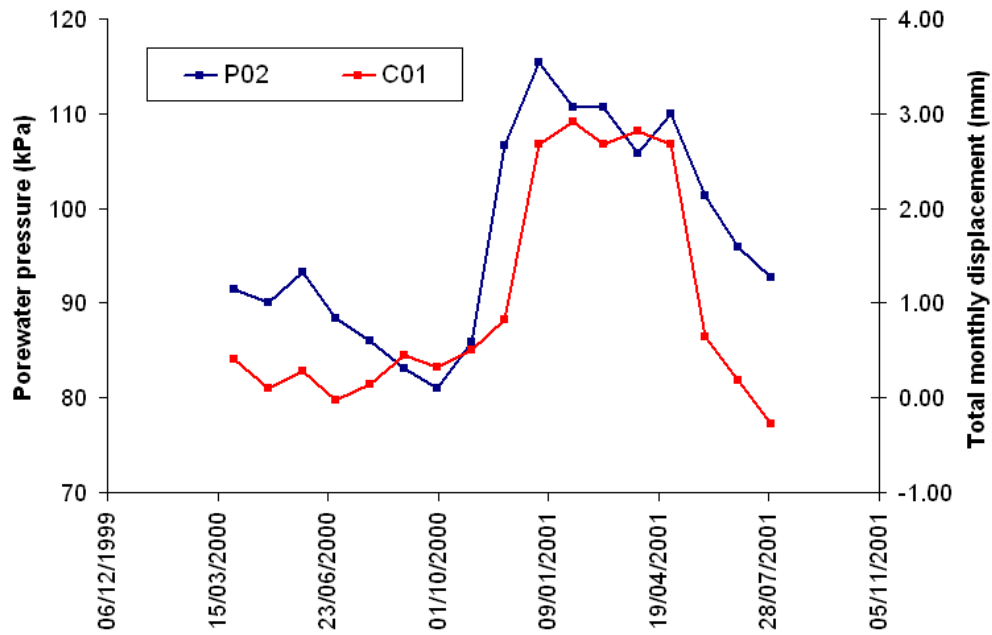


Figure 5.61 Comparison of porewater pressures in P02 and total monthly displacement at C01 between 15/03/2000 and 28/07/2001

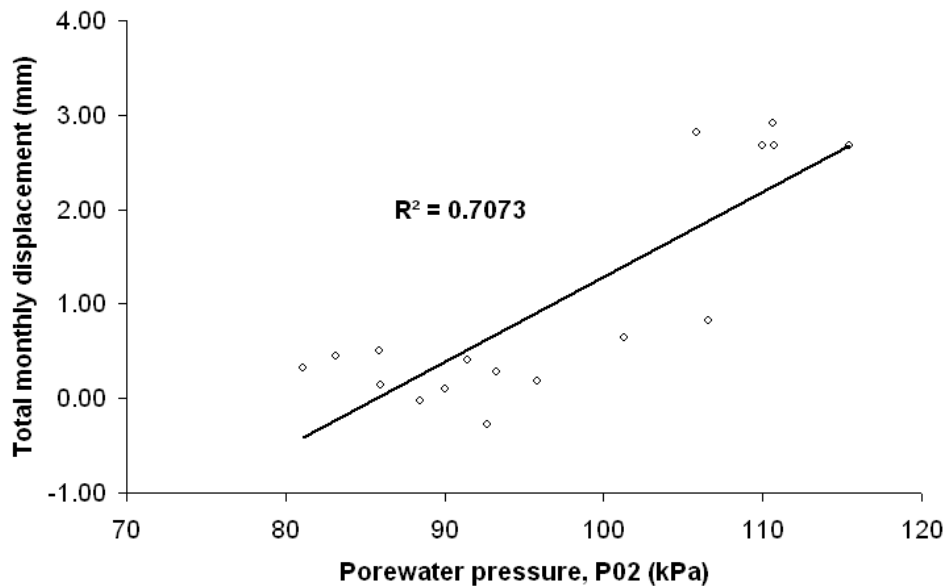


Figure 5.62 Relationship between porewater pressure in P02 and total displacement at C01

When the period of accelerated movement recorded at C01 and C02 is plotted with total monthly rainfall it is possible to observe that the displacement rate patterns mirror the rainfall record (Fig 5.63)

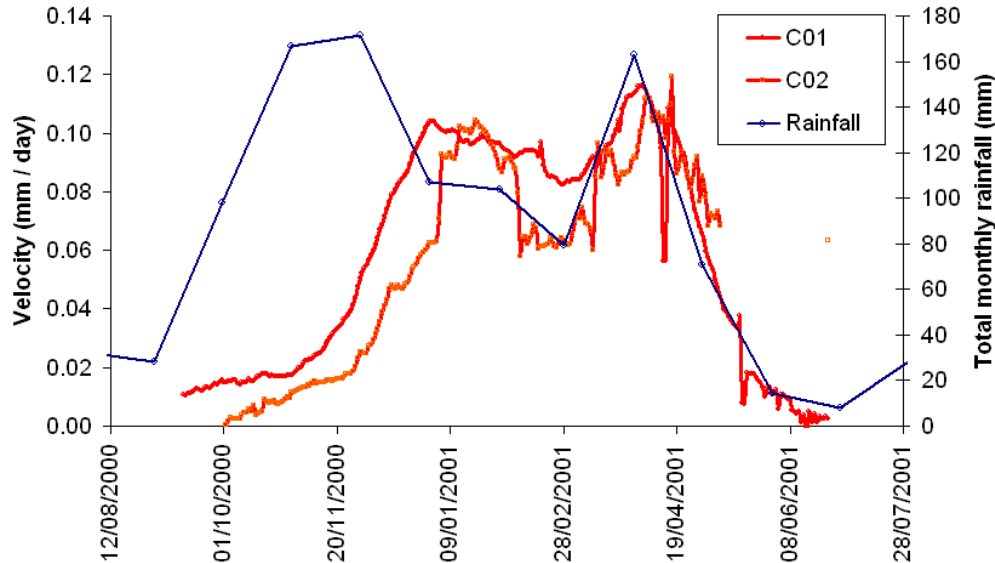


Figure 5.63 Relationship between velocity measured at the Newport Road (C01 and C02) and total monthly rainfall between 23/06/2000 and 28/07/2001

The results are consistent with previous research carried out at this site in which long-term historical rainfall records have been compared to landslide events and movement records (Moore *et al.*, 2007; Lee and Moore, 1991). This research has revealed a statistically significant relationship between the preceding four month rainfall and ground movement, suggesting that the antecedent rainfall characteristics is a significant factor in triggering ground movement and landsliding within the Undercliff.

The ground movement records at C01 have been plotted as total monthly displacement with the four month running average total monthly rainfall (Fig 5.65). The graph illustrates a similar pattern in both displacement and rainfall which when plotted together provides a statistically significant linear trend with an R^2 value of 0.74 (Fig 6.65).

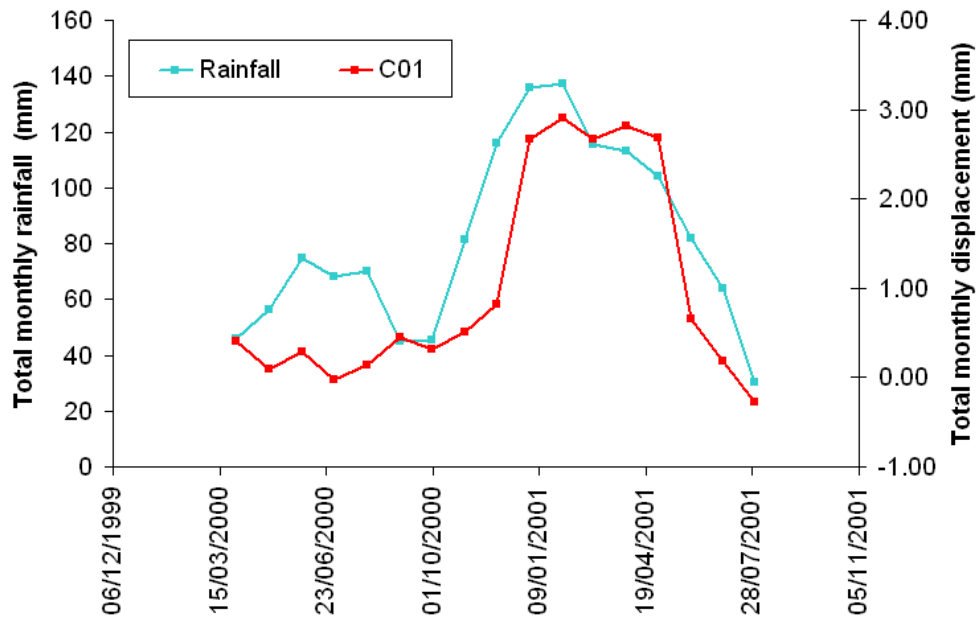


Figure 5.64 Comparison of the 4 month running average total monthly rainfall and total displacement at C01 between 15/03/2000 and 28/07/2001

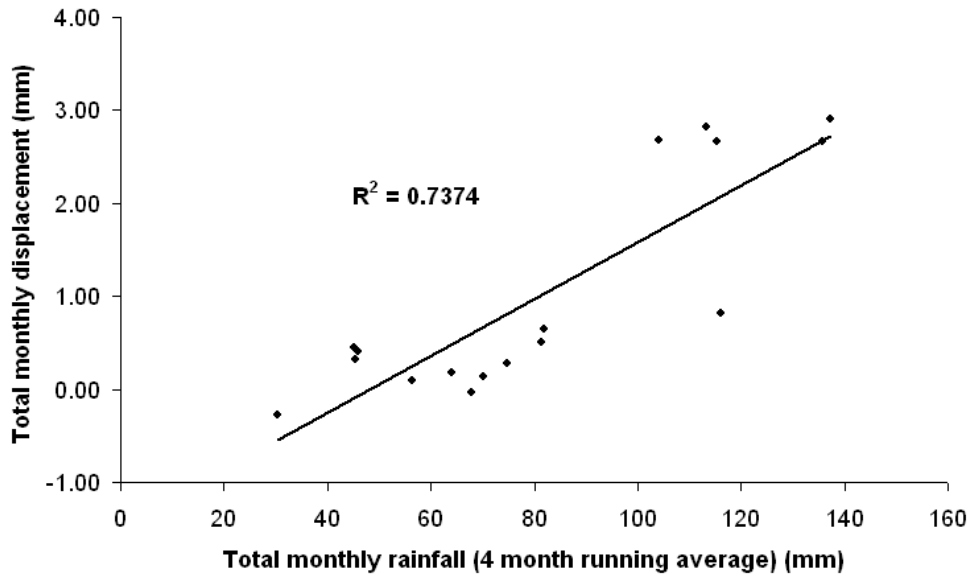


Figure 5.65 Relationship between 4 month running average total monthly rainfall and total displacement at C01

5.5 Chapter summary

This chapter has analysed the spatial and temporal distribution of ground movement within the Ventnor landslide complex to develop a greater understanding of the existing landslide model, the nature of a patterns of movement occurring within the site and the sensitivity of the landslide to the internal groundwater regime and external rainfall characteristics at the site.

The monitoring data made available from the Council's landslide management strategy has provided a new insight into the spatial distribution of ground movement. The results have illustrated that the landslide comprises of three distinct units: First, a lower tier landslide incorporating the area of Park Avenue and is currently displacing along bedding controlled shear surface confirmed at 73 m bgl. The shear surfaces are seated in the Gault Clay and in Sandrock 2d. Second, an upper tier landslide that extends from the Lowtherville Graben to Park Avenue, which comprises of a series of deep seated translational blocks that are moving along a bedding controlled shear surface 95 m bgl at the base of Gault Clay. Third, an additional lower tier landslide unit has been identified in the area of the Esplanade with an unconfirmed shear surface. This landslide unit is also subject to ongoing settlement and is likely to actively unload the Upper tier landslide above.

In addition the analysis has revealed a series of distinct movement patterns which vary within each of the landslide units and are interpreted to be influenced by potentially different causal mechanisms.

A pattern of seasonal settlement and uplift observed within settlement cells SC03, SC06 and SC11. Analysis of the settlement records has demonstrated uplift correlates with elevated porewater pressures measured at P02, whilst settlement corresponds with the lowering of porewater pressures. This uplift and settlement cycle has been observed at other landslide sites (e.g .Zhou *et al.*, 2010) and has been linked to localised changes in soil moisture causing wetting and drying cycles. These effects occur at shallow depths around the settlement cell and are therefore not the result of landslide movement.

An ongoing slow creep pattern of movement has been observed in the settlement cells, crackmeters and inclinometers whilst suggest the all three landslide units are subject to continued ongoing movement. The movements appear to suggest some consistency to 'stick-slip' observed by previous authors (e.g, Petley *et al.*, 2005c; Allison and Brunnsden, 1990). Given the minor fluctuations in displacement observed these 'stick-slip' movements, which is best identified in the velocity data were minor fluctuations are observed within the longer term trend of near constant displacement rate. The exact causal mechanism of this movement remains to be fully understood as the patterns of movement do not relate to the seasonal variations in the measured porewater pressures. A close correlation between cumulative rainfall and the stick-slip movement has been observed. This may suggest that the landslides are in a state marginal stability and require only minor rainfall inputs to promote movement albeit at an initially very low creep rate (6 to 10 mm / yr)

A specific period of accelerated ground creep has been recorded at the Lowtherville Graben only. This period of accelerated ground creep occurred winter period of 2000 and 2001 and is consistent with the graded movement patterns previously observed at other sites (e.g. Petley *et al.*, 2002; 2005c; Allison and Brunnsden, 1990), and laboratory based studies. Analysis of this period of ground acceleration in $1/v - t$ space has demonstrated an asymptotic trend consistent with movement along a pre-existing shear surface or ductile shear zone (Petley *et al.*, 2005c; Ng and Petley, 2009). This period of accelerated ground creep appears to occur above a specific porewater pressure threshold. Once surpassed the rate and duration of accelerated creep correlates linearly with the measured porewater pressures.

A clear correlation between this period of ground movement, porewater pressure and antecedent rainfall has been established. A four month running average of total monthly rainfall shows a strong linear correlation with the graded ground movement. The three month lag between rainfall and porewater pressure response indicates that potential landslide displacement

rates under various groundwater and antecedent rainfall scenarios could be forecast to provide an early warning to residents and the Council.

Chapter 6: Laboratory Results

6.1 Introduction

This chapter presents the results of laboratory testing designed to study the progressive development and post failure behaviour of the landslide shear surface materials sampled from Ventnor landslide complex.

The detailed landslide monitoring analysis presented in Chapter 5 has confirmed that a series of movement patterns operate over different spatial and temporal scales, with the control being a deep shear surface at the base of the Gault Clay (Fig 5.4). Correlation of these movement patterns with porewater pressure and antecedent rainfall characteristics recorded at the site have highlighted their significance in driving these landslide movement patterns.

This analysis has formed the basis of the laboratory testing, which is focused on two materials extracted from the landslide shear surface (Table 4.3). These comprise the basal Gault Clay Formation and the transition zone of the Gault into the underlying Carstone referred to in this study as the Gault-Carstone transition zone. These materials have collected from both intact cores, during the rotary drilling of two deep boreholes (BH5 and BH4) (Halcrow, 2006) and excavated from appropriate locations local to the site (Fig 4.1) as stratigraphic-equivalent undisturbed block samples (BS).

The physical properties of these two materials have been investigated to determine the key soil properties of particle size, Atterberg limits, specific gravity and natural moisture content. The plasticity of both materials has been defined using a plasticity chart.

Standard geotechnical testing has been undertaken to define the both the peak and residual strength failure envelopes in both the Gault Clay and Gault-Carstone transition zone. This has been studied using both Isotropically Consolidated Undrained (ICU) stress path tests using the triaxial cell and standard direct shear tests using the back pressured shear box.

The progressive development of shear surfaces in intact materials has been studied under a series of failure scenarios by varying the initial consolidation and stress histories of samples and through studying failure under varying pore pressure reinflation (PPR) rates on intact samples. A range of test scenarios have been developed using both Isotropically Consolidated Drained (ICD) testing and pore pressure controlled direct shear testing using the back pressured shear box (BPSB).

The subsequent post failure behaviour of the two materials has been investigated using remoulded samples subject to different rates of pore pressure reinflation through a series of PPR ICD and BPSB tests.

Finally a long creep test has been conducted on an intact Gault clay sample to study the nature of failure at constant mean effective stress.

The results provide a new insight into the development and behaviour of shear surfaces under pore pressure induced failure conditions.

6.2 Physical Properties

The physical properties of the Gault Clay and the Gault-Carstone transition zone samples are summarised in Table 6.1.

The results indicate that a range of natural moisture contents were observed in the Gault Clay samples which ranged from 13% in BH4 samples up to 17% in Gault Clay samples extracted from BS and BH5. Natural moisture contents were generally lower in the Gault-Carstone transition zone which average 14%.

Table 6.1 Physical properties of the Gault Clay and Gault-Carstone transition samples

Physical Properties	Gault Clay (BH4)	Gault Clay (BH5)	Gault Clay (BS)	Gault/ Carstone transition zone (BH5)
Particle size:				
Sand (%)	44.87	46.61	47.70	70.40
Silt (%)	48.59	39.28	40.40	24.70
Clay (%)	6.54	14.10	11.90	4.90
Specific gravity (Gs)	2.72	2.73	2.70	2.69
Loss on Ignition (%)	2.45	5.02	3.69	1.76
Mc (%)	13	17	17	14
Liquid limit (%)	51	56	30.11	35
Plastic limit (%)	19	21	21.18	17
Plasticity index	32	35	8.93	18
Bulk density (mg/ m ³)	2.213-2.241	2.069	2.069-2.21	1.983
Dry density (Mg / m ³)	1.896-1.911	1.66	1.702-1.911	1.701

Particle size analysis (Fig 6.1) illustrates some variability across the Gault Clay samples. Gault Clay from BH5 show Clay contents ranging 14.10% with silt contents of 39.28% and sand content of 46.61%. Similar particle size characteristics can be observed in BS samples which show a slightly lower Clay content of 14.10% and comparable silt and sand contents of 40.40% and 47.70% respectively. The basal Gault Clay in BH4, however, shows significantly lower Clay content of 6.54% and much higher silt contents of 48.59%.

Analysis of particle size data of the Gault-Carstone transition zone material collected in BH5 illustrate a material with much lower clay content of 2.69%, a silt content of less than 24.70% and approximately 70.40% sand-sized particles.

Particle size analysis results have been compared with previous studies of the Gault Clay during the 2005 ground investigation (Halcrow, 2006) (Fig 6.2). The results indicate similar particle size characteristics across the two studies although moderately lower clay percentages and higher sand percentages are observed in the current study. The results of both studies, however, suggest that Gault Clay at Ventnor is generally coarser than in many other parts of the UK, where clay contents can range up to 65% (BGS, 1995).

The Atterberg limit results (Fig 6.3) indicate that the Gault Clay samples comprise high plasticity clay in BH4 and BH5 and a low plasticity clay in BS, as defined in accordance with BS5930 (1981). The plastic limits of the Gault samples ranged between 19% and 22% with liquid limits ranging between 30% in BS and 56% in BH5. Significantly lower plasticity was observed in BS which relates specifically to the surprisingly low liquid limit. The Atterberg limits observed in the Gault-Carstone transition zone demonstrate a low to medium plasticity clay material with a lower plastic limit at 17% and a liquid limit at 35%. This is consistent with the particle size analysis, which illustrates a greater sand content in the Gault-Carstone transition zone.

The measured Atterberg limits have been compared with previous physical properties testing performed on Gault clay samples from Ventnor (Halcrow, 2006) (Fig 6.4). Previous studies illustrate a significant scatter in Gault Clay characteristics. Whilst the majority of samples described and intermediate to high plasticity clays, as defined in accordance with BS5930 (1981), a number of samples can be defined as intermediate to high plasticity clays. In addition some further results indicate clays of low or very low plasticity. Previous tests show an overall range in plastic limits from 18% to 38% with a median value of 23%.

The Gault Clay plasticity characteristics from BH4 and BH5 are consistently lower than the ranges of median plastic and liquid limits of 23% to 32% and 68% to 80% reported by the BGS (1995) for other Gault Clay sites in the UK. The lower plasticity characteristics observed during this study are consistent with the observation of coarsening of the Gault toward the base of the Formation (Halcrow, 2006).

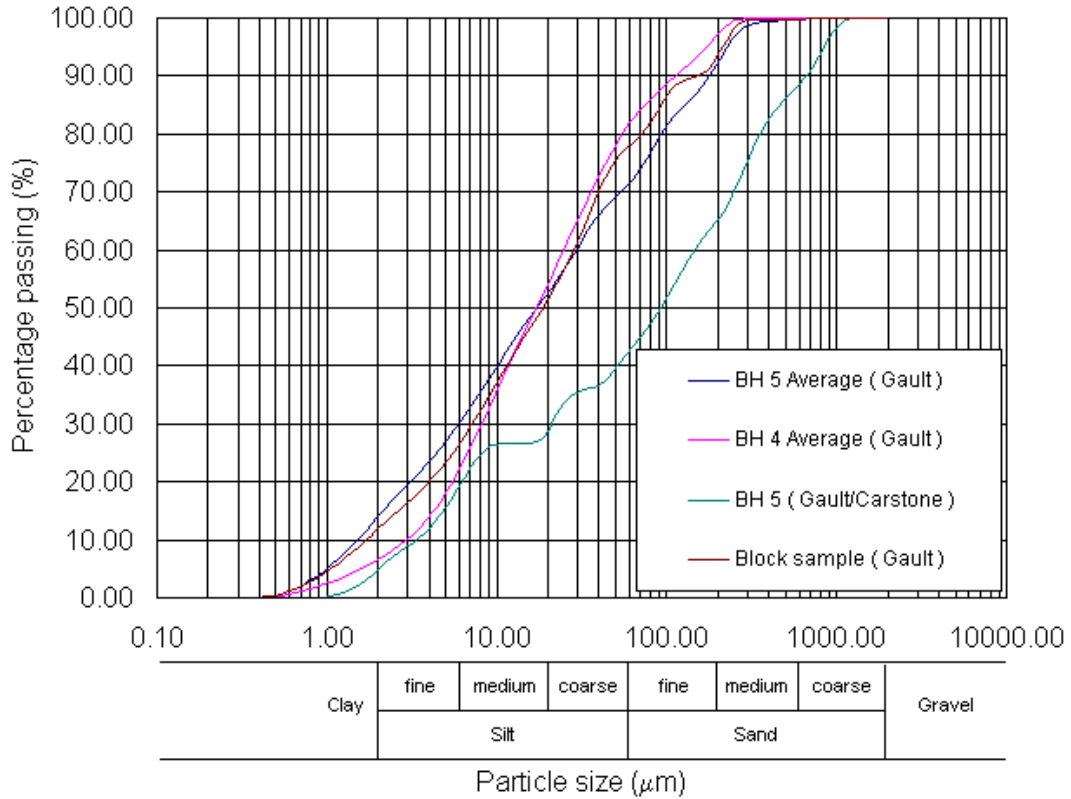


Figure 6.1 Particle size distribution chart for Gault Clay samples collected from BH4, BH5 and BS and Gault- Carstone transition zone in BH5

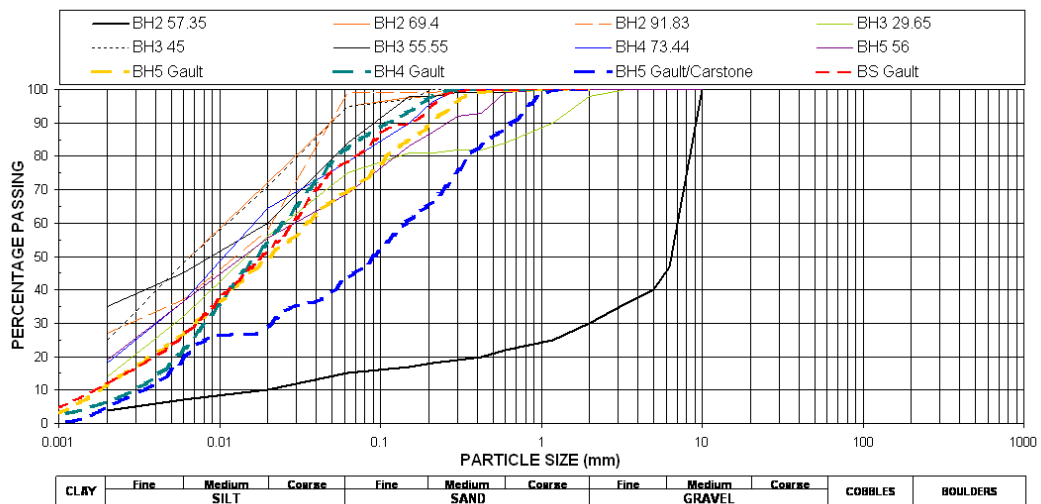


Figure 6.2 Comparison of particle size distribution with previous laboratory testing during the previous ground investigations by the Isle of Wight Council (after Halcrow, 2006)

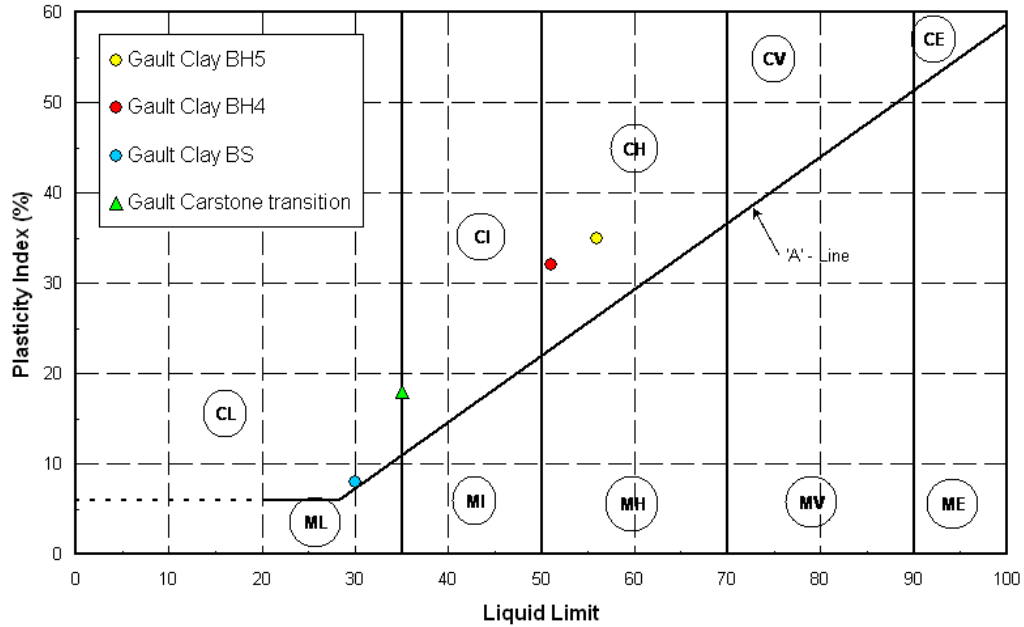


Figure 6.3 Material classification of Gault Clay and Gault/ Carstone transition samples using the Plasticity chart (after BSI, 1981)

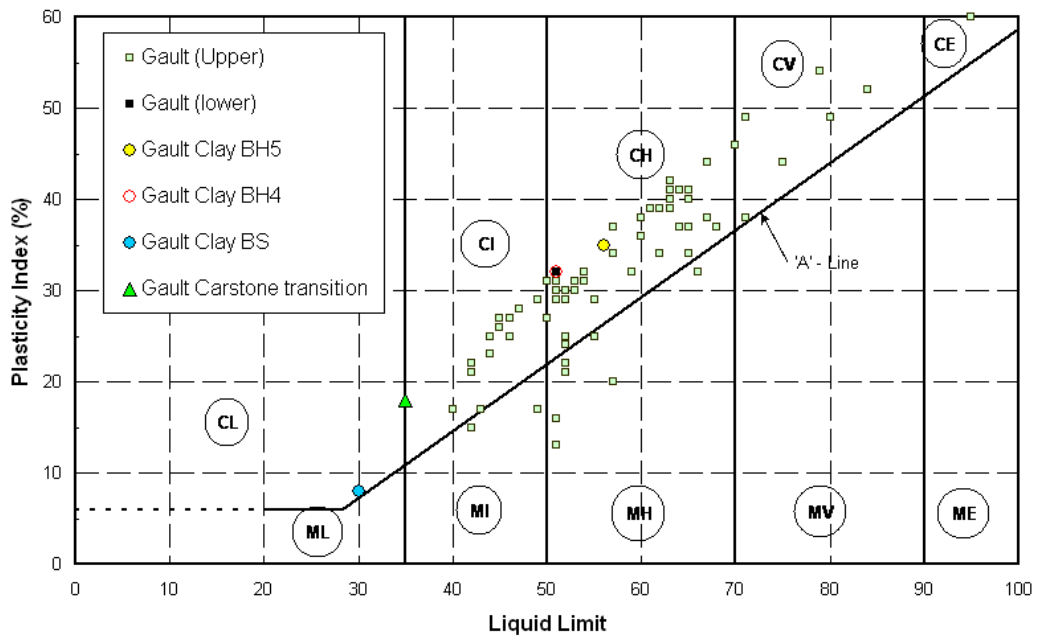


Figure 6.4 Comparison of Atterberg limits in relation to previous testing on the Gault Clay at Ventnor

6.3 Geotechnical testing

To undertake this study a suite of laboratory tests has been conducted using both the triaxial cell and the back pressured shear box apparatus. A breakdown of the geotechnical testing undertaken is provided in Tables 6.2 to 6.5

Table 6.2 Isotropic consolidated undrained (ICU) tests

Test Reference	Material	Confining pressure (kPa)	Strain rate during shear	PPR rate (kPa/hr)	Sample Reference	Sample condition
ICU1	Gault	250	0.01	N/A	BS	intact
ICU2	Gault	350	0.01	N/A	BS	intact
ICU3	Gault	450	0.01	N/A	BS	intact
ICU4	Gault	450	0.01	N/A	BS	intact
ICU5	Gault	550	0.01	N/A	BS	intact
ICU6	Gault	550	0.01	N/A	BS	intact
ICU7	Gault	150	0.01	N/A	BS	intact

Table 6.3 Isotropic consolidated drained (ICD) pore pressure re-inflation (PPR) tests

Test Reference	Material	Confining pressure (kPa)	Stress path (kPa)	Strain rate during shear	PPR rate (kPa/hr)	Sample Reference	Sample condition
ICD1	Gault	250	400	0.01	10	BS	intact
ICD2	Gault	350	400	0.01	10	BS	intact
ICD3	Gault	450	400	0.01	10	BS	intact
ICD4	Gault	350	400	0.01	10	BS	intact
ICD6	Gault	350	400	0.01	18	BS	intact
ICD7	Gault	350	400	0.01	5	BS	intact
ICD8	Gault	450	500	0.01	10	BS	intact
ICD9	Gault	550	600	0.01	10	BS	intact
ICD10	Gault	350	400	0.01	10	BH4	Intact
ICD11	Gault	350	400	0.01	10	BH5	Intact
ICDR1	Gault	350	400	0.01	10	BS	remoulded
ICDR2	Gault	350	400	0.01	18	BS	remoulded
ICDR3	Gault	350	400	0.01	5	BS	remoulded
ICD13	Gault	350	400	0.01	Slow creep	BH5	intact

Table 6.4 Direct shear cut plane shear box (CPSB) tests

Test Reference	Material	Confining pressure kPa	Stress path kPa	Strain rate during shear	PPR rate (kPa/h)	Sample Reference	Sample condition
CPSB1	Gault - Carstone transition	300	N/A	0.01	N/A	BH5	intact
CPSB2	Gault - Carstone transition	600	N/A	0.01	N/A	BH5	intact
CPSB3	Gault - Carstone transition	900	N/A	0.01	N/A	BH5	intact

Table 6.5 Back pressured shear box (BPSB) pore pressure reinflation (PPR) tests

Test Reference	Material	Confining pressure kPa	Stress path kPa	Strain rate during shear	PPR rate (kPa/hr)	Sample Reference	Sample condition
BPSB1	Gault - Carstone transition	600	250	0.01		BH5	intact
BPSB1R	Gault - Carstone transition	600	250	0.01		BH5	remoulded
BPSB2	Gault - Carstone transition	250	150	0.01		BH5	intact
BPSB3	Gault Clay	250	150	0.001		BH5	intact
BPSB4	Gault Clay	750	150	0.001		BH5	intact

6.3.1 Saturation stage

The majority of intact Gault samples showed only minor increases or decreases (less than 1%) in axial length (L), volume (V) and void ratio during saturation (Table 6.6). Samples ICD8, ICD9, and ICD11 however showed increases in axial length, and volume of greater than 1% suggesting that the samples may have lost moisture prior to testing. Reductions in sample volume of 1.511% and 2.081% were also observed in samples ICU5 and ICU6. Remoulded Gault sample (ICDR2) recorded the larger decreases in sample volumes of between 2.2% and 9.84% during saturation indicating the moisture content was too high during remoulding.

The Gault Carstone-transition samples illustrated similar variability during saturation with samples CPSB 1and CPSB2 decreasing in sample volume and height whilst samples CPSB3, CPSB1 and CPSB1R swelling during saturation. Despite these variations the saturation is not believed to have had a significant impact on the geotechnical testing.

Table 6.6 Change in ICU and ICD sample dimensions during the saturation of Gault Clay samples

Test Reference	Before saturation		After saturation		% change		B- value
	L0 (mm)	V0 (mm ³)	Lsat (mm)	Vsat (mm ³)	L (%)	V (%)	
ICD1	75.23	83266	75.62	82737	0.518	-0.635	99.2
ICD2	76.01	81774	75.90	82280	-0.145	0.619	98.8
ICD3	75.71	86407	76.14	86291	0.568	-0.134	99.6
ICD4	77.03	84172	77.07	83680	0.052	-0.585	99.4
ICD5	75.98	83065	76.64	82387	0.869	-0.816	99.0
ICD6	75.92	85879	76.27	85030	0.461	-0.989	99.8
ICD7	76.00	85149	75.92	84862	-0.105	-0.337	98.2
ICD8	77.22	88574	78.18	89224	1.243	0.734	99.0
ICD9	75.74	86098	76.78	85068	1.373	-1.196	99.8
ICD10	74.38	83040	74.83	82471	0.605	-0.685	98.8
ICD11	75.10	84579	75.43	83341	0.439	-1.464	99.0
ICD12	75.72	85826	76.51	85541	1.043	-0.332	97.6
ICD13	75.87	85371	76.26	83972	0.514	-1.639	99.4
ICDR1	74.46	87405	75.46	88578	1.343	1.34	100.4
ICDR2	76.62	87171	77.17	78593	0.718	-9.840	101.0
ICDR3	76.44	87435	77.00	88064	0.733	0.719	99.6
ICU1	75.79	82728	75.97	81985	0.237	-0.898	98.0
ICU2	76.73	83533	76.96	82880	0.300	-0.782	98.6
ICU3	74.78	84493	75.02	83982	0.321	-0.605	98.6
ICU4	75.97	85044	76.18	84592	0.276	-0.531	98.6
ICU5	77.09	84460	77.20	82702	0.143	-2.081	99.2
ICU6	75.73	85116	76.25	83830	0.687	-1.511	98.4

Table 6.7 Change in CPSB and BPSB sample dimensions during the saturation of Gault-Carstone interface samples

Test Reference	Before saturation		After saturation		% change	
	H0 (mm)	V0 (mm ³)	Hsat (mm)	Vsat (mm ³)	H (%)	V (%)
CPSB1	21.20	212000	21.17	211690	-0.142	-0.146
CPSB2	20.74	207380	20.54	205300	-0.964	-1.00
CPSB3	21.37	213720	21.51	215130	0.655	0.655
BPSB1	21.00	210050	21.16	211570	0.7619	0.7236
BPSB1R	22.06	220610	22.10	221030	0.1813	0.1904

6.3.2 Consolidation stage

All ICD and ICU triaxial samples underwent an initial phase of isotropic consolidation before a shear force was applied. The consolidation curves for both ICU and ICD testing on intact Gault Clay samples have been constructed at a range confining pressures ranging from 250 kPa to 550 kPa (Appendix 1, Fig A1). Whilst the results demonstrate some variability in behaviour between the samples there is a general trend of increased volumetric strain occurring in samples consolidated at higher mean effective stress. Plotting volumetric strain on a logarithmic scale illustrates that there is some variation in the nature of the consolidation curves (Fig 6.5) with samples ICD89 and ICU4 consolidating rapidly in comparison to final volumetric strains when compared to majority of samples.

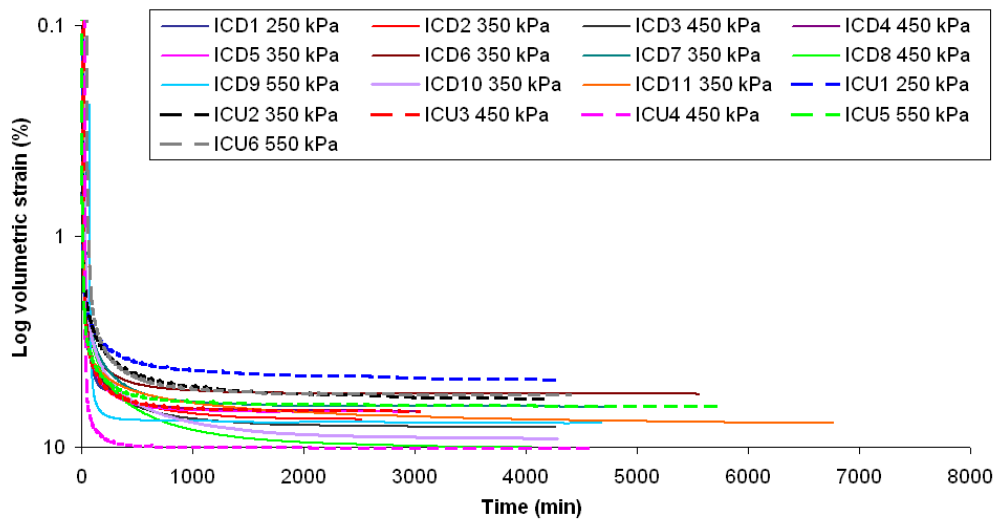


Figure 6.5 Volumetric strain plotted on a log scale against time for ICD and ICU Gault Clay samples at effective stress 250, 350, 450 and 550 kPa

Comparison of the initial void ratios of each sample (Appendix A, Fig A2) illustrates the variability in samples tested although each sample showed comparable behaviour during consolidation (Appendix A, Fig A3). This is reflected in the change in void ratio (Appendix A, Fig A4) and final void ratios (Appendix A, Fig A5) which show similar variability to the initial void ratio.

Consolidation curves from the remoulded Gault Clay samples ICDR1, ICDR2 and ICDR3 illustrate relatively consistent behaviour although with less change in volumetric strain being observed in sample ICDR3 (Appendix A, Fig A6). The nature of the consolidation curves however is consistent (Fig 6.6), which indicates the consistent nature of the samples tested. This is further supported by only minor variability observed in the initial void ratios (Appendix A, Fig A7) and final void ratio (Appendix A, Fig A8). As expected more significant changes in void ratio during consolidation were identified in the remoulded samples (Appendix A, Fig A9) when compared to the intact samples (Appendix A, Fig A10).

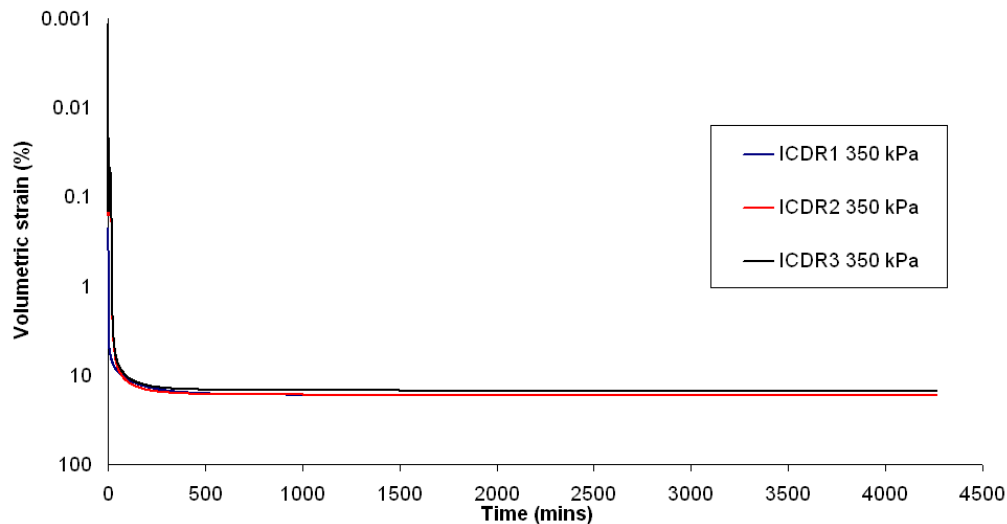


Figure 6.6 Log volumetric strain against time for remoulded ICD Gault Clay samples at effective stress of 350 kPa

Samples tested in the BPSB were subject to a ramped consolidated phase in which the axial load was increased linearly through the consolidation to allow for sample drainage and to prevent the development of positive porewater pressures.

During consolidation of the Gault - Carstone transition material samples axial displacements increased linearly as axial load increased (Appendix A, Fig A11). The results of the consolidation demonstrate greater displacement in samples subjected to higher axial loads (Appendix A, Fig A12). This can be

observed in the vertical strain – time curves which demonstrate that greater vertical strain can be observed in samples consolidated to higher mean effective stresses (Fig 6.7). The results demonstrate consistent behaviour during the consolidation in the Gault Carstone material (Appendix A, Fig A13).

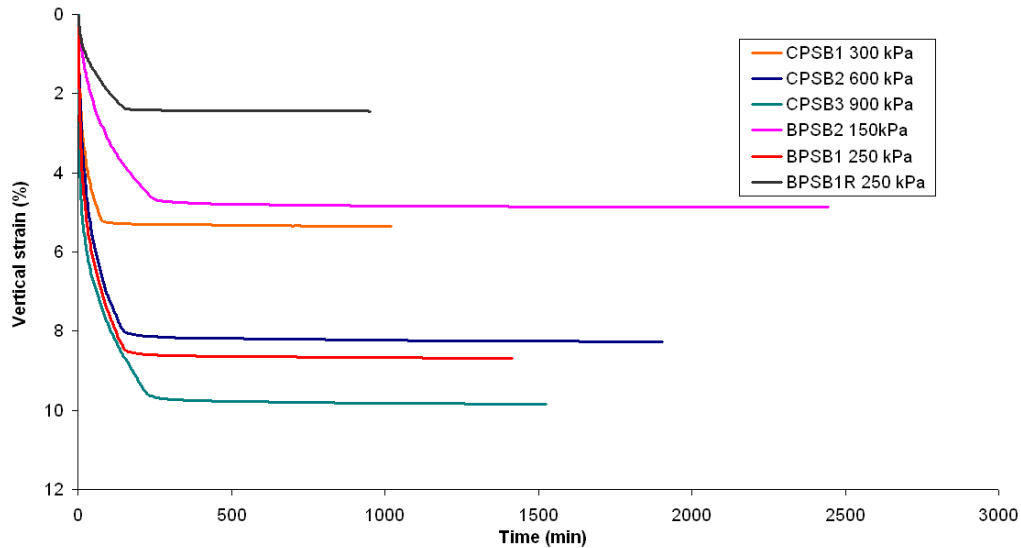


Figure 6.7 Consolidation curve for Gault-Carstone transition zone samples at effective stress of 150, 200, 300, 600 and 900 kPa

Gault Clay samples tested in the BPSB were subjected to a ramped consolidation phase through the linear increase in normal load until the pre-determined mean effective stress was reached (Appendix A, Fig A14). Sample BPSB3 however shows a stepped pattern in consolidation which was associated with a power cut during testing. During this time axial load reduced slightly until loading could recommence. Whilst this has caused a stepped pattern in the consolidation behaviour this is believed to have had no impact on the sample which continued to consolidate once the increase in axial load continued (Appendix A, Fig A15). The consolidation curves (Fig 6.8) illustrate that despite the stepped pattern in the consolidation of sample BPSB3 the samples consolidated as expected.

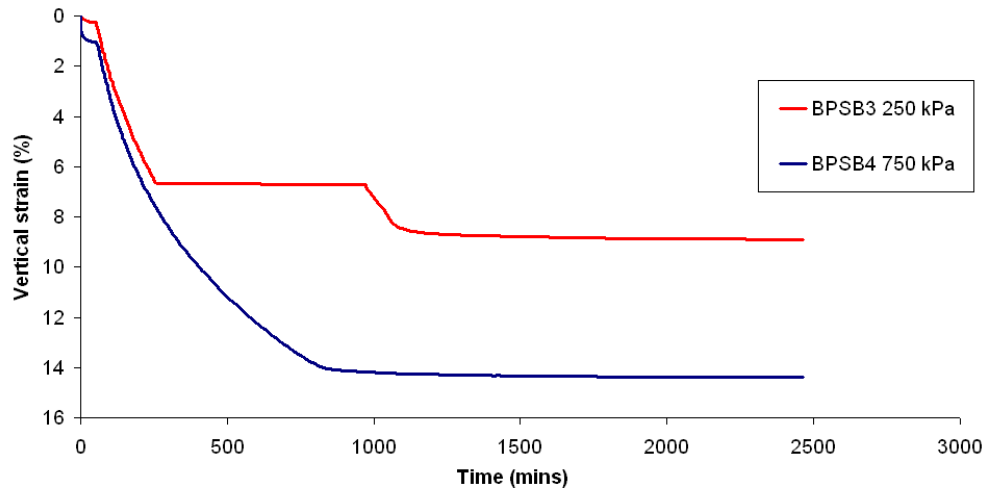


Figure 6.8 Vertical strain against time for Gault Clay samples at effective stress of 150 and 250 kPa

6.3.3 Material failure envelopes

In all ICU samples the deviator stress initially increased rapidly with minimal (>1 %) initial sample strain (Appendix A, Fig A16). In each sample deviator stress peaked at between 2.11 % and 3.55 % axial strain and then reduced before reaching c.5% strain, thereafter strain continued at near constant p' . The results show that samples failing at higher q demonstrated a larger reduction in q after peak strength. The results indicate that all samples failed at relatively low axial strain (Table 6.8), with the strain at failure increasing with increased p' .

The behaviour observed is consistent with brittle failure characteristics in overconsolidated clays (e.g. Cripps and Taylor, 1981; Burland, 1990). These brittle failure characteristics are further supported by the condition of samples at failure, which reveal a singular shear surface associated with stress concentration along a single fracture zone (Plate 6.1)

Table 6.8 Axial strain (%) at failure during ICU testing

Sample reference	Confining pressure (kPa)	p' (kPa)	q' (kPa)	ϵ_a (%)
ICU1	250	341	536	2.36
ICU2	350	472	650	2.11
ICU3	450	767	1322	2.49
ICU4	450	755	1224	3.55
ICU6	550	911	1360	2.89



Plate 6.1 Classic Brittle failure through shear surface development sample ICU1

The sample stress paths (Appendix A, Fig A17) demonstrate classic behaviour for overconsolidated clays during undrained shear (Craig, 1993). These are depicted as an initial increase in both deviator stress (q') and mean effective stress which produces a curved stress path until peak strength (peak q) is reached. Both p' and q then reduce (with generally a larger reduction of q) until the samples reaches a lower stress state. Once the lower stress is

reached the samples ICU1 and ICU 3 illustrate a decrease in p' and q whilst samples ICU4 and ICU6 increase p' and q . Sample ICU3 shows anomalous behaviour after peak strength suggesting a testing error occurred.

The results of the ICU tests have been used to determine the peak strength envelope (i.e. the maximum shear stress) based on the sample stress paths (Fig 6.9). The stress paths indicate clear variability in both peak and residual strength which demonstrates the heterogeneous nature of the Gault Clay being studied. In particular sample ICU2 shows lower peak strength characteristics when compared to the other samples. The overall failure envelope indicates a strong material with high cohesion.

The failure envelope has been studied further by including two additional tests from Carey (2002) on the stress path plot (Fig 6.10). Using these results suggest that the peak strength failure envelope could have a lower cohesion and indicates that sample ICU1 failed at an anomalously high deviator stress. The results again demonstrate the heterogeneous nature of the Gault Clay.

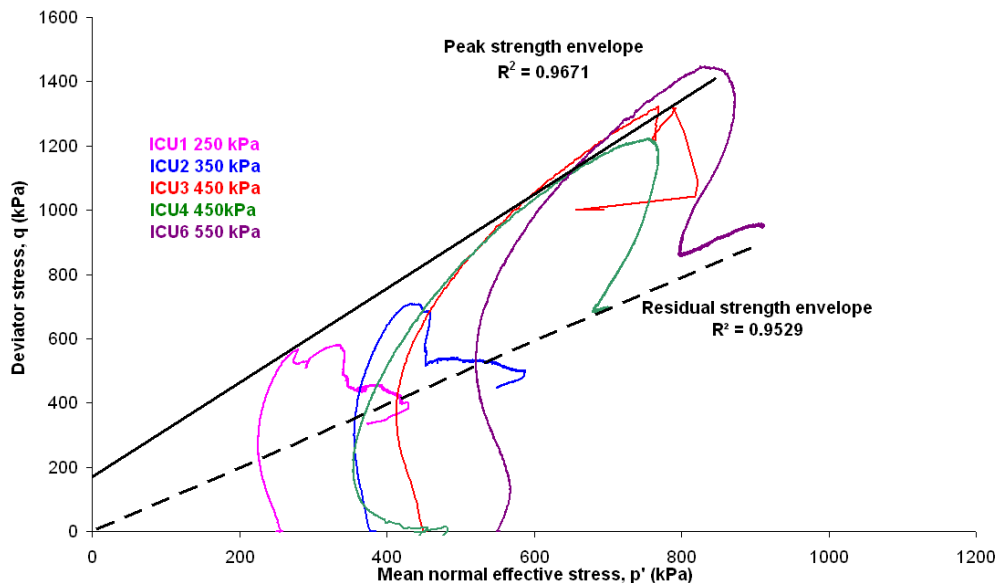


Figure 6.9 Peak and residual strength envelope, undrained triaxial cell testing

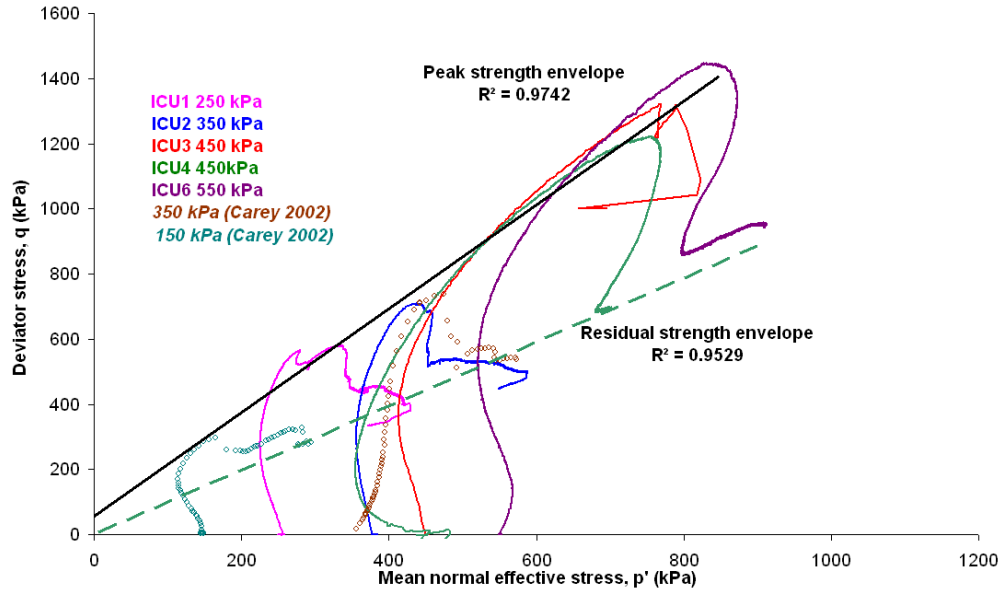


Figure 6.10 Peak and residual strength envelope, undrained triaxial cell testing (including results from Carey, 2002)

The peak and residual strength envelopes have also been calculated using standard Mohr's Circle technique (Head, 1998). Using this method a peak ϕ' value for the Gault of 35.13° and c' of 46.80 kPa is determined (Fig 6.11) and a residual ϕ' value of 26.60° and a c' of 0 kPa (Fig 6.12). The Mohr circles constructed do not plot consistently. Again this illustrates the variation in sample strengths and provides further evidence of the heterogeneity of the Gault Clay.

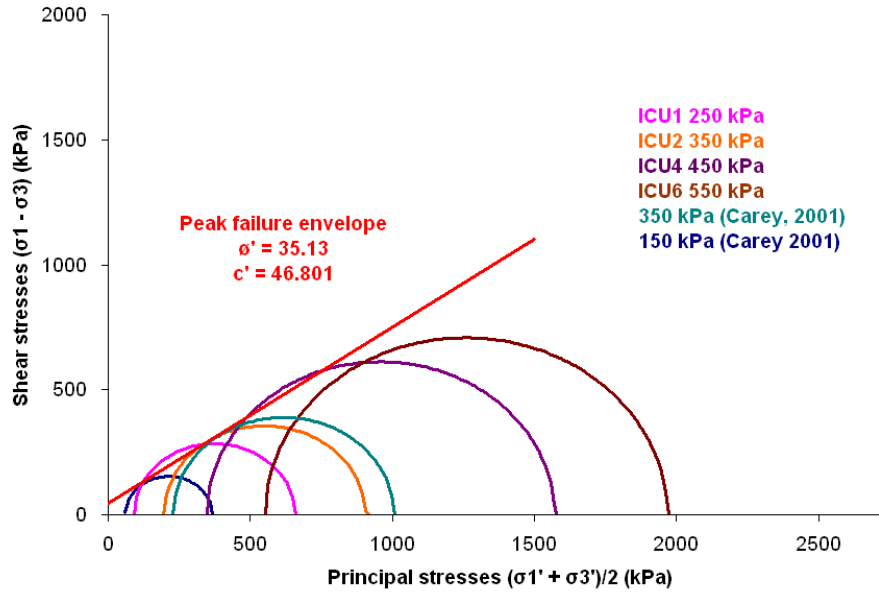


Figure 6.11 Construction of the peak strength failure envelope for ICU tests using the Mohr Coulomb approach

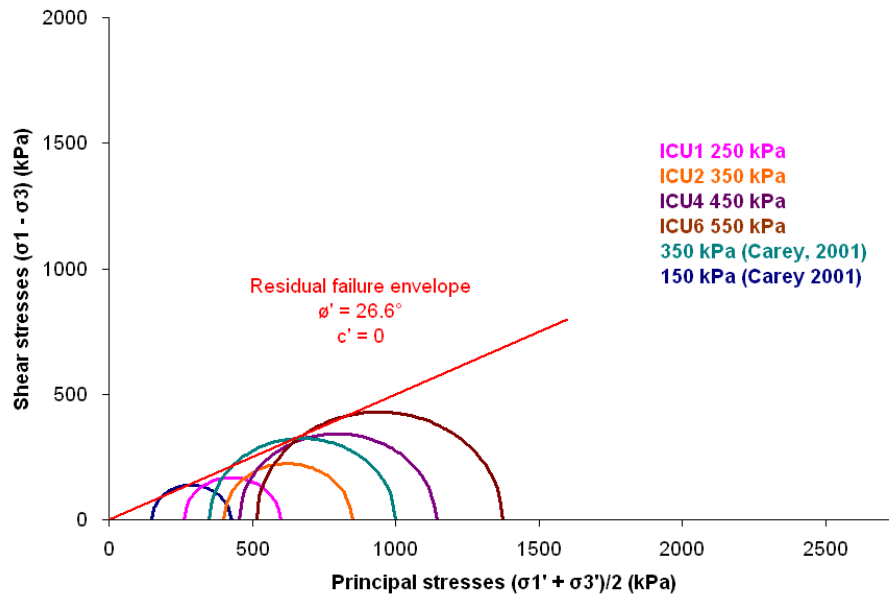


Figure 6.12 Construction of the residual strength failure envelope for ICU tests using the Mohr Coulomb approach

These residual strength characteristics have been compared with previous shear strength parameters calculated for the Gault Clay (Table 6.9). The results indicate higher ϕ'_r values than suggested by a series of ring shear tests undertaken in the previous Halcrow investigation (Halcrow, 2006). This

previous study suggests the residual strength of the Gault ranges from 4.9° to 22.7°. The results generally indicated higher ϕ'_r values in the upper and lower Gault and lower ϕ'_r values in the middle Gault. These ϕ'_r parameters are higher than a range of between 7.5° and 20° suggested for the St Catherine's Point landslide (Hutchinson *et al.*, 1991). Residual strength parameters determined using the ring shear apparatus are generally slightly lower than those determined using shear box apparatus or those which operate in landslides calculated by back-analysis (Hutchinson *et al.*, 1991). Skempton (1985) observed that back analysis of slopes, in which failure had occurred, yielded residual strengths that were within the limits of variation of shear box tests, and these were some 1 to 2° higher than those from ring shear tests. In tests on London Clay and Upper Lias Clay, Chandler and Skempton (1974) noted larger differences of the order of 5 to 6°. The results therefore indicate that the residual strength parameters determined during this study are similar to those previously presented.

Table 6.9 Comparison of residual strength values proposed for the Gault Clay

Source	Material type	Type	c_r (kPa)	ϕ'_r (°)
Halcrow (2006)	Upper Gault	Ring shear	0	16.5
Halcrow (2006)	Middle Gault	Ring shear	0	9.0
Halcrow (2006)	Lower Gault	Ring shear	0	15.0
Hutchinson <i>et al.</i> (1991)	Gault – St Catherine's landslide	Shear box	0	7.5-20.0
Current data	Base of Gault	ICU	0	26.6

The failure envelope of the Gault-Carstone transition material has been studied in direct shear using the back pressured shear box. In these tests intact samples were tested to determine peak strength and then, following failure, were subjected to a series of reversals along the existing plane to establish residual strength characteristics of the materials. The tests are referred to as cut plane shear box (CPSB) tests.

During the initial shear phase of the CPSB tests, the Gault-Carstone samples demonstrated an initial period of increasing shear stress with minimal change in horizontal displacement (Appendix A, Fig A18) until between 1.5 mm to 2.0 mm horizontal displacement was achieved. Following this point horizontal displacement continued with minor changes in shear stress.

Analysis of percentage vertical strain during the initial shear phase (Appendix A, Fig A19) demonstrated that samples CPSB2 and CPSB3 were subject to increased vertical strain with horizontal displacement whilst sample BPSB1 showed an initial increase in vertical strain followed by a prolonged period of decreasing vertical strain. These results therefore suggest that sample CPSB1 underwent dilation (increasing void ratio) whilst samples CPSB2 and CPSB3 underwent contraction (decreasing in void ratio).

The results of the CPSB tests have been used to construct the peak and residual failure envelope for the Gault-Carstone transition material. The peak and residual strength results from sample CPSB2 were significantly lower than observed in the other tests (Fig 6.13), which may indicate that this was a sample with possible pre-existing shears.

The failure envelope has therefore been constructed using the results from samples CPSB1 and CPSB3. These results indicate a peak strength ϕ' of 31.0° and c' of 102.7 kPa and a residual strength ϕ' of 33.5° and c' of 0 kPa (Fig 6.14). The strength characteristics are indicative of an over-consolidated material and reflect similar characteristics to the intact Carstone, which is located immediately beneath in the landslide shear surface identified in section 5.2.1.

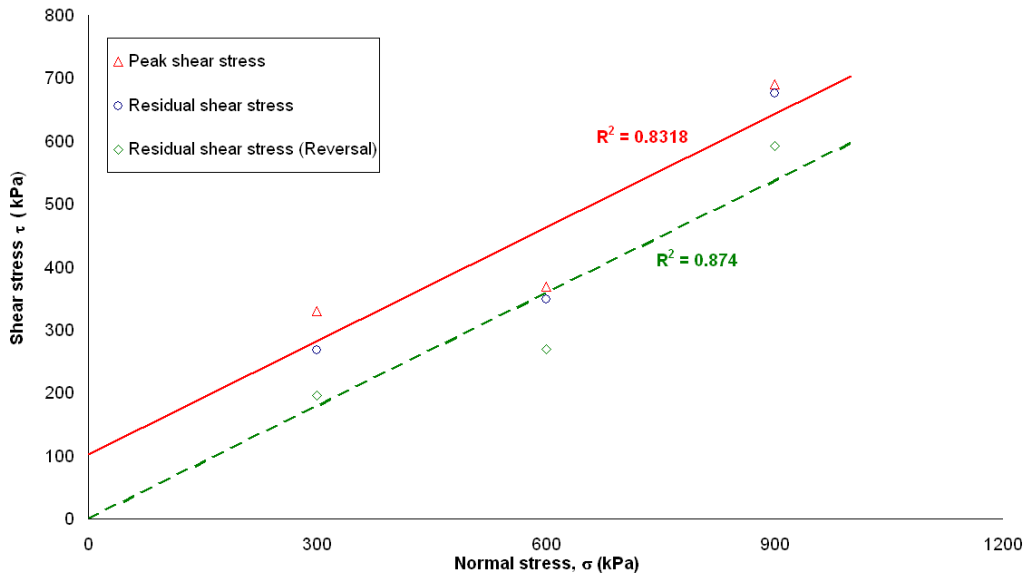


Figure 6.13 Peak and residual shear stress against normal stress using all CPSB tests on the Gault/ Carstone transition zone material

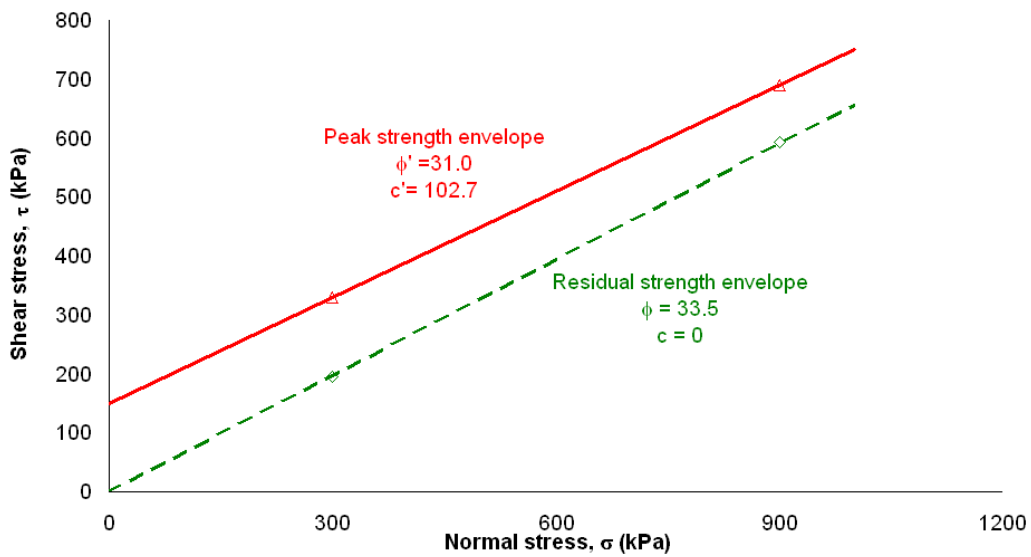


Figure 6.14 Construction of the peak and residual strength envelope failure envelope, Gault/ Carstone transition material

6.4 Specialist Pore pressure reflation (PPR) testing

A series of isotropically-consolidated drained pore pressure reflation (PPR) tests were undertaken on Gault Clay samples to investigate the mechanism shear surface development under varying mean effective stress scenarios. A series of PPR tests have been undertaken along various stress paths and under different PPR scenarios (Fig 6.15). These test conditions have been developed to study the following research questions:

1. Can PPR testing be used to construct a failure envelope, and how does this compare to the standard undrained failure envelope in the triaxial cell?
2. How does the consolidation history of the shear surface materials affect the development of the shear surface to failure?
3. How does the rate of pore pressure reflation affect the development of the shear surface to failure?
4. How does the behaviour during different porewater pressure scenarios behave when at residual strength?
5. Is the nature of shear surface development different in the Gault Carstone transition material and can this be compared to the Gault Clay in direct shear using the Back pressured shear box.

Each research question is presented separately and, in each case, has been sub-divided into two sections associated with the key stages of the test procedure. These are:

- stress path results associated with drained initial shear phase, which following consolidation, brought the samples to a pre-defined stress state below the defined failure envelope prior to reflation testing; and
- stress path test results and displacement behaviour to failure during pore pressure reflation phase, where samples passed through the failure envelope by reducing the mean effective stress. This was achieved by maintaining a constant deviator stress whilst linearly increasing pore pressure in the sample at different rates.

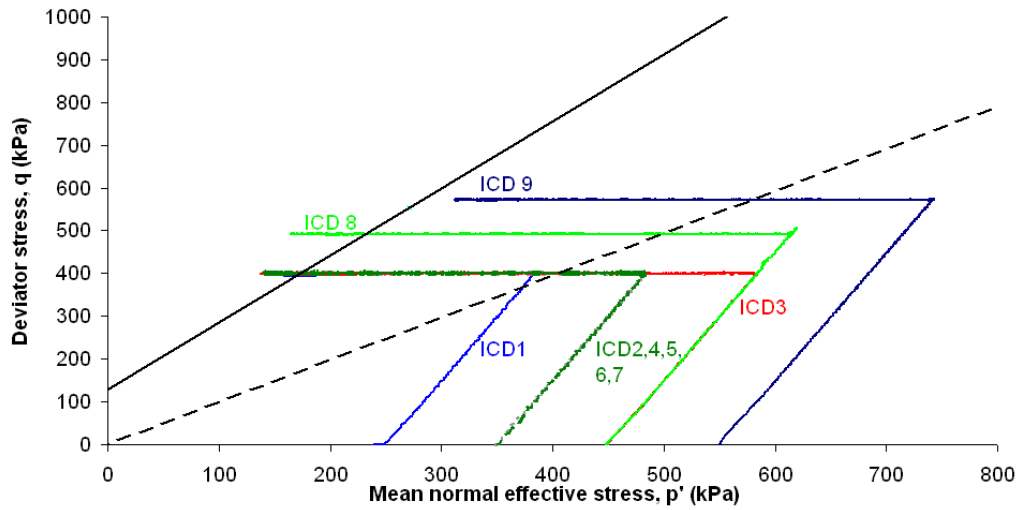


Figure 6.15 ICD stress path testing programme

6.4.1 Can PPR testing be used to construct a failure envelope, and how does this compare to the standard undrained failure envelope in the triaxial cell?

The suitability of PPR testing as a method for calculating the material failure envelope has been studied using three PPR ICD tests (ICD4, ICD8 and ICD9). In these tests the displacement to failure was measured at three constant deviator stresses ($q = 400, 500$ and 550 kPa) following consolidated at three different mean effective stresses ($p' = 350, 450$ and 550 kPa) at a linear pore pressure reinflation rate of 10 kPa/ hr (Fig 6.16).

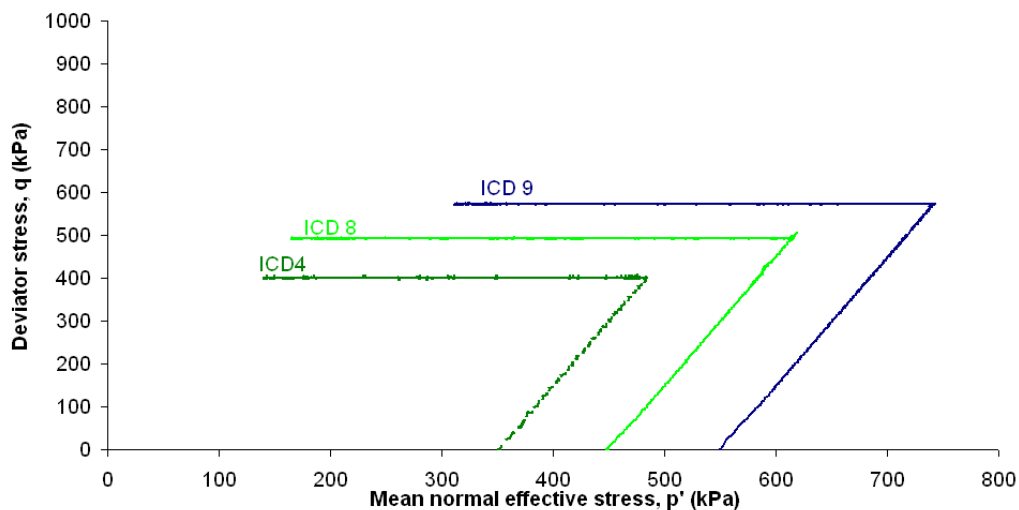


Figure 6.16 ICD PPR stress paths at constant deviator stress $400, 500$ and 550 kPa from effective stresses $350, 450$ and 550 kPa

6.4.1.1 Sustained initial shear stage

All three tests separate demonstrated consistent linear drained stress paths to different deviator stresses (Appendix A, Fig A20). Samples ICD4 and ICD8 consolidated at lower mean effective stresses reached higher axial strains of 0.8% at the same deviator stress (Appendix A, Fig A21) although ultimately higher strains of above 1.2% were achieved in samples ICD8 and ICD9 resulting from the initial drained shear being sustained to 500 kPa and 550 kPa respectively. Sample ICD8 showed anomalous behaviour between 0.6% and 1.0% axial strain as the sample continued to strain at constant deviator stress. Following this deviator stress increased again toward the end of the shear stage. Similar behaviour is evident when volumetric strain is plotted against axial strain (Appendix A, Fig A22). The axial strain in sample ICD8 increased at lower volumetric strains than ICD4 and ICD9, which demonstrated consistent behaviour to 0.8% strain. It is anticipated that the variation in behaviour in sample ICD8 is likely to be associated with a reduction in axial strain which would have had minimal impact on the overall performance of the test.

6.4.1.2 Pore pressure reinflation

The relationship between displacement rate and p' along the three separate drained stress paths during the PPR stage (Fig 6.17) indicates that samples ICD4 and ICD8 progressed through a period of fluctuating displacement rates at during the early stages of deformation where displacement rates were below (>0.001 mm/min). Following this a period of steadily increasing displacement rate was experienced in both samples before hyperbolic acceleration started to develop at 0.001 mm/min. Sample ICD9 shows different behaviour with an initial period of increasing displacement rate to 0.0001 mm/min followed by a period of linearly increasing displacement rate to 0.01 mm/min. Final acceleration to failure occurred as an exponential increase in displacement rate at a relative high displacement rate of 0.01 mm/min in comparison to ICD4 and ICD8.

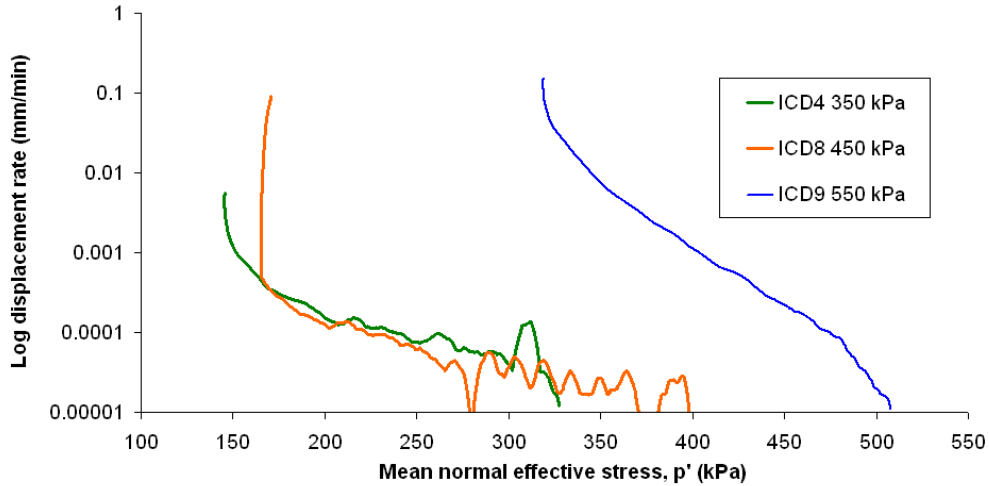


Figure 6.17 Displacement rate against p' , at constant q of 400, 500 and 550 kPa, samples ICD4, ICD8 and ICD9

The different behaviour observed in these samples is illustrated further by viewing the PPR stage in $1/v - p'$ space (Fig 6.18). Samples ICD4 and ICD8 clearly show a period of fluctuation $1/v - p'$ at mean effective stresses followed by a linear trend to failure. Conversely sample ICD9 shows a clear asymptotic trend from a much higher mean effective stress of 480 kPa to failure at 350 kPa. Regression analysis (Fig 6.19) of the final stages to failure in all sample illustrates the statistical significance of the linear trend in samples IC4 and ICD8 and the asymptotic trend in samples ICD9

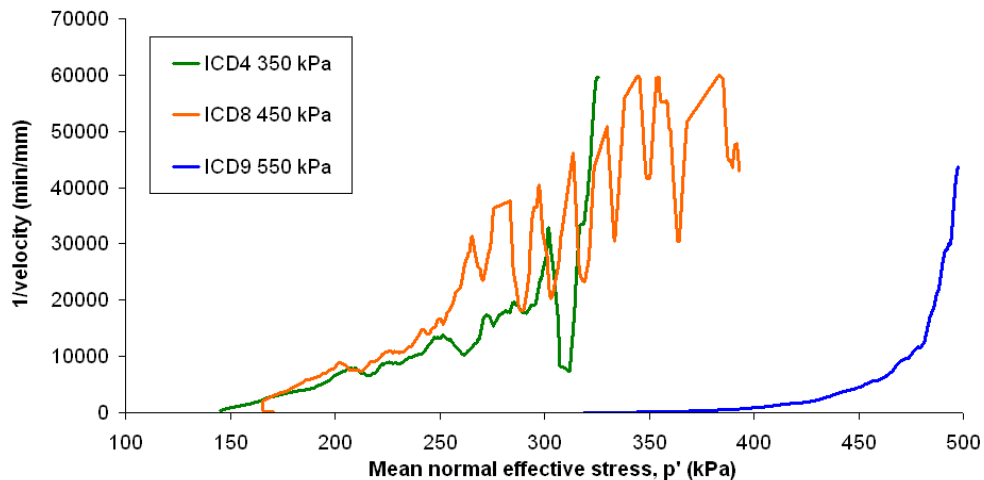


Figure 6.18 $1/v$ against p' at constant q of 400, 500 and 550 kPa, samples ICD4, ICD8 and ICD9

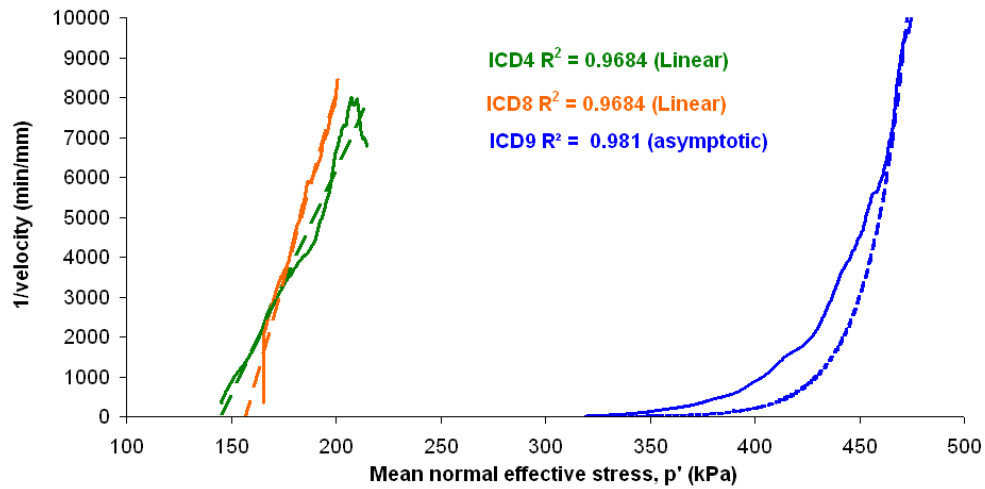


Figure 6.19 Regression analysis of displacement to failure in $1/v - p'$ at constant q of 400, 500 and 550 kPa, samples ICD4, ICD8 and ICD9

Time to failure analysis of these three samples indicates that sample ICD4 failed later than sample ICD8 despite being subjected to both a higher initial mean effective stress ($p' = 550$ kPa). Similarly the $1/v - t$ against time graph (Fig 6.20) demonstrates that acceleration to failure occurs earlier in sample ICD9 when compared with ICD8, which was undertaken along at $q = 550$ kPa (Fig 6.21). The $1/v - t$ space plots indicate that sample ICD9 is either a significantly weaker Gault sample or potentially that the sample failure is ductile at higher confining pressures as has been observed in other mudrocks at high stresses (Petley, 1999).

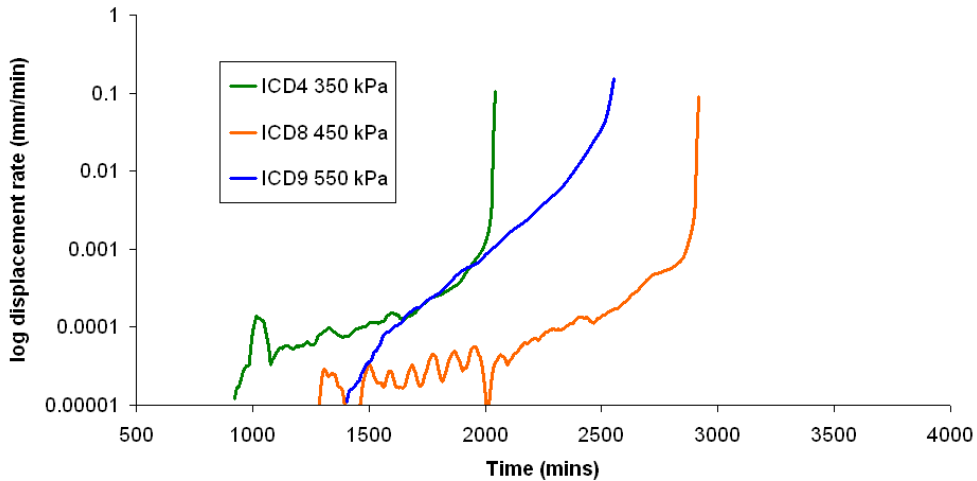


Figure 6.20 Displacement rate against time at constant q of 400, 500 and 550 kPa, samples ICD4, ICD8 and ICD9

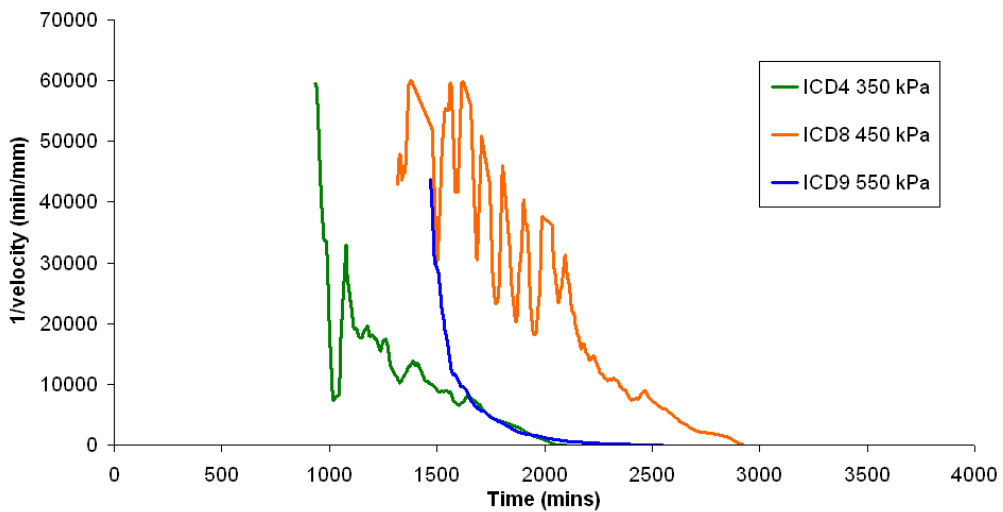


Figure 6.21 $1/v - t$ at constant q of 400, 500 and 550 kPa, samples ICD4, ICD8 and ICD9

Sample volume change data illustrates that in all three samples volume increase through time as porewater pressures are inflated (Fig 6.22). This illustrates that all three samples dilated during the test as failure developed. This is a clear indication that sample ICD9 is likely to be a weaker sample as shear surface contraction would be expected during ductile failure at high mean effective stresses.

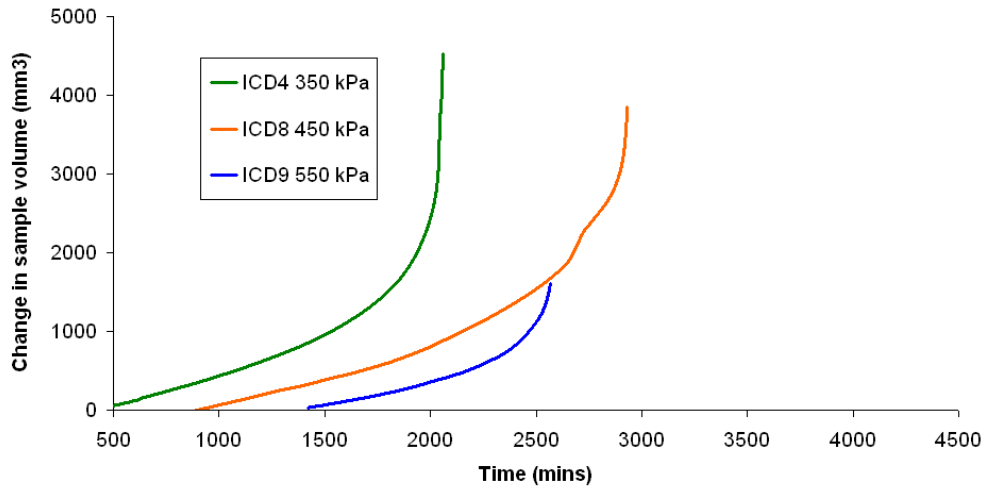


Figure 6.22 Change in sample volume through time at constant q of 400, 500 and 550 kPa, samples ICD4, ICD8 and ICD9

The results of these three tests have been compared with ICU failure envelope presented in section 6.3.3. The ICU failure envelope is believed to be representative of the stress states in the PPR testing as undrained testing allows pore pressure generation in the sample during failure unlike standard drained testing where pore pressures are able to dissipate. Similarly in the PPR testing whilst the test is drained the continually increasing porewater pressures in the sample are anticipated to generate similar conditions as would be observed in an undrained test. At present there is no specification for determining the failure envelope in brittle materials at constant deviator stress. Hence failure has been determined at a specific displacement rate of 0.1 mm/min at which point failure is developing in all three samples

Comparison of the PPR results with the ICU failure envelope indicate that failure in the PPR testing occurred at lower mean effective stresses in samples ICD8 and ICD4 and at a similar mean effective stress in sample ICD9 (Fig 6.23). This result may indicate that the samples tested in the PPR testing were naturally stronger than the ICU samples. Given the ductile nature of failure in sample ICD9, which occurs close to the brittle failure envelope, this is likely to be the case.

When the failure conditions are considered with the ICU failure envelope excluding previous Gault testing undertaken in 2002 during the ICD PPR samples fail either at or close to the previously defined failure envelope, with the exception of sample ICD8 (Fig 6.24). The results of this analysis indicate clear variability in the samples strengths of the Gault Clay. Clearly, however, the results suggest failure of the weaker ICD9 test before the peak strength envelope and failure of sample ICD4 and ICD8 immediately after the peak strength envelope.

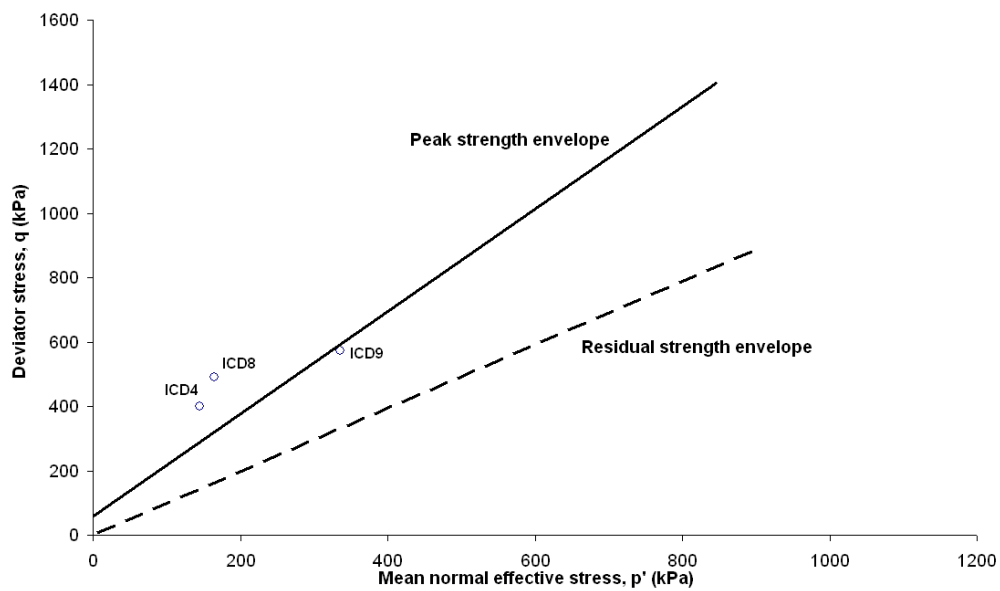


Figure 6.23 Comparison of p' at failure of PPR testing and the ICU failure envelope inclusive of Carey 2002 tests

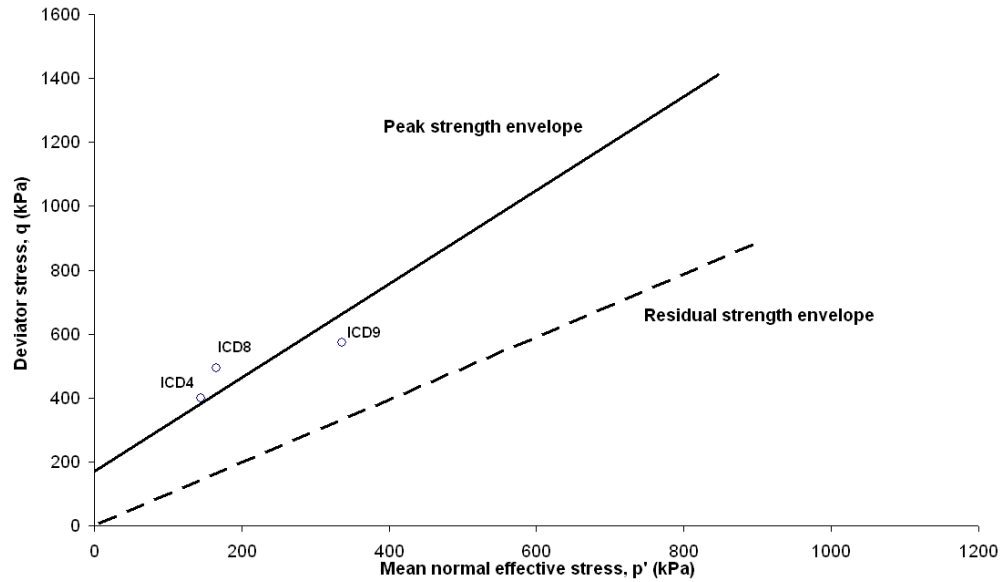


Figure 6.24 Comparison of p' at failure of PPR testing and the ICU failure envelope based on thesis results

Analysis of the failure envelope through the construction of Mohr circles (Fig 6.25) supports the variable strength observed throughout the testing. Using all three Mohr circles suggests failure envelope (a) with a lower ϕ' of 23.96° and significantly higher c' of 177 kPa than was observed in the ICU testing (section 6.3.3). The results however have indicated that sample ICD9 is a weaker sample and therefore may have failed close to residual strength and further indicates a higher ϕ' and c' values of 34.99° and 110 kPa respectively.

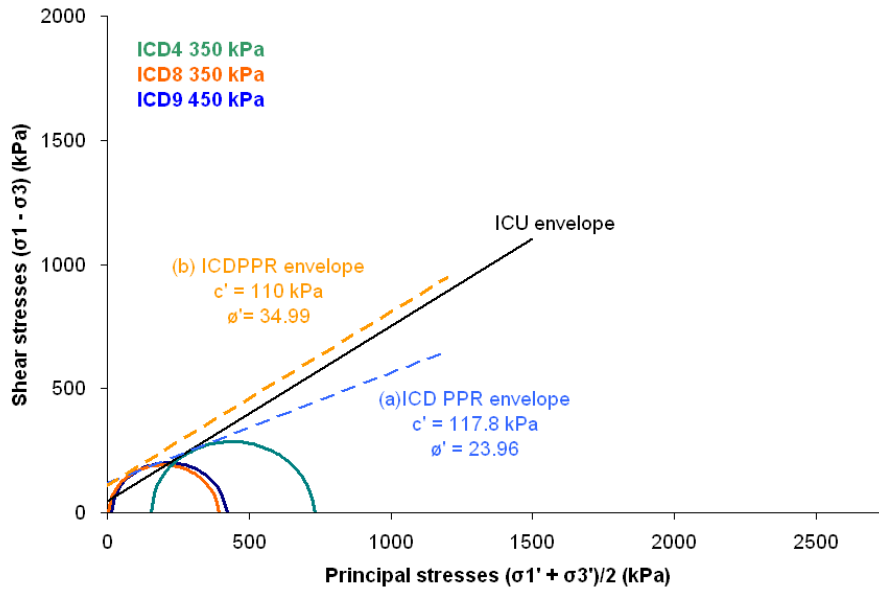


Figure 6.25 Comparison of the ICD PPR and ICU peak failure envelope constructed from samples ICD4, ICD8 and ICD9 and PPR rate = 10 kPa/hr

6.4.2 How does the consolidation history of the shear surface materials affect the development of the shear surface to failure?

To study the implications of the consolidation history of the shear surface materials a series of tests were conducted at constant deviator stress ($q = 400$ kPa) at a linear pore pressure reinflation rate of 10 kPa/hr following consolidation to three different mean effective stresses ($p' = 250, 350, 450,$ kPa) (Fig 6.26).

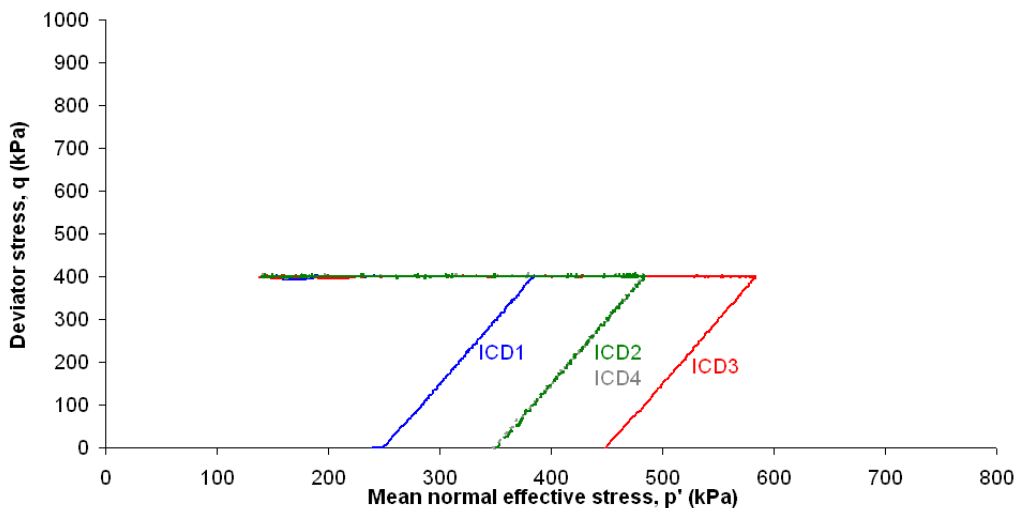


Figure 6.26 ICDPPR stress paths at constant deviator stress 400 kPa from effective stresses 350, 450 and 550 kPa

6.4.2.1 Sustained initial shear stage

The initial drained shear phase for samples ICD1, ICD2, ICD3 and ICD4 show linear drained stress paths to $q = 400$ kPa (Appendix A, Fig A23). Each sample underwent an initial phase of increasing deviator stress at low axial strain (Appendix A, Fig A24). At approximately 0.2% strain however a linear relationship in deviator stress and axial strain was observed in all tests with samples undertaken at lower initial confining pressure reaching higher axial strains. There is a notable variation in the axial strains observed in samples ICD2 and ICD4 which reached 0.8% to 1.2% axial strain respectively. This is likely to represent variability in strength of the samples. Vertical strains (Appendix A, Fig A25) demonstrate that greater changes in vertical strain are associated with ICD3 (initial $p' = 450$ kPa) in comparison to ICD1 (initial $p' = 250$ kPa).

6.4.2.2 Pore pressure re-inflation

A consistent pattern of displacement rate to failure is observed in all four tests (Fig 6.27). The results demonstrate that each test was subject to an initial period of fluctuation displacement rates to about 0.0001 mm/min. A period of steadily increasing displacement rates is then observed between 0.001mm/min and 0.001 mm/min before hyperbolic accelerations in displacement are observed. With the exception of sample ICD2 the results demonstrate that higher displacement rates can be observed at higher mean effective stresses in samples subject to lower mean effective stresses during consolidation which indicates that increased sample stiffness increases the pore pressure required to promote the initiation of failure.

Despite the different consolidation histories of each sample a hyperbolic acceleration to failure in displacement rate appears to occur in all tests at very similar mean effective stresses of $p' = 138$ to 145 kPa. This indicates that whilst stiffness modifies the pre-failure behaviour of the shear surface, the p' at failure is only marginally affected as can be shown in the variability of p' values at failure in samples ICD2 and ICD4.

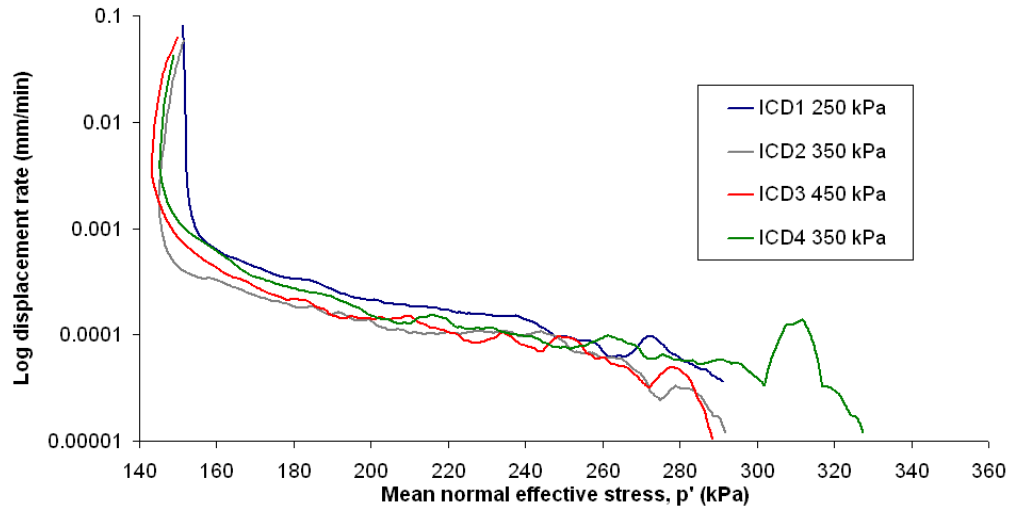


Figure 6.27 Displacement rate against p' , at constant q of 400 kPa, samples ICD1, ICD2, ICD3 and ICD4

Analysis of these results in $1/v - p'$ space (Figure 6.28) illustrates that all samples show consistent behaviour to failure. This comprises a clear rapid decrease and subsequent recovery in $1/v$ as the mean effective stresses continue to decrease followed by a period of fluctuation (saw-tooth pattern) $1/v$ values prior to the development of a negative linear trend to failure. Regression analysis of the final period of the test clearly demonstrates a statistically significant linear trend in all samples which develops from $p' = 240$ to 210 kPa (Fig 6.29). Again minor differences in the steepness of the curve are observed in samples ICD1, ICD4 and ICD3, which suggest that the linear trend may steepen with increasing sample stiffness. This would indicate that samples subject to greater initial mean effective stresses would be subject to more rapid failures. Again the initial consolidation phase appear to have only a limited impact on this as demonstrated by the variability of behaviour in samples ICD4 and ICD2

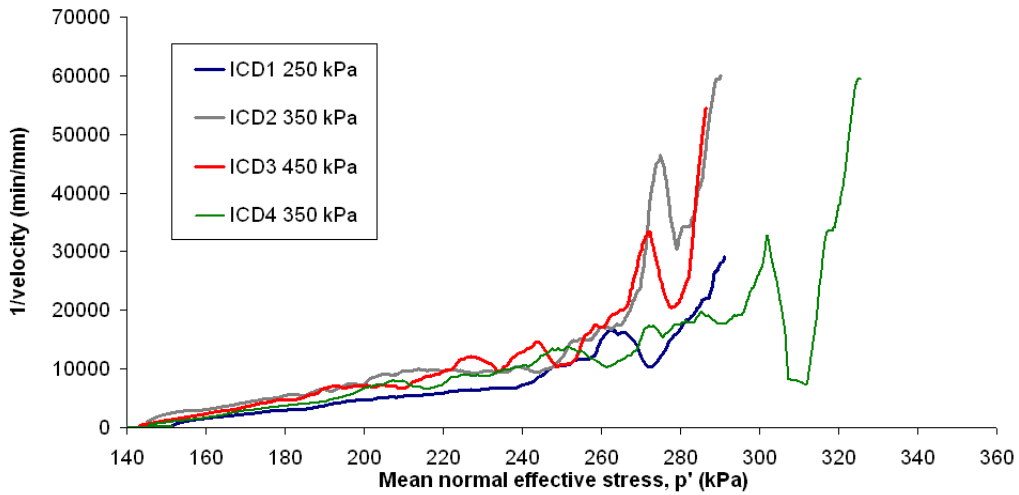


Figure 6.28 1/ velocity against p' at constant q of 400kPa, samples ICD1, ICD2, ICD3 and ICD4

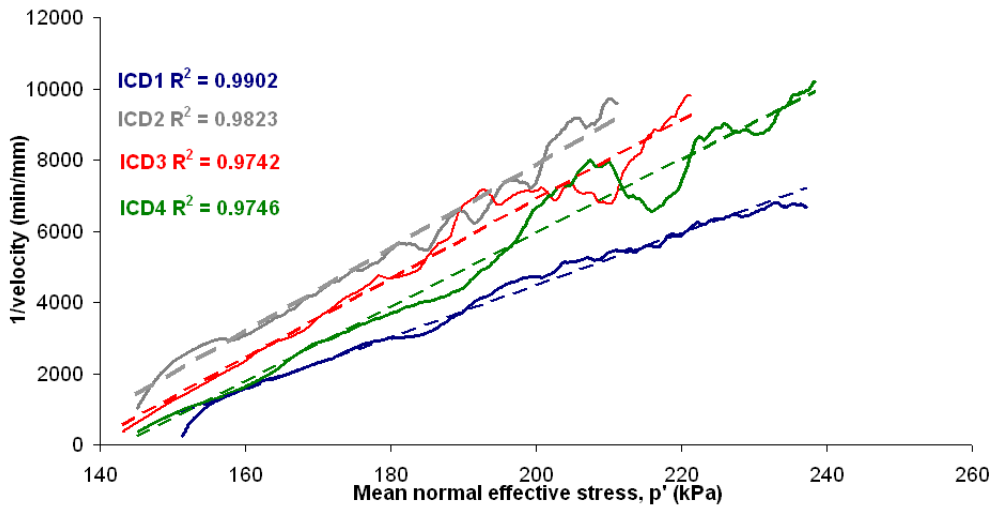


Figure 6.29 Regression analysis of displacement to failure in $1/v - p'$ at constant q of 400 kPa, samples ICD1, ICD2, ICD3 and ICD4

Analysis of the time to failure characteristics of these tests illustrates that samples consolidated at higher p' failed later than those subject to lower p' during consolidation (Fig 6.30). This is logical given that samples tested from higher initial p' start PPR further from the failure envelope. This is demonstrated more clearly in the $1/v - t$ space which the negative linear trend

to failure develops later for samples consolidated to a higher initial p' (Fig 6.31).

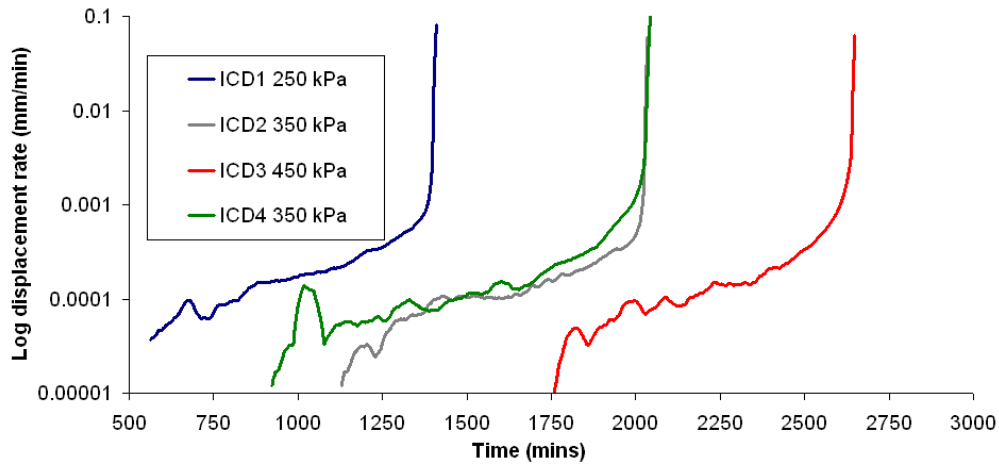


Figure 6.30 Displacement rate against time at constant q of 400 kPa, samples ICD1, ICD2, ICD3 and ICD4

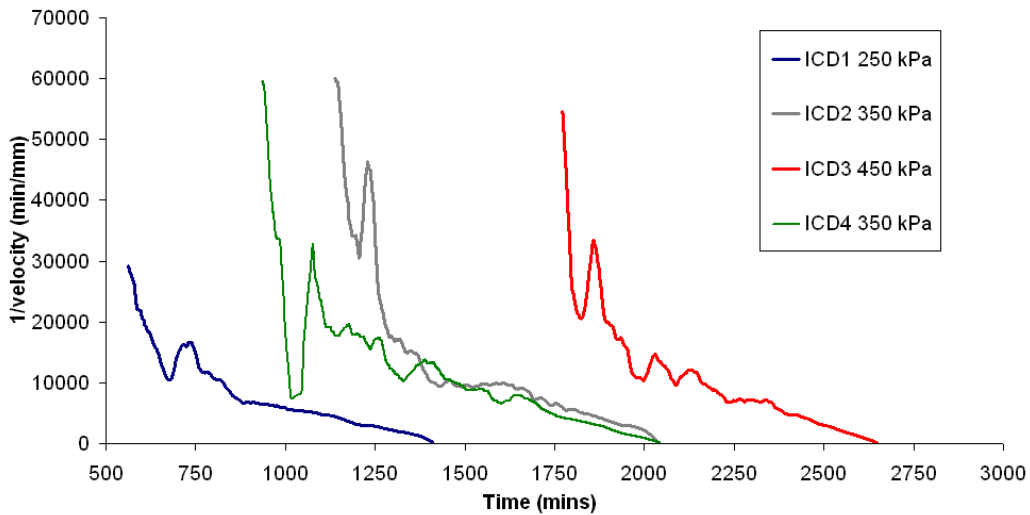


Figure 6.31 $1/v - t$ at constant q of 400 kPa, samples ICD1, ICD2, ICD3 and ICD4

Analysis of the change in sample volume during the PPR stage shows consistent increasing volume to failure in each sample (Fig 6.32). This provides clear evidence that the linear trend occurs as a result of dilation of the shear surface consistent with brittle shear surface development (Petley *et al.*, 2005a).

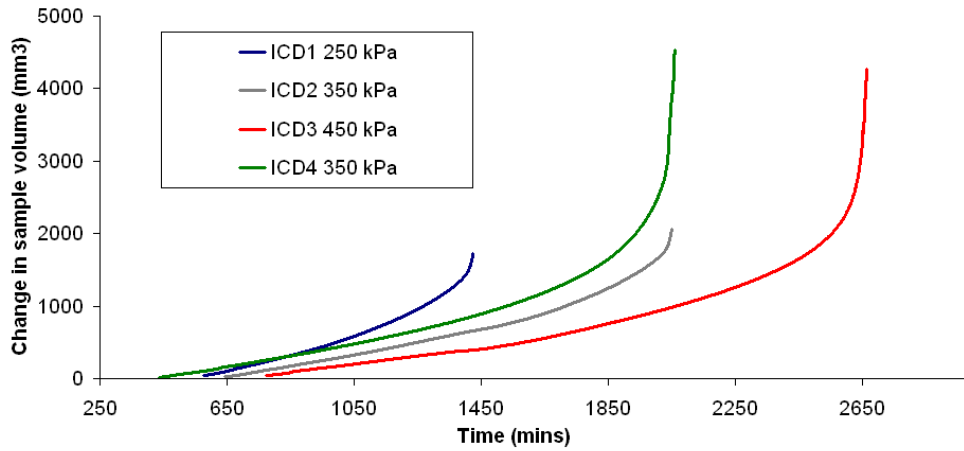


Figure 6.32 Change in sample volume through time at constant q of 400 kPa, samples ICD1, ICD2, ICD3 and ICD4

6.4.3 How does the rate of pore pressure reinflation affect the development of the shear surface to failure?

To study the impact of the rate of pore pressure reinflation three tests were conducted where displacement to failure was generated at constant deviator stress ($q = 400$ kPa) using three different linear pore pressure reinflation rates (5, 10, 18 kPa/hr) following consolidation at standard initial confining pressure ($p' = 350$ kPa) (Fig 6.33).

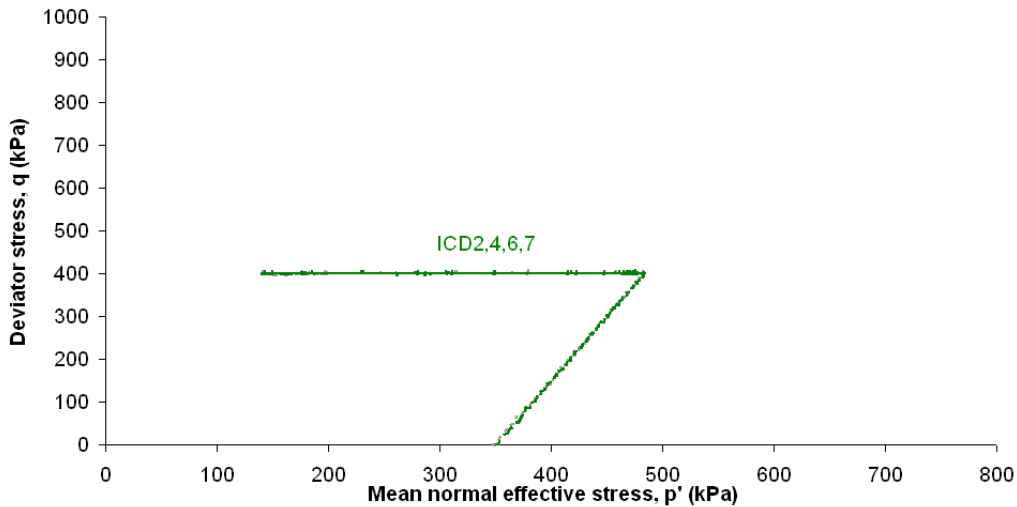


Figure 6.33 ICDPPR stress paths at PPR rates of 5, 10, 18 kPa/hr at constant q of 400 kPa from initial p' of 350kPa

6.4.3.1 Sustained initial shear

The drained stress paths during the initial drained shear phase for ICD samples tests from an initial confining mean effective stress of 350 kPa demonstrated a straight line consistent with the early phase of a standard drained shear to the pre-determined deviator stress ($q = 400$ kPa) (Appendix A, Fig A26). Axial strains during this period of initial drained shear range between 0.8 and 1% (Appendix A, Fig A27). During the initial phase of shear axial and volumetric strains were seen to increase with a general decrease in volumetric strain (Appendix A, Fig A28).

6.4.3.2 Pore pressure reinflation

The acceleration of sample deformation to failure in relation to the pore pressure condition has been analysed by plotting the test results in $1/v - p'$ space (Fig 6.34). The results illustrate a clear negative linear trend to final failure, which occurred at $p' = 140$ to 142 kPa in all samples. The tests illustrate a clear saw-tooth pattern in $1/v - p'$ to failure (Fig 6.35), which reduces toward failure ($p' = 200$ kPa). Analysis of the final period of linearity to failure (Fig 6.36) illustrates a statistically significant linear trend in each test. Interestingly the results illustrate a steepening of the linear trend with reducing mean effective stress. The results indicate that the rate of pore pressure reinflation had limited impact on the mean effective stress at which brittle failure was generated.

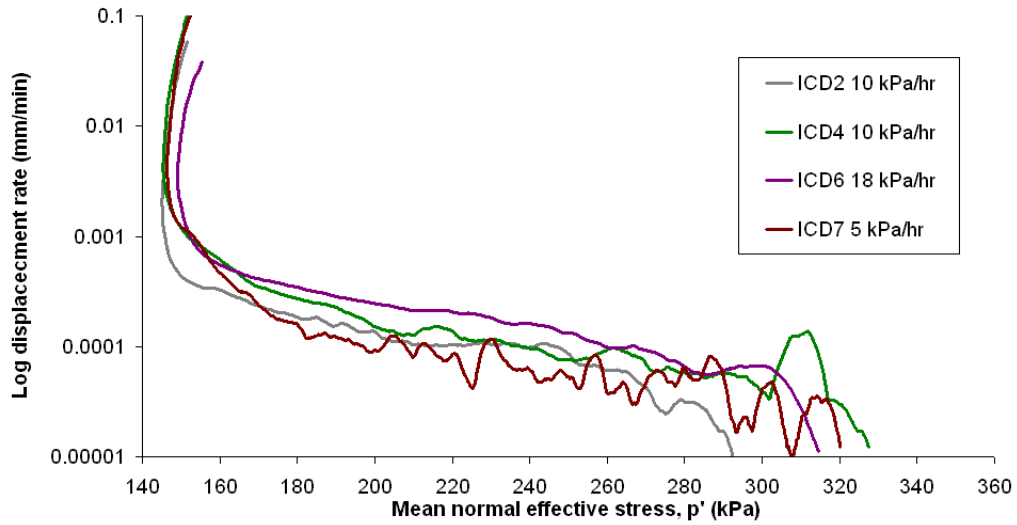


Figure 6.34 Displacement rate against p' , at constant q of 400 kPa, samples ICD21, ICD4, ICD6 and ICD7

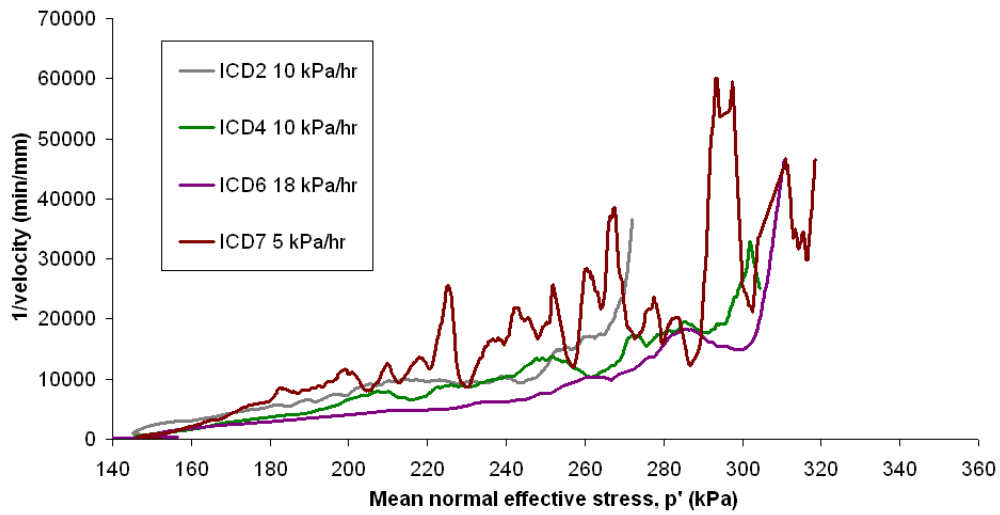


Figure 6.35 1/ velocity against p' at constant q of 400kPa, samples ICD2, ICD4, ICD6 and ICD7

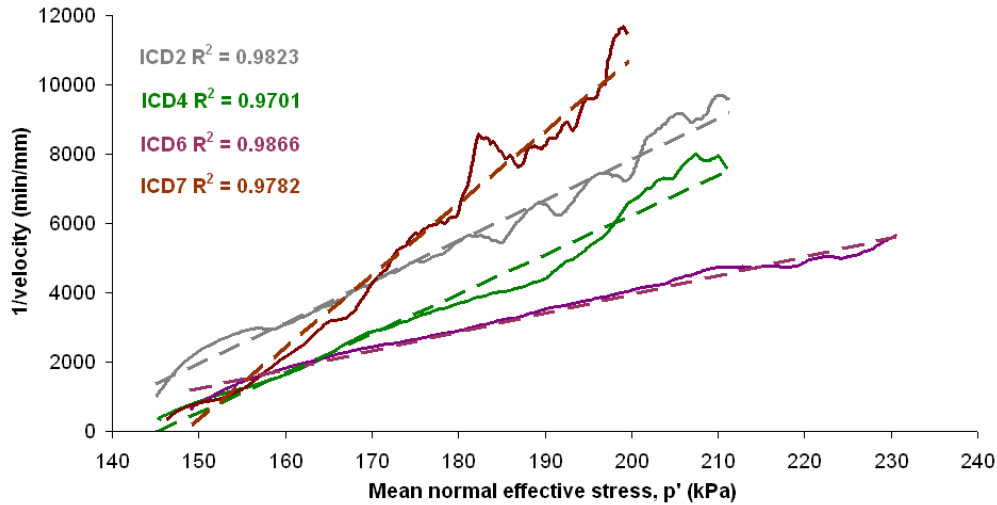


Figure 6.36 Regression analysis of displacement to failure in $1/v - p'$ at constant q of 400 kPa, samples ICD2, ICD4, ICD6 and ICD7

The rate of pore pressure reinflation also demonstrates impacts on the time of failure in samples tested under the same stress path conditions (Fig 6.37). The graph illustrates that failure in samples subject to slower rates of pore pressure reinflation occurred later, with the exception of the rapid pore pressure test, which does not demonstrate the same patterns of deformation to failure. The time to failure however was shown to have little to no impact on the development $1/v - t$ space relationship (Fig 6.38). Sample volume data suggests dilation to failure as was observed in the previous intact PPR testing on Gault Clay (Fig 6.39).

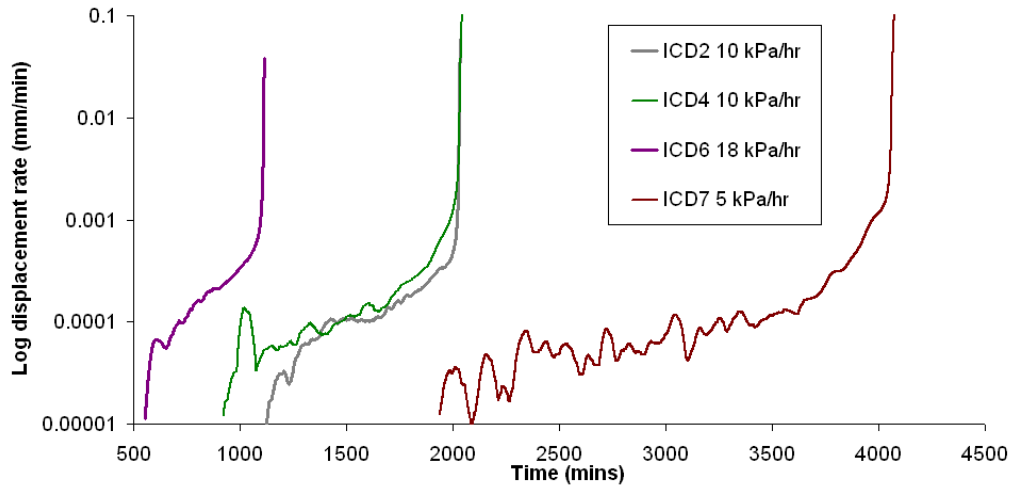


Figure 6.37 Displacement rate against time at constant q of 400 kPa, samples ICD2, ICD4, ICD6 and ICD7

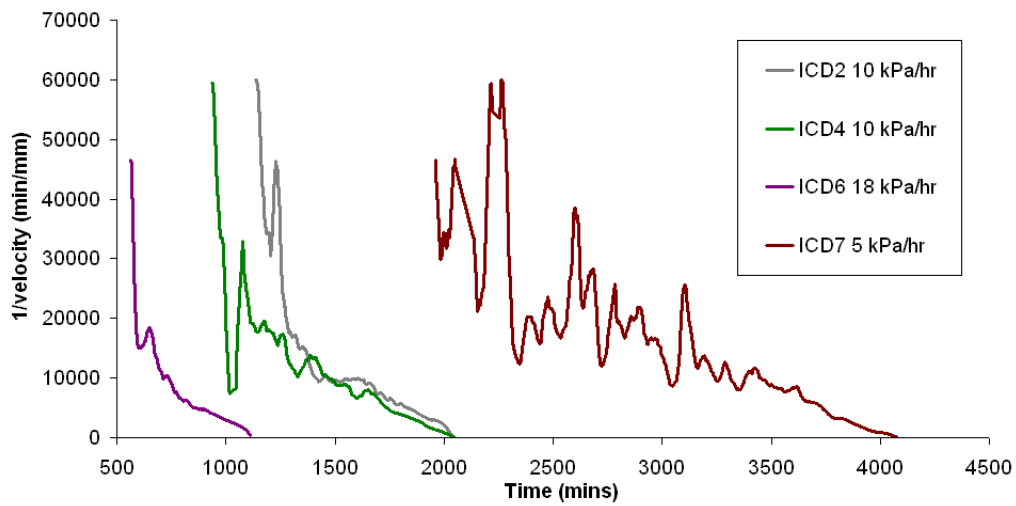


Figure 6.38 $1/v - t$ at constant q of 400 kPa, samples ICD2, ICD4, ICD6 and ICD7

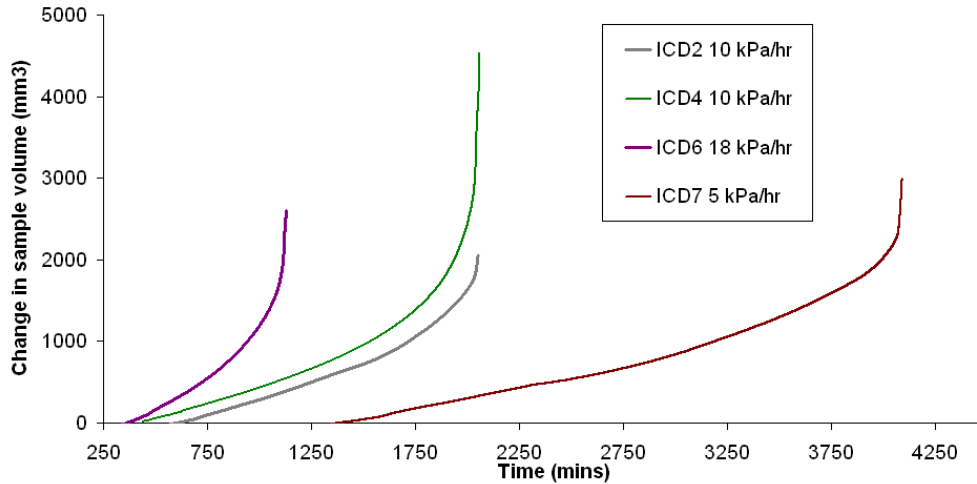


Figure 6.39 Change in sample volume through time at constant q of 400 kPa, samples ICD1, ICD2, ICD3 and ICD4

6.4.4 How does a material behaviour during different porewater pressure scenarios behave post-failure?

To study the potential implications of differential pore pressure reinflation rates on the displacement to failure of pre-failed soils a series of remoulded samples were studied under a series of PPR scenarios. Three remoulded samples were tested at constant stress ($q = 400$ kPa) using three different rates of pore pressure reinflation (5, 10, 18 kPa/ hr) following consolidation at a standard initial confining pressure ($p' = 350$ kPa) (Fig 6.40).

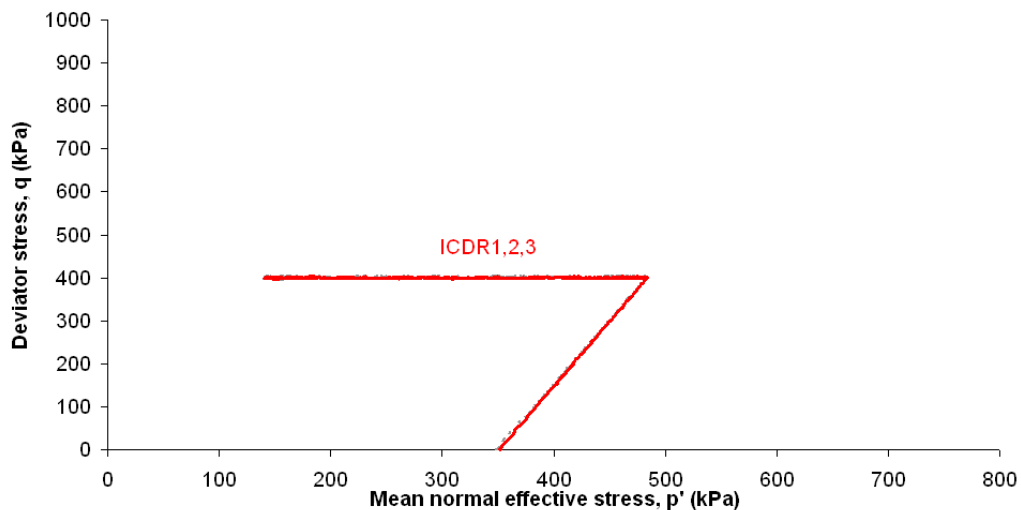


Figure 6.40 ICDPPR stress paths for remoulded samples at PPR rates of 5, 10, 18 kPa/hr at constant q of 400 kPa from initial p' of 350kPa

6.4.4.1 Sustained initial shear

The initial drained shear of ICD tests on remoulded samples revealed consistent linear stress paths (Appendix A, Fig A29). Axial strain rates during the initial drained shear phase are significantly higher (3.5% to 4%) than the intact samples (Appendix A, Fig A30). This characteristic is also mirrored in the volumetric strains of between 1.5% and 2% (Appendix A, Fig A31). The different volumetric strains observed during this phase in the remoulded samples suggest that there is some variability in the sample properties.

6.4.4.2 Pore pressure reinflation

Analysis of the PPR stage of the three remoulded tests illustrates an exponential increase in displacement rates to failure with reducing mean effective stress (Fig 6.41). Interestingly during the early stages of PPR when mean effective stresses are high the initial displacement rates are higher in samples subjected to higher pore pressure reinflation rates. This relationship is observed until $p' = 270$ kPa when displacement rates increase more rapidly in the samples subject to lower rates of PPR.

Analysis of this phase in $1/v - p'$ space (Fig 6.42) illustrates that failure occurs at a mean effective stress of 170 kPa, which indicates that the period of displacement measured after this p' is likely to relate to post failure movements in the sample. The $1/v - p'$ analysis indicates that samples progress to failure at the same mean effective stress. Regression analysis of these displacement rates demonstrates that in all cases a statistically significant asymptotic trend is observed (Fig 6.43) which is consistent with ductile deformation previously observed in both laboratory based testing (Ng and Petley, 2009) and in specific landslide systems such as the Tessina landslide (Petley *et al.*, 2005).

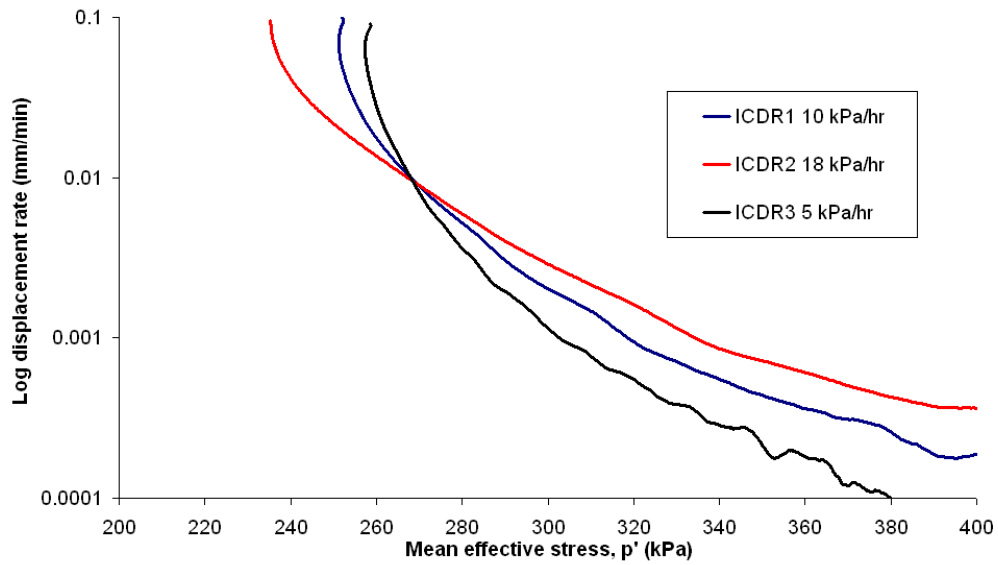


Figure 6.41 Displacement rate against p' , at constant q of 400 kPa, samples ICDR1, ICDR2 and ICDR3

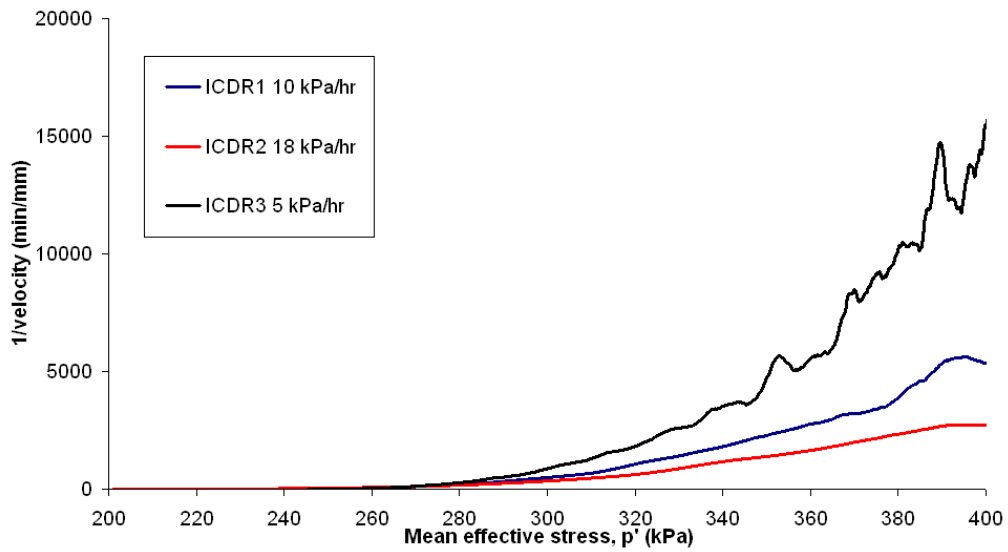


Figure 6.42 1/ velocity against p' at constant q of 400kPa, samples ICDR1, ICDR2 and ICDR3

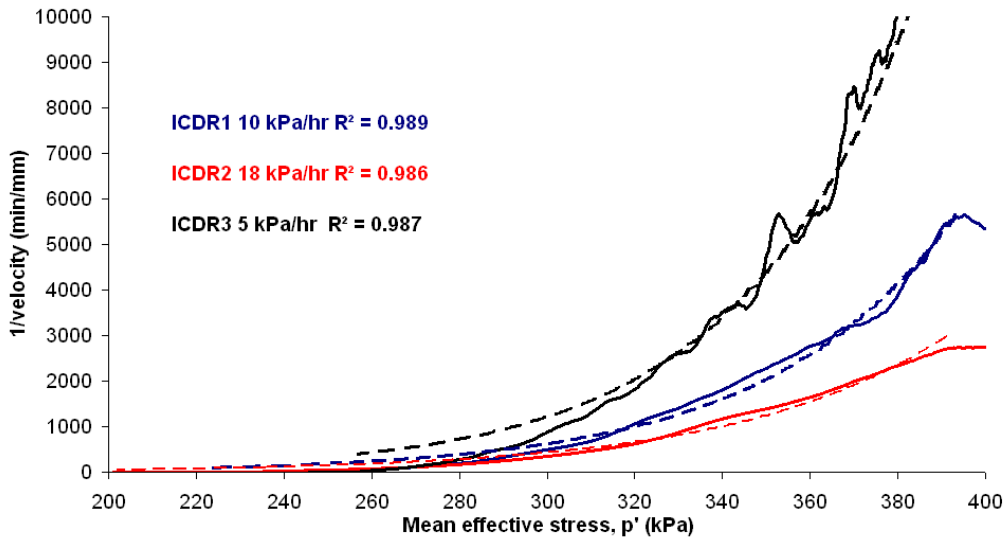


Figure 6.43 Regression analysis of displacement to failure in $1/v - p'$ at constant q of 400 kPa, samples ICDR1, ICDR2 and ICDR3

Remoulded samples tested show consistent time-dependent failure as the intact ICD samples (Fig 6.44). Analysis of these results in $1/v - t$ space (Fig 6.45) reveals a consistent asymptotic trend to failure as observed in ductile deformation (e.g. Ng, 2007).

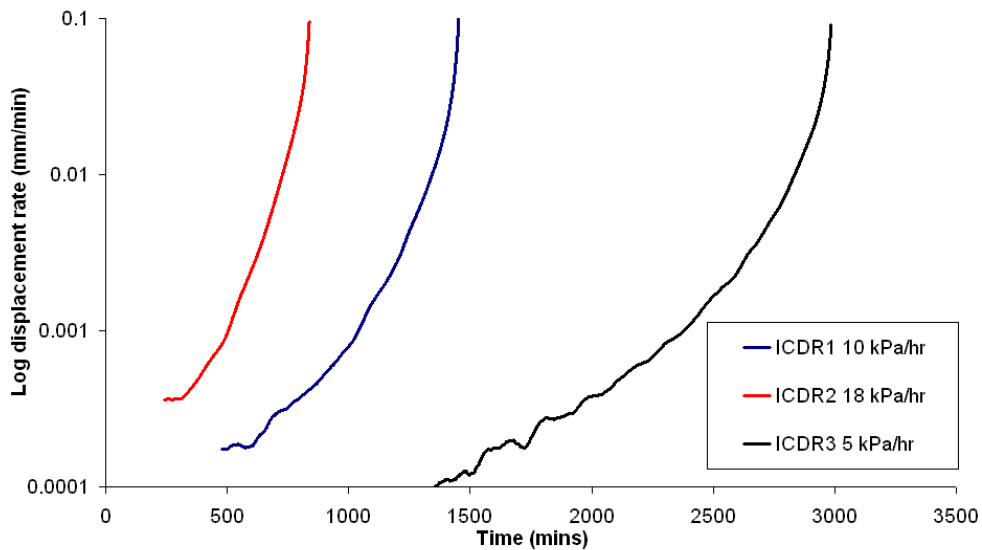


Figure 6.44 Displacement rate against time at constant q of 400 kPa, samples ICDR1, ICDR2 and ICDR3

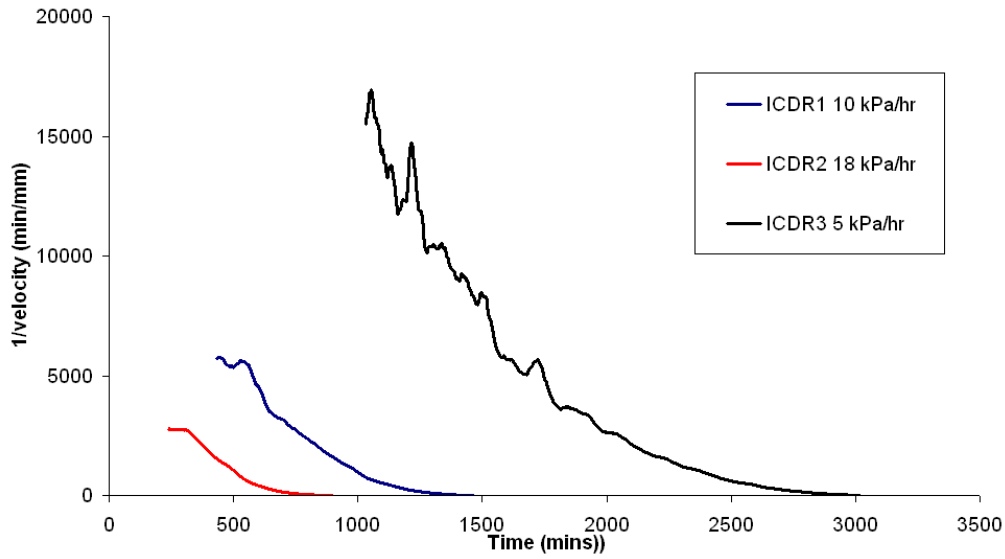


Figure 6.45 $1/v - t$ at constant q of 400 kPa, samples ICDR1, ICDR2 and ICDR3

Analysis of the change in sample volume (Fig 7.46) during these tests provides evidence of sample dilation to failure in all three tests. This result concurs with previous studies on non-cohesive soils in which ductile failure occurred through sample dilation (Ng and Petley, 2009).

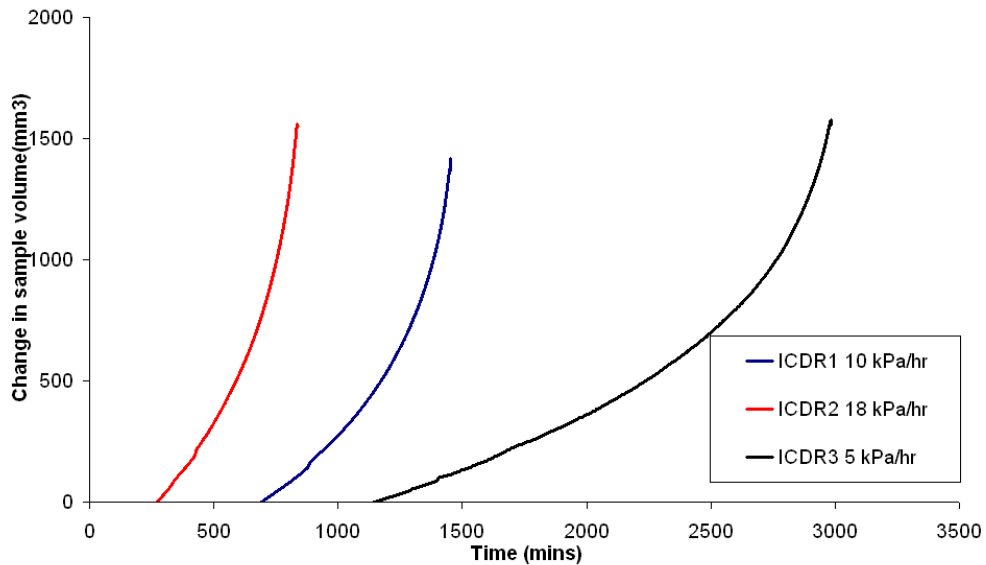


Figure 6.46 Change in sample volume through time at constant q of 400 kPa, samples ICDR1, ICDR2 and ICDR3

6.4.5 Variability of Gault Clay across sites

To determine whether variability in the deformation behaviour of the Gault Clay from different sampling sites a set of tests have been conducted on samples of the intact Gault collected in BH4, intact Basal Gault sampled in BH5 and BS samples collected from Gore Cliff (Fig 4.1). In these tests samples were consolidated to $p' = 350$ kPa. Following this stage deviator stress was raised in each sample to $q = 400$ kPa before failure was initiated at constant q at a standard PPR rate of 10 kPa/hr (Fig 6.47).

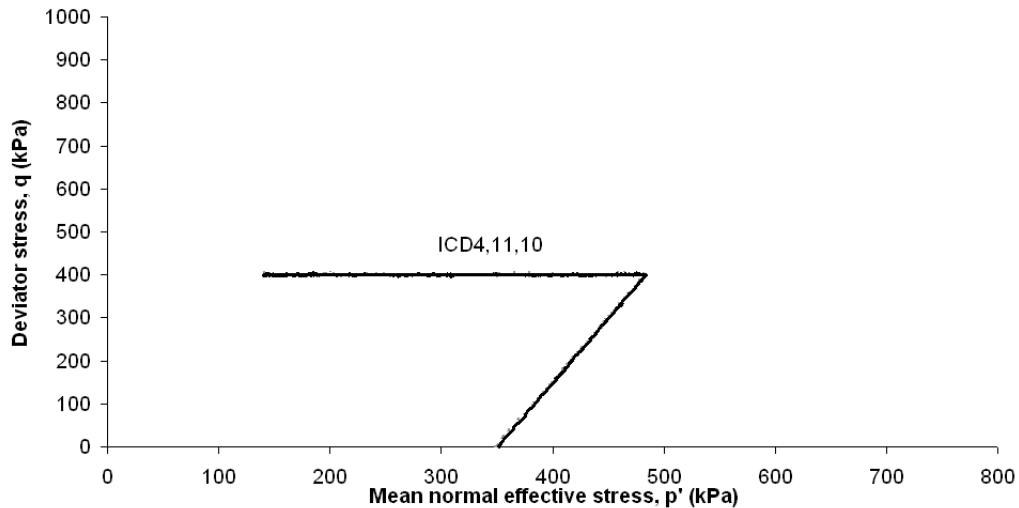


Figure 6.47 ICDPPR stress paths for Gault Clay samples taken from BH4, BH5 and BS at PPR rates of 5, 10, 18 kPa/hr at constant q of 400 kPa from initial p' of 350kPa

6.4.5.1 Sustained initial shear

The drained stress paths during the initial drained shear phase for each ICD sample demonstrated a straight line to the pre-determined deviator stress ($q = 400$ kPa) consistent with the early phase of a standard drained shear (Appendix A, Fig A32). Axial strains during this period of between 0.6% and 0.8%. Much larger axial strains of up to 2.5%, however, were observed in ICD11 during the same period. Similarly the percentage volumetric strains

recorded in sample ICD11 reached 0.35% (Appendix A, Fig A33). Volumetric strains (Appendix A, Fig A34) recorded in ICD4 and ICD10 also ranged from 0.28% in IC4 and to 0.15% in ICD10. The results suggest that sample stiffness varied between the three boreholes which may indicate that the disturbance of the Gault varies across the site.

6.4.5.2 Pore pressure reinflation

Analysis of the PPR stage of these tests demonstrates different displacement rate behaviour to failure in each sample (Fig 6.48). Sample ICD4 showed an initial period of accelerated displacement rate between $p' = 330$ kPa and 300 kPa, followed by a period of near linear increase in displacement rate between $p' = 300$ kPa and 150 kPa, at which point the displacement rate increased hyperbolically. An initial increase in displacement rate was not observed in sample ICD5 until $p' = 190$ kPa. Following this a period of fluctuating displacement rates was observed to 145 kPa before a hyperbolic acceleration to failure was observed. In contrast sample ICD11 demonstrated a much larger increase in displacement rates between $p' = 230$ kPa to $p' = 210$ kPa. Following this period a near linear increase displacement rates was observed between $p' = 210$ kPa and 150 kPa before acceleration to final failure occurs. This indicates more significant pre-failure deformation occurred in sample ICD11 extracted from BH4 when compared with to ICD4 and ICD10.

Analysis of these patterns of displacement in $1/v - p'$ space illustrates a clear linear trend to failure in samples ICD4 and ICD10 (Fig 6.49). Conversely sample ICD11 shows a clear asymptotic trend in $1/v$ to failure. Regression analysis of these displacement rates (Fig 6.50) demonstrates that a negative linear trend to failure is observed in samples ICD4 and ICD10 consistent with brittle failure and a statically significant asymptotic trend is observed in sample ICD11 which is consistent with ductile deformation.

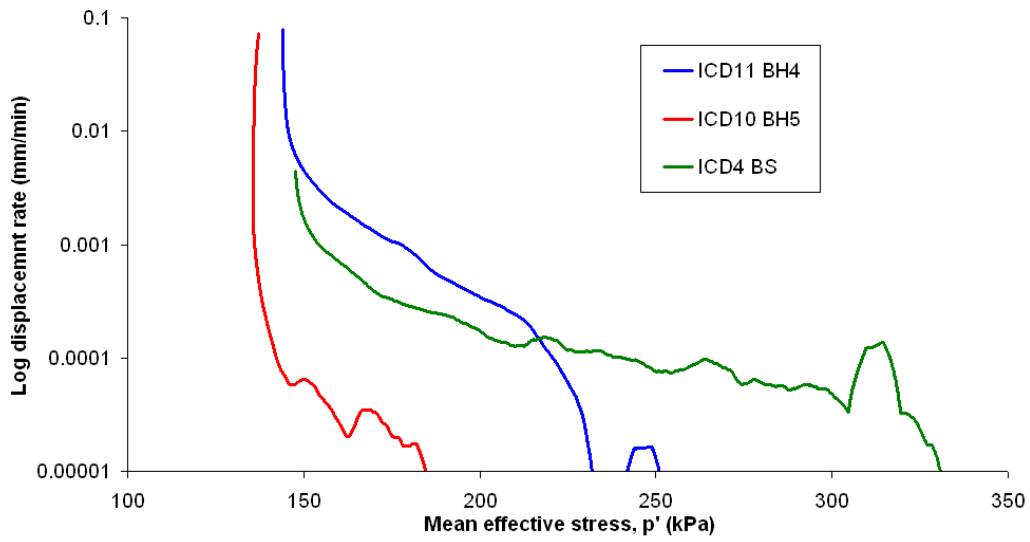


Figure 6.48 Displacement rate against p' , at constant q of 400 kPa, samples ICD4, ICD10 and ICD11

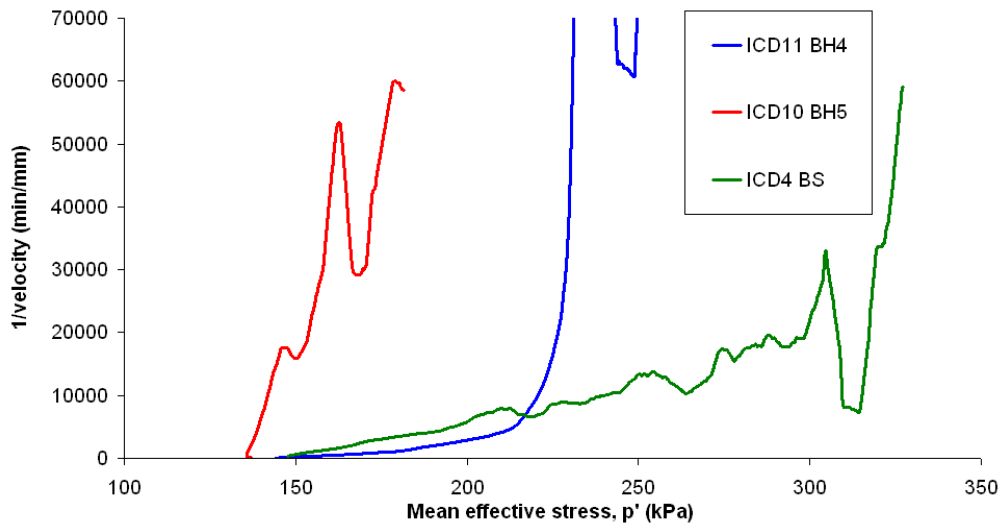


Figure 6.49 1/ velocity against p' at constant q of 400kPa, samples ICD4, ICD10 and ICD11

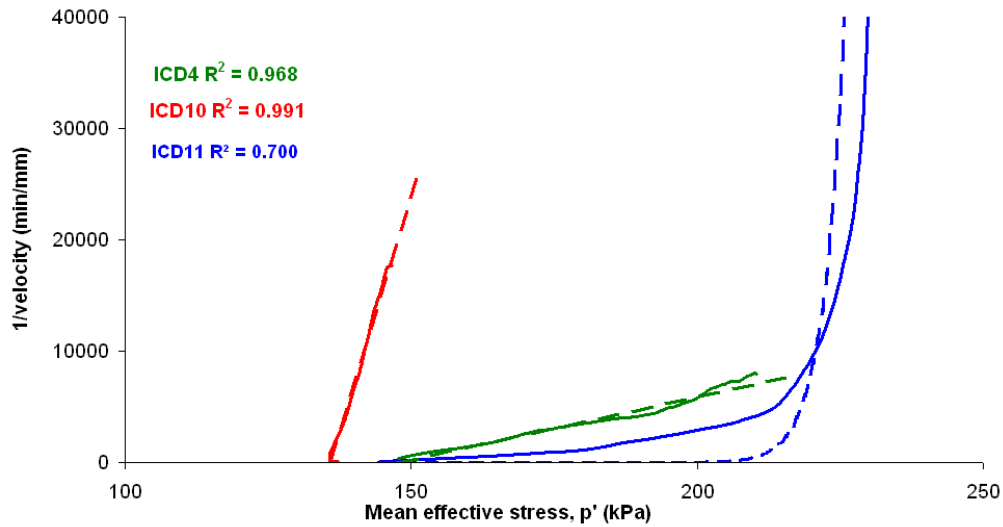


Figure 6.50 Regression analysis of displacement to failure in $1/v - p'$ at constant q of 400 kPa, samples ICD4, ICD10 and ICD11

Analysis of these patterns through time (Fig 6.51) reveals that sample ICD11 undergoes the largest increase in displacement rate prior to final failure which indicates a larger proportion of pre-failure strain has occurred in the sample. Sample ICD10 undergoes a shorter period of pre-failure displacement prior to final failure whilst sample ICD4 is subjected to a prolonged period of linearly increasing displacement rate. The results indicate that the variation in the $1/v - t$ space trends to failure may relate to the degree of pre-failure strain that is able to occur in the sample at p' values above failure (Fig 6.52). Sample volumes are shown to increase to failure illustrating dilative behaviour (Fig 6.53), consistent with the previous testing on intact Gault Clay samples.

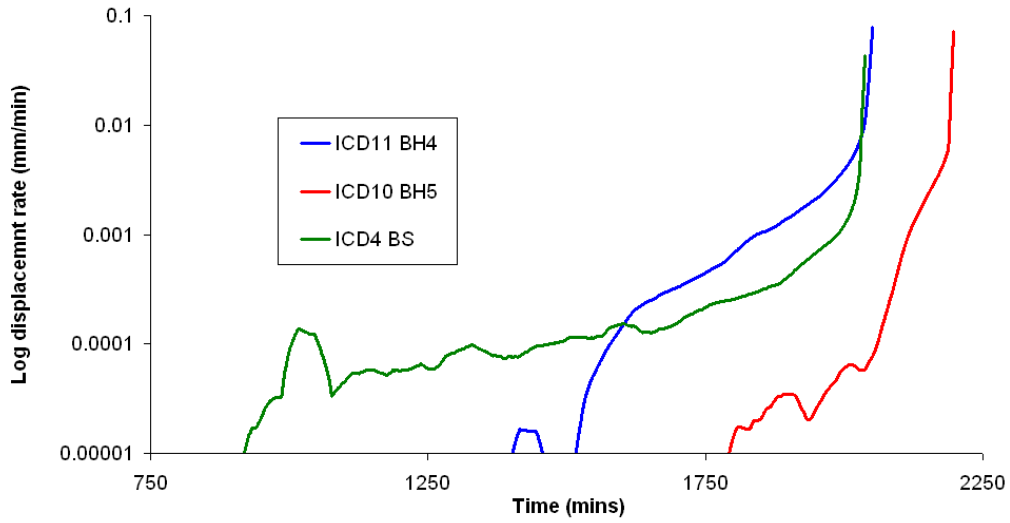


Figure 6.51 Displacement rate against time at constant q of 400 kPa, samples ICD4, ICD10 and ICD11

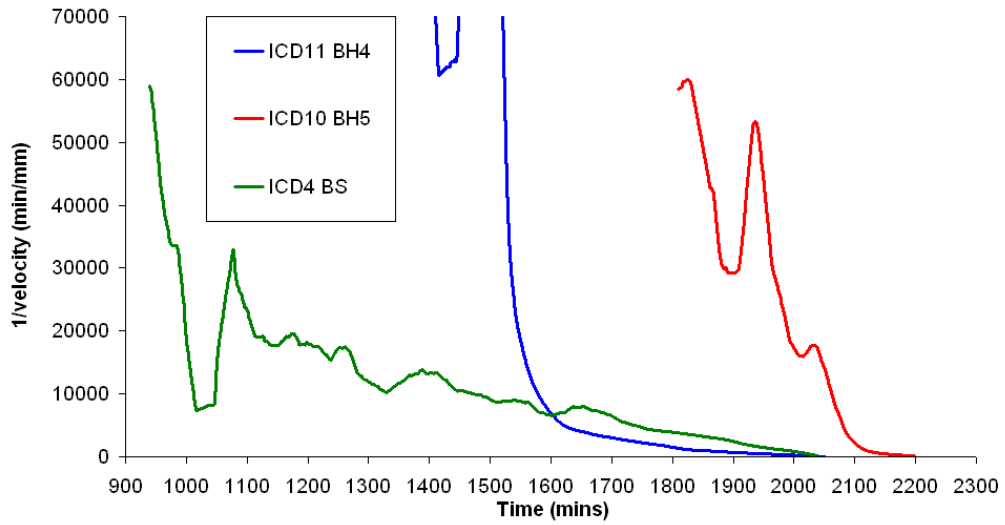


Figure 6.52 $1/v - t$ at constant q of 400 kPa, samples ICD4, ICD10 and ICD11

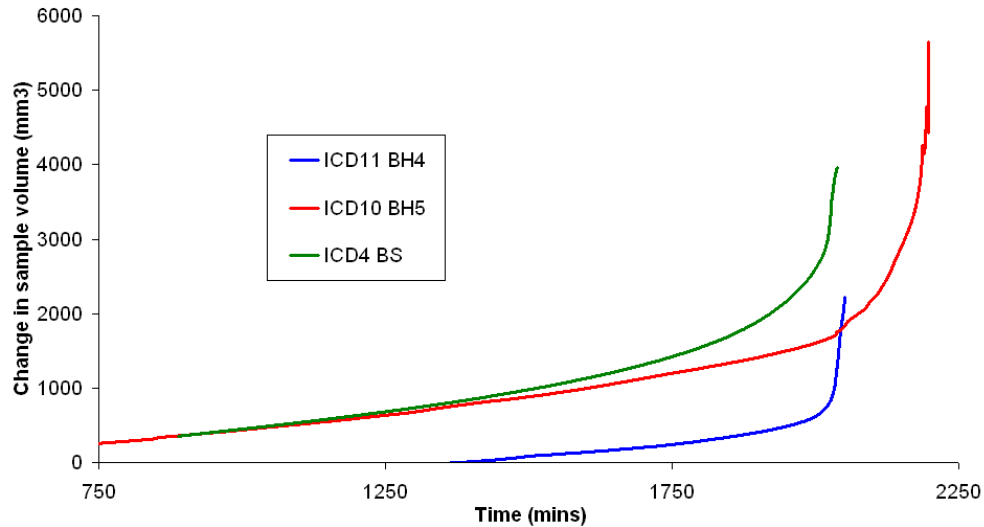


Figure 6.53 Change in sample volume through time at constant q of 400 kPa, samples ICD4, ICD10 and ICD11

6.4.6 *Is the nature of shear surface development different in the Gault Carstone interface material, and can this be compared to the Gault Clay?*

A series of porewater pressure reinflation tests were undertaken on the Gault Carstone transition material using the specialist back pressured shear box (BPSB). A further series of tests were undertaken on the Gault Clay samples from BH5 to assess the variable behaviour of the two materials and to cross correlate behaviours with the triaxial cell tests

Figure 6.54 and Figure 6.55 demonstrate the test stress paths undertaken in both materials and their relationship with the peak and residual strength envelopes calculated for these materials using standard ICU and CPSB samples (section 6.3.3).

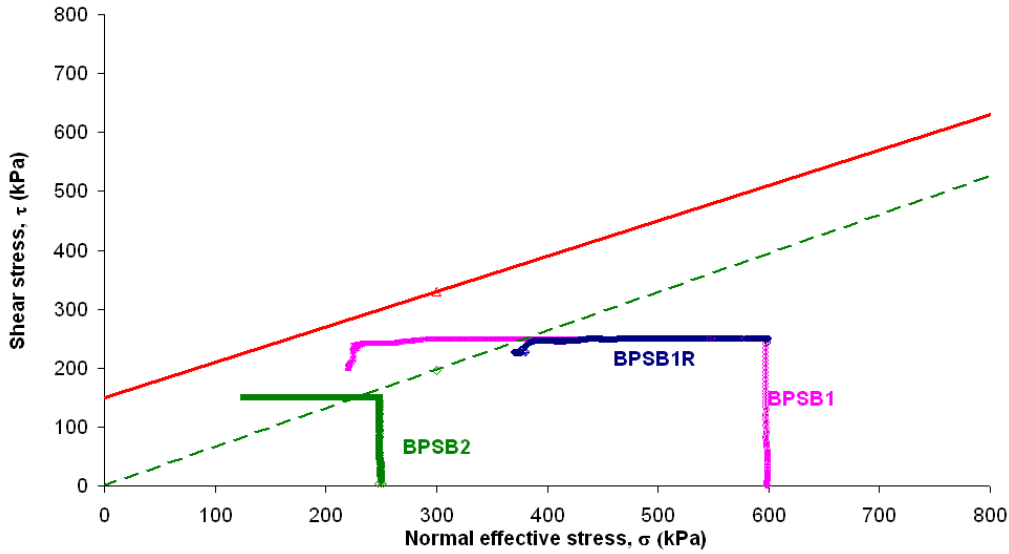


Figure 6.54 BPSB stress path testing programme, Gault-Carstone transition

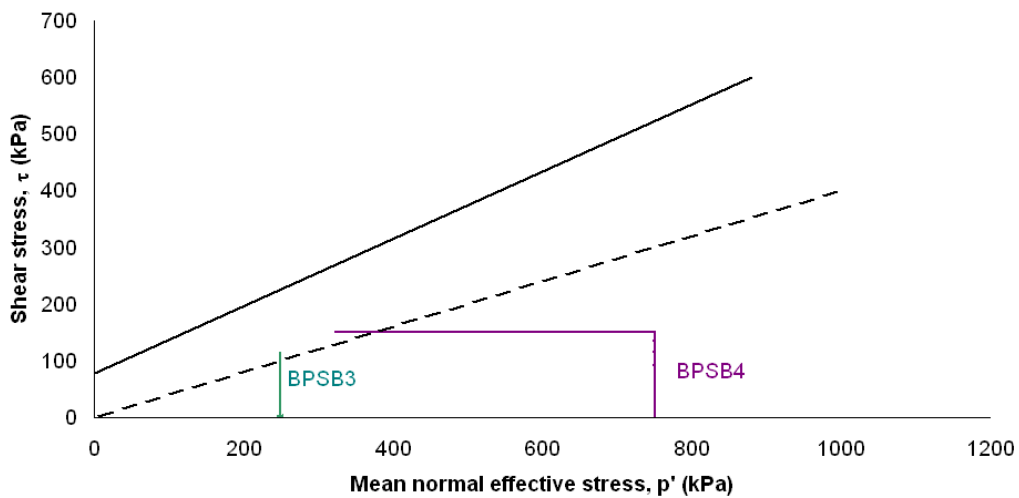


Figure 6.55 BPSB stress path testing programme, Gault Clay

6.4.6.1 Sustained initial shear

The sustained initial shear stage in the Gault Carstone transition material illustrates an initial increase in shear stress but only a minimal change in horizontal displacement (Appendix A, Fig A35). Each test sample begins to curve suggesting increased displacement over smaller changes in stresses toward the end of the sustained initial shear phase. Significant horizontal displacement occurred in the remoulded sample BPSB1R indicating that the sample is significantly weaker than the intact sample.

During this period vertical strain remain relatively consistent in the intact samples BPSB1 and BPSB2 with larger vertical strains (up to 3.5%) measured in the remoulded sample, suggesting significant displacement has occurred in the sample prior to the PPR stage (Fig Appendix A, A36).

The sustained initial shear stage in the Gault Clay demonstrates an initial high increase in shear stress with minimal change in horizontal displacement (Fig 6.56). Significant displacement was observed at low strain in sample BPSB3 before flattening at 110 kPa at which point displacement continued at constant stress. Sample BPSB4 however reaches a stress 140 kPa with only minimal change in the sample strain. The different displacement characteristics of the two samples are further highlighted in the change in vertical strain (Fig 6.57) during the initial shear stage. The results illustrate that sample BPSB3 failed during the initial shear stage before PPR could be initiated. The early failure of the sample is likely to have been due to a pre-existing shear or zone of weakness within the sample, which led to failure occurring at residual strength. As a consequence the PPR characteristics of this sample are not considered in section 6.4.5.2.

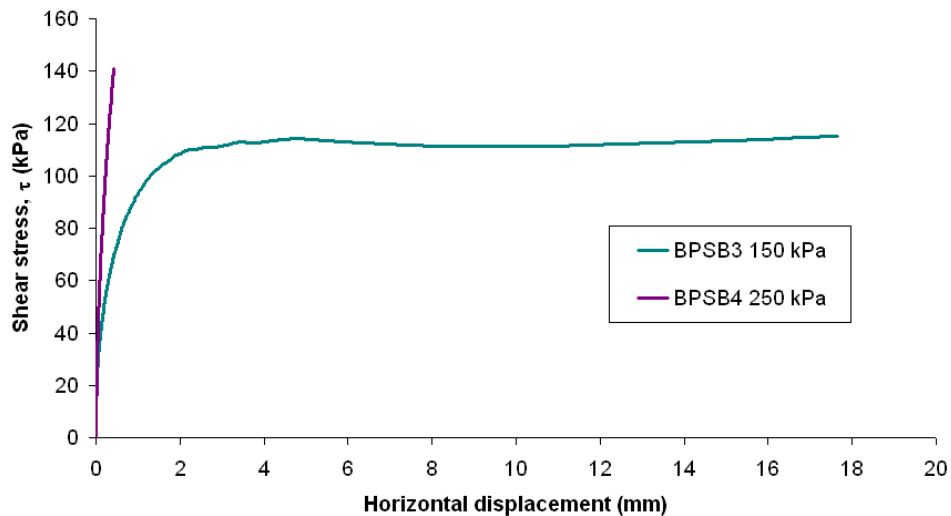


Figure 6.56 Shear stress against horizontal displacement during initial shear stage, Gault Clay samples BPSB3 and BPSB4

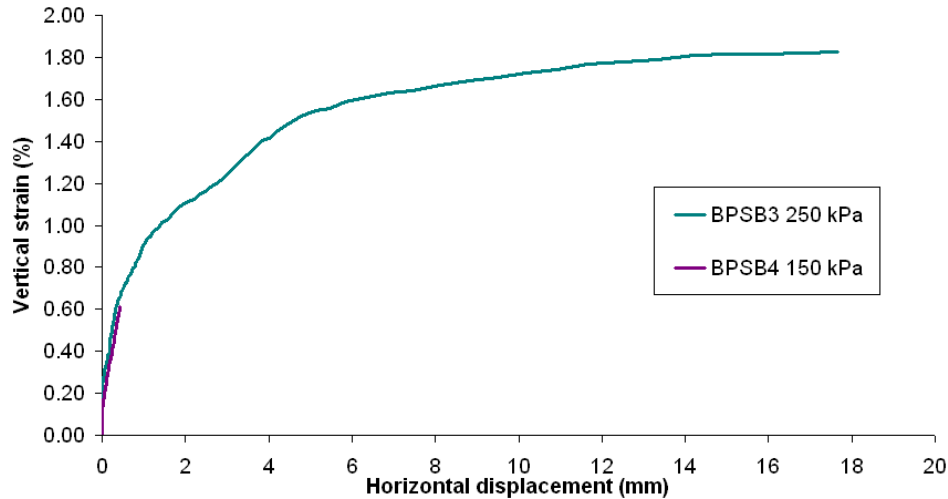


Figure 6.57 Vertical strain against horizontal displacement during initial shear stage, Gault Clay samples BPSB3 and BPSB4

6.4.6.2 Pore pressure reinflation

Analysis of the PPR stage of intact sample BPSB1 and remoulded sample BPSB1R undertaken along the same stress path ($q = 250$ kPa) (Fig 6.58) illustrates an initial period of rapidly increasing displacement rates between 600 and 500 kPa in both samples. Following this period a near linear increase in displacement rate is observed in both samples with displacement rates in the remoulded sample increasing more rapidly at lower p' values. Following this a distinct stepped pattern to failure can be observed in the remoulded sample. Intact BPSB1, however, maintains a near-linear increase in log displacement rate until a distinct hyperbolic increase is observed at $p' = 220$ kPa.

There is a distinct asymptotic trend at high p' in both samples (Fig 6.59) which is then maintained to failure at $p' = 400$ kPa in remoulded sample BPSB1R. Following this initial asymptotic trend in intact sample BPSB1 is followed by a short increase in $1/v - p'$ space at $p' = 530$ kPa followed by a period of asymptotic trend in $1/v - t$ space between $p' = 530$ kPa to $p' = 230$ kPa. Following this a linear trend is observed to $p' = 220$ kPa (Fig 6.60).

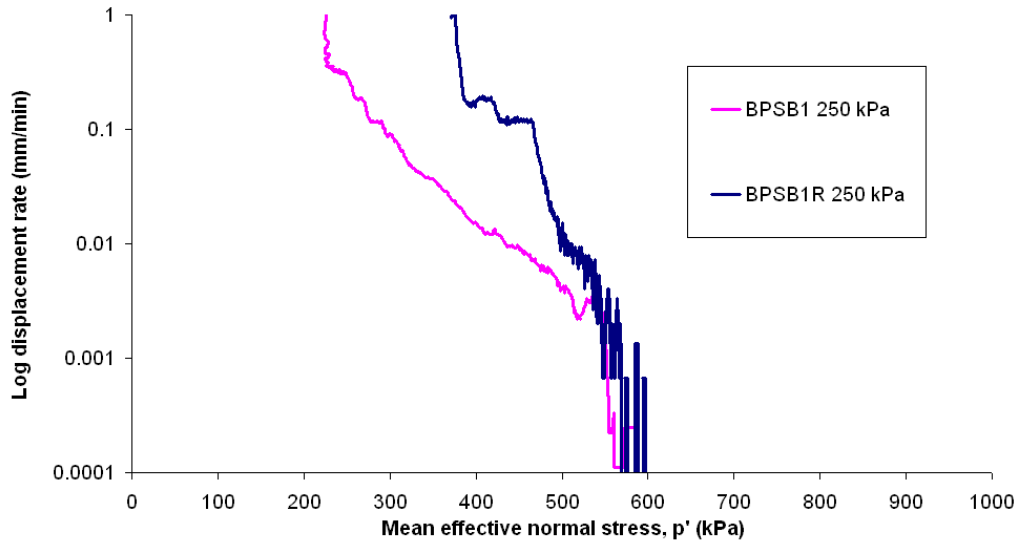


Figure 6.58 Displacement rate against p' at constant $q = 250$ kPa from initial $p' = 600$ kPa, samples BPSB1 and BPSB1R

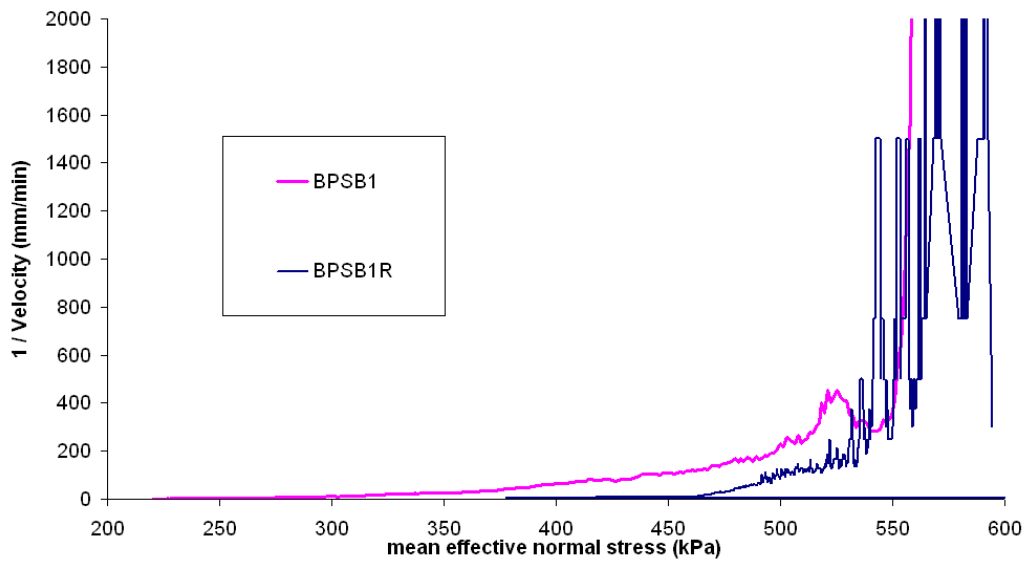


Figure 6.59 $1/v - p'$ at constant $q = 250$ kPa from initial $p' = 600$ kPa, samples BPSB1 and BPSB1R

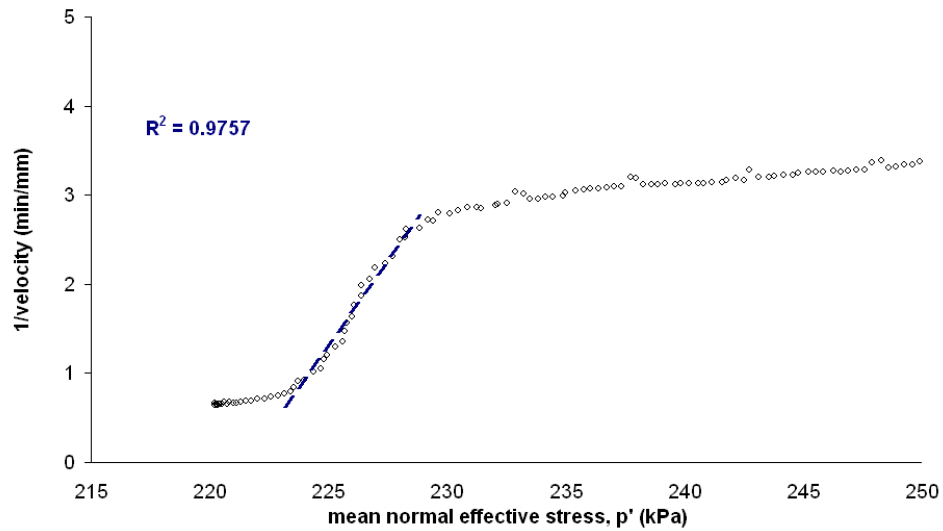


Figure 6.60 BPSB1 Final phase of linearity to failure in intact sample BPSB1

Analysis of displacement rates against time (Fig 6.61) illustrates similar patterns of behaviour in both the remoulded and intact Gault-Carstone transition zone samples. As expected remoulded sample BPSB1R demonstrates displacement to failure earlier than the intact sample with a clear stepped pattern of increasing displacement rate to failure. Intact sample BPSB1 however shows a near linear increase in log displacement rate (indicating exponential acceleration) through time before the final period of acceleration to failure at high displacement rates. This prolonged exponential phase is observed in $1/v - t$ space as a prolonged asymptotic trend with linearity occurring at very low $1/v$ rates (Fig 6.62).

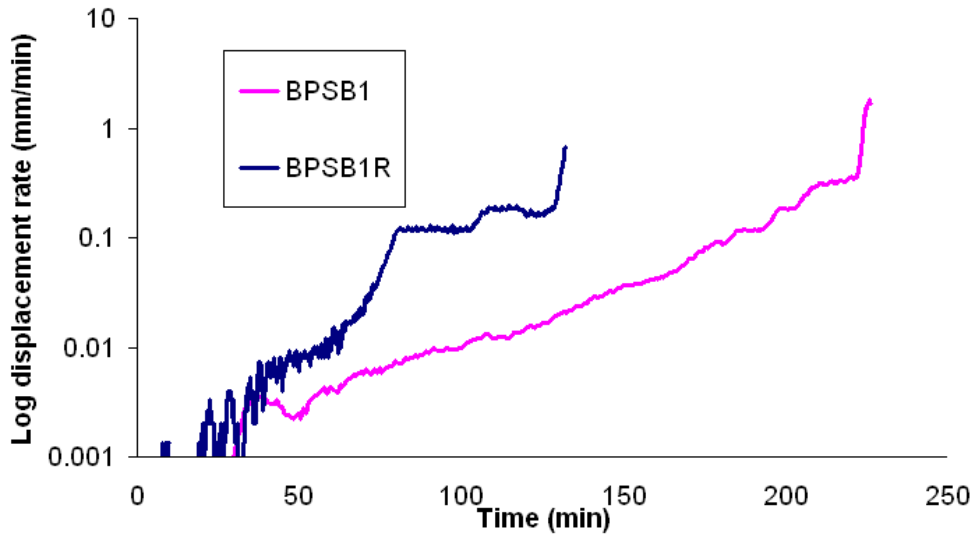


Figure 6.61 Displacement rate against time at constant $q = 250 \text{ kPa}$ from initial $p' = 600 \text{ kPa}$, samples BPSB1 and BPSB1R

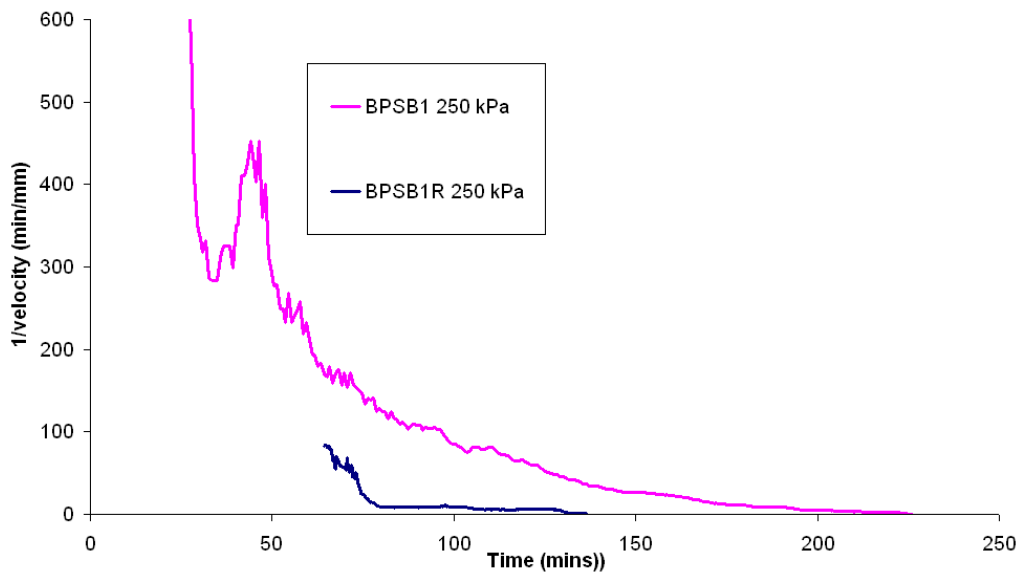


Figure 6.62 $1/v - t$ at constant $q = 250 \text{ kPa}$ from initial $p' = 600 \text{ kPa}$, samples BPSB1 ad BPSB1R

Intact sample BPSB2 illustrates a very different pattern of behaviour in displacement rate against time (Fig 6.63). The sample underwent a period of varying displacement rate at a low displacement rate to $p' = 200 \text{ kPa}$, followed by a period of increasing displacement rate. At $p' = 140 \text{ kPa}$ the sample appears to have undergone a sudden increase in displacement rate, which reduces before acceleration to final failure. The behaviour may suggest

fracturing in the sample. The displacement rates show a clear linear trend to failure when plotted in $1/v - p'$ (Fig 6.64) consistent with brittle shear surface development.

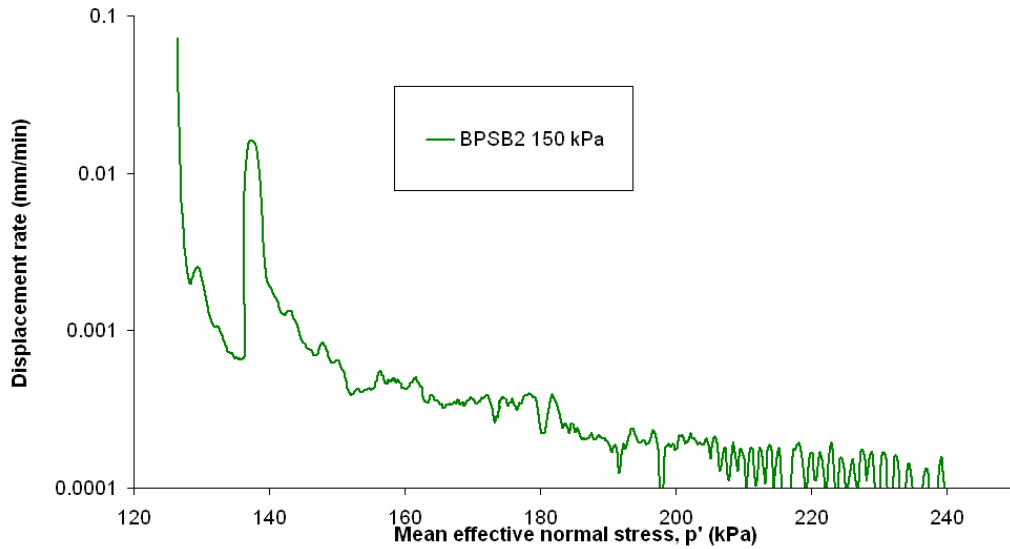


Figure 6.63 Displacement rate against p' at constant $q = 150 \text{ kPa}$ from initial $p' = 250 \text{ kPa}$, sample BPSB2

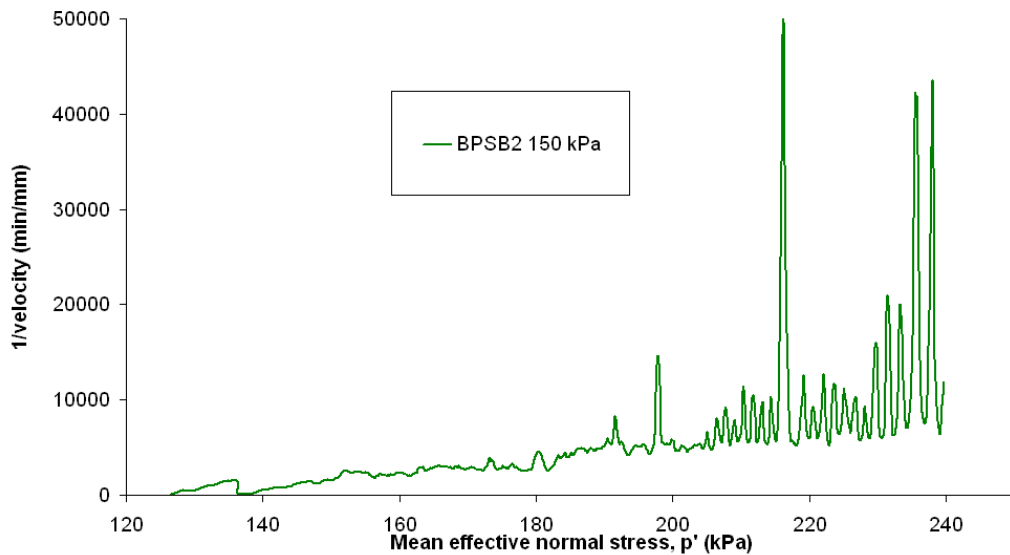


Figure 6.64 $1/v - p'$ at constant $q = 150 \text{ kPa}$ from initial $p' = 250 \text{ kPa}$, sample BPSB2

Analysis of displacement rates against time demonstrate the progressive development to failure through time (Fig 6.65) which, as expected, demonstrates a linear trend to failure in $1/v - t$ (Fig 6.66) .

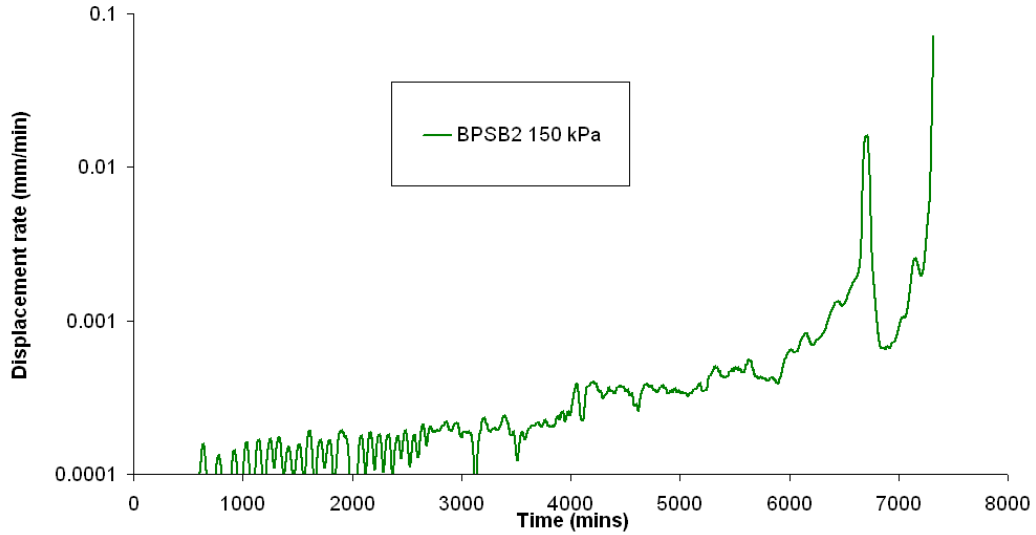


Figure 6.65 Displacement rate against time at constant $q = 150 \text{ kPa}$ from initial $p' = 250 \text{ kPa}$, sample BPSB2

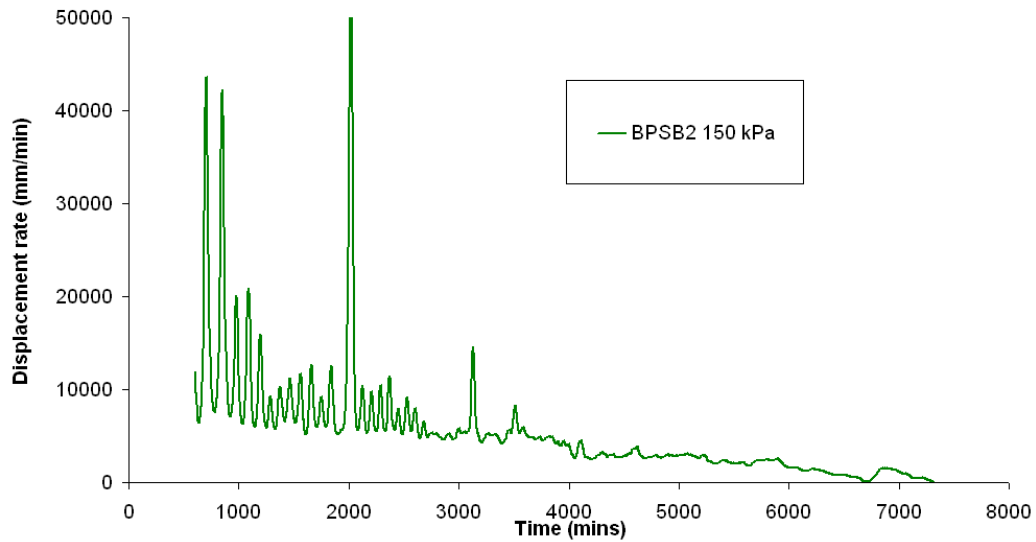


Figure 6.66 $1/v - t$ at constant $q = 150 \text{ kPa}$ from initial $p' = 250 \text{ kPa}$ sample BPSB2

Back pressured shear box testing on the Gault Clay sample BPSB4 (Fig 6.67) showed a near constant displacement rate through time without the development of acceleration to failure as observed in the triaxial cell testing (section 6.4). The data during the PPR stage indicate a slow increase in displacement at near constant displacement without consistent with

secondary creep. It is likely that given the high initial consolidation pressure ($p' = 750$ kPa) and subsequent low deviator stress ($q = 250$ kPa) that porewater pressure were not sufficient to reduce p' to the failure envelope. As a consequence failure was not successfully initiated.

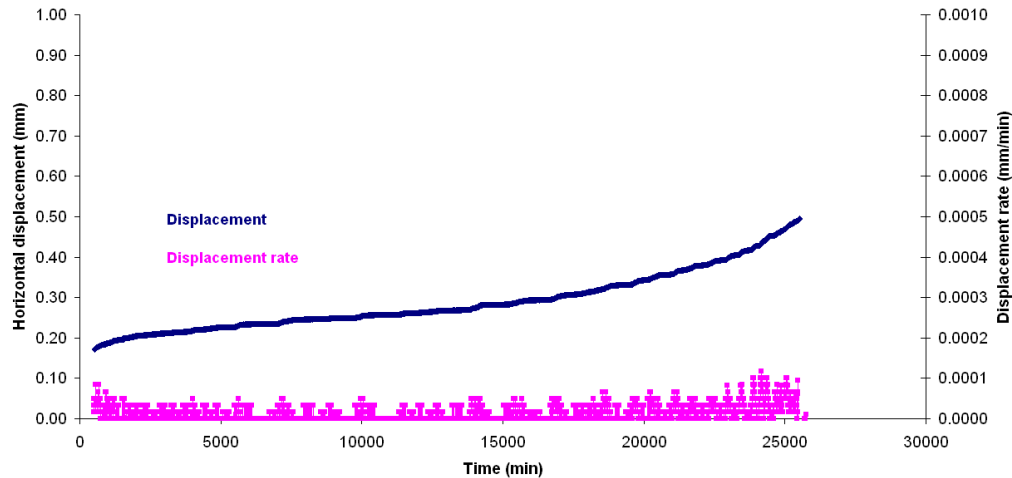


Figure 6.67 Displacement and displacement rate against time at constant $q = 250$ kPa from initial $p' = 750$ kPa, sample BPSB4

6.5 PPR results in relation ICU and ICD PPR failure envelopes

The specialist pore pressure reinflation testing has demonstrated a number of patterns in displacement which vary as a result of the properties of the material sampled and tested. The behaviour observed falls into two distinct categories.

1. Brittle materials fail due to the formation of a singular shear surface as the sample dilates. Samples that behave in this way are generally intact cohesive materials and in all cases demonstrate a negative linear trend in both $1/v - t$ space and $1/v - p'$ space to failure.
2. Conversely, ductile deforming materials do not fail along singular shear surface but barrel across a larger deformation zone as the sample dilates. Samples that have been shown to behave in this manner have low or no cohesion such as remoulded pre-deformed clay samples or

intact sandstones. In all cases they show an asymptotic trend in $1/v - t$ space and $1/v - p'$ space to failure.

When the ICD PPR samples undertaken at $p' = 400$ kPa have been analysed in relation the ICU and CIDPPR peak strength envelopes (Fig 6.68) it can be demonstrated that the linear trend develops from the ICU failure envelope and significantly before the ICD PPR failure envelope. This demonstrates that whilst failure appears to occur at a critical p' of 150 kPa this occurs at a mean effective stress before both the ICU and ICDPPR peak strength envelopes have been reached.

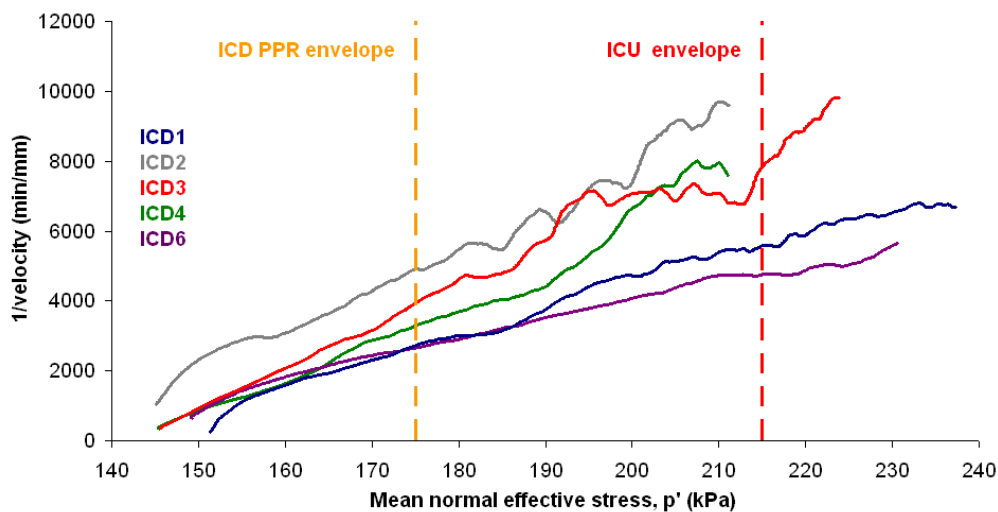


Figure 6.68 Relationship between $1/v - p'$ and ICU and ICDPPR failure envelopes, intact Gault Clays samples

Linear behaviour observed, in the Gault-Carstone transition material, occurs at p' values below the peak strength envelope, with a stepped asymptotic trend observed from a p' above the residual strength envelope (Fig 6.69). Analysis of this pattern of behaviour in $\log v - p'$ (Fig 6.70) demonstrates this period of exponential acceleration followed by a period constant displacement rate before final failure develops. This mechanism of shear surface development is consistent with assessment of crack development (Kilburn and Petley, 2003) (Appendix A, Fig A37) (Main, 2000) in which displacement rate (crack growth) slows prior to final failure as a result of micro-crack saturation

(Petley *et al*, 2005a; Main, 2000). At this stage further micro-cracks are unable to develop and therefore displacement rates remain constant temporarily as only crack growth mechanisms are acting to deform the shear surface. Through this process final failure would occur as a single shear surface formed from a period of near constant displacement rate. Sample BPSB1 indicates that this brittle cracking process may develop from below the peak strength envelope

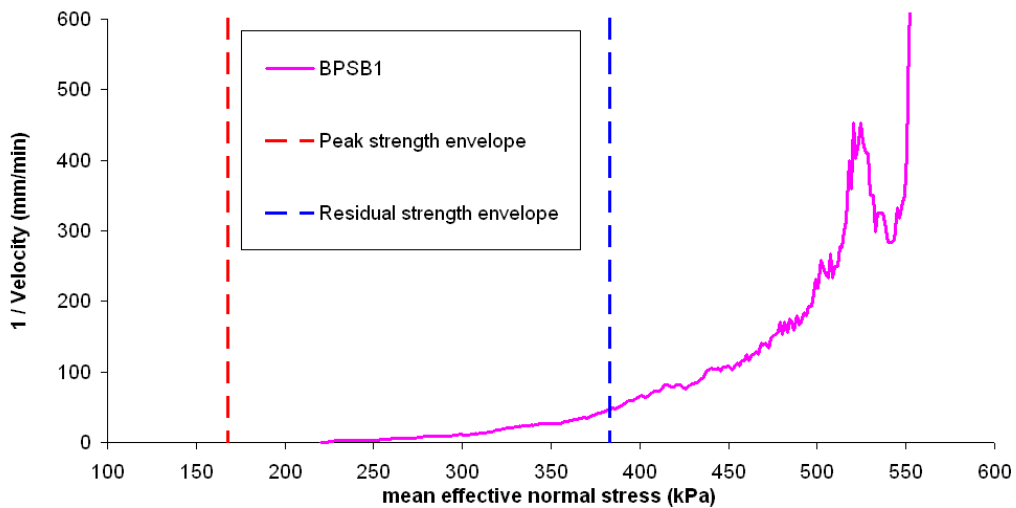


Figure 6.69 Relationship between $1/v - p'$ and the peak and residual strength envelopes, intact Gault-Carstone interface material

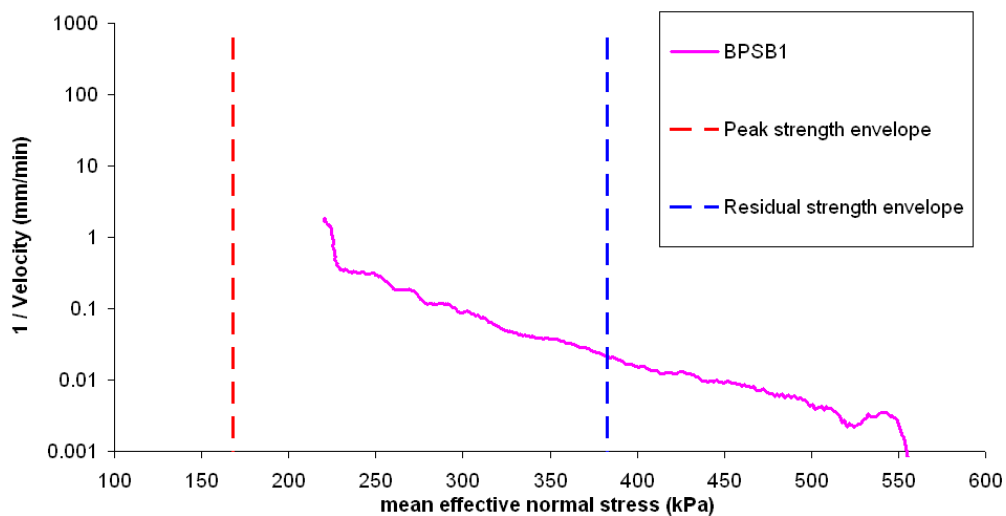


Figure 6.70 Relationship between displacement rate against p' and the peak and residual failure envelopes, intact Gault-Carstone interface material

Asymptotic behaviour was shown to develop after the ICU residual strength envelope. This is shown in sample ICD9 where the asymptotic trend develops from $p' = 500$ kPa with final failure occurring before both the ICU and ICDPPR failure envelope had been reached (Fig 6.71). Similar asymptotic behaviour was observed in the remoulded Gault Clay samples (ICDR1, ICDR2 and ICDR3). When the $1/v - p'$ plots are considered in relation to the failure envelop (Fig 6.72) it is clear displacement to failure occurs after the residual strength envelope has been reached but before the peak strength envelope can be reached.

Interestingly the remoulded PPR testing on the Gault-Carstone transition material, however, indicates the development of displacement to failure from a p' above the residual strength envelope (Fig 6.73) develops once the residual strength envelope is surpassed in all three tests with final failure occurring at p' above the ICU peak strength failure envelope.

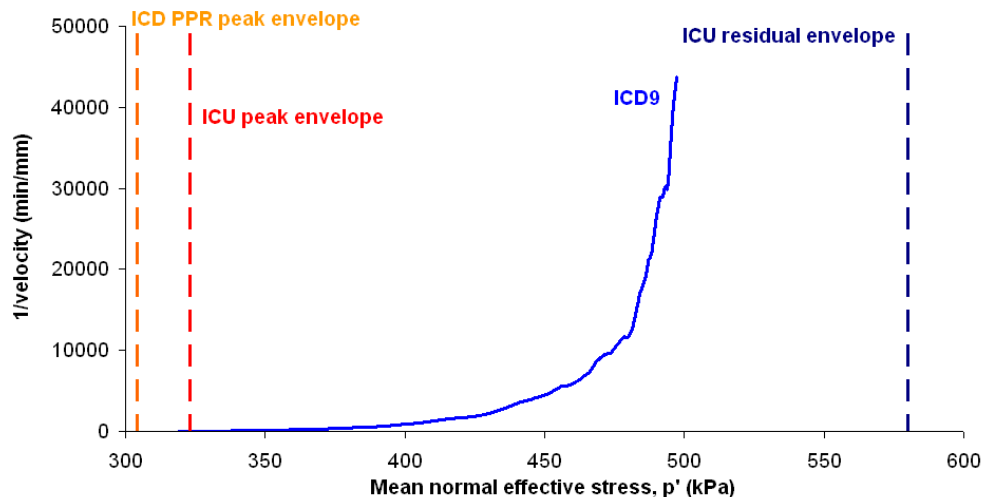


Figure 6.71 Relationship between $1/v - p'$ and the peak (ICU, ICD PPR) and ICU residual strength envelopes, intact Gault sample from $p' = 500$ kPa

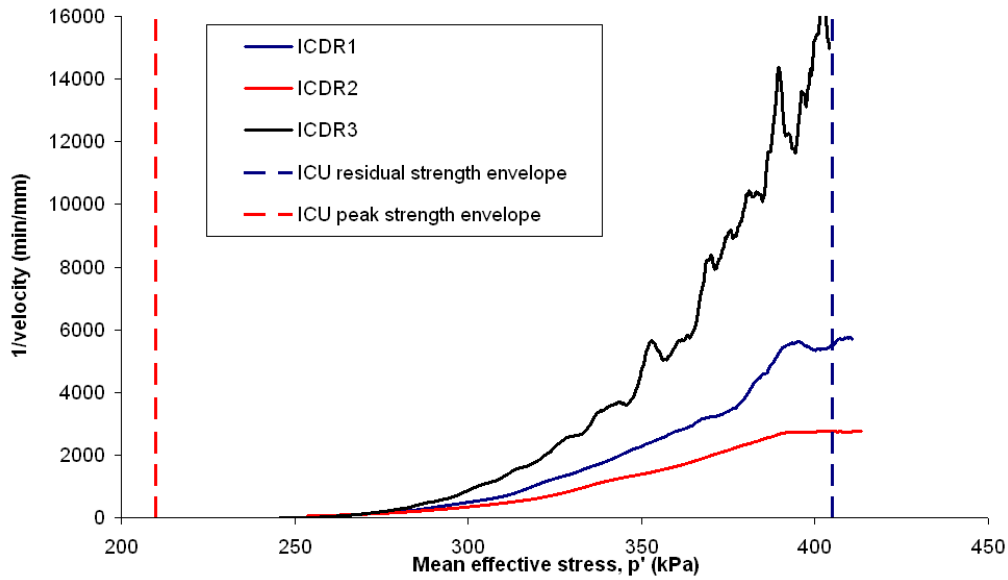


Figure 6.72 $1/v - p'$ plots for remoulded (ICD PPR) Gault samples

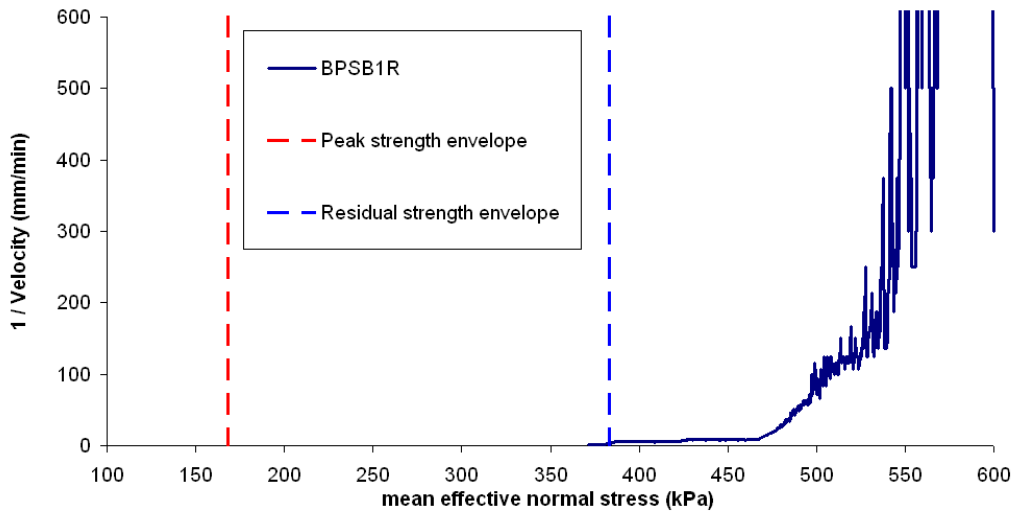


Figure 6.73 $1/v - p'$ plot for remoulded (BPSB) Gault-Carstone transition samples

6.6 Can failure be initiated from a constant p' long creep test?

Finally, an additional long creep test was undertaken. In this test, pore pressures were raised gradually and then held constant. The test lasted 524 days. The aim of this test was to assess the hypothesis that brittle failure

could develop in the Gault Clay at constant p' and q from below the peak strength envelope.

An intact sample of Gault Clay (ICD12) was initially consolidated to $p' = 350$ kPa, during which its behaviour was consistent with the previous ICD tests (Appendix A, Fig A38). Following this the sample was subjected to an initial drained shear to $q = 400$ kPa, before pore pressures were increased at a rate of 10 kPa / hr on the $q = 400$ kPa stress path (Appendix A, Fig A39).

Analysis of the PPR stage through time illustrates a steeper pattern of displacement during the early stages of the test associated with the staged increases in porewater pressure (Fig 6.74). After each increment the sample was held at constant pore pressure for a period of 24 hours or until no further displacement was observed. Initially pore pressures were raised at 5 kPa/ hr. As p' reduced toward the peak strength envelope the length of the PPR stages were reduced to 30 minutes and the hold phases were extended to ensure no stress induced displacement was occurring.

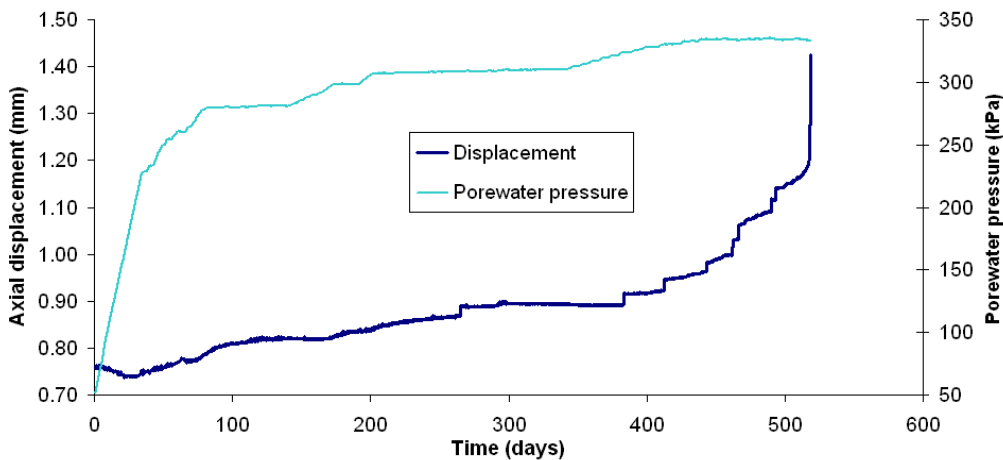


Figure 6.74 Displacement and pore water pressure through time

During the final stage of the test the back pressure was held constant for 81 days to prevent any increase in the sample pore pressures and subsequent change in the sample p' (Fig 6.75). Analysis of displacement rates during this period indicate that the sample accelerated to failure on day 81 of the final

testing stage (day 524 of the total testing period) at constant stress. Analysis of the displacement rates indicate an initial period of fluctuating displacement rates consistent with the behaviour of intact Gault Clay tests studied in the linear PPR testing. The initial acceleration and decelerations in displacement appear occur as a result of sudden increases in sample volume which is indicative of sample dilation as a result of shear surface development (Fig 6.76).

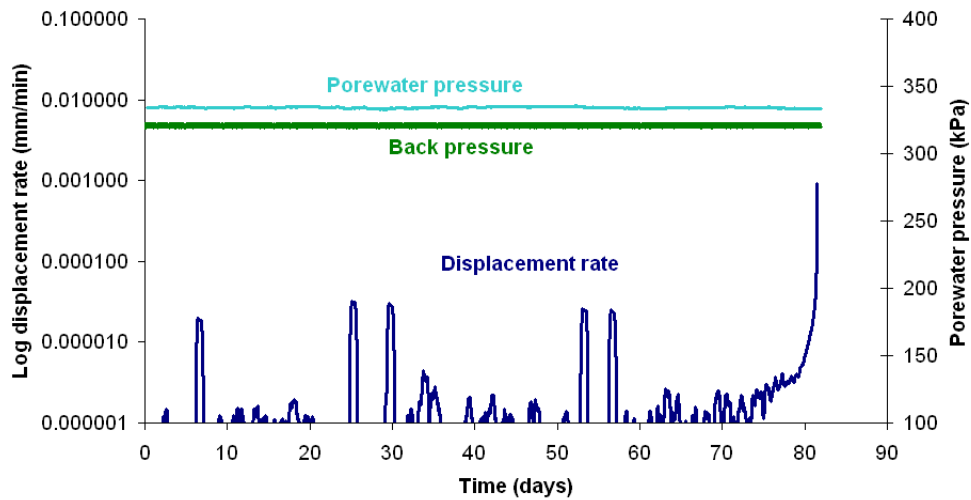


Figure 6.75 Displacement rate to failure at constant back pressure and porewater pressure

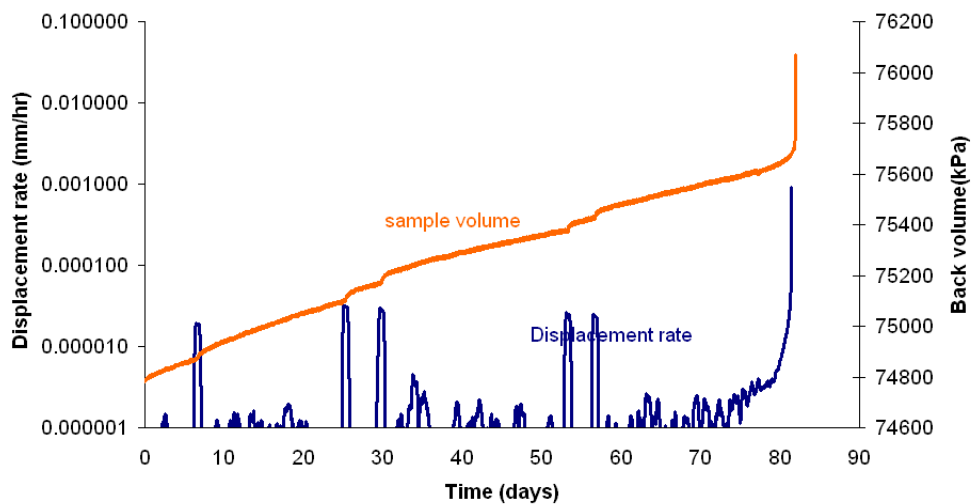


Figure 6.76 Comparison of sample volume and displacement rate at constant p' to failure

The progressive development of failure appears to occur from day 70 as a series 'saw-tooth' pattern movements until a hyperbolic curve in acceleration rate is observed from day 77 (Fig 6.77). Analysis of these displacement rates in $1/v - t$ space (Fig 6.78) indicates the same pattern of $1/v$ to failure as observed in previous linear PPR tests. Sample failure occurred following the development of a negative linear trend to failure from day 77. Regression analysis (Fig 6.79) of this final period of shear surface development indicates a statistically significant linear trend which develops some 4 days prior to failure.

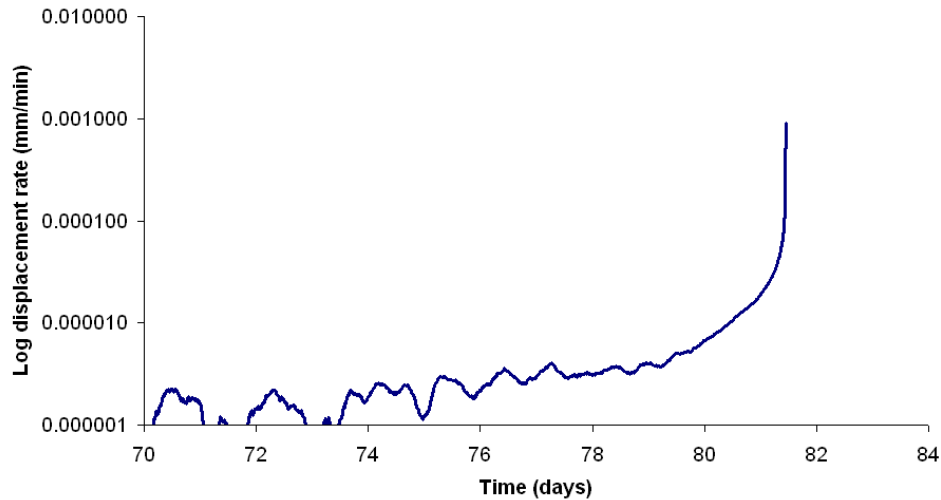


Figure 6.77 Displacement rate against time during last 11 days of the long creep test

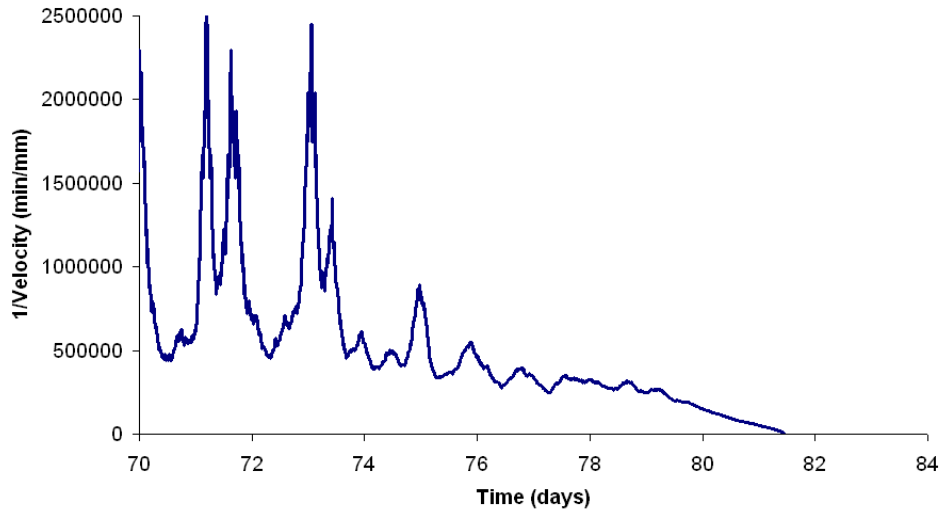


Figure 6.78 $1/v - t$ during final 11 days of long creep test

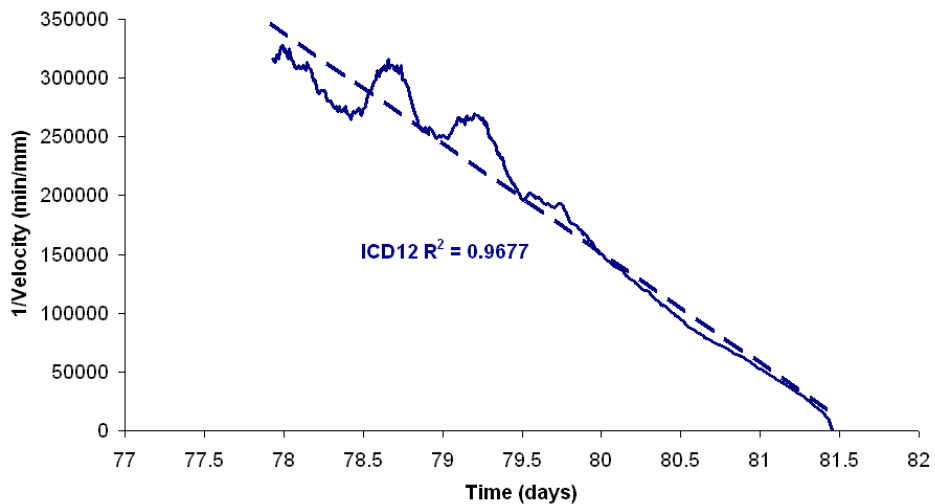


Figure 6.79 Regression analysis of the linear trend in $1/v - t$ space

Given that the nature and pattern of shear surface development is consistent in both the linear PPR testing and constant stress test it is possible to conclude that, in certain circumstances there is a time dependent element to failure which allows the progressive development of a brittle shear surface at constant stress from below the peak strength envelope. The results therefore prove for the first time that the progressive cracking model (Kilburn and Petley, 2003) provides a credible mechanism for the development of shear surfaces in brittle materials.

6.7 Chapter summary

A suite of laboratory tests has been undertaken to study the development and behaviour of shear surfaces on samples collected from the Ventnor landslide and equivalent sites. Sampling of these materials were specifically collected from the base of the Gault Clay and the underlying transition zone between the Gault and the Carstone where landslide shear surface and evidence of ground movement have been observed and discussed in Chapter 5.

6.7.1 Classification of material physical and standard geotechnical properties

Physical properties tests have been conducted on both materials to determine their material properties. The results have confirmed that the Gault is a high plasticity clay with a natural moisture content of 14-17%. Particle size analysis has confirmed high percentages of clay (6.54-14.10%) and silt sized particles (39.28-48.59%). Conversely the Gault-Carstone transition material had a higher sand content (70.40%) and lower clay component (4.90%).

Standard ICU tests have been used to establish the shear strength parameter of the Gault Clay samples and identify the peak and residual shear strength envelope using the Mohr column analysis (Fig 6.11; 6.12). The resultant stress paths demonstrated classic brittle failure behaviour as generally observed in cohesive over-consolidated clays (Burland, 1990). This comprised a rapid reduction in deviator stress required to maintain sample deformation after the peak strength was reached.

A series of direct shear box tests were undertaken on the Gault-Carstone transition zone material using the back pressure shear box to identify the peak and residual strength envelope (Fig 6.14). The results demonstrate a peak c' value of 102.7 kPa and ϕ' value of 31.0° and a residual c' value of 0 kPa and ϕ' value of 33.5°.

6.7.2 Types of failure

A series PPR tests were undertaken on both the Gault Clay and Gault-Carstone transition zone material to study the influence of mean effective

stress on the development of the shear surfaces. The testing has confirmed two distinct types of failure as summarised in Table 6.10.

The majority of intact samples failed through the development of a singular shear surface (brittle failure). In this instance failure occurs through an initial period of fluctuating displacement rates that have a distinctive 'saw-tooth' pattern in displacement rate at high mean effective stresses. This pattern of behaviour generally develops as the p' value passes through the residual strength envelope and significantly before the material peak strength is reached. These fluctuations gradually reduce into a near linear increase in displacement rate in which displacement rates rise gradually. This finally develops into a hyperbolic acceleration in displacement to failure. In all cases a negative linear trend in $1/v - p'$ could be observed to failure consistent with previously published laboratory results (Petley *et al.*, 2005). Interestingly the Gault-Carstone transition material underwent a prolonged period of pre failure deformation which led to the development of the hyperbolic acceleration in strain rate occurring at much higher displacement rates than the Gault Clay.

All remoulded samples and those deemed to be disturbed prior to testing (e.g. ICD9 and ICD11) failed as a result of ductile deformation where a singular shear surface was unable to form. In this mode of failure smooth exponential accelerations in displacement rate were observed from much higher mean effective stresses and sample failure generally at a much higher mean effective stress which were typically significantly above the peak strength envelope and soon after the residual strength envelope. The displacement rates when analysed in $1/v - p'$ space showed a statistically significant asymptotic trend consistent with previous published laboratory results on residual soils (Petley and Ng, 2009).

6.7.3 The influence of failure scenario on shear surface development

Analysis of Gault Clay samples where failure was initiated at a constant deviator stress $q = 400$ kPa at three different initial mean effective stresses ($p' = 250, 350, 450$ kPa) at a PPR rate of 10 kPa / hr underwent brittle failure. The results have demonstrated failure that occurred at similar mean effective

stresses regardless of the initial confining pressure to which the sample had been subjected. Interestingly, however, samples subject to higher initial confining pressures during consolidation underwent less pre-failure displacement, which led to an increasing steepness of the linear trend with increasing p' . This result indicates that sample stiffness may impact on the speed at which the shear surface develops.

A second set of ICD Gault Clay samples where failure was initiated at a constant deviator stress ($q=400$ kPa) from an initial mean effective stress ($p'=350$ kPa) were undertaken at three pore pressure reinflation rates (5, 10, 18 kPa/hr) to assess the influence of pore pressure reinflation rate on the development of the shear surface. The results have demonstrated that failure occurred at similar mean effective stresses through brittle failure at similar mean effective stresses regardless of the pore pressure reinflation rate. Interestingly, samples subjected to lower rates of pore pressure reinflation underwent less pre-failure displacement, leading to an increase in the steepness of the linear trend to failure. The results suggest, therefore, that limited shear surface development occurs in samples where pore pressures are raised slowly which in turn leads to a more rapid failure development at a critical value of p' .

A series of remoulded Gault samples which were subjected to the same PPR testing criteria illustrated ductile failure from the residual strength envelope. The results further showed an increase in the steepness of the asymptotic curve with decreasing PPR, consistent with the intact behaviour.

Analysis of tests undertaken under the same conditions on Gault Clay material from separate sample locations (BH4, BH5 and BS) demonstrated different behaviour during ICD PPR testing with failure occurring at a higher mean effective stress in BH4 in comparison to BH5 and BS. The results indicate that the behaviour of the Gault varies spatially, which may provide insight into the nature of its deposition and movement history.

Table 6.10 Summary ICD and BPSB PPR laboratory results

Test	Material	Confining pressure (kPa)	Stress path (kPa)	PPR rate (kPa/hr)	Sample reference	Sample condition	Failure mode	Failure pattern in $1/v - t$ space
ICD1	Gault	250	400	10	BS	intact	Brittle	**Lin
ICD2	Gault	350	400	10	BS	intact	Brittle	**Lin
ICD3	Gault	450	400	10	BS	intact	Brittle	**Lin
ICD4	Gault	350	400	10	BS	intact	Brittle	**Lin
ICD6	Gault	350	400	18	BS	intact	Brittle	**Lin
ICD7	Gault	350	400	5	BS	intact	Brittle	**Lin
ICD8	Gault	450	500	10	BS	intact	Brittle	**Lin
ICD9	Gault	550	600	10	BS	intact	Ductile	*Asymp
ICD10	Gault	350	400	10	BH4	Intact	Brittle	**Lin
ICD11	Gault	350	400	10	BH5	Intact	Ductile	*Asymp
ICDR1	Gault	350	400	10	BS	remoulded	Ductile	*Asymp
ICDR2	Gault	350	400	18	BS	remoulded	Ductile	*Asymp
ICDR3	Gault	350	400	5	BS	remoulded	Ductile	*Asymp
ICD13	Gault	350	400	Long creep	BH5	intact	Brittle	Lin
BPSB1	Gault - Carstone	600	250	10	BH5	intact	Brittle	**Lin
BPSB1R	Gault - Carstone	600	250	10	BH5	remoulded	Ductile	*Asymp
BPSB2	Gault - Carstone	250	150	10	BH5	intact	Brittle	**Lin

*Asymp = Asymptotic **Lin = Linear

6.7.4 The long creep test

Following the results of the linear PPR testing it was hypothesised that given the development of displacement at p' above the peak strength envelope, failure could be initiated at constant p' and constant q as a result of the internal sample deformation. To study this hypothesis a slow creep test was carried out in which PPR was raised slowly raised and held over a number of months. The test demonstrated for the first time that brittle failure could be generated at constant stress. The failure behaviour was consistent with the brittle failures observed in the linear PPR tests. The failure initiated from a p' above the ICD PPR envelope indicating for the first time that time dependent failure can occur without change in sample stress. This illustrates that in these circumstances failure is controlled by the long-term internal deformation of the sample.

The results provide a new insight into the significance of material properties in the formation of landslide shear surface under different effective stress conditions. Most significantly the results confirm the presence pre-failure

creep (increasing displacement rate at constant stress) which for the first time provides a mechanism for time dependent failure in slopes.

Chapter 7: Discussion

7.1 Introduction

This chapter combines the results of specialist laboratory testing on samples collected from the shear zone of the Ventnor landslide complex with the interpretation of surface monitoring data from both the site and relevant the literature. The results are used to evaluate the stages of progressive development and post failure behaviour of landslide failures (Fig 7.1) and to further consider the mechanisms of movement currently operating within the Ventnor landslide. The potential implications this interpretation may have on its future behaviour are also discussed.

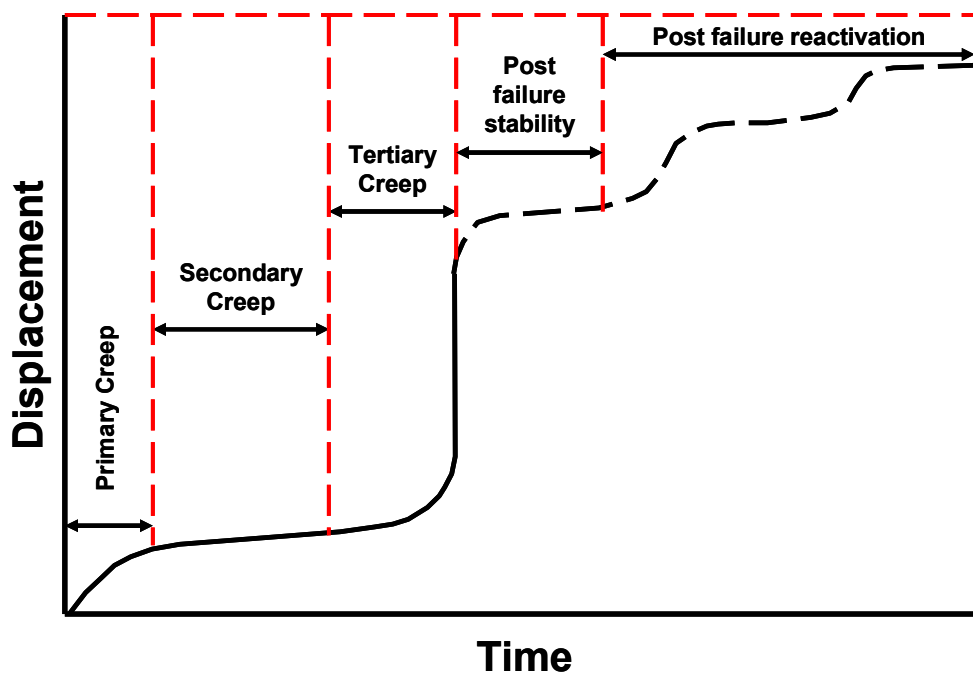


Figure 7.1 Concept of progressive landslide development and post failure creep (adapted from Varnes, 1978; Petley and Allison, 2006)

The specialist testing results are analysed to assess the mechanisms of shear surface development in different materials, in relation in particular to the phases of creep previously observed by Varnes (1978) (Section 7.2 – 7.5). The patterns observed in the laboratory are calibrated with landslide

monitoring data to evaluate the relationships between shear surface processes and surface movement patterns. The stages of shear surface development are considered in relation to the undrained peak and residual strength failure envelope (Section 7.6, 7.7), in order to determine the role of mechanical parameters in controlling the stability of a slope (Section 7.8).

The PPR test results are used as the basis to propose mechanisms for the progressive development of shear surfaces, from the onset of movement through failure to post-failure behaviour (Section 7.8). These progressive mechanisms of shear surface development explain the phenomenon of 'Saito linearity' and are used to evaluate previously published models of progressive landslide development (Section 7.9).

The results of the study provide new insight in to the present and potential future behaviour of the Ventnor landslide complex (Section 7.10) and form the basis of an improved model for the progressive development and post failure behaviour of deep-seated landslides in over-consolidated clays (Section 7.11). The implications of this new knowledge for the understanding of rainfall and groundwater induced landslide development are then discussed (Section 7.12).

7.2 Pre-failure displacement patterns in intact materials

The initiation of movement in landslides was identified by Varnes (1978) as a period of Primary creep. This pre-failure behaviour had previously been observed in laboratory testing on intact Hanley Clay samples (Campanella and Vaid, 1974). In these examples, Primary creep was characterised by an initially high displacement rate which decelerated through time to a constant or near constant displacement rate.

Primary creep movement patterns have, thus far, been difficult to confirm from the monitoring of real landslide systems although this is not surprising given that monitoring is usually started after initial movement has occurred. In the case of the New Tredegar landslide for example, initial displacement rates in the monitoring records show an almost linear increase in displacement

through time, suggesting an initial increase in displacement rate (velocity) to an almost constant displacement rate without deceleration (Fig 7.2a). Analysis of this phase of movement (Carey *et al.*, 2007) in $1/v$ - t spaces reveals an asymptotic trend (Fig 7.2b).

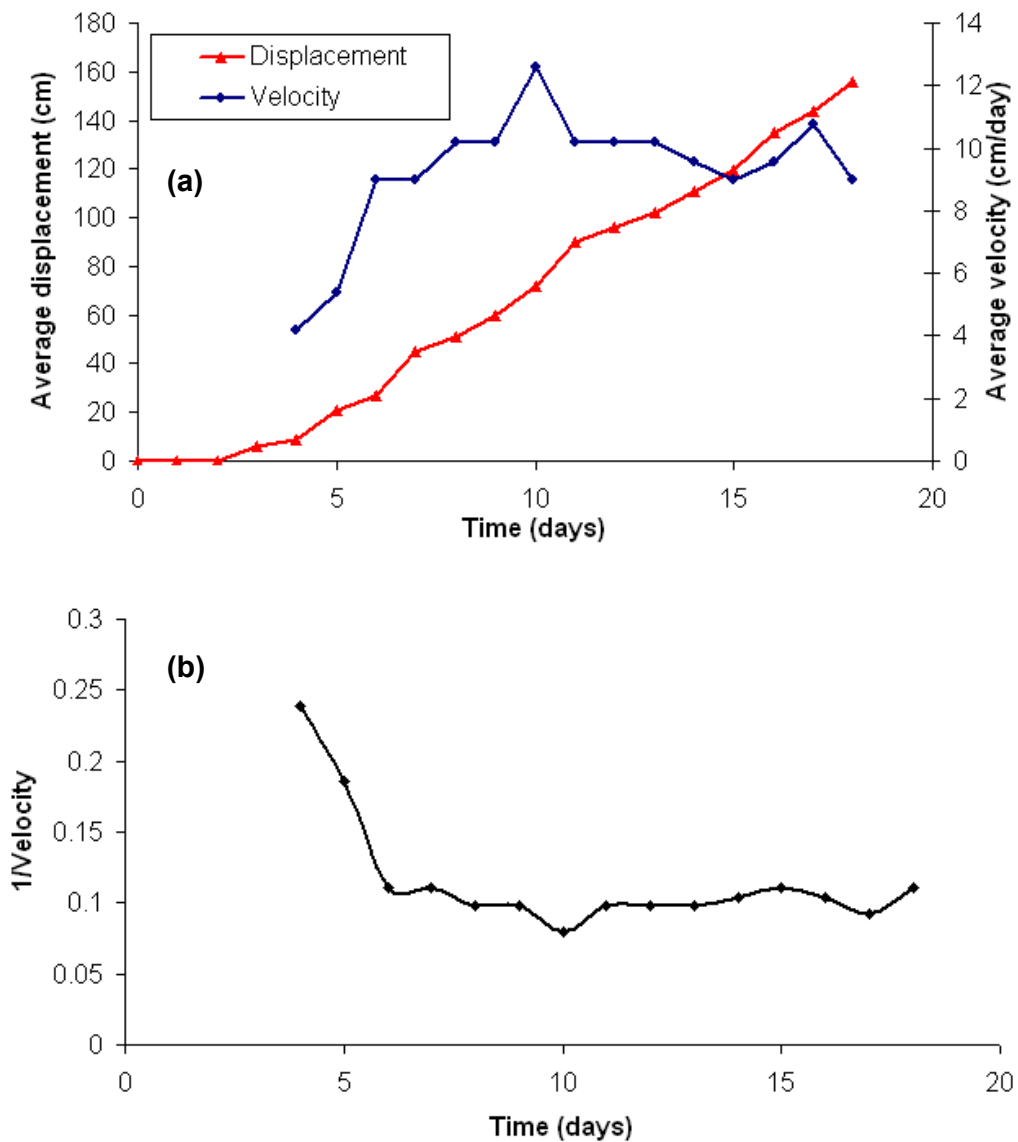


Figure 7.2 Potential Primary creep New Tredegar Landslide (a) Displacement and displacement rate (b) $1/v$ - t space (after Carey *et al.*, 2007).

Similarly, analysis of ICD PPR testing on intact Gault samples does not provide clear evidence for a Primary phase of creep during the initiation of displacement. The onset of movement is characterised by dilative behaviour as sample volume increases (Fig 7.3a) and as back volume decreases (Fig 7.3b).

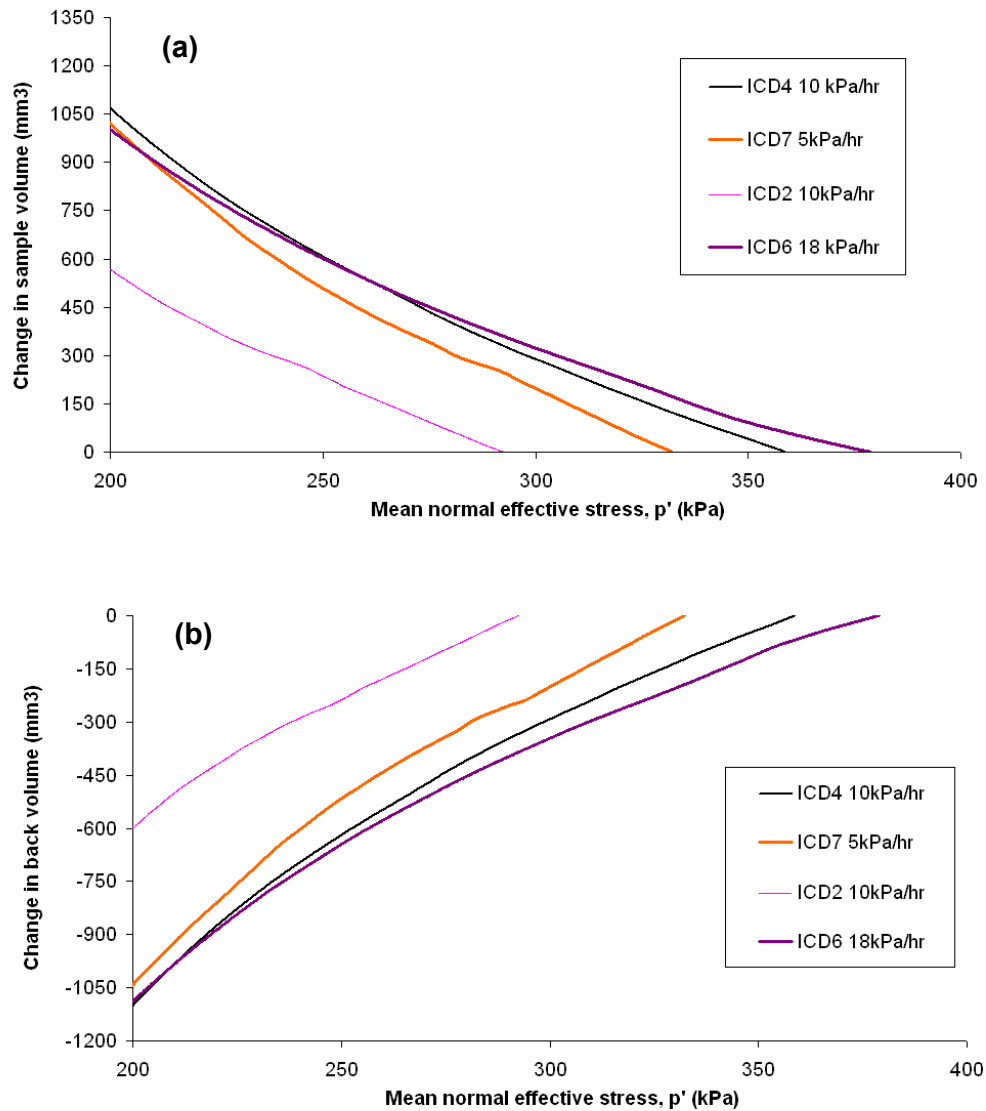


Figure 7.3 Initiation of displacement in intact Gault ICD PPR tests (a) Change in sample volume plotted against p' (b) Change in back volume plotted against p'

Displacement rate during this period demonstrates a near linear increase with reducing mean effective stress, for all the intact Gault Clay samples (Fig 7.4a). The displacement rate has a distinctive fluctuating pattern, characterised by a series of large asymptotic trends in $1/\text{velocity} - p'$ space (Fig 7.4b). This fluctuation in displacement rate suggests movement initiation occurs at very low displacement rates through a 'stick-slip' process (Allison and Brunsten, 1990).

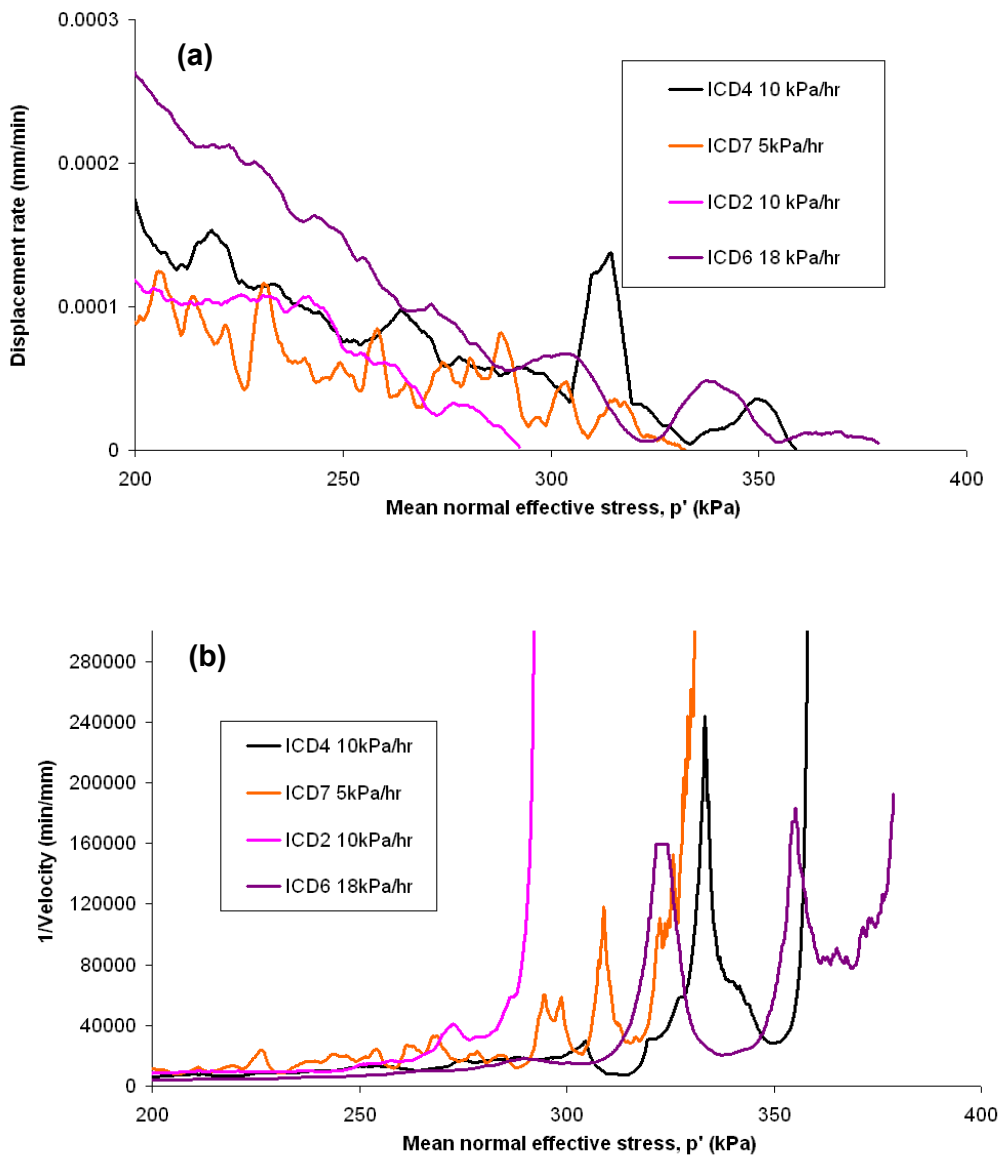


Figure 7.4 Initiation of displacement in intact Gault ICD PPR tests (a)

Displacement rate – p' (b) $1/V - p'$

The patterns of deformation recorded in laboratory testing are consistent with the surface movement patterns of landslides at very low displacement rates. Landslide monitoring records collected by Vibert and Arnould (1987) from the La Clapiere landslide, Saint-Etienne-de-Tinee, France, demonstrates short term variability in displacement rates at very low movement rates, which plots as large asymptotic trends in $1/v - t$ space. Similarly, monitoring records of rock fracturing obtained prior to rockfalls (Monma, *et al.*, 1987) illustrate a period of short term increases in displacement rate followed by long periods where very low or no displacement is observed.

PPR testing on the Gault-Carstone transition zone material using the BPSB illustrates a similar behaviour, with a linear increase in displacement rate corresponding to a linear reduction in back volume and increased sample volume (Fig 7.5a and 7.5b). The sample volume remains relatively unchanged during this phase of deformation, although the increase in sample volume toward the end of this stage relates to increases in the rate of deformation (Fig 7.5a).

Analysis of this behaviour in $1/v - p'$ space demonstrates a clear asymptotic trend with reducing mean effective stress (Fig 7.6), consistent with the movement observations at New Tredegar (Fig 7.6). In this initial phase, linear movement is consistent with previous PPR testing results in which linear deformation has been successfully linked to increasing sample void ratio (Ng, 2007). This dilative behaviour was interpreted as 'push and climb' deformation associated with inter-particle movements within the residual soils at very low displacement rates (Ng and Petley, 2007).

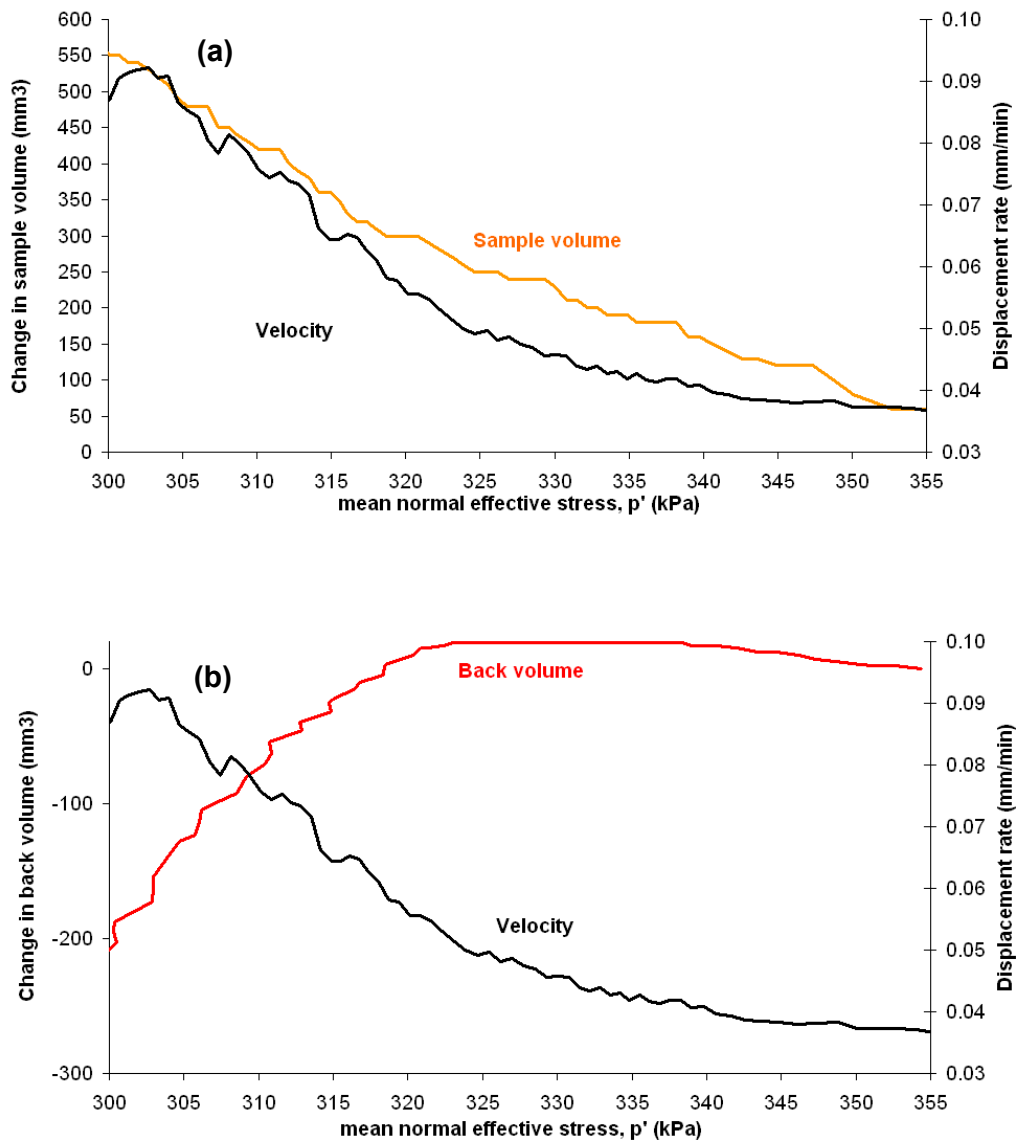


Figure 7.5 Initial deformation of intact Gault Carstone transition BPSB test (a) Sample volume and displacement rate – p' (b) Change in back volume and displacement rate – p'

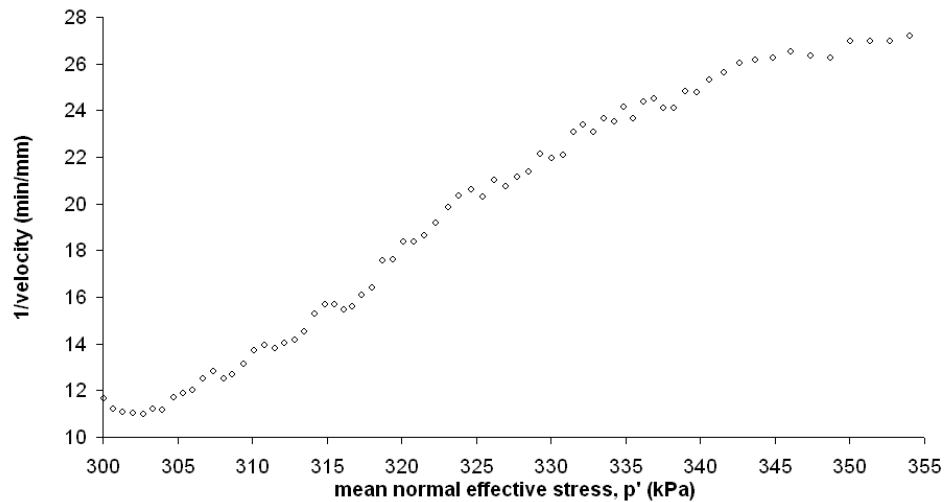


Figure 7.6 initial deformation of intact Gault Carstone transition BPSB test in $1/v - p'$ space

The PPR testing on intact samples demonstrates that the initial dilative behaviour observed in both the Gault Clay and the Gault-Carstone transition zones are not characteristic of Primary creep. This is in keeping with movement observations for landslides (Carey *et al.*, 2007; Reid *et al.*, 2008). Given that Primary creep is hypothesised as a period of strain hardening (Petley and Allison, 2006) which occurs at very low initial displacement rates it is plausible that such a phase of creep occurred during the earlier initial shear stage. At these low displacement rates it is very unlikely that standard landslide monitoring practices (e.g. daily marker surveys, inclinometer measurements, crackmeter measurements) would have been installed in sufficient time to provide accurate records of this movement phase. Landslide monitoring records generally start after significant deformation (e.g. tension crack development, ground settlement) has occurred at a given site, in which case Primary creep would not be detected. In the case of New Tredegar, site monitoring commenced following a ground movement event (Knox, 1927; Bentley and Siddle, 2000) and as a consequence the monitoring records available are unlikely to provide evidence of the Primary creep phase. The results demonstrate the need for full scale landslide simulation in natural slopes to understand the mechanisms controlling this phase of movement.

Previous studies, in which failures have been deliberately triggered, in instrumented slopes, through controlled increases in pore pressure (e.g. Cooper *et al.*, 1989) have provided a remarkable insight into the development of failure and would provide new knowledge of the mechanisms of Primary creep.

This initial phase of observed movement is, however, consistent with the early phase of Secondary creep, which is characterised by a period of purely plastic deformation at a near constant but slightly increasing rate of displacement (Varnes, 1978). The onset of Secondary deformation has been argued to represent a period in which strain hardening and strain softening processes are in approximate balance (Petley and Allison 2006). The PPR results, however, demonstrate this may occur as a progressive change in dominance from hardening to softening processes.

Similar behaviour has been observed in landslide monitoring records as a series of stepped accelerations (Fig 7.7a). These steps in displacement lead to a fluctuating pattern of asymptotic movements in $1/v - t$ space (Fig 7.7b) consistent with the PPR tests in intact Gault Clay samples.

Following the initial period of linear acceleration, the Gault-Carstone transition zone material develops a stepped change in displacement rate that correlates with a distinct decrease in back volume (Fig 7.8a) and increasing sample volume (Fig 7.8b). This illustrates that sample is dilating as the mean effective stress continues to reduce. This demonstrates that the mechanism of shear surface development during the phase of creep is related to dilation, as progressive deformation occurs within the shear zone. This shows a distinct change from the micro-cracking process observed in the Gault Clay samples. As a consequence a series of asymptotic trends in $1/v - t$ are observed (Fig 7.9).

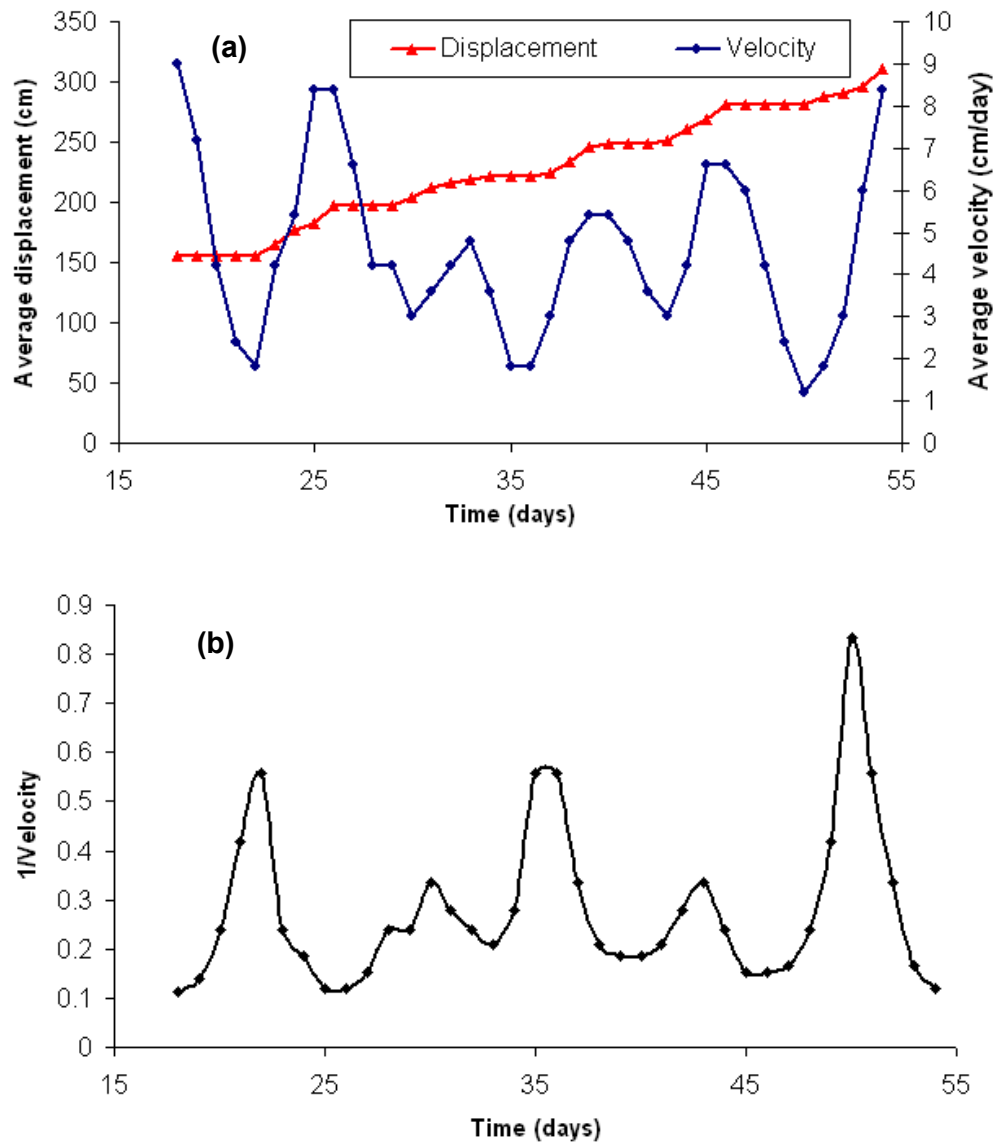


Figure 7.7 Secondary creep, New Tredegar (a) average displacement and displacement rate (b) 1/velocity against time

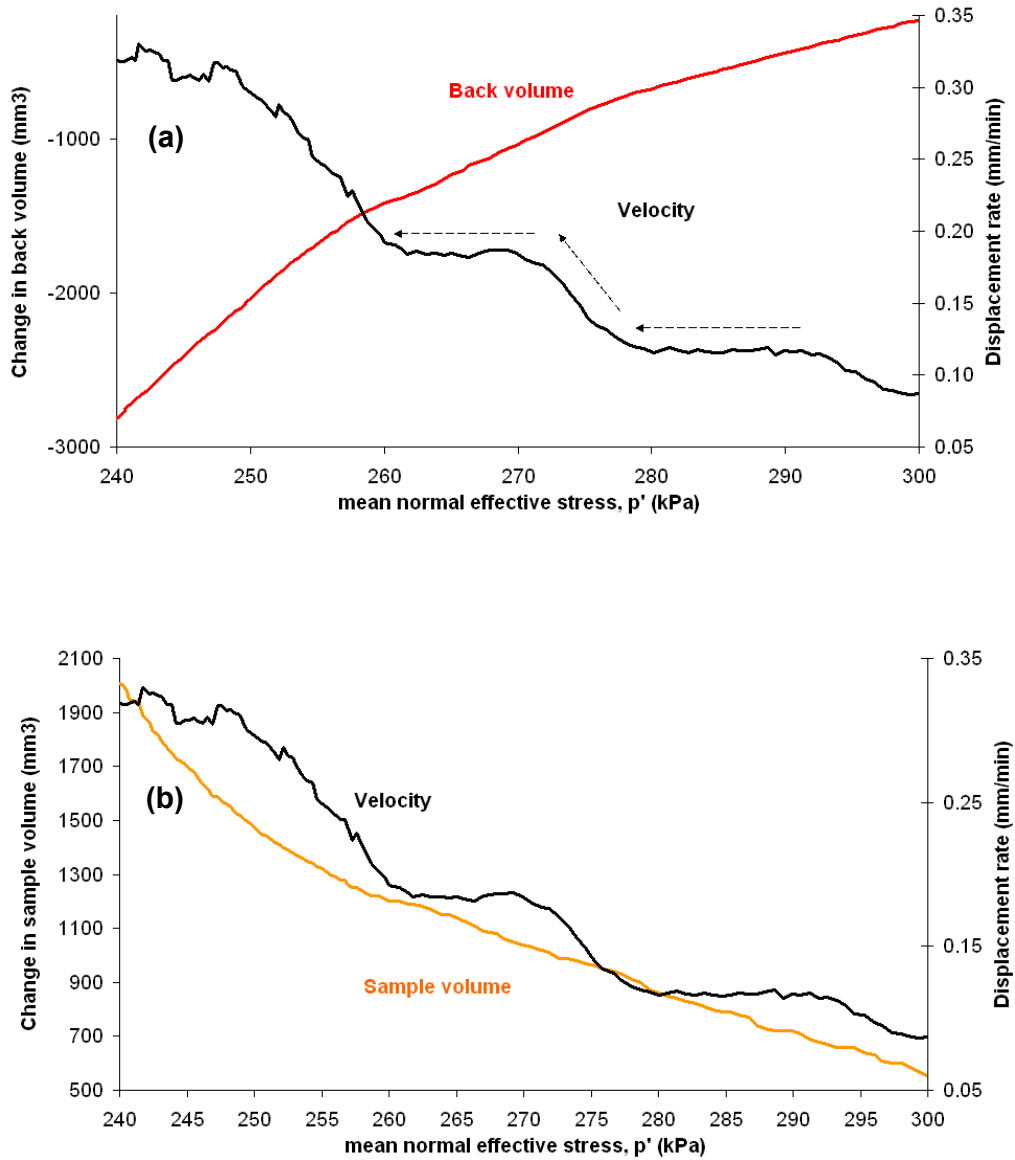


Figure 7.8 Deformation of intact Gault Carstone transition BPSB test (a) displacement rate and back volume against p' (b) displacement rate and sample volume against p'

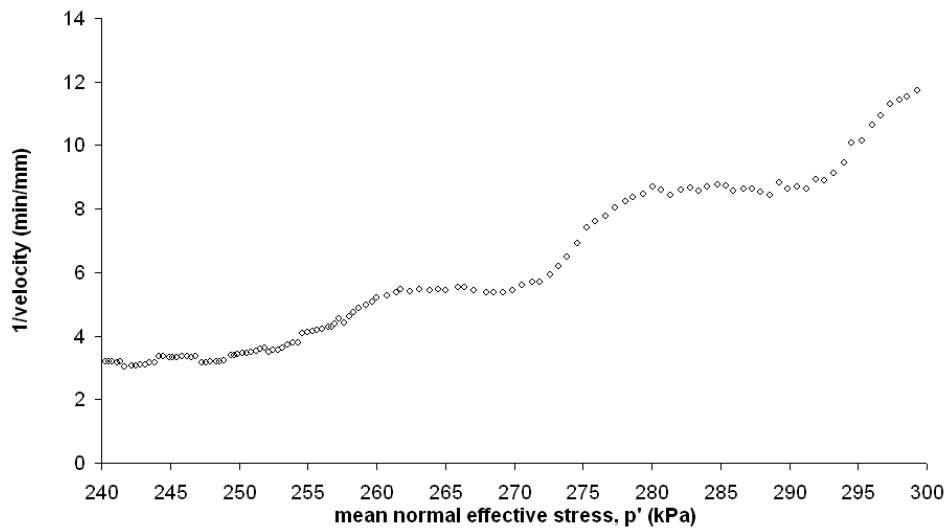


Figure 7.9 Deformation of Gault- Carstone transition BPSB test in $1/v - p'$ space

Similar stepped increases in strain have been observed by Ng (2007), who related this phase of displacement to localised sliding between particles within the shear zone. These patterns of behaviour have been observed in landslides such as 'graded movements' in Wealden Clay mudslides on the Dorset coast (Allison and Brunsden, 1990) and Tessina, northern Italy (Petley *et al.*, 2005c). In the case of these landslides these patterns of movement have been associated with purely plastic deformation under variable pore pressure and associated soil permeability. This type of movement, however, is also consistent with crack widening and crack coalescence behaviour in intact over-consolidated clay samples (Kilburn and Petley, 2003) as observed at New Tredegar.

The stepped increase in displacement rate with reducing mean effective stress in intact materials is likely to represent a later phase of Secondary creep, associated with the development and widening of micro-cracks within the shear zone. Whilst this process is likely to be occurring in both the intact Gault and Gault-Carstone transition material, it is clear that this process is occurring to a larger extent in the transition material, in which lower cohesion but higher frictional strength has been observed.

7.3 Pre-failure behaviour in remoulded materials

Remoulded Gault samples show similar dilative behaviour during PPR testing. Initial displacements correspond with increasing sample volume (Fig 7.10a) / decreasing back volume (Fig 7.10b) as the mean effective stress is reduced.

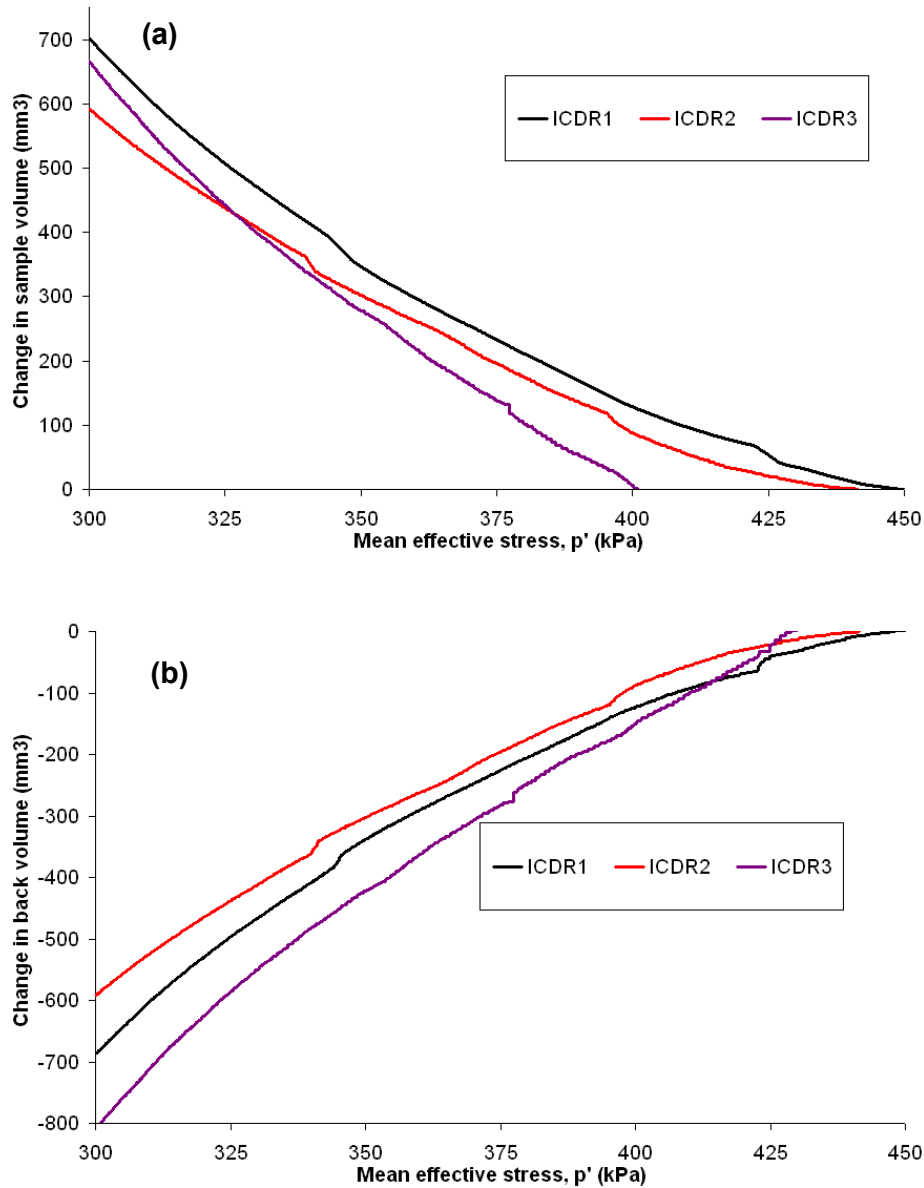


Figure 7.10 Initial displacements in remoulded Gault ICD PPR tests (a) change in sample volume against p' (b) change in back volume against p'

The samples demonstrate different patterns in displacement rate during this period (Fig 7.15a). Displacement rates in the remoulded samples increase

with decreasing mean effective stress, demonstrating a smooth exponential curve (Fig 7.11a). This can be plotted as an asymptotic trend in $1/\text{velocity} - p'$ space (Fig 7.11b), consistent with the ductile or plastic deformation experienced in non-cohesive materials (Ng, 2007).

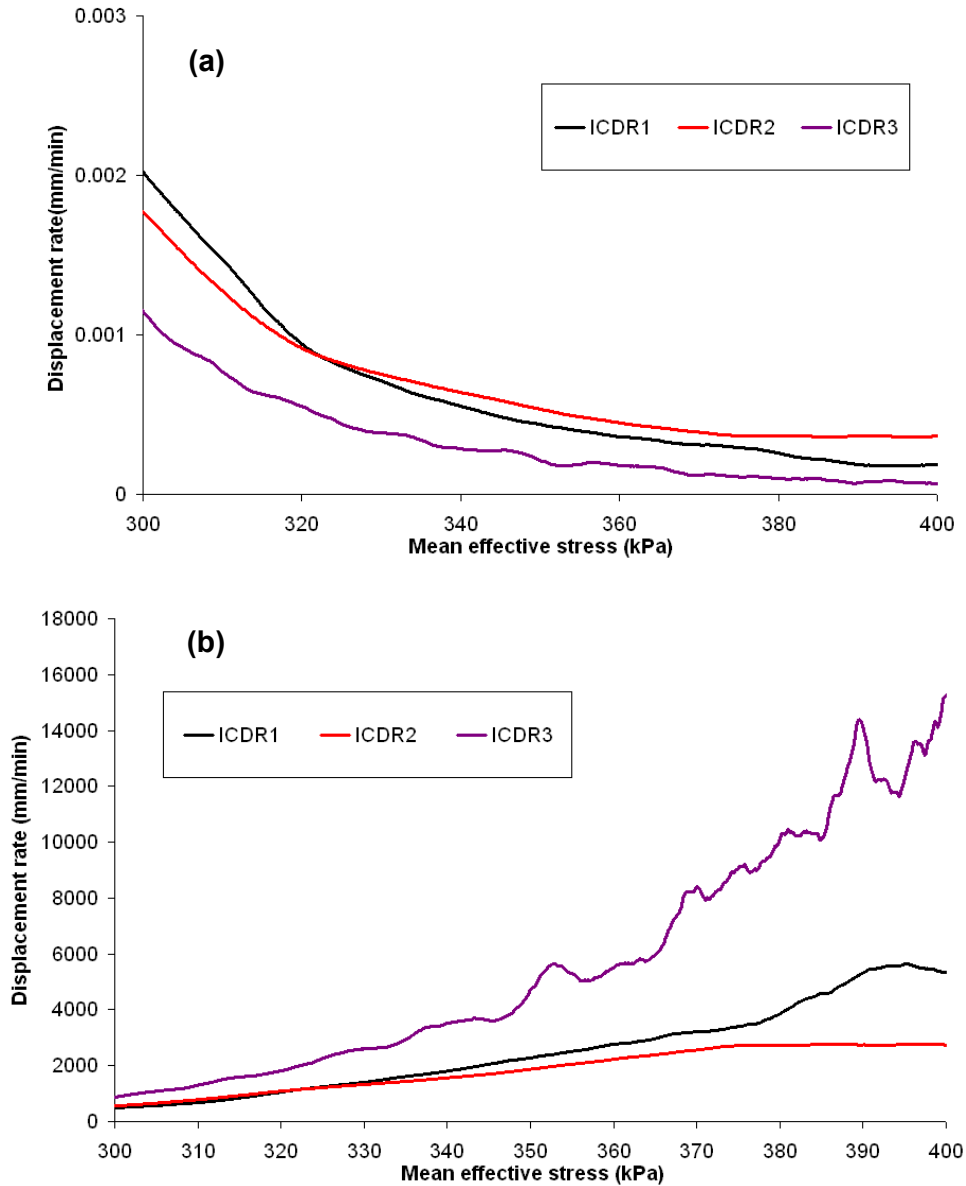


Figure 7.11 Initiation of displacement in remoulded Gault ICD PPR tests (a) Displacement rate against p' (b) $1/v - p'$ space

7.4 Acceleration to final failure in intact materials

Tertiary creep occurs as the mean effective stress continues to reduce in the sample. During this phase displacement rates begin to develop rapidly until a hyperbolic acceleration occurs, often from low strain rates. This type of acceleration to failure has been linked to the final development of a singular shear surface in landslides and can occur rapidly as stress concentrates along a very thin shear zone (Main, 2000), as shown at New Tredegar (Fig 7.12a). This hyperbolic acceleration to failure is characterised by a negative linear trend in $1/v - t$ space (Fig 7.12b), the so-called 'Saito linearity'.

The Tertiary creep phase observed in the intact Gault Clay samples develops through continued sample dilation, as illustrated by the rapid reduction in back volume (Fig 7.13a) and corresponding increase in sample volume to failure (Fig 7.13b). During this phase the displacement rates show a clear hyperbolic acceleration to failure in the intact Gault Clay samples (Fig 7.14a). This period of deformation has been plotted in $1/v - p'$ as a series of negative linear trends (Fig 7.14b).

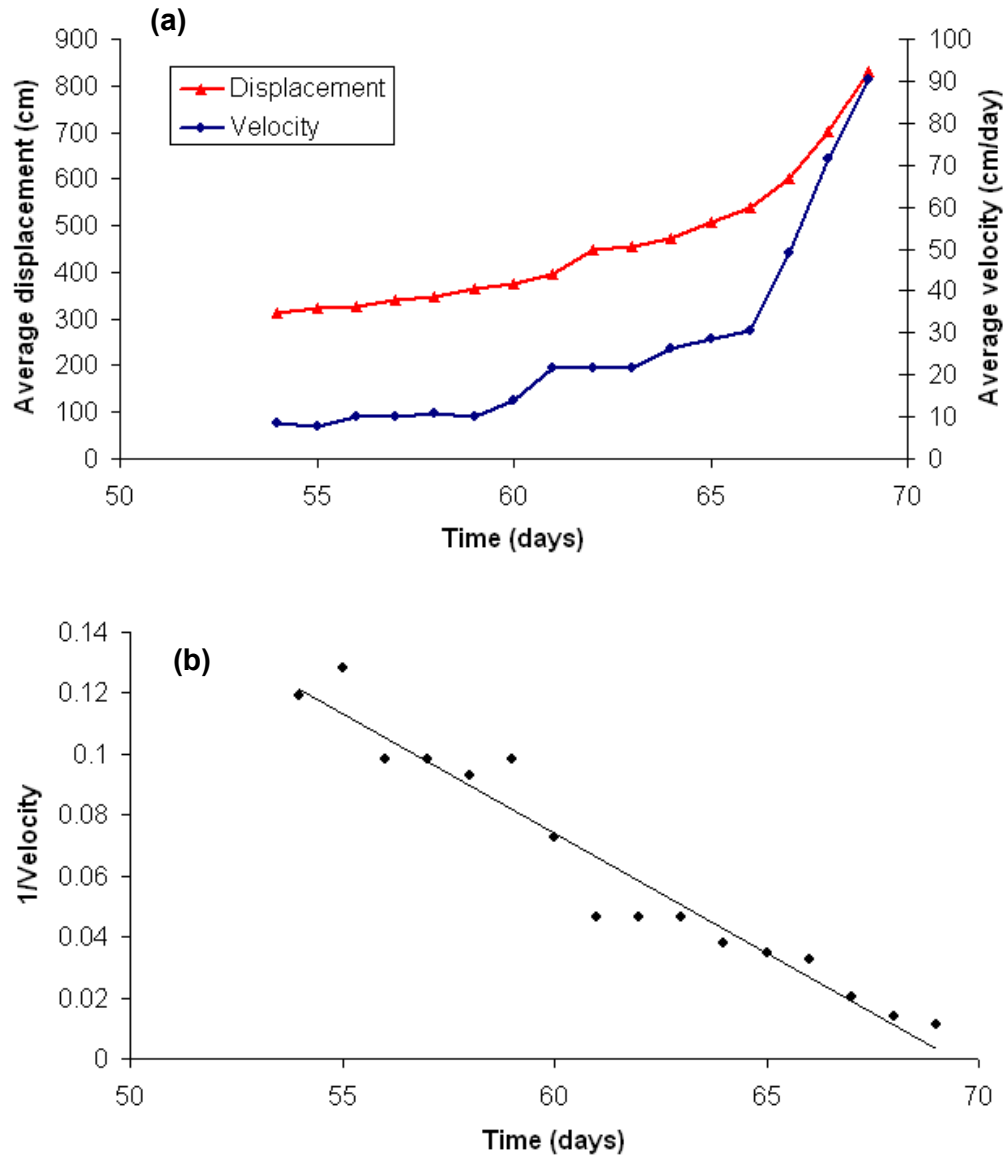


Figure 7.12 Acceleration to failure, New Tredegar (a) displacement and velocity against time (b) $1/v - t$ space

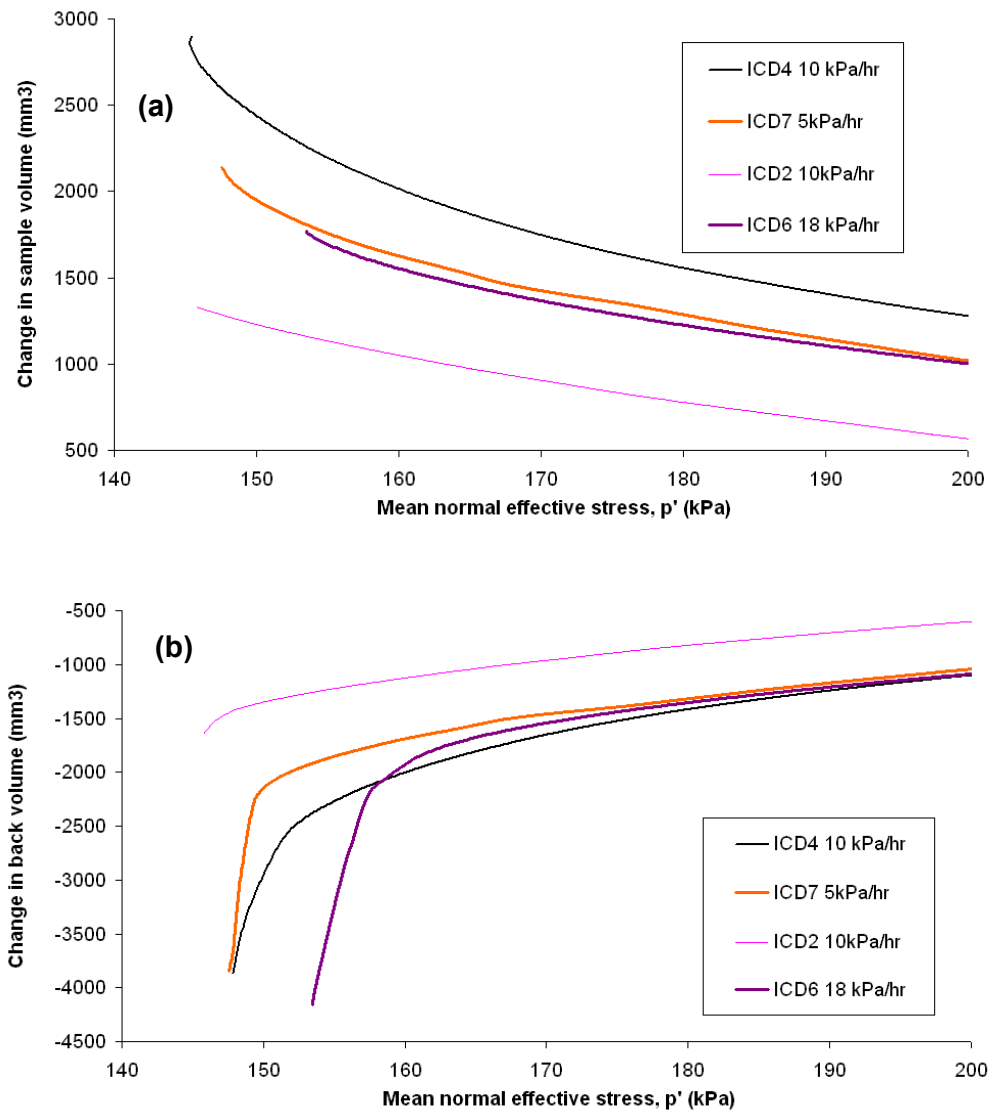


Figure 7.13 Acceleration to failure in intact Gault ICD PPR tests (a change in sample volume against p' (b) change in back volume against p'

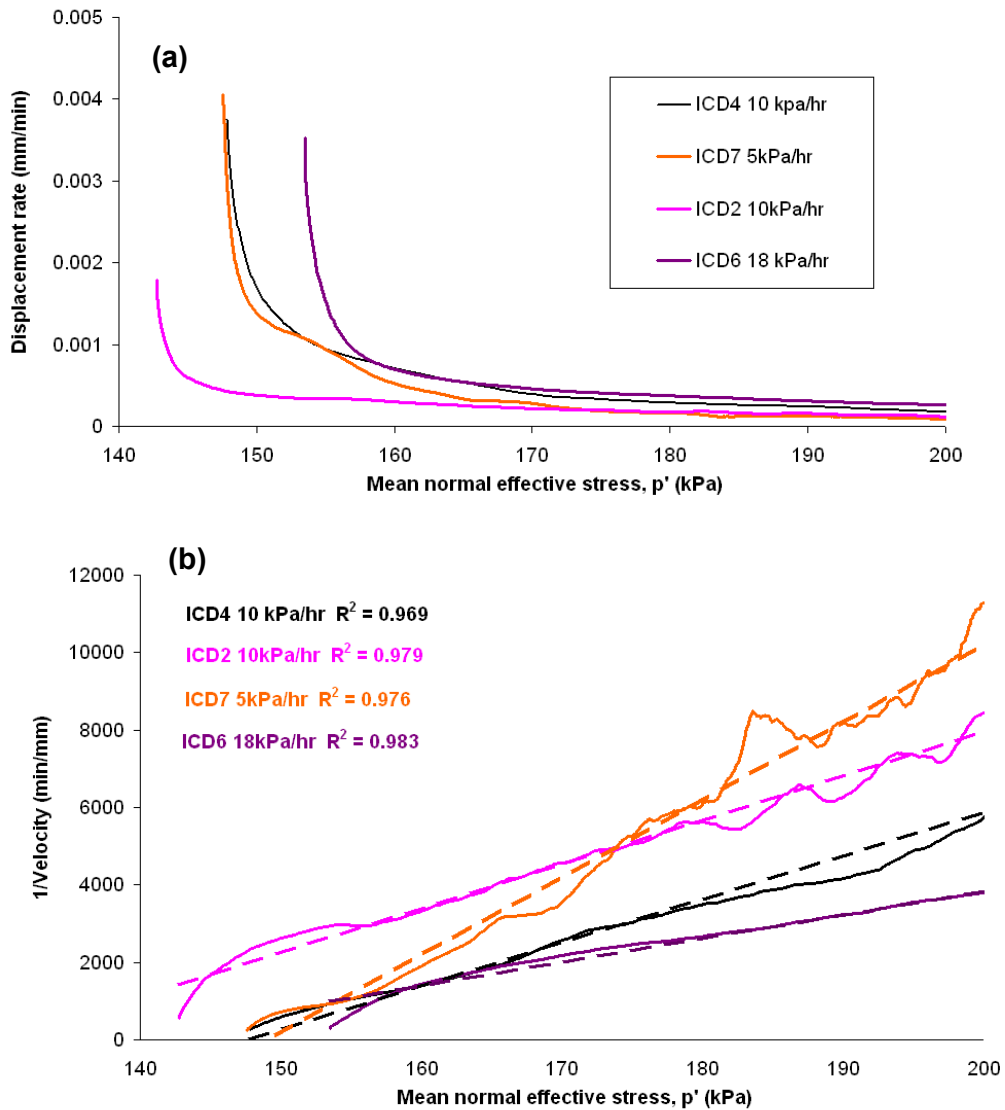


Figure 7.14 Acceleration to failure in Intact Gault ICD PPR tests (a) displacement rate against p' (b) $1/v - p'$ space

The fluctuations from the linear trend in $1/v - p'$ space suggest that the shear surface develops through a 'stick-slip' fracturing mechanism, causing minor increases and decreases in mean effective stress as the shear surface develops. This type of behaviour demonstrates a period of shear development in which micro-cracks begin to coalesce as the stresses within the material concentrate along a singular shear surface as described by Main (1999, 2000). As this occurs, the micro-cracks encounter stress concentration at the

crack tips, promoting further deformation and, as a consequence an acceleration in displacement rate. The extension and coalescence of cracks will cause a localised reduction in shear stress as dilation causes a temporary local reduction in porewater pressure. As pore pressures begin to increase again the stresses acting at the crack tips are further elevated, resulting in consequent increases in displacement rate.

The rapid increase in sample volume, and the corresponding decrease in back volume is indicative the development of a fracture developing within the sample which allows sample to displace rapidly along a single shear surface. The negative linear trend in $1/v - p'$ space (Saito linearity) during this stage therefore may indicate the development of a singular shear surface to failure in the intact Gault Clay samples.

The Tertiary creep phase for the Gault-Carstone interface occurs with a corresponding decrease in back volume (Fig 7.15a) and increase in sample volume (Fig 7.15b) consistent with the Gault. The pattern of displacement rate shows a period of constant displacement rate to a mean effective stress of 235 kPa, prior to the accelerating displacement rate to failure. Analysis of the displacement rate in $1/v - p'$ space demonstrates that a linear trend is generated at a low mean effective stress and high displacement rate (Fig 7.16). This suggests that the final development of a shear surface occurred toward the end of the test at a high strain rate after a significant period of pre-failure deformation.

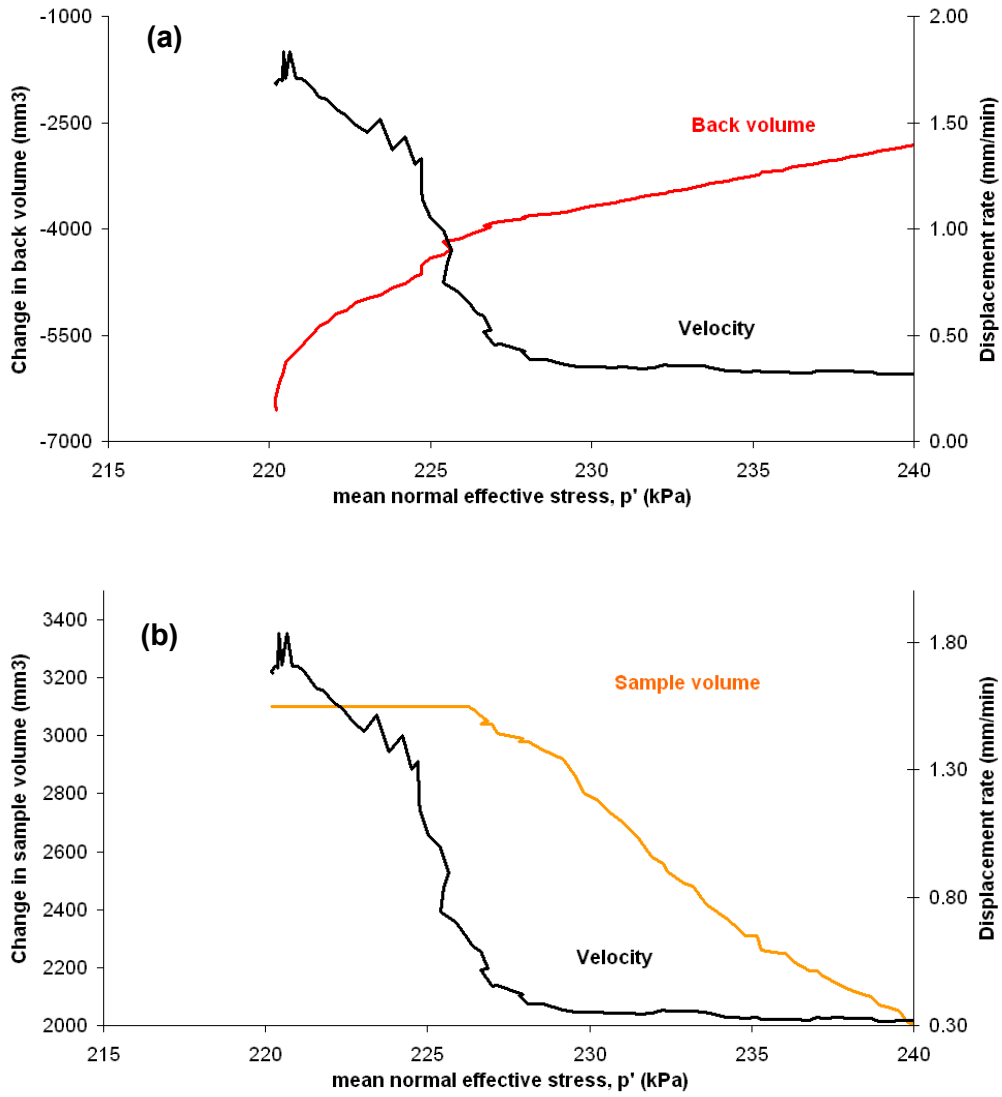


Figure 7.15 Acceleration to failure in Gault Carstone transition BPSB test (a) displacement rate and back volume against p' (b) displacement rate and sample volume against p'

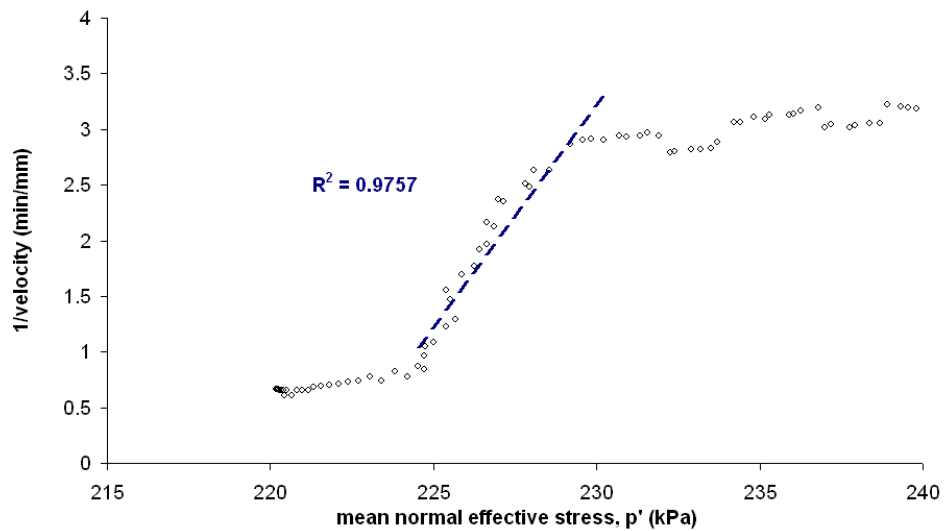


Figure 7.16 Acceleration to failure in Gault Carstone transition BPSB test in $1/v - p'$ space

7.5 Acceleration to failure in remoulded materials

As the remoulded Gault Clay samples accelerate to failure a decrease in back volume (Fig 7.17a), indicating an increase in sample volume (Fig 7.17b) is observed. This is consistent with dilative behaviour as observed by Ng and Petley (2009). During this phase of movement displacement rates accelerate exponentially (Fig 7.18a), suggesting continued strain weakening through plastic deformation. This acceleration pattern is consistent with the generalised sliding deformation mechanism observed by Ng and Petley (2009). Generalised sliding initiates as mean effective stress (p') continues to reduce through the progressive mobilisation of increased solid particles within the shear zone. These patterns of displacement rate have been observed as graded movements in pore pressure induced mudslides (e.g. Allison and Brunsden, 1996) The results confirm that failure in the remoulded Gault Clay samples occurs through ductile deformation through generalised sliding as soil particles mobilise within the shear zone. This pattern of deformation creates a distinct asymptotic trend in $1/\text{velocity} - p'$ space (Fig 7.18b).

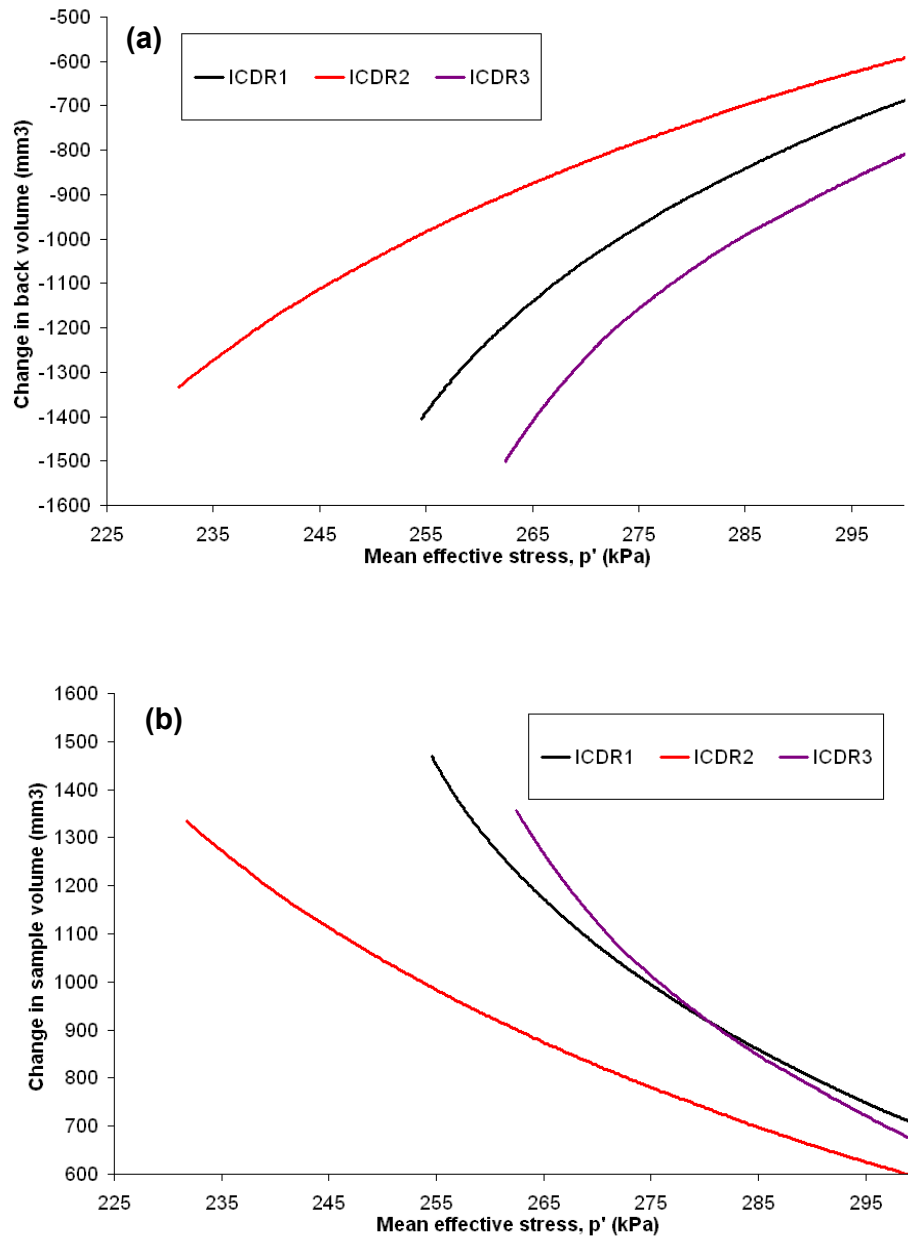


Figure 7.17 Acceleration to failure in remoulded Gault ICD PPR tests (a) change in back volume against p' (b) change in sample volume against p'

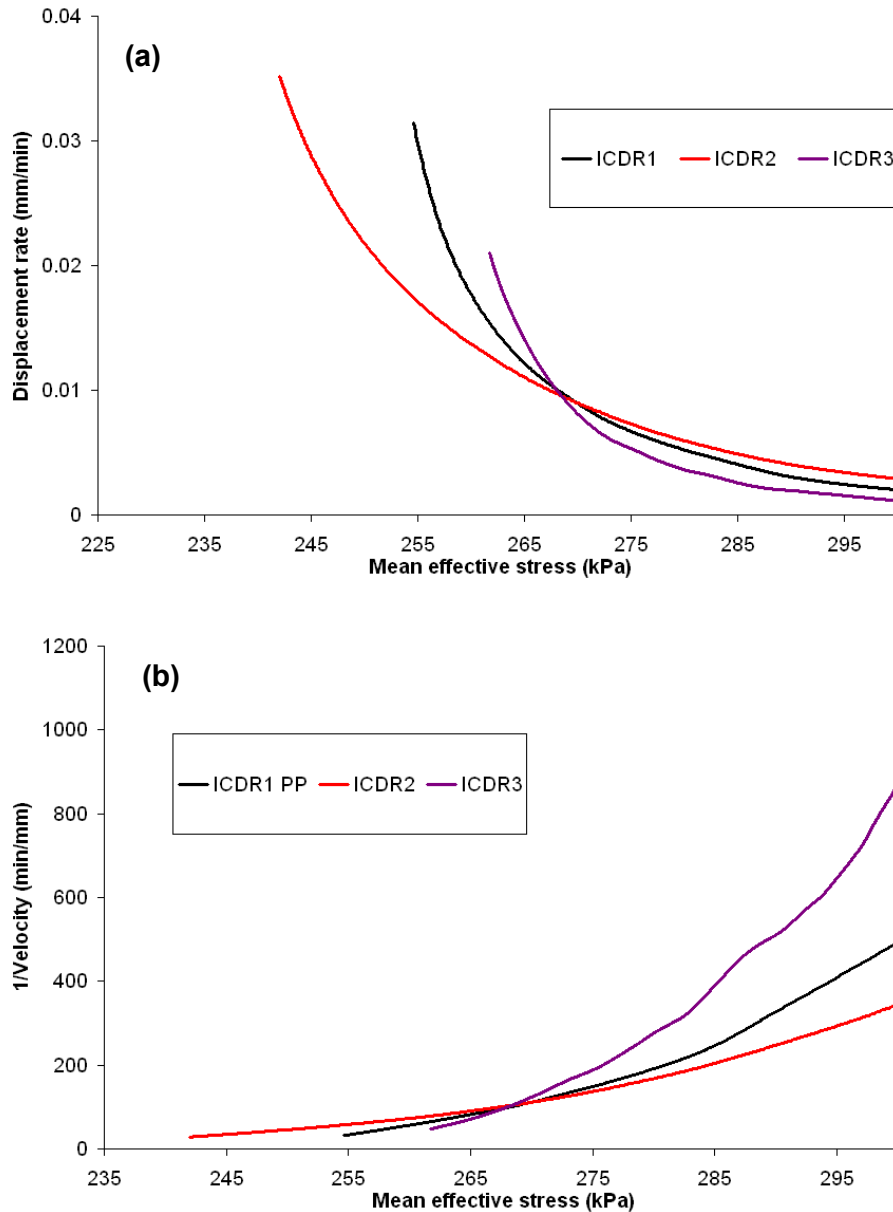


Figure 7.18 Acceleration to failure in remoulded Gault ICD PPR tests (a) displacement rate against p' (b) $1/v - p'$ space

These results are consistent with patterns of acceleration associated with ductile landslide failures where movement accelerates to a constant rate of displacement for any given effective stress state. Movement patterns, consistent with these findings, have been observed in several landslides including the Tessina landslide (Fig 2.17, Chapter 2) (Petley et al., 2005c) and mudslide accelerations on the Dorset Coast (Allison and Brunsden, 1990).

7.6 Relationship between movement patterns and failure envelopes

The results from the PPR tests confirm the mechanisms and patterns of deformation to failure in the different materials tested. The results from the intact Gault Clay tests confirmed the long established notion that intact natural stiff clays exhibit brittle shearing behaviours at low to intermediate confining pressures (Georgiannou and Burland, 2006). This behaviour results from the formation of a singular shear surface, with an associated rapid reduction in shear strength, and the subsequent displacement of a rigid block of material along this surface (e.g. Bishop *et al.*, 1965; Burland, 1990; Georgiannou and Burland, 2006).

Whilst much attention has been devoted to the strength of slip surfaces shortly after their formation (e.g. Burland, 1990; Burland *et al.*, 1996), far less attention has been placed on the initiation of slip surfaces (Georgiannou and Burland, 2006). The few studies that have been conducted have generally involved compression approaches (e.g. Drescher *et al.*, 1990) and have demonstrated the formidable experimental difficulties in the reliable detection of the onset of strain localisation (e.g. Viaggiani *et al.*, 1993). As a consequence there has been some debate over the role of peak strength in shear formation, in particular whether this represents a clearly definable strength at which point strain localisation and subsequent shear surface development occurs (e.g. Finno and Rhee, 1993). Alternatively, Burland (1990) concluded that slip surface formation was initiated close to the peak strength in stiff natural clays, suggesting that the peak shear stress is the consequence of the formation of the discontinuity, rather than the cause of it. Further studies, using undrained tests on similar materials, have concluded that strain localisation can be initiated well before peak strength at the maximum stress ratio q/p' (Viggiani *et al.*, 1993). Whilst these developments have assisted in developing a greater understanding of the mechanisms of shear surface development, the formation and growth of shear zones remains to be fully understood and may vary considerably from material to material.

The identification of pre-failure deformation patterns in the PPR testing provides an opportunity to consider how these differing patterns of

deformation relate to the undrained peak and residual strength failure envelope. The series of ICD PPR tests on intact Gault Clay samples demonstrated that the majority of samples develop final failure at a relatively consistent mean effective stress of 150 kPa for a deviator stress of 400 kPa. The variability in effective stress at final failure shown in these tests could be explained through sample variation, as identified in the consolidation and initial shear stages of testing (see Chapter 6).

Analysis of the axial strain characteristics of the intact Gault Clay samples reveals that failure does not occur at a specific strain (Fig 7.19a). The testing illustrates that, generally, samples subjected to higher initial confining pressure progress to failure from lower percentage strains than samples subjected to lower initial confining pressures, despite the fact that each test has been conducted along the same stress path ($q = 400$ kPa). This result is consistent with previous studies which concluded that samples tested from a lower initial confining pressure have a greater degree of recoverable strain or elasticity when compared with samples subjected to higher initial confining pressures (e.g. Bjerrum, 1967; Skempton, 1969). Similar analyses of samples tested under the same confining pressure conditions, but subjected to different rates of pore pressure reinflation, demonstrate no clear relationship between pre-failure strain and pore pressure reinflation rate (Fig 7.19b)

The mean effective stress at failure has been analysed in relation to the undrained peak and residual strength failure envelope calculated from ICU tests on intact Gault (see section 6.3.3). Fig 7.20a and 7.20b plot sample displacement rates against p' for intact tests undertaken at constant mean effective stress ($q = 400$ kPa). The figures demonstrate consistently that final sample failure occurs after the undrained failure envelope has been surpassed. The graphs further demonstrate that initial displacements begin at p' values below the residual strength envelope.

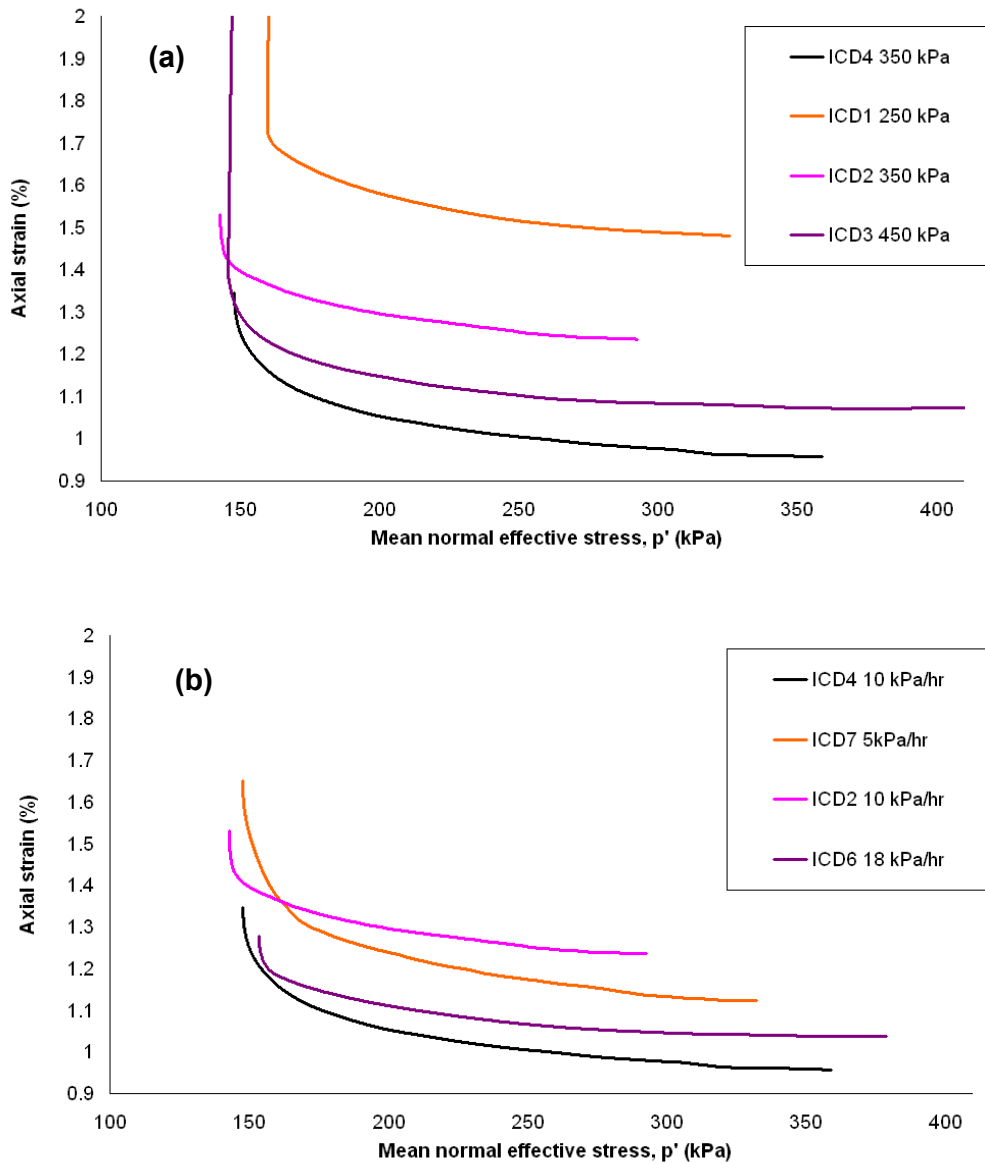


Figure 7.19 Axial strain to failure of intact Gault ICD PPR tests at 400kPa (a) undertaken at different initial confining pressures (b) undertaken at different PPR rates

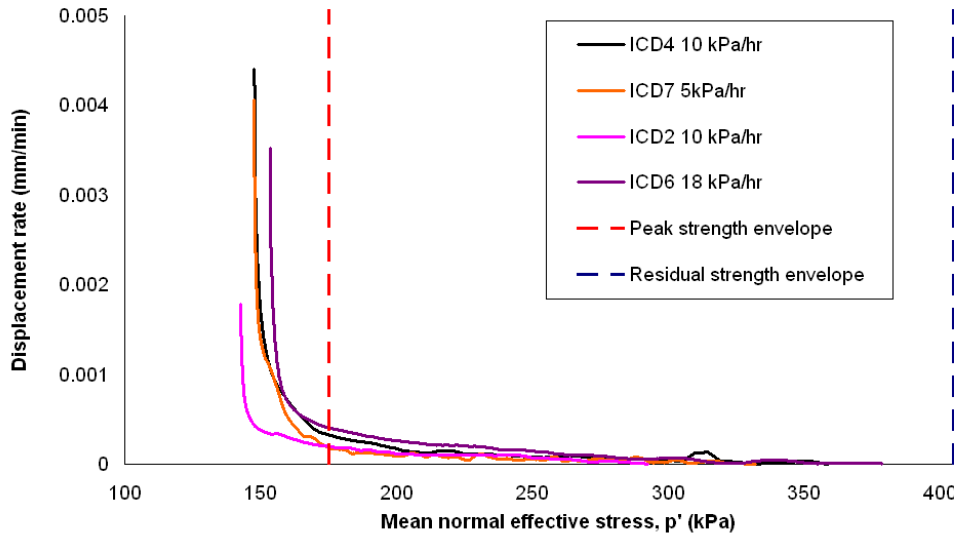


Figure 7.20 Displacement to failure of intact Gault ICD PPR tests at 400kPa in relation to the undrained failure envelopes (a) undertaken at different initial confining pressures (b) undertaken at different PPR rates

A clear relationship between sample behaviour and the peak and residual strength envelope can be shown by considering a single PPR test on intact Gault Clay (Fig 7.21). The graph demonstrates an early asymptotic trend in $1/v - p'$ space occurs at very low displacement rates as the mean effective stress continues to reduce. This occurs at p' below the residual strength envelope but significantly higher than the peak strength envelope. This period of pre-failure displacement is illustrated in $1/v - p'$ space as a distinct saw tooth pattern of deformation at a near constant displacement rate. The development of the linear trend in $1/v - p'$ space occurs during Tertiary creep and develops before the peak strength envelope is reached. In the case of over-consolidated clays the peak strength envelope would appear to represent the stage at which micro-cracks begin to coalesce to form a singular shear surface.

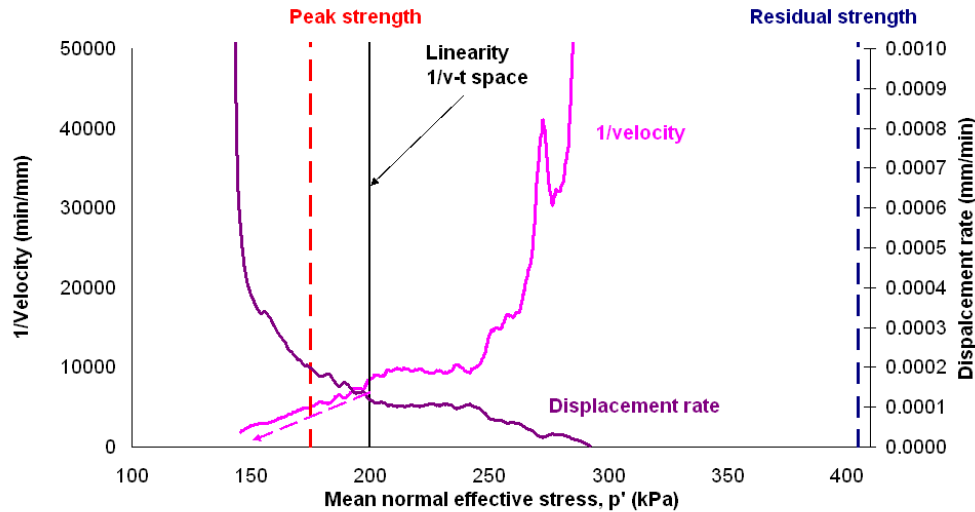


Figure 7.21 $1/v-p'$ and displacement rate against p' in relation to undrained failure envelopes, sample ICD2, PPR 10 kPa/hr, 400kPa

These patterns of movement are consistent with previous PPR laboratory tests on Foxmould samples collected from the Black Ven landslide, Dorset (Petley and Allison, 2006). Similarly, these tests demonstrated that the negative linear trend in $1/v - p'$ space developed before the peak strength envelope had been reached.

The results of this study are broadly consistent with the findings of Burland (1990) in demonstrating that the peak stress in over-consolidated Clays represents the point at which a singular shear surface develops. As a consequence, shear surface development may be initiated at or close to the peak strength envelope.

Similar analysis carried out on sample ICD9 which was undertaken at a $p' = 550$ kPa shows contrasting behaviour (Fig 7.22). In this case failure occurred at a p' value greater than the undrained peak strength failure envelope, indicating that the sample did not reach peak strength. The pattern of displacement rate to failure is clearly exponential, creating an asymptotic trend to failure in $1/v - p'$. The results may indicate that the stresses in the test were sufficiently high to prevent strain localisation along a shear surface and,

as a consequence, ductile failure occurred across a larger shear zone. Similar behaviour has been observed in mudrock failure undertaken under high stress conditions (e.g. Petley, 1999).

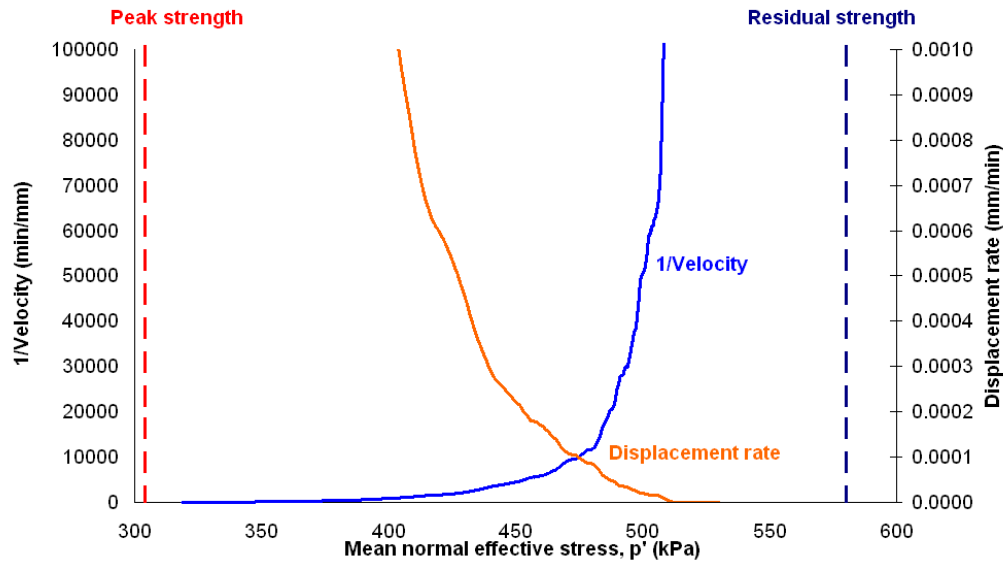


Figure 7.22 $1/v-p'$ and displacement rate against p' in relation to undrained failure envelopes, sample ICD9, PPR 10 kPa/hr, 550kPa

Results from the remoulded ICD PPR Gault Clay tests demonstrate different behaviour to the intact samples, with strain initiation occurring in the samples at significantly higher mean effective stresses (Fig 7.23a). As the mean effective stress continues to decrease the strain increases almost linearly, until an exponential acceleration in strain to failure is observed. Tests conducted at higher rates of pore pressure reinflation (in contrast), illustrate initially lower strain rates at a given mean effective stress. However, there appears to be a certain critical displacement rate at which the mean effective stress changes more rapidly in samples undertaken at a lower pore pressure reinflation rate (Figure 7.23b). This pore pressure rate dependency has been previously observed by Ng and Petley (2009) who suggested that pore pressure rate fluctuations could be more significant than the actual pore pressure level in ductile materials. It is plausible that the rate of pore pressure reinflation may be responsible for controlling strain at higher mean effective stresses, whilst the sample yield may be reached at a specific mean effective

stress, in which case acceleration occurs from a lower strain rate in samples inflated more slowly.

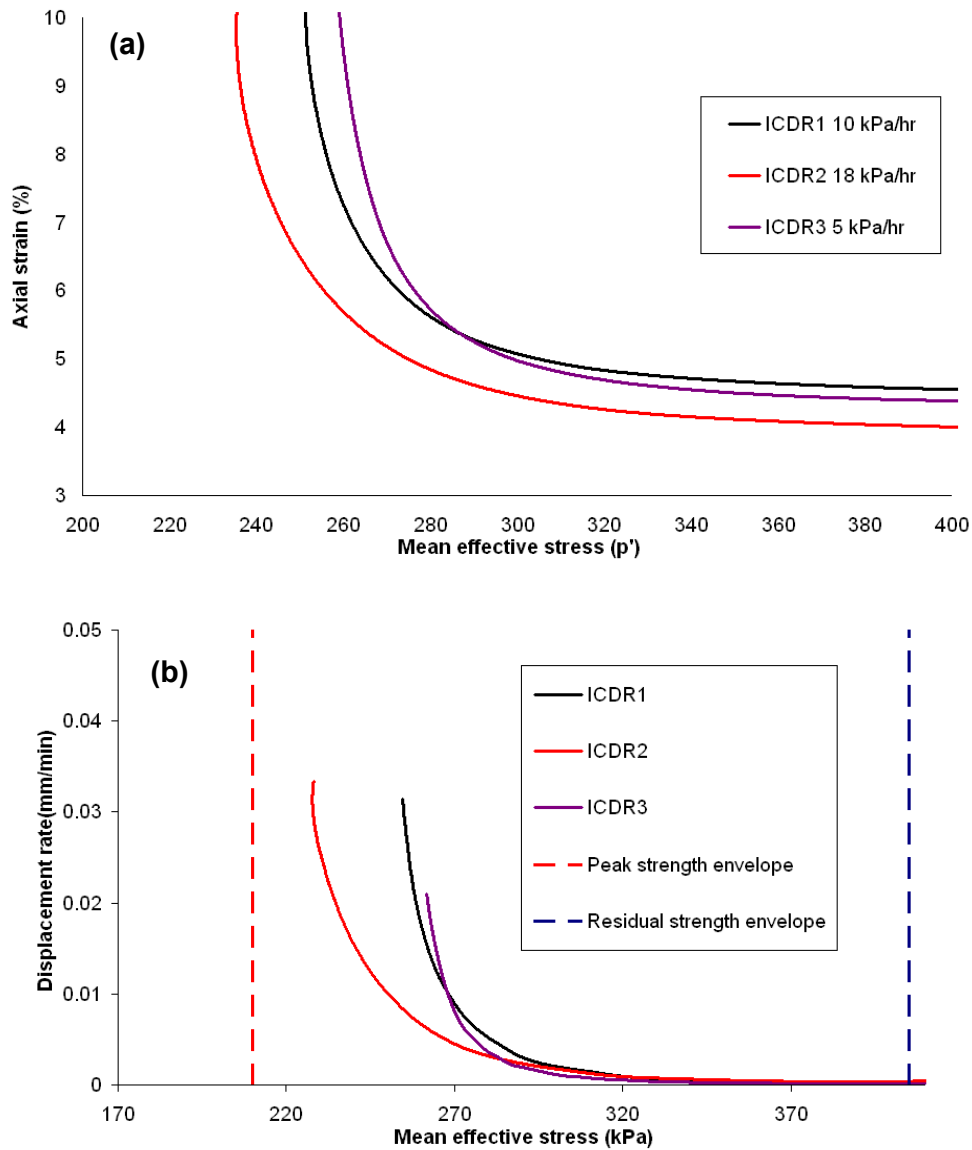


Figure 7.23 Deformation to failure in remoulded Gault PPR tests in relation to the undrained failure envelope, (a) axial strain against p' (b) displacement rate against p'

Figure 7.24 graphs the patterns of $1/v - p'$ and displacement rate against p' during the ICDR PPR test. The graph demonstrates that a distinct asymptotic trend in $1/v - p'$ space occurs from the residual strength envelope and is

associated with a critical mean effective stress at which displacement rates begin to increase. Subsequently, failure occurs before the mean effective stress reaches the peak strength envelope. The results indicate that deformation in the remoulded Gault occurs as the sample reaches the material residual strength envelope.

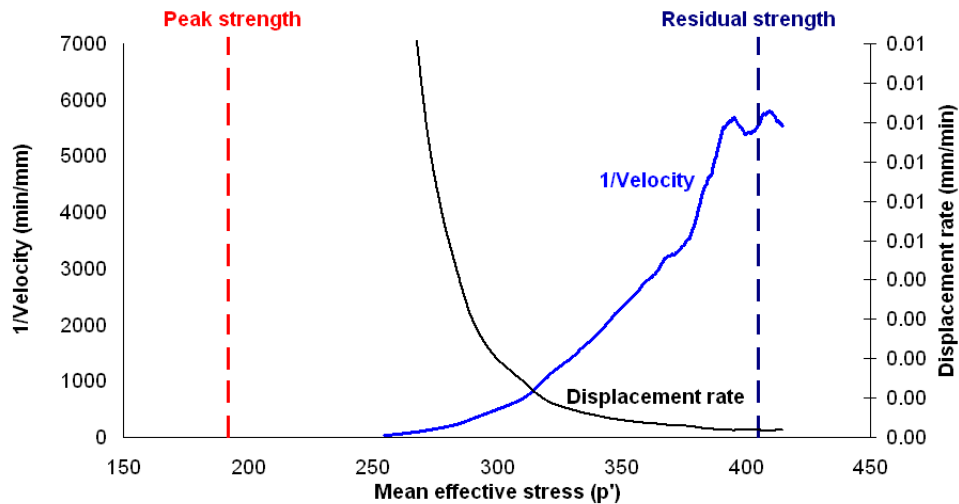


Figure 7.24 $1/v-p'$ and displacement rate against p' in relation to undrained failure envelopes, sample ICDR2, PPR 10 kPa/hr, 400kPa

7.7 Failure behaviour at constant stress – The long term creep test

The PPR testing has demonstrated the significance of mean effective stress during pore pressure reinflation in controlling the development of the shear surface in the different materials tested. It is important to note that these tests have been carried out using a linear pore pressure reinflation rate. Such a change in conditions may not replicate true landslide conditions as a continuous reduction in mean effective stress is unlikely to occur along a landside shear surface. The design of the tests could therefore mask any time dependent failure mechanisms associated with progressive shear surface development and present an artificially low mean effective stress at failure.

This study has proposed the hypothesis that brittle failure could occur at constant mean effective stress once low level creep is initiated in the sample. In this failure scenario the sample reaches a critical mean effective stress in

which pre-failure deformation is initiated and, through time, the sample will progressively displace to final failure without undergoing a change in stress. In over-consolidated clays this failure should occur through crack propagation producing a negative linear in $1/v - t$ space from a mean effective stress above the peak failure envelope.

To assess this hypothesis a long creep test has been undertaken (test ICD12). In this test the sample was subjected to the standard initial confining pressure of 350 kPa and initial drained shear of 400 kPa. The slow creep test was carried out over a period of 524 days (Fig 7.25a). As hypothesised, the test provides evidence of the development of time dependent failure, in which a hyperbolic acceleration to failure occurred without any further increase in porewater pressure (Fig 7.25b). During the final stage of the test back pressure was held constant for 81 days prior to failure, providing evidence that failure occurred at constant mean effective stress (Fig 7.25c).

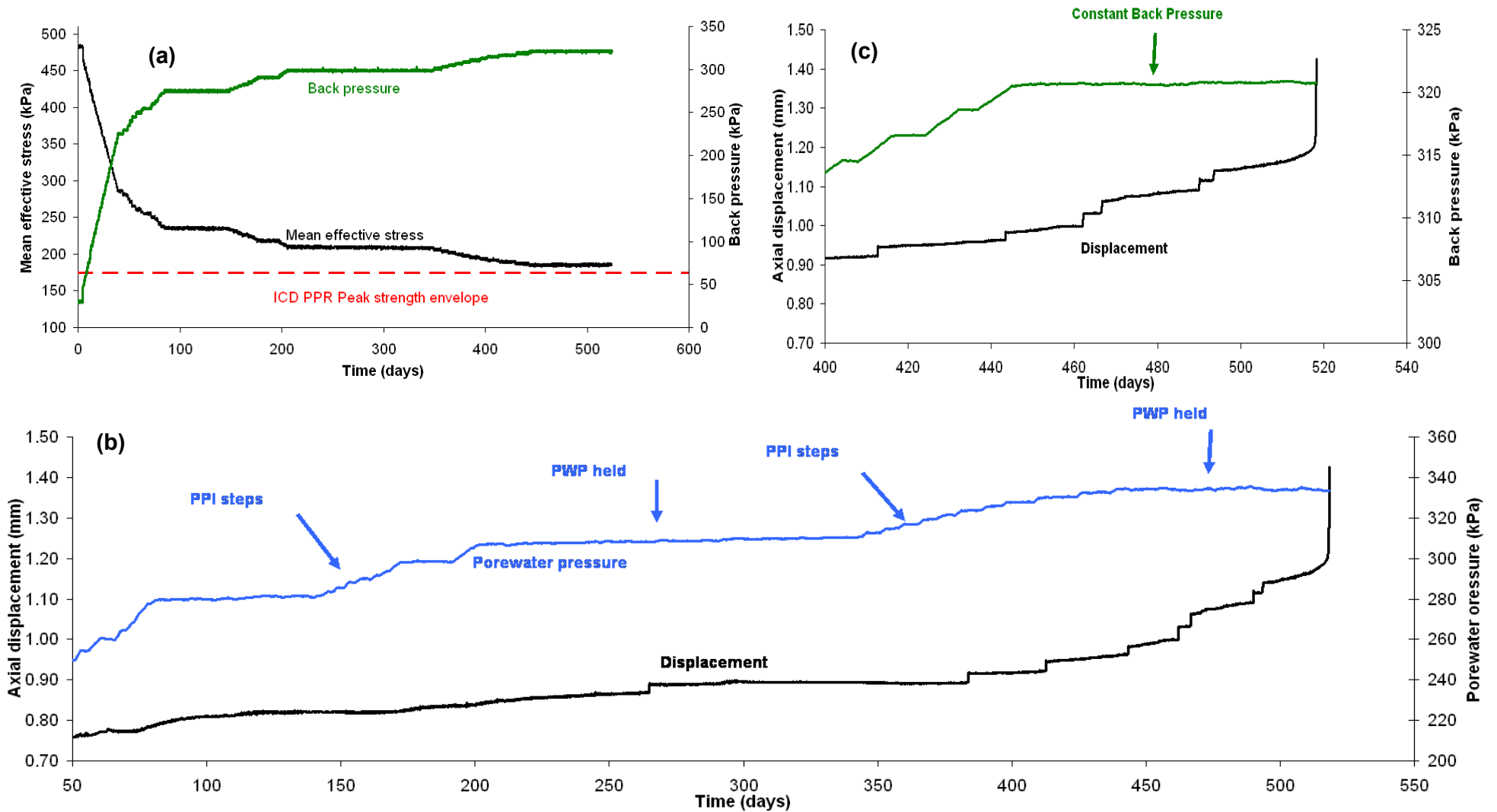


Figure 7.25 The long creep test (a) Comparison of back pressure and mean effective stress in relation to the failure envelope (b) Comparison of porewater pressure and sample displacement throughout the full test (c) Comparison of sample displacement and back pressure to failure.

Analysis of the final 81 days of the long creep test (Fig 7.26a) demonstrates that the sample accelerated to failure at constant porewater pressure, from a background of very low displacement rates. During this period the sample mean effective stress was held constant at 190 kPa whilst the sample volume continued to increase, indicating deformation was occurring at very low displacement rates (Fig 7.26b).

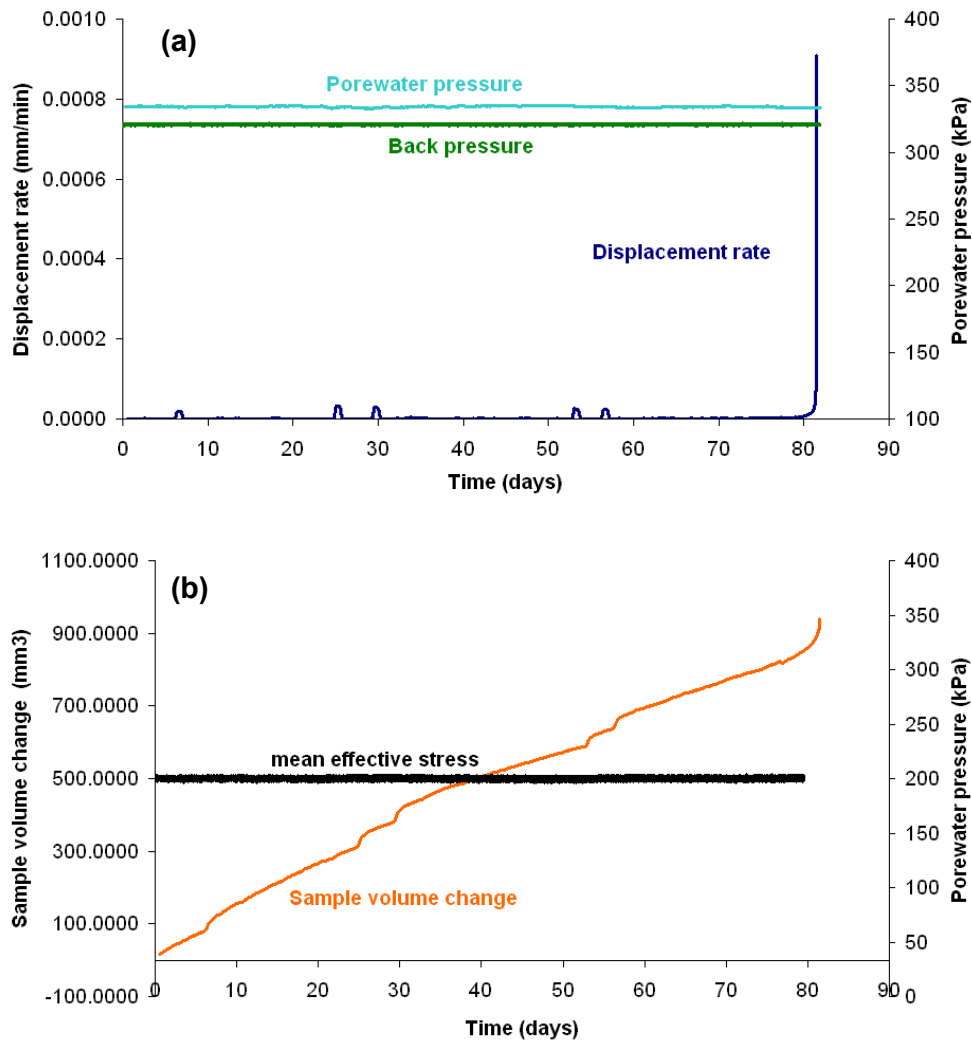


Figure 7.26 Deformation to failure during the final stage of the long creep test

(a) Comparison of displacement rate with sample porewater pressure and back pressure, (b) Comparison of change in sample volume and sample mean effective stress

The sample demonstrated dilation during deformation with an approximately constant decrease in back volume observed to failure. Interestingly though a series of steps in the back volume are observed which corresponding to period of increased displacement rates within the sample (Fig 7.27). This suggests that the sample was undergoing micro-scale crack propagation. As micro cracking develops a distinct increase in velocity is observed which corresponds to a drop in back volume. This occurs as pore pressures are locally dissipated as the sample dilates as cracking occur. This causes a rapid reduction in displacement and a decrease in back volume as the cell tries to increase porewater pressures again to sustain the PPR rate.

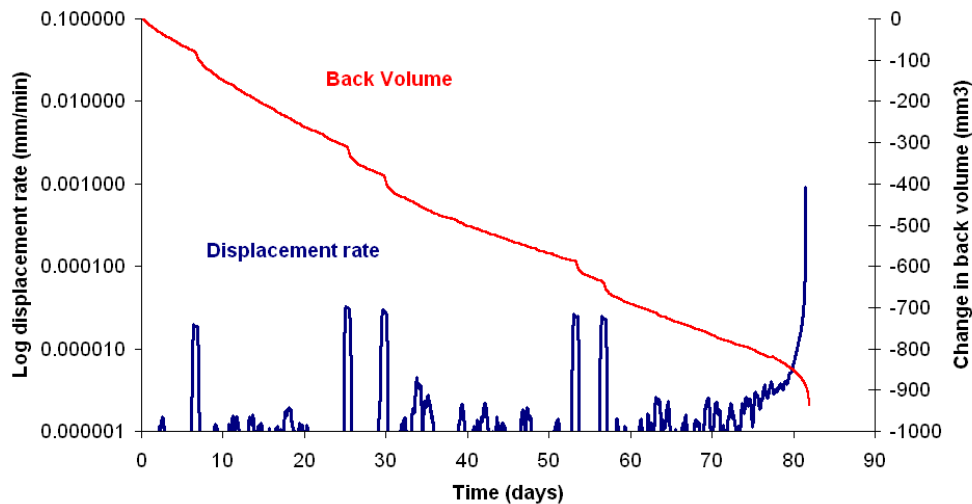


Figure 7.27 Comparison of log displacement rate and back volume during final stage of long creep test

During this final testing period, the subtle deformation rate patterns reveal an initial period of varying displacement rates phase of the final stage (Fig. 7.28). This is followed by a short period of stepped creep movement. Following this a constant creep rate is re-established, although at a higher rate of strain, which culminates in a final acceleration to failure. Minor fluctuations are observed in the displacement rate, which is mirrored by the changes in back volume. These increases and decreases in back volume indicate that the triaxial cell is pushing water in and out of the sample to maintain porewater pressure and maintain a constant p' . This provides further evidence of cracking processes operative at the shear surface which would cause the

localised pore pressure dissipation in the sample during crack growth and dilation. The displacement rate then progressively develops until acceleration to final failure is observed. This indicates the formation of a singular shear surface occurred as observed in brittle failure.

These patterns of progressive shear surface development are consistent with those confirmed in the linear pore pressure reinflation testing, suggesting that failure occurred at constant stress through brittle cracking. This is further supported by the $1/v - t$ plot (Fig 7.29) which shows the distinct saw tooth pattern of movement prior to the development of a linear trend to failure in $1/v - t$ at constant mean effective stress.

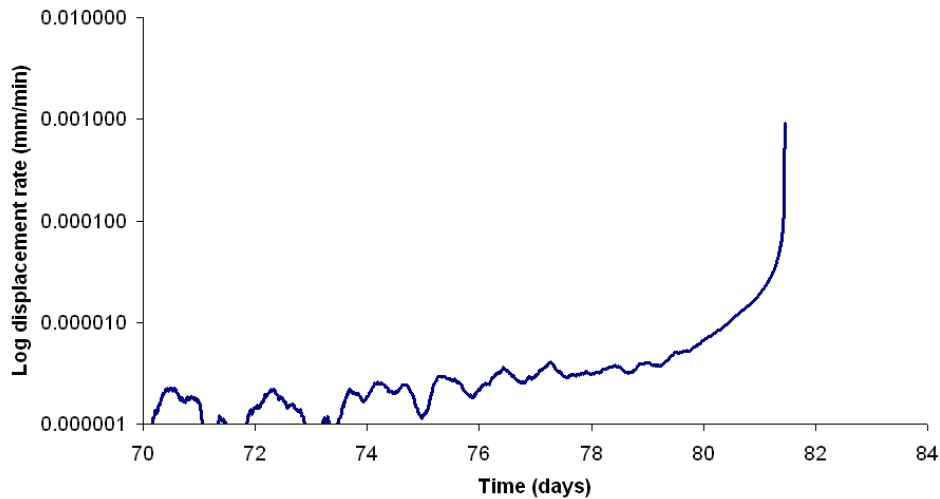


Figure 7.28 Displacement rate plotted on a log scale against time

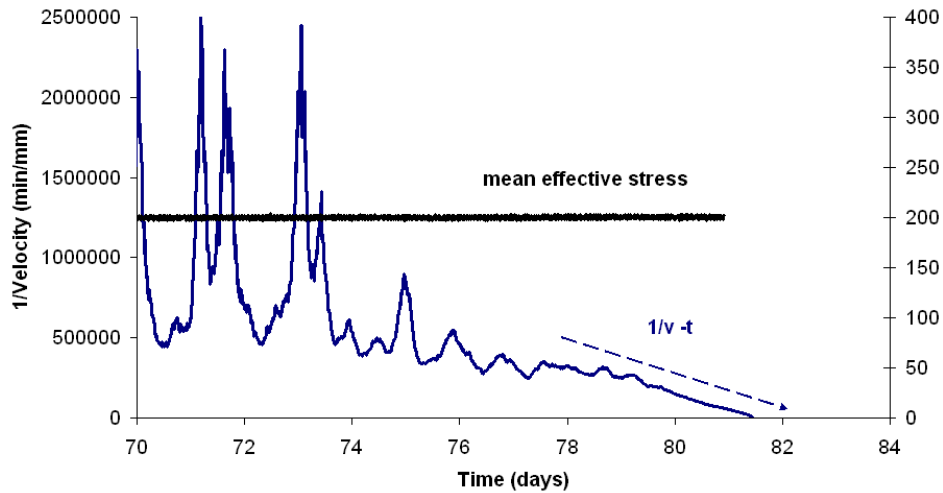


Figure 7.29 $1/v - t$ plot for the long term creep test at constant mean effective stress

Displacement rates from the intact Gault Clay samples (ICD2 and ICD4) tested under linear pore pressure reinflation at the same initial mean effective stress ($p' = 350$ kPa) and deviator stress ($q = 400$ kPa) can be compared directly to the same period of strain development in the slow creep test. This has been undertaken by normalising the time between the initiation of displacement rates and final failure at 0.1 mm/min (Fig 7.30). The assessment demonstrates clear similarities in the patterns of deformation occurring in the linear PPR test and the long creep test with a period of fluctuating displacement rates associated with micro-cracking.

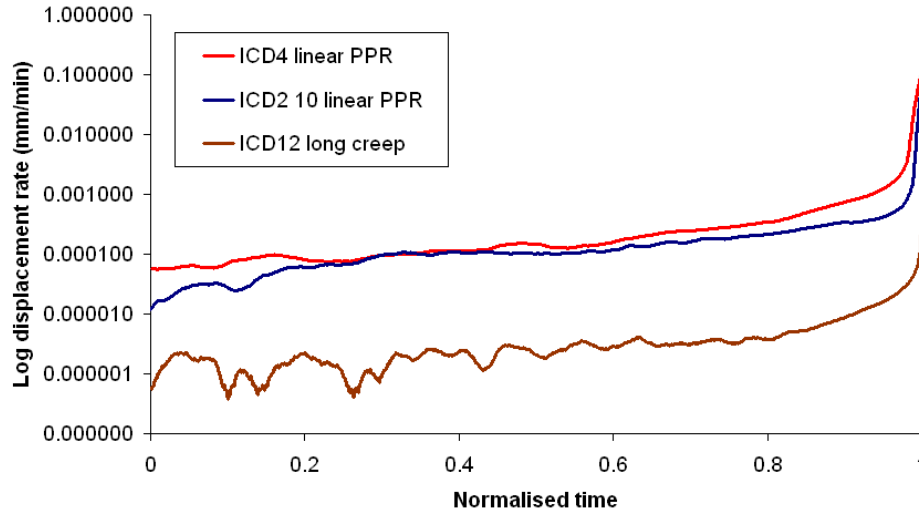


Figure 7.30 Comparison of displacement rates to failure through linear PPR and during the long creep test

These Tertiary creep phases have been compared in $1/v - t$ space (Fig 7.31a), which demonstrate similar patterns to failure, although at different rates. Analysis of the final stage of failure (Fig 7.31b) for all tests suggests that linearity occurs from at a similar stage in the pattern of deformation, although the onset of linearity occurs earlier in the linear PPR tests when compared to the long creep test.

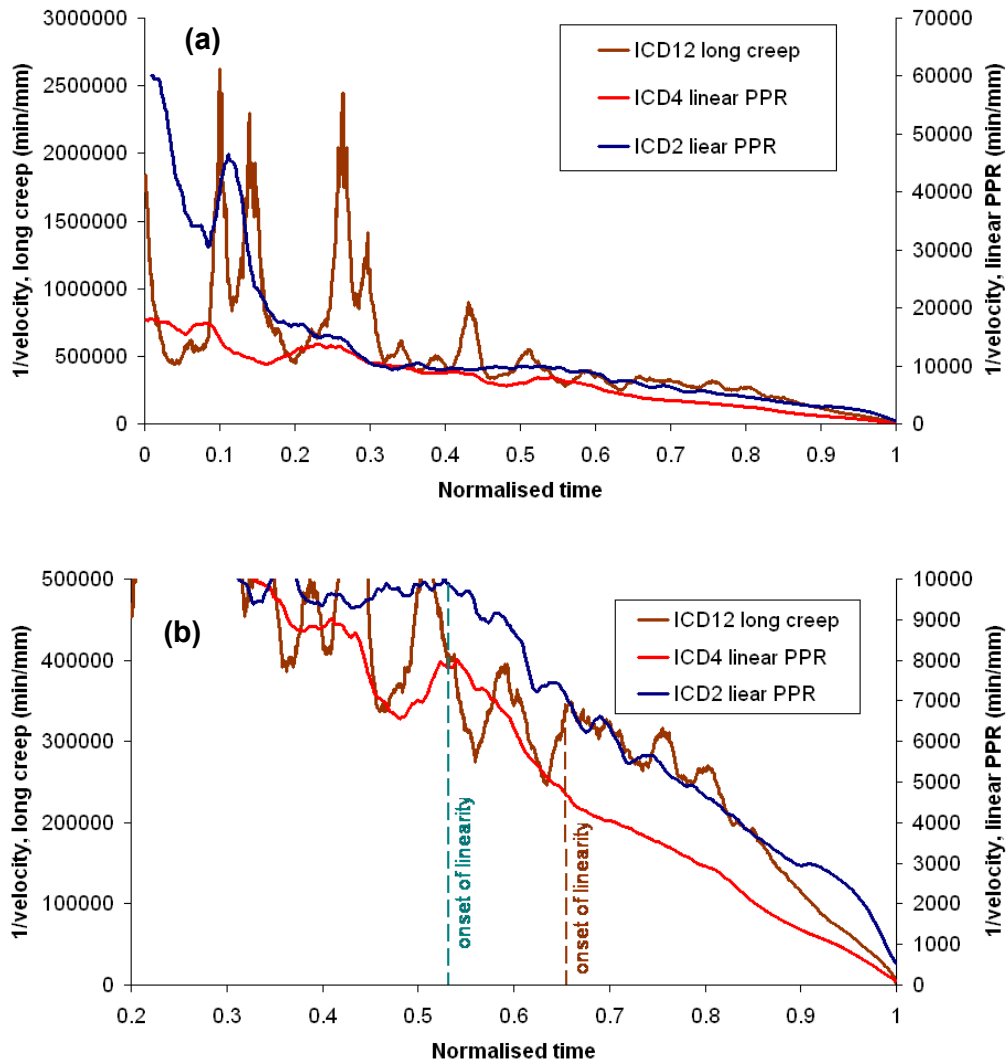


Figure 7.31 Comparison of linear PPR and long creep test (a) $1/v - t$ (b) $1/v - t$ during final stages of failure

The results confirm that brittle failure in the Gault Clay can occur at constant stress from a higher mean effective stress than the failure envelope. Similar patterns of development to failure have been observed in previous catastrophic landslides events such as the 1960 Vaiont landslide (e.g. Voight 1989). Consistent with the long creep test, monitoring records from the Vaiont disaster confirmed that failure progressively developed without change in the stress state within the slope.

7.8 Patterns of deformation

The PPR testing has confirmed three distinct patterns of progressive deformation during reducing mean effective stress, based on the mechanisms of shear surface development and the properties of the materials being tested.

These comprise:

- a. Brittle deformation of intact over-consolidated Gault Clay
- b. Brittle deformation of intact samples of the Gault-Carstone transition material
- c. Ductile deformation of remoulded samples

Figure 7.32 demonstrates the phases of movement to failure of these three materials. The figure demonstrates that, as porewater pressures are raised in the intact sample to point A (Fig 7.32(i) a and b)), the mean effective stress in the sample reduces to the residual strength envelope (Fig 7.32 (ii) a and b). This line represents the post failure strength component of the shear surface controlled by the frictional resistance of randomly aligned soil particles (Schofield and Wroth, 1968), and therefore represents the minimum strength of the material. As the mean effective stress passes through this minimum strength envelope the weakest aligned soil particles will become mobilised. Therefore, any additional stress applied to the sample from this point will be placed at the higher strength components of the shear surface. As a consequence, it is likely that this imbalance in strength within the shear zone allows for the onset of Primary creep. Whilst this is still not fully understood it is hypothesised that this phase of deformation is likely to occur at or close to the residual strength envelope. The pattern of deformation displayed (Fig 7.32 (iii) a and b) is believed to represent a phase of strain hardening, as the rate of displacement reduces following an initially high displacement rate. This strain hardening process is consistent with damage mechanics (Main, 2000; Marlet *et al.*, 2005) and can be observed as an asymptotic trend in $1/v - t$ space (Fig 7.32 (iv) a and b).

In both intact materials the mean effective stress continues to decrease between points A and B as porewater pressures are increased (Figure 7.32 (i)

a). Point B in both cases represents a state in which the mean effective stress is sufficiently reduced to allow the development of micro-cracks within the weakest sections of the shear zone. This micro-cracking processes most likely initiates where the weakest cohesive bonds and lowest inter-particle friction is occurring in the sample. This secondary stage of deformation represents the dominance of progressive strain weakening within the sample. Whilst in most previous models (e.g. Varnes,1983) this phase is observed as a period of plastic deformation at a constant displacement rate, these results have revealed subtle variations in the pattern of deformation rate (Fig 7.32 (iii) a) which is emphasised in the $1/v - t$ space plots. Between points B and C the Gault Clay reveals a distinct saw tooth pattern in $1/v - t$ space at very low displacement rates (Fig 7.32 (iv) a). This pattern of behaviour is consistent with the micro-cracking process proposed by (Kilburn and Petley, 2003) and the fracturing processes observed in damage mechanics (Main, 2000) where localised micro-cracks lead to small irregular increases in displacement as the mean effective stress continues to reduce.

Between Points B and C the Gault-Carstone interface materials reveal a different pattern of behaviour in which larger, graded movements are observed. This is explained by the fact that the interface material has a lower cohesive strength than the intact Gault Clay, which has relatively low peak σ' (number) strength but high c' (number). As a consequence a larger proportion of the shear strength can be mobilised in the interface material during Secondary creep, leading to the onset of Secondary creep occurring closer to the residual strength envelope (Fig 7.32(ii) b) and the development of higher and more distinct displacement rates during the Secondary creep phase (Fig 7.32 (iii) b) as micro-cracks are able to develop over a broader area of the shear zone. As a consequence the displacement patterns in $1/v - t$ space occur as a either a singular or series of smaller asymptotic trends (Fig 7.32(iv) b) consistent with displacement occurring in a wider shear zone rather than along a defined shear surface.

When point C is reached in the intact materials (Fig 7.32(i) a and b) displacement rates accelerate hyperbolically to final failure. The development

of this hyperbolic displacement rate occurs as the mean effective stress reduces toward the peak strength envelope (Fig 7.32(ii) a and b) when sufficient stress has been applied to the shear surface to allow for the coalescence of the micro-cracks. As these cracks coalesce and interact the stress is concentrating continually on a smaller surface area of the shear surface, leading to the hyperbolic increase in crack growth (Fig 7.32(i) a and b) and subsequent acceleration to failure and a final singular shear surface is formed. In the Gault Clay (Fig 7.32(ii) a) this stage of displacement has been shown to occur close to the peak strength envelope from a relative low displacement rate, which correlates with a more distinct negative linear trend to failure in $1/v-t$ space (Fig 7.32(iv) a). Conversely the Gault-Carstone interface has been shown to develop this phase of hyperbolic acceleration from a much higher displacement rate (Fig 7.32(iii) b) which corresponds to a less and much later development of the linear trend in $1/v-t$ space (Fig 7.32(iv) b).

As the remoulded Gault Clay samples (Fig 7.32(ii) c) pass through the residual strength envelope a larger proportion of soil particles will be mobilised and therefore ductile deformation is initiated in the form of an exponential acceleration in displacement (Fig 7.32(iii) c) and subsequent asymptotic trend in $1/v - t$ space (Fig 7.32(iv) c). As previously observed by Ng and Petley, (2009) it can be argued that this process of deformation initiates as 'push and climb' before developing into 'localised sliding' as the frictional resistance of the shear surface progressively reduces through both deformation and the increasing porewater pressure. As the mean effective stress continues to reduce (Fig 7.32(ii) b) as porewater pressure increases in the sample further soil particles within the shear zone are progressively mobilised until generalised sliding occurs. At this stage the strains continue to accelerate exponentially until a constant displacement rate is achieved and the sample barrels consistent with ductile failure.

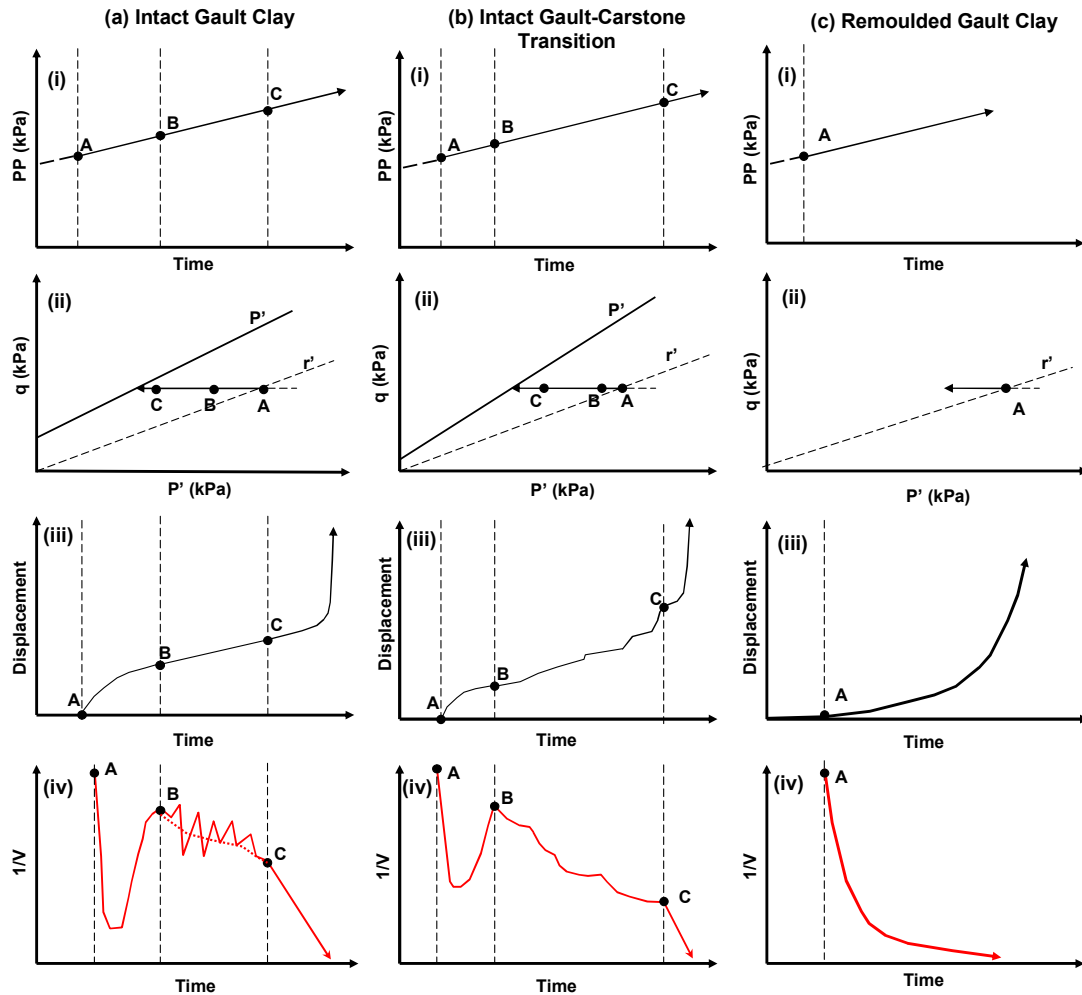


Figure 7.32 Progressive shear surface development patterns observed in PPR test

7.9 The relationship to previous progressive models of shear surface development

The PPR testing on both intact and remoulded samples has provided new detail on the processes of progressive landslide development initially observed by Terzaghi (1950). A number of previous models have been hypothesised to explain this phenomenon (e.g. Varnes, 1983; Bjerrum, 1967; Helmseter et al., 2004; Hlemseter and Sornette, 2004; Petley *et al.*, 2005a). Whilst these models have been used to explain landslide development, insufficient information has been presented to explain the subtlety and variability of landslide movement patterns in varying materials and stress

conditions. These models can now be reviewed against these new testing results.

7.9.1 Progressive Failure (Bjerrum, 1967)

The progressive failure model for cohesive materials hypothesised by Bjerrum (1967) considers the development to failure of slopes in over-consolidated clay slopes. Whilst the PPR testing results confirm the conceptual model of shear surface development the model proposed by Bjerrum is largely based on the development of failure in homogenous slopes which are driven by initial change in stress state (e.g. slope cutting). The model therefore considers a delay to failure created by an initial change in the deviator stress which leads to a localised increase in stress above the peak strength envelope. The slow creep test provides evidence for the initiation of movement at both a constant deviator and mean effective stress from below the peak strength envelope. This suggests that the time dependent propagation to failure can occur before the peak strength is reached and therefore shear surface development is occurring at a stress state between the peak strength and residual strength envelopes.

7.9.2 Three phase creep (Varnes, 1983)

The classic three phase creep to failure model has not been fully identified during this investigation. In particular the evidence for Primary creep, associated with a phase of strain hardening during initial creep has not been observed in either PPR laboratory testing or in the monitoring records of the vast majority of landslides.

Secondary creep has been observed in all testing and is characterised by a relatively uniform period of creep at a constant displacement rate. Whilst this trend is generally consistent with Varnes observations the subtle variability in displacement rate during PPR cannot be accounted for by purely plastic deformation. These stepped increases in displacement rate can be accounted for by the development and lengthening of micro-cracks within the shear zone as this micro-crack development allows for localised sliding in remoulded soils and fracture development as stresses are transferred over a smaller

remaining intact sections of the shear surface in brittle materials. This micro-cracking process during Secondary creep further accounts for the increased deformation in the Gault-Carstone interface transition material where cohesion is lower and subsequently samples are less brittle.

Tertiary Creep as described by Varnes occurs as period of rapid acceleration to failure. Whilst this has been observed in all samples the pattern of this curve has been observed as a exponential acceleration in remoulded samples and a hyperbolic acceleration in the intact samples, which is not considered in the Varnes model. These different patterns of displacement to failure can be related to the generation of distributed deformation in remoulded and ductile samples and as shear surface propagation through crack coalescence in intact cohesive materials. The results have shown that this phase of Tertiary creep can occur at different strain conditions depending on the brittleness of the sample.

7.9.3 Slider block models (Helmsetter et al., 2004)

The state- and rate- dependent velocity model has been suggested as physical model to explain the acceleration of landslides such as the Vaiont and La Clapiere landslides using the state and velocity dependent friction law established in laboratory testing and used to model earthquake friction. Whilst this method has been used successfully to explain the accelerating phase of these landslides the potential for this method to explain the subtle patterns of behaviour observed in this suite of tests is limited.

The slider-block model is limited in its ability to explain the subtle variation in behaviour between each of the intact and remoulded samples tested and particularly the fluctuation in displacement rate during decreasing porewater pressure and mean effective stress. The slide-block model would indicate that each period of acceleration should have lead to a reduction in friction and therefore promoted further movement as opposed to halting immediately after a creep phase. These 'stick-slip', and graded movements provide real evidence in both real landslide systems and laboratory based testing of periods of deceleration during deformation to failure which can not be

explained by an increase in friction. The long creep test further demonstrates acceleration to failure at constant mean effective stress, which within this model, would imply a conditionally stable regime. This implies that final patterns of behaviour observed in this study cannot be accounted for within the state and rate dependent model.

7.9.4 Crack propagation (Petley et al., 2005a)

The concept of crack propagation as conceptualised by Petley et al., (2005a) considers the development of a slope failure through the development of micro-cracks due to elevated porewater pressures. This model successfully combines laboratory based testing with landslide monitoring analysis to conclude that micro-cracking occurs during periods of elevated porewater pressure when the mean effective stresses in the slope are sufficiently reduced below a key threshold to promote irreversible deformation of the materials at the shear surface. The continued fluctuations in pore pressure allow for the progressive deterioration of the shear surface until cracks coalesce to form a singular shear surface. As the strength of the shear surface develops the stresses acting on the slope are concentrated over a smaller area leading to displacement rates accelerating catastrophically as a hyperbolic curve.

Whilst this mechanism of shear surface development provides a clear explanation of the negative linear trend to failure observed, it fails to provide a full understanding of the subtle variation in patterns of movements in Secondary deformation and how these relate to the materials properties and the mechanics of shear surface development operating in a slope. These subtle patterns of deformation have important ramifications for understanding the mechanisms of shear surface development and require further investigation before more sophisticated landslide hazard warning systems can be implemented.

7.10 Implications for the Ventnor Undercliff landslide

The results of the PPR tests and associated interpretation of the different patterns of progressive shear surface development provides a new framework to assess the mechanisms of creep occurring in the basal shear zone of landslide systems and the implications this may have on the future behaviour of the landslide complex.

The results of Ventnor landslide monitoring analysis (Chapter 5) provide an opportunity to evaluate the applicability of this approach and to consider the potential future behaviour of an active deep-seated landslide complex. Of particular concern is the development of the 'Lowtherville Graben' which may relate to reactivation of pre-existing landslide and this may indicate the formation of a new feature which may be subject to catastrophic failure in the future (e.g. e.g. Hutchinson and Bromhead, 2002; Barton, 2007).

The results of the analysis presented in Chapter 5 are summarised in Table 7.1, providing a record of ground movement in the Town from 1949 to 2009. The review demonstrates relatively consistent annual ground movement through time in a number of different locations. These records show that the majority of monitoring sites have been moving by less than 5 mm per year, which appears consistent across both the short term and long term monitoring records.

Spatial analysis of the movement records has confirmed three distinct zones of ground movement, which relate to the differential movement of three discrete landside blocks as suggested by the site geomorphology and spatial distribution of damage (section 5.2). Whilst inclinometer records (Fig 5.4) have revealed for the first time that a greater degree of movement is occurring in Lower Ventnor, the most significant damage, through settlement and horizontal displacement, has been observed at the Newport Road associated with 'the Lowtherville Graben'. These findings are consistent with the historical records, although illustrate that the entire landslide complex is currently undergoing ground movement with damage focused along the current headscarp and between the key landslide units.

Table 7.1 Summary of ground movement records Ventnor (after Moore et al., 2007a)

Location	Monitoring period	Movement rate (mm/yr)
Newport Road	1982-1983	19.7 to 39
Newport Road	1988	28
Newport Road	1995-2009	6.4 (crack extension) 33.2 (settlement)
Lowtherville Graben	1982-1983	26.9 to 29.9
Lower Gill's Cliff Road	1982-1983	8 to 16.5
Ocean View Road	1982-1983	6
Bath Road	1982-1983	0
Bath Road	1988**	0 to 2
Bath Road	1995-2009***	-0.06 (crack closure) 22 (settlement)
Esplanade	1949-1988	20 (heave)

*Note * after Chandler (1984) ** after Woodruff (1989) ***Council records*

Detailed temporal analysis of the automated crackmeter and settlement cells analysis (Chapter 5) has shown two distinct patterns of ground movement at the graben associated with landslide deformation, which is observable in both horizontal and vertical displacement records (Fig 7.33). Analysis illustrates a period of continuous ground movement (zone A) where ground displacement occurs as a series of 'stick - slip' movements. This period of creep is characterised by very low ground movement rates during which time displacement rates fluctuate and are not affected by changes in groundwater level. In addition a period of prolonged ground acceleration is recorded (zone B) during the winter of 2000 and 2001. Following this ground movement reduces and the continuous ground displacements continue (zone C).

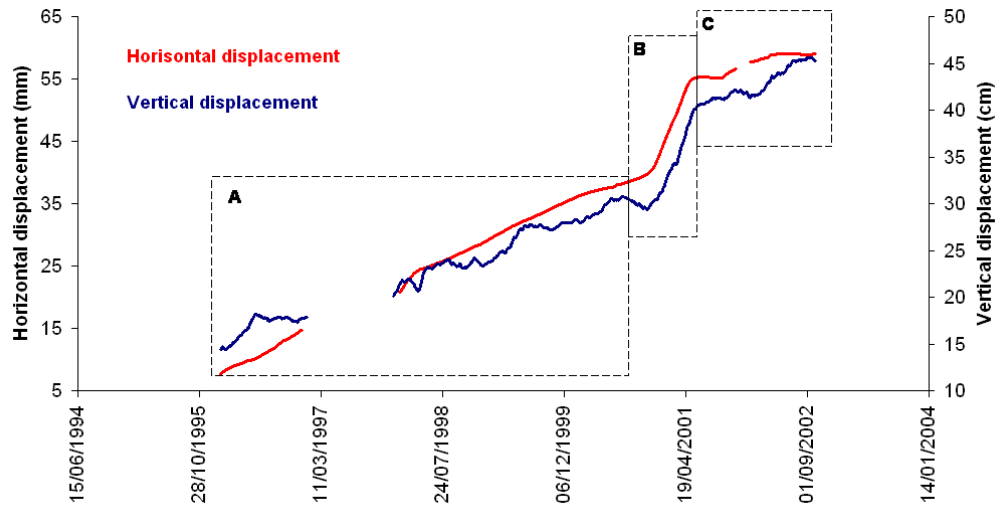


Figure 7.33 Comparison of settlement and extension behaviour at the Lowtherville Graben between 1995 and 2002

These periods of ground movement have been converted into velocity to assess and analyse mechanisms of displacement during a distinct period of accelerated ground creep. These two patterns of ground movement have been analysed with groundwater monitoring from the site to evaluate the landslide displacement behaviour in relations to the deformation behaviour observed in the PPR testing to consider whether the mechanisms of shear surface displacement can be inferred from the ground movement behaviour of the landslide.

A relationship between the velocity recorded at the Lowtherville Graben and porewater pressures recorded at the Winter Gardens has been established (Fig 7.34). The results show that the ongoing creep occurs through a period of fluctuating displacement rates below 0.05 mm / day between October 1995 and October 2000. This behaviour is consistent with 'stick - slip' movements observed at low displacement rates in mudslide (Allison and Brunsden, 1990) and the very slow movements (Type 1) identified within the Tessina landslide (Petley *et al*, 2005c). The increase in velocity in the winter period of 2000/01, however, clearly highlights the velocity reached above 0.15 mm/ day and, during this period, porewater pressures reached of over 110 kPa; the highest recorded porewater pressures in this dataset. Whilst only one period of

ground acceleration is observed in the dataset it can be concluded that accelerated ground creep, measured in the graben, occurred once a critical pore pressure threshold had been exceeded. This therefore illustrates that acceleration in ground creep is associated with a reduction in mean effective stress to a critical threshold. This type of movement has been observed in other landslide systems as graded movement (e.g. Allison and Brunsden: 1990; Petley *et al.*, 2005c) and is consistent with generalised sliding behaviour observed in laboratory testing by Ng and Petley (2007).

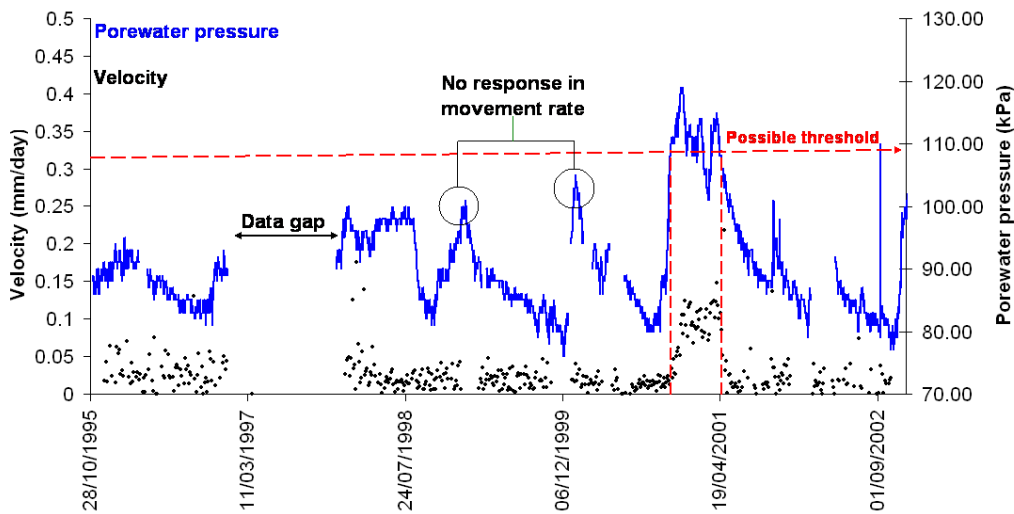


Figure 7.34 Comparison of ground movement behaviour and porewater pressure characteristics

Threshold relationships have been confirmed from similar monitoring records at the Jinnosuke-dani Landslide in Japan for the period between February 2000 and October 2001 (Wang *et al.*, 2007) and for the Fosso San Martino slide, France (Bertini *et al.*, 1986). Such relationships have been successfully used at Lyme Regis, Dorset to determine critical porewater pressure thresholds as a method of early warning system of future ground movement risk (Brunsden, 2002).

Analysis of the period of accelerated ground creep shows has a distinct exponential increase in velocity through time until a velocity reaches a peak which is sustained for approximately 20 days before reducing to a background

rate of 0.05 mm / day, similar to the rates occurring prior to the creep acceleration (Fig 7.35). This pattern of ground movement is consistent with previous observations of graded movement patterns observed at other sites (Allison and Brunsden, 1990; Brunsden, 2002; Petley *et al.*, 2005c).

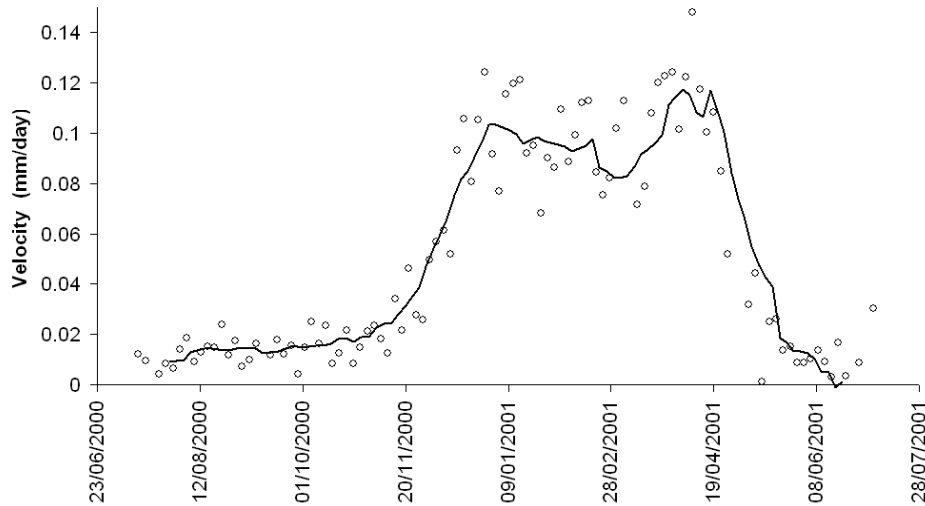


Figure 7.35 Ground movement velocity measured at the Lowtherville Graben (23/06/2000 – 28/07/2001)

This period of accelerated creep has been analysed in $1/v - t$ space (Fig 7.36). The graph shows a distinctive asymptotic trend which is consistent with non-brittle shear surface movement. The graph demonstrates an initial period of rapidly reducing $1/v$ before the landslide reaches a maximum velocity depicted here by the flattening of the $1/v - t$ trend. This type acceleration to a constant creep rate has been observed at other landslide sites such as Tessina (Petley *et al.*, 2005c) and Worbarrow Bay (Allison and Brunsden, 1996), both of which were associated with movement along a ductile deformation zone or pre-existing shear surface.

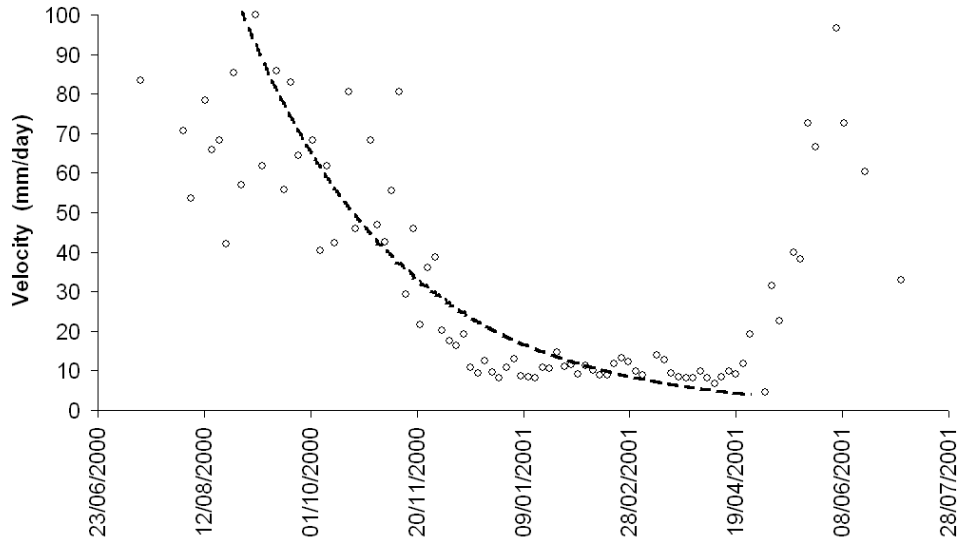


Figure 7.36 Ground movement pattern at the Lowtherville Graben in $1/v - t$ space (23/06/2000 – 28/07/2001)

Analysis has successfully demonstrated a relationship between porewater pressure and velocity, above a specific porewater pressure threshold, through the winter period of 2000-2001 (Fig 7.37). Through this period a correlation between porewater pressure and velocity has been demonstrated (section 5.4.3). The graph shows a relatively consistent relationship between velocity and increasing porewater pressures from 12/8/2000 to 20/12/2000. After a velocity of 0.12 mm / day is achieved however this relationship weakens with higher velocities being sustained during a period of porewater pressure decline. This suggests that once graded movement is initiated, velocity increases linearly with increasing porewater pressure, but once the inertia in the landslide body is overcome the movement generates momentum which cannot be immediately dissipated when porewater pressures are reduced.

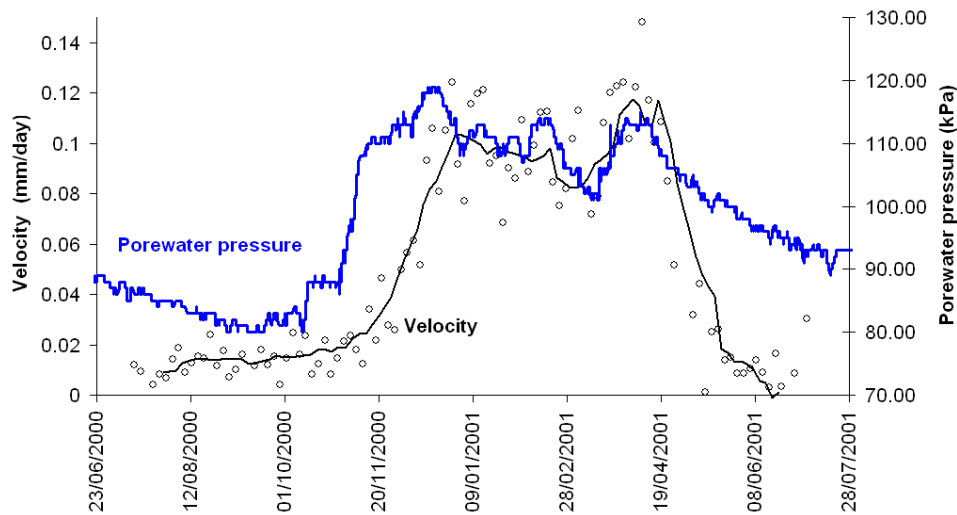


Figure 7.37 Comparison between ground movement velocity and porewater pressure (23/06/2000 – 28/07/2001)

In various landslides subject to continued episodes of creep acceleration close relationships have been established between landslide velocities and groundwater levels (e.g. Wang *et al.*, 2007; Brunsden, 2002). Despite this, research describing the dynamics of these relations remains scarce (Gonzalez *et al.*, 2008).

Further analysis of the phases of acceleration and deceleration between 2000 and 2001 has been conducted by plotting average daily porewater pressures against the corresponding average daily velocities (Fig 7.38). The results demonstrate that in this instance porewater pressures were approximately 2 kPa higher during the acceleration phase to initiate the velocities as were experienced during the deceleration phase.

Similar research on a Japanese landslide by Nakamura (1984) concluded that landslide movement during the rising limb of groundwater level was larger than that observed in the lower limb of the same water table. Similar analysis carried out by Bertini *et al.* (1984, 1986) and Picarelli (2004) showed different velocities for the rising and lowering limb of piezometric levels. Similarly observations made by Van Asch *et al.*, (2007) suggest that for a given

groundwater level velocities were higher during the rising limb and lower as the water table decreases. This is not consistent with the Ventnor results.

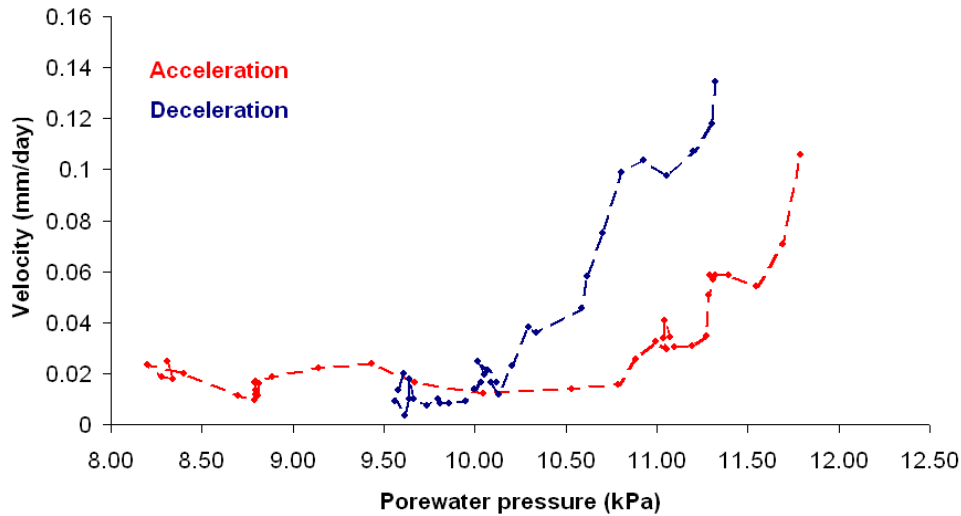


Figure 7.38 Relationship between ground movement rate and porewater pressure, Ventnor

Analysis undertaken by Gonzelaz *et al.*, (2008) of slow movements of the Vallcebre landslide in the eastern Pyrenees of a series of ground movements between 1996 and 1998 revealed a variety of behaviours. Gonzelaz *et al.* (2008) proposed a simple conceptual model based on the infinite slope which concluded that in most cases a reversible behaviour in velocities occurs due to constant viscous component acting within the landslide mass. In the some instance however a hysteretic effect (e.g. Nakamura, 1984; Bertini *et al.*, 1986) may be observed associated with a non-constant viscous component or changes in the conditions acting upon the landslide. In the case of Ventnor it would appear that a constant viscous component is operational at the shear surface which provides evidence for movement along a pre-existing shear zone.

Comparison between the Ventnor monitoring records and the results from the PPR testing demonstrates that the current behaviour and patterns of ground movement can be related to the mechanisms of shear surface deformation observed in remoulded Gault (Fig 7.32 c). The patterns of ground movement

confirm that accelerated ground creep occurs above a given porewater pressure threshold and once this threshold is achieved movement accelerates as porewater pressures increase until a constant velocity is achieved. The inclinometer data summarised in Chapter 5 (Fig 5.4) confirms that this shear surface is seated at the base of the Gault Clay some 98 m bgl at BH2 in Upper Ventnor and 73 m bgl BH4 in Lower Ventnor. Given that PPR testing confirmed brittle failure in the intact Gault Clay it is possible to conclude from this analysis that the landslide is currently undergoing post failure creep along a pre-existing landslide shear surface.

Under groundwater induced conditions therefore the landslide would remain marginally stable whilst the location of the landslide on the stress state graph remains below the residual strength envelope. For accelerated ground creep to occur the porewater pressures acting at the landslide shear surface would need to be elevated to a sufficiently high level to cause the required reduction in mean effective stress to place the landslide above the residual strength envelope on the stress state graph. The PPR testing has demonstrated that the stress state required is associated with the residual strength envelope. Once the stress state reaches the residual strength envelope the friction strength acting at the shear surface is no longer able to resist the stresses acting to promote ground movement and acceleration occurs.

7.11 A model of progressive failure in a landslide

The results of this investigation confirm the concept of the progressive development of landslide shear surfaces initially proposed by Bjerrum (1967) and subsequently developed Petley *et al.* (2005a; 2005b).

For simplicity the model presented considers progressive shear surface development to failure of a slope cut in a natural cohesive material (e.g. slope cutting in clay) which has not been subject to recent modifications in porewater pressure.

Following the formation of the slope, porewater pressures slowly increase through groundwater recharge to form a water table. Initially the groundwater levels are comparatively low such that the slope remains stable (Fig 7.39(1)).

An additional increase in porewater pressure, however, leads to a further reduction in the mean effective stress which passes through the minimum strength envelope (Fig 7.39(2)). In this state, on a micro-scale, the weakest component of the slope strength (the frictional resistance between preferential aligned particles) is fully mobilised. Whilst Primary creep is still not fully understood it is hypothesised in this model that this phase of creep occurs at this stage as particles realign and the sample contracts within a relatively broad shear zone leading to increase in sample strength. At this stage any further reduction in mean effective stress cannot be resisted by this component of the shear surface and therefore this stress is passed on to other strength components within the slope. Following this period of elevated porewater pressure groundwater levels may reduce back to their previous level below the minimum strength envelope and no further movement is experienced.

Further fluctuations in groundwater level may not be sufficient to cause any further deformation until another period of sustained elevated ground water is experienced. As the mean effective stress reduces high localised stresses will become sufficient to break the weakest cohesive bonds and the micro-cracking processes as described by Kilburn and Petley (2003) will be initiated in weakest sections of the shear zone (Fig 7.39(2)). At this stage localised micro-scale deformations within the shear zone may be observed as measurable strain. If porewater pressures are reduced within the shear zone the micro-cracking process will terminate and no further deformation will take place, and it is likely that continued reductions in mean effective stress will be required to continue the micro-cracking process.

Previous models have concluded that in certain slopes micro-cracking occurs when the mean effective stress is sufficiently reduced below a given threshold (Petley *et al.*, 2007b). Previous interpretations (Petley and Allison, 2006) have

concluded that this critical effective stress relates to the point at which the mean effective stress is reduced below the material residual strength envelope. This study, however, demonstrates that this critical effective stress can vary depending on the material properties with more cohesive materials requiring mean effective stresses to reduce significantly below the residual or minimum strength envelope. As the mean effective stress reduces to this condition a greater proportion of the shear surface can no longer sustain any further increase in shear and, as a consequence, this excess stress will be passed on to the higher strength components and in particular the cohesive bonds. At this stage stress is concentrated over a smaller proportion of the shear zone and will become sufficient to break the weakest cohesive bonds through the micro-cracking processes described by Kilburn and Petley (2005)(Fig 7.39(3)). At this stage localised micro-scale deformations within the shear zone may be observed as Secondary creep as strain weakening forces become dominant in the sample. During this stage if porewater pressures are reduced within the shear zone the micro-cracking process will terminate and no further Secondary creep will take place and further reductions in mean effective stress through pore pressure increases will be required to continue the micro-cracking process. This strain weakening process during Secondary creep therefore may be active within a slope over a range of potential time frames from hours to millennia in which time the slope is progressively weakening toward final failure.

Further episodes of elevated porewater pressures will lead to continued micro-crack development within the shear zone and during this time shear stresses will become increasingly focused at the crack tips (Main, 2000) further increasing the differential stresses within the shear zone and weakening the slope. As the mean effective stress is reduced further shear stresses acting at the tips of micro-cracks will become increasingly localised to break stronger cohesive bonds and causing the crack lengthening of existing micro-cracks. This process is well-described in the damage mechanics literature as localisation (Main, 2000; Logan, 2007) and indicates the initiation of a shear surface within the slope. As strain localisation develops the shear stresses in the slope operate over a progressively smaller

component of intact material. This crack lengthening process initially occurs as a series of stepped increases in strain producing a 'saw tooth' pattern in displacement rate. It is hypothesised that this pattern is related to localised pore pressure inflation and dilation as cracks lengthen and coalesce.

Eventually the shear zone is saturated by micro-cracking and further weakening can only occur through the process of crack lengthening alone, such that the shear stress is concentrated along a singular shear surface (Fig 7.39(4)). This may lead to a temporary reduction in displacement rate. Strain then begins to increase as further lengthening and coalescence of crack occurs along an increasingly smaller proportion of the shear surface increasing the rate at which cohesive bonds break and fracturing develops along a singular shear surface. At this stage the strain rates become hyperbolic as the shear surface runs away to failure. Analysis of the slow creep test illustrates that this process can occur at constant stress and therefore the hyperbolic acceleration to final failure can be controlled by the internal mechanisms of strain development as opposed to alterations in the deviator or mean effective stresses.

As the pore pressures continue to increase the effective stress is reduced to the failure initiation line. This line appears to be at or close to the peak strength failure envelope. Previous hypotheses have suggested that at this stage the micro-cracking density becomes sufficiently high that the micro-cracks are able to coalesce (Main 2000). At this stage stresses are concentrate at the crack tips, allowing for the widening and coalescence of the micro-cracks, until a singular shear surface forms. This process of shear surface development is consistent with the development of negative linearity in $1/v$ – time space which predicts the final point of shear surface development and acceleration.

ICD PPR undertaken on the Gault where porewater pressures are raised linearly through time indicates that failure occurs at a critical mean effective stress for any given deviator stress. Clearly further research in this field is required to understand the relationship between these two parameters more

closely but the results demonstrate that a specific mean effective stress may not result in certain strain condition and therefore linearity in $1/v - t$ space may be controlled by a critical strain rate rather than stress condition.

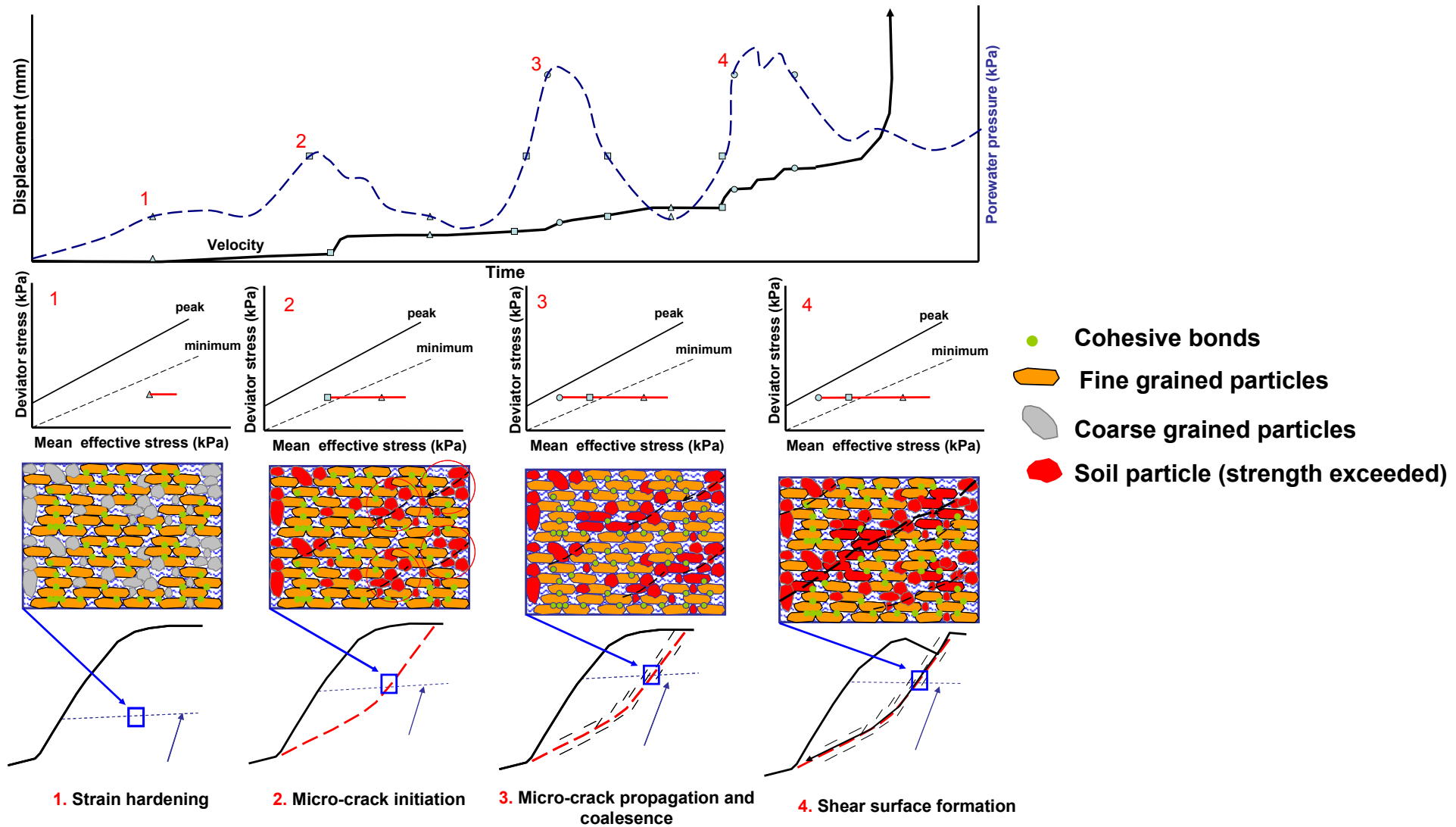


Figure 7.39 A conceptual model for the progressive development of a first time landslide

Following final development of a singular shear surface post failure movement in the form of landslide creep occurs when the mean effective stress is sufficiently reduced on the stress state graph to exceed the residual strength envelope. The correlation of the asymptotic trend developing at or close to the residual strength envelope in the specialist PPR testing demonstrates that these movements occur where little or no cohesion is apparent in the sample and therefore the slope strength is controlled by the frictional component of the landslide. Similarly the close correlation of ground movement rate and porewater pressure recorded in the Ventnor landslide demonstrates that once the mean effective stress is reduced below the residual strength envelope the rate of movement is proportional to the porewater pressure. The porewater pressure threshold observed in many landslides (e.g. Wang *et al.*, 2007) is likely to relate to the mean effective stress state at or close to the residual strength envelope in marginally stable landslides

7.12 Implications for understanding rainfall and groundwater induced landslides

The analysis of the PPR testing and landslide monitoring records have been used to successfully propose a new model for the progressive development and post failure behaviour of landslides developed in over-consolidated clays. The model provides a new insight into development of landslides and their subsequent behaviour under groundwater induced conditions which can now be addressed.

The model provides an explanation of why under certain circumstances landslides can occur rapidly without the development of features indicative of pre-failure.

The model further explains why in many circumstances acceleration to failure may not occur in certain conditions where significant slope creep has been observed, final catastrophic failure does not occur. The model suggests that ductile deformation and movement along pre-existing shear surface accelerate to a final creep rate which is related to the porewater pressure increase at the landslide shear surface. The results of this study therefore

demonstrate that rapid acceleration in these circumstances is difficult to generate without significant rises in porewater pressure within the landslide shear zone. This result is consistent with the laboratory findings of Petley and Ng (2009) who demonstrate the relationship between porewater pressure and movement in soils sample using a stepped PPR profile.

The revised model has demonstrated why many landslides and landslide accelerations are triggered by high antecedent rainfall which elevate porewater pressures and reduce the mean effective stress of the landslide shear surface until accelerated movement can occur (Fig 7.40).

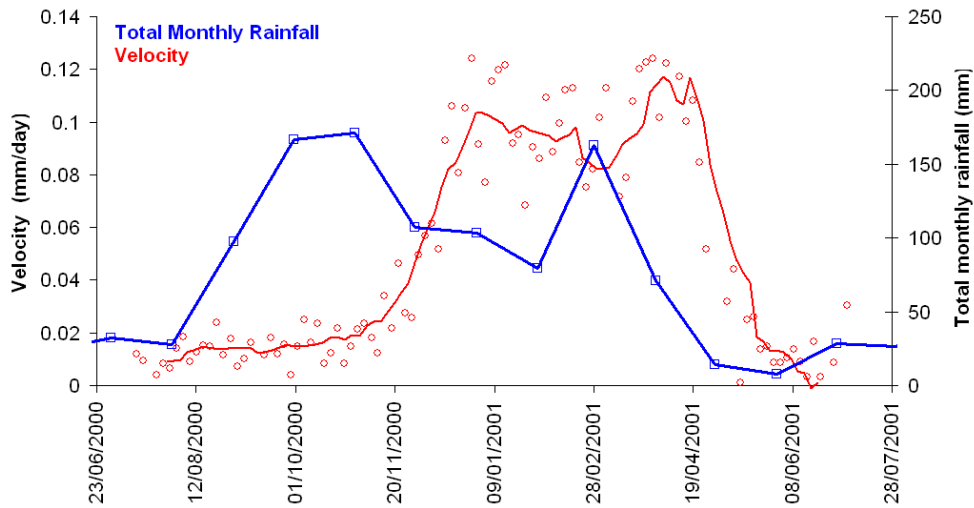


Figure 7.40 Total monthly rainfall and ground acceleration relationship, Ventnor

Whilst rainfall and ground movement response relationships have been used to account for the spatial distribution of marginally stable and unstable areas of the Undercliff (Moore *et al.*, 2007a) the revised model provides an explanation as to why this approach is often inappropriate for first time failures. The model proposed demonstrates that in certain circumstances first time failures can occur without the need for any significant change in porewater pressure.

The difficulty in establishing a direct relationship between rainfall frequency events and landslides has been established by a number of authors (e.g. Lee and Moore, 1991; Lee and Clarke, 2002). This can be shown in the analysis of the four month Winter Effective Rainfall (WER) data with reported landslide events in the Undercliff (Lee and Moore, 1991) (Fig 7.41). The analysis illustrates that whilst, in certain circumstances, reported landslides have correspond with high four month WER in many circumstances landslides have occurred following low four month WER which is consistent with the proposed model. This demonstrates that caution should be advised when rainfall data is being used to forecast the potential for future first time landslide events.

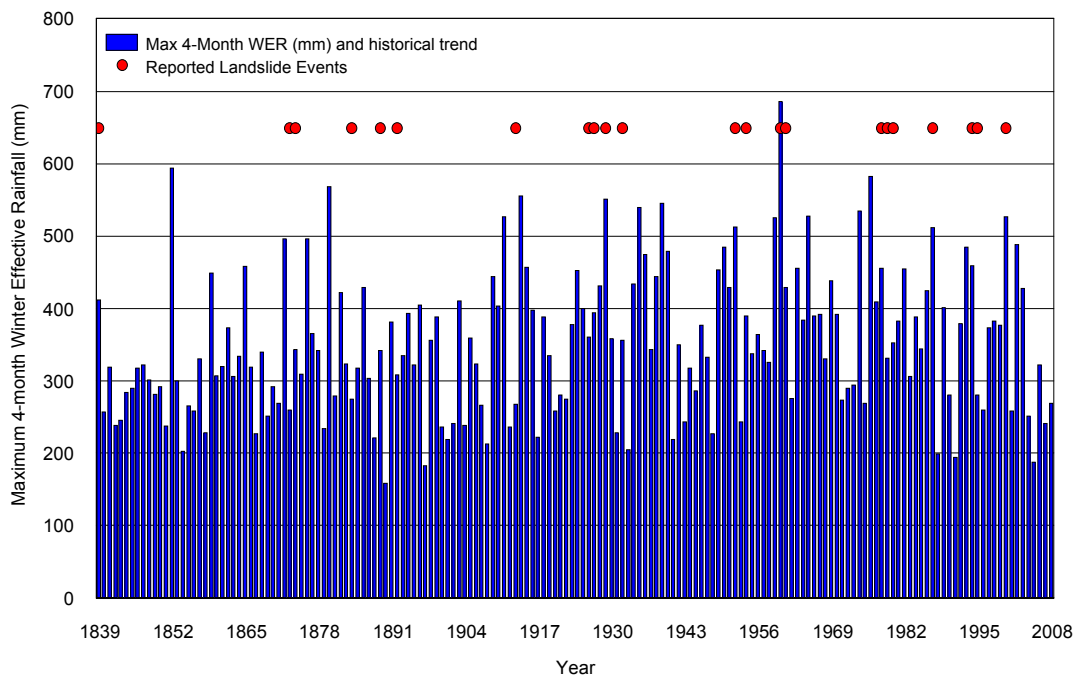


Figure 7.41 Landslide events in relation to Maximum 4 month WER within the Undercliff (after Moore et al., 2007a)

Similarly, since the late 1950's wet year sequences have broadly coincided with landslide activity years on the Lyme Regis Coastal Slopes and the timing of major reactivations within the Black Ven Spittles mudslide complex (REF). This general pattern is also supported by landslide movement data and road damage dates for the inland slopes of the Char valley (Brunsdon and

Chandler, 1996). There are, however, a number of particularly wet periods where no landslide events have been recorded.

Clark *et al.* (1995) were able to demonstrate extensive 1994 landslide movements at Blackgang, within the Isle of Wight Undercliff, were linked to almost continuous, and at times intense, rainfall over the previous month. Analysis of these rainfall records, however, indicated that this was only the thirteenth wettest winter since 1839. Wetter winters had not led to similar movements.

These studies provide clear evidence that whilst extreme and prolonged rainfall events are often a major trigger of landslides, predicting landslide failures through these techniques are problematic. This study has provided evidence to suggest that this is because the timing and cause of the landslide events is partially governed by the internal deformation of materials at the landslide shear surface. The model presented demonstrates how progressive shear development may cause a slope to fail at a lower than anticipated mean effective stresses and subsequently at lower than anticipated rainfall thresholds. Understanding landslide risk therefore requires an understanding of the internal properties of the slope as well as the external factors which may impact upon it.

Chapter 8: Conclusion

8.1 Key findings

This study has successfully combined the analysis of landslide monitoring records with the results of a series of specialist laboratory tests, which were undertaken to replicate groundwater induced landslide failure conditions. The assessment of this data has been used to; study the mechanisms of progressive shear surface development in deep-seated landslides under groundwater induced conditions; analyse how these mechanisms vary in different shear surface materials, and evaluate the implications this has subsequently on landslide post-failure behaviour.

8.1.1 Patterns of deformation to failure

The study indicates that the formation of shear surfaces in deep-seated landslides is partially controlled by the properties of the basal shear surface materials. Failure in over-consolidated cohesive materials usually occurs through brittle deformation, as strain localises along a singular shear surface. The results have been analysed to consider the patterns of deformation that are observed in a slope progressing to final failure. These patterns have been compared with the three phase creep model initially proposed by Varnes (1983).

The Primary creep phase of deformation could not be confirmed during the study despite being observed in previous investigations (e.g. Campanella and Vaid, 1974; Varnes, 1983). Whilst this phase of deformation is still not fully understood it is hypothesised that Primary creep occurs through strain hardening processes, which develop when the stress conditions in the material reach the residual strength envelope. The pattern of behaviour suggests strain hardening is occurring at the shear zone, causing strain initiation.

Intact Gault Clay testing showed an initial period of increasing displacement rate during shear surface dilation. This period of deformation is characterised by fluctuating displacement rates, which create a distinct 'saw tooth pattern'.

This behaviour is consistent with crack propagation micro-crack development during the early stages of Secondary creep and the early phases of movement in first time landslides (Carey *et al.*, 2007). This Secondary creep phase occurs following a reduction in mean effective stress which exceeds the residual strength envelope.

The Tertiary creep phase develops to failure as the stress continues to reduce toward the peak strength envelope. This phase of shear surface development is observed as a hyperbolic acceleration in displacement rate and a negative linear trend in $1/v - t$ space. This behaviour is consistent with the findings of Saito (1963) and the patterns of movement observed in landslides undergoing first time failure (Voight, 1988, 1989; Petley *et al.*, 2002; Petley and Petley, 2006; Carey *et al.*, 2007). The results reveal that, in the Gault Clay, this linear trend in $1/v - t$ develops before the stress state at the shear surface reaches the peak strength envelope. As a consequence, peak strength represents a stage of deformation at which a singular shear surface is developing to failure as strain localisation allows the rapid propagation and coalescence of micro-cracks. This finding is supported by the results of previous studies of brittle failure mechanisms in overconsolidated Clays (e.g. Burland *et al.*, 1990).

The Intact Gault-Carstone transition zone material also demonstrates brittle failure characteristics although with subtly different behaviour through Secondary and Tertiary creep phases of deformation. Initially the Secondary creep phase occurs as a constant increase in displacement rate with reducing mean effective stress. This pattern of creep initiation and corresponding sample dilation is broadly consistent with the micocracking process observed in the intact Gault Clay samples. As the mean effective stress continues to reduce a distinct stepped pattern of creep is established, which comprises a series of exponential accelerations in displacement rate with reducing mean effective stress. This phase of movement is expressed as a series of asymptotic trends in $1/v - t$ space. Following this, continued reduction in the mean effective stress leads to a final hyperbolic acceleration at high displacement rates, illustrated by linearity in the final period of acceleration in $1/v - t$ space.

The remoulded Gault Clay tests at high initial confining pressures do not demonstrate Saito linearity to failure in $1/v - t$ space. In these tests displacement rates were shown to increase exponentially with decreasing mean effective stress. This phase of movement is expressed as an asymptotic trend in $1/v - t$ space. The patterns of deformation observed in PPR testing were consistent with landslide movement patterns observed in ductile or purely plastic shear zones where strain localisation, and subsequent shear surface propagation do not develop. (e.g. Allison and Brunsden, 1990; Petley *et al.*, 2002; Petley *et al.*, 2005c). The stages of deformation observed with the behaviour observed in specialist testing undertaken on non-cohesive soils (Ng, 2007; Ng and Petley, 2009).

8.1.2 Time dependent failure at constant stress

Following the results of the PPR testing, using linear increases in porewater pressure, a long creep test has been undertaken to consider whether time dependent failure can occur in landslides subjected to constant stress conditions. The long creep test successfully accelerated to final failure at a constant stress before peak strength was reached. The sample underwent brittle failure through the development of a distinct singular shear surface and demonstrated the same distinct patterns of pre-failure deformation as observed in the intact Gault PPR testing. This test has, for the first time, demonstrated how progressive landslide failure can occur consolidated clay as a result of time dependent deformation. The patterns of deformation were found to be consistent with previous catastrophic landslide events in which no distinct change in porewater pressure was observed in the slope prior to failure (e.g. Wataru, and Tsukasa, 2004).

8.1.3 The Progressive failure of landslides

A refined model of the progressive development and post-failure behaviour of landslide complexes has been proposed. The model demonstrates that the onset of shear surface develops through a series of stages, during periods where the mean effective stress is reduced in a slope. The model proposes that this processes progresses through Primary, Secondary and Tertiary

creep as a result of a micro-cracking mechanism, activated in the slope during periods when the stress state of the slope exceed the minimum strength envelope. Following this, additional micro-crack formation and propagation occur during periods when this threshold is exceeded. The micro-cracks eventually lengthening and coalesce causing strain localisation and the formation of a singular shear surface. As the shear surface develops the rapid reduction in strength leads to the acceleration to failure of the landslide, until the landslide comes to rest at a marginally stable state.

Following failure, subsequent post failure movements are controlled by stresses acting along the pre-defined shear surface. In the majority of cases the remaining strength component will comprise the frictional resistance of the soil particles within the shear surface. Post-failure creep, therefore, will occur when stress state of the landslide exceeds the residual strength envelope of the shear surface material. In the case of Ventnor once this stress state is achieved the rate of movement relates to the amount of porewater pressure elevated beyond the residual strength envelope.

The model has been validated using the patterns of landslide movement observed in the Ventnor landslide complex and tested as a potential method of assessing present and potential future landslide behaviour. Two patterns of movement have been observed in the Ventnor monitoring record. The first is ongoing slow displacement, which occurs through a 'stick-slip' process commonly observed at other landslide sites (e.g. Allison and Brunsden, 1990; Petley *et al.*, 2005c). A second period of accelerated ground displacement is observed which occurs above a specific porewater pressure threshold and is consistent with the graded movement patterns observed by Allison and Brunsden (1990). The patterns of movement link successfully to the deformation behaviour observed in the remoulded materials and the mechanisms of creep analysed by Ng and Petley (2009). As a consequence it is possible to conclude that the present landslide movement patterns recorded in Ventnor are the result of movements along a marginally stable, pre-existing shear surface and indicate that the rapid development of the landslide in Upper Ventnor is less likely to occur than previously thought.

The implications of this model have been considered in relation to groundwater and rainfall induced landslides. The model successfully explains why, on a number of occasions, landslide movement can be linked directly to extreme or intense rainfall events (e.g. Ventnor, Lyme Regis, Fosso San Martino and Jinnosuke-dani landslides). Further to this the model explains why the majority of large first time landslides that undergo catastrophic failure are, in most cases, preceded by a trigger event such as elevated groundwater levels (e.g. Petely and Petley, 2006) volcanic or seismic activity (e.g. Voight, 1989) and prolonged or intense rainfall events (e.g. Brand, 1981; Anderson and Sitar, 1995). Conversely, there have been a number of cases where large catastrophic landslide events have occurred without any determinable triggering event or following a significant reduction in porewater pressures (e.g. Vaiont landslide). This model, complemented with evidence from a novel slow creep PPR, has demonstrated time dependent failure for the first time. This process can occur when stresses acting within an intact slope are below peak strength. This time dependent mechanism of shear surface development can occur over very long time periods and therefore offers an explanation for this phenomenon.

These results have important implications for understanding the development and post failure behaviour of deep-seated landslides, their mechanisms and their relationship to the patterns of movement observed at the ground surface. The results confirm that a greater appreciation of these relationships could be a powerful tool in the management of future landslide risk.

8.2 Limitations

This discussion has successfully demonstrated the relationship between landslide movement patterns and the mechanisms of shear surface deformation occurring within the basal shear zone of deep seated landslides under elevated porewater pressure conditions. Whilst the results of this investigation demonstrate real progress in the understanding and interpretation of landslide behaviour, caution is needed in the application of such techniques to the conditions observed in natural deep-seated landslide

conditions. In using this dataset the limitations of the data presented should be understood.

The mechanisms of failure development considered have focused only on the Gault Clay, and Gault-Carstone transition materials sampled from field sites within or local to Ventnor. The results have been used to propose understanding model of landslide behaviour in brittle clays. Whilst the results have been used successfully to interpret the behaviour of the movement patterns experienced within the Lowtherville Graben, caution must be used in applying this behaviour to other over-consolidated clays which by their nature may vary considerably in their material compositions and mechanical behaviour.

Both triaxial cell testing and BPSB testing are undertaken on relatively small samples which are inferred to be representative of the field conditions. Such small samples may not reflect the potential variability of soil conditions across the site and are highly unlikely to reflect any larger scale regional geological or geomorphological features which may be inherent in the landscape. Thus, geomorphological and geological investigations are important in conjunction with the specialist laboratory based testing developed in this study if such methods are used to interpret ground behaviour at different sites in the future.

The study has benefitted from the continuous monitoring records made available by the Isle of Wight Council. These records are further complimented by a great body of ground movement measurements and observations within the published records. The study has focused largely on the movement patterns of the Lowtherville Graben and has successfully correlated antecedent rainfall, groundwater and ground movement through out the period 1995 to 2001. Whilst this provides a reasonable record to analyse ground movement behaviour it should be recognised that only one major period of ground acceleration was observed in the records. Although this has provide an excellent opportunity to understand the behaviour of the landslide, further calibration with future periods of ground acceleration may assist in improving our understanding of ground behaviour at the site. New

monitoring systems, including replacement crackmeters and settlement cells, were being installed during this study and have yet to be calibrated. Future studies should look to update this investigation with new data from the site when it is made available.

The automated ground movement records have focused the location of the graben and whilst the study has provided a new interpretation of the nature and development of this feature, it may not be reflective of the movement patterns being experienced within the wider landslide system. In particular the Council has established a series of permanent movement marker stations to undertake annual differential GPS surveys across the town. At present there is insufficient data to draw any clear understanding of movement patterns from these records, but in the future such survey information will provide an invaluable source of spatial movement records which will improve our understanding of the behaviour and interactions of different units within the landslide complex.

Automated groundwater measurements have been used from the Winter Gardens in Lower Ventnor, which provides groundwater records for both the upper and lower water tables observed in Ventnor. Whilst the readings have been instrumental in establishing the relationship between antecedent rainfall, groundwater levels and ground movement, the data should be treated cautiously as these readings may not represent the actual pore pressures operating in upper Ventnor. It is the intention of the Council to install and automated piezometers at the base of the Gault Clay in central Ventnor and therefore it is hoped that this relationship can be developed more accurately using future porewater pressure readings from the landslide shear surface.

8.3 Recommendations for further research

Whilst this research has provided new knowledge of the mechanisms and processes operating in deep seated landslide complexes, further research could be considered in order to advance understanding of groundwater induced landslide mechanisms.

The PPR testing undertaken has been designed to replicate field conditions for groundwater-induced failure. Whilst the testing has successfully demonstrated the relationship between mean effective stress and time dependent failure at constant stress, it should be recognised that these tests do not replicate the cyclical patterns of increasing and decreasing porewater pressures within the landslide. It is clear that different patterns of pore pressure re-inflation caused by heavy or prolonged rainfall may impact the development of the shear surface differently. As a consequence further testing, which takes into account pore pressure cycles and in which porewater pressures are reduced as failure develops, should be undertaken to understand this behaviour further.

Movement within pre-existing landslides has been studied using remoulded samples in laboratory testing. It is recognised that pre-existing shear surface in brittle materials would be better represented by a pre-cut singular shear surface along which weakening processes such as polishing, and hardening processes such as chemical cementing, may occur. Further creep testing through short periods of pore pressure re-inflation on pre-cut tri-axial or back pressured shear box samples would be beneficial to study these processes more accurately.

The patterns of movement recorded at Ventnor provide one of the most detailed monitoring records of a UK deep-seated landslide. The patterns of movement, however, have revealed only one single period of accelerated ground creep during the winter period of 2000 to 2001. Whilst clear relationships between this event and groundwater and rainfall have been established at the site it must be recognised that further monitoring may provide additional periods of accelerated ground creep that may assist in refining this relationship. In addition, the automated groundwater records at the site have been shown to be measuring groundwater in a lower landslide unit and may not be directly representative of the porewater pressure conditions impacting the graben. Automation of piezometers in Upper Ventnor would allow specific porewater pressure thresholds to be considered which may lead to further accelerated ground movement at the graben. The results

further indicate the need for further full-scale tests on cut slopes, which have previously provided invaluable datasets of ground movement (e.g. Cooper *et al.*, 1998).

This study has demonstrated how a combined method of detailed field monitoring, geomorphological assessment and geotechnical testing can provide a detailed understanding of complex landslide systems, their mechanisms of movement and their potential future behaviour. Furthermore, detailed instrumentation and long term monitoring would allow the consideration of important parameters such as critical porewater pressure thresholds, which may be used as hazard warning alert criteria or inform on the design of cost effective landslide mitigation measures. Surprisingly the installation of such detailed networks in the UK is rare, although such analytical approaches would provide very cost effective approaches to managing future landslide risk.

References

- Aleotti, P. and Chowdurry, R. 1999. Landslide hazard assessment; summary review and new perspectives. *Bulletin of Engineering Geology and Environment*. 58: 21-44.
- Allison, R.J. 1989. Rates and mechanisms of change in hard rock coastal cliffs. *Zeichtschrift fur Geomorphologie Supplement Band*, 73: 125-138.
- Allison, R.J. 1996. Slope and slope processes. *Progress in Physical Geography*. 20(4): 453-465.
- Allison, R. and Brunnsden, D., 1990. Some mudslide movement patterns. *Earth Surface Processes and Landforms*, 15: 297-311.
- Anderson, S.A and Sitar, N., 1995. Analysis of rainfall-induced debris flow. *ASCE Journal of Geotechnical Engineering*, 121(7): 544-552.
- Barton, M.E. Sleep demons and terrified horses: Determining the onset of instability. In: In: R McInnes, J Jakeways, H Fairbank, and E Mathie (Editors), *Proceedings of the International Conference Landslides and Climate Change, Ventnor Isle of Wight*. Taylor & Francis, London. pp. 475-480.
- Basset, R.H. 1979. Time dependent creep in rock and soil structures. *Creep in Engineering Materials*. pp. 11-37.
- Bass, M.A. 1954. A study of the characteristics and origins of some major areas of landsliding in the Eastern Pennines and Isle of Wight. Thesis (unpublished), University of Sheffield.
- Bentley, S.P. and Siddle, H.J., 2000. New Tredegar Landslide, Rhymney Valley, In: *Landslide and landslide management in South Wales*.
- Bertini, T., Gugusi, F., D'Elia, B. and Rossi-Doria, M. 1984. Climatic conditions and slow movements of colluvial covers in central Italy. *Proceedings of the 4th International Symposium on Landslides, Toronto, Canada*. 1. pp. 367-376.

- Bertini, T., Gugusi, F., D'Elia, B. and Rossi-Doria, M. 1986. Lenti movimenti di versante nell'Abruzzo Adriatico: Caratteri e criteri di stabilizzazione. *Proceedings. XVI Convngno Nazionale di Geotecnica, Bolgogna maggio*. pp. 91-100.
- Bird, E. 1997. *The Shaping of the Isle of Wight; with an excursion guide*. Ex Libris: Whilshire.
- Bishop, A.W. and Henkel, D.J. 1962. *The Measurement of Soil Properties in the Triaxial Test*. Edward Arnold, London. pp. 228.
- Bishop, A.W., Webb, D.L. and Lewin, P.I. 1965. Undisturbed specimens of clay from the Ashford Common shaft: strength effective stress relationship. *Geotechnique*, 15(1): 1-31.
- Bishop, A.W. and Lovenbury, H.T. 1969. Creep characteristics of two undisturbed clays. Proceeding of the 7th International Conference on Soil Mechanics and Foundation Engineering. 1. pp. 29-27.
- Bishop, A.W. and Wesley, L.D. 1975. A hydraulic triaxial apparatus for controlled stress path testing. *Geotechnique*, 25(4): 657-670.
- Bjerrum, L. 1967. Progressive failure in slopes of over-consolidated plastic clay and clay shales. *Journal of the Soil Mechanics Foundation Division of the American Society of Civil Engineers*, 93: 1-49.
- Brabb, E.E. 1989. Landslides – extent and economic significance in the United States, In Brabb, E.E. and Harrod, B.L., (Editors) *Landslides – extent and economic significance*: Rotterdam, Netherlands, A.A. Balkema. pp. 25-50.
- Brabb, E.E. 1991. The world landslide problem. *Episodes*, 14: 52-61.
- Brand, E.W., (1981). Some thoughts on rain-induced slope failure. *Proceedings 10th International Conference on Soil Mechanics and Foundation Engineering, San Francisco*. Balkkema. Pp. 2541-2578.
- British Geological Survey. 1995. Engineering geology of British rocks and soils: Gault clay.

- British Standards Institute (BSI).1981. *Code of Practice for Site Investigations*. BS 5930: 1981.
- British Standards Institute (BSI).1990a. *British Standard Methods of Test for Soils for Civil Engineering Purposes. Part 1: General Requirements and Sample Preparation*. BS 1377: Part 1.
- British Standards Institute (BSI). 1990b. British Standards Methods of Test for Soils for Civil Engineering Purposes. Part 8: *Shear strength tests (effective stress)*. BS 1377: Part 8.
- Bromhead, E.N., Curtis, R.D. and Schofield, W. 1988. Observation and adjustment of a geodetic survey network for measurement of landslide movement. In: C Bonnard (Editor), *Landslides, Proceedings of the 5th International Symposium on Landslides, Lausanne*. pp. 383-386.
- Bromhead, E.N, and Ibsen, M.-L. 2007. Folkestone warren landslides and the impact of the past rainfall record. In: R McInnes, J Jakeyways, H, Fairbank, and E Mathie (Editors), *Proceedings of the International Conference Landslides and Climate Change, Ventnor Isle of Wight*. Taylor & Francis, London. pp. 17-24.
- Brunsdon, D. 1973. The application of systems theory to the study of mass movement, *Geologica. Applicata e Indrogeologi*, University of Bari, 8(1): 185-207.
- Brunsdon, D. 1984. Mudslides. In: D Brunsdon and D.B Prior (Editors), *Slope Instability*, Wiley: Chichester. pp. 363-418.
- Brunsdon, D. 1985. Landslide types, mechanisms, recognition, identification. In: C.S Morgan (Editor), *Landslides in the South Wales Coalfield, Proceedings Symposium*, 1-3 April 1985, The Polytechnic of South Wales. pp. 19-28.
- Brunsdon, D. 1993. Mass movement; the research frontier and beyond: a geomorphological approach. *Geomorphology*, 7: 85-128.
- Brunsdon, D.N. 2002. The fifth Glossop lecture: Geomorphological roulette for engineers and planners: some insights into an old game. *Quarterly Journal of Engineering Geology and Hydrogeology*, 35: 101-142.

- Burland, J.B., 1990. On the compressibility of shear strength of natural clays. *Geotechnique*, 40(3): 329-378.
- Burland, J.B., Rampello, S., Georgiannou, V.N. and Calabresi, G. 1996. A laboratory study of the strength of four stiff clays. *Geotechnique*, 46(3): 491-514.
- Campanella, R.G. and Vaid, Y.P. 1974. Triaxial and plane strain creep rupture of an undisturbed clay. *Canadian Geotechnical Journal*, 11: 1-10.
- Carey, J.M. 2002. Determining Landslide behaviour through the Analysis of Landslide Movement Patterns and Material Geotechnical Properties. The Undercliff, Isle of Wight. MSc Dissertation (unpublished), University of Durham.
- Carey, J.M., Moore, R., Petley, D.N. and Siddle, H.J. 2007. Pre-failure behaviour of slope materials and their significance in the progressive failure of landslides. In: R McInnes, J Jakeways, H Fairbank, and E Mathie (Editors), *Proceedings of the International Conference Landslides and Climate Change, Ventnor Isle of Wight*. Taylor & Francis, London. pp. 207-215.
- Carrara, A; Guzzetti, M; Cardinali, M and Reichenbach, P. 1999. Use of the Technology in the Prediction and Monitoring of Landslide Hazard. *Natural Hazards*. 20: 117-135.
- Casagli, N., Filippo, C., Del Ventisette. and Luzi, G. (2010). Monitoring, prediction, and early warning using ground based radar interferometry, *Landslides*. 7:291-301.
- Chandler, M.P. 1984. The Coastal landslides forming the Undercliff of the Isle of Wight. Ph. D. Thesis (unpublished), Imperial College, University of London.
- Chandler, R.J. and Skempton, A.W. 1974. The design of permanent cutting slopes in stiff fissured clays. *Geotechnique*, 24(4): 457-466.
- Chelli, A., Mandrone, G. and Truffelli, G. 2006. Field investigations and monitoring as tools for modelling the Rossena castle landslide (Northern Appennines, Italy). *Landslides*, 3: 252-259.
- Chigira, M., Wu, X., Inokuchi, T. and Wang, G. 2010. Landslides induced by the 2008 Wenchuan earthquake, Sichuan, China. *Geomorphology*, 118: 225-238.

- Clark, A.R., Lee, M.E. Moore, R. 1994. The development of a ground behaviour model for the assessment of landslide hazard in the Isle of Wight Undercliff and its role in supporting major development infrastructure projects. *Proceedings 7th International Congress International Association of Engineering Geology*, Lisbon, 6. pp. 4901-4913.
- Clark, A., Moore, R. McInnes, R.G. 1995. Landslide response and management, Blackgang, Isle of Wight. *Proceedings of the 30th Conference of Rivers and Coastal Engineers, Keele, UK. Ministry of Agriculture, Fisheries and Food.*
- Conforth, D.N. 2005. *Landslides in Practice: Investigation, Analysis, and Remediation / Preventative Options in Soils*, Jon Wiley: New York.
- Cooper, M.R., Bromhead, E.N., Petley, D.J. and Grant, D.I., 1998. The Selbourne cutting stability experiment. *Geotechnique*. 48: 83-101.
- Costa, J.E. and Schuster, R.L. 1987. *The Formation and Failure of Natural Dams, US Geological Survey Open- File Report*. pp. 87-392.
- Couperthwaite, S.L. and Marshall, R.G. 1989. Slope instability poses complex problems for pipeline design. *Technology Oil and gas Journal*, 85.
- Craig, R.F. 1992. Soil Mechanics. Spon Press, London, pp. 102-103.
- Crozier, M.J. 1984. Field assessment of slope instability. In: D Brunnsden and S Prior (Editors). *Slope Instability*, Wiley: Chichester. pp. 103-142.
- Cruden, D.M. 1991. A simple definition of a landslide. *Bulletin International Association for Engineering Geology*, 43: 27-29.
- Culling, W.E. 1963. Soil creep and the development of hillside slopes. *Journal of Geology*, 71: 127-161.
- Culling, W.E. 1983. Rate - process theory in geomorphic soil creep. *Catena Supplement*, 4: 191-214.
- Dai, F.C., Lee, C.F., Wang, S.J. and Feng, Y.Y., 1999. Stress-strain behaviour of a loosely compacted volcanic-derived soil and its significance to rainfall-induced fill slope failures. *Engineering Geology*, 53: 359-370.

- Dai, F.C. and Lee, C.F., 2002. Landslide characteristics and slope instability modelling using GIS, Lantau Island, Hong Kong. *Geomorphology*, 42(3-4): 213-228.
- de Freitas, M.H. 2009. The Ninth Glossop lecture: Geology: its principles, practice and potential for Geotechnics. *Quarterly Journal of Engineering Geology and Hydrogeology*, 42(4): 395-441.
- Dias, A. 2000. Assessment and interpretation of geotechnical instrument data from the Undercliff, Isle of Wight. MSc Dissertation (unpublished), University of Portsmouth.
- Dikau, R., Brunsden, D., Schrott, L. and Ibsen, M-L (Editors) 1996. *Landslide Recognition: Identification, Movement and Causes*. John Wiley & Sons: Chichester. pp. 1-13.
- Dixon, N. and Bromhead, E.N. 1991. The mechanics of first time slides in the London Clay cliff at the Isle of Sheppey, England. *Proceedings of the International Conference on Slope Stability Engineering: Developments and Applications, Isle of Wight, UK, April 15-18*. pp. 277-282.
- Dixon, N. and Bromhead, E.N. 2002. Landsliding in London Clay coastal cliffs. *Quarterly Journal of engineering Geology and Hydrogeology*, 35(4): 327-343.
- Department of the Environment (DOE). 1991. *Coastal landslip potential assessment: Isle of Wight Ventnor, Contract PECD 7/1/272*. Prepared by Geomorphological Services Limited.
- Donoghue, D. 1986. Review and analysis of slow mass movement mechanisms with reference to a Weardale catchment, N. England. *Zeitschrift fur Geomorphologie Supplementband*, 60: 41-54.
- Downton, M.W. and Pielke, R.A. (2005). How accurate are Disaster Loss Data? The case of U.S. Flood Damagem. *Natural Hazards*. 35: 211-228
- Drescher, A., Vardoulakis, I. and Han, C. 1990. A biaxial apparatus for testing soil. *Geotechnical testing Journal ASTM*, 13(3): 226-234.

- Dunnicliff, J. 1997. Warm-Up time for inclinometer probes- a reminder. *Geotechnical News Magazine*, 15(1): 41-42.
- Dunning, S.A; Rosser, N.J. Petley, D.N. and Massey, C.R. (2006). Formation and failure of the Tsatichhu landslide dam, Bhutan. *Landslides*, 3(2): 107-113.
- EDM-DAT. 2005. *The OFDA/CRED International Disaster Database*. Université Catholique de Louvain – Brussels – Belgium. <http://www.emdat.be/maps-disaster-types>
[Accessed on March 15](#), 2009.
- Eisbacher, G.H. and Clague, J.J. 1980. Urban landslides in the vicinity of Vancouver, British Columbia, with special reference to the December 1979 rainstorm. *Canadian Geotechnical Journal*, 18: 205-216.
- EPOCH (European Community Programme). 1993. *Temporal Occurrence and Forecasting of Landslides in the European Community*. 3 Volumes, Contract No. 90 0025.
- Evans, S.G., Bishop, N.F., Smoll, L.F., Murillo, P.V., Delaney, K.B and Oliver-Smith, A. 2009. A re-examination of the mechanism and human impact of catastrophic mass flows originating on Nevado Huascarán, Cordillera Blanca, Peru in 1962 and 1970. *Engineering Geology*, 108:96-118.
- Finno, R.J. and Rhee, Y. 1993. Consolidation, pre- and post- peak shearing responses from internally instrumented biaxial compression device. *Geotechnical Testing Journal ASTM*, 16(4): 496-509.
- Fish, P.R., Moore, R, and Carey, J.M. 2006. Landslide geomorphology of Cayton Bay, North Yorkshire, UK. *Proceedings of the Yorkshire Geological Society*, 56 (1): 5-14.
- Flentje, P.N., Chowdhury., R.N., Tobin, P. and Brizga, V. 2005. Towards real-time risk management in an urban area, In: Hungr, Fell, Couture and Eberhardt (eds) *Landslide Risk Management*, Taylor & Francis: London. pp. 741-751.
- Fort, D.S., Clark, A.R., Savage, D.T. and Davis, G.M. 2000. Instrumentation and monitoring of coastal landslides at Lyme Regis, Dorset. *Landslides in Research*

- Engineering and Practice, Proceedings of the 8th International Conference on Slopes and Landslides, Cardiff.* pp. 573-578.
- Foster, C. Gibson, A.D, and Wildman, G. 2008. The New national landslide database and landslide hazard assessment of Great Britain. *First World Landslide Forum Tokyo*, 18-20 Nov 200. pp. 203-206.
- Federico, A., Popsecu, M., Fidelibus, C. And Interno, G. 2004. On the prediction of the time of occurrence of a slope failure: a review: In W.A. Lacerda, M. Ehrlich, S.A.B. Fontoura and A.S.F. Sayao (Editors), *Landslide: Evaluation and Stabilization. Proceedings of the 9th International Symposium on Landslides, Rio de Janeiro, June 28-July 2, 2004.* Leiden: A.A. Balkema, pp. 979-1188.
- Fukuzono, T., 1985. A new method for predicting the failure time of a slope. *Proceedings of 4th International Conference and Field Workshop on Landslides, 1985, Tokyo*, pp. 145-150.
- Fukuzono, T. 1989. A simple method for predicting failure the failure time of slope using reciprocal of velocity. *Technology for Disaster Prevention, Science and Technology Agency, Japan and International Co-operation Agency, Japan*, 13: pp.111-128.
- Fukuzono, T. 1990. Recent studies on the time prediction of slope failures. *Landslide News*, 4: 9-12.
- Furuya, G., Sassa, K., Hiura, H and Fukuoka, H. 1999. Mechanisms of creep movement caused by landslide activity and underground erosion in crystalline schist, Shikoku Island, Southwestern Japan. In: T Sakuma and K Yagi (Editors), *Proceedings of the 8th International Conference on Creep and Fracture of Engineering Materials and Structures.* pp. 171-174
- GDS Instruments. 2005. The GDS Laboratory Users Handbook. *GDSLAB v2 Handbook.*
- GDS Instruments. 2008. The GDS Triaxial Testing System Hardware Handbook (Advanced and Standard). *GDS Hardware Handbook.*

- Georgiannou, V.N. and Burland, J.B. 2006. A laboratory study of slip surface formation in an intact natural stiff clay. *Geotechnique*, 56(8); 551-559.
- Geomorphological Service Limited in association with Rendel Palmer and Tritton, 1986/87. *Review of Research into Landsliding in Great Britain: Reports to the Environment*. Series A: Regional review of landsliding – regional atlases of country maps at 1:25,000 scale, regional reports. Landslide database.
- Geomorphological Services Limited. 1987. *Review of research into landsliding in Great Britain: Series E, National summary and recommendations*. Technical report to Department of the Environment.
- Gokceoglu, C. and Sezer, E. 2009. A statistical assessment on international landslide literature (1945 – 2008). *Landslides*, 6; 345-351.
- Griffiths, J.S., Hutchinson, J.N., Brunsdon, D.N., Petley, D.J and Fookes, P.G. 2004. The reactivation of a landslide during the construction of the Ok Ma tailings dam, Papua New Guinea. *Quarterly Journal of Engineering Geology and Hydrogeology*, 37: 317-325.
- Gonzalez, D.A., Ledesma, A. And Corominas. 2008. The viscous component in slow moving landslides: A practical case. In: Chen et al. (Editors) *Landslides and Engineered Slopes*, Taylor and Francis Group: London. pp. 237-242.
- Gueguen, Y. and Besuelle, P. 2007. Damage and localization: two key concepts in rock deformation studies. In; H. Lewis and G.D. Couples (eds) *The Relationship between Damage and Localisation, Geological Society Special Publication No. 289*. pp. 7-17.
- Halcrow. 2006. *Ventnor Undercliff, Isle of Wight Coastal Instability Risk: Interpretative Report and Quantitative Risk Analysis*. Technical Report to the Isle of Wight Council.
- Hancox, G.T., McSaveney, M.J., Manville, V.R. and Davies, T.R. 2005. The October 1999 Mt Adams rock avalanche and subsequent landslide dam-break flood and effects in Poerua River, Westland, New Zealand. *New Zealand Journal of Geology and Geophysics*. 48: 683-705.

- Hayashi *et al.*, 1989. On the forecast of time to failure of slope (II): Approximate forecast in early period of tertiary creep. *Journal of Japanese Landslide Society*, 25(3): 11-16.
- Helmstetter, A., Sornette, D., Grasso, J.R., Andersen, V., Gluzman, S. and Pisarenko, V. 2003. Slider-block friction model for landslides: implication for prediction of mountain collapse. *Journal of Geophysical Research*, 109 (B02): 409-432.
- Helmstetter, A. and Sornette, D. 2004. Slider block friction model for landslides: application to Vaiont and La Clapiere landslides. *Journal of Geophysical Research*, 109 (B02): 210-225.
- Hutchinson, J.N. 1965. A reconnaissance of coastal landslides in the Isle of Wight. Note No. EN 35.65. Watford: Building Research Station.
- Hutchinson, J.N. 1967. The free degradation of London Clay cliffs. *Proceedings of the Geotechnical Conference*, Oslo, 1. pp.113-118.
- Hutchinson, J.N. 1968. Mass movement. In: R.W, Fairbank (ed.), *Encyclopedia of Geomorphology*, Reinhold Book Corporation: London. pp. 688-696.
- Hutchinson, J.N. 1969. A reconsideration of the coastal landslides at Folkestone Warren, Kent. *Geotechnique*, 19: 6-38.
- Hutchinson, J.N. 1976. Coastal landslides in cliffs of Peistocene deposits between Cromer and Overstrand, Norfolk England. *Laurits Bjerrum Memorial Volume*, Norwegian Geotechnical Institute, Oslo. pp. 155-182.
- Hutchinson, J.N. 1984. Landslides in Britain and their counter measures, *Journal of Japan Landslide Society*. 12:1-25.
- Hutchinson, J.N. 1986a. A sliding-consolidation model for flow slides, debris flows and avalanches. *Canadian Geotechnical Journal*, 32: 610-623.
- Hutchinson, J.N. 1986b. Cliffs and shores in cohesive materials: geotechnical and engineering geological aspects. In: M. G Skafel (Editor) *Proceedings Symposium on Cohesive Shores*, Burlington, Ontario, Canada: Assocaite

- Committee for Research on Shoreline Erosion and Sedimentation; and National Research Council Canada. pp. 1-44.
- Hutchinson, J.N. 1987a. Mechanisms producing large displacements in landslides on pre-existing shears. *Memoir of the Geological Society of China*, 9: 175-200.
- Hutchinson, J.N. 1987b. Some coastal landslides of the southern Isle of Wight. In: K.E Barber (Editor), *Wessex and the Isle of Wight, Field Guide*, Cambridge: Quaternary Research Association. pp. 123-135.
- Hutchinson, J. N. 1988. General Report. Morphological and geotechnical parameters of landslides in relation to geology and geohydrology. *Proceedings of the 5th International Symposium on Landslides, Lausanne*, 1. pp. 3-35.
- Hutchinson, J.N. 2001a. The Fourth Glossop Lecture, Reading the ground: morphology and geology in site appraisal. *Quarterly Journal of Engineering Geology and Hydrogeology*, 34: 7-50.
- Hutchinson, J.N. 2001b. Landslide risk- to know, to foresee, to prevent, *Geologia Tecnica and Abientale*, 9: 3-24.
- Hutchinson, J.N. and Bhandari, R.K. 1971. Undrained loading, a fundamental mechanism of mudflows and other mass movements. *Geotechnique*, 21: 353-358.
- Hutchinson, J.N., Bromhead, E.N. and Lupini, J.F. 1980. Additional observations on the Folkestone Warren landslides. *Quarterly Journal of Engineering Geology*, 13: 1-32.
- Hutchinson, J.N., Bromhead, E.N. and Chandler, M.P. 1991a. Investigations of the landslides at St Catherines Point, Isle of Wight. In: R.J Chandler (Editor), *International Conference on Slope Stability Engineering-Development and Applications*, London: Thomas Telford. pp. 213-218.
- Hutchinson, J.N. and Bromhead, E.N. 2002. Keynote Paper: Isle of Wight landslides. In: R.G McInnes and J Jakeways (Editors), *Instability Planning and Management: Seeking Sustainable Solutions to Ground Movement Problems*,

- Proceedings of International Conference, Ventnor*. Thomas Telford: London, pp. 3-70.
- Hutchinson, J.N., Brunsten, D. and Lee, E.M. 1991b. The geomorphology of the landslide complex at Ventnor, Isle of Wight. In: R.J. Chandler (Editor) *International Conference on Slope Stability Engineering- Developments and Applications*, London: Thomas Telford. pp. 157-168.
- Hutchinson, J.N., Chandler, M.P. and Bromhead, E.N. 1985. A review of current research on the landslides forming the forming the Undercliff of the Isle of Wight with some practical implications. *Conference Proceedings, Problems associated with the coastline*, Newport Isle of Wight. pp. 17-18.
- Iverson, R.M. 2005. Regulation of landslide motion by dilatancy and pore pressure feedback. *Journal of Geophysical Research – Earth Surface*, 110 (F2): Article no – F02015.
- Julian, M. and Anthony, E. 1996. Aspects of landslide activity in the Mercantour Massif and the French Riviera, Southern France. *Geomorphology*, 15: 275-289.
- Kilburn, C.J. and Petley, D.N. 2003. Forecasting giant, catastrophic slope collapse: lessons from Vajont Northern Italy. *Geomorphology*. 54: 21-32.
- Knox, G. 1927. Landslides in the South Wales Valleys. *Proceedings of the South Wales Institute of Civil Engineers*, 43: 161-281.
- Korup, O. 2005. Geomorphic hazard assessment of landslide dams in South Westland, New Zealand: fundamental problems and approaches. *Geomorphology*. 66, 167-188.
- Lacey, G.N. 1972. Observations on Aberfan. *Journal of Psychosomatic Research*, 16: 257-260.
- Lee, E.M. 2009. Landslide risk assessment: the challenge of estimating the probability of landsliding. *Quarterly Journal of Engineering Geology and Hydrogeology*, 42(4): 445-458.

- Lee, E.M., Audibert, J.M.E., Hengesh, J.V. and Nyman, D.J. 2009. Technical Note: Landslide-related ruptures of the Camisea pipeline system, Peru. *Quarterly Journal of Engineering Geology and Hydrogeology*, 42(2): 251-259.
- Lee, E.M. and Brunsden, D. N. 2000. Coastal landslides of southern England: mechanisms and management. In: E.N. Bromhead., N. Dixon and M'L Ibsen (eds) *Landslides: in research theory and practice. CD-ROM*.
- Lee, E.M. and Moore, R. 1991. Coastal Landslip Potential Assessment: Isle of Wight Undercliff, Ventnor, Technical Report, Department of the Environment.
- Lee, E.M. and Moore, R. 2007. Ventnor Undercliff: development of landslide scenarios and quantitative risk assessment. In: R McInnes, J Jakeways, H, Fairbank and E Mathie (Editors), *Proceedings of the International Conference Landslides and Climate Change, Ventnor Isle of Wight*. Taylor & Francis, London. pp.17-24.
- Logan, J.M. 2007. The progression from damage to localization of displacement observed in laboratory testing of porous rocks. In H Lewis and G. D Couples (Editors), *The Relationship between Damage and Localization*, Geological Society Special Publication No. 289 pp. 75-87.
- Long, A.J. and Tooley, M.J. 1995. Holocene sea-level and crustal movements Hampshire and Southeast England, United Kingdom. In: Frinkl Jr. (Editor), *Holocene Cycles: Climate, Sea Levels and Sedimentation, Journal of Coastal Research*, Special Issue 17. pp. 299-310.
- Liu, C.-N. 2009. Progressive failure mechanism in one-dimensional stability analysis of shallow slope failures. *Landslides*, 6: 129-137.
- Main, I.G. 1999. Applicability of time-to-failure analysis to accelerated strain before earthquakes and volcanic eruptions. *Geophysical Journal International*, 139: F1-F6.
- Main, I.G., 2000 . A damage mechanics model for power-law creep and earthquake aftershock and foreshock sequences. *Geophysical Journal International*, 142(1): 151-161.

- Malet, J.P., van Asch, Th. W.J., van Beek, R. and Maquaire, O. (2005). Forecasting the behaviour of complex landslides with a spatially distributed hydrological model. *Natural Hazards and Earth System Sciences*, 5: 71-18.
- McCahon, C.P., Carling, P.A., Pascoe, D. 1987. Chemical and ecological effects of a Pennine peat slide. *Environmental Pollution*, 45: 275– 289.
- Mikkelsen, P.E. 2003. Advances in inclinometer data analysis. In: F. Myrvoll (Editor) *Proceedings of the 6th International Symposium on Field Measurement in Geomatics*, Oslo, Norway. pp 13.
- Mills, A.J., Moore, R., Carey, J.M. and Trinder, S.K. 2007. Recent landslide impacts in Scotland: Possible evidence of climate change? In: R McInnes, J. Jakeways, H, Fairbank and E Mathie (Editors) *Proceedings of the International Conference Landslides and Climate Change, Ventnor Isle of Wight*. Taylor & Francis, London. pp. 99-106.
- Monma, K., Kojima, S, and Kobayashi, T. 2000. Rock slope monitoring system and rock fall prediction. *Landslides News*, 13: 33-34.
- Moore, R. 1986. Fairlight Landslips; the location form and behaviour of coastal landslides with respect to toe erosion. Geography Department, Kings College London, Occasional Papers, 27.
- Moore, R. and Brunsden, D. (1996). A physio-mechanism of seasonal mudsliding. *Geotechnique*. Vol XLVI (2), 259-278.
- Moore, R. Lee, E.M. and Clark, A.R. 1995. *The Undercliff of the Isle of Wight: a review of ground behaviour*. Cross Publishing: London.
- Moore, R., Carey, J.M., Mills, A., Martin, S., Trinder, S., Kerry, L., Leask, G. and Simmons, A. 2006. Recent landslide impacts on the UK Scottish road network: investigation in the mechanisms, causes and management of landslide risk. *Proceedings International Conference on Slopes, Malaysia*, pp. 223-237.
- Moore, R., Carey, J.M., McInnes, R. G. and Houghton, J.E.M. 2007a. Climate Change, so what? Implications for ground movement and landslide event frequency in the Ventnor Undercliff, Isle of Wight. In: R.J McInnes, J Jakeways,

- H Fairbank and E Mathie (Editors), *Proceedings of the International Conference Landslides and Climate Change, Ventnor Isle of Wight*. Taylor & Francis, London. pp. 335-344.
- Moore, R., Turner, M.D., Palmer, M.J. and Carey, J.M. 2007b. The Ventnor Undercliff: Landslide model, mechanisms and causes, and the implications of climate change induced ground behaviour risk. In: R. J McInnes., J Jakeways., H Fairbank, and E Mathie (Editors), *Proceedings of the International Conference Landslides and Climate Change, Ventnor Isle of Wight*. Taylor & Francis, London. pp. 365-375.
- Moriwaki, H., Inokuchi, T., Hattanji, T., Sassa, K., Ochiai,H., and Wang, G. 2004. Failure processes in a full-scale landslide experiment using a rainfall simulator. *Landslides*, 1:277-288.
- Nakamura, H. 1984. Landslides in silts and sands mainly in Japan. *Proceedings of the 4th International Symposium on Landslides, Toronto*, 1. pp. 155-185.
- Ng, K-Y. 2007. Mechanisms of Shallow Rainfall-induced Landslides in Residual Soils in Humid Tropical Environments. Thesis (Unpublished), University of Durham.
- Ng, K-Y. and Petley, D.N. 2009. The use of pore pressure reinflation testing in landslide management in Hong Kong. *Quarterly Journal of Engineering Geology and Hydrogeology*. 42:487-498.
- Orense, R., Farooq, K. and Towhata, I. 2004. Deformation behaviour of sandy slopes during rainwater infiltration. *Soils and Foundations*, 44(2): 15-30.
- Pachauri, A.K. and Pant, M. 1992. Landslide hazard mapping based on geological attributes. *Engineering Geology*. 32, 81-100.
- Palmer, M.P., Carey, J.M. and Turner, M.D. 2007. Litho-stratigraphy of the Ventnor Undercliff and determination of critical horizons through borehole geophysics. In R.J McInnes., J Jakeways., H Fairbank, and E Mathie (Editors) *Proceedings of the International Conference Landslides and Climate Change, Ventnor Isle of Wight*. Taylor & Francis, London. pp. 365-375.

- Parry, R.H.G. 1960, Triaxial compression and extension tests on remoulded saturated clay. *Geotechnique*, 10: 166-180.
- Penman, H.L. 1948. Natural evaporation from open water, bare soil, and grass. *Proceedings of the Royal Society, London, U.K*, A193. pp. 120–145.
- Petley, D.N. 1999. Failure envelope of mudrocks at high confining pressures. In: A.C Alpin, A.J Fleet and J.H.S Macquaker (Editors), *Muds and Mudstones: Physical and Fluid Flow Properties*, Geological Society of London, Special Publications, 158. pp. 61-71.
- Petley, D.N. 2004. The evolution of slope failures: mechanisms of rupture propagation. *Natural Hazards and Earth System Sciences*, 4: 147-152
- Petley, D.N. and Allison, R.J. 1997. The mechanics of deep-seated landslides. *Earth Surface Processes and Landforms*, 22: 747-758.
- Petley, D.N. and Allison, R.J. 2006. On the movement of landslides. *International Conference on Slopes, Malaysia*, Special lecture. pp. 115-137.
- Petley, D.N., Bulmer, M.H.K. and Murphy, W., 2002. Patterns of movement in rotational and translational landslides. *Geology*, 30 (8): 719-722.
- Petley, D.N. and Bulmer, M.H. 2004. The application of Earth observation technologies for landslide disaster mitigation. *Proceedings of the CEOS Workshop, November 2004, Beijing*.
- Petley, D.N., Higuchi, T., Petley, D.J., Bulmer, M.H. and Carey, J., 2005a. The development of progressive landslide failure in cohesive materials. *Geology*, 33(3): 201-204.
- Petley, D.N., Higuchi, T., Dunning, S., Rosser, N.J., Petley, D.J., Bulmer, M.H. and Carey, J., 2005b. A new model for development of movement in progressive landslides. In: O Hungr, R Fell, R Couture and E Eberhardt (Editors), *Landslide Risk Management*, A.T. Balkema, Amsterdam. pp. 201-204.
- Petley, D.N., Mantovani, F., Bulmer, M.H. & Zannoni, A. 2005c. The use of surface monitoring data for the interpretation of landslide movement patterns. *Geomorphology*, 66:133-147.

- Petley, D.N. and Petley, D.J., 2006. On the initiation of large rockslides: perspectives from a new analysis of the Vaiont movement record. In: S.G Evans, G S Mugnozza, A Strom and R.L Hermanns (Editors), *Landslides from Massive Rock Slope Failure*. NATO Science Series IV: Earth and Environmental Sciences. Springer: Dordrecht. pp. 77-84.
- Petley, D.N., Hearn, G.J., Hart, A., Rosser, N.J., Dunning, S.A., Oven, K., and Mitchell, W.A. 2007. Trends in landslide occurrence in Nepal. *Natural Hazards*, 43: 23-44.
- Petley, D.N. 2008. On climate and landslides in Asia. In H Marui (Editor), *Proceedings of the World Landslide Forum Satellite Conference, Sendai, Japan*. Japan Landslide Society. pp. 1-11.
- Petley, D.N., Rosser, N.J., Karim, D., Wali, S., Ali, N., Nasab, N. and Shaban, K. 2010. Non-seismic landslide hazards along the Himalayan Arc. In: Williams, A.L., Pinches, G.M., Chin, C.Y., McMorran, T.J. and Massey, C.I. (Editors) *Geologically Active*. CRC Press, London, pp. 143-154..
- Picarelli L. and Russo C. 2004. Mechanics of slow active landslides and interaction with man-made works. *Key Note Lecture, 9th International Symposium on Landslides, Rio de Janeiro*, vol. 2.
- Picarelli, L., Urciuoli, G., and Russo, C. 2004. Effects of groundwater regime on the behaviour of clayey slopes. *Canadian Geotechnical Journal*, 41: 467-484.
- Pitts, J. and Brunnsden, D. 1987. A reconsideration of the Bindon landslide of 1839. *Proceedings of the Geological Association of London*, 89: 1-18.
- Prior, D.B. and Stephens, N. 1972. Some movement patterns of temperate mudflows: examples from north-east Ireland. *Bulletin of the Geological Society of America*, 83: 2533-2544.
- Reid, M.E., Baum, R.L., LaHusen, R.G. and Ellis, W.L. 2008. Capturing landslide dynamics and hydrologic triggers using near-real-time monitoring. In: Chen *et al.* (Editors) *Landslides in Engineered Slopes*, Taylor & Francis Group: London. pp. 179-191.

- Rosser, N. J., Petley, D. N., Lim, M., Dunning, S. A. & Allison, R. J. 2005. Terrestrial laser scanning for monitoring the process of hard rock coastal cliff erosion. *Quarterly Journal of Engineering Geology and Hydrogeology*, 38: 363-376.
- Saito, M. (1965). Forecasting the time and occurrence of a slope failure. *Proceedings of the 6th International Conference on Soil Mechanics and Foundation Engineering*. 2. pp. 537-541.
- Saito, M. 1969. Forecasting time of slope failure by tertiary creep. *Proceedings of the 7th International Conference on Soil Mechanics and Foundation Engineering, Mexico*. pp. 677-683.
- Saito, M. 1980. Semi-logarithmic representation for forecasting slope failure. *Proceedings of the International Symposium on Landslides*, 1. pp. 321-324.
- Salt, G. (1988). Landslide mobility and remedial measures. *Proceedings of the 6th International Conference on Slopes and Landslide*, 1. pp. 757-762.
- Salvati, P., Bianchi, C., Rossi, M and Guzzetti, F. 2010. Societal landslide and flood risk in Italy. *Natural Hazards and Earth System Sciences*, 10: 465-483.
- Sassa, K. (1989). Geotechnical Classification of Landslides. *Landslide News*. 3, 21-24
- Schofield, A. and Wroth, P. 1968. *Critical State Soil Mechanics*. McGraw –Hill: London. pp. 222-223.
- Seed, H.B. and Wilson, S.D. 1967. The Turnagain Heights Landslide, Anchorage, Alaska. *Journal of Soil Mechanics and Foundation Engineering*, 93: 325-353.
- Selby, M.J. 1993. *Hillslope Materials and Processes; Second Edition*. Oxford University Press, Oxford, England, pp. 270.
- Skempton, A.W. 1964. The long-term stability of clay slopes. *Geotechnique*. 14(20): 75-101.
- Skempton, A.W. 1969. Long term stability of clay slopes, *Geotechnique*. 14(2): 77-101.

- Skempton, A.W. 1985. Residual strength of clays in landslides, folded strata and the laboratory. *Geotechnique*, 35(1): 3-18.
- Skempton, A.W. and Hutchinson, J.N., 1969. Stability of natural slopes and embankment foundations, state-of-the-art report. *Proceedings of the 7th International Conference on Soil Mechanics and Foundation Engineering, Mexico*, 4, pp. 291-340.
- Sornette, D., Helmstetter, A., Andersen, J.V., Gluzman, S., Grasso, J.R. and Pisarenko, V. 2004. Towards landslide predictions: two case studies. *Physica A-Statistical Mechanics and Its Applications*, 338(4): 605-632.
- Stark, T.D. and Choi, H. 2008. Slope inclinometers for landslides. *Landslides*, 5 (3); 339-350.
- Stephens, N., Creighton., J.R, and Hannon, M.J. 1975. The late Pleistocene period in north eastern Ireland: an assessment. *Irish Geography*, 8: 1-23.
- Terzaghi, K., 1950. Mechanisms of landslides. In: *Geological Society of America (Editors), Application of Geology to Engineering Practice*: Geological Society of America, New York. pp. 83-123.
- The Weather Channel, UK and Ireland. 2010. Averages and records for Isle of Wight Climate, United Kingdom. <http://uk.weather.com/weather/climatology/UKXX11881>. Accessed on April 5, 2009.
- Thornthwaite, C. W. 1948. An approach toward a rational classification of climate. *Geographical Review*, 38 (1): 55-94.
- Tigila, A., Ladanza, C and Spizzichino, D. 2010. Quality assessment of the Italian Inventory using GIS processing, *Landslides*. 7(4); 455-470.
- Tomalin, D. 2000. Geomorphological evolution of the Solent Seaway and the Severance of Wight: A Review. In: M Collins and K Ansell (Editors), *Solent Science - A Review*, Amsterdam:Elsevier. pp. 9-10.
- Transportation Research Board. 2008. Use of Inclinometer fro Geotechnical Instrumentation on Transportation Project, state of practice. Transportation

research Circular Number E-C129. Transportation Research Board of National Academies

- Tsai, T.-L. 2008. The influence of rainstorm pattern on shallow landslide. *Environmental Geology*, 53(7): 1563-1569.
- Tsukomoto, 2002. Determination of shear strength of Hawaiian residual soil subjected to rainfall induced landslides. *Geotechnique*, 52; 143-144.
- Ulusay, R. and Aksoy, H. 1994. Assessment of the failure mechanism of a highwall slope under spoil pile loadings at a coal mine. *Engineering Geology*, 38:117-134.
- Van Ash, Th.J.W., Van Beek, L.P.H. and Bogaard, T.A. 2007. Problems in predicting the mobility of slow moving landslides. *Engineering Geology*, 91:46-55.
- Varley, P.M., Warren, C. D., Rankin, W.J. and Harris. 1996. Site investigations. In C. S Hart, M. B Varley and C. D Warren (Editors) *Engineering Geology of the Channel Tunnel*. Thomas Telford: London. pp. 11-33.
- Varnes, D.J. 1958. Landslide types and processes. Highways Research Board, Special Report, Washington DC, 29. pp. 20-47.
- Varnes, D.J. 1978. Slope movement types and processes. In: R Schuster and R Krizek (Editors), *Landslide Analysis and Control. Special Report 176. National Research Council (U.S)*. Transportation Research Board., National Academy of Sciences, Washington, D.C. pp. 11-33.
- Varnes, D.J. 1983. Time-deformation relations in creep to failure of earth materials. *Proceeding of the 7th Southeast Asian Geotechnical Conference, 22-26, November 1982, Hong Kong*. pp. 107-1302.
- Velegrakis, A., Dix, J.K. and Collins, M.B. (1999). Late Quaternary evolution of the upper reaches of the Solent River, Southern England, based upon marine geological evidence. *Journal of the Geological Society, London*, 156: 73-87.
- Vibert, C. and Arnould, M. 1987. An attempt at predicting the failure of a mountainous slope: The 'La Clapiere' Slide at Saint-Etienne-de-Tinee (France). *Landslide News*, 1:4-6.

- Viggiani, G., Rampello, S., Georgiannou, V.N. and Bardanis, M.E. 2001. A laboratory study of post-rupture strength. *Geotechnique*, 51(8), 665-675.
- Voight, B. 1988. A relation to describe rate dependent material failure. *Science*, 243, 200-203.
- Voight, B. 1989. A method for prediction of volcanic eruptions. *Nature*, 332: 125-130.
- Wang, G. and Sassa, K. 2003. Pore-pressure generation and movement of rainfall-induced landslides: effects of grain size and fine particle content. *Engineering Geology*, 69: 109-125.
- Wang, F.W., Sassa, K, and Wang, G.H. 2003. Mechanisms of the long-runout Hiegaesi Landslide, triggered by heavy rainfall. *Landslides*. 14/15:15-19.
- Wang, F., Okuno, T. and Matsumoto, T. 2007. Deformation characteristics and influential factors for the giant Jinnosuke-dani landslide in the Haku-san Maountain area, Japan. *Landslides*, 4(1): 19-31.
- Watry, S.M. and Ehlig, P.L. 1995. Effect of test method and procedure on measurements of residual shear strength of bentonite from the Potuguese Bend landslide. *Geological Society of America Review, Engineering Geology*, 10: 13-38.
- Wataru, N. and Tsukasa, E. 2004. Occurrence of delayed failure and deformation of ground with excavation on the tuff of Paleogene Kobe Group, Kobe district, SW Japan. *Journal of the Japan Landslide Society*, 41(4): 33-43.
- Whitaker, W. 1910. The Water supply of Hampshire (including the Isle of Wight). *Memoirs of the Geological Survey of Great Britain England and Wales*. London: H.M.S.O.
- White, H.J.O (1921). A short account of the geology of the Isle of Wight. *Memoirs of the Geological Survey of Great Britain England and Wales*. London: H.M.S.O.
- Winter, M.G., Shackman, L. and Mcgregor, F. 2007. Landslide management and mitigation on the Scottish road network. In: R McInnes, J Jakeyways., H Fairbank and E Mathie (Editors), *Proceedings of the International Conference*

Landslides and Climate Change, Ventnor Isle of Wight. Taylor & Francis, London. pp. 249-258.

Wong, H.N. and Ko, F.W.Y. 2006. Evolution of slope engineering practice and landslide risk management in Hong Kong. *International Conference on Slopes, Malaysia*, pp. 487-494.

Woodruff, M.1986. Monitoring of ground movement in Ventnor. Technical Report to South Wight Borough Council.

Yin, Y; Zheng, W; Lui Y; ZAng, J, and Li, X. (2010). Integration of GPS with InSAR to monitoring of the Jiaju landslide in Sichuan, China, *Landslides*, 7 (3); 359-365.

Zhou, Y.D., Cheuk, C.Y. and Tham, L.G. 2009. Deformation and crack development of a nailed loose fill slope subject to water infiltration. *Landslides*, 6; 299-308.

Zhou, Y.D., Tham, L.G., Kwong, A.K.L. and Tang, X.W.2010. Mechanism of drying induced rebound movements in a soil slope in Sai Kung, Hong Kong. *Engineering Geology*, 116: 86-94.

Zhu, J.-H. and Anderson, S.A., 1998. Determination of shear strength of Hawaiian residual soil subjected to rainfall-induced landslides. *Geotechnique*, 48(1): 73-82.

Appendix A: Laboratory Testing Results

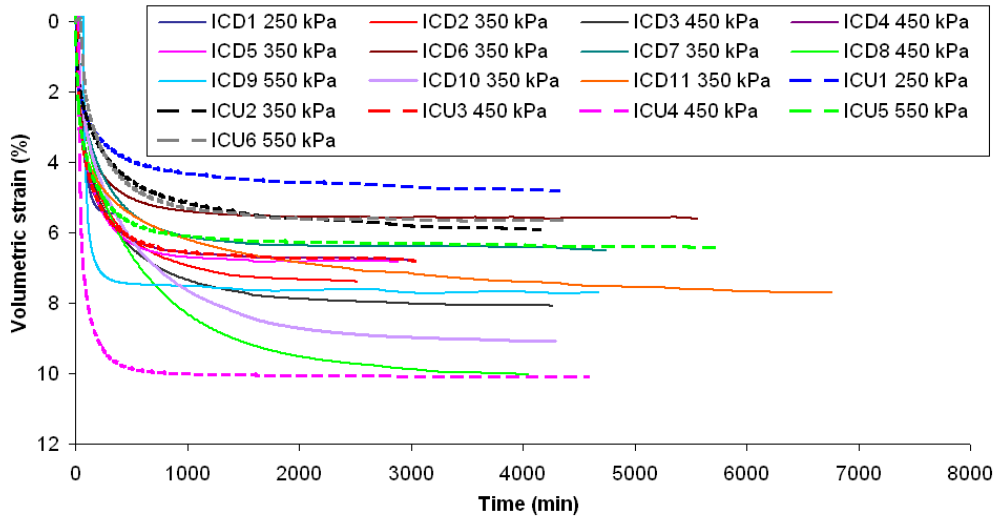


Figure A1 Consolidation curves for ICD and ICU Gault Clay samples at effective stress 250, 350, 450 and 550 kPa

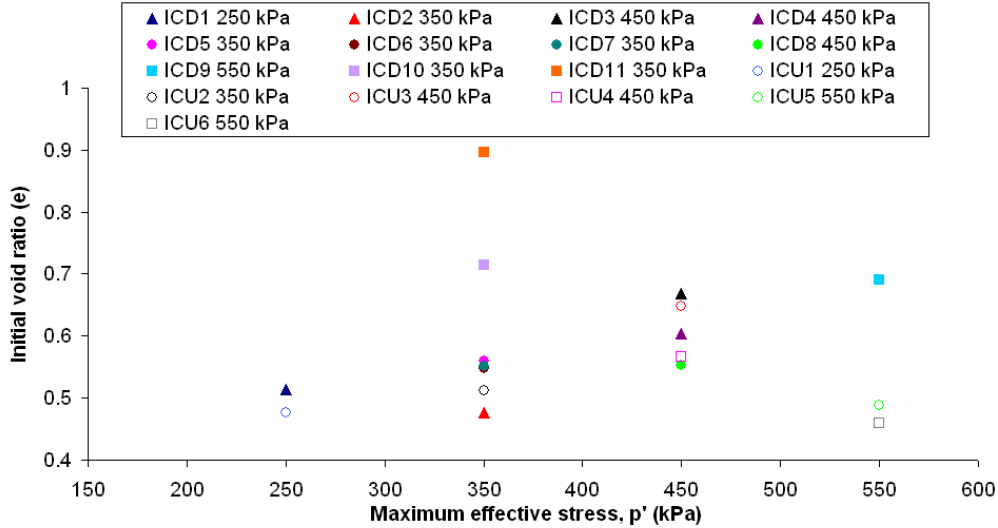


Figure A2 Initial void ratio against maximum effective stress (p') for ICD and ICU Gault Clay samples at effective stresses 250, 350, 450 and 550 kPa

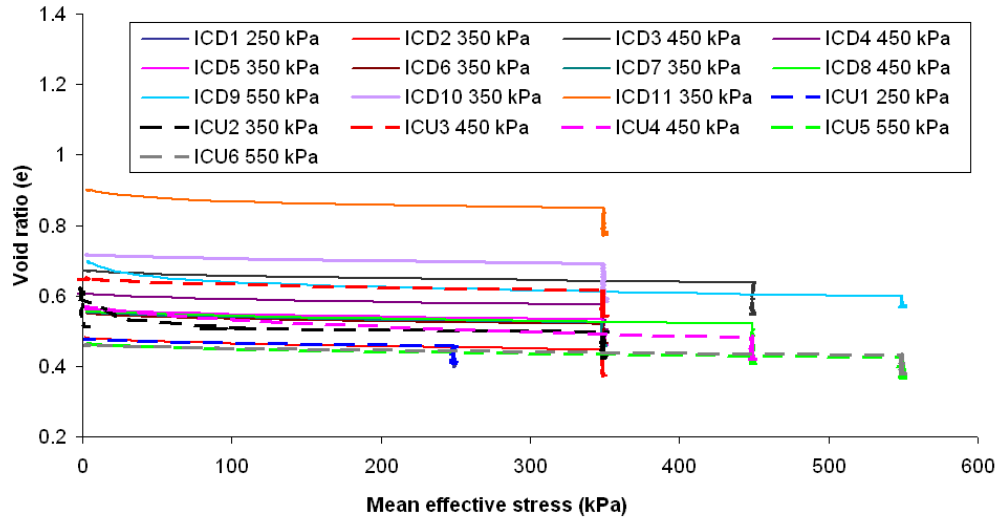


Figure A3 Void ratio against mean effective stress for ICD and ICU Gault Clay samples at effective stresses 250, 350, 450 and 550 kPa

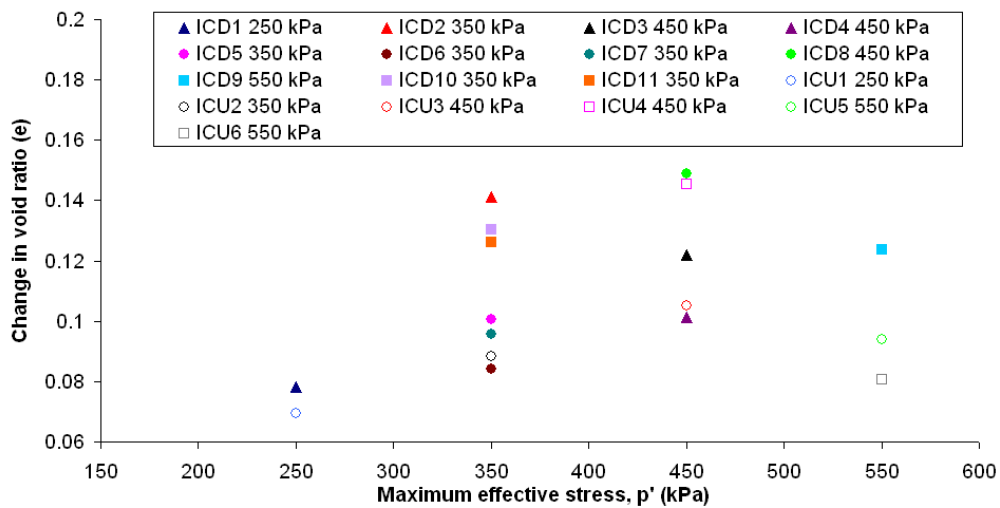


Figure A4 Change in void ratio against mean effective stress for ICD and ICU samples at effective stresses 250, 350, 450 and 550 kPa

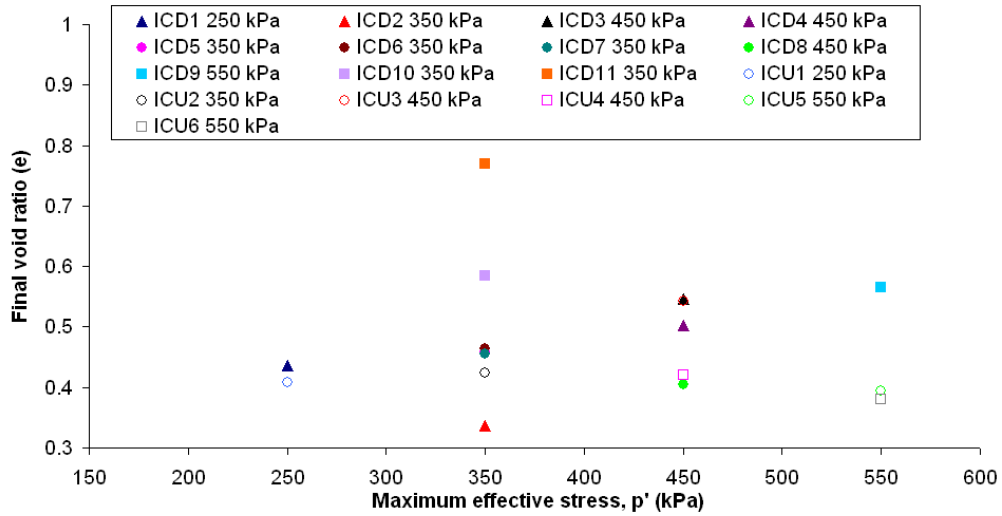


Figure A5 Final void ratio against mean effective stress for ICD and ICU samples at effective stresses 250, 350, 450 and 550 kPa

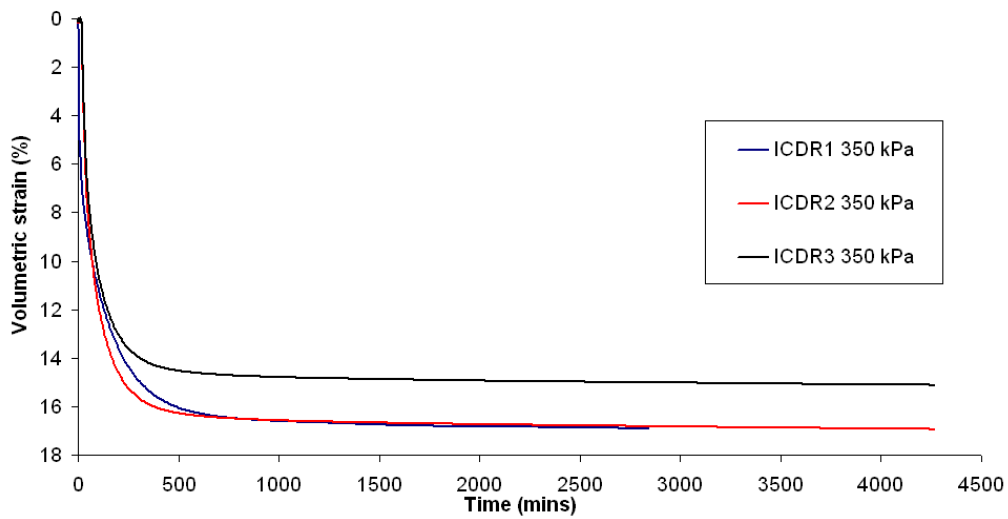


Figure A6 Consolidation curves for remoulded ICD Gault Clay samples at effective stress of 350 kPa

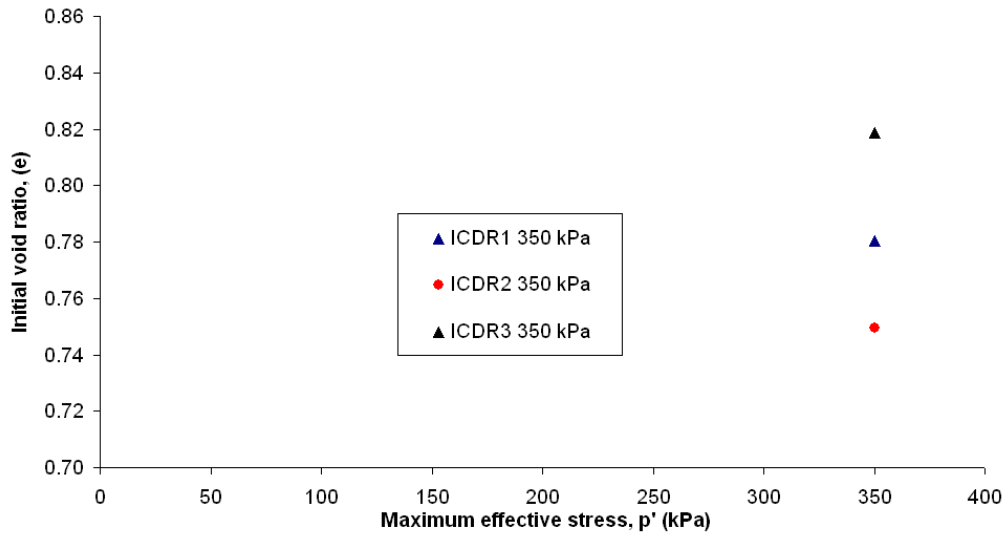


Figure A7 Initial void ratio against mean effective stress for remoulded ICD Gault Clay samples at effective stress of 350 kPa

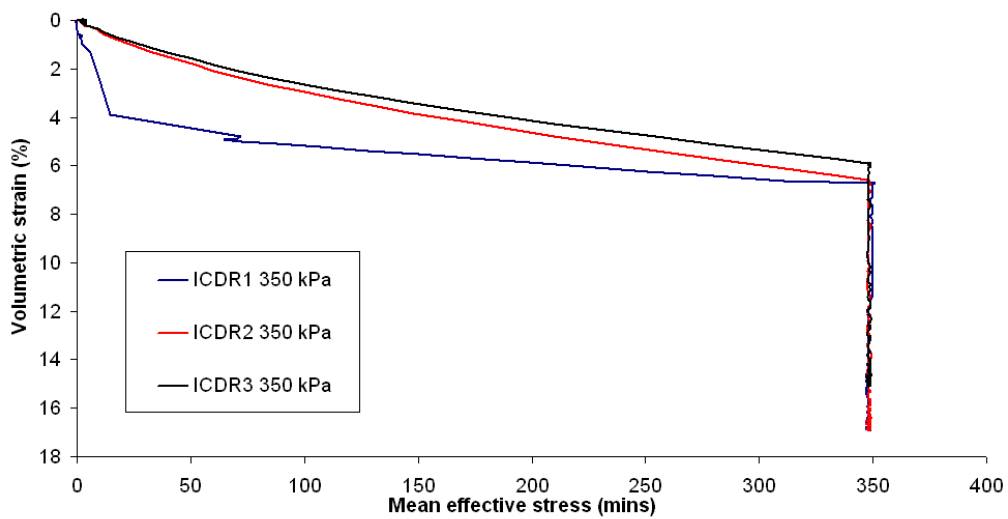


Figure A8 Volumetric strain against mean effective stress for remoulded ICD Gault Clay samples at effective stress of 350 kPa

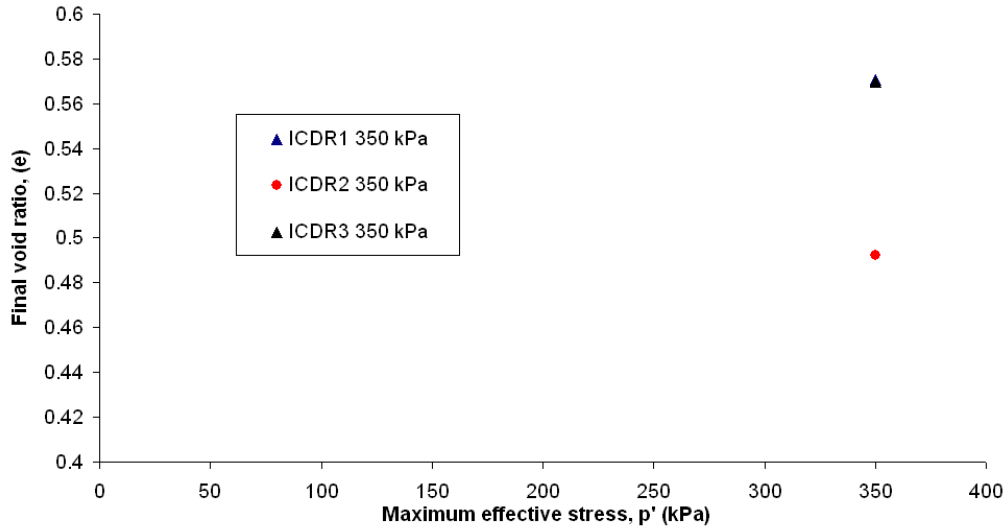


Figure A9 Final void ratio against mean effective stress for remoulded ICD Gault Clay samples at effective stress of 350 kPa

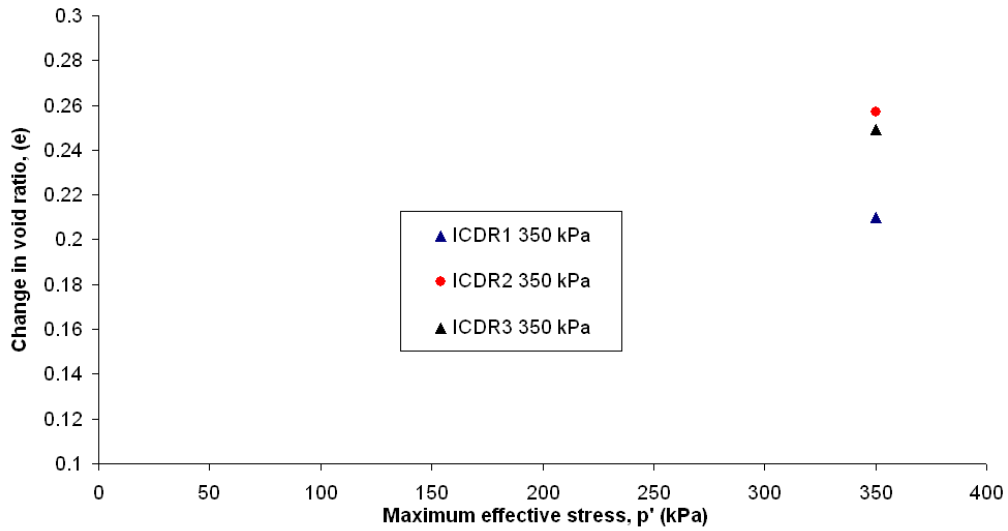


Figure A10 Change in void ratio against mean effective stress for remoulded ICD Gault Clay samples at effective stress of 350 kPa

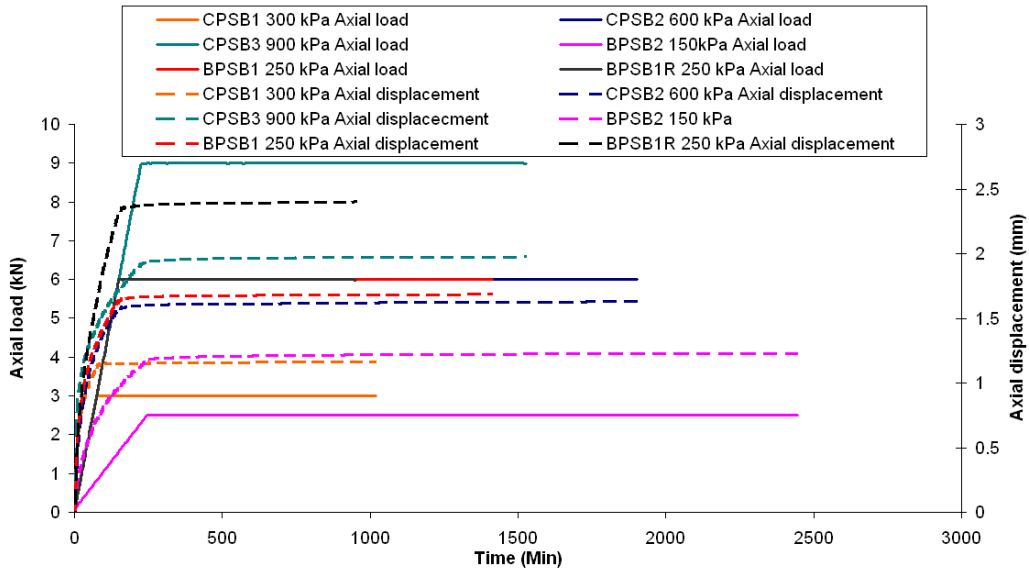


Figure A11 Change in axial load and axial displacement through time for Gault–Carstone transition zone sample at effective stress of 150, 250, 300, 600 and 900 kPa

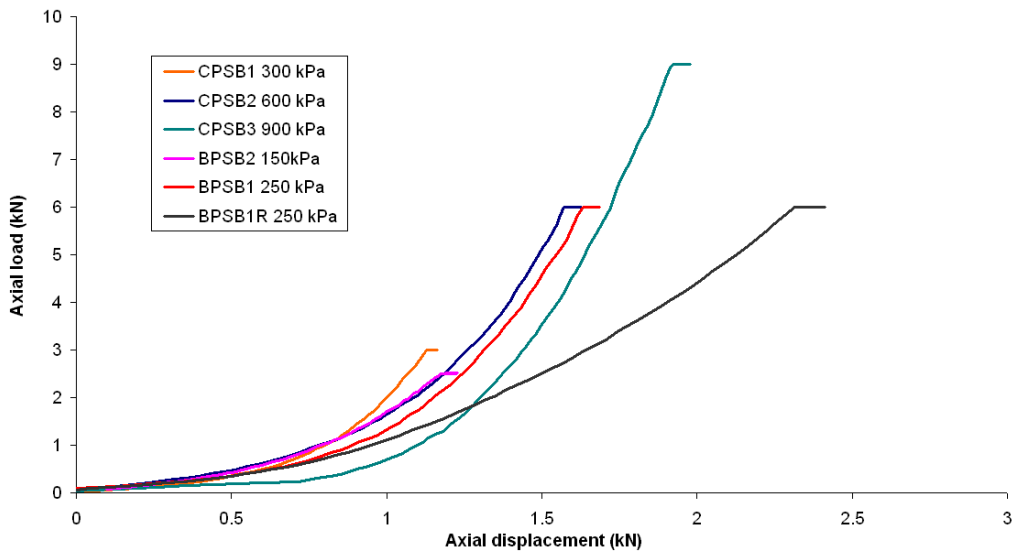


Figure A12 Axial load against axial displacement for Gault – Carstone transition zone samples at effective stress of 150, 250, 300, 600 and 900 kPa

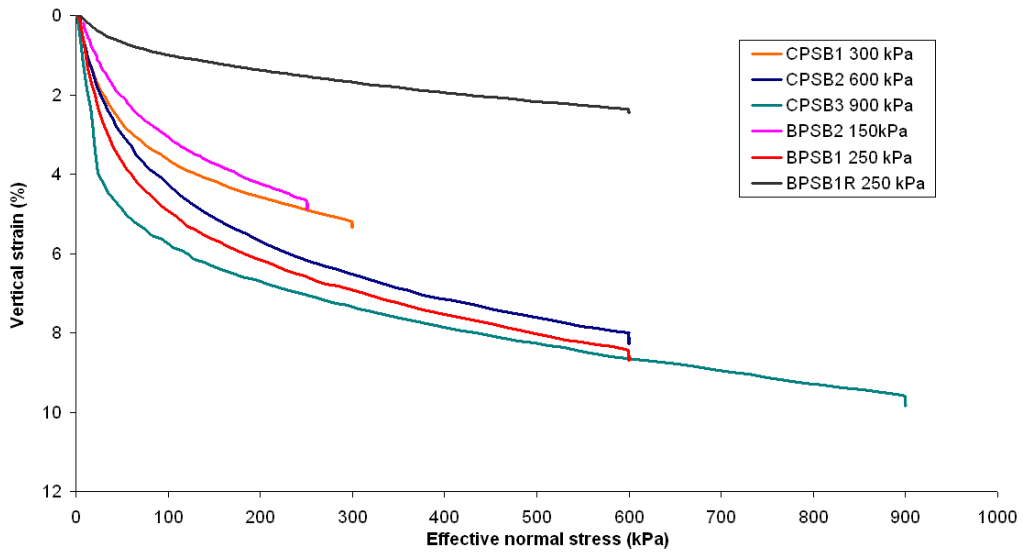


Figure A13 Vertical strain against effective normal stress for Gault – Carstone transition samples at effective stress of 150, 250, 300, 600 and 900 kPa

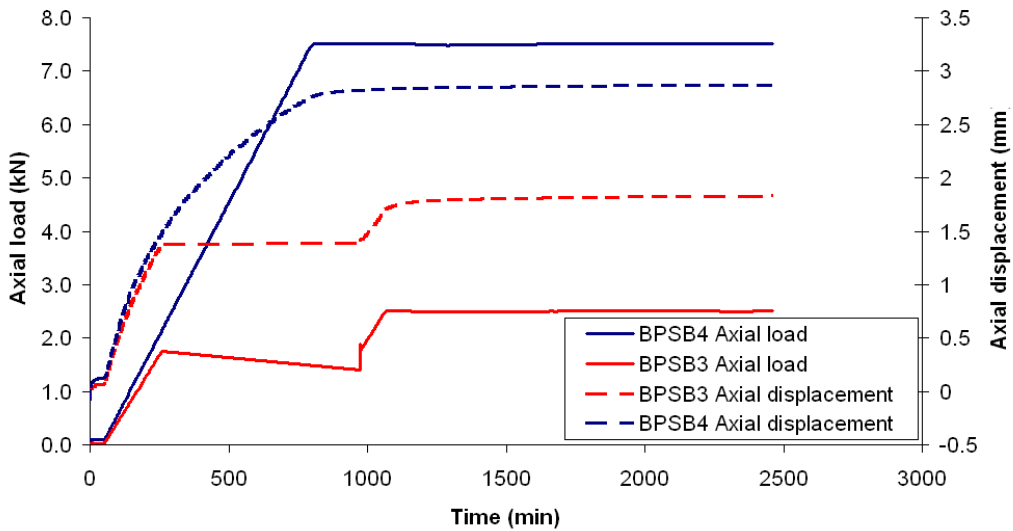


Figure A14 Change in axial load and axial displacement through time for Gault Clay samples at effective stress of 150 and 250 kPa

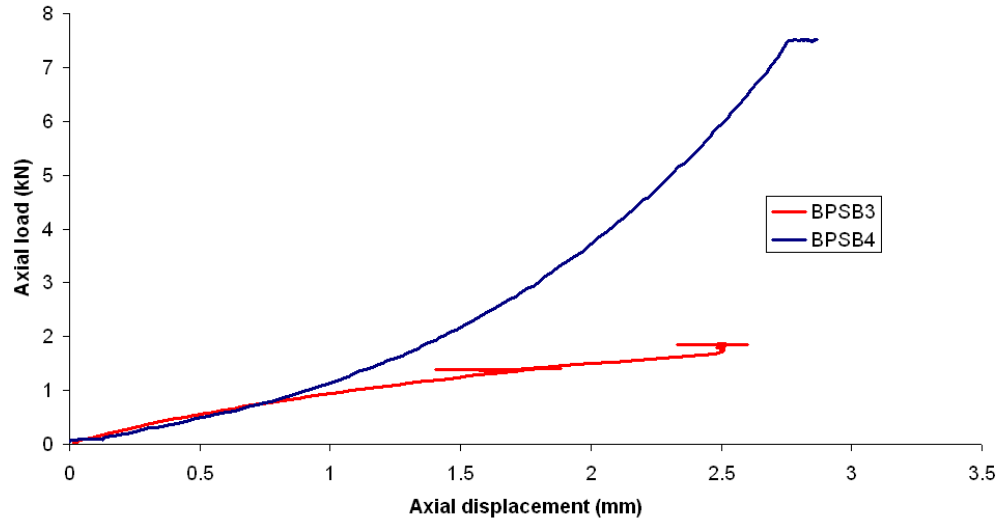


Figure A15 Axial load against axial displacement for Gault Clay samples at effective stress of 150 and 250kPa

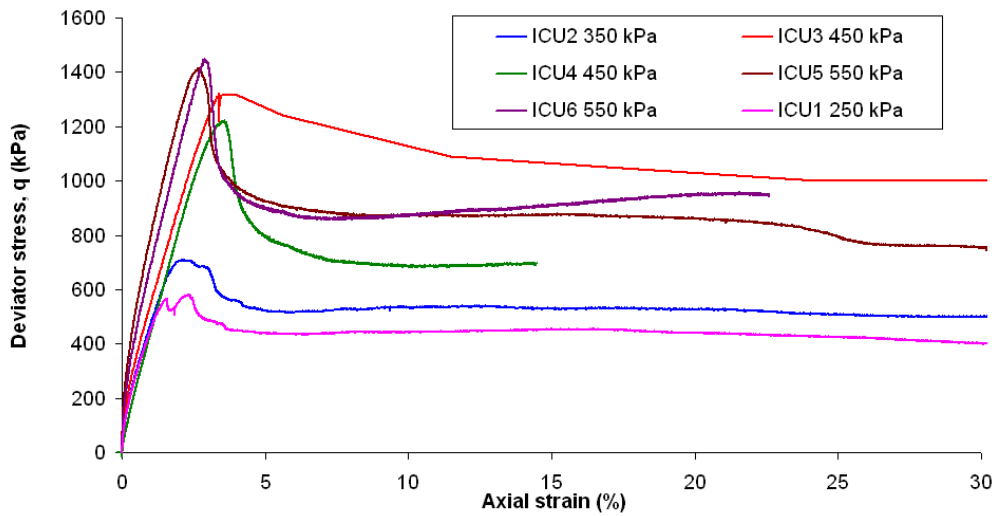


Figure A16 Classic brittle failures through shear surface development in ICU samples

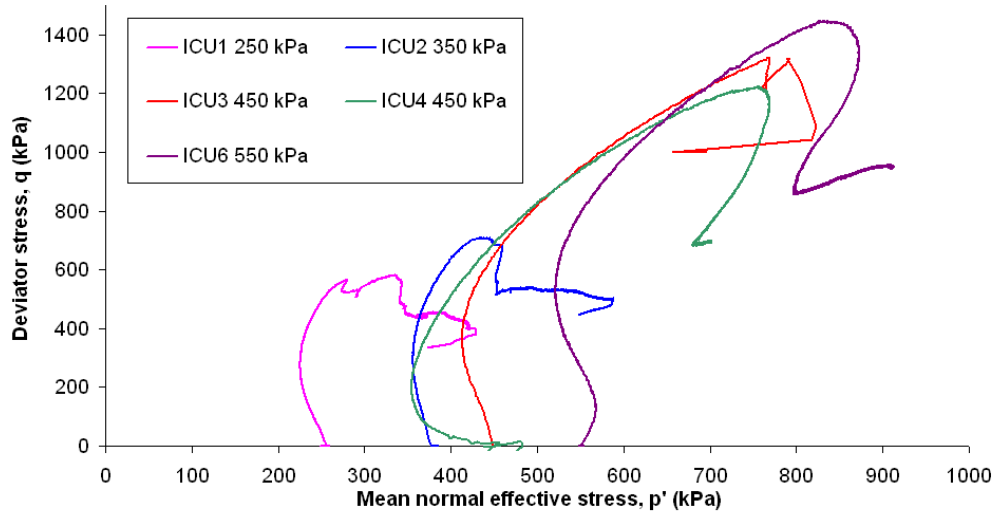


Figure A17 Standard stress path for the undrained triaxial tests on the Gault Clay

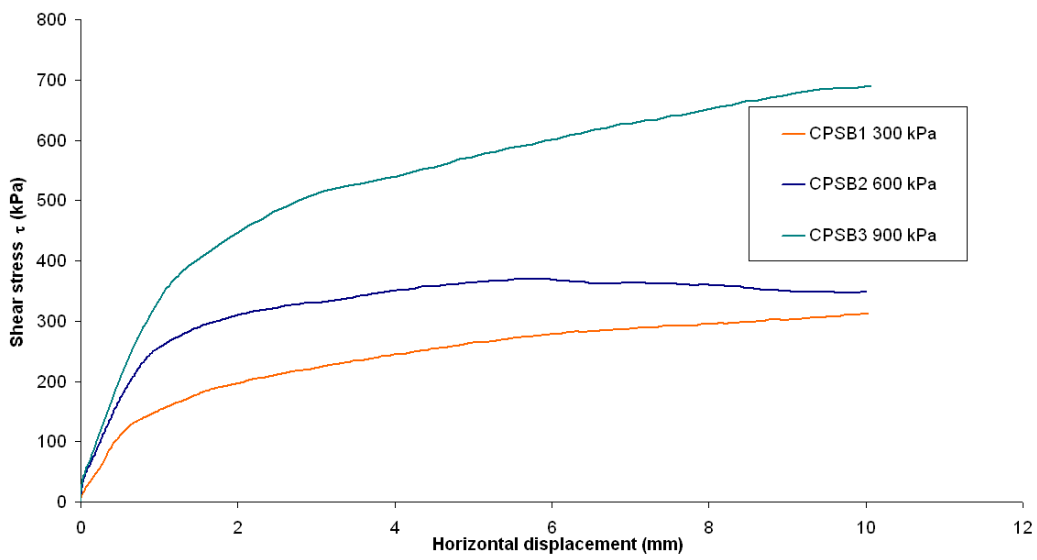


Figure A18 Shear stress against horizontal displacement during CPSB testing on the Gault -Carstone transition samples at effective stresses 300, 600 and 900 kPa

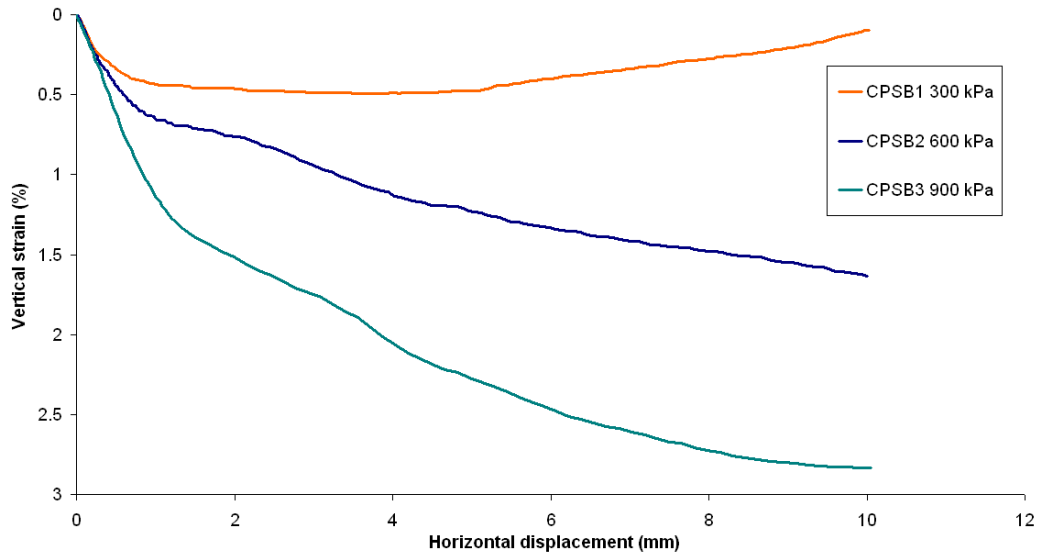


Figure A19 Vertical strain against horizontal displacement during CPSB testing on the Gault -Carstone transition samples at effective stresses 300, 600 and 900 kPa

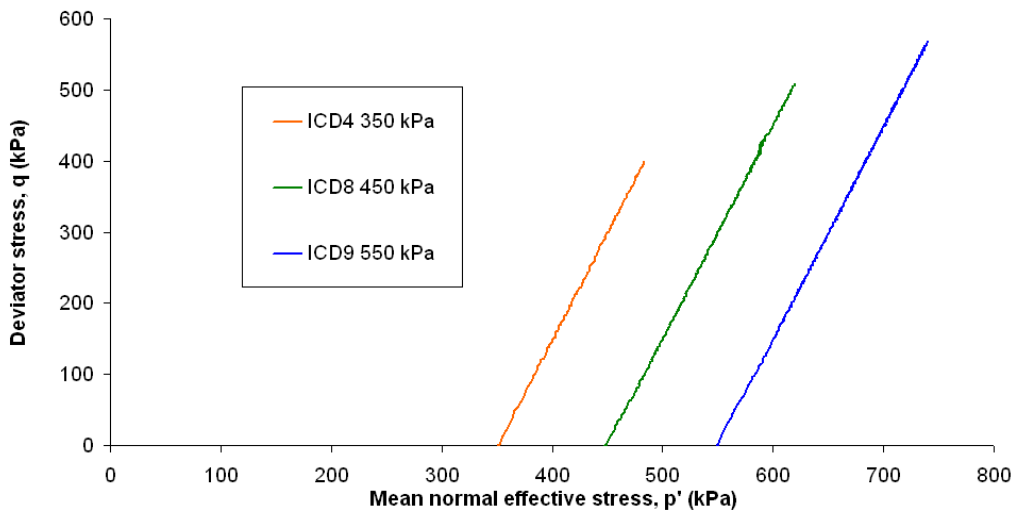


Figure A20 Stress paths during initial drained shear to 400 500 and 550 kPa, samples ICD4, ICD8 and ICD9

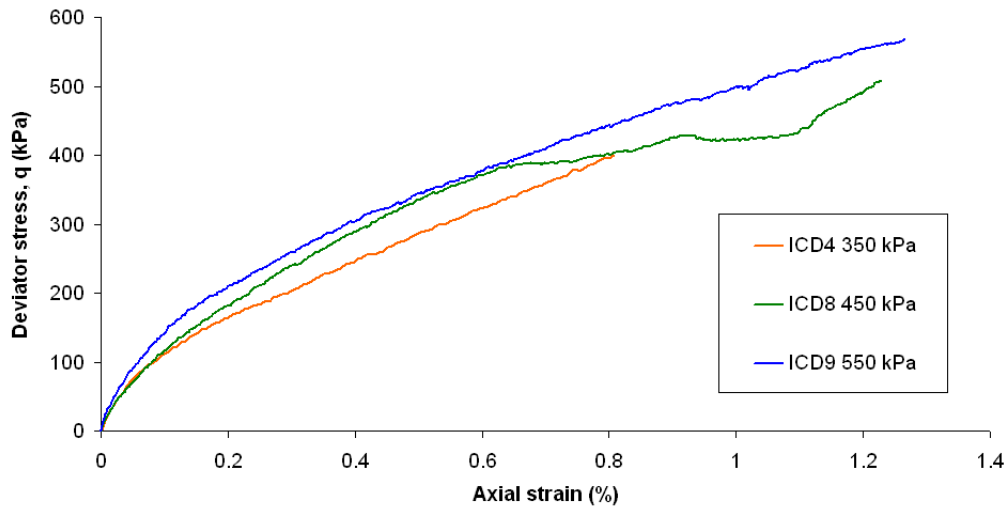


Figure A21 Stress strain relationship during initial drained shear to 400, 500 and 550 kPa, samples ICD4, ICD8 and ICD9

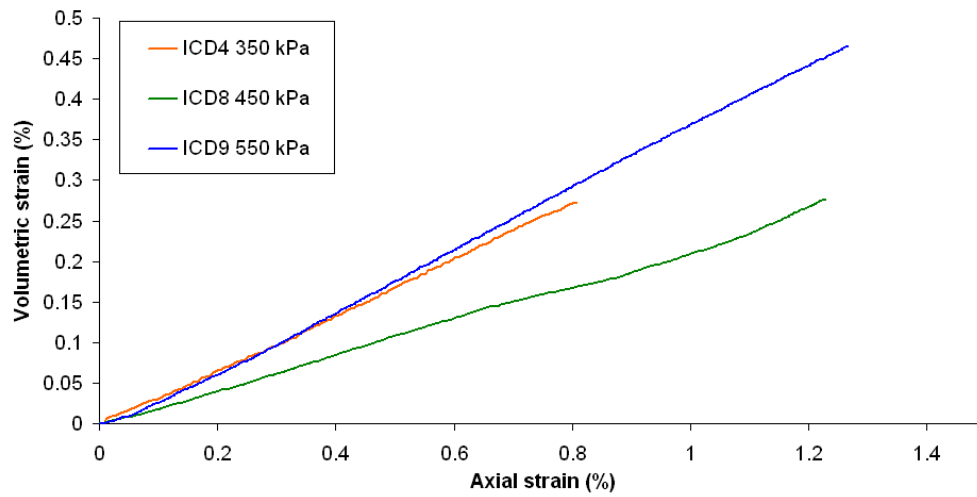


Figure A22 Sample volume change during initial drained shear to 400, 500 and 550 kPa, samples ICD4, ICD8 and ICD9

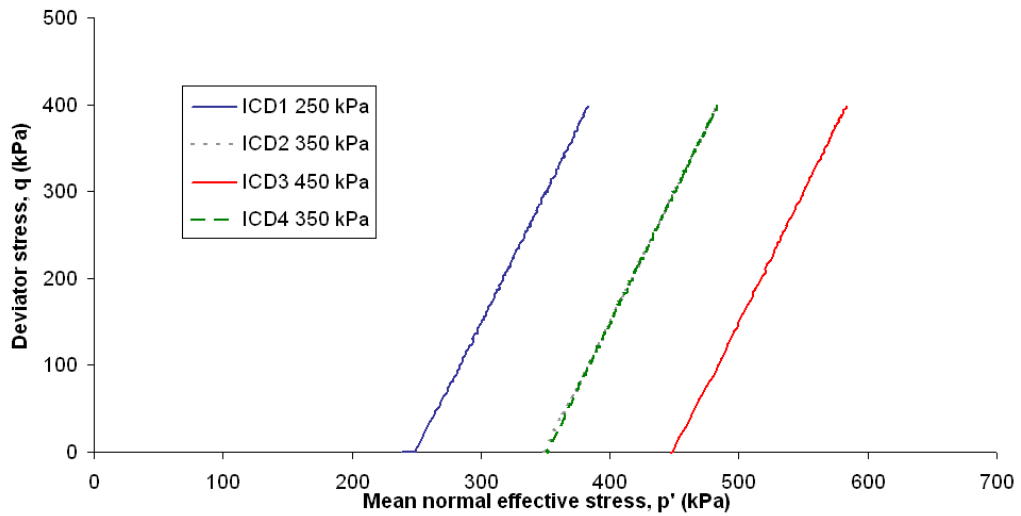


Figure A23 Stress paths during initial drained shear to 400 kPa, samples ICD1, ICD2 ICD3 and ICD4

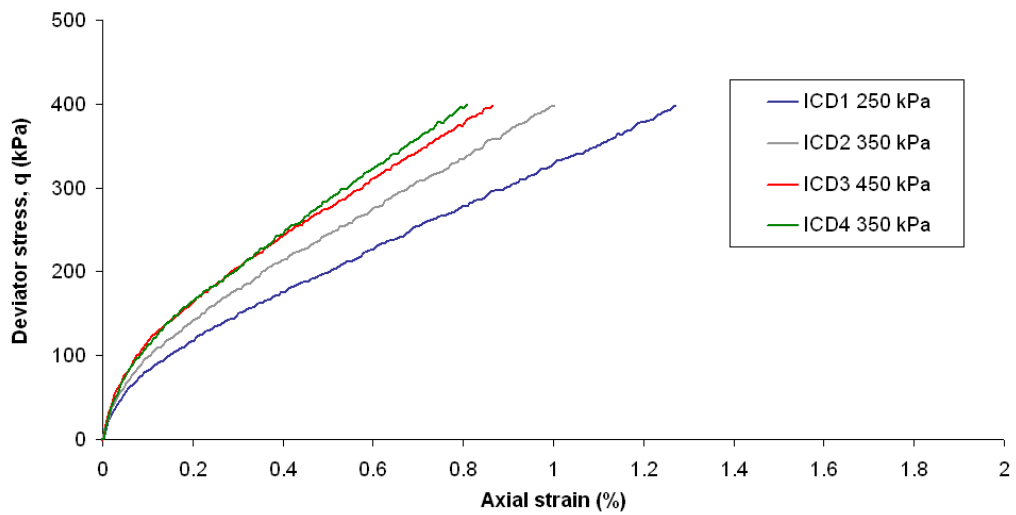


Figure A24 Stress strain relationship during initial drained shear to 400 kPa, samples ICD1, ICD2 ICD3 and ICD4

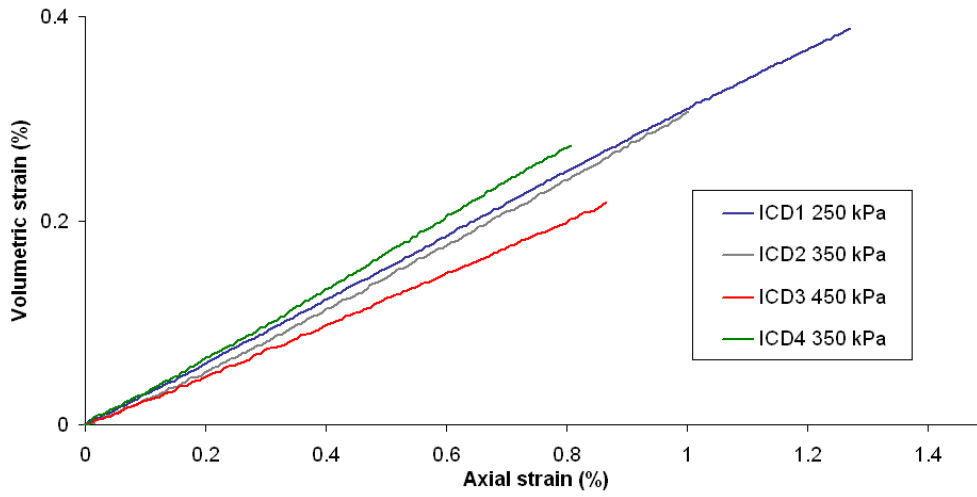


Figure A25 Sample volume change during initial drained shear to 400 kPa, samples ICD1, ICD2 ICD3 and ICD4

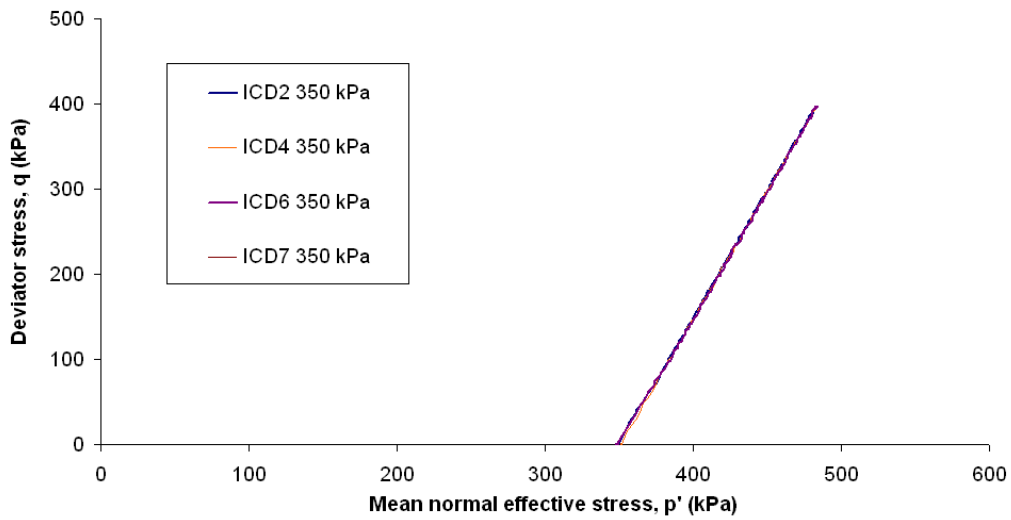


Figure A26 Stress paths during initial drained shear to 400 kPa, samples ICD2, ICD4, ICD6 and ICD7

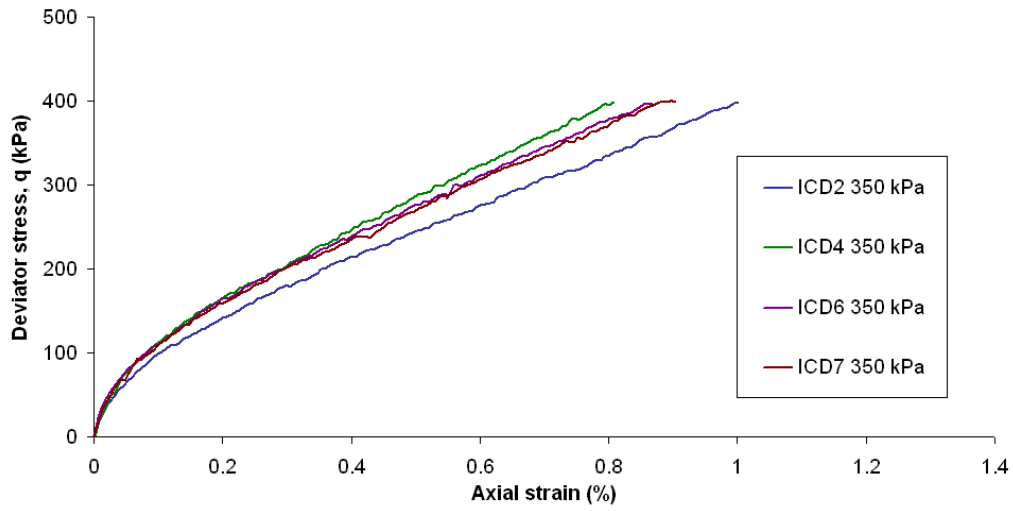


Figure A27 Stress strain relationship during initial drained shear to 400 kPa, samples ICD2, ICD4, ICD6 and ICD7

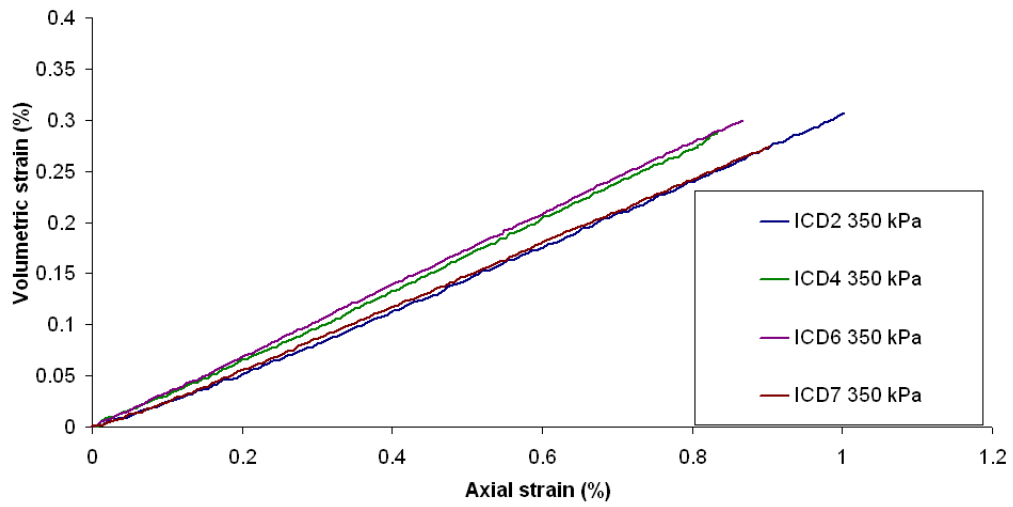


Figure A28 Sample volume change during initial drained shear to 400 kPa, samples ICD2, ICD4 ICD6 and ICD7

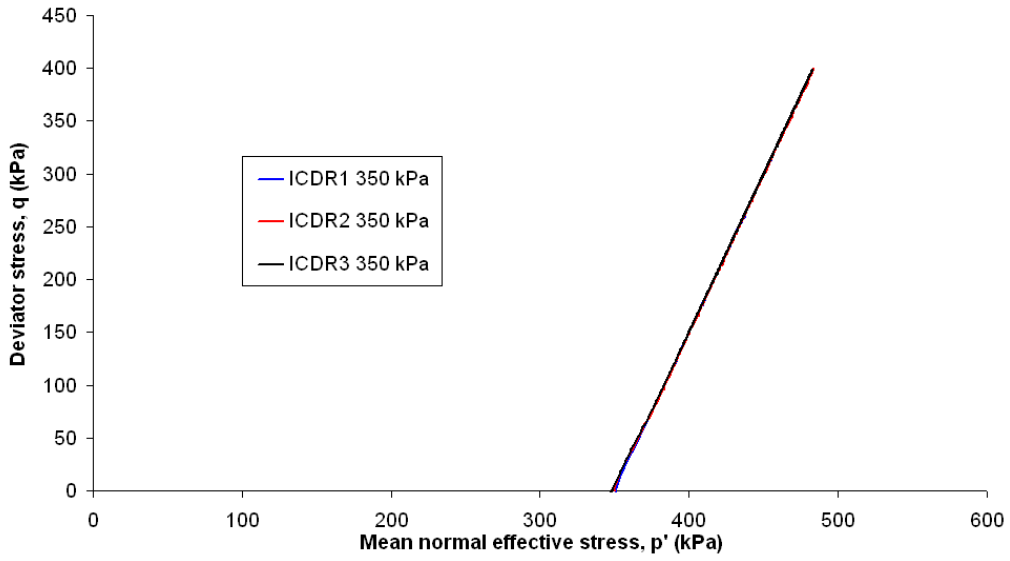


Figure A29 Stress paths during initial drained shear to 400 kPa, samples ICDR12, ICDR2 and ICDR3

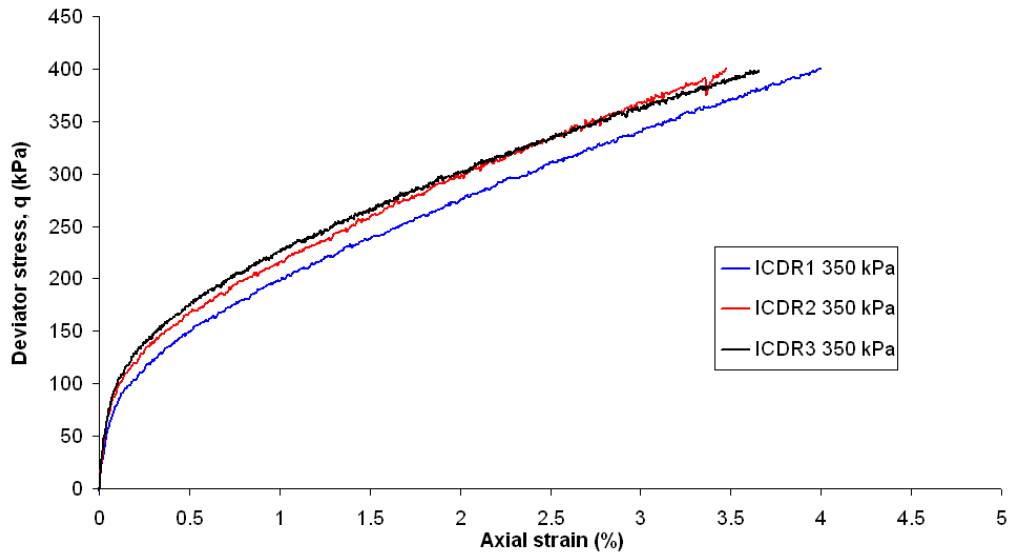


Figure A30 Stress strain relationship during initial drained shear to 400 kPa, samples ICDR1, ICDR2 and ICDR3

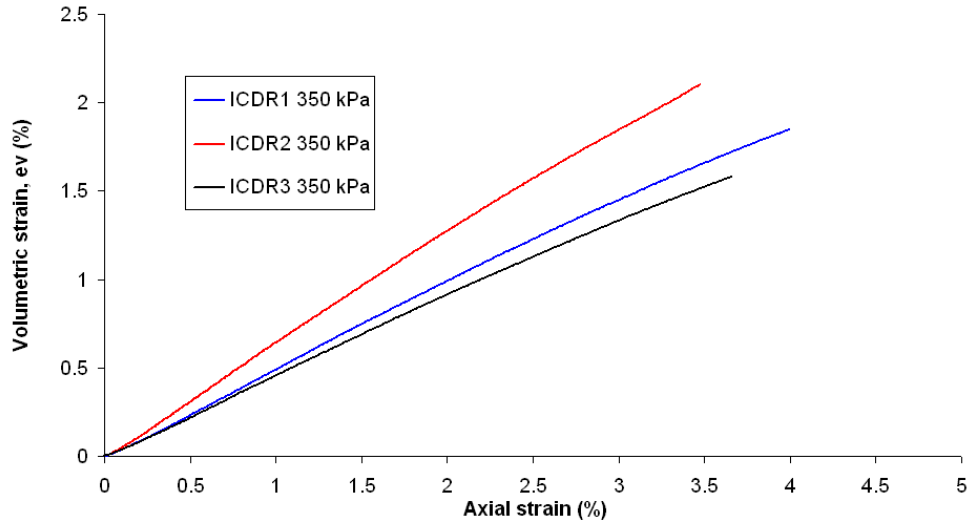


Figure A31 Sample volume change during initial drained shear to 400 kPa, samples ICDR1, ICDR2 and ICDR3

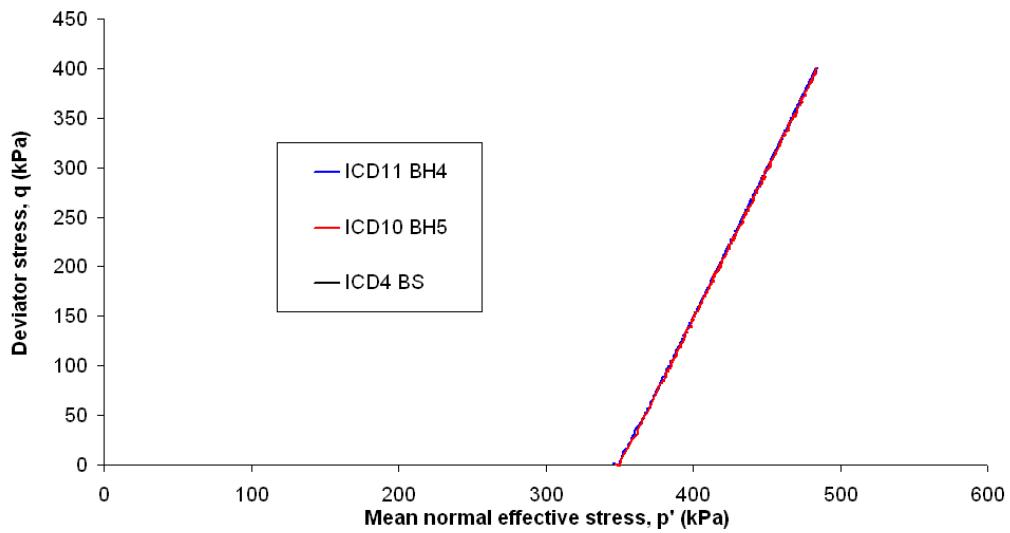


Figure A32 Stress paths during initial drained shear to 400 kPa, samples ICD4, ICD10 and ICD11

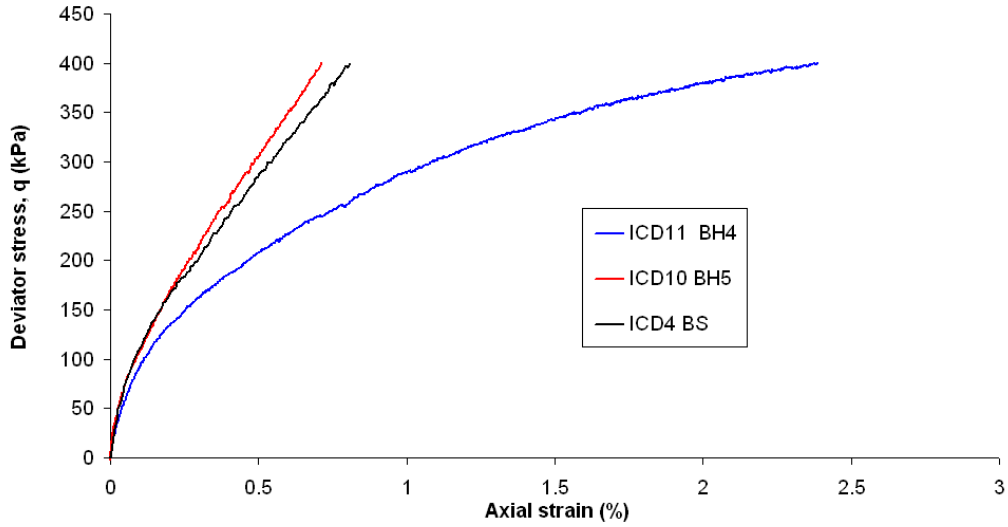


Figure A33 Stress strain relationship during initial drained shear to 400 kPa, samples ICD4, ICD10 and ICD11

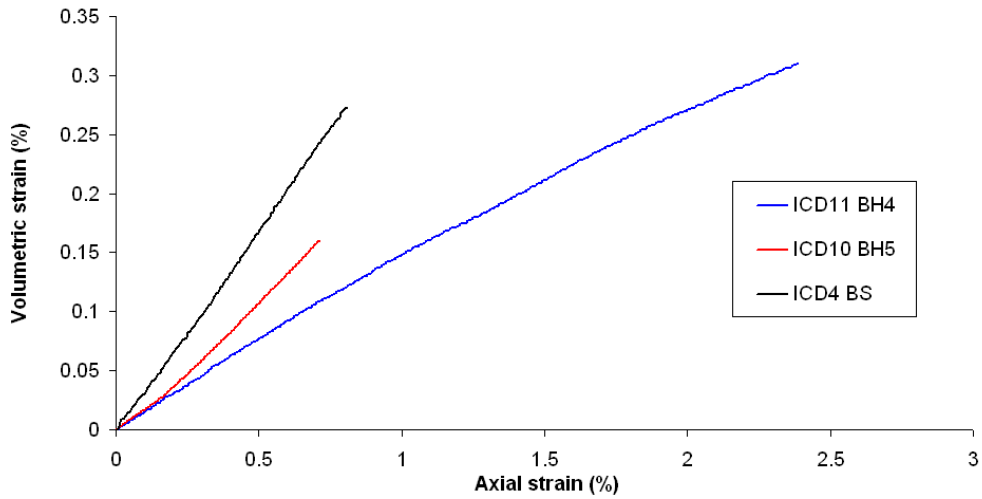


Figure A34 Sample volume change during initial drained shear to 400 kPa, samples ICD4, ICD11 and ICD10

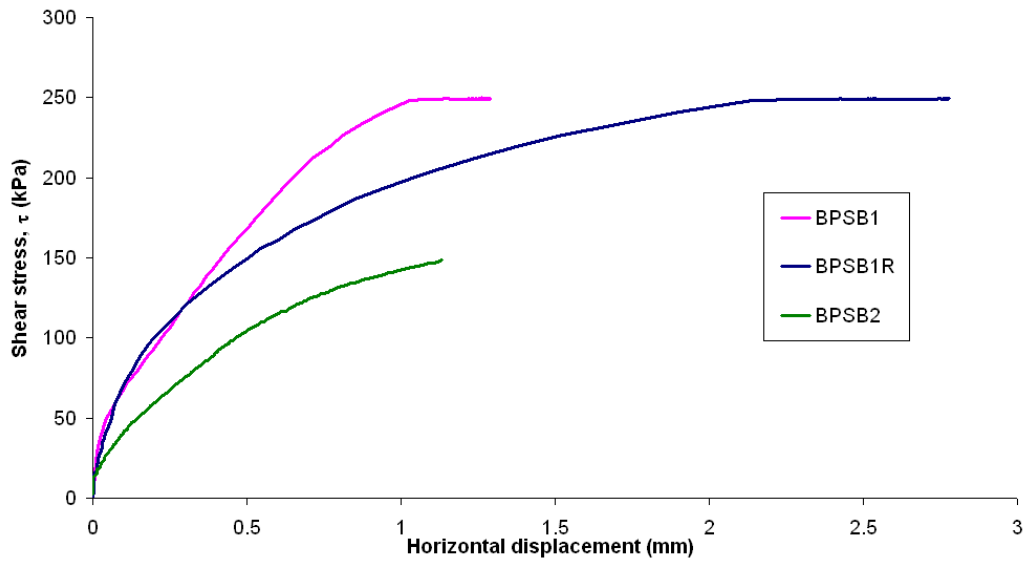


Figure A35 Shear strain against horizontal displacement during initial shear stage, Gault-Carstone transition sample BPSB1, BPSB1R and BPSB2

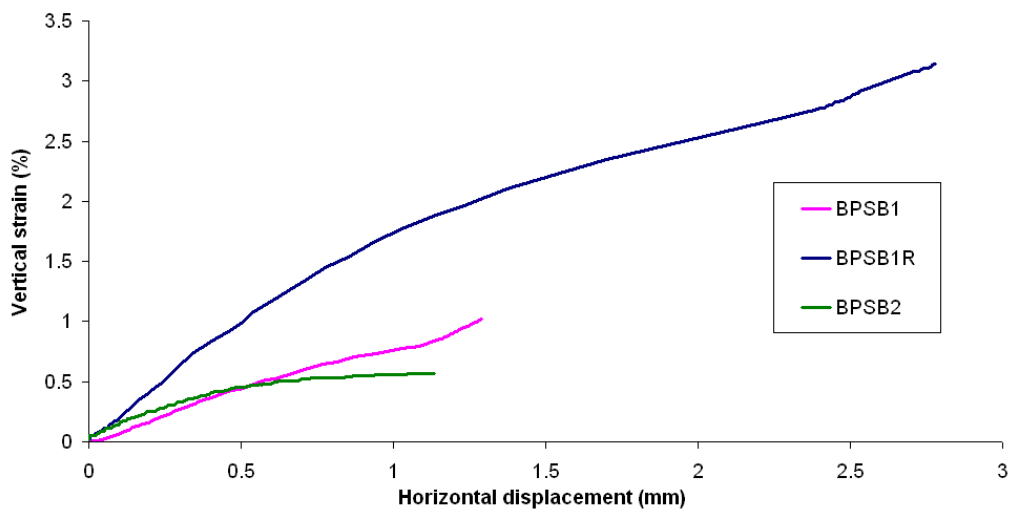


Figure A36 Vertical strain against horizontal displacement during initial shear stage, Gault Carstone transition samples BPSB1, BPSB1R and BPSB2

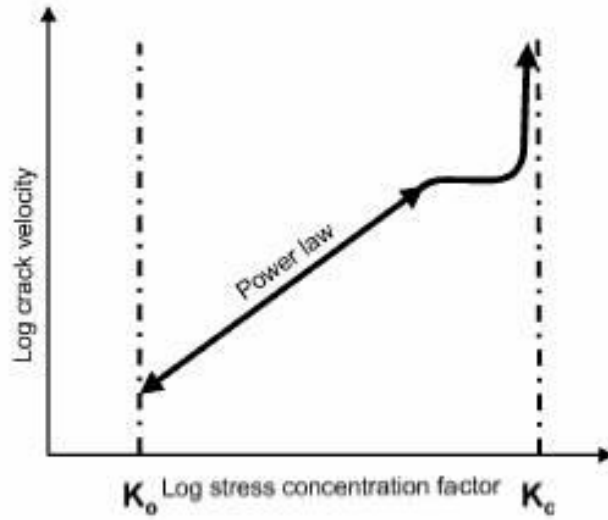


Figure A37 Model of shear surface development (after Main, 2000)

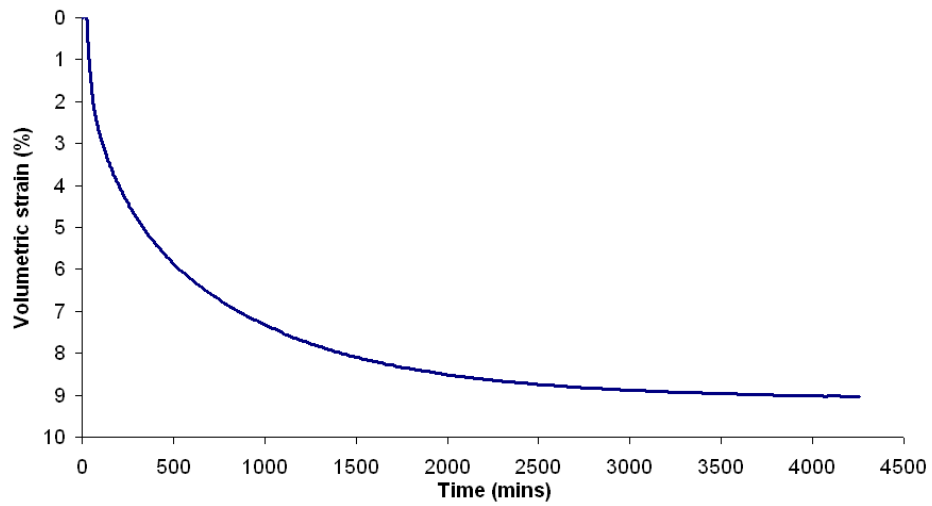


Figure A38 The consolidation curve for the long term creep test

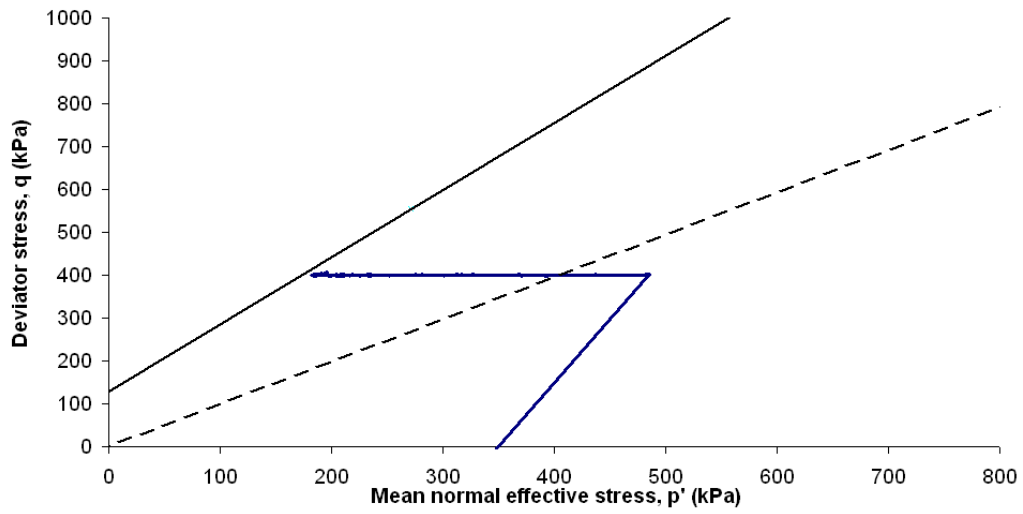


Figure A39 The long term creep test stress path through initial drained shear and PPR